D 2018

U.PORTO

FEUP FACULDADE DE ENGENHARIA
UNIVERSIDADE DO PORTO

DEFORMATION BEHAVIOUR OF SEMI CRYSTALLINE POLYMERS UNDER DIFFERENT STRESS STATES

JOÃO PEDRO MANAIA

TESE DE DOUTORAMENTO APRESENTADA

À FACULDADE DE ENGENHARIA DA UNIVERSIDADE DO PORTO EM, 29 DE NOVEMBRO, 2018

PROGRAMA DOUTORAL EM LÍDERES PARA AS INDÚSTRIAS TECNOLÓGICAS

SUPERVISOR AT FEUP: **PROF. DR. FRANCISCO A. PIRES**

CO-SUPERVISOR AT FEUP: **PROF. DR. ABÍLIO M. P. DE JESUS**

THANK YOU FOR EVERYTHING!

FOR MY LOVING PARENTS, **JORGE MANAIA** AND **MARIA HELENA MANAIA**

THANK YOU FOR EVERYTHING!

Abstract

The mechanical behaviours of High-Density Polyethylene (HDPE), Polypropylene (PP) and Polyamide 6 (PA 6) semi crystalline polymers were investigated under various stress states, strain rates and temperatures. The elastic and initial yielding behaviours were the primary focus of this research. Nevertheless the complete viscoplastic domain as well as the microstructural deformation and failure mechanisms also deserved relative attention.

The biaxial yielding of the semi crystalline polymers was investigated from a series of biaxial loading tests (pure shear, combined shear and tension/compression, pure tension/compression) using the Arcan testing Apparatus. In order to investigate a wider range of stress states, flat and cylindrical notched specimens with different curvature radii were also tested. More conventional mechanical tests, such as uniaxial tension on dumbbell specimens and uniaxial compression tests on cylindrical regular shape were also examined to provide better insights on the stress state effects.

The proposed testing programme aimed at covering distinct stress triaxiality and Lode angle values allowing the understanding of their influence on the yield behaviour of the semi crystalline polymers. Also, various complementary analysis techniques were used to characterize the thermal properties and crystallinity degree using Differential Scanning Calorimetry (DSC) and viscoelastic properties using Dynamical Mechanical Analysis (DMA). The Scanning Electron Microscopy (SEM) was also applied to examine the evolution of the materials microstructural features at failure for different mechanical testing conditions.

In the domain of constitutive modelling, the capabilities of the von Mises and Drucker-Prager yield models were investigated. They were identified with a selected set of testing data and further applied to simulate the nonlinear yield behaviour of the investigated materials for the conditions explored with the Arcan tests. While the von Mises is only sensitive to the second invariant of the stress tensor, the Drucker-Prager yield model shows also dependency on the first and third invariants of the stress tensor.

The tensile tests on dumbbell and cylindrical notched specimens, also in compression tests on cylindrical regular and cylindrical notched specimens were the basis for the Drucker-Prager model calibration, covering different stress triaxialities. Simulations of the biaxial loading tests as well the tensile results of flat notched specimens, were used to assess the accuracy of the yield models, comparing the experimental load-displacement curves with numerical simulation.

The Drucker-Prager yield model allowed an improved description of the available experimental results as compared with the von Mises model, demonstrating the necessity of accounting for pressure dependency in the yield models formulation of semi crystalline polymers. Deviations observed in the predicted and experimental results obtained with the Drucker-Prager yield model are very likely attributed to third invariant stress tensor effects not properly explored in the Drucker-Prager yield model calibration.

Acknowledgements

The work presented in this thesis was accomplished between 2014 and 2018. This period of time was thoroughly different from the rest of my life both personally and intellectually. These four years of my research were funded by FCT (Fundação para a Ciência e a Tecnologia) under a PhD grant with reference PD/BD/52346/2013.

I would like to express my acknowledgments to ***NORTE-01-0145-FEDER-000022 - SciTech - Science and Technology for Competitive and Sustainable Industries***, I&D project co-funded by Programa Operacional Regional do Norte ("NORTE2020"), through the Fundo Europeu de Desenvolvimento Regional (FEDER).







There are many people who have contributed to the work presented in this thesis directly and indirectly. Without their help and support it would not be possible to finish the current work.

I would like to take this opportunity to thank my thesis Supervisor, Prof. Dr. Francisco A. Pires and Co-supervisor Prof. Dr. Abílio M. P. de Jesus, for allowing me to develop my approach intending a contribution to polymers science. They offered many helpful suggestions, also introduce me to the field of polymers science and opened my eyes to improvement. Both gave me a very satisfying appreciation for mechanics, a feat for which I am grateful. One would have to search high and far to find better supervisors (though, I doubt better supervisors exist).

I would also like to acknowledge the help I received from Eng. Rui Silva, Eng. Miguel Figueiredo, Technology Testing Lab director, and Dr. Ricardo Carbas and prof. Lucas Silva, Adhesive Lab responsible. They have contributed to the data appearing in this thesis. All tests would not have been possible without their help and support or without the testing equipment provided in the testing laboratories.

I am grateful to Carla Monteiro for her immediate help and support in solving complex administrative issues. To my colleagues Vitor Anes, Marcia Baptista, João Reis and Duarte Dinis, with whom I got to share my best and worst times and besides all the fun moments they contributed a lot to the development of my thesis. Also, for creating a pleasant working environment at a high knowledge level. Many of you have contributed to unforgettable stories. Thank you all!

Certainly, more people have helped me along the difficult path leading to graduate school and a sense of accomplishment. It is not possible to include them all here. I would like to express my deepest thanks to my parents, Jorge Alberto Manaia and Maria Helena Manaia for their continuing support of my study from elementary school all the way to the PhD degree. For their unwavering support and encouragement, I am happy and proud to dedicate this thesis to them.

Finally, I would like to thank those, who know who they are, for making the past four and half year a valuable time in my life.

Contents

Abstract **3**

Acknowledgements **5**

1 Introduction **31**

1.1 Motivation 31
1.2 Objectives 32
1.3 Scope 33
1.4 Outline of Thesis 33

2 Behaviour of Semi Crystalline Polymers **35**

2.1 Structure of Semi Crystalline Polymers 35
2.1.1 Polymer Crystallinity *37*
2.1.2 Quiescent Crystallization *38*
2.1.3 Inhomogeneous and Shish-Kebab Structures *40*
2.2 Deformation of Semi Crystalline Polymers 42
2.2.1 Microstructural Deformation of Semi Crystalline Polymers Under Tensile Strength *42*
2.2.2 Fragmentation of Crystalline Lamellae *47*
2.2.3 Cavitation *48*
2.2.4 Microfibril Formation *50*
2.3 Thermal Transitions in Semi Crystalline Polymers 51
2.3.1 Amorphous Polymers *52*
2.3.2 Semi Crystalline Polymers *53*
2.3.3 Specific Volume *53*
2.4 Evaluation of Mechanical and Physical Properties of Polymers 54
2.4.1 Tensile Test *54*
2.4.2 Compression Test *57*
2.5.3 Dynamic Mechanical Analysers (DMA) *58*
2.4.4 Testing of Physical Properties - Differential Scanning Calorimetry (DSC) *59*
2.4.5 Microstructure Observation by Scanning Electron Microscopy (SEM) *60*
2.4.6 Notched Specimens – Literature Review *60*
2.6 Mechanical Testing under Multiaxial Stress States 64
2.6.1 Arcan Standard Configuration (One Pin) - Analytical Formulas *64*
2.6.2 Arcan Clamped Configuration (Two Pin) - Analytical Formulas *65*
2.6.3 Arcan Apparatus - Literature Review *66*
2.6.4 Butterfly Specimens – Literature Review *68*
2.7 Constitutive Modelling, Stress Triaxiality and Lode Angle Parameter 70
2.7.1 Stress Invariants, Stress Triaxiality and Lode Angle Parameter *71*
2.7.2 von Mises Yield and Drucker-Prager Yield Criteria *73*
2.7.3 Linear Drucker-Prager Model *74*
2.8 The Materials in this Study 76
2.8.1 Polyethylene (PE) *76*
2.8.2 Polypropylene (PP) *78*
2.8.3 Polyamide (PA) / Nylon *80*

3 Experimental Details **83**

3.1 Specimens Production – Mould Injection 83
3.2 Machining of Specimens 85

3.3 Specimens Geometry 85
3.3.1 Tensile Specimens - Geometry 85
3.3.2 Tensile Specimens - Analytical Formulas for Stress Analysis 88
3.3.3 Compression Specimens - Analytical Formulas for Stress Analysis 91
3.3.4 Butterfly Specimen - Geometry, Stress Triaxiality and Analytical Formulas 92
3.3.5 Dynamic Mechanical Analysis (DMA) Specimens 95
3.3.6 Specimen for Differential Scanning Calorimetry (DSC) Experiments 95
3.4 Arcan Apparatus 96
3.5 Testing Machines, Testing Matrix and Testing Conditions 97
3.5.1 Mechanical Tests at Room Temperature (RT) 98
3.5.2 Mechanical Tests at 50 °C (Constant Temperature) 101
3.5.3 Differential Scanning Calorimetry (DSC) 102
3.5.4 Dynamic Mechanical Analysis (DMA) 104
3.5.5 Scanning Electron Microscopy (SEM) 105

4 Experimental Results and Discussion 107

4.1 High-Density Polyethylene (HDPE) 107
4.1.1 Tensile Tests at Room Temperature 108
4.1.2 Combined Tensile/Shear Tests at Room Temperature 113
4.1.3 Combined Tensile/Shear Tests at Temperature of 50°C 118
4.1.4 Compression Tests at Room Temperature 122
4.1.5 Combined Compression/Shear Tests at Room Temperature 124
4.1.6 Combined Compression/Shear Tests at Temperature of 50°C 127
4.1.7 Differential Scanning Calorimetry (DSC) 130
4.1.8 Dynamic Mechanical Analysis (DMA) 132
4.2 Polypropylene (PP) 133
4.2.1 Tensile Tests at Room Temperature 134
4.2.2 Combined Tensile/Shear Tests at Room Temperature 138
4.2.3 Combined Tensile/Shear Test at Temperature of 50°C 142
4.2.4 Compression Tests at Room Temperature 145
4.2.5 Combined Compression/Shear Tests at Room Temperature 147
4.2.6 Combined Compression/Shear Tests at Temperature of 50°C 150
4.2.7 Differential Scanning Calorimetry (DSC) 153
4.2.8 Dynamic Mechanical Analysis (DMA) 155
4.3 Polyamide 6 (PA 6) 156
4.3.1 Tensile Tests at Room Temperature 156
4.3.2 Combined Tensile/Shear Tests at Room Temperature 160
4.3.3 Combined Tensile/Shear Test at Temperature of 50°C 164
4.3.4 Compression Tests at Room Temperature 167
4.3.5 Combined Compression/Shear Tests at Room Temperature 169
4.3.6 Combined Compression/Shear Tests at Temperature of 50°C 172
4.3.7 Differential Scanning Calorimetry (DSC) 175
4.3.8 Dynamic Mechanical Analysis (DMA) 177
4.4 Discussion and Concluding Remarks 178
4.4.1 Tensile Tests at Room Temperature - HDPE, PP and PA 6 179
4.4.2 Combined Tensile/Shear and Compression/Shear Tests - HDPE, PP and PA 6 180
4.4.3 Compression Tests at Room Temperature - HDPE, PP and PA 6 181
4.4.4 DSC and DMA - HDPE, PP and PA 6 182
4.4.5 HDPE, PP, PA 6 Mechanical Behaviour Discussion 184

5 Fracture Surface Analysis 187

5.1 Triaxiality and Temperature 187
5.2 Analysis of Flat Notched Specimens Fracture Morphologies under Tension at Stress Triaxialities: 0.62 to 0.84 188
5.3 Analysis of Cylindrical Notched Specimens Fracture Morphologies under Tension at Stress Triaxialities: 0.39 to 0.64 191
5.4 Analysis of Combined Tensile/Shear Loading Fracture Morphologies at Stress Triaxialities: 0 to 0.58 194
5.4.1 Pure Tension (α = 90°) – Stress Triaxiality: 0.58 194
5.4.2 Combined Tension/Shear (α = 30°) – Stress Triaxiality: 0.19 196
5.4.3 Pure Shear (α = 0°) – Stress Triaxiality: 0 199
5.5 Discussion and Concluding Remarks 202
5.5.1 Flat and Cylindrical Notched Specimens 202
5.5.2 Combined Tensile/Shear Loading Fracture Morphologies 205

6 Plasticity Model Calibration and Verification – Drucker-Prager and von Mises 209

6.1 Drucker-Prager and von Mises Calibration and Verification - High-Density Polyethylene (HDPE) 211
6.1.1 Yield Stress Determination 211
6.1.2 Numerical Calibration 212
6.1.3 Numerical Verification 219
6.1.4 Drucker-Pager Model - Stress Triaxiality and Lode Angle Parameter 224
6.2 Drucker-Prager and von Mises Calibration and Verification - Polypropylene (PP). 229
6.2.1 Numerical Calibration 230
6.2.2 Numerical Verification 235
6.2.3 Drucker-Pager Model - Stress Triaxiality and Lode Angle Parameter 239
6.3 Drucker-Prager and von Mises Calibration and Verification - Polyamide 6 (PA 6). 243
6.3.1 Numerical Calibration 243
6.3.2 Numerical Verification 249
6.3.3 Drucker-Pager Model - Stress Triaxiality and Lode Angle Parameter 252
6.4 Discussion and Concluding Remarks 256

7 Conclusions and Future Studies 259

7.1 Conclusions: Chapter 4 Experimental Results and Discussion 259
7.2 Conclusions: Chapter 5 Fracture Surface Analysis 262
7.3 Conclusions: Chapter 6 Plasticity Model Calibration and Verification – Drucker-Prager and von Mises 264
7.4 Future Studies 265

8 Appendix 267

8.1 Arcan Apparatus 267
8.1.1 Arcan Apparatus Technical Drawings - All Details and Dimensions 267
8.1.2 Arcan Apparatus Modifications - Technical Drawings 268
8.2 All SEM Micrographs 270
8.2.1 All SEM Micrographs – Flat Notched Specimens – HDPE, PP and PA 6 270
8.2.2 All Micrographs – Cylindrical Notched Specimens – HDPE, PP and PA 6 280
8.2.3 All SEM Micrographs –Butterfly Specimens – HDPE, PP and PA 6 286

9 References 321

List of Figures

From Chapter: 2 Behaviour of Semi Crystalline Polymers

Figure 1 - From the left to the right: linear, branched, and cross-linked polymer molecules [4]..... 36

Figure 2 - Tensile strength and melt viscosity versus molecular weight [4]..... 36

Figure 3 - Crystalline and amorphous regions [15]..... 37

Figure 4 - Sheaves of lamellar crystals: (1) 3PbO 2SiO crystal grows, (2) PE/LDPE 61/39 blend crystallized [19]..... 38

Figure 5 – (1) PLM image of PE banded spherulites; scale bars are 25 µm, (2) Diagram of polymer spherulite with chain-folded lamellae [19, 23]..... 38

Figure 6 - Examples of spherulites obtained by polymer crystallization under quiescent conditions. PLM image of polyethylene spherulites [23]..... 39

Figure 7 - PLM images of a PE molecular mass fraction M_w of 30.6 kDa, crystallized at different temperatures [19]..... 39

Figure 8 - (1) Optical micrographs of cross-section injection-mould specimen of polyethylene at position near to the injection-moulding gate, (2) middle of the specimen and (3) far from the gate [26]..... 40

Figure 9 - Shish-Kebab structure [23]..... 42

Figure 10 - Stress-strain diagram [4]..... 43

Figure 11 - Models of deformation in amorphous region: (1) undeformed, (2) interlamellar shear, (3) interlamellar separation and (4) stack rotation [43]..... 43

Figure 12 - Scheme of the crystalline and amorphous lamellae with their stress transmitters [49]..... 44

Figure 13 - HDPE tensile stress-strain curves at 23 °C and increasing strain rates [55]..... 45

Figure 14 - Variation of true elastic modulus of poly(ethylene-*co*-vinyl acetate) with 12 wt % of counits (PEVA-12) with true strain: *T* = (1) 25 °C, (2) 42 °C, (3) 58 °C and (4) 71 °C [56]..... 46

Figure 15 – SEM micrographs. Evolution of internal structure of PP specimens deformed in horizontal direction at different temperatures. Morphology at different strain is presented: initial, 0.3, 0.7 and 1.2 [57]..... 47

Figure 16 - Schematic diagrams illustrating (1) fine and (2) coarse chain slip [17]..... 48

Figure 17 - AFM height images of equatorial region of a spherulite for two strain levels 10 and 15%. On the images are indicated the void formation (1), the growth (2) and the coalescence of cavities (3) [59]..... 49

Figure 18 - Stress-strain curves of polypropylene obtained from tensile and compression: curve 1, compression experiment and curve 2, tensile experiment [60]..... 49

Figure 19 - (1) True stress-strain curve for injection-moulded HDPE specimen. Numbers below are the strains. (2) Volume strain of HDPE specimen as a function of strain [61]..... 50

Figure 20 - Microfibrils pulled out at the crack of polyoxymethylene (POM) single crystals [62]..... 51

Figure 21 - Five regions of viscoelastic behaviour for amorphous polymer. Also illustrated is effect of cross-linked polymers (dashed line) [4]..... 52

Figure 22 - The typical PVT-behaviour of an (1) amorphous (polycarbonate) and (2) semi-crystalline polymer (polyethylene). The open symbols characterise the equilibrium state of the polymers, whereas the solid symbols the transition ranges [65]..... 54

Figure 23 - Test specimens type 1A and 1B, shape [42, 69]..... 56

Figure 24 (1) The relationship of the applied sinusoidal stress to strain is shown, with the resultant phase lag (δ) and strain. (2) Stress–strain behaviour of a purely elastic material [71]..... 58

Figure 25 - Arcan standard configuration..... 64

Figure 26 - Arcan clamped configuration..... 65

Figure 27 - Shape and dimensions (in mm) of Mohr and Henn designed butterfly specimen with the flat gauge section of uniform thickness [111]..... 68

Figure 28 - Detailed geometry of Bay designed specimen with a gauge section with a double curvature profile [8]..... 69

Figure 29 - Schematic of Dunand and Mohr proposed specimen [112]..... 69

Figure 30 - Principal stress space with hydrostatic and deviatoric stresses defined by the pressure and Lode Angle parameters [8]..... 72

Figure 31 - Dependence of the fracture mechanism and strain on the stress triaxiality [92]..... 73

Figure 32 - Drucker–Prager yield surface in $J_1 - \sqrt{J_2}$ plane [125]..... 74

Figure 33 - Typical yield surfaces of the linear model in the deviatoric plane [121]..... 75

Figure 34 - Schematic of hardening for the linear model in the p–t plane [121]..... 76

Figure 35 - Structural unit repeat of polyethylene (PE) [9]..... 76

Figure 36 - Crystalline regions (atomic force microscopy images): (1) HDPE (2) LDPE [40]..... 77

Figure 37 - Structural unit repeat of Polypropylene (PP) [9]..... 79

Figure 38 - Structural unit repeat of Polyamide 6 (PA 6) [9]..... 80

From Chapter: 3 Experimental Details

Figure 39 - (1) and (2) designed injection mould attached to the injection moulding machine, (3) mould with unextracted test specimens..... 83

Figure 40 - Notched circular tensile bars geometries tested in tension [142]..... 86

Figure 41 - Dumbbell specimen Type 1A. Dimensions in mm..... 87

Figure 42 - Flat notched specimen. (1) Radius 30 and (2) radius 5. Dimensions in mm..... 87

Figure 43 - Cylindrical notched specimen. (1) Radius 30 and (2) radius 5. Dimensions in mm..... 87

Figure 44 - FE results in terms of stress distribution in the gauge section..... 88

Figure 45 – Axis direction: (1) cylindrical and (2) flat notched..... 90

Figure 46 - Compression specimen. Cylindrical shape (blue) and cylindrical notched shape (red). Dim. in mm..... 92

Figure 47 - Butterfly specimen shape. Dimensions in mm..... 93

Figure 48 - FE results in terms of stress distribution of butterfly specimen under positive vertical displacement, along the loading angle..... 94

Figure 49 - (1) Locations of butterfly specimen from which the specimens were cut, (2) DMA specimen shape. Dimensions in mm..... 95

Figure 50 - Specimen for differential scanning calorimetry (DSC). Dimensions in mm..... 96

Figure 51 - (1) Designed arcan apparatus with the butterfly specimen, (2) α = 0° (pure shear) and (3) α = 90° (pure tension/compression)..... 96

Figure 52 - Modifications in arcan apparatus for temperature testing..... 97

Figure 53 - (1) Servohydraulic MTS 810 universal testing machine and (2) MTS 634.25 axial extensometer..... 98

Figure 54 - Butterfly specimen at four different loading angles, (1) α = 0° (pure shear), (2) and (3) α = 30°, 60° (both combined shear and tension/compression) and (4) α = 90° (pure tension/compression)..... 100

Figure 55 - Instron environmental chamber and Instron 3367 loading machine..... 101

Figure 56 - (1) DSC. TA Instruments DSC Q20 and (2) DMA. TA instruments model Q800..... 103

Figure 57 - DMA experimental framework..... 104

Figure 58 - SEM instrument FEI Quanta 400FEG ESEM..... 106

From Chapter: 4 Experimental Results and Discussion

Figure 59 - Tensile load-displacement curves of (1) Dumbbell, (2) flat notched 5 and (3) flat notched 30 specimens (HDPE, Room Temperature)..... 108

Figure 60 - Tensile load-displacement curves of (1) cylindrical notched 5 and (2) cylindrical notched 30 specimens (HDPE, Room Temperature)..... 109

Figure 61 - Load-displacement curves for HDPE resulting from combined tensile/shear loading at RT: influence of crosshead speeds for each loading angle..... 114

Figure 62 - Load-displacement curves for HDPE resulting for combined tensile/shear loading at RT: effect of loading angle for given crosshead speeds..... 115

Figure 63 - Load-displacement curves for HDPE resulting from combined tension/shear loading at RT and 50 °C: influence of crosshead speeds for each loading angle..... 119

Figure 64 - Load-displacement curves for HDPE resulting for combined tensile/shear loading at temperature of 50 °C: influence of resulting in combined tension/shear for given crosshead speeds.... 120

Figure 65 - Compression load-displacement curves of (1) cylindrical and (2) cylindrical notched specimens..... 122

Figure 66 - Load-displacement curves during biaxial loading for negative vertical displacement, for a given loading angle (α = 90°, 60°, 30°, and 0°) and distinct crosshead speeds of 1, 20 and 200 mm/min, at RT..... 125

Figure 67 - Load-displacement curves for negative vertical displacement at RT, for a given crosshead speed and distinct loading angles (α = 90°, 60°, 30°, and 0°)..... 125

Figure 68 - Load-displacement curves during biaxial loading (α = 90°, 60°, 30°, and 0°) under a negative vertical displacement and room temperature or constant temperature of 50 °C..... 128

Figure 69 - Load-displacement curves in a negative vertical displacement under constant temperature of 50 °C. Effects of loading angles for fixed crosshead speed..... 129

Figure 70 - DSC curves for HDPE virgin/injected injected material..... 131

Figure 71 - (1) DSC curves for HDPE at true strains of 0.5 and 1, (2) red dashed line is the longitudinal section investigated in the DSC..... 132

Figure 72 - Results of DMA experiments: the storage modulus (E') as function of temperature (°C) and frequency for HDPE..... 133

Figure 73 - Tensile load-displacement curves of (1) Dumbbell, (2) flat notched 5 and (3) flat notched 30 specimens (PP, Room Temperature)..... 135

Figure 74 - Tensile load-displacement curves of (1) cylindrical notched 5 and (2) cylindrical notched 30 specimens (PP, Room Temperature)..... 135

Figure 75 - Load-displacement curves for PP resulting from combined tension/shear loading at RT: influence of crosshead speeds for each loading angle..... 138

Figure 76 - Load-displacement curves for PP resulting for combined tensile/shear loading at RT: effect of loading angle for a given crosshead speeds..... 139

Figure 77 - Load-displacement curves for PP resulting from combined tension/shear loading at RT and 50 °C: influence of crosshead speeds for each loading angle..... 143

Figure 78 - Load-displacement curves for PP resulting for combined tensile/shear loading at temperature of 50 °C: influence of resulting in combined tension/shear for given crosshead speeds..... 143

Figure 79 - Compression load-displacement curves of (1) cylindrical and (2) cylindrical notched specimens..... 146

Figure 80 - Load-displacement curves for PP resulting from combined compression/shear loading at RT: influence of crosshead speeds for each loading angle..... 148

Figure 81 - Load-displacement curves for PP resulting for combined compression/shear loading at RT: effect of loading angle for a given crosshead speeds..... 148

Figure 82 - Load-displacement curves for PP resulting from combined compression/shear loading at RT and 50 °C: influence of crosshead speeds for each loading angle..... 151

Figure 83 - Load-displacement curves for PP resulting for combined compression/shear loading at 50 °C: effect of loading angle for given crosshead speeds..... 152

Figure 84 - DSC curves for PP virgin/injected material..... 154

Figure 85 - (1) DSC curves for PP at true strains of 0.5 and 1, (2) red dashed line is the longitudinal section investigated in the DSC..... 155

Figure 86 - Results of DMA experiments; the storage modulus (E') as function of temperature (°C) for and frequency effects on PP..... 156

Figure 87 - Tensile load-displacement curves of (1) Dumbbell, (2) flat notched 5 and (3) flat notched 30 specimens (PA 6, Room Temperature)..... 157

Figure 88 - Tensile load-displacement curves of (1) cylindrical notched 5 and (2) cylindrical notched 30 specimens (PA 6, Room Temperature)..... 157

Figure 89 - Load-displacement curves for PA 6 resulting from combined tension/shear loading at RT: influence of crosshead speeds for each loading angle..... 161

Figure 90 - Load-displacement curves for PA 6 resulting for combined tensile/shear loading at RT: effect of loading angle for given crosshead speeds…… 162

Figure 91 - Load-displacement curves for PA 6 resulting from combined tension/shear loading at RT and 50 °C: influence of crosshead speeds for each loading angle…… 165

Figure 92 - Load-displacement curves for PA 6 resulting for combined tensile/shear loading at 50 °C: influence of resulting in combined tension/shear for given crosshead speeds…… 165

Figure 93 - Compression load-displacement curves of (1) cylindrical and (2) cylindrical notched specimens…… 167

Figure 94 - Load-displacement curves for PA 6 resulting from combined compression/shear loading at RT: influence of crosshead speeds for each loading angle…… 170

Figure 95 - Load-displacement curves for PA 6 resulting for combined compression/shear loading at RT: effect of loading angle for given crosshead speeds…… 170

Figure 96 - Load-displacement curves for PA 6 resulting from combined compression/shear loading at RT and 50 °C: influence of crosshead speeds for each loading angle…… 173

Figure 97 - Load-displacement curves for PA 6 resulting for combined compression/shear loading at 50 °C: effect of loading angle for given crosshead speeds…… 173

Figure 98 - DSC curves for PA 6 virgin/injected material…… 175

Figure 99 - (1) DSC curves for PA 6 at true strains of 0.5 and 1, (2) red dashed line is the longitudinal section investigated in the DSC…… 176

Figure 100 - Results of DMA experiments; the storage modulus (E') as function of temperature (°C) and frequency effects on PA 6…… 178

Figure 101 - Results of DMA experiments; the storage modulus (E') and loss factor, tan (δ) as function of temperature (°C) on PA 6…… 178

Figure 102 – Tensile load-displacement curves of cylindrical notched R 5 for: (1) HDPE, (2) PP and (3) PA 6; and cylindrical notched R 30 for: (4) HDPE, (5) PP and (6) PA 6 at RT…… 184

Figure 103 – Load-displacement curves resulting from tensile loading on: (1) HDPE, (2) PP and (3); and shear loading on: (4) HDPE, (5) PP and (6) PA 6 at RT…… 185

From Chapter: 5 Fracture Surface Analysis

Figure 104 – SEM of tensile deformed long chain ethylene - propylene copolymers, showing the fibrillation type of fracture, during tensile straining [175]…… 189

Figure 105 – SEM fracture surfaces for flat notched specimens with *R 5*, for HDPE, PP and PA 6. Note that in the first column the geometry of specimen and fracture surface location are indicated by the black square…… 189

Figure 106 – SEM fracture surfaces for flat notched specimens with *R 30*, for HDPE, PP and PA 6. Note that in the first column the geometry of specimen and fracture surface location are indicated by the black square…… 190

Figure 107 - SEM fracture surfaces for cylindrical notched specimens with *R 5*, for HDPE, PP and PA 6. Note that in the first column the geometry of specimen and fracture surface location are indicated by the black square…… 192

Figure 108 - SEM fracture surfaces for cylindrical notched specimens with *R 30*, for HDPE, PP and PA 6. Note that in the first column the geometry of specimen and fracture surface location are indicated by the black square..... 193

Figure 109 - SEM images of butterfly specimens fractured for tensile loading at room temperature for HDPE, PP and PA 6. In the first column the geometry of specimen and fracture surface location are indicated by the black square..... 195

Figure 110 - SEM images of butterfly specimens fractured for tensile loading at temperature of 50 °C for HDPE, PP and PA 6. In the first column the geometry of specimen and fracture surface location are indicated by the black square..... 196

Figure 111 - SEM images of butterfly specimens fractured for combined tensile/shear loading α = 30° at room temperature for HDPE, PP and PA 6. In the first column the geometry of specimen and fracture surface location are indicated by the black square..... 197

Figure 112 – High magnifications (1) PP peripheric-central region and (2) PA 6, central fracture region. 198

Figure 113 - SEM images of butterfly specimens fractured for combined tensile/shear loading α = 30° at temperature of 50 °C for HDPE, PP and PA 6. In the first column the geometry of specimen and fracture surface location are indicated by the black square..... 199

Figure 114 - SEM images of butterfly specimens fractured for shear loading at room temperature for HDPE, PP and PA 6. In the first column the geometry of specimen and fracture surface location are indicated by the black square..... 200

Figure 115 - SEM images of butterfly specimens fractured for shear loading at temperature of 50 °C for HDPE, PP and PA 6. In the first column the geometry of specimen and fracture surface location are indicated by the black square..... 201

Figure 116 – High magnification of PP fracture surface at extremities..... 202

Figure 117 - SEM fracture surfaces for flat notched specimens with *R 5* and *R 30*, for HDPE, PP and PA 6 at central localization..... 204

Figure 118 - SEM fracture surfaces for cylindrical notched specimens with *R 5* and *R 30*, for HDPE, PP and PA 6 at central localization..... 204

Figure 119 - SEM images of butterfly specimens fractured for tensile loading at room temperature for HDPE, PP and PA 6 at central localization..... 205

Figure 120 - SEM images of butterfly specimens fractured for combined tensile/shear loading at room temperature and at temperature of 50 °C for HDPE, PP and PA 6 at central localization..... 206

Figure 121 - SEM images of butterfly specimens fractured for shear loading at room temperature for HDPE, PP and PA 6 at central localization..... 207

From Chapter: 6 Plasticity Model Calibration and Verification – Drucker-Prager and von Mises

Figure 122 – Initial loading conditions of the specimens geometries in the plane of stress triaxiality and Lode angle parameter [8, 112]..... 210

Figure 123 – Yield stress determination, example of procedure used for tensile test on dumbbell with crosshead speed of 20 mm/min. The value 14.2 MPa (σ_{zz}) is depicted in Table 110 in tensile dumbbell column..... 212

Figure 124 –True stress-strain curves for all 5 specimens geometries, for each crosshead speed. Only one curve is displayed for each specimen geometry and crosshead speed..... 214

Figure 125 - (1) The equivalent stress and pressure of Table 111 are plotted. (2) Hardening curves for 1, 20 and 200 mm/min crosshead speed..... 215

Figure 126 – Comparison of the numerical simulations with experimental results. Tensile load-displacement curves of (1) Dumbbell, (2) cylindrical notched 5 and (3) cylindrical notched 30 specimens (HDPE, Room Temperature)..... 218

Figure 127 - Comparison of the numerical simulations with experimental results. Compression load-displacement curves of (1) cylindrical and (2) cylindrical notched specimens (HDPE, Room Temperature)..... 219

Figure 128 – Butterfly model, boundary constrains..... 221

Figure 129 – Comparison of the numerical simulations with experimental results. Tensile load-displacement curves of (1) flat notched 5 and (2) flat notched 30 specimens (HDPE, Room Temperature)..... 221

Figure 130 - Comparison of the numerical simulations with experimental results. Load-displacement curves for HDPE resulting from combined tensile/shear loading at RT. Loading angles: (1) $\alpha = 90°$, (2) $\alpha = 60°$, (3) $\alpha = 30°$ and (4) $\alpha = 0°$..... 222

Figure 131 - Comparison of the numerical simulations with experimental results. Load-displacement curves for HDPE resulting from combined compression/shear loading at RT. Loading angles: (1) $\alpha = 90°$, (2) $\alpha = 60°$ and (3) $\alpha = 30°$..... 223

Figure 132 – Locations from where the strain and corresponding stress states were extracted, for each specimen geometry. Red dot, centre and blue dot, outside surface..... 225

Figure 133 - Evolution of the (1) stress triaxiality and (2) Lode angle parameter with respect to plastic strain at centre, for all specimens geometries in study..... 226

Figure 134 - Evolution of the (1) stress triaxiality and (2) Lode angle parameter with respect to plastic strain at outside surface, for all specimens geometries in study..... 226

Figure 135 - Effect of stress triaxiality and Lode angle parameter on the equivalent plastic strain of HDPE based on the experimental and numerical results. (1) At centre and (2) at outside surface..... 229

Figure 136 –True stress-strain curves for all 5 specimens geometries, for each crosshead speed. Only one curve is displayed for each specimen geometry and crosshead speed..... 231

Figure 137 - (1) The equivalent stresses and pressures of Table 120 are plotted. (2) Hardening curves for 1, 20 and 200 mm/min crosshead speed..... 232

Figure 138 – Comparison of the numerical simulations with experimental results. Tensile load-displacement curves of (1) Dumbbell, (2) cylindrical notched 5 and (3) cylindrical notched 30 specimens (PP, Room Temperature)..... 234

Figure 139 - Comparison of the numerical simulations with experimental results. Compression load-displacement curves of (1) cylindrical and (2) cylindrical notched specimens (PP, Room Temperature).. 235

Figure 140 – Comparison of the numerical simulations with experimental results. Tensile load-displacement curves of (2) flat notched 5 and (3) flat notched 30 specimens (PP, Room Temperature). 236

Figure 141 - Comparison of the numerical simulations with experimental results. Load-displacement curves for PP resulting from combined tensile/shear loading at RT. Loading angles: (1) $\alpha = 90°$, (2) $\alpha = 60°$, (3) $\alpha = 30°$ and (4) $\alpha = 0°$..... 237

Figure 142 - Comparison of the numerical simulations with experimental results. Load-displacement curves for PP resulting from combined compression/shear loading at RT. Loading angles: (1) α = 90°, (2) α = 60° and (3) α = 30°..... 238

Figure 143 - Evolution of the (1) stress triaxiality and (2) Lode angle parameter with respect to plastic strain at centre, for all specimens geometries in study..... 240

Figure 144 - Evolution of the (1) stress triaxiality and (2) Lode angle parameter with respect to plastic strain at outside surface, for all specimens geometries in study..... 240

Figure 145 - Effects of stress triaxiality and Lode angle parameter on the equivalent plastic strain of PP based on the experimental and numerical results. (1) At centre and (2) at outside surface..... 243

Figure 146 –True stress-strain curves for all 5 specimens geometries. Only one curve is displayed for each specimen geometry and crosshead speed..... 245

Figure 147 - (1) The equivalent stresses and pressures of Table 126 are plotted. (2) Hardening curves for 1, 20 and 200 mm/min crosshead speed..... 246

Figure 148 – Comparison of the numerical simulations with experimental results. Tensile load-displacement curves of (1) Dumbbell, (2) cylindrical notched 5 and (3) cylindrical notched 30 specimens (PA 6, Room Temperature)..... 248

Figure 149 - Comparison of the numerical simulations with experimental results. Compression load-displacement curves of (1) cylindrical and (2) cylindrical notched specimens (PA 6, Room Temperature)..... 249

Figure 150 – Comparison of the numerical simulations with experimental results. Tensile load-displacement curves of (2) flat notched 5 and (3) flat notched 30 specimens (PA 6, Room Temperature)..... 250

Figure 151 - Comparison of the numerical simulations with experimental results. Load-displacement curves for PA 6 resulting from combined tensile/shear loading at RT. Loading angles: (1) α = 90°, (2) α = 60°, (3) α = 30° and (4) α = 0°..... 251

Figure 152 - Comparison of the numerical simulations with experimental results. Load-displacement curves for PA 6 resulting from combined compression/shear loading at RT. Loading angles: (1) α = 90°, (2) α = 60° and (3) α = 30°..... 252

Figure 153 - Evolution of the (1) stress triaxiality and (2) Lode angle parameter with respect to plastic strain at centre, for all specimens geometries in study..... 253

Figure 154 - Evolution of the (1) stress triaxiality and (2) Lode angle parameter with respect to plastic strain at outside surface, for all specimens geometries in study..... 253

Figure 155 – Effects of stress triaxiality and Lode angle parameter on the equivalent plastic strain of PA 6 based on the experimental and numerical results. (1) At centre and (2) at outside surface..... 256

From Appendices:

Figure 156 - Designed Arcan Apparatus – isometric and orthogonal views..... 271

Figure 157 - Designed Arcan Apparatus – exploded view and dimensions of components..... 271

Figure 158 - Designed Arcan Apparatus - range of biaxial loading angles (α = 0°: shear; α = 90°: tension/compression)..... 272

Figure 159 - Arcan Apparatus Modifications - intermediate grips modification to avoid rotation of specimens gripping..... 272

Figure 160 - Arcan Apparatus Modifications - designed specimen extra-clamping device..... 273

Figure 161 - Arcan Apparatus Modifications – extra drilled holes for extra specimen clamps..... 273

Figure 162 – SEM fracture surfaces for flat notched specimens with *R 5* for HDPE at RT. Localization: near surface..... 274

Figure 163 – SEM fracture surfaces for flat notched specimens with *R 5* for HDPE at RT. Localization: central..... 275

Figure 164 – SEM fracture surfaces for flat notched specimens with *R 30* for HDPE at RT. Localization: central and near surface..... 276

Figure 165 – SEM fracture surfaces for flat notched specimens with *R 30* for HDPE at RT. Localization: near surface..... 277

Figure 166 – SEM fracture surfaces for flat notched specimens with *R 5* for PP at RT. Localization: central and near surface..... 278

Figure 167 – SEM fracture surfaces for flat notched specimens with *R 30* for PP at RT. Localization: central and near surface..... 279

Figure 168 – SEM fracture surfaces for flat notched specimens with *R 30* for PP at RT. Localization: near surface..... 280

Figure 169 – SEM fracture surfaces for flat notched specimens with *R 5* for PA 6 at RT. Localization: central and near surface..... 281

Figure 170 – SEM fracture surfaces for flat notched specimens with *R 30* for PA 6 at RT. Localization: central and near surface..... 282

Figure 171 – SEM fracture surfaces for flat notched specimens with *R 30* for PA 6 at RT. Localization: near surface..... 283

Figure 172 – SEM fracture surfaces for cylindrical notched specimens with *R 5* for HDPE at RT. Localization: central and near surface..... 284

Figure 173 – SEM fracture surfaces for cylindrical notched specimens with *R 30* for HDPE at RT. Localization: near surface..... 285

Figure 174 – SEM fracture surfaces for cylindrical notched specimens with *R 5* for PP at RT. Localization: central and near surface.....286

Figure 175 – SEM fracture surfaces for cylindrical notched specimens with *R 30* for PP at RT. Localization: central..... 287

Figure 176 – SEM fracture surfaces for cylindrical notched specimens with *R 5* for PA 6 at RT. Localization: central and near surface..... 288

Figure 177 – SEM fracture surfaces for cylindrical notched specimens with *R 30* for PA 6 at RT. Localization: central and near surface..... 289

Figure 178 - SEM images of butterfly specimens fractured for tensile loading at RT for HDPE. Localization: near surface..... 290

Figure 179 - SEM images of butterfly specimens fractured for tensile loading at RT for HDPE. Localization: central..... 291

Figure 180 - SEM images of butterfly specimens fractured for tensile loading at RT for HDPE. Localization: near surface..... 292

Figure 181 - SEM images of butterfly specimens fractured for combined tension/shear loading α = 30° at RT for HDPE. Localization: near surface..... 293

Figure 182 - SEM images of butterfly specimens fractured for combined tension/shear loading α = 30° at RT for HDPE. Localization: central..... 294

Figure 183 - SEM images of butterfly specimens fractured for shear loading at RT for HDPE. Localization: central and near surface..... 295

Figure 184 - SEM images of butterfly specimens fractured for tensile loading at temperature of 50 °C for HDPE. Localization: central and near surface..... 296

Figure 185 - SEM images of butterfly specimens fractured for combined tension/shear loading α = 30° at temperature of 50 °C for HDPE. Localization: central and near surface..... 297

Figure 186 - SEM images of butterfly specimens fractured for combined tension/shear loading α = 30° at temperature of 50 °C for HDPE. Localization: near surface..... 298

Figure 187 - SEM images of butterfly specimens fractured for shear loading at temperature of 50 °C for HDPE. Localization: near surface and central..... 299

Figure 188 - SEM images of butterfly specimens fractured for shear loading at temperature of 50 °C for HDPE. Localization: near surface..... 300

Figure 189 - SEM images of butterfly specimens fractured for tensile loading at RT for PP. Localization: near surface and central..... 301

Figure 190 - SEM images of butterfly specimens fractured for combined tension/shear loading α = 30° at RT for PP. Localization: near surface.....302

Figure 191 - SEM images of butterfly specimens fractured for combined tension/shear loading α = 30° at RT for PP. Localization: near surface..... 303

Figure 192 - SEM images of butterfly specimens fractured for combined shear loading at RT for PP. Localization: near surface and central..... 304

Figure 193 - SEM images of butterfly specimens fractured for combined shear loading at RT for PP. Localization: near surface..... 305

Figure 194 - SEM images of butterfly specimens fractured for tensile loading at temperature of 50 °C for PP. Localization: near surface..... 306

Figure 195 - SEM images of butterfly specimens fractured for tensile loading at temperature of 50 °C for PP. Localization: central..... 307

Figure 196 - SEM images of butterfly specimens fractured for combined tension/shear loading α = 30° at temperature of 50 °C for PP. Localization: central..... 308

Figure 197 - SEM images of butterfly specimens fractured for combined tension/shear loading α = 30° at temperature of 50 °C for PP. Localization: near surface..... 309

Figure 198 - SEM images of butterfly specimens fractured for shear loading at temperature of 50 °C for PP. Localization: centre..... 310

Figure 199 - SEM images of butterfly specimens fractured for shear loading at temperature of 50 °C for PP. Localization: near surface..... 311

Figure 200 - SEM images of butterfly specimens fractured for tensile loading at RT for PA 6. Localization: near surface and central…… 312

Figure 201 - SEM images of butterfly specimens fractured for tensile loading at RT for PA 6. Localization: near surface…… 313

Figure 202 - SEM images of butterfly specimens fractured for combined tension/shear loading α = 30° at RT for PA 6. Localization: near surface and centre…… 314

Figure 203 - SEM images of butterfly specimens fractured for combined tension/shear loading α = 30° at RT for PA 6. Localization: near surface…… 315

Figure 204 - SEM images of butterfly specimens fractured for combined tension/shear loading α = 30° at RT for PA 6. Localization: near surface…… 316

Figure 205 - SEM images of butterfly specimens fractured for shear loading at RT for PA 6. Localization: near surface and centre…… 317

Figure 206 - SEM images of butterfly specimens fractured for shear loading at RT for PA 6. Localization: centre…… 318

Figure 207 - SEM images of butterfly specimens fractured for shear loading at RT for PA 6. Localization: near surface…… 319

Figure 208 - SEM images of butterfly specimens fractured for tensile loading at temperature of 50 °C for PA 6. Localization: near surface…… 320

Figure 209 - SEM images of butterfly specimens fractured for tensile loading at temperature of 50 °C for PA 6. Localization: centre…… 321

Figure 210 - SEM images of butterfly specimens fractured for combined tension/shear loading α = 30° at temperature of 50 °C for PA 6. Localization: centre…… 322

Figure 211 - SEM images of butterfly specimens fractured for combined tension/shear loading α = 30° at temperature of 50 °C for PA 6. Localization: near surface…… 323

Figure 212 - SEM images of butterfly specimens fractured for shear loading at temperature of 50 °C for PA 6. Localization: near surface…… 324

List of Tables

From Chapter: 2 Behaviour of Semi Crystalline Polymers

Table 1 - ISO 527 part 1 recommended testing speed [55, 66]..... 55
Table 2 - Test specimens type 1A and 1B, dimensions [42, 69]..... 56
Table 3 - Shear compression specimens (SCS)..... 61
Table 4 - Shear tensile specimens..... 61
Table 5 - Combined tension and shear - Torsional tubing specimens..... 62
Table 6 - Biaxial loading tests - cruciform specimen..... 62
Table 7 - Notched tensile specimens..... 63
Table 8 - Notched compression specimens..... 63
Table 9 - Low-Density and High-Density Polyethylene properties [2, 9]..... 77
Table 10 - Dow™ HDPE KT 10000 UE, technical information [129]..... 78
Table 11 - Sabic® PP PHC27, technical information [133]..... 80
Table 12 - Promyde® B30 PMID, technical information [134]..... 81

From Chapter: 3 Experimental Details

Table 13 - Specifications and set parameters of the injected moulded specimens..... 84
Table 14 - Machine Specifications - Euro Inj D200 [136]..... 84
Table 15 - Recommended machining conditions for thermoplastics according to ISO 2818 [138]..... 85
Table 16 - Basic material properties assigned (HDPE)..... 88
Table 17 - Stress/strain analytical formulas, stress triaxiality and lode angle used in this research 94
Table 18 - MTS 810 universal testing machine specifications [147]..... 98
Table 19 - MTS 634.25 axial extensometer specifications [148]..... 99
Table 20 - Total number of tensile tests..... 99
Table 21 - Total number of compression specimens..... 99
Table 22 - Total number of butterfly specimens used in combined tensile/shear loading..... 100
Table 23 - Total number of butterfly specimens used in combined tensile/shear loading..... 101
Table 24 - Instron 3367 universal testing machine specifications [149]..... 101
Table 25 - Total number of butterfly specimens used in combined tensile/shear loading..... 102
Table 26 - Machine Specifications – DSC Q20 [150]..... 103
Table 27 - Parameters used in DSC analyses..... 103
Table 28 - Total number of DSC tests..... 103
Table 29 - DMA Machine Specifications – DMA Q800 [151]..... 104
Table 30 - Parameters used in DMA analyses..... 104

Table 31 - Total number of butterfly specimens used in SEM observations..... 105

Table 32 - Total number of flat and cylindrical notched specimens used in SEM observations..... 105

From Chapter: 4 Experimental Results and Discussion

Table 33 - Load and displacement values for dumbbell specimen at selected deformation stages (all values are averaged) (HDPE)..... 110

Table 34 - Deformation patterns and corresponding load and displacement values for flat notched 5 specimens at three deformation stages (all values are averaged) (HDPE)..... 110

Table 35 - Deformation patterns and corresponding load and displacement values for flat notched 30 specimens at three deformation stages (all values are averaged) (HDPE)..... 110

Table 36 - Deformation patterns and corresponding load and displacement values for cylindrical notched 5 specimens at three deformation stages (all values are averaged) (HDPE)..... 111

Table 37 - Deformation patterns and corresponding load and displacement values for cylindrical notched 30 specimens at three deformation stages (all values are averaged) (HDPE)..... 111

Table 38 - Deformation patterns and corresponding load and displacement values for butterfly specimen at $\alpha = 90°$ (pure tension) at RT (all values are averaged) (HDPE)..... 115

Table 39 - Deformation patterns and corresponding load and displacement values for butterfly specimen at $\alpha = 60°$ (combined tension/shear) at RT (all values are averaged) (HDPE)..... 116

Table 40 - Deformation patterns and corresponding load and displacement values for butterfly specimen at $\alpha = 30°$ (combined tension/shear) at RT (all values are averaged) (HDPE)..... 116

Table 41 - Deformation patterns and corresponding load and displacement values for butterfly specimen at $\alpha = 0°$ (pure shear) at RT (all values are averaged) (HDPE)..... 117

Table 42 - Fracture appearance and corresponding load and displacement values for butterfly specimen at $\alpha = 90°$ (pure tension) at 50 °C (all values are averaged) (HDPE)..... 120

Table 43 - Fracture appearance and corresponding load and displacement values for butterfly specimen at $\alpha = 60°$ (combined tension/shear) at 50 °C (all values are averaged) (HDPE)..... 121

Table 44 - Fracture appearance and corresponding load and displacement values for butterfly specimen at $\alpha = 30°$ (combined tension/shear) at 50 °C (all values are averaged) (HDPE)..... 121

Table 45 - Fracture appearance and corresponding load and displacement values for butterfly specimen at $\alpha = 0°$ (pure shear) at 50 °C (all values are averaged) (HDPE)..... 121

Table 46 - Deformation patterns and corresponding load and displacement values for cylindrical specimen at three deformation stages (all values are averaged) (HDPE)..... 123

Table 47 - Deformation patterns and corresponding load and displacement values for cylindrical notched specimen at two deformation stages (all values are averaged) (HDPE)..... 123

Table 48 - Deformation patterns and corresponding load and displacement values for butterfly specimens loaded at $\alpha = 90°$ (pure compression) at RT (all values are averaged) (HDPE)..... 126

Table 49 - Deformation patterns and corresponding load and displacement values for butterfly specimens loaded at $\alpha = 60°$ (combined compression/shear) at RT (all values are averaged) (HDPE)..... 126

Table 50 - Deformation patterns and corresponding load and displacement values for butterfly specimens loaded at $\alpha = 30°$ (combined compression/shear) at RT (all values are averaged) (HDPE)..... 127

Table 51 - Deformation patterns and corresponding load and displacement values for butterfly specimens loaded at α = 0° (pure shear) at RT (all values are averaged) (HDPE)..... 127

Table 52 - Fracture appearance and corresponding load and displacement values for butterfly specimen loaded at α = 90° (pure compression) at 50 °C (all values are averaged) (HDPE)..... 129

Table 53 - Fracture appearance and corresponding load and displacement values for butterfly specimen loaded at α = 60° (combined compression/shear) at 50 °C (all values are averaged) (HDPE)..... 129

Table 54 - Fracture appearance and corresponding load and displacement values for butterfly specimen loaded at α = 30° (combined compression/shear) at 50 °C (all values are averaged) (HDPE)..... 130

Table 55 - Characteristic load and displacement values for butterfly specimens loaded at α = 0° (pure compression) at 50 °C (all values are averaged) (HDPE)..... 130

Table 56 - Thermal properties and crystallinity of HDPE determined by DSC, injected material..... 131

Table 57 - Influence of deformation on thermal properties and crystallinity of HDPE determined by DSC, deformed specimens..... 132

Table 58 - Load and displacement values for dumbbell specimen at selected deformation stages (all values are averaged) (PP)..... 136

Table 59 - Deformation patterns and corresponding load and displacement values for flat notched 5 specimens at three deformation stages (all values are averaged) (PP)..... 136

Table 60 - Deformation patterns and corresponding load and displacement values for flat notched 30 specimens at three deformation stages (all values are averaged) (PP)..... 136

Table 61 - Deformation patterns and corresponding load and displacement values for cylindrical notched 5 specimens at three deformation stages (all values are averaged) (PP)..... 137

Table 62 - Deformation patterns and corresponding load and displacement values for cylindrical notched 30 specimens at three deformation stages (all values are averaged) (PP)..... 137

Table 63 - Deformation patterns and corresponding load and displacement values for butterfly specimens loaded at α = 90° (pure tension) at RT (all values are averaged) (PP)..... 140

Table 64 - Deformation patterns and corresponding load and displacement values for butterfly specimens loaded at α = 60° (combined tension/shear) and RT (all values are averaged) (PP)..... 140

Table 65 - Deformation patterns and corresponding load and displacement values for butterfly specimens loaded at α = 30° (combined tension/shear) at RT (all values are averaged) (PP)..... 141

Table 66 - Deformation patterns and corresponding load and displacement values for butterfly specimens loaded at α = 0° (pure shear) and RT (all values are averaged) (PP)..... 141

Table 67 - Fracture appearance and corresponding load and displacement values for butterfly specimen at α = 90° (pure tension) at 50 °C (all values are averaged) (PP)..... 144

Table 68 - Fracture appearance and corresponding load and displacement values for butterfly specimen at α = 60° (combined tension/shear) at 50 °C (all values are averaged) (PP)..... 144

Table 69 - Fracture appearance and corresponding load and displacement values for butterfly specimen at α = 30° (combined tension/shear) at 50 °C (all values are averaged) (PP)..... 145

Table 70 - Fracture appearance and corresponding load and displacement values for butterfly specimen at α = 0° (pure shear) at 50 °C (all values are averaged) (PP)..... 145

Table 71 - Deformation pattern and corresponding load and displacement values for cylindrical specimen at three deformation stages (all values are averaged) (PP)..... 147

Table 72 - Deformation pattern and corresponding load and displacement values for cylindrical notched specimen at two deformation stages (all values are averaged) (PP)..... 147

Table 73 - Deformation patterns and corresponding load and displacement values for butterfly specimen at α = 90° (pure compression) at RT (all values are averaged) (PP)..... 149

Table 74 - Deformation patterns and corresponding load and displacement values for butterfly specimen at α = 60° (combined shear/compression) at RT (all values are averaged) (PP)..... 149

Table 75 - Deformation patterns and corresponding load and displacement values for butterfly specimen at α = 60° (combined shear/compression) at RT (all values are averaged) (PP)..... 150

Table 76 - Deformation patterns and corresponding load and displacement values for butterfly specimen at α = 60° (pure shear) at RT (all values are averaged) (PP)..... 150

Table 77 - Deformation pattern and corresponding load and displacement values for butterfly specimen at α = 90° (pure compression) at 50 °C (all values are averaged) (PP)..... 152

Table 78 - Deformation pattern and corresponding load and displacement values for butterfly specimen at α = 60° (combined shear/compression) at 50 °C (all values are averaged) (PP)..... 152

Table 79 - Deformation pattern and corresponding load and displacement values for butterfly specimen at α = 30° (combined shear/compression) at 50 °C (all values are averaged) (PP)..... 153

Table 80 - Deformation pattern and corresponding load and displacement values for butterfly specimen at α = 0° (pure shear) at 50 °C (all values are averaged) (PP)..... 153

Table 81 - Thermal properties and crystallinity of PP determined by DSC, virgin material..... 154

Table 82 - Thermal properties and crystallinity of PP determined by DSC, deformed specimens..... 155

Table 83 - Load and displacement values for dumbbell specimen at selected deformation stages (all values are averaged) (PA 6)..... 158

Table 84 - Deformation patterns and corresponding load and displacement values for flat notched 5 specimens at three deformation stages (all values are averaged) (PA 6)..... 159

Table 85 - Deformation patterns and corresponding load and displacement values for flat notched 30 specimens at three deformation stages (all values are averaged) (PA 6)..... 159

Table 86 - Deformation patterns and corresponding load and displacement values for cylindrical notched 5 specimens at three deformation stages (all values are averaged) (PA 6)..... 159

Table 87 - Deformation patterns and corresponding load and displacement values for cylindrical notched 30 specimens at three deformation stages (all values are averaged) (PA 6)..... 160

Table 88 - Deformation patterns and corresponding load and displacement values for butterfly specimens loaded at α = 90° (pure tension) at RT (all values are averaged) (PA 6)..... 162

Table 89 - Deformation patterns and corresponding load and displacement values for butterfly specimens loaded at α = 60° (combined tension/shear) and RT (all values are averaged) (PA 6)..... 163

Table 90 - Deformation patterns and corresponding load and displacement values for butterfly specimens loaded at α = 30° (combined tension/shear) and RT (all values are averaged) (PA 6)..... 163

Table 91 - Deformation patterns and corresponding load and displacement values for butterfly specimens loaded at α = 0° (pure shear) and RT (all values are averaged) (PA 6)..... 164

Table 92 - Fracture appearance and corresponding load and displacement values for butterfly specimen at α = 90° (pure tension) at 50 °C (all values are averaged) (PA 6)..... 166

Table 93 - Fracture appearance and corresponding load and displacement values for butterfly specimen at α = 60° (combined tension/shear) at 50 °C (all values are averaged) (PA 6)..... 166

Table 94 - Fracture appearance and corresponding load and displacement values for butterfly specimen at α = 30° (combined tension/shear) at 50 °C (all values are averaged) (PA 6)..... 166

Table 95 - Fracture appearance and corresponding load and displacement values for butterfly specimen at α = 0° (pure shear) at 50 °C (all values are averaged) (PA 6)..... 167

Table 96 - Deformation pattern and corresponding load and displacement values for cylindrical specimen at three deformation stages (all values are averaged) (PA 6)..... 168

Table 97 - Deformation pattern and corresponding load and displacement values for cylindrical notched specimen at two deformation stages (all values are averaged) (PA 6)..... 169

Table 98 - Deformation patterns and corresponding load and displacement values for butterfly specimen at α = 90° (pure compression) at RT (all values are averaged) (PA 6)..... 171

Table 99 - Deformation patterns and corresponding load and displacement values for butterfly specimen at α = 60° (combined shear/compression) at RT (all values are averaged) (PA 6)..... 171

Table 100 - Deformation patterns and corresponding load and displacement values for butterfly specimen at α = 30° (combined shear/compression) at RT (all values are averaged) (PA 6)..... 171

Table 101 - Deformation patterns and corresponding load and displacement values for butterfly specimen at α = 0° (pure shear) at RT (all values are averaged) (PA 6)..... 172

Table 102 - Deformation pattern and corresponding load and displacement values for butterfly specimen at α = 90° (pure compression) at 50 °C (all values are averaged) (PA 6)..... 174

Table 103 - Deformation pattern and corresponding load and displacement values for butterfly specimen at α = 60° (combined shear/compression) at 50 °C (all values are averaged) (PA 6)..... 174

Table 104 - Deformation pattern and corresponding load and displacement values for butterfly specimen at α = 30° (combined shear/compression) at 50 °C (all values are averaged) (PA 6)..... 174

Table 105 - Deformation pattern and corresponding load and displacement values for butterfly specimen at α = 0° (pure shear) at 50 °C (all values are averaged) (PA 6)..... 174

Table 106 - Thermal properties and crystallinity of PA 6 determined by DSC, virgin material..... 176

Table 107 - Thermal properties and crystallinity of PA 6 determined by DSC, deformed specimens..... 177

Table 108 – Principal thermal properties of HDPE, PP and PA 6 determined by DSC, virgin material and deformed..... 182

From Chapter: 5 Fracture Surface Analysis

Table 109 – Summary of stress triaxialities, whose fracture surfaces were observed by SEM..... 188

From Chapter: 6 Plasticity Model Calibration and Verification – Drucker-Prager and von Mises

Table 110 - Elastic Modulus, stress components in tension and compression on yield at room temperature for HDPE..... 213

Table 111 - The von Mises equivalent stress (q) and hydrostatic pressure (p), are displayed..... 215

Table 112 – Drucker Prager hardening in tension points for HDPE..... 216

Table 113 - Basic material properties assigned..... 216

Table 114 - Mesh models, element type, element shape, geometric order, number of elements and nodes..... 217

Table 115- Mesh models, element type, element shape, geometric order, number of elements and nodes..... 220

Table 116 – Displacements from where the stress triaxiality , Lode angle parameter and equivalent plastic strain were determined..... 225

Table 117 - Stress triaxiality and Lode angle parameter values obtained from numerical simulations. The initial stress triaxiality values calculated from the analytical formulas are listed in the second column... 227

Table 118 - Stress triaxiality and Lode angle parameter values obtained from numerical simulations. The initial stress triaxiality values calculated from the analytical formulas are listed in the second column... 227

Table 119 – Elastic Modulus, yield loci, stress components in tension and compression at room temperature for PP..... 230

Table 120 - The von Mises equivalent stress (q) and hydrostatic pressure (p), are displayed..... 232

Table 121 – Drucker Prager hardening in tension, points for PP..... 233

Table 122 - Basic material properties assigned..... 233

Table 123 - Stress triaxiality and Lode angle parameter values obtained from numerical simulations. The initial stress triaxiality values calculated from the analytical formulas are listed in the second column... 241

Table 124 - Stress triaxiality and Lode angle parameter values obtained from numerical simulations. The initial stress triaxiality values calculated from the analytical formulas are listed in the second column... 241

Table 125 – Elastic Modulus, yield loci, stress components in tension and compression at room temperature for PA 6..... 244

Table 126 - The von Mises equivalent stress (q) and hydrostatic pressure (p), are displayed..... 246

Table 127 – Drucker Prager hardening in tension, points for PA 6..... 247

Table 128 - Basic material properties assigned..... 247

Table 129 - Stress triaxiality and Lode angle parameter values obtained from numerical simulations. The initial stress triaxiality values calculated from the analytical formulas are listed in the second column... 254

Table 130 - Stress triaxiality and Lode angle parameter values obtained from numerical simulations. The initial stress triaxiality values calculated from the analytical formulas are listed in the second column... 254

Nomenclature

Letters

A	Area
A_o	Cross-Section Area of the Specimen in the Initial State
a	Actual Minimum Radius of the Specimen
a_0	Minimum and Initial Radius of the Centre of the Median Cross-Section
C_p	Heat Capacity
d	Initial Cross-Section Diameter
d_m	Cohesion of the Material
E	Elastic Modulus
E^*	Complex Modulus
E'	Storage Modulus
E''	Loss Modulus
F	Applied Force
i	Smallest Radius of Inertia
I_1	First Stress Invariant
J_2	Second Deviatoric Stress Invariant
K	Ratio of the Yield Stress in Triaxial Tension to the Triaxial Compression
l	Specimen Length
l_o	Original Length
l_1	Instantaneous Length Followed Force Application
ln	Natural Log
I_y	Smallest Axial Inertia Moment
p	= σ_h
q	= σ_{eq}
R	Reaction Force
R_n	Notch Radius
r	Third Invariant of the Deviatoric Stress (Drucker-Prager)
T_g	Glass Transition Temperature
T_m	Melting Temperature
t	Actual Minimum Ligament Thickness of the Specimen
t_0	Initial Ligament Thickness of the Specimen
x	Current Radial Abscissa in the Cross Section

Symbols

α	Loading Angle
β	Slope of the Linear Yield Surface in the *p*–*t* stress plane
β_x	Stiffness Ratio
y	Diameter of Cylindrical Specimens
δ	Displacement
δ_f	Loss Factor tan
ΔH_f	Measured Melting Enthalpy
ΔH^0_f	Perfect Polymer Crystal
ε_A	Strain Amplitude
ε_{c^*}	Maximum Nominal Compressive Strain
ε_e	Engineering Strain
ε_{eq}	Equivalent Strain

ε_t	True Strain
ε_t^{pl}	The True Plastic Strain
η	Stress Triaxiality
θ	Lode Angle
$\overline{\theta}$	Normalized Lode Angle
λ	Slenderness Ratio
ν	Poisson Ratio
ξ	Normalized Third Deviatoric Stress
π	Pi
σ	Stress
σ_A	Stress Amplitude
σ_c	If Hardening is Defined by the Uniaxial Compression Yield Stress
σ_e	Engineering Stress
σ_{eq}	von Mises Equivalent Stress
σ_h	Hydrostatic Pressure
σ_t	If Hardening is Defined by the Uniaxial Tension Yield Stress
σ_t	True Stress
σ_{xx}	Normal Stress in Biaxial Loading
σ_{xy}	Shear in Biaxial loading
$\sigma_{xx}, \sigma_{yy}, \sigma_{zz}$	Maximum, Medium and Minimum Principal Stress, Respectively
$\sigma_x, \sigma_y, \sigma_z$	Principal Stresses
$\emptyset_{cw}$	Crystal Weight Fraction

1 Introduction

This chapter outlines the motivation and the objectives of the present thesis. The methodology followed to achieve the aims of the thesis is also described. Finally, the contents of the thesis are presented and shortly discussed.

1.1 Motivation

Nowadays it would be nearly impossible to imagine a world without plastics. It was not until the nineteenth century that attempts were made to develop a synthetic polymeric material and the first success was based on an organic material derived from cellulose, by Alexander Parkes. The first truly synthetic polymer did not come along until 1909, when Leo Baekeland, created a liquid resin, which he named Bakelite. During the Second World War, materials such as nylon and polyethylene appeared on the scene. The breakthrough landmark in the commercial production of polyethylene began in 1953, with the Karl Ziegler discovery of catalysts for its polymerization under mild temperatures and pressures. Building on Ziegler's discovery, Giulio Natta synthetises the polypropylene. This discovery was recognized by a Nobel Prize [1, 2].

Thermoplastics are one of the fastest advancing and expanding materials, since they are inexpensive substitutes for metals, concrete, and timber, becoming the material of choice due to low cost, ease of processing, large weight savings, corrosion resistance, design freedom, lack of conductivity (heat and electrical), low-density relative to metals coupled with high strength and the possibility of being designed "by man to his own specifications". Also they are easily recycled and a variety of different processing methods are used to convert raw material into finished products [1, 3, 4]. Thermoplastics are finding applications in almost all areas of human activity as many of the things we use as well as in diverse areas of engineering applications such as pressure vessels liners [4].

Throughout the years, several authors were interested in the mechanical response of thermoplastics under uniaxial stress states, stress-strain rate effects, temperature effects, neck propagation, viscoplasticity and yielding. Nevertheless, under combined biaxial stress states, the material properties of thermoplastics or any other material can be different from the properties measured under uniaxial tension/compression or shear tests [5]. Also, references to biaxial loading tests combined with the effect of temperature, for semi crystalline polymers are not abundant in the literature. Therefore, due to the lack of relevant data and for the successful behaviour prediction during in-service phase, there is a need to better understand the thermoplastic's mechanical properties and behaviour under a variety of loading conditions and temperature effects. However, this is not easy because of the complex microstructure of semi crystalline polymers [6].

The mechanical properties in the elastic domain and yielding, are generally influenced by the molecular structure and orientation, inhomogeneous structure, molecular weight, degree of crystallinity and the thickness of the crystallite lamellae, as for example, the elastic modulus. Essentially, the elastic modulus is not only determined by the intrinsic properties of crystal and amorphous domains, but also by the interface between both domain boundaries. Temperature

is also an important factor for the mechanical properties since it governs the molecular mobility and thus may strongly modify the various deformation processes [6, 7].

In addition, the continuum progress in computational mechanics has been essential in the development of technological advances and have allowed engineers to analyse complex structural components, assess structural reliability and optimize structural designs, being one of the most important links in product development cycles. Therefore, the yielding of materials is an important issue in the industrialized world, because the static design verification has to be performed accounting for the onset of yielding or onset of plastic deformation or for ultimate stresses, taking into account the service temperatures and the loading rates. Design verification demands for reliable data, which may be obtained by rigorous experimental testing programs [8].

1.2 Objectives

This thesis is concerned with the experimental characterization, analysis and discussion of the deformation behaviour of semi crystalline polymers. Relationships such as load-displacement / stress-strain and temperature effects as well as proprieties such as yield point and elastic modulus are investigated. Also, it aims to develop a proper and comprehensive understanding of the micromechanical processes of deformation. The materials to be addressed in this monograph are High-Density Polyethylene (HDPE), Polypropylene (PP) and Polyamide 6 (PA 6), three semi crystalline thermoplastics. In order to accomplish this purpose, both complex specimen geometries, produced by injection moulding and a biaxial testing apparatus (Arcan), will be designed. Also, extensive laboratory tests performed at different crosshead speeds and different temperatures will be performed. The objectives of this research are:

- To define the methodology and methods for data collection, which includes the design of various complex specimen shapes and the design of a multiaxial testing apparatus,
- To carry out an extensive experimental program, which includes specimens with different geometries, and considering different crosshead speeds: 1, 20 and 200 mm/min and temperatures: room temperature (RT) and constant temperature of 50 °C,
- To identify, investigate and describe the deformation/damage mechanisms,
- Calibration of von Mises and Drucker-Prager yield criteria based on experimental results to determine the parameters employed in the material model,
- Verification of identified constitutive models by means of numerical simulations of the biaxial experimental results under tension and compression loading, using butterfly specimens, and the tensile flat notched specimens experimental results, by comparing the experimental load-displacement curves with numerical counterparts,
- To understand the effects of stress triaxiality and Lode angle parameter on the onset of plastic domain behaviour.

1.3 Scope

- The intention of this research is to investigate the stress state effects on the yield response of HDPE, PP and PA 6, using three complementary experimental approaches: one combining tension/shear and compression/shear in a plane stress state; other imposing a triaxial stress state and another one more conventional, such as uniaxial tension and compression tests.
- The more conventional specimen's geometry under tension and compression are: dumbbell and cylindrical.
- The triaxial stress state effects will be examined by means of tests using flat and cylindrical notched specimens with different curvature radii in order to set different triaxial stress states in the median cross-section.
- The biaxial yield response will be measured from a series of biaxial loading (pure shear, combined shear and tension/compression, pure tension/compression) in a positive and negative vertical displacement using butterfly specimens.
- The majority of tests will be carried out at room temperature. A small batch of biaxial loading tests will be performed in an environmental chamber at constant temperature of 50°C.
- All tests will be carried out at three crosshead speeds of 1, 20 and 200 mm/min.
- Analytical expressions are used in order to calculate the local stresses and strains in the elastic regime, and therefore, allowing the yield points to be extracted.
- Differential Scanning Calorimetry (DSC) and Dynamical Mechanical Analysis (DMA) will be used to characterize the thermal properties, crystallinity degree and viscoelastic properties.
- Scanning Electron Microscopy (SEM) will be used to examine the microstructural features of the tested material fracture surfaces and correlate them with the loading conditions.
- The von Mises and the Drucker-Prager plasticity models parameters, are determined from stress-strain results obtained from: tensile tests on dumbbell and cylindrical notched specimens, and compression tests on cylindrical and cylindrical notched specimens.
- The true stress versus plastic strain data from the tensile test on dumbbell specimen is used as input data points (yield stress and plastic strain) in both, Drucker-Prager and von Mises yield model parameters, to define the isotropic hardening function.
- The aim of calibrating the material constitutive models, is to verify by means of numerical simulation of the biaxial loading experimental results and the tensile results of flat notched specimens, the accuracy of the proposed constitutive models, by comparing the experimental load-displacement curves with numerical simulation.
- The stress triaxiality and lode angle results at the viscoplastic domain of each specimen are collected and analysed.

1.4 Outline of Thesis

The present monograph consists of seven chapters. The first chapter, which is an introduction, presents the general framework of the thesis. Chapter 2 introduces and discusses some topics with main focus on macromolecular structure and basis of polymer behaviour. In a sequential manner, various aspects of polymers are introduced with the emphasis gradually shifting from structural aspects to mechanical and physical properties. Therefore, the main topics on

polymers comprised in this chapter are: molecular structure, molecular weight, polymer crystallinity, quiescent crystallization vs inhomogeneous and shish-kebab structures formed in injection moulding, stress-strain behaviour, microstructural deformation under elastic and plastic domains, thermal transitions, mechanical and physical tests, typical fracture surface properties, arcan apparatus and butterfly specimens in the context of mechanical testing. von Mises Yield and Drucker-Prager Yield Criterion, as well as the required basics of ductile fracture such as stress state parameters, stress triaxiality and Lode angle parameter, are briefly explained.

Chapter 3 details all the experimental program so that a clear understanding of testing procedures is attained. It is more focused in a quantitative picture of polymers behaviour, evaluation and characterization. The different specimen geometries, the mechanical and physical testing protocols are described in accordance with the standards. A major focus is given to the evolution of the mechanical properties of polymers as these often constitute the most important consideration and dictate the use of specific polymers in diverse applications.

Chapter 4 discusses polymer properties under two main headings - mechanical and physical, providing explanations on a molecular and structural basis for the observed mechanical behaviours. The results of mechanical test are presented in the form of load-displacement curves. In Chapter 5, by using of a Scanning Electron Microscope, the specimen's fracture surface topographies are analysed. Scanning Electron Microscope micrographs allowed to identify modes of deformation. The effects of notch profile radii on HDPE, PP and PA 6 fracture behaviour have been studied as well the biaxial fracture morphologies were investigated from a series of biaxial loadings under tensile loadings.

The capability of Drucker-Prager and von Mises yield criteria to capture the nonlinear material response at various stress, is explored in Chapter 6. The material models and the calibration of material parameters from the material tests, are presented. Also, the FE model simulations results are verified and discussed. A summary of the concluding remarks and future studies is finally given in Chapter 7.

2 Behaviour of Semi Crystalline Polymers

The main intent of this chapter is to introduce the fundamental concepts that explain the deformation mechanisms of the examined materials (semi crystalline polymers), with regard to the existing literature. The stress state parameters, stress triaxiality and Lode angle parameters are briefly explained.

2.1 Structure of Semi Crystalline Polymers

Polymers are derived from organic products, mainly produced from petroleum or natural gas raw materials. The word polymer is derived from the Greek "-mer" for the basic unit and "poly-mer" for many repeating units. Polymeric materials are characterized by long-chain molecular structures, which are produced when many thousands of small monomer molecules join up to form macromolecules with repeated unit [9]. The process of transformation of monomer molecules into a polymer molecule is known as polymerization [10].

The monomer molecules have strong bonds among themselves, a covalent backbone* formed by carbon atoms and have weak secondary bonds between adjacent polymer chains [4]. These weak bonds, are also called Van der Waals bonds as they are the result of small attractive forces between side atoms along the chain. The weaker secondary bonds are relatively easy to disrupt, with moderate heat, without rupturing the covalent bonding [3, 4, 11]. Most polymers are based on carbon atoms in combination with other atoms, such as hydrogen (very often) and sometimes oxygen, chlorine, fluorine, phosphorous, and silicon. Also, other polymer chains can be connected to the main chain. The number of different combination possibilities is wide, as well as the variety of different polymer types [12].

Polymers can exhibit a range of different molecular structures, which are related to the physical arrangement of monomer molecules along the chain. The molecular structure of a fully polymerized polymer has a strong influence on their unique properties and can be grouped into one of three major types: linear, branched, and cross-linked (Figure 1) [9]. In linear polymers, long chains of connected monomers are arranged in a linear sequence. A common example is the High-Density Polyethylene [10]. Branched polymers are linear polymers with irregular side chains of the same polymer attached to the main chain; lastly the cross-linked or network polymer contains short side chains (cross links) that connect different polymer chains forming a complex three-dimensional "network". Unlike linear and branched polymers, cross-linked polymers do not melt upon heating and do not dissolve in solvents [13, 14].

The molecular structure is the basis for the polymers classification in thermoplastics or thermosets. Thermosets are cross-linked polymers and become permanently hard during their formation. Both linear and branched polymers are thermoplastic which means, they can be melted/softened and reversibly hardened as a function of temperature and may be processed

*Note: a covalent bond is a chemical bond that involves the sharing of electron pairs between atoms.

by a variety of moulding, blowing and extrusion techniques. The type of branching has a profound effect on the spatial arrangement of the polymer chains, and hence on properties. The presence of branches disturbs the regular arrangement of the polymer chains, and therefore crystallinity decreases as branching increases; also physical properties such as viscosity and elasticity are affected by the amount and type of branching [4, 9].

Thermoplastics comprise the three materials included in this study: High-Density Polyethylene, Polypropylene and Polyamide 6 [14].

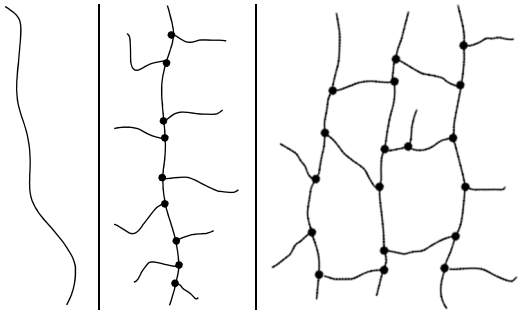


Figure 1 – From the left to the right: linear, branched, and cross-linked polymer molecules [4].

The physical properties of a polymer, such as its strength and melting temperatures are strongly dependent on the length of the polymer chain and by the molecular weight distribution. A largely low molecular weight polymer will display different mechanical and thermo-physical properties from the ones with high molecular weight [4, 9]. The relationship between tensile strength and melt viscosity versus molecular weight is depicted in Figure 2.

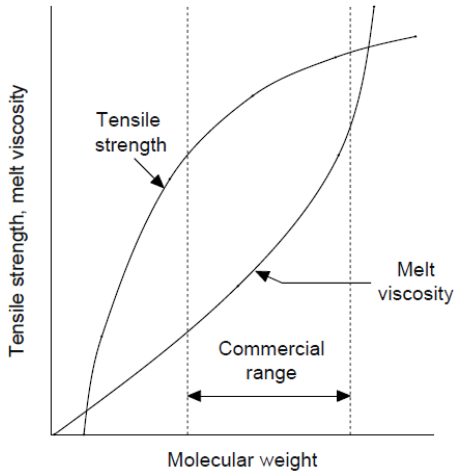


Figure 2 - Tensile strength and melt viscosity versus molecular weight [4].

As can be seen from the figure above, as the molecular weight is increased, strength properties and melt viscosity or resistance to flow also tends to increase. Polymers with high molecular weight have a smaller number of chain ends in a given volume when compared with low molecular weight polymers. Therefore, increasing molecular weight tends to decrease the chain

mobility, due to the increase in chain interactions (intermolecular forces) and entanglements which come with increased chain length. These interactions and entanglements results in a higher glass transition temperature value and an improvement in the mechanical properties. Other properties that dependent on the molecular weight, are: elastic modulus and softening point [3].

2.1.1 Polymer Crystallinity

Structurally, polymers in solid state may be amorphous or crystalline. If crystalline polymers contain some amorphous regions, they are then referred to as semi crystalline. Therefore, semi crystalline polymers have both crystalline and amorphous regions, with the crystalline region embedded in the remaining amorphous domains (Figure 3). While metals and ceramics can be fully crystalline, in thermoplastics the degree of crystallinity usually varies between 10 and 80%. The degree of crystallinity is an important physical parameter since it reflects the polymer morphology and determines various mechanical properties [4].

Amorphous polymers are composed of tangled macromolecular chains, with randomly arrangement in space, somewhat like a bowl of cooked spaghetti. These entanglements (branched polymers) might cause the polymer chains to behave as a network, packing together irregularly enough to form a crystal. Therefore, high degree of short and long chain branching, results in loose packing of the chains and low degree of crystallinity. Although polymer chains can be arranged into a regular crystalline structure. Crystallinity region occurs when linear polymer chains are structurally oriented in a uniform and well-defined spatially manner, which is characterized by translational symmetry [9, 15].

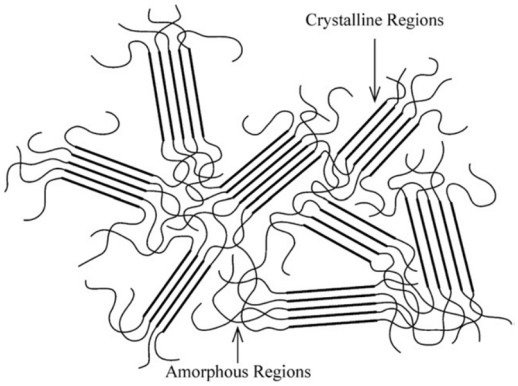


Figure 3 - Crystalline and amorphous regions [15].

Crystallinity has a number of important effects on the end-use properties of a polymer. Physical properties of crystalline polymers are influenced by the spherulite size and overall crystallinity, which are affected by the types of nucleation, crystal growth rate and the characteristics of individual folded chains. Increasing the degree of crystallinity increases hardness, tensile strength, impact strength, friction and wear, corrosion resistance and opacity [16]. Crystalline polymers are more dense than amorphous polymers because of a more compact packing of

aligned polymer chains in the crystalline regions [13, 15]. Amorphous polymers are usually less rigid, more easily deformed, often transparent and have lower melting points [1].

2.1.2 Quiescent Crystallization

Polymer crystallization follows an ordered structures hierarchy, which begins with the crystal nucleation. When slowly cooled from the melt in the absence of flow, so-called quiescent crystallization, semi crystalline polymers often show a spherulitic morphology (spherical aggregates of the lamellar crystallines). The crystallisation starts from certain points, spherulite centres and then the lamellae grow along the radial direction [17–19]. The majority of nascent spherulites appear as sheaves of lamellar crystals as the examples in Figure 4 [19].

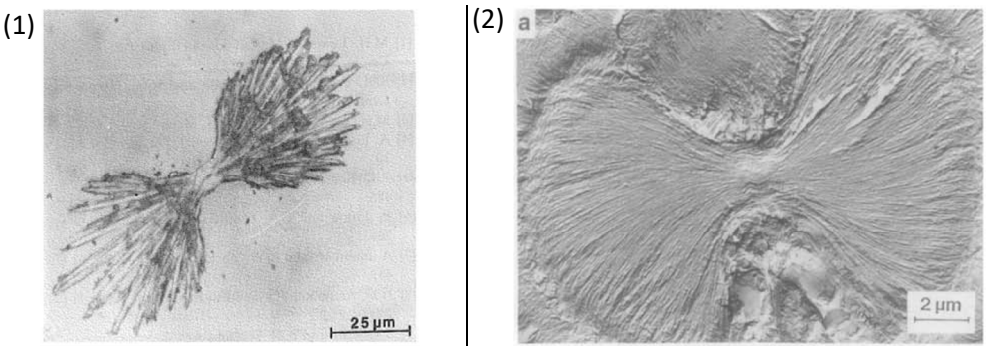


Figure 4 – Sheaves of lamellar crystals: (1) 3PbO 2SiO crystal grows, (2) PE/LDPE 61/39 blend crystallized [19].

While growing, the crystalline layers are being twisted along the radial direction of the spherulite. This effect can be observed as concentric light-dark rings in polarized light micrographs (PLM) such as in Figure 5 (1) [19]. Other techniques, such as electron and atomic force microscopy (AFM) [20] and x-ray diffraction (XRD) [21] provided the evidences for the twisted structures. Twisted lamellae are also reported to have an S-shaped cross-section when they are cut perpendicularly to the growth direction (Figure 5 (2)). This structure is explaned based on the reorientation of polymer chains and the stress on the lamellar surfaces and self-induced fileds during crystallization [22].

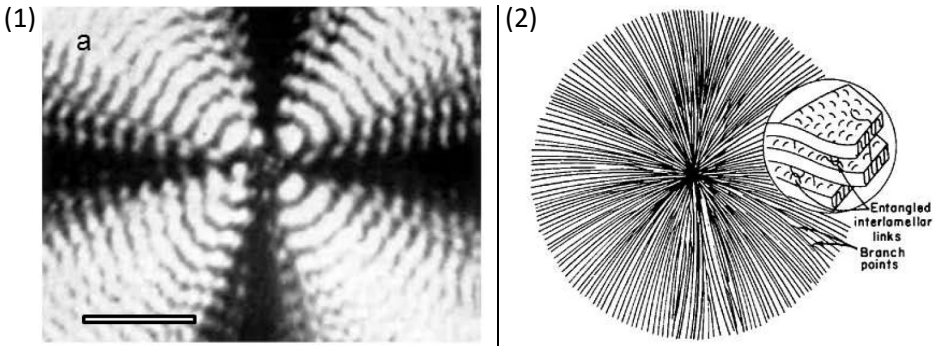


Figure 5 - (1) PLM image of PE banded spherulites; scale bars are 25 µm, (2) Diagram of polymer spherulite with chain-folded lamellae [19, 23].

In the beginning, spherulites are located distantly and have a round shape, however, when the boundaries come in contact, spherulites acquire a polyhedron shape (Figure 6). In semi crystalline polymers the inter-spherulite space is filled with amorphous material [17–19].

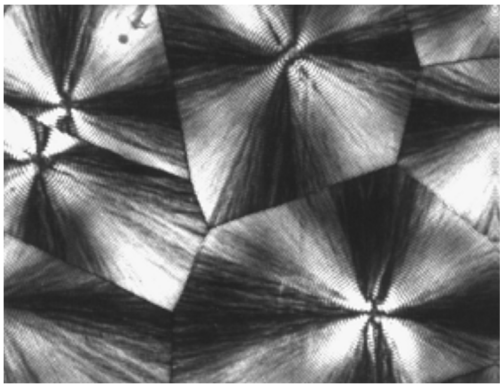


Figure 6 – Examples of spherulites obtained by polymer crystallization under quiescent conditions. PLM image of polyethylene spherulites [23].

Each spherulite consists of a radial lamellar stack, consisting of alternating layers of crystalline lamellae and non-crystalline domains, both entities have thickness in a nanometre range and are organised like composite sandwich structure. The average size of lamellae and their curvature, as well as the type of their organization into spherulites are strongly dependent upon molecular weight, crystallization conditions and the degree of branching of chains [18, 24]. The polarized light microscopy observations (PLM), reveals morphological changes with crystallization temperature. A common example is illustrated in Figure 7 for Polyethylene (PE) fraction. For larger crystallization temperatures (smaller undercooling ΔT = melting temperature T_m – crystallization temperature T_c) the growth rate is reduced and the spherulites appear coarser, less regular and less dense [19].

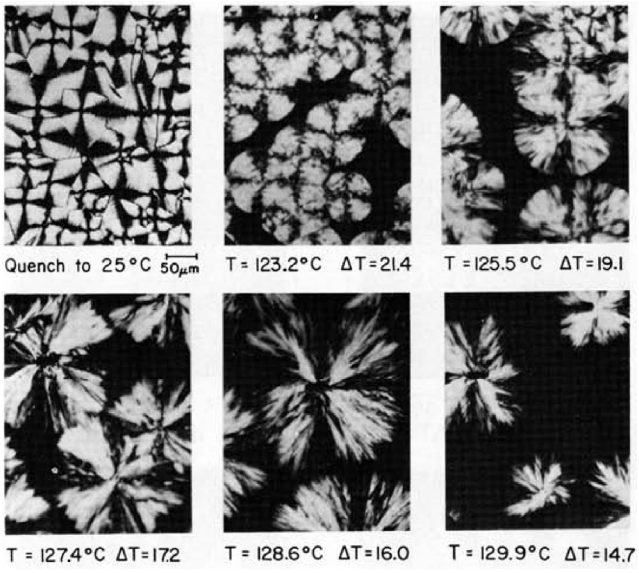


Figure 7 - PLM images of a PE molecular mass fraction M_w of 30.6 kDa, crystallized at different temperatures [19].

2.1.3 Inhomogeneous and Shish-Kebab Structures

In injection moulded semi crystalline polymers, the shear flow at the moulding filling stage induces high orientation and extension of molecules. Therefore, the crystalline structure and morphology are affected and can be quite different from what is observed under quiescent crystallization conditions. Beyond the spherulites morphology, shish-kebabs, lamellae row-structures and an inhomogeneous multiphase skin can be shaped [25].

Inhomogeneous Structure

Investigations on injection-moulding specimens of semi crystalline polymers, show a multiphase layer structure along the cross-section perpendicular to the melt flow. The morphology of these multiphase layers is strongly dependent on processing temperatures, flow rate, pressure and have different thicknesses along flow direction. The inhomogeneous structure, affects physical properties such as dimension stability, elastic modulus and tensile strength [26, 27].

Multiphase morphology of semi crystalline polymers can be partitioned into three or more layered structures. Schrauwen et al. [26], analysed the morphology formed during processing and deformation behaviour of thin, injection-moulded polyethylene and polypropylene specimens. Optical micrographs of polyethylene were taken from three positions: near to the injection-moulding gate (1), middle of the specimen (2) and far from the gate (3), as illustrated in Figure 8. From the optical micrographs, four structural layers can be distinguished: a skin layer (A), a transition layer (B), a shear layer (C) and an isotropic core (D) as well as a reduction of the oriented layers thickness at increasing distances from the injection gate (A, B and C) [26, 27].

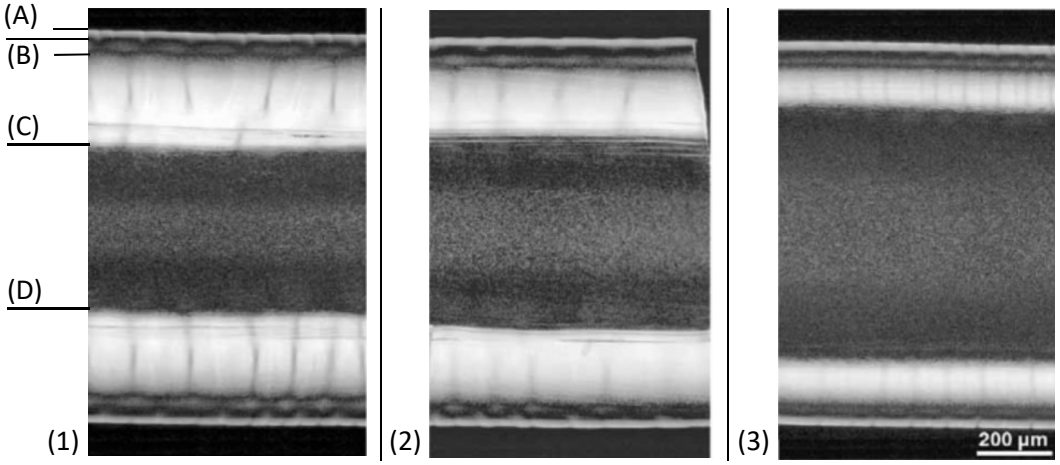


Figure 8 - (1) Optical micrographs of cross-section injection-mould specimen of polyethylene at position near to the injection-moulding gate, (2) middle of the specimen and (3) far from the gate [26].

The skin, transition and shear layer (intermediate layer) are non-spherulitics and consists of high oriented structures along the flow direction. These layers are formed due to strong flows before and during crystallization, the stress field and rapid cooling rate induced by the cold walls of the mould. Under these conditions crystalline structures like shish-kebabs or lamellae row

structures are formed. On the other hand, the absence of flow shear and lower cooling rate in the core layer, results in isotropic spherulite structures with a low molecular orientation. Although, the number and thickness of the layers might change with moulding conditions, thermoplastic composition (chemical composition, molecular weight and molecular weight distribution), flow rate and pressure [28–30].

Guo et al. [31] and Viana [32] found that the skin layer thickness decreases with increasing the melt temperature and injection flow rate, while the spherulite size directly increases with the mould temperature. Pantani et al. [33] observed that higher holding pressure could promote molecular orientation in polypropylene mainly due to increased relaxation time under higher pressure. Stern et al. [34] showed that the elastic modulus of a polypropylene depends not only on the degree of crystallinity but also on the crystalline orientation and the crystal thickness. They also showed that the tensile strength of a polymer is proportional to its molecular weight.

Still from Schrauwen et al. [26] study, it was observed that differences in the microstructure have a drastic influence on the mechanical response of specimens cut at different locations and orientations from the injection-moulded plate, which range from brittle fracture (perpendicular to flow and near the injection point) , to neck formation (perpendicular to flow but far from the injection point) and homogeneous deformation (parallel to flow), in which a low level of extended chains and a high level of oriented lamellae were found [26].

With respect to the inhomogeneous multiphase structure, two negative concerns to mechanical properties arise: (1) the residual stress produced by different levels of crystal orientation (anisotropic skin layer and isotropic core layer), and (2) the existence of a larger proportion of disordered crystals in the core layer [35].

Shish-kebab Structures

Shish-kebab structure has been intensively studied since it was first reported by Pennings and Kiel [36] in 1965. They found that the shish-kebabs are readily produced when dilute solutions of polyethylene were cooled under conditions of continuous stirring. Under shear flow, the crystalline morphology changes and oriented crystalline structures such as stacked lamellae (row-structure) and a shish-kebab morphology are observed. In contrast to the spherulitic morphology formed under quiescent crystallization condition, shish-kebab crystals have anisotropic microstructures, which consists of a long central core (shish) surrounded by lamellar crystals (kebabs) periodically attached perpendicularly along the shish. It is believed that the shish is formed by crystallization of completely stretched polymer chains and the kebabs are coiled chain lamella crystals. The schematic representation of shish-kebab morphology is depicted in Figure 9 [25, 37].

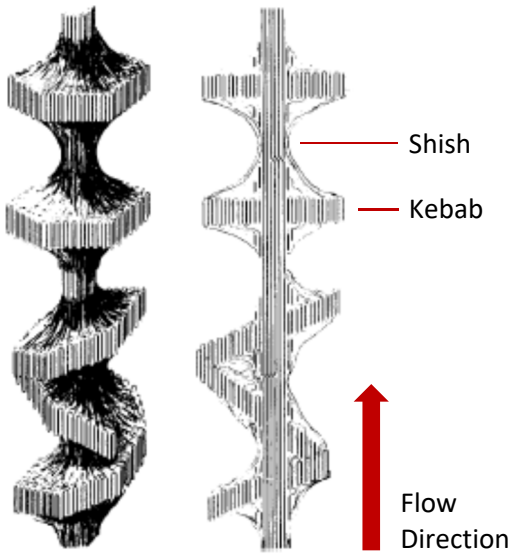


Figure 9 – Shish-Kebab structure [23].

2.2 Deformation of Semi Crystalline Polymers

Mechanical studies on semi crystalline polymers show that properties such as tensile strength, and limit elongation are associated with the deformation and rearrangement of crystalline and amorphous phase. The imposed loadings draw crystalline lamellae and amorphous phase into viscoelastic and viscoplastic deformation. The deformation of semi crystalline polymers is complex, multistage and is strongly dependent on the underlying structure as well as on external parameters such as applied stress, strain rate, temperature and pressure and they are often accompanied by volume change during their viscoplastic deformations [25, 38].

2.2.1 Microstructural Deformation of Semi Crystalline Polymers Under Tensile Strength

The search for a relationship between molecular structure and mechanical properties of semi crystalline polymers has been the subject of considerable research in the past [39]. It is known that the stress-strain curves provides useful information about yielding behaviour and deformation mechanisms of polymer [40].

The mechanisms that govern the process of tensile deformation of semi crystalline polymers at low and constant rate along the true stress-strain curves, show different regimes and draws crystal lamellae and amorphous parts into viscoelastic and plastic deformation. Viscosity and elasticity are the characteristic properties of fluids and solid bodies. The characteristic feature of viscoelastic behaviour is the time dependence of polymer properties. A deformation is time-dependent if the material responds with a delay to changes of the load [41]. A typical stress-strain curve of semi crystalline polymers under tension for a constant rate of loading is depicted in Figure 10. The behaviour of the stress-strain curves for compression and shear is quite similar except that the magnitude and the extension to which the curve is followed are different [4].

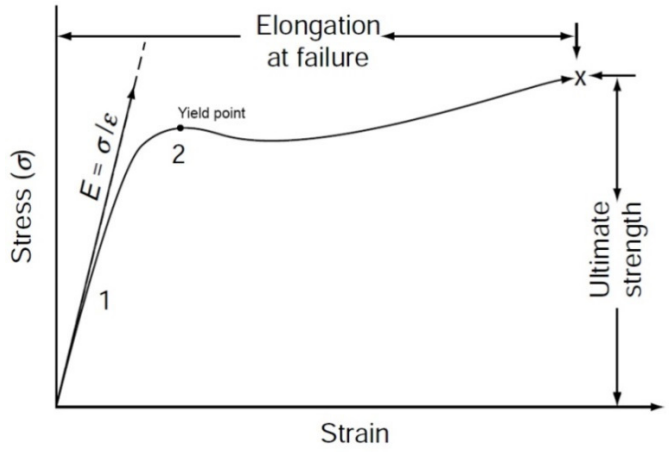


Figure 10 – Stress-strain diagram [4].

Observing Figure 10, it is possible to identify the following deformation regimes:

Elastic Domain: From the Figure 10, the initial portion of the stress-strain curve up to point 1 is linear and it follows Hooke's law, which states that for an elastic material (modulus of elasticity E) the stress is proportional to the strain and the deformation is recoverable and nearly instantaneous, when the load is removed. At small to moderate strains, deformation manifests itself mainly through amorphous layers. The deformation of the amorphous phase can lead to a combination of stack rotation interlamellar shear and/or separation (Figure 11) [4, 42, 43].

Interlamellar shear involves parallel lamellar shear to each other with the amorphous layer undergoing shear. It is established that the recoverable deformation can be attributed to the reversible interlamellar shear due to the amorphous structure. Interlamellar separation is responsible for thickening of inter-crystalline layers when induced by tensile load perpendicular to the lamellar surface. Changes in the lamellae separation are accompanied by transversal contractions so that the deformation must involve a change in volume. Stacks can be easily rotated under the action of the stress. Stack rotation can help the strain accommodation by crystals, as taking place simultaneously with interlamellar shear and interlamellar separation. There is neither release in the existing molecular links nor permanent displacement of the molecules relative to each other [4, 41, 42].

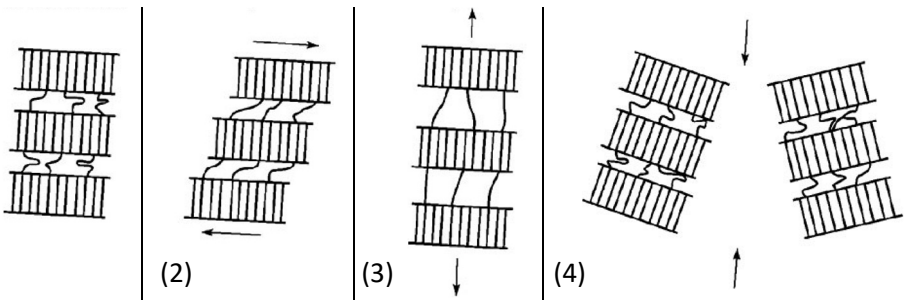


Figure 11 - Models of deformation in amorphous region: (1) undeformed, (2) interlamellar shear, (3) interlamellar separation and (4) stack rotation [43].

At higher stresses, between points 1 and 2, the response becomes nonlinear and eventually reaches a maximum, the so-called engineering yield stress. This response involves the whole assembly of molecules. Deformations are associated with the onset of isolated inter and intra-lamellar slip process. At the point of maximum curvature, begins a collective activity of slip motions of crystal blocks of crystalline lamellae. The deformations may be recoverable [4, 41].

Plastic Domain: Beyond point 2 (yield point), the first point on the stress-strain curve at which an increase in strain occurs without the increase in stress, the extensions are not recoverable. After yield point, the stress drops due to the localization of the plastic deformation in an unpredictable place of the specimen that contains a mechanical weakness, which generates stress concentration [44]. In semi crystalline polymers the plastic deformation involves both the crystalline and the amorphous phase. The mechanisms by which the plastic deformation is produced in the crystalline lamella are assigned mainly to the crystallographic slip process. The elementary crystallographic slip process is characterized by gliding of molecular chains along each other on crystallographic slip planes within the crystalline lamella [25, 38, 45].

Due to the strong connectivity of crystalline and amorphous phases through tie molecules (molecule chain, which may run through several crystalline and amorphous regions), entanglements, loose chain folds and crossing chains, upon stretching the crystallographic mechanisms are accompanied by interlamellar deformation and they can only deform simultaneously. Tie molecule is a long molecular chain which connects two neighbouring lamellar crystals. Emanates from one lamella, crosses the amorphous layer and connects the adjacent crystalline phase. Tie molecules provides strength and impact resistance to the assembly crystalline-amorphous phase [46, 47]. According to Humbert et al. [48, 49] elements such as tie molecules and entanglements are considered as stress transmitters through stacks of crystalline lamellae, and they are responsible for an increase of elastic modulus of confined amorphous layers (Figure 12).

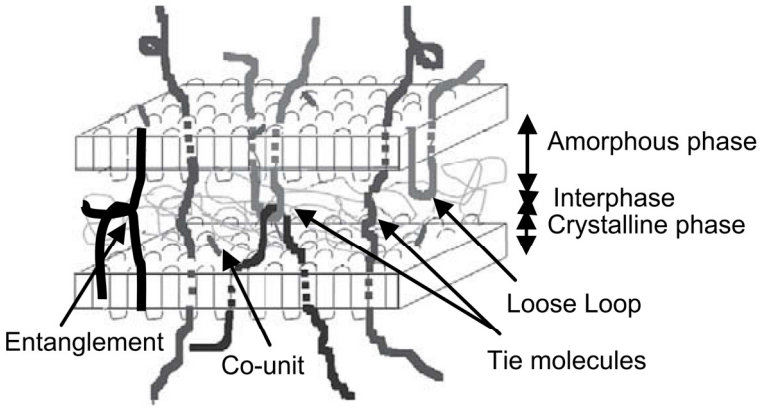


Figure 12 - Scheme of the crystalline and amorphous lamellae with their stress transmitters [49].

At larger strains, an orientation of the macromolecules takes place as a result of plastic deformation, which will trigger the resistance to deformation and might cause strain hardening due to the stretching of the amorphous entangled network. From this point on the crystallites controls the whole plastic deformation kinetics, while the amorphous layers merely adjust

themselves to the deformation. The plastic deformation begins with shape changes of polymer chains and chain fragmentation in the amorphous phase crystallites. At this point, the crystalline microstructure starts to collapse until breakdown due to advanced slip and a high stress generated in adjacent amorphous layers [17, 50–54].

Deformation continues until the moment of strain hardening process following by necking (cross-section reduction), which is regarded as the point where the polymer loses its integrity and gradually is transformed into fibrils morphology. It can be understood considering that once the tie molecules connecting adjacent lamellae reach their maximum elongation, further stretching requires higher energy processes, such as pulling tie molecules out from the lamellae, lamellar fracture, or rupture of tie molecules. The onset of necking localization may be determined by an increase in temperature or by a structural or material imperfection. Deformations are associated with the fragmentation of the crystalline lamellae into crystal blocks, followed by cavitation and microfibril formation along the tensile direction, disentanglements of the amorphous network [17, 50–53].

The values of stress at critical points 1, 2 and beyond point 2 may change significantly with degree of crystallinity, strain rate and temperatures, while the strains at which these transitions take place are nearly invariant over various strain rates and drawing temperatures. This fact complies with the general assumption that semi crystalline polymers are a heterogeneous system in which at low stresses or strains the forces transmitted by the interconnected crystallites dominate, whereas at high strains the rubber-like network forces are superior (amorphous phase) [46]. Additionally, to the viscoelastic and elastoplastic response of amorphous and crystalline phases, deformation of semi crystalline polymers is also controlled by the strain rate dependence, which is reflected in the variation of the initial elastic modulus. An increase in strain rate results in increasing the stress and the initial elastic modulus [17]. The tensile stress-strain response of a high-density polyethylene (HDPE) pulled at a number of different rates at 23 °C is displayed in Figure 13 [55].

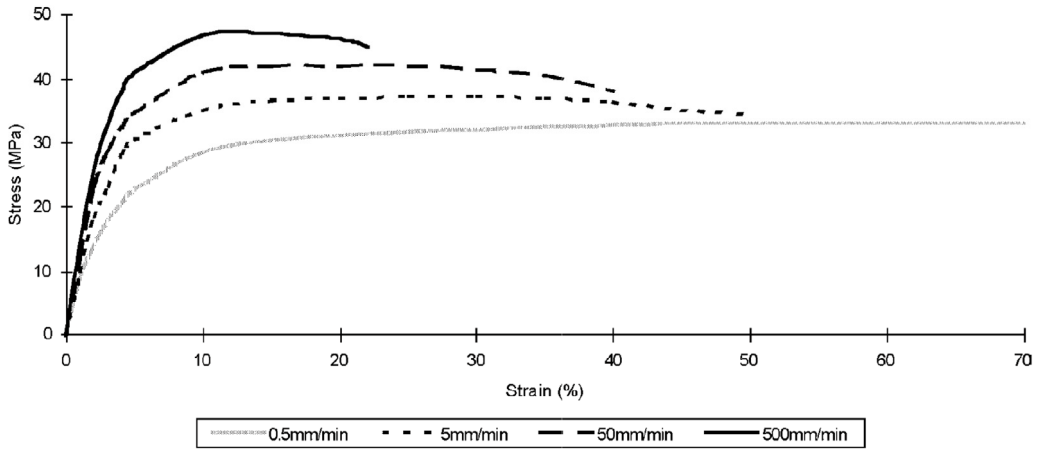


Figure 13 - HDPE tensile stress-strain curves at 23 °C and increasing strain rates [55].

From Figure 13, two distinct features are observed, first lack of any noticeable yield point in the lowest rate. At low rate of extension and at larger strains, the polymer macromolecules have

the time necessary to induce an orderly alignment just enough to accept the increase in deformation, whilst maintaining a constant tensile stress to the applied force. At higher strain rates, both the propensity of the material to form a yield point and to exhibit brittle behaviour, becomes clear [55].

Tensile deformation of various polyethylenes were studied over a range of temperatures by Hong and Strobl [56]. Figure 14 depicts the evolution of the true elastic modulus (E_{cm}) with the imposed true strain (ε_H) at four different temperatures for various strains. It is observed at 25 °C a strong decrease of E_{cm} as a first reaction to the tensile deformation. Beyond point C, E_{cm} increases again due to the onset of fibrillation and strain hardening. Mainly, three features are revealed: (1) tensile drawing leads to the reduction of E_{cm} , (2) E_{cm} decreases with temperature and (3) the yield point is associated with a drop in the stiffness (point B). The temperature dependence of the true elastic modulus can be interpreted as an indication of weakening and decoupling of links between the lamella blocks with increase in temperature and strain.

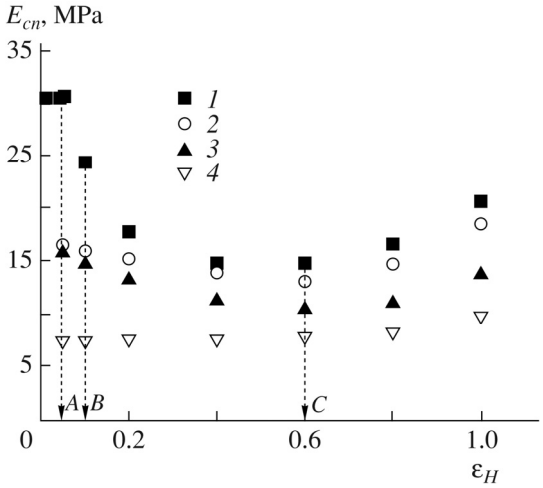


Figure 14 - Variation of true elastic modulus of poly(ethylene-*co*-vinyl acetate) with 12 wt % of counits (PEVA-12) with true strain: *T* = (1) 25 °C, (2) 42 °C, (3) 58 °C and (4) 71 °C [56].

Pawlak and Galeski [57] subjected polypropylene thick films to tensile drawing at various temperatures from the room temperature to 100 °C. Morphological alterations during drawing were followed by wide-angle X-ray scattering, small-angle X-ray scattering and scanning electron microscopy (SEM) of sectioned and etched specimens, volume strain measurement, and light transparency measurement at various level of strain. The stress-strain curves were correlated with morphological observations. From SEM scans, the morphological changes during deformation are illustrated in Figure 15. It is observed that: spherulitic structure is clearly visible, the changes of morphology with deformation depend on the deformation temperature and strain, at 25 °C and at 0.3 strain some cavities appear. They are elongated perpendicularly to the deformation direction, at the strain up to 1.2 there is a high lamellae orientation. The spherulitc becomes unrecognizable; the evolution of morphology of deformed PP proceeds differently when strained at higher temperature of 70 °C and 100 °C. At these temperatures the cavitation phenomenon does not occur and lamellae do not fragment up to the strain of 1.2.

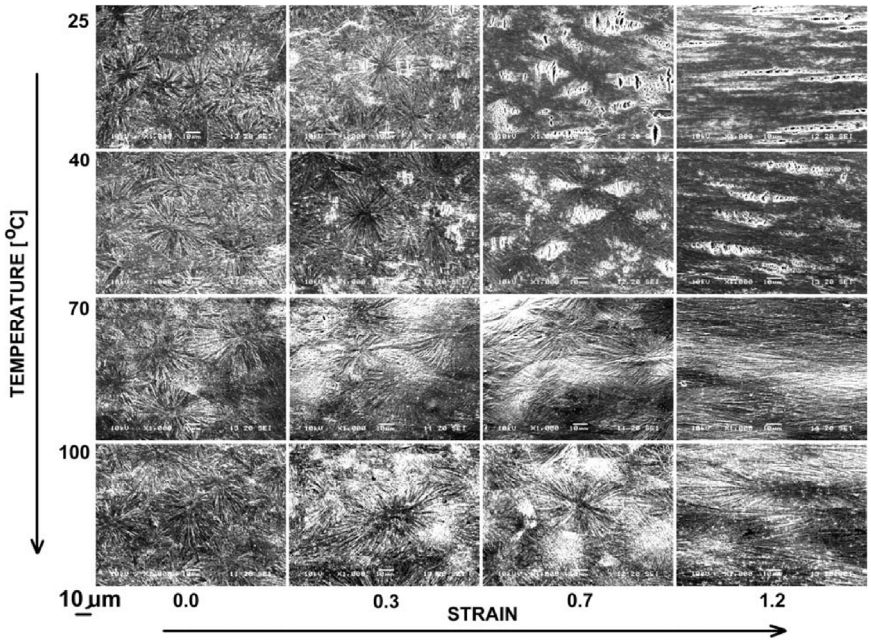


Figure 15 – SEM micrographs. Evolution of internal structure of PP specimens deformed in horizontal direction at different temperatures. Morphology at different strain is presented: initial, 0.3, 0.7 and 1.2 [57].

Studies of a broad range of polyethylenes deformed in plane-strain compression by Bartczak [58] demonstrated that the transitions at critical points 1 and 2 (Figure 10) follow a similar process of deformation mechanisms as in tensile deformation. However, beyond point 2, the strong constraints intrinsic to compression mode result mostly in the lamella cooperative kinking. This contrast to the tensile deformation, which results in fragmentation of crystal lamellae and formation of the fibrillar morphology.

Bartczak [58] summarized the compression deformation mechanisms in critical points (Figure 10), as follow: (1) end the elastic proportionality and beginning of isolated inter and intra-lamellar slip process, (2) widespread slip events and onset of collective crystallographic slips and interlamellar shear, (beyond point 2) temporary lock of the interlamellar shear of the amorphous layers due to straining of tie molecules causes some stress concentration in lamellae, resulting in the slip localization and lamellae cooperative bending, kinking and/or limited fragmentation. At some stage, due to full stretch of the molecular network in amorphous layer, the stress increases and leads to an extensive fragmentation of lamellar structure into smaller blocks. At higher stress, the strain generated by stretching of the entanglements network, results in the destruction of the lamellae and the amorphous components.

2.2.2 Fragmentation of Crystalline Lamellae

Beyond point 2 (yield point) of Figure 10, the stress runs to a critical value causing fragmentation of crystalline lamellae into separate blocks and microfibril formation. Several structural features occurring at moderate plastic strains (yield point) are relevant to crystallographic process.

Lamellar slip is the dominant type of plastic deformation and is mainly associated with two types of crystallographic slip mechanisms: the fine (homogeneous) and coarse chain (heterogeneous, block) slips (Figure 16). The fine slip is characterized by multiple lattice displacements along chain axis. These displacements cause tilting of the folded chains with respect to lamellar surface and might induce reorientation of crystalline lamellae. Whereas, the coarse chain slip occurs on a few parallel crystallographic planes, resulting in displacement of its multiple pieces relative to each other without tilting of the chain axes. Coarse slip take place in lamellae which are defected or have block sub-structure [43, 46]. Fine slip was found the predominant mode in semi crystalline polymers, including polyethylene and polyamide 6, at Room Temperature and low or moderate strains, under compression and tension [43].

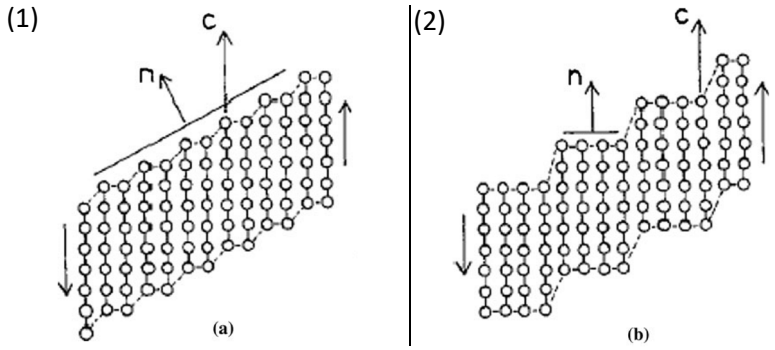


Figure 16 - Schematic diagrams illustrating (1) fine and (2) coarse chain slip [17].

2.2.3 Cavitation

Cavitation phenomenon is observed during deformation in many semi crystalline polymers and corresponds to formation of numerous microvoids (cavities) inside amorphous phase between lamellae. At the beginning, the cavities exhibit ellipsoidal shape, oriented perpendicular to the tensile direction. Then, during necking the cavities are elongated and oriented along the tensile direction. Usually the cavities can be detected by visual observation of stress whitening or by small angle X-ray scattering (SAXS) [46, 59]. Among the available microscopic methods, Pawlak et al. [59] reported that, Seguela group examined morphological changes in deformed of poly(1-butene) spherulites by using atomic force microscopy (AFM) (Figure 17).

It is reported in the literature that cavitations can be related with yielding, as cavity formation is necessarily a damage. Also performed experiments in compression and shear demonstrated that cavitation is specific of deformation of solely uniaxial tension. Consequently, the comparison of a tensile with a compression test which avoids cavitation has allowed concluding that cavitation can affect the macroscopic yield stress [43, 48].

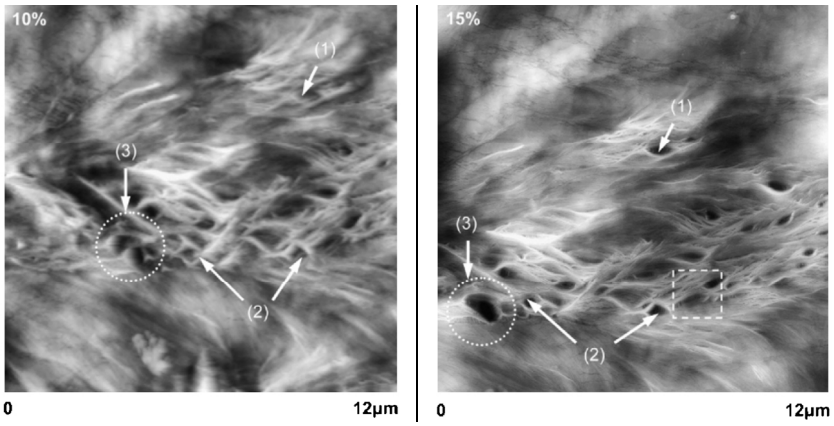


Figure 17 – AFM images of equatorial region of a spherulite for two strain levels 10 and 15%. On the images are indicated the void formation (1), the growth (2) and the coalescence of cavities (3) [59].

Considerable escalation of cavitation during cold drawing was reported by Pawlak and Galeski in polymers such as polypropylene and high-density polyethylene, leading to decrease of yield stress and yield strain. Whereas polymers with small crystals such as low-density polyethylene (LDPE) and Polyamide 6, cavities are not observed. The explanation for such differences in deformation was that in tensile drawing of semi crystalline polymers there is a competition between cavitation and activation of crystal plasticity. Polymers with crystals of higher plastic resistance (thicker lamellae), cavitation occurs first; while for polymers with crystals of lower plastic resistance, deformation occur first, this was observed for LDPE. Cavitation changes the macroscopic yield stress. This phenomenon could be observed form the curves of tensile and compression experiments (Figure 18) obtained by Pawlak and Galeski [60].

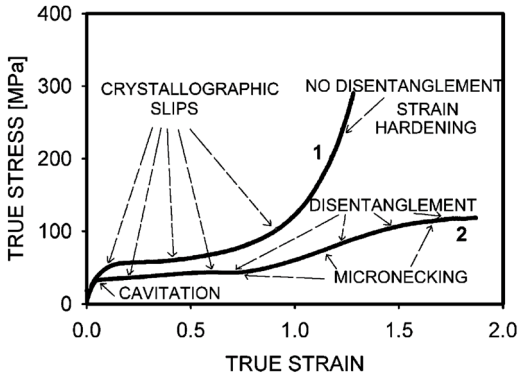


Figure 18 – Stress-strain curves of polypropylene obtained from tensile and compression: curve 1, compression experiment and curve 2, tensile experiment [60].

The cavitation process is usually initiated at the stress level close to the yield point. Pawlak [61] studied the development of cavities with deformation, both for skin layer and volume of injection moulded high-density polyethylene specimen. It was shown that cavitation in high-density polyethylene depends on the orientation of the crystalline lamellae, as it was observed in the skin layers of injection moulded material, where the cavities were formed readily as early

as at 1% of elongation at the macroscopic stresses of 2 MPa. Cavitation in the core of the same injection-moulded high-density polyethylene specimen was observed at yield above 10% of elongation at the stress 30 MPa. Cavities formed in the skin layer do not influence the yielding process.

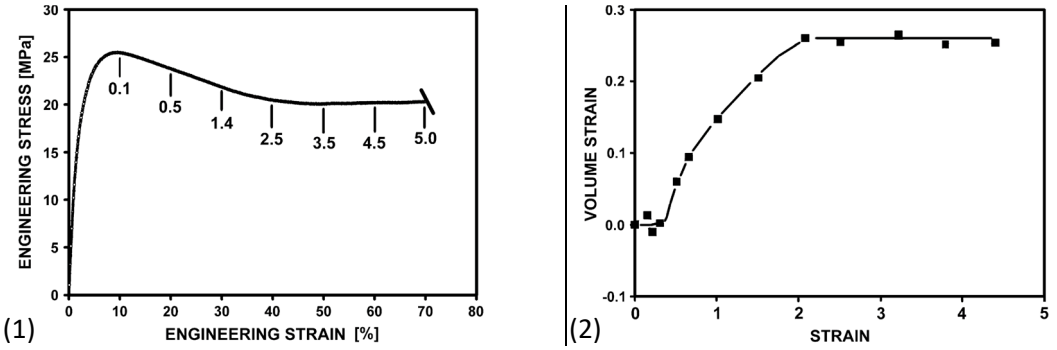


Figure 19-(1) True stress-strain curve for injection-moulded HDPE specimen. Numbers below are the strains. (2) Volume strain of HDPE specimen as a function of strain [61].

The true stress-strain curve for tensile deformation of injection-moulded high-density polyethylene specimen is shown in Figure 19 (1) and respective changes in the volume strain are depicted in Figure 19 (2). The increase of volume due to cavitation is seen for strains in the range of 0.3 and 2. The region of constant volume strain is a result of strong localization of deformation in neck [61].

According to Humbert et al. [48], two parameters are governing cavitation and crystalline shearing on polyethylene: density of stress transmitters (tie molecules and entanglements) and crystal thickness. Cavitation occurs when the stress in the system exceeds a certain critical stress needed for cavitation. They calculated the dependences of those stresses as a function of crystal thickness and showed that certain critical thickness exists, above which the cavitation is more probable. Also, the onset of cavitation was followed up by small angle X-ray scattering in-situ tensile test. It was found that, depending on polyethylene microstructural and molecular parameters, cavitation can be avoided or, on the contrary, appears before or after yielding. In the case of polyethylenes with thicker crystalline lamella, the cavities initiate before yielding, while polyethylenes with thinner crystalline lamella the cavities initiate after yielding. In high-density polyethylene the phenomenon of cavitation generally appeared close to yielding. The cavity volume is found to be higher when the molecular weight is low. Low molecular weights generate fewer entanglements during crystallization, which favours a larger amount of cavities.

2.2.4 Microfibril Formation

The phenomena of cold drawing following necking of semi-crystalline polymers involves conversion of spherulite structure into an oriented microfibrous structure. Microfibril formation seems to be restricted to the high-strain stage and tensile deformation. Peterlin [62] proposed that microfibrils formation process was associated with the fragmentation of the lamellar

crystals into blocks that were reorganized into a new crystalline oriented assembly, via chain unfolding from the fracture surface of the crystal blocks, during cold drawing. Figure 20 depicts, the microfibrils originate at the crack edges at micronecks which transform the lamellae into the fully oriented fibre structure.



Figure 20 - Microfibrils pulled out at the crack of polyoxymethylene (POM) single crystals [62].

The microfibrils contain completely oriented folded chain crystalline blocks alternating with amorphous layers in axial direction. During the deformation process, the temperature increases in the neck, which imparts mobility to the chains in the crystal blocks. However the deformation does not produce enough heat for complete melting [62]. Intrinsic material parameters, such as crystallinity, and external parameters, such as temperature or strain-rate, influence the phenomena of cold drawing hardening and thereby the neck profile [44].

Jiang et al. [63] argumented, that upon tensile deformation, block slippage within the crystalline lamellae takes place firstly, followed by the stress-induced fragmentation and recrystallization. In their work, the micro-structural evolution of HDPE at different deformation ratios after stretching at different temperatures by means of combined synchrotron small-angle X-ray scattering and wide-angle X-ray scattering technique was investigated. It was found that a common sequence of deformation processes is active in specimens elongated below 100 °C, whereas deforming the specimen at the temperature of 120 °C, the original lamellar crystallites melt and recrystallize. The crystal blocks form with their normal parallel to the stretching direction.

2.3 Thermal Transitions in Semi Crystalline Polymers

Polymers have a quite significant level of change in physical properties over a relatively small change in temperature, which are largely determined by their molecular structure and the resulting bonding relations. The two major thermal transitions in polymers are the glass

transition temperature (T_g) and the melting temperature (T_m). Most physical properties of polymers change significantly around glass transition temperature, including the viscosity, elastic modulus and strength [4].

2.3.1 Amorphous Polymers

Polymers with low degree of crystallinity (largely amorphous), the glass transition temperature will determine the maximum service temperature, since above that temperature, the polymer change from hard to a soft rubbery state and ultimately becomes a viscous liquid at higher temperatures without any sharp transition [4]. The glass transition marks the onset of extensive motion of atoms and molecule segments, causing the polymer to lose its molecular cohesion. Beyond stiffness, other changes in properties are noticeable, such as specific volume, elastic modulus and hardness [3].

Figure 21, illustrates the five regions of viscoelastic behaviour for amorphous polymers: (a-b) glassy region, (b-c) glass transition temperature, (c-d) rubbery plateau, (d-e) rubbery flow region and (e-f) liquid flow region, explained as follows:

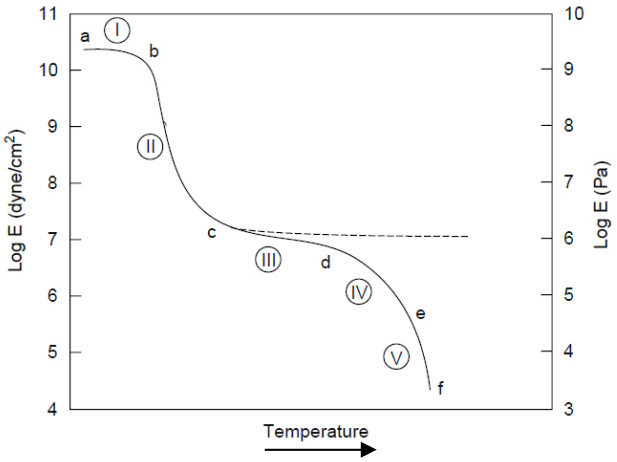


Figure 21 - Five regions of viscoelastic behaviour for amorphous polymer. Also illustrated is effect of cross-linked polymers (dashed line) [4].

- Glassy region (a-b): the polymer is glassy, rigid and brittle. At low temperatures, the chains cannot rotate or move in space [4].

- Glass transition (b-c): is the glass transition region temperature, also called primary relaxation or *α* process. It is related to the motion of long sections of polymer chains and short main chain segments relative to others, additionally several side chains might move as a unit within a macromolecule. The behaviour of polymers in this region is best described as leathery [4, 42].

- Rubbery plateau (c-d): in this region, entanglements act as temporary crosslinks in a network with a flexible-chained polymer. Two possible deformation cases are distinguished. First, if the polymer is linear (structure), the solid line is followed on which the modulus drops off slowly

with increasing temperature. The length of the plateau is governed primarily by the molecular weight of the polymer; the higher the molecular weight, the longer the plateau. Second, if the polymer is cross-linked, the dashed line is followed [4, 42].

- Rubbery flow region (d-e): the polymer is in the rubbery flow region. The polymer exhibits both rubber elasticity and flow properties. Does not occur for cross-linked polymers [4].

- Liquid flow region (e-f): is the liquid flow region which is reached at higher temperatures [4].

2.3.2 Semi Crystalline Polymers

For semi crystalline polymers (high degree of crystallinity) the glass transition temperature is only of secondary importance. For them it is the melting temperature, which will limit the maximum operating temperature. This is due to the presence of both the amorphous and crystalline phases. At melting temperature, the crystalline domains lose their structure or melt, whereas in the glass transition temperature the amorphous domains lose the structural mobility of the polymer chains and become rigid glasses. Increasing the degree of crystallinity increases the melting temperature. Between glass transition and melting temperatures, semi crystalline polymers tend to behave as a tough and leathery material. Semi crystalline polymers are used at temperatures lying above glass transition and below melting temperature. In a perfectly crystalline polymer no glass transition would be observed, due to the absence of disordered polymer chains [4].

2.3.3 Specific Volume

The different thermal response in the transition from a rigid solid to an eventually liquid state can be graphically represented as the change in specific volume. Commonly, the specific volume of polymers is measured as a function of pressure and temperature using the technique of dilatometry. The measured quantity, the specific volume, reflects accurately the state and the changes of state of materials [64]. It is commonly referred to as Pressure-Volume-Temperature behaviour or PVT-behaviour. The change of volume for an amorphous and a semi crystalline polymer with increasing temperature is shown in Figure 22 [65].

From Figure 22 it is observed that, polycarbonate shows a glass transition, detectable as a change in the slope of the volume temperature dependency. Polyethylene shows a melting transition, resulting in a step-like increase of specific volume in dependence on temperature [65].

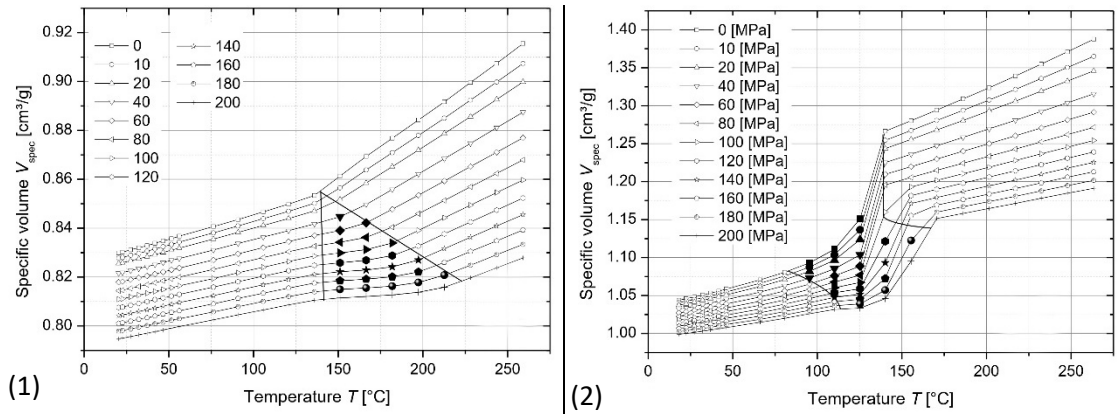


Figure 22 - The typical PVT-behaviour of an (1) amorphous (polycarbonate) and (2) semi-crystalline polymer (polyethylene). The open symbols characterise the equilibrium state of the polymers, whereas the solid symbols the transition ranges [65].

2.4 Evaluation of Mechanical and Physical Properties of Polymers

2.4.1 Tensile Test

Tensile testing is the most frequently used approach for structure or component performance research. Young's modulus, stress and strain at yield point, and stress and strain at break point (which are indications for cold-drawn ability) are some important properties associated with a tensile test [9, 55].

Tensile testing machines are designed to elongate specimens of materials at a constant rate and monitoring both the force required to pull a material apart and the displacement that the material undergoes as a result of the applied force at a constant deformation rate [4, 9, 55]. The degree to which a material strains depends on the magnitude of the imposed stress. This stress is defined as the force per unit area given as follows [9, 55, 66]:

$$Stress\ (\sigma)\ (MPa) = \frac{Force\ (F)\ (N)}{Area\ (A)\ (mm^2)}\ . \tag{2.1}$$

Stress (σ) is the force applied to produce deformation in a unit area of a test specimen and the ratio of applied load to the original cross-sectional area and is expressed in MPa. It should be noted that the nominal stress or engineering stress which is measured in tensile test is based upon the original dimensions of the cross-sectional area prior to the application of any force, whereas the true stress is the applied load divided by the actual cross-sectional area (the changing area with respect to time) of the specimen at that load [9, 41, 55, 66].

The strain is defined as the amount of deformation per unit length of the material due to the applied load, and is given as follows [9, 55, 66]:

$$Engineering\ Strain\ (\%) = \frac{l_1 - l_o}{l_o} \times 100\,. \tag{2.2}$$

Where l_o is the original length of the test specimen before any load is applied, l_1 is the instantaneous length followed force application and $(l_1 - l_o)$ is the amount of elongation. It is common practice to express as a dimensionless ratio and it is also known as nominal strain or engineering strain (ε_e), whereas true strain or logarithmic strain (ε_t) equals the natural log of the quotient of current length over the original length as given by equation [9, 55, 66]:

$$True\ Strain\ = \ln\left(\frac{l_1}{l_o}\right). \tag{2.3}$$

The relationship between stress and strain in the linear elastic regime is known as the elastic modulus (Young modulus) (E) and is usually measured in GPa [9, 55, 66]:

$$Elastic\ Modulus\ (GPa) = \frac{Stress\ (MPa)}{Strain \times 1000}. \tag{2.4}$$

Test method, specimens and ISO 527-1 / ISO 527-2: A comprehensive set of standards that cover the tensile testing of plastic materials, has been drawn up and covered in the various parts of ISO 527, which includes the testing of moulding compounds, films and sheets, as well as fibre composite materials [42, 66].

The tensile testing machine should be of the constant rate of crosshead movement type, consisting of one fixed and one movable members, both carrying self-aligning grips. Self-aligning grips are required to hold the specimen. The movable member shall move with a uniform, controlled velocity with respect to the fixed member [67]. A uniaxial loading and stress state should be generated in the specimen. The two parameters that are measured during a tensile test are load and displacement. The load cell measures the magnitude of the applied load on the specimen. The two most common methods existing for displacement measurement are: machine crosshead motion (the displacement of the crosshead is assumed to be the specimen displacement) and extensometer which measures the elongation between two designated points within the gauge length of the test specimen as this is stretched. With load, displacement and time data, the stress in the specimen and the amount of deformation, or strain, can be calculated for each time increment and result in a stress-strain diagram as show in Figure 10 [68].

Ultimate strength, elongation, and elastic modulus can be obtained from the stress-strain diagram. For determining elastic modulus the slope of the initial tangent is measured (Figure 10) [4]. The speed of testing is the relative rate of motion of the crosshead during the test. ISO 527-1 specifies that any testing machine used shall be capable of maintaining the speeds of testing given in Table 1. The most frequently employed speed of testing is 5 mm/min and 50 mm/min [55, 66].

Table 1 - ISO 527 part 1 recommended testing speed [55, 66].

Speed (mm/min)	Tolerance (%)
1, 2, 5, 10	± 20
20, 50, 100, 200, 500	± 10

Test specimens for tensile tests can be prepared in many different ways such as injection moulded or compression moulded. The specimens may also be prepared by machining operations from materials in sheet, plate, slab or similar forms [41]. A minimum of 5 specimens are required by ISO 527-1 for each direction tested and if different speeds are used for modulus and ultimate strength then separate sets of specimens will be needed. The preferred test specimens that are applicable to this standard (ISO 527-2) are either dumbbell Type 1A or 1B, see Figure 23 and Table 2, with type 1A being used for directly moulded specimens and type 1B for machined specimens [55, 66, 69].

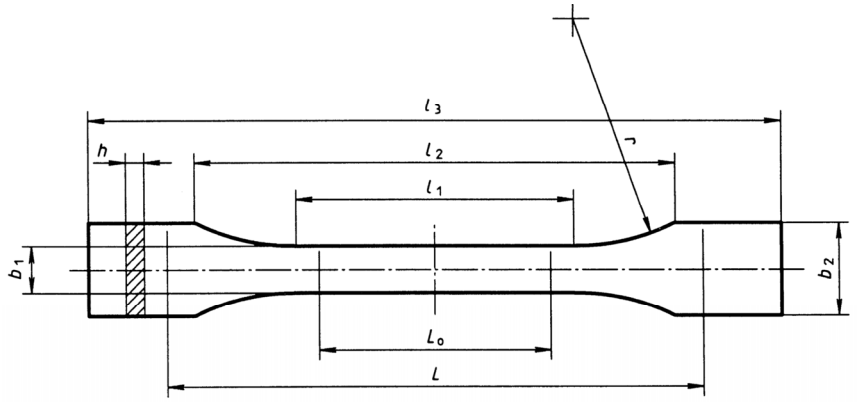


Figure 23 - Test specimens type 1A and 1B, shape [42, 69].

Table 2 - Test specimens type 1A and 1B, dimensions [42, 69].

	Type 1A (mm)	**Type 1B (mm)**
l_3	≥150	≥150
l_2	104 to 113	106 to 120
l_1	80 ± 2	60 ± 0.5
b_2	20 ± 0.2	20 ± 0.2
b_1	10 ± 0.2	10 ± 0.2
h	4.0 ± 0.2	4.0 ± 0.2
L_0	50.0 ± 0.5	50.0 ± 0.5
L	115.0 ± 1	$l_2 + 5$
r	20 to 25	≥60

Since the tensile properties of some plastics change rapidly with small changes in temperature, it is recommended that tests are conducted in the standard laboratory atmosphere of 23 ± 2°C and 50 ± 5 percent relative humidity [41, 66].

Data acquired by tensile testing can be influenced by the state and properties of the moulding specimen (chemical structure, viscosity, molecular weight and its distribution), the process employed to prepare the specimen (morphology, residual stresses, orientation degree of crystallinity and machining), specimen geometry (dumbbell specimens or flat specimens), test conditions (regarding temperature and crosshead speed) and any occurring damage mechanisms, which can lead to a wide spectrum of material values [41, 42].

2.4.2 Compression Test

Compressive properties describe the behaviour of the material when it is subjected to a compressive load and uniform rate of loading. Under compressive load, a homogenous uniaxial stress state arises in the test specimen, which corresponds to normal stress and strain distributed uniformly over the cross-section [41]. The resulting compression stress and strain can be calculated using the same equations of the tensile test [42].

ISO 604 standard specifies test methods and specimen geometry aiming at the evaluation of compressive properties of reinforced and unreinforced rigid plastics under defined conditions. The universal testing machine used for tensile testing can also be used for compressive testing of various materials. The compression takes place between parallel steel plates and strain is normally measured by machine crosshead displacement [70].

The shape of the specimen can be quite varied in terms of the cross-section and the slenderness ratio. The standard allows the use of right prisms, cylinders or tubes for cross section. Specimens for compression testing must have very flat and parallel end faces. Specimens may be prepared by machining or moulding [42, 55]. ISO 604 specifies the following equation for defining an adequate ratio between specimen dimensions and the clamping length between compression plates [70]:

$$\varepsilon_{c^*} \leq 0{,}4 \left(\frac{y}{l}\right)^2 . \tag{2.5}$$

In this equation, ε_{c^*} is the maximum nominal compressive strain occurring during the test; l is the specimen length and y is the diameter if the specimen is a cylinder, the outer diameter if it is a tube. An y/l ratio not less than 0.08 is recommended for measuring the compression modulus and for other compressive tests not less than 0.4. Two preferred specimen sizes are: for modulus, length = 50 mm, width = 10 mm and thickness = 4 mm and for strength, length = 10 mm, width = 10 mm and thickness = 4 mm. The requirements for test speed are chosen from 1, 2, 5, 10 or 20 mm/min, the choice depends on the nature of the material and the measurement being made. Hence, for the standard specimens, the most appropriate speed for modulus and for the strength of brittle materials is 1 mm/min, and 5 mm/min for the strength of ductile materials. A minimum of 5 specimens are required by ISO 604 for each specimen in the case of isotropic materials [42, 55, 70].

Another factor affecting the geometric dimensions of specimens in compression test is the buckling. In order to minimize that occurrence, the slenderness ratio λ, must be 10 or at least 6. The slenderness ratio is defined as the ratio of specimen length l to the smallest radius of inertia i of its base area [42]:

$$\lambda = \frac{l}{i} . \tag{2.6}$$

The smallest radius of inertia of base area i of the specimen results from [42]:

$$i = \sqrt{\frac{I_y}{A_o}} . \tag{2.7}$$

Whereby, I_y is the smallest axial inertia moment and A_o is the cross-section area of the specimen in the initial state. For the specimens in study the I_y and A_o are calculated using the fallowing equations. Where, d is the initial cross-section diameter [42]:

$$I_y = \frac{\pi d^4}{64} \quad \text{and} \quad A_0 = \frac{\pi d^2}{4} \cdot \tag{2.8}$$

In the compression test, the interfacial friction between the specimen and the compression plates and the consequent barrelling of specimens are factors that affect axisymmetric compression and the uniaxial compressive stress state. This expresses itself in hindered deformation of the base areas. Therefore, the plastic deformation zone will be located in the centre of the test specimen. To minimize this influence, friction between specimen and compression plates can be reduced by lubricants or by Teflon sheets between the specimen or load/unloading schemes [42].

2.5.3 Dynamic Mechanical Analysers (DMA)

Dynamic mechanical analysis enables simultaneous study of both elastic and viscous behaviour of materials measured during a linear temperature scan under heating conditions. Also, DMA can be used to determining a value of the glass transition temperature of the material and identify transitions corresponding to other molecular motions [67].

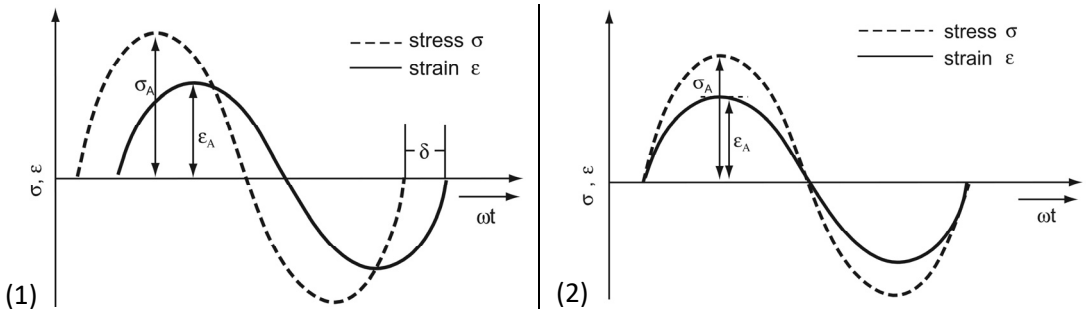


Figure 24 – (1) The relationship of the applied sinusoidal stress to strain is shown, with the resultant phase lag (δ) and strain. (2) Stress–strain behaviour of a purely elastic material [71].

When an oscillatory force is applied in dynamic mechanical analysis to characterize viscoelastic properties, the specimen is subjected to sinusoidal alternating mechanical loading at constant frequency and constant amplitude. From this oscillatory force the resulting strain is measured [72, 73]. By measuring both the amplitude of the deformation at the peak of the sine wave and the lag between the stress and strain sine waves, properties like the stiffness (modulus), the viscosity caused by viscoelastic changes taking place in the specimen and damping can be calculated (Figure 24 (1)) [71, 72].

The time dependence of material behaviour can be characterized by varying the frequency. The complex modulus (*E**) is the ratio of stress amplitude (σ_A) to strain amplitude (ε_A) and represents the stiffness of the material. The magnitude of the complex modulus is [71]:

$$|E^*| = \frac{\sigma_A}{\varepsilon_A} \cdot \tag{2.9}$$

The complex modulus is composed of the storage modulus (E') (in-phase component) and its mechanical damping, the loss modulus (E'') (out of phase component). The ratio between the loss modulus and storage modulus is the loss factor tan (δ) and represents mechanical damping or internal friction in a viscoelastic system [42]. According to ISO 6721-1, the storage modulus E'measures the stored energy during the oscillation period, representing the elastic portion, by contrast the loss modulus measures the energy dissipated as heat during the oscillation, representing the viscous portion [74].

The material is perfectly elastic when the stress and strain are in phase (δ= 0) and the complex modulus becomes equivalent to storage modulus, therefore (*E*=* E'). Steel is an example of an almost purely elastic material (Figure 24 (2)) [71].

The specimen geometry may be in rectangular form. Due to the numerous types of dynamic mechanical analysers, specimen size is not fixed by this test method. In many cases, specimens measuring between 1 × 5 × 20 mm and 1 × 10 × 50 mm are suitable [74].

2.4.4 Testing of Physical Properties - Differential Scanning Calorimetry (DSC)

Differential scanning calorimetry is an analytical tool for characterizing the physical properties of a polymer measured as functions of temperature and/or time. DSC enables determination of the melting temperature and crystallization, glass transition temperature**,** amount of crystallinity and caloric quantities as specific heat capacity (C_p) and its integral over temperature, measured via calorimetry [42, 75]. The crystal weight fraction ($\emptyset_{cw}$) is calculated as the ratio of the measured melting enthalpy (ΔH_f) and the theoretical melting enthalpy of a perfect polymer crystal (ΔH^0_f). For HDPE, PP and PA 6 considered in this research are: 293 J/g, 209 J/g and 188 J/g, respectively [5, 76].

$$\emptyset_{\mathrm{cw}} = \frac{\Delta \mathrm{H}_f}{\Delta \mathrm{H}_f^0} \cdot \tag{2.10}$$

The most common mode of operation of a DSC is heating or cooling at constant rates. According to ISO 11357, the test specimens, in solid state might be in the form of a powder, pellets or granules small enough to fit in a small holder within an adiabatic enclosure [77]. DSC commonly is composed of a measurement chamber with two specimen positions, one for the test specimen under investigation and other for a reference specimen (an empty crucible or an inert material) [13].

The rate of temperature changes for a given amount of heat will differ between the test and reference specimens. This difference depends on the composition of the test specimen contents as well as physical changes such as phase transitions [9]. As test and reference specimens are

subjected to identical temperature, more or less heat will be needed to provide to the test specimen in order to keep the temperature of both nearly identical. Whether less or more heat must flow to the test specimen depends on whether the process is exothermic or endothermic. The primary outcome of such an experiment is heat flow rate as a function of time. If temperature of the specimen position is known, data can be represented as heat flow rate versus temperature [42, 75].

2.4.5 Microstructure Observation by Scanning Electron Microscopy (SEM)

Scanning electron microscopy, is a useful tool for investigating the micro- and nano-structural characteristics of solid objects with excellent depth of field. SEM is a type of electron microscope that produces images of a specimen by scanning the surface with a focused beam of electrons in a vacuum and using the scattered secondary electrons to create highly magnified image of the material surface [41].

The electrons interact with atoms in the specimen at various depths, producing various signals that contain information about the specimen's surface topography and composition. The electron beam is scanned in a raster scan pattern, and the beam's position is combined with the detected signal to produce an image. The SEM uses a PC to control the electron beam, to select the signals, and to record as well as to store the digital image(s) [78].

Specimens for SEM have to be prepared to withstand the vacuum conditions and high energy beam of electrons and have to be of a size that will fit on the specimen stage. Specimens are generally mounted rigidly to a specimen holder or stub using a conductive adhesive. Electrically non-conducting specimens such as HDPE, PP and HDPE are usually coated with an ultrathin coating of electrically conducting material, deposited on the specimen [79]. SEM has been used for a broad range of polymer studies and applications, including surface roughness, adhesive failures, fractured surfaces, networks, and phase boundaries in blends [9].

2.4.6 Notched Specimens – Literature Review

Specimens generating different stress states have been suggested in several studies. Some of these specimens are in Table 3, Table 4, Table 5, Table 6, Table 7 and Table 8:

These specimens are used to extract a variety of properties including elastic and plastic behaviour, yield stress and fracture strain. However, each of these specimens introduces a limit on some of the desirable characteristics of the experimental configuration such as: large non-uniformity of stress in the gauge region and rely on numerical analysis for experimental interpretation, because in most experiments the local stress state cannot be calculated based on force measurements using analytical formulas. A hybrid experimental-numerical approach is therefore required. Although altogether, these specimens provide a large variety of stress combinations [80]. From the above literature review it can be highlighted that the specimens already used with polymers materials, are: shear compression specimens (Table 3), cruciform specimen (Table 6) and cylindrical notched tensile specimens (Table 7).

Table 3 – Shear compression specimens (SCS).

Shear Compression Specimens (SCS)

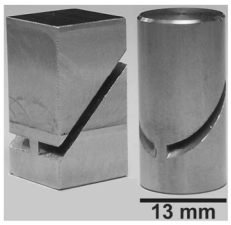
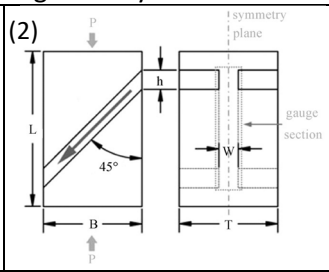
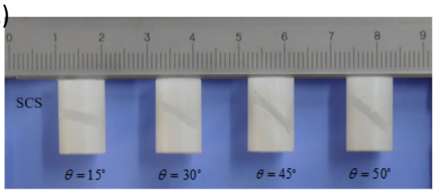
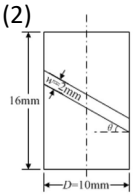
Specimen geometry	Author, material and description
(1)  (2) 	Ames et al.[81]. Stainless steel. (1) SCS Beam-type geometry (left) and cylinder-type geometry (right). (2) Layout of the SCS geometry. The relevant geometrical parameters, as well as the directions of uniaxial loading (P) and the resulting shear displacement are indicated.
(1)  (2) 	Duan et al. [82]. Polyamide 66 (PA66). (1) The SCS geometry consists of two slots machined at different angles θ (15°, 30°, 45° and 50°) with respect to the longitudinal axis. (2) Layout of the SCS geometry.

Table 4 – Shear tensile specimens.

Shear Tensile Specimens

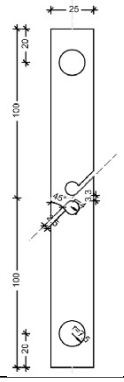
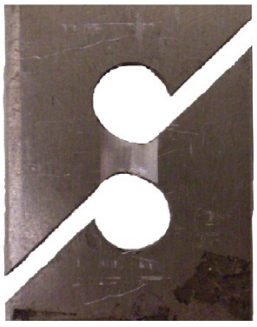
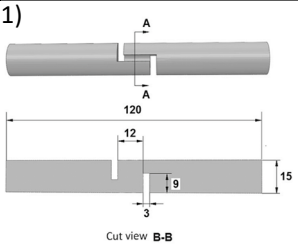
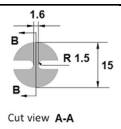
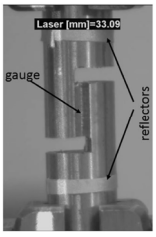
Specimen geometry	Author, material and description
(1)  (2) 	Brunig et al. [83]. Aluminium alloy. (1) Geometry of the flat shear specimen. (2) Specimen detail.
(1)   (2) 	Dorogoy and Rittel [84]. 1020 cold drawn steel. (1) The quasi static specimen dimensions. (2) A mounted specimen in the servo hydraulic machine.

Table 5 - Combined tension and shear – Torsional tubing specimens.

Combined Tension and Shear – Torsional Tubing Specimens

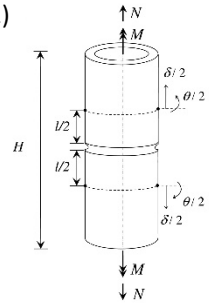
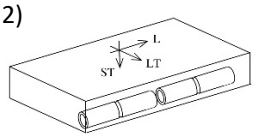
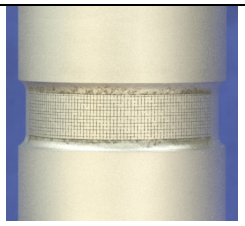
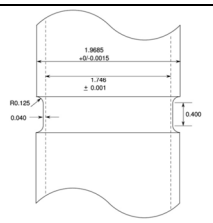
Specimen geometry	Author, material and description
(1)  (2) 	Barsoum and Faleskog [85]. High-strength steel - Weldox 420 and Weldox 960. (1) Configuration of the double notched tube specimen. Tests were performed on circumferentially double notched tube specimens subjected to a combination of tensile and torsional loading. (2) The orientation of the specimen with respect to the rolled plate.
(1)  (2) 	Haltom et al. [6]. Al-6061-T6. (1) Tubular specimen used in the tension-torsion radial stress experiments. Photograph showing the square grid placed on the test section. (2) Drawing showing the test section.

Table 6 – Biaxial loading tests – cruciform specimen.

Biaxial Loading Tests – Cruciform Specimen

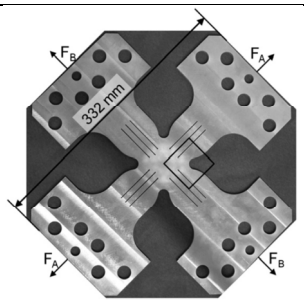
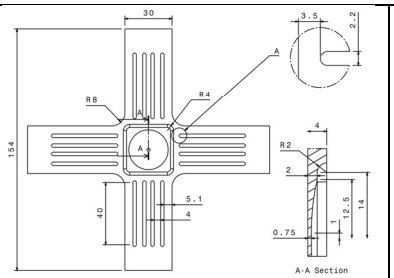
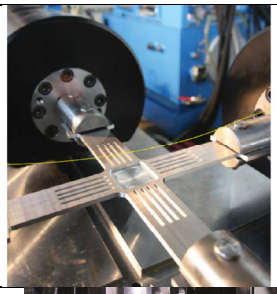
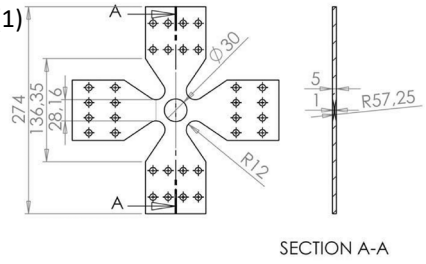
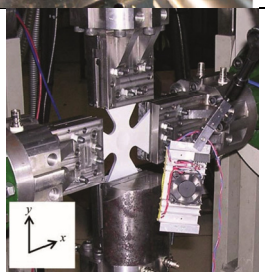
Specimen geometry	Author, material and description
	Kulawinski et al.[86]. Metastable austenitic stainless cast steel. Cruciform specimen of static biaxial planar testing was developed by FE simulations to achieve a uniform stress and strain distribution in the measuring field.
(1)  (2) 	Leotoing et al.[87]. Aluminium alloy. (1) Specimen shape and dimensions. (2) Cruciform specimen tested by a servohydraulic machine with four independent actuators.
(1)  (2) 	Ognedal A. [88] HDPE and PVC (1) Specimen shape and dimensions. (2) Biaxial tension specimen in the Astree testing machine.

Table 7 – Notched tensile specimens.

Notched Tensile Specimens

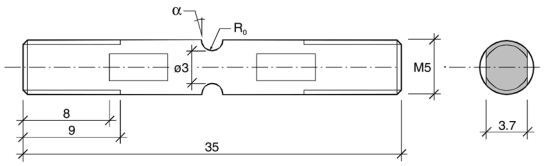
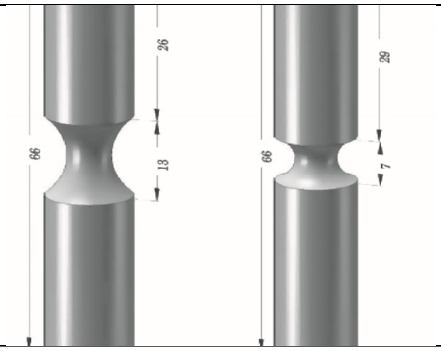
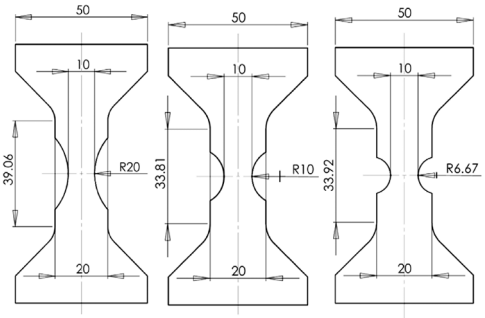
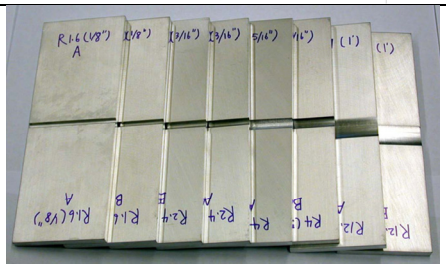
Specimen geometry	Author, material and description
	Borvik et al. [89]. Weldox 460 E steel. Geometry and dimensions of notched test specimens for high rate tests with R_0 = 0.4 mm and 0.8 mm and R = 2 mm. Tension Bar (in mm). For manufacturing reasons, the side faces of the notch were inclined at an angle α = 17.5° to the normal of the specimen axis.
	Hachour et al.[5]. High-density polyethylene (HDPE). Shape and dimensions of the notched round bar specimens (All dimensions are in mm).
	Dunand and Mohr [90]. TRIP780 steel. Flat tensile specimens with different circular cutouts.
	Bai and Wierzbicki [8][91] Aluminium 2024-T351. Tensile tests of flat grooved plates. The width of the specimens is 50 mm. Four types of radii of the grooves are machined: 12.7 mm, 3.97 mm, 2.38 mm, and 1.59 mm.

Table 8 – Notched compression specimens.

Notched Compression Specimens

Specimen geometry	Author, material and description
	Bao and Wierzbicki [92]. 2024-T351 aluminium alloy. The specimens were machined as large diameter round bars with a notched small gauge section in the middle. The deformation is very localized in the gauge section and fracture initiation occurred at the equatorial area.

2.6 Mechanical Testing under Multiaxial Stress States

Some possible test methods and specimens configurations, for composite laminate materials under uniaxial and multiaxial, in-plane and out-of-plane loading conditions are reviewed by Olsson, in which both biaxial arcan apparatus and arcan specimen are included [93]. Arcan specimen was developed to produce and measure a uniform plane stress condition in solid specimens within the minimum gauge section being subjected to shear and tensile/compressive loading. Originally arcan specimen was proposed as a monolithic, plane circular with anti-symmetric cut outs, resulting in a small and central test zone. The monolithic arcan specimen were cut out of a single plate and could be directly installed into a universal testing machine [94].

The original version of arcan specimen has been modified and improved, resulting in two main components: the butterfly specimen, which is joined on either side with two half-circular grips, also known as arcan apparatus. The geometric parameters of arcan apparatus and butterfly specimen (notched or not) are chosen in order to guarantee the uniformity of stresses at significant section. Furthermore, by adding an array of loading holes in both half-circular grips, it became possible to achieve arbitrary combinations of biaxial loadings (pure shear, combined shear and tension/compression, pure tension/compression) [93, 95].

There are two possible configurations for the arcan apparatus: the standard configuration, which allows the arcan grips to rotate; and the clamped configuration, which prohibits rotations of the arcan grips [95].

2.6.1 Arcan Standard Configuration (One Pin) - Analytical Formulas

The joint between the arcan grips and the testing machine is a single pin (Figure 25). Horizontal and vertical displacements are controlled at the joint, but rotations of the grips are allowed [95].

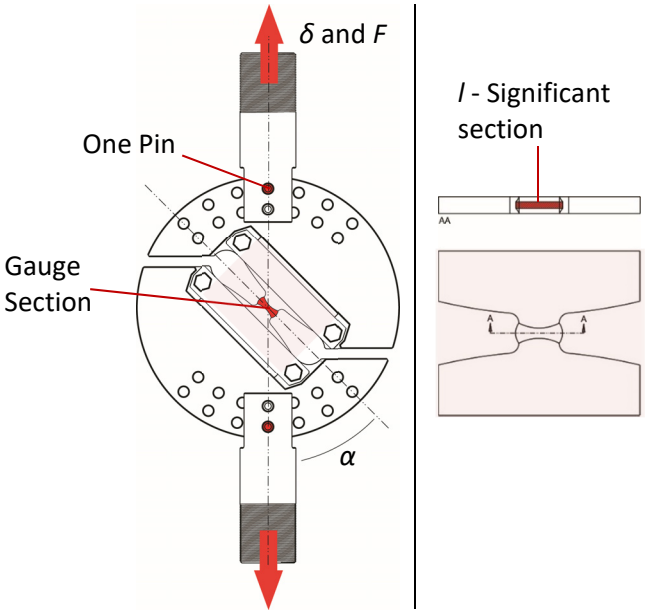


Figure 25 - Arcan standard configuration.

Figure 25 is the schematic of modified arcan apparatus with a butterfly-shaped specimen subjected to a displacement (δ) at a loading angle α (from 0° to 90°) and the section (l) (the significant section of the test specimen). F is the vertical force (applied force). Since section l is expected to be under uniform plane stress, the average stress and shear in the significant section can be estimated with the following arcan equations [94]:

$$Stress\ (\sigma_{xx})\ (MPa) = \frac{F}{Area} sin\ (\alpha)\ , \tag{2.11}$$

$$Shear\ (\sigma_{xy})\ (MPa) = \frac{F}{Area} cos\ (\alpha)\ . \tag{2.12}$$

2.6.2 Arcan Clamped Configuration (Two Pin) - Analytical Formulas

With two pins, not only the horizontal and vertical displacements are controlled, avoiding any out-of-plane motion, but also prohibit the rotations between arcan assemblies. Since arcan grips and butterfly specimen are aligned along the loading axis, the measurement of the vertical force (F), is not influenced. However, when the testing machine applies a vertical force, a perpendicular reaction force (R), is generated. The presence of a reaction force is the basic difference between the current set-up (Figure 26) and the original arcan apparatus (one pin). In the original design by Arcan, the apparatus is joined to the testing machine by a single loading pin, thus allowing rotations, resulting in zero reaction force [95].

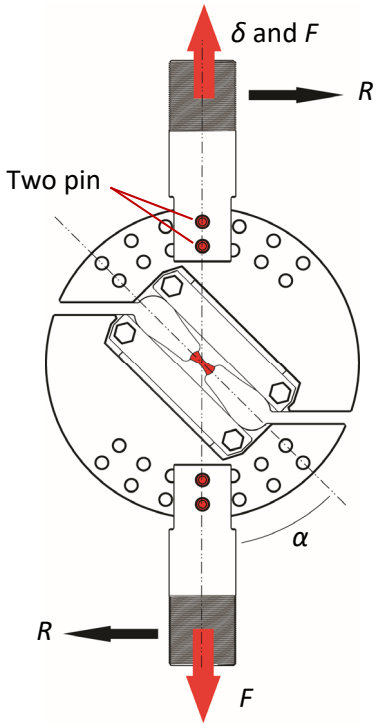


Figure 26 - Arcan clamped configuration.

If α is the biaxial loading angle, then the normal stresses and shear at the central section are [96]:

$$Stress\ (\sigma_{xx})(MPa) = \frac{F}{Area} sin\ (\alpha) - \frac{R}{Area} cos\ (\alpha)\ , \tag{2.13}$$

$$Shear\ (\sigma_{xy})(MPa) = \frac{F}{Area} cos\ (\alpha) + \frac{R}{Area} sin\ (\alpha)\ . \tag{2.14}$$

If the elastic properties of the plastic are known beforehand and the specimen is tested in the linear elastic regime, then it is not necessary to include a load cell in order to measure the reaction force during biaxial loading. Using theoretical and finite element analyses, Mohr and Doyoyo derived expressions for the average shear (σ_{xy}) and average normal stresses (σ_{xx} and σ_{yy}) at the central section of the specimen in the elastic regime [95–98].

$$Stress\ (\sigma_{xx}\ )(MPa) = \left(\frac{\beta_x\ sin \propto}{(1 - \beta_x) \cos^2 \propto + \beta_x}\right) \times \frac{F}{Area}\ , \tag{2.15}$$

$$Stress\ (\sigma_{yy}\ )(MPa) = \nu \times \sigma_{xx}\ , \tag{2.16}$$

$$Shear\ (\sigma_{xy})(MPa) = \left(\frac{cos \propto}{(\beta_x - 1) \sin^2 \propto + 1}\right) \times \frac{F}{Area}\ . \tag{2.17}$$

Where β_x is the specimen stiffness ratio. For an isotropic specimen with elastic Poisson's ratio of ν, the stiffness ratio is [95–97]:

$$Stiffness\ ratio\ (\beta_x)\ = \frac{2}{1 - \nu}\ . \tag{2.18}$$

The absence of rotations using arcan clamped configuration is indispensable for the biaxial testing of soft materials like those concerned in this study, high density polyethylene, polypropylene and polyamide 6, in order to prevent the out-of-plane displacements. Without clamping, the two arcan grips could rotate with respect to each other and cause undesired deformation localization at the ends of the significant section of a butterfly specimen. Furthermore, with the clamping configuration the localization of deformation is controlled, as a consequence of the specimen shape and forced to occur along the significant section [96].

2.6.3 Arcan Apparatus - Literature Review

While the arcan specimen was primarily designed for the biaxial testing of fibre-reinforced composites, other improvements have shown that the modified arcan apparatus set up can also be used with cellular solids, metallic, fibre-reinforced composites, plastic materials as well as on spot welds connections.

Arcan apparatus with cellular solids materials: A failure criterion for Nomex honeycomb core under combined out-of-plane compressive and shear loading has been determined using arcan apparatus in its clamped configuration, by Petras and Sutcliffe [99]. Doyoyo and Wierzbicki [96] used the arcan apparatus to investigate and determine the yield surface of ductile isotropic and

brittle anisotropic closed-cell aluminium foams. They also extended the originally arcan specimen to butterfly-shaped honeycomb and metallic foams specimen. Zou et al. [97] investigated the yield behaviour of closed-cell aluminium alloy foams with arcan apparatus. Combined compression-shear tests under four loading rates were conducted in order to determine their initial yield surface. Also, the influence of the loading rate on the initial yield surface under multiaxial loading conditions, was investigated.

Arcan apparatus with metallic materials: The effect of stress states on the ductile fracture of Docol 600DL steel has been studied extensively at low strain rates, by Gruben et al. [100]. The tests were conducted on a series of specimens with different geometries in order to create different combinations of stress states. The tests ranged from plane-strain to shear tests. The arcan apparatus was modified based on the original arcan specimen and the test series were carried on a new designed notched specimen. Ghahremaninezhad and Ravi-Chandar [101] have used a modified arcan test to study the ductile fracture of polycrystalline Al 6061-T6. The deformation and failure evolution were examined under some combinations of tension and shear or compression and pure shear.

Arcan apparatus with fibre-reinforced composites: The mixed-mode interlaminar fracture behaviour in woven carbon fibre/polyetherimide was investigated, by Choupani [102]. Experiments were performed on modified arcan specimen. With the same test specimen configuration and by varying the angle from 0° to 90°, a wide range of mixed-mode, mode-I (pure opening) and pure mode-II (in-plane shearing) data were obtained experimentally. Nikbakht and Choupani [103] studied experimentally and numerically, the behaviour of interlaminar fracture of woven carbon/epoxy composite. A modified version of arcan specimen was employed to conduct mixed-mode, mode I and mode II fracture tests. Different loading angles, ranging from 0° to 90° made possible different mixed mode ratios. All loading conditions were generated by the same type of specimen configuration. Similar approach was applied by Gning et al. [104] to determine the material fracture behaviour of glass/epoxy composite. Butterfly-shaped specimens have been extensively tested and were loaded in pure shear, pure tension and combined shear coupled with tension. For all specimens, the fracture localization was more or less located in the significant section. Fracture phenomenology in terms of mechanism and load levels was described.

Cognard et al. [105] analysed the mechanical behaviour of composites and their adhesive bonded assemblies under tensile-shear out-of-plane loadings, using a modified arcan set up. Numerical studies were developed in order to analyse and optimize the design of such system. Hung and Liechti [106] examined the strain fields and their uniformity in laminate specimens under shear loading. Arcan type specimens with various fibre orientations were obtained from a single plate of unidirectional fibre reinforced thermoplastic. The strains were measured using moiré interferometry. El-Hajjar and Haj-Ali [107] designed an arcan apparatus and a butterfly specimen to measure the in-plane shear modulus, nonlinear stress-strain response of fibre reinforced plastic under shear combined with different biaxial stress conditions.

Arcan apparatus with semi crystalline polymers: The method initially proposed by Arcan et al. was used by Mae [108] to investigate the material ductility of polypropylene (PP) blended with ethylene-propylene rubber (EPR) and talc fillers. Butterfly specimens were tested to fracture

under pure shear, pure tension, combined tension and shear at various loading velocities. Hachour et al. [5] examined the mechanical response of high density polyethylene (HDPE) under different stress states and verified the classical yield criteria by comparison with the results of the measurement of biaxial yield envelope. The yield behaviour of HDPE material was investigated from a series of biaxial tension/shear and compression/shear tests using butterfly-shaped specimens with a modified Arcan apparatus.

Arcan apparatus on spot welds connections: In order to investigate the failure characteristics of spot-welded plates, Langrand and Combescure [109] adopted an experimental set-up based on the Arcan test principles. The spot-welded plates were tested under quasi-static and dynamic loading conditions and in pure and combined opening/shear modes.

2.6.4 Butterfly Specimens – Literature Review

The literature includes some variations on the butterfly specimens. The original specimen proposed by Mohr features a flat gauge section of uniform thickness [94]. Wierzbicki et al. [110] modified that geometry by including a complex lofted surface into the gauge section to assure that fracture always occurs at the same location, resulting in a specimen with a non-flat gauge section, which reduces the possibility of crack formation at the boundaries. The new specimen design is tested in combined tension/compression and shear in order to investigate failure of metals at low triaxiality.

A similar specimen shape was designed by Mohr and Henn (Figure 27) [111]. The gauge section of a specimen has been designed such that fracture initiation are most likely to initiate within the specimen gauge section, under all loading combinations. The advantages are: the ability to generate a wide range of stress states using only one type of specimen and the fact that one finite element model is needed for all load conditions. The butterfly specimen was subjected to combined tension and shear loading. Due to the heterogeneity of the stress and strain fields in the specimen gauge section, they made use of a finite element model to determine the stress and strain at the location of fracture initiation.

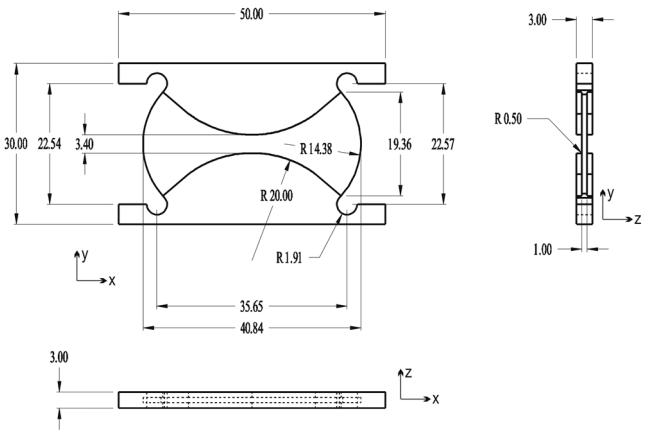


Figure 27 - Shape and dimensions (in mm) of Mohr and Henn designed butterfly specimen with the flat gauge section of uniform thickness [111].

Bai [8] modified this geometry by including a second curvature (Figure 28), resulting in a specimen with a non-flat gauge section, similar to that presented by Wierzbicki. Regardless of the specimen geometry, a hybrid experimental-numerical approach is required to determine the stress and strain states at the onset of fracture.

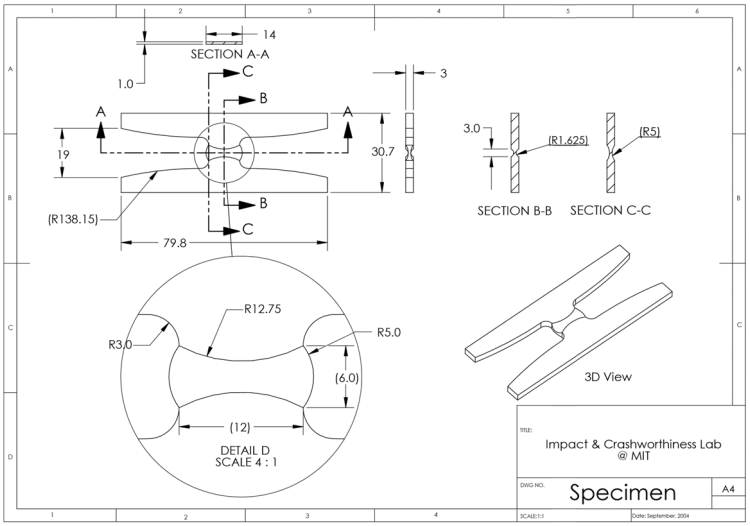


Figure 28 - Detailed geometry of Bay designed specimen with a gauge section with a double curvature profile [8].

The butterfly specimen designed by Mohr and Henn has been developed further by Dunand and Mohr [112] by optimizing the specimen shape to increase the homogeneity of the stress and strain fields at the specimen centre and to reduce experimental errors, through the use of more advanced plasticity models for the identification of the loading path to fracture. The specimen features an abrupt change in thickness between the gauge section and the specimen shoulders (Figure 29).

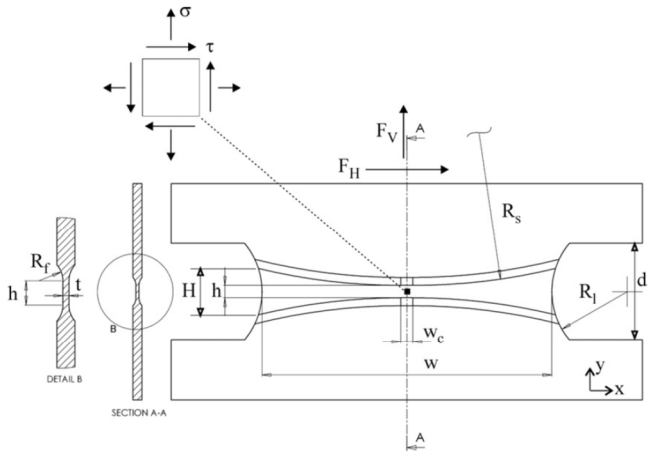


Figure 29 - Schematic of Dunand and Mohr proposed specimen [112].

2.7 Constitutive Modelling, Stress Triaxiality and Lode Angle Parameter

Tresca (1864) and von Mises (1913), proposed the most widely used yield criteria developed for crystalline isotropic materials. In the von Mises yield criterion, it is assumed that yielding of a ductile material begins when the second deviatoric stress invariant, J_2 reaches a critical value. This theory assumes that the hydrostatic pressure and the third invariant of the deviatoric stress have no effect on plastic yielding [113]. The Tresca yield criterion, also known as the maximum shear stress theory, simply compares the maximum state of shear stress in the material with a critical value to determine whether plastic yielding will occur. On the basis of this yield criterion was the observation that plastic strains appear by crystallographic gliding under acting shear stresses. Tresca yield surface has dependence on second deviatoric stress invariant J_2 and the third deviatoric stress invariant J_3, which can be also concluded as Lode dependence, however have no hydrostatic pressure dependence [114].

The criteria of Tresca and von Mises have been found the most applicable to plastic yielding in metals, both of these criteria neglect any effect of hydrostatic stress components. These two models are the basis, for new yield criterion extensions. For example, the Drucker-Prager yield criterion, is an extension of the von Mises yield criterion including pressure dependency via the first stress invariant, I_1 [114].

Pae and Bhateja [115] have shown on their quasi-static experiments on polymers, that increased hydrostatic confining pressure results in an increased yield strength and decreased strain to failure in tension. This pressure dependence, also manifests itself in differences between the tensile and compressive yield stresses, where the yield stress often is found to be higher in compression than in tension.

Wilson [116] conducted experiments on 2024-T351 aluminium cylindrical notched specimens to investigate the effect of hydrostatic tensile stress on yielding. Finite element analyses using von Mises, and Drucker-Prager yield functions were performed. von Mises results overestimated experimental load-displacement curves by 10 to 65% depending on the notch radii, whereas the Drucker-Prager results essentially matched the experimental test data. Drucker-Prager model along with its optimized models have been successfully employed to simulate the response behaviour of pressure-dependent material, such as granular-alike soils, rocks and other alike pressure-dependent materials, such as in plastics [114].

Brunig et al. [83, 117] similar to the Drucker-Prager yield condition proposed a yield criterion as a function of the first stress invariant to describe the effect of the hydrostatic pressure on metal plasticity. Later added the third deviatoric stress invariant in the yield criterion to describe the deformation of metals. Bai and Wierzbicki [91] introduced a yield criterion that is a function of pressure and Lode angle and compared their model with experimental tests conducted on 2024-T351 aluminium alloy. Modified versions of Tresca, von Mises, and Drucker-Prager yield criteria, involving the hydrostatic component of the stress tensor, are used by different authors such as Bowden and Jukes [118], Raghava et al. [119] and Ghorbel [120] in order to describe the yield behaviour of different polymers.

2.7.1 Stress Invariants, Stress Triaxiality and Lode Angle Parameter

If a material is assumed to be isotropic, the yield stress surface can be formulated in terms of three invariants of the stress tensor $\boldsymbol{\sigma}$, defined as the hydrostatic pressure [121]:

- Hydrostatic pressure: $p = -\sigma_h = -\frac{1}{3}\, trace\,(\boldsymbol{\sigma}) = -\frac{I_1}{3}$, (2.19)

where, $I_1 = (\sigma_x + \sigma_y + \sigma_z)$ and $\sigma_x, \sigma_y, \sigma_z$ are the direct stresses of the stresses tensor ;

- von Mises equivalent stress: $q = \sigma_{eq} = \sqrt{\frac{3}{2}}\,(\boldsymbol{S}{:}\boldsymbol{S}) = \sqrt{3\,J_2}$, (2.20)

where, $J_2 = \frac{1}{6}[(\sigma_1 - \sigma_2)^2 + (\sigma_2 - \sigma_3)^2 + (\sigma_3 - \sigma_1)^2]$; (2.21)

- Third invariant of deviatoric stress: $r = (\frac{9}{2}\boldsymbol{S}{:}\boldsymbol{S}{:}\boldsymbol{S})^{\frac{1}{3}}$, (2.22)

where $\boldsymbol{S}$ is the deviatoric stress tensor, defined as: $\boldsymbol{S} = \boldsymbol{\sigma} + p\boldsymbol{I}$. (2.23)

$\boldsymbol{I}$ is the second order identity tensor. Note that the parameter p is positive in compression, but σ_h is positive in tension.

The stress triaxiality η is defined as the ratio between hydrostatic stress σ_h and von Mises equivalent stress σ_{eq}:

$$\eta = \frac{-p}{q} = \frac{\sigma_h}{\sigma_{eq}}\,. \tag{2.24}$$

The Lode Angle differentiates the stress state between tension, shear and compression. In Figure 30, the three coordinate systems which describe the stress state for isotropic materials are illustrated. A particular stress state can be represented by a point in a three dimensional cartesian coordinate system with (σ_1, σ_2, σ_3), which is the first cartesian coordinate system, the second is the cylindrical coordinate system (σ_h, σ_{eq}, θ), and the third is the spherical coordinate system ($\sigma_{eq}, \eta, \theta$) [8].

The geometrical representation of Lode angle is shown in Figure 30. The Lode angle θ is related to the normalized third deviatoric stress invariant ξ through [8]:

$$\xi = \left(\frac{r}{q}\right)^3 = \cos(3\theta)\,. \tag{2.25}$$

Since the range of the Lode angle is $0 \leq \theta \leq \pi/3$, the range of ξ is $-1 \leq \xi \leq 1$. The Lode angle can be normalized by the following equation according to Bai [8].

$$\overline{\theta} = 1 - \frac{6\theta}{\pi} = 1 - \frac{2}{\pi}\, arccos\,(\xi) \qquad (-1 \leq \overline{\theta} \leq 1)\,. \tag{2.26}$$

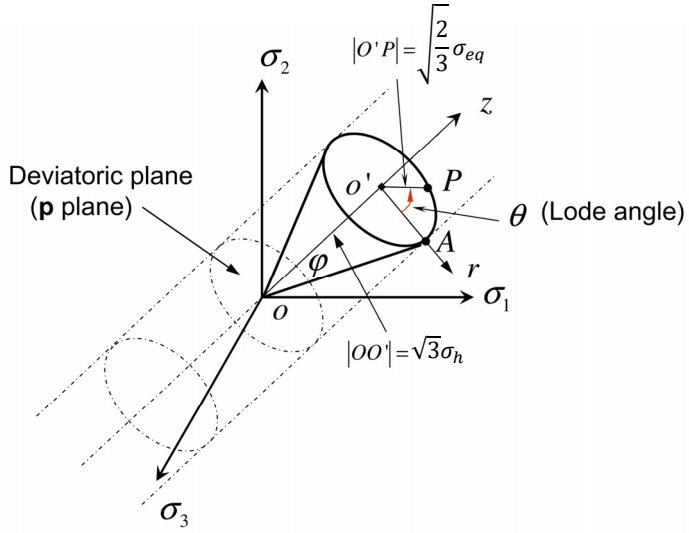


Figure 30 - Principal stress space with hydrostatic and deviatoric stresses defined by the pressure and Lode Angle parameters [8].

Theoretical and experimental studies showed that the stress triaxiality and Lode angle parameters are the two most important parameters controlling ductile fracture in metals under quasi-static loading at room temperature [122]. Bao [123] and Bao and Wierzbicki [92], performed an extensive series of experiments on 2024-T351 involving tensile tests on unnotched and notched cylindrical specimens, compression tests and shear tests. Experiments on fracture tests on butterfly specimens under combined tension/shear/compression loading, were studied by Wierzbicki et al. [110]. The mentioned tests have proven that the material ductility depends on both stress triaxiality and the Lode angle parameter. The effect of the hydrostatic pressure is responsible for controlling the size of the yield surface whereas the effect of the third invariant of stress deviator is responsible for the shape of the yield surface [8].

The effect of hydrostatic pressure and lode angle can be uncoupled and determined from a separate series of experiments. Bai and Wierzbicki [91] on tensile tests used the cylindrical and flat notched specimens to study the effect of stress triaxiality with the introduction of different notch radii at constant Lode parameter for a particular type of specimen, whereas to study the effect of the Lode angle parameter on metal plasticity, they conduct tensile tests on cylindrical ($\overline{\theta} = 1$) and flat notched ($\overline{\theta} = 0$) specimens with the same range of stress triaxiality, however with different corresponding lode angle parameter values.

A literature review shows that experimental investigations on the influence of Lode angle parameter on material yielding are scarce. Bai [8] proposed a pressure and Lode dependent yield function. It has been found that the plasticity model parameters obtained from 2024-T351 tensile flat notched specimens require between 12%-16% Lode angle parameter correction, while the required correction for hydrostatic pressure is relatively small.

The inherent stress state created within the gauge section of the specimen is largely dependent on the specimen geometry and the direction in which the load is applied. The experimental research performed by Bao and Wierzbicki [92] showed the dependence of the fracture mechanisms and strain on the stress triaxiality (Figure 31). It is observed that equivalent strain

to fracture differs for specimens under different stress triaxialities. In the range of negative stress triaxiality, shear fracture dominates in compression test. The equivalent strain to fracture of 0.2 at $\eta = 0$, corresponds to the pure shear test. The equivalent strain peak of 0.45 at $\eta = 0.4$, corresponds to the tensile test on the smooth round bar. Between $\eta = 0$ and $\eta = 0.4$, fracture may develop as a combination of shear and void growth modes. Beyond $\eta = 0.4$, the equivalent strain to fracture decreases with increasing the stress triaxiality, fracture occurs due to void formation in tensile tests on pre-notched specimens.

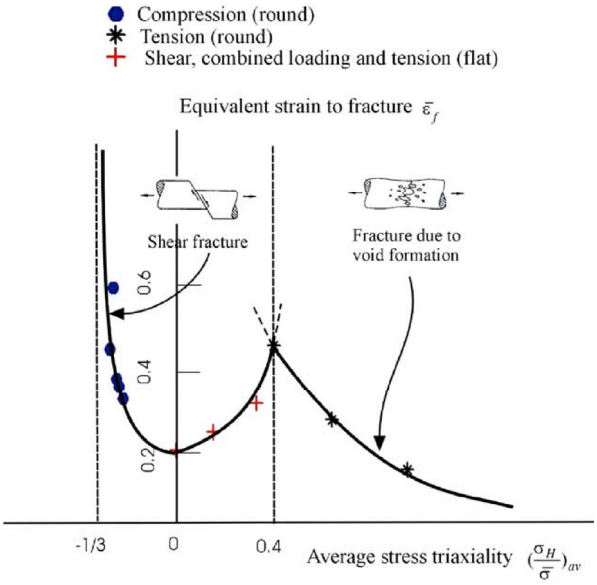


Figure 31 - Dependence of the fracture mechanism and strain on the stress triaxiality [92].

The above defined set of parameters $(\eta, \overline{\theta})$ can be used to describe the stress state. The normalized Lode angle $\overline{\theta} = 1$ corresponds to the axisymmetric tension and uniaxial tension, $\overline{\theta} = 0$ corresponds to shear (or plastic plane strain) loading condition and $\overline{\theta} = -1$ corresponds to the axisymmetric compression and uniaxial compression. When the material under goes a combined multiaxial stress state, $\overline{\theta}$ is between above values [8, 122].

2.7.2 von Mises Yield and Drucker-Prager Yield Criteria

von Mises yield criterion has been used to successful predict yield behaviour of metals, however, many non-metallic materials, such as polymers, are characterized by strain hardening and necking as a result of increasing hydrostatic pressure. Structures made of these pressure-dependent materials would typically exhibit different stress limits in tension and compression, showing differences between the stress-strain curves in uniaxial tension and uniaxial compression. The phenomenon of inequality of the tensile and compressive yield strengths is known as the strength-differential effect. It can be also denoted as an asymmetric effect [124].

In such a case, the von Mises criterion is not appropriate and the Drucker-Prager criterion is available as one of the simplest alternative plasticity yield models. Also, it is important to point,

out that the Drucker-Prager yield criterion is an extension of the von Mises yield criterion to include pressure dependence via the first stress invariant, I_1 [124].

The difference between the Drucker-Prager yield criterion and pressure-insensitive criteria, such as von Mises criterion in the $I_1 - \sqrt{J_2}$ plane of the stress space, is shown in Figure 32. The original von Mises yield criterion states that the yield surface only depends on the second invariant of the deviatoric stress tensor. This theory assumes that the hydrostatic pressure and the third invariant of the deviatoric stress have no effect on plastic yielding and the material is incompressible in the plastic regime. The latter is a line parallel to the abscissa while the former is an inclined line [125].

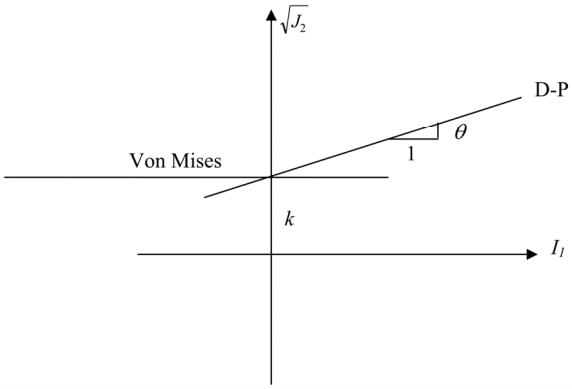


Figure 32 - Drucker–Prager yield surface in $I_1 - \sqrt{J_2}$ plane [125].

The plastic yielding behaviour of polymers is well known to be sensitive to the hydrostatic pressure. Because of its hydrostatic dependency, the Drucker-Prager yield criterion should result in more accurate modelling of geometries that have a high hydrostatic stress influence such as notches. Drucker-Prager yield criterion was found to be useful for the modelling of some polymeric and composite materials that exhibit significant different yield behaviour in tension and compression [121].

2.7.3 Linear Drucker-Prager Model

To represent the asymmetry of the elastic plastic transition phase under tensile and compressive loadings, the linear extended Drucker-Pager yield criterion built in commercial software Abaqus, is referred. The linear model is written in terms of all three stress invariants and described in [121]:

$$F = t - p\tan\beta - d = 0\,, \tag{2.27}$$

Where the deviatoric stress t measure is defined as:

$$t = \frac{1}{2}q\left[1 + \frac{1}{K} - \left(1 - \frac{1}{K}\right)\left(\frac{r}{q}\right)^3\right].$$

(2.28)

p is hydrostatic pressure, q is von Mises equivalent stress, $tan\beta$ represents the yielding sensitivity to hydrostatic pressure, β is the slope of the linear yield surface in the *p–t* stress plane and is referred as the friction angle, K is the ratio of the yield stress in triaxial tension to the yield stress in compression and r is the third invariant of the deviatoric stress (or Lode angle parameter). This function is sketched in Figure 33. When $K = 1$ implies that the yield surface is the von Mises circle in the deviatoric principal stress plane, thus $t = q$, also when $\beta = 0$, the classical pressure independent von Mises criterion is obtained [121].

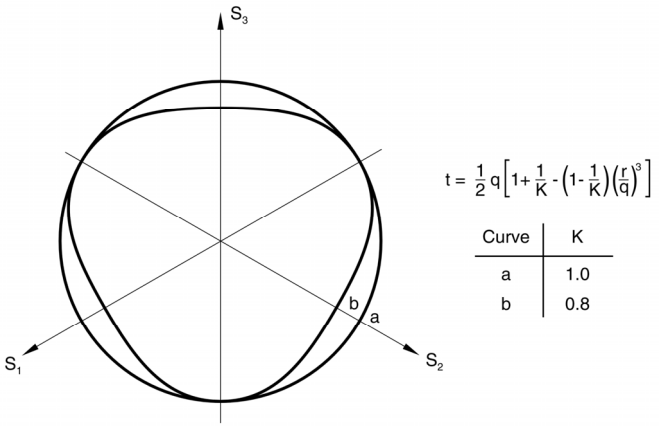


Figure 33 - Typical yield surfaces of the linear model in the deviatoric plane [121].

d is the cohesion of the material and represents the isotropic hardening, as illustrated in Figure 34. Where [121]:

$d = \left(1 - \frac{1}{3}\tan\beta\right)\sigma_c$ if hardening is defined by the uniaxial compression yield stress, σ_c (2.29)

$d = \left(\frac{1}{K} + \frac{1}{3}\tan\beta\right)\sigma_t$ if hardening is defined by the uniaxial tension yield stress, σ_t. (2.30)

In Figure 34, p represents the hydrostatic component of current stress point. The invariant t is a distance of the current stress point to the hydrostatic axis, and therefore represents the magnitude of deviatoric stress [121].

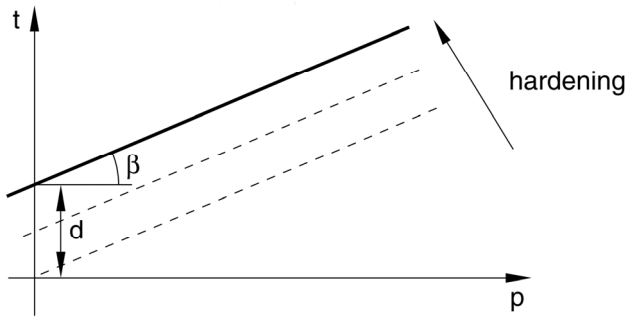


Figure 34 - Schematic of hardening for the linear model in the *p–t* plane [121].

2.8 The Materials in this Study

All tests in this monograph have been performed on the materials described in the following sections.

2.8.1 Polyethylene (PE)

Polyethylene is a semi crystalline polymer made from polymerization of ethylene. PE can easily be arranged into crystals, due to its perfectly regular and orderly molecular chain [4]. The monomer molecule, the ethylene, can be seen as a pair of methylene groups, which consists of two hydrogen atoms bound to a carbon atom, along the molecular chain (=CH_2). Polyethylene macromolecule is illustrated in Figure 35, where *n* is the number of repeat units and might vary between 10^3 and 10^6 [9].

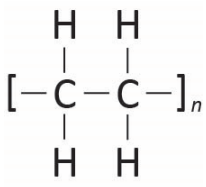


Figure 35 – Structural unit repeat of polyethylene (PE) [9].

Density is directly related to crystalline content. Polyethylene grades are mainly classified according to their density or branching structure. The two main grades of mass-produced Polyethylene, are [126]:

Low-Density Polyethylene (LDPE): Polymers with densities ranging from about 0.915 to 0.935 g/cm^3. Low-density Polyethylene have a substantial concentration of high degree of short and long chain branching which inhibits the crystallization process resulting in relatively low densities [127]. Therefore the crystalline lamellae are less ordered, thinner and shorter than in HDPE as shown in Figure 36 (2) [40]. The higher degree of branching, the more compact a polymer chain is and the more irregular the structure becomes. This increases amorphous content contributing to LDPE properties, such as ease of processing and film transparency [126].

High-Density Polyethylene (HDPE): Polymers with densities ranging from 0.940 to 0.970 g/cm^3. HDPE has a mostly long linear chain (lower degree of branching), therefore has stronger intermolecular forces. HDPE is chemically the closest in structure to polyethylene. Therefore, crystallizes easily and to a high degree (over 80%). Because of its regular arrangement along the polymer chain, HDPE exhibits better mechanical properties and higher density [127]. The crystalline region in which chains fold and orient themselves into highly ordered thick lamellae as shown in Figure 36 (1) [40].

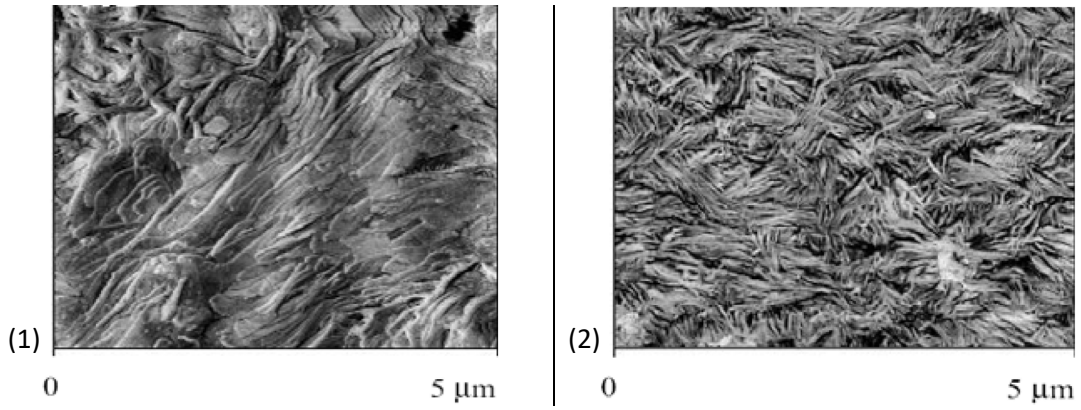


Figure 36 – Crystalline regions (atomic force microscopy images): (1) HDPE (2) LDPE [40].

Most of differences in properties between Low-Density and High-Density Polyethylene can be attributed to the degree of branching. Different degrees of branching results in several changes in properties such as the degree of crystallinity and morphology. Higher crystallinity increases density, hardness, tensile strength and melting point, while low crystallinity offers good processability and better transparency [4, 128]. Low-Density and High-Density Polyethylene properties are shown in Table 9 [2, 9].

Table 9 – Low-Density and High-Density Polyethylene properties [2, 9].

Properties	**Low-Density Polyethylene**	**High-Density Polyethylene**
Melting Point	≈ 110 °C	≈ 130 °C
Crystallinity	Low crystallinity due to irregular packing (50-60% Crystalline).	Highly crystalline (>90% Crystalline) due to long linear chains which results in regular packing.
Flexibility	Due to lower crystallinity is more flexible than HDPE.	More rigid than LDPE due to higher crystallinity.
Tensile Strength	Low tensile strength due to irregular packing of polymer chains.	High tensile strength as consequence of regular packing of polymer chain.
Transparency	Relative transparency since it is more amorphous than HDPE.	Less transparent than LDPE due to high crystalline degree.
Density	0.915 to 0.935 g/cm^3	0.940 to 0.970 g/cm^3
Heat Resistance	Poor heat resistance. Density drops off above room temperature (RT).	Softens on heating above 100 °C.
Low Temperatures	Both LDPE and HDPE become brittle at very low temperatures (below -80 °C).	

High-density polyethylene is largely being used in engineering components due to its good wear resistance and impact strength, low gas permeability and high toughness [5]. HDPE is known to display nonlinear responses during loading /unloading and depends on external parameters such as strain rate, temperature, but also on morphological parameters such as degree of crystallinity, molecular structure and weight distribution, which themselves are determined by thermo-mechanical history experienced by the polymer during processing of the product [18, 38, 40].

Low-Density Polyethylene is mainly used for film extrusion applications such as shopping bags as well as rotational moulding for industrial containers. Other typical applications include lightweight food packaging structures, wire and cable insulation, adhesives and sealants, while High-Density Polyethylene is used more often to make containers (bottled water) and automotive fittings. It is also used in pipes for canalisation, injection moulded products, packaging and housewares [2, 15, 128].

Dow™ HDPE KT 10000 UE, High Density Polyethylene Resin (semi crystalline polymer) is provided by Dow Chemical Company (Dow) and is an UV stabilized resin with high molecular weight distribution. Dow reports that it has excellent stiffness, good impact strength to injection moulded parts at minimum warpage. The crystalline melting temperature for the polymer is 250 °C. Supplier technical information for Dow™ HDPE KT 10000 UE, is listed in Table 10 [129].

Table 10 - Dow™ HDPE KT 10000 UE, technical information [129].

	Properties	Units	Polyethylene (HDPE)	Test Method
Physical	Density	g/cm^3	0,964	ASTM D792
	Melt Flow Rate (MFR) (190°C/2,16Kg)	g/10 min	8	ISO 1133
Mechanical (Tensile Strength)	Yield Stress (Compression) (50mm/min)	MPa	29	ASTM D638
	Stress at Break (Compression) (50mm/min)	MPa	32	
	Strain at Break (50mm/min)	%	800	
	Elastic Modulus – 1% Secant (Compression) (1mm/min)	MPa	1050	ASTM D790
Impact	Tensile Impact	KJ/m^2	77	ASTM D1822
Hardness	Shore D	-	66	ISO 868
Thermal	Vicat Softening Temperature	°C	131	ISO 306/A

2.8.2 Polypropylene (PP)

Polypropylene is a semi crystalline polymer with linear chain form. Polypropylene shows a similar structure to polyethylene, with one of the hydrogen atoms replaced by a methyl group, which is an alkyl derived from methane, containing one carbon atom bonded surrounded by three hydrogen atoms (- CH_3). Figure 37 is the representation of Polypropylene molecular structure [9].

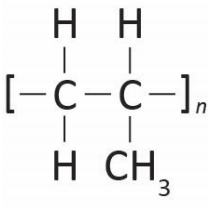


Figure 37 – Structural unit repeat of Polypropylene (PP) [9].

The presence of the methyl group restricts the rotation of the chain producing a stronger but less flexible polymer than polyethylene. The density of polypropylene is between 0.895 and 0.92 g/cm³. Polypropylene shows several attractive properties such as low density, high strength, high melting point, stiffness and dimensional stability also good chemical and moisture resistance. However, polypropylene itself has low elasticity, has poor impact resistance and is very brittle at low temperatures. Also has narrow thermal processing window due to it sharp transition from semi crystalline solid to a melt, which does not ease its use in processing operations such as deep draw thermoforming or extrusion coating [2, 9]. The three main types of polypropylene generally available are [130]:

- Homopolymers are a blend of polypropylene homopolymer with a catalyst, which is an additional substance that increases the rate of a chemical reaction. Polypropylene homopolymer is the stiffest of the three propylene types and have the highest tensile strength at yield, however they have less impact resistance especially below 0°C. In the natural state, they are translucent [130].

- Random Copolymers are a blend of polypropylene homopolymer with a small amount of ethylene (<5%). Adding ethylene monomer, decreases the polymer crystallinity, lowers the melting point and also makes the polymer more transparent. Polypropylene random copolymer is the most flexible with the lowest tensile strength of the three and have better room temperature (RT) impact than homopolymers but share the same relatively poor impact resistance at low temperatures [130].

- Impact Copolymers are a blend of polypropylene homopolymer with an ethylene propylene rubber (EPR). This copolymer has intermediate stiffness, tensile strength and has low impact strength with high toughness due to the presence of EPR. As a rule, the more the ethylene monomer added, the greater the impact resistance with correspondingly lower stiffness and tensile strength. Polypropylene impact copolymers are used in a wide range of applications including automotive components, pipe applications, household, food containers, toys and bottles [130–132].

Sabic® PP PHC27 is a semi crystalline polymer and a multipurpose polypropylene impact copolymer. Saudi Basic Industries Corporation (SABIC) reports that it has high impact resistance also at low temperatures, good stiffness, excellent flow properties, low warpage and narrow molecular weight distribution. Typical property values for Sabic® PP PHC27, are listed in Table 11 [133].

Table 11 - Sabic® PP PHC27, technical information [133].

	Properties	Units	Polypropylene (PP)	Test Method
Physical	Density	g/cm^3	0,905	ASTM D792
	Melt Flow Rate (MFR) (230°C/2,16Kg)	g/10 min	14	ISO 1133
Mechanical (Tensile Strength)	Yield Stress (50mm/min)	MPa	22	ISO 527
	Stress at Break (50mm/min)	MPa	19	
	Strain at Break (50mm/min)	%	600	
	Elastic Modulus - 1% Secant (1mm/min)	MPa	1200	ASTM D790
Impact	Charpy Impact Notched (23 °C)	KJ/m^2	31	ISO 179
Hardness	Shore D	-	60	ISO 868
Thermal	Vicat Softening Temperature	°C	145	ISO 306/A

2.8.3 Polyamide (PA) / Nylon

Polyamide is a macromolecule with repeating units linked by amide (-CO-NH-) bonds. Polyamides are crystalline polymers with high molecular weight. Polyamides sometimes are called nylons due to the trade name given by the manufacturer, DuPont. There are several types of polyamide types, such as polyamide 6, polyamide 11, polyamide 12 and polyamide 66, which provides a broad range of properties available. Polyamides in general, have excellent mechanical properties with fatigue and abrasion resistance, stability at elevated temperatures, fire resistance, good processability, low friction, high toughness and outstanding gas barrier properties. All polyamides tend to absorb moisture that can affect their properties and dimensional stability [2].

Polyamide 6 (Nylon 6)

Polyamide 6 has the notation 6, due to the number of carbon atoms contained in the structural repeat unit [1]. Polyamide 6 is employed in a wide range of uses, including automotive applications such as interior, exterior, air conditioning systems, vents and electric fittings, electric applications such as plugs and connectors, consumer products such as ski boots and kitchen utensils [14]. Figure 38 is the representation of Polyamide 6 molecular structure [9].

$$[-NH-(CH_2)_5-CO-]_n$$

Figure 38 – Structural unit repeat of Polyamide 6 (PA 6) [9].

Promyde® B30 PMID is a Polyamide 6 impact modified, heat stabilized with equilibrated mechanical properties, optimal flow, excellent impact resistance, efficient mold filling and easy

mold release provided by Nurel Engineering Polymers. The values for Promyde® B30 PMID are taken from the manufacturer's data sheet and given in Table 12 [134].

Table 12 - Promyde® B30 PMID, technical information [134].

	Properties	Units	Polyamide 6 (PA 6)	Test Method
Physical	Density	g/cm^3	1,13	ASTM D792
	Melt Flow Rate (MFR) (275°C/5Kg)	g/10 min	80	ISO 1133
Mechanical (Tensile Strength)	Yield Stress (23°C, 50mm/min)	MPa	35 - 75	ISO 527
	Stress at Break (23°C, 50mm/min)	MPa	85	
	Strain at Break (23°C, 50mm/min)	%	70 - 180	
	Elastic Modulus (23°C, 1mm/min)	MPa	1100 - 2800	
Impact	Charpy Impact Notched (23 °C)	KJ/m^2	8	ISO 179
Hardness	Shore D	-	84	ISO 868
Thermal	Melting Temperature (DSC) (10°C/min)	°C	222	ISO 3146

3 Experimental Details

The physical and mechanical testing of polymers consist of investigation, characterization and provision of data. An experimental program was designed such that it provides insight in the yield behaviour and fracture initiation of HDPE, PP and PA 6 over a wide range of stress states. It includes experiments on dumbbell specimen Type 1A, flat and cylindrical notched specimens with two different notch radii and butterfly specimen at four different loading angles, (1) α = 0° (pure shear), (2) and (3) α = 30°, 60° (both combined shear and tension/ compression) and (4) α = 90° (pure tension/ compression) at room temperature.

In addition, part of experiments in butterfly specimens are performed at constant temperature of 50 °C. Also, viscoelastic characterization is performed using Dynamic Mechanical Analyses (DMA) allowing the evaluation of storage modulus E', loss modulus E'' and loss factor tan (δ). Differential Scanning Calorimetry (DSC) has been used to study the changes in the tested material crystallinity and the melting temperature T_m. Scanning electron microscopy (SEM) is proposed to examine the fracture morphology.

The present investigation is more particularly focused on the yielding conditions determination. Here after, a detailed description of the experimental techniques for the characterization of the materials under study are reported. The study of literature analytical formulas for specimen's stress states analysis, are also included. Prior to the presentation of the test results, an analysis of the assigned geometries is performed using the Finite Element Method.

3.1 Specimens Production – Mould Injection

Specimen preparation is an essential part of any experimental research work. Different heating/cooling profiles, different applied pressures during preparation, details of mould configuration or even if there was any cutting or machining involved might result in significant differences in the specimen properties as well as in the results from test data. Therefore, cautious and consistent specimens preparation for polymers are important, because both physical and mechanical properties are dependent on how the materials are prepared [55].

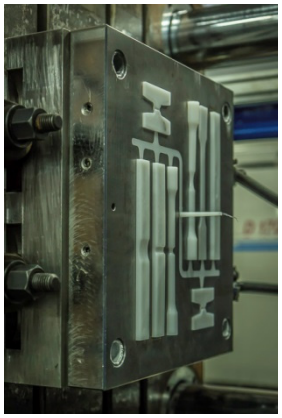
(1)  (2)  (3) 

Figure 39 – (1) and (2) designed injection mould attached to the injection moulding machine, (3) mould with unextracted test specimens.

A designed injection mould made of steel was used to produce the specimens (Figure 39). The main components of the mould are the mould plates with the mould cavities. Each half is attached to the injection moulding machine. One mould half is allowed to slide, so that the mould can be opened and closed along the partition line, whereas the other mould plate is fixed to a stationary platen and is aligned with the nozzle of the injection machine. The mould plates are provided with channels for cooling, heating and venting. The ejection pins are provided in the mould core. Some post processing was required, such as removing the solidified channels of the mould or trim from the specimens the excess material [135].

Since the specimen properties depends on the selected processing method and mould parameters (pressure, time and temperature), as well as the type of machine used, it is crucial to state the specifications such as the setting parameters of the machine and the moulding conditions for the materials (Table 13). All the specimens were injection moulded on a Euro Inj D200, by Lien Yu Machinery Co. Lt, a screw type injection moulding machine. The most relevant characteristics of the equipment can be found in Table 14. The polymers used in this study were: Dow™ HDPE KT 10000 UE, Promyde® B30 PMID and Sabic® PP PHC27 both supplied in granular form (cylindrical strand-cut pellets).

The melt temperature on the nozzle was set to 190 °C both for HDPE and PP and 240 °C for PA; the hold pressure at the nozzle was set to 7.5 MPa for the three semi crystalline thermoplastics. The holding time was set to 15 s, 4 s and 10 s for the HDPE, PP and PA 6; the total cooling time was 85 s, 30 s and 35 s; also, the mould surface temperature was set to 10 ^{o}C, 20 ^{o}C and 40 ^{o}C and the injection speeds were set in order to obtain the same polymer front velocity, which were 28 m/s, 90 m/s and 30 m/s, respectively for HDPE, PP and PA 6.

Table 13 - Specifications and set parameters of the injected moulded specimens.

Parameters	**Units**	**Polyethylene (HDPE)**	**Polypropylene (PP)**	**Polyamide (PA)**
Screw Filling	s	9.4	14.5	8.4
First Injection	s	5.5	1.5	4.7
Second Injection	s	15	4	10
Mould Cooling	s	85	30	35
Cycle Time	s	115	45	60
Injection Pressure	MPa	7.5	7.5	7.5
Nozzle Temperature	^{o}C	190	190	240
Nozzle Injection Speed	m/s	28	90	30
Mould Surface Temperature	^{o}C	10	20	40

Table 14 – Machine Specifications - Euro Inj D200 [136].

Parameters	**Units**	**Euro Inj D200**
Screw Diameter	mm	45
Screw L/D Ratio	L/D	22.2
Number of Heating Zones	qty	5
Max Injection Pressure	bar	2125
Max Locking Force	Tonne	200

Note: After injection of the material into the mould is complete, the screw remains stationary for some time to hold the plastic in the mould under pressure (holding time). However, during cooling some shrinkage of the part may occur. The packing of material in the injection stage allows additional material to flow into the mould and reduce the amount of visible shrinkage (second injection). The cooling stage starts at the solidification of a thin section at cavity entrance (gate), starting from that instant no more material can enter or exit from the mould [135].

3.2 Machining of Specimens

The majority of the specimens were produced in final shape using injection moulding, requiring any small finishing operations, such as burr removal. However, machining processes were used as secondary operations on injection moulded specimens in order to obtain some of the required specimen geometries. Machining plastic is not the same as machining metal, therefore there are several key differences, such as: plastics exhibit greater thermal expansion than metals, which increases tool friction and the rate of heat generation; plastics dissipate heat at a slower rate than metals and plastics have lower melting temperatures than metals. Considering these differences HDPE, PP and PA 6 were machined at low cutting speeds and feed rates. Because of heat build-up both in specimen and in the tool, compressed air was used as coolant medium in order to prevent deformations, stresses, colour changes or even melting [137].

The main machining processes used were: turning and milling. Table 15 provides information from ISO 2818 about recommended machining conditions [138]. Compression specimens were processed using the turning operation in which the workpiece material is rotated while a single point cutting tool is moved parallel to the axis of rotation, removing unwanted material to create the desired cylindrical and axially symmetric shape [12]. Dynamic mechanical analysis specimens were processed using routing operations which is a type of milling operation, on existing injection specimens [139]. In this process, routing was done automatically with CNC machine tools.

Table 15 - Recommended machining conditions for thermoplastics according to ISO 2818 [138].

Process	Rotational Speed (rev/min)	Cutting Edge Angle (α)	Cutting Speed (mm/min)	Feed Rate (mm)
Turning	500 to 1000	5 to 15	30 - 200	0.2 - 0.4
Milling	180 to 500	-	70 - 250	0.2 - 0.5

3.3 Specimens Geometry

3.3.1 Tensile Specimens - Geometry

In conventional uniaxial tension tests, the dumbbell specimen geometry is often proposed with calibrated gauge portion of constant cross-section. Because of plastic instabilities involved in semi crystalline polymers, a non-uniform state of stress and strain occurs, with necking

appearing in any place of gauge length. In order to avoid this effect, notches in the specimen geometry are included in a well-defined region of the specimen to succeed local measurements. When a notched specimen is loaded, local stress and strain concentrations are generated in the notch area. The stresses often exceed the yield limit of the material in the well-defined region around the notch root [140].

The main reasons to include notches in the specimen geometry, are: (1) to maintain nearly uniform plane stress condition in the centre of gauge section, (2) the plastic deformation and the onset of fracture processes is confined to the notched region, (3) there is no need to introduce an imperfection in a numerical model to trigger the onset of localized deformation [141] and (4) in cylindrical notched specimens the neck develops uniquely from the centre of the specimen, with simpler axisymmetric distributions of the stresses and strains [140].

Experiments on cylindrical notched tensile bars made of semi crystalline polymers are found in the literature [5, 142]. Castagnet and Deburck [142] studied the influence of the microstructure on mechanical behaviour and cavitation in a semi-crystalline polymer. The tensile experiments were performed on specimens with different shapes: dumbbell and axisymmetric tensile bars with three different curvature radii. Geometries of axisymmetric notched bars are described in Figure 40. The minimal diameter is equal to 9 mm for all specimens but the length of the non-uniformly reduced section varies from a shape to another.

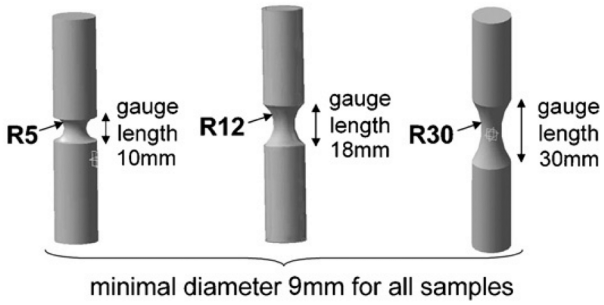


Figure 40 - Notched circular tensile bars geometries tested in tension [142].

Uniaxial tensile tests are performed on dumbbell shape specimens Type 1A with uniform rectangular cross-section. Flat and cylindrical notched specimens with two different notch radii: R = 30 mm and R = 5 mm, were also considered. Dumbbell specimen Type 1A is the specimen preferred for thermoplastic moulding materials, according to ISO 527-2 [69]. For flat notched specimens, the notch is positioned such that the specimen width decreases from 10 mm in its remote section to 5 mm at the specimen centre. Cylindrical notched specimens have 190 mm in length, the minimal cross section diameter is 5 mm, and the remote diameter is 10 mm. Both ends of cylindrical notched specimens were prepared by M14 threads for mounting in the tensile machine. The shapes and dimensions of the specimens are illustrated in Figure 41, Figures 42 (1) and (2) and Figures 43 (1) and (2). All dimensions are in millimetres (mm).

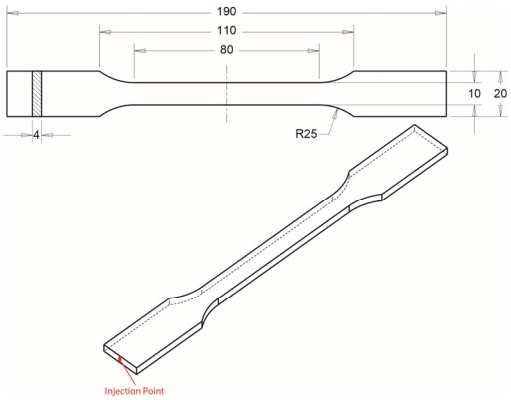


Figure 41 - Dumbbell specimen Type 1A. Dimensions in mm.

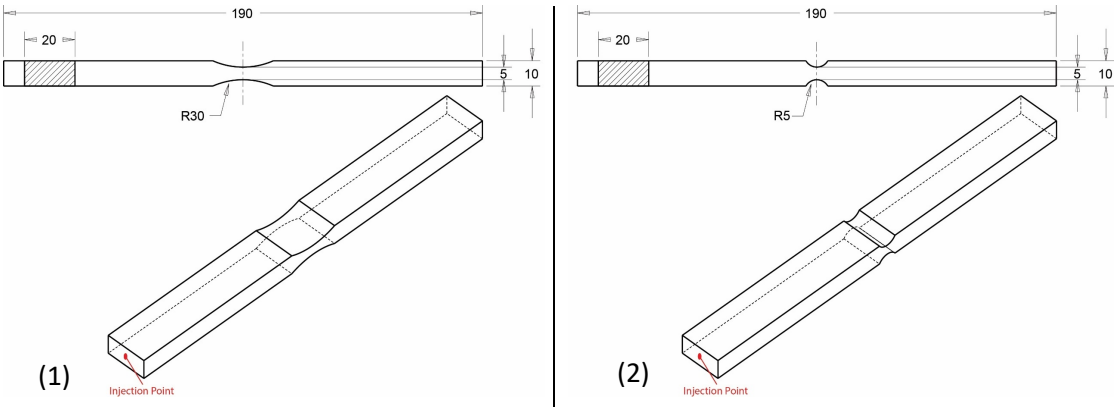


Figure 42 - Flat notched specimen. (1) Radius 30 and (2) radius 5. Dimensions in mm.

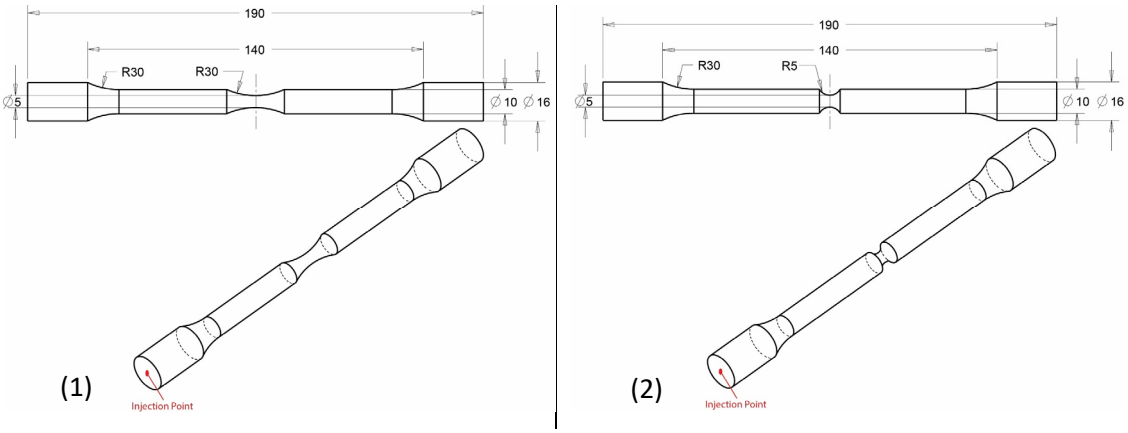


Figure 43 - Cylindrical notched specimen. (1) Radius 30 and (2) radius 5. Dimensions in mm.

The designed flat cylindrical notched specimens were analysed, by 3D FE calculations performed using Abaqus version 6.16. Eight-node linear solid element, C3D8R, with reduced integration, was used to construct the models. More detailed information about mesh is given in chapter 6 Plasticity Model Calibration and Verification – Drucker-Prager and von Mises. Note that the mesh is sufficiently refined in the gauge section. The FE calculations in tension confirmed that

the gauge section of the specimens is where the stresses are concentrated and onset of fracture processes is expected. Figure 44 presents elastic FE results in terms of stress distribution in the leading direction. The basic materials properties applied are listed in Table 16.

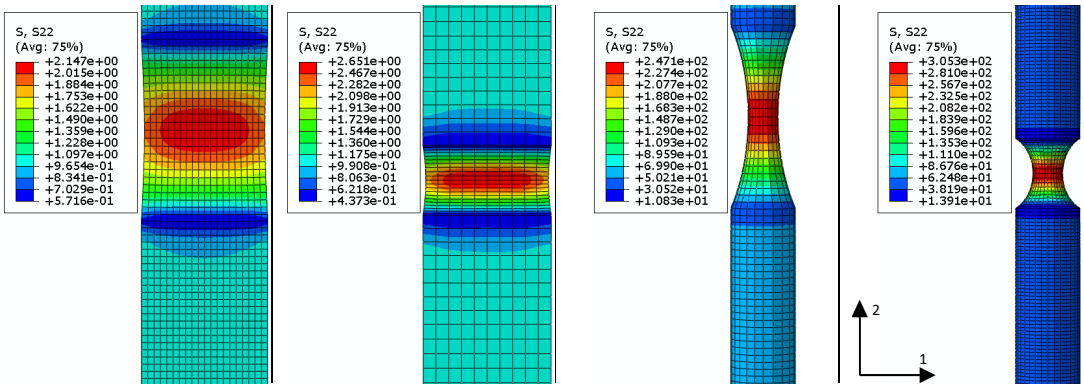


Figure 44 - FE results in terms of stress distribution in the gauge section.

Table 16 - Basic material properties assigned (HDPE).

Elastic Modulus (MPa)	Poisson's Ratio [76]	Mass Density (g/cm^3) [76]
1061	0.4	0.964

3.3.2 Tensile Specimens - Analytical Formulas for Stress Analysis

Dumbbell specimen: The true stress was obtained from the measured force values and strain from the extensometer measurements. The engineering and true stress–strain curves are calculated using standard methods as follows [143]:

$$Engineering\ Stress\ (\sigma_e) = \frac{F}{A_o = (w \times h)} \quad \Big| \quad True\ Stress\ (\sigma_t) = \sigma_e(1 + \varepsilon_e), \quad (3.1)$$

$$Engineering\ Strain\ (\varepsilon_e) = Extensometer \quad \Big| \quad True\ Strain\ (\varepsilon_t) = ln(1 + \varepsilon_e). \quad (3.2)$$

Where, F is the applied force A_o is the cross-sectional area of specimen before deformation has taken place (w is the width and h is the thickness of the rectangular cross-section) [143]. The different tensile specimens are characterized by distinct values of stress triaxiality, η. The stress triaxiality is defined as the ratio between hydrostatic stress σ_h and von Mises equivalent stress σ_{eq}. For dumbbell specimens the initial stress triaxiality is $\eta = 1/3$ [8]. It is referred as initial since triaxiality evolves with deformation and varies throughout the specimen.

Triaxial stress state effects (different triaxialities) were examined by means of tests using flat and cylindrical notched specimens with two different notch radii: *R* 5 and *R* 30 in order to set different triaxial stress states in the median cross-section.

Cylindrical notched specimen: The effect of stress triaxiality (or pressure) on the yield stress will be studied in particular. In a specimen subjected to necking, the stress state in the specimen is no longer uniaxial, nor homogeneous. This multiaxial stress state leads to high hydrostatic stresses. Due to this phenomenon, it is possible for axial yield stress of notched specimens to be greater than that of smooth specimens [88, 143].

The applied tensile load induces a multiaxial (triaxial) stress state in the minimal cross section. The formula of stress triaxiality was first derived by Bridgman, who had analysed the stress distribution in cylindrical metal specimens with different notches. Bridgman's formulas involve the relationship between the smallest cross section a and the notch radius R. At the centre of the median cross-section the stress triaxiality ratio η is maximum and is defined as the ratio of the hydrostatic stress σ_h and the von Mises equivalent stress σ_{eq}, using the Bridgman formula [8, 144]:

$$\eta = \frac{\sigma_h}{\sigma_{eq}} = \frac{1}{3} + \ln(1 + \frac{a_0}{2R}) \text{ ,} \tag{3.3}$$

where R is the notch radius, a_0 is the minimum and initial radius of the centre of the median cross-section and ln is the natural logarithm. If $R \to 0$ the equation above is not valid, and if $R \to \infty$, the geometry of the specimen tends to that of a smooth cylindrical for which stress triaxiality ratio η is = 1/3 [8, 145]. Bridgman formula was revisited by Bao and Wierzbicki [8] using finite element simulation, being proposed a correction factor of $\sqrt{2}$.

$$\eta = \frac{\sigma_h}{\sigma_{eq}} = \frac{1}{3} + \sqrt{2}\ln(1 + \frac{a_0}{2R}) \cdot \tag{3.4}$$

An initial minimum radius a_0 of 2.5 mm was chosen for the two geometries. The initial stress triaxiality ratio is then equal to 0.39 and 0.64 for *R* 30 and *R* 5 specimens, respectively. The stress triaxiality ratio increases inversely to the notch radius of specimens [8].

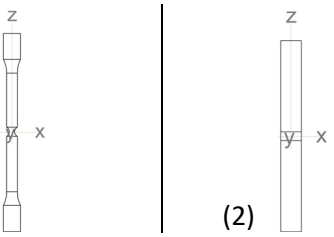
Castagnet and Deburck [142] (from the same study above referenced) measured the actual cross section area by employing a digital image correlation software linked to a CCD camera and the elongation of the specimen. By plotting the radial strain against axial strain of the gauge length for specimens with different radii, they showed that the change of the diameter (radial strain) was lower for higher triaxialities.

In this research, on cylindrical notched specimens, two measurement methods were performed, at same time one with the extensometer for axial displacements strain measurements and other using digital camera, for local measurements of radial cross section reduction. The cross-section of a cylindrical notched specimen presents a triaxial stress state that can be approximately calculated using the following Bridgman formula, for equivalent strain [8, 123]:

$$\varepsilon_{eq} = 2\ln(\frac{a_0}{a}) \cdot \tag{3.5}$$

where a_0 is the initial minimum radius of the centre of the median cross-section and a is the actual minimum radius of the specimen. In his research, Bridgman assumed that the strains to be constant over the neck cross section [5].

As described, evolution of the minimal cross section diameter was measured along the test by a digital camera, followed by image analysis. The actual length of the cross section was obtained from images taken with the digital camera and treated with an image analysis software. Although the contrast created between the background and the specimen, some discrepancy of the method, resulting from the pixel selection, lead to scatter during threshold operation.



(1) (2)

Figure 45 – Axis direction: (1) cylindrical and (2) flat notched.

By assuming perfectly plastic material, deforming with no volume change and with a homogeneous axial strain in the minimal cross section, Bridgman demonstrated that both radial (σ_{xx} and σ_{yy}) and axial stresses (σ_{zz}) can be expressed as follows [8, 144]:

$$\sigma_{xx} = \sigma_{yy} = \sigma \ln\left(\frac{a^2 + 2aR - x^2}{2aR}\right), \tag{3.6}$$

$$\sigma_{zz} = \sigma \left(1 + \ln\left(\frac{a^2 + 2aR - x^2}{2aR}\right)\right). \tag{3.7}$$

In Figure 45 (1) Z is the loading direction. These equations show that decreasing the notch radius results in an increase in the maximum load for a given value of equivalent stress. Where, x is the current radial abscissa in the cross section, $x = 0$ corresponding to the centre of the cross section. Accordingly, by decreasing the notch radius R for a given value of a, one can expect higher peak stress. The average axial stress σ can be defined as the applied force F over the cross section A [144].

Boisot et al. [144] performed a comparison between both numerical and analytical models proposed by Bridgman and experimental data. They found that, although the effects of triaxiality were overestimated by Bridgman formula, the peak stress values calculated by both analytical and numerical methods were rather similar. They reported that Bridgman formula was valid up to the peak load, however overestimates the stress in the plastic regime. Also, in Bridgman's analyses, no strain hardening, strain rate effects, pressure sensitive or plastic dilatation were taken into account [88].

Flat notched specimen: A formula is derived for the stress triaxiality inside the notch of a flat notched plane strain specimen, by Bai et al. [8]. Test results on 2024-T351 aluminium alloy and finite element simulations corroborated this formula. At the centre of the median cross-section the stress triaxiality ratio η is maximum ($x = 0$) and is given by the following equation:

$$\eta = \frac{\sigma_h}{\sigma_{eq}} = \frac{\sqrt{3}}{3}\left(1 + 2\ln\left(1 + \frac{t}{4R}\right)\right). \tag{3.8}$$

Where t, is the ligament thickness of the flat notched specimen, R is the notch radius and ln is the natural logarithm. The detailed derivation can be found in [8]. An initial minimum ligament thickness t of 5 mm was chosen for the two geometries used in this work. Equation above implies that the range of stress triaxiality at the centre of a plane strain specimen is $\eta \geq 1/\sqrt{3}$. The initial stress triaxiality ratio is equal to 0.62 and 0.84 for *R* 30 and *R* 5 specimens, respectively. The lower the curvature radius, the higher the stress triaxiality ratio.

The strain stresses are determined as follows [8] (Figure 45 (2) Z is the loading direction):

$$\varepsilon_{eq} = \frac{2}{\sqrt{3}} \ln(\frac{t_0}{t}), \tag{3.9}$$

$$\sigma_{xx} = \frac{2}{\sqrt{3}} \sigma (\frac{1}{2} + \ln\left(\frac{a^2 + 2aR - x^2}{2aR}\right)), \tag{3.10}$$

$$\sigma_{yy} = \frac{2}{\sqrt{3}} \sigma \ln(\frac{a^2 + 2aR - x^2}{2aR}), \tag{3.11}$$

$$\sigma_{zz} = \frac{2}{\sqrt{3}} \sigma(1 + \ln\left(\frac{a^2 + 2aR - x^2}{2aR}\right)). \tag{3.12}$$

where t_0 is the initial ligament thickness of the specimen, and t is the actual minimum ligament thickness of the specimen, x is the current radial abscissa in the cross section, $x = 0$ corresponding to the centre of the cross section, R is the notch radius, a is the actual half ligament thickness of the specimen, σ average axial stress [8].

3.3.3 Compression Specimens - Analytical Formulas for Stress Analysis

Cylindrical specimens with a slenderness ratio λ of 8 (for more details read section: 2.4.2 Compression Tests, equation 2.6), were applied in compression tests. Barrelling effect near the equator and buckling phenomena, were minimized with selected slenderness ratio ($l/i = 8$). Like for necking in tension, the barrelling effect in compression, is a testing difficulty resulting from geometrical imperfections and friction, responsible to create a non-homogeneous strain field which also brings difficulties and extra efforts in performing numerical simulations. In theory, a homogeneous strain field should imply a perfect lubrication between the plates and the specimen. Unfortunately, the ideal sliding is quasi impossible to reach, as acknowledged by numerous authors [146].

Besides cylindrical specimens, notched cylindrical specimens based on the work by Bao and Wierzbicki [92], were also considered. This specimen shape, with a notched small gauge section in the middle, removes the effect of barrelling due to friction and localized the deformation in the gauge section such that fracture initiation is most likely occurred at the equatorial area. The specimens shape and dimensions for compression are illustrated in Figure 46. The specimens were cut from cylindrical notched specimen with radius 5.

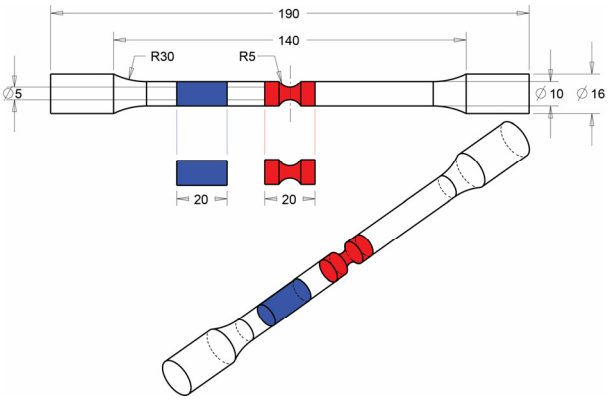


Figure 46 – Compression specimen. Cylindrical (blue) and cylindrical notched (red). Dimensions in mm.

Cylindrical Specimen: The true stress was obtained from the measured force values and strain from the displacement measurements by the MTS 810. The engineering and true stress–strain curves are calculated using standard methods as follows [143]:

$$Engineering\ Stress\ (\sigma_e) = \frac{F}{A_o = (\pi\ a^2)} \quad \Big| \quad True\ Stress\ (\sigma_t) = \sigma_e(1 + \varepsilon_e). \tag{3.13}$$

$$Engineering\ Strain\ (\varepsilon_e) = \frac{l_1 - l_o}{l_o} \quad \Big| \quad True\ Strain\ (\varepsilon_t) = ln(1 + \varepsilon_e). \tag{3.14}$$

Where, F is the applied force, A_o is the cross-sectional area of specimen before deformation has taken place, a circumference radius, l_o is the original length of the specimen before any load is applied, l_1 is the instantaneous length followed force application and $(l_1 - l_o)$ is the measured displacement [143]. A negative stress triaxiality ratio η is equal to -1/3 for the cylinders specimens in compression.

Cylindrical notched specimen: Analytical Formulas are the same as detailed in section: 3.3.2 Tensile Specimens - Analytical Formulas for Stress Analysis, equations 3.4 to 3.9. In this case, the negative stress triaxiality is = -0.64. For both tension and compression tests, the true axial stress was obtained from the measured force values and the current diameter of the specimen monitored optically in its mid-plane.

3.3.4 Butterfly Specimen - Geometry, Stress Triaxiality and Analytical Formulas

For the biaxial testing of HDPE, PP and PA 6, a butterfly specimen was designed. The specimen dimensions and shape are shown in Figure 47. Note that a similar specimen shape was designed by Bai, for 2024-T351 aluminium alloy and A710 steel [8].

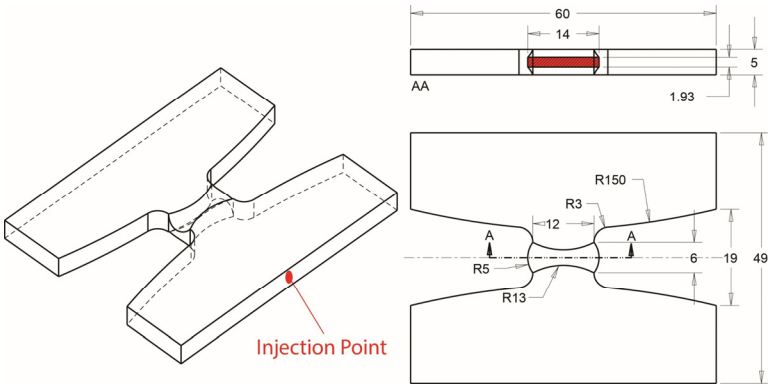


Figure 47 - Butterfly specimen shape. Dimensions in mm.

The thicknesses of the specimen significant section and the specimen shoulders are 1.9 and 5.0 mm, respectively. This difference is chosen such that the specimen shoulders deform elastically, while the central gauge section exhibits large plastic deformations. Also, the shoulders dimensions provide sufficient gripping area. Another design particularity is the complex loft surface in the gauge section of the specimen, which lowers the likelihood of fracture in the vicinity of the specimen boundaries. The tensile strains along the free boundaries are further reduced [112]. Consequently, the fracture is most likely to initiate near the specimen centre in the gauge section under all loading combinations and at the same time the specimen experience a wide range of stress states (stress triaxiality).

The stress triaxiality η is defined by the ratio of hydrostatic stress σ_h and the von Mises equivalent stress σ_{eq} [112].

$$\eta = \frac{\sigma_h}{\sigma_{eq}} = \frac{\text{sign}(\sigma)}{\sqrt{3 + 12(\frac{\tau}{\sigma})^2}} \,. \tag{3.15}$$

The stress triaxiality is zero for shear dominant loading ($\sigma/\tau \to 0$) while it approaches its maximum value of $\eta = 1/\sqrt{3}$ as the pure tension becomes dominant ($\sigma/\tau \to \infty$) [112]. To sum up, the biaxial loading allows exploring initial stress triaxialities ranged from 0 for pure shear (α = 0°) to 0.58 for pure tension (α = 90°). For α = 30° and 60° (both combined tension and shear) the stress triaxiality are: 0.19 and 0.38, respectively [112].

Mohr and Doyoyo proposed analytical formulas for the average shear (σ_{xy}) and average normal stresses (σ_{xx} and σ_{yy}) at the central section of the specimen in the elastic regime, which were already explained in section: 2.6.2 Arcan Clamped Configuration (Two Pin) - Analytical Formulas, equations 2.15 to 2.18. The specimen stiffness ratios β_x, where directly calculated from the equation $\beta_x = 2/(1-\nu)$ using the elastic Poisson ratio of 0.4, 0.38 and 0.3, respectively for HDPE, PP and PA6, taken from [76].

The designed butterfly specimen was analysed by 3D FE calculations performed using Abaqus version 6.16. The 3D FE mesh of the butterfly-shaped specimen, is a twenty-node linear brick element with reduced-integration, C3D20R. More detailed information about mesh is given in chapter 6. Note that the mesh is sufficiently refined in the gauge section. The FE calculations in

tension confirmed that the gauge section of the butterfly specimen is where the plastic deformation and the onset of fracture processes are confined. Also, due to the notch in the gauge section the stresses are non-uniform.

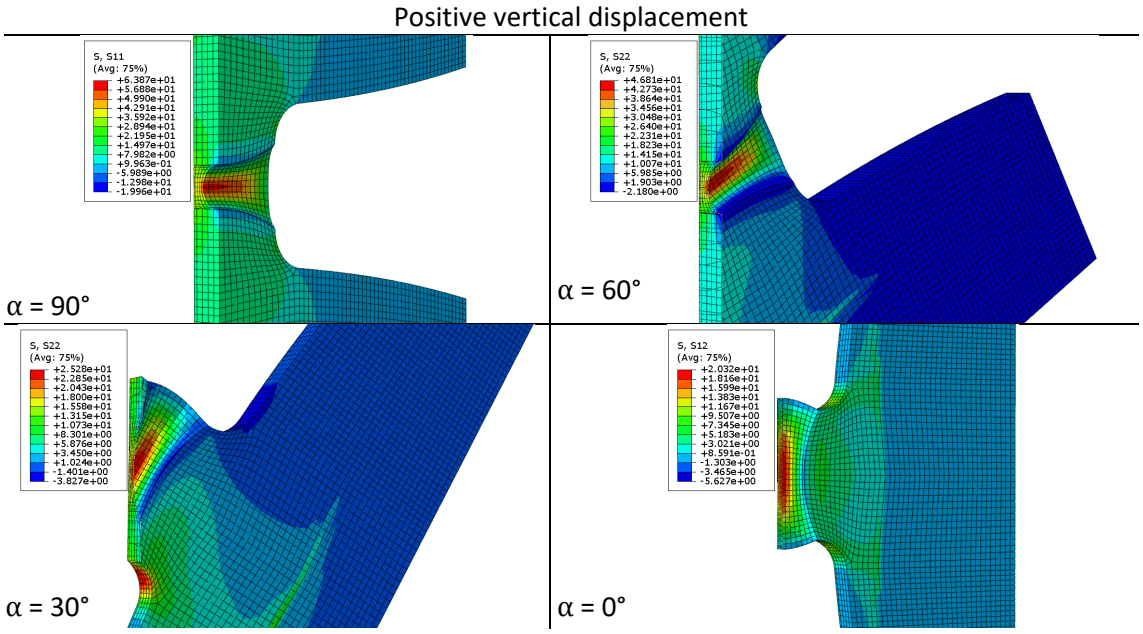


Figure 48 - FE results in terms of stress distribution of butterfly specimen under positive vertical displacement, along the loading angle.

Table 17 – Stress/strain analytical formulas, stress triaxiality and lode angle used in this research.

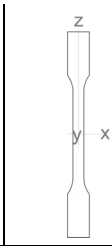
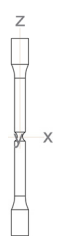
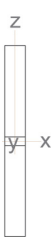
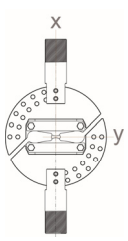
					
	Dumbbell	**Cylindrical Notched**	**Flat Notched**	**Cylindrical (compression)**	**Arcan Clamped Configuration/ Butterfly Specimen**
σ_{xx}	-	$\sigma \ln(\frac{a^2+2aR-x^2}{2aR})$	$\frac{2}{\sqrt{3}}\sigma(\frac{1}{2}+\ln(\frac{a^2+2aR-x^2}{2aR}))$	-	$\left(\frac{\beta_x \sin\propto}{(1-\beta_x)\cos^2\propto+\beta_x}\right)\times\frac{F}{A}$
σ_{yy}	-		$\frac{2}{\sqrt{3}}\sigma\ln(\frac{a^2+2aR-x^2}{2aR})$	-	$\nu\times\sigma_{xx}$
σ_{zz}	$\sigma_e=\frac{F}{A_o}$ $\sigma_t=\sigma_e(1+\varepsilon_e)$	$\sigma(1+\ln(\frac{a^2+2aR-x^2}{2aR}))$	$\frac{2}{\sqrt{3}}\sigma(1+\ln(\frac{a^2+2aR-x^2}{2aR}))$	$\sigma_e=\frac{F}{A_o}$ $\sigma_t=\sigma_e(1+\varepsilon_e)$	-
σ_{xy}	-	-	-	-	$\left(\frac{cos\propto}{(\beta_x-1)\sin^2\propto+1}\right)\times\frac{F}{A}$
ε	$\varepsilon_e=Extenso.$ $\varepsilon_t=ln(1+\varepsilon_e)$	$\varepsilon_{eq}=2\ln(\frac{a_0}{a})$	$\varepsilon_{eq}=\frac{2}{\sqrt{3}}\ln(\frac{t_0}{t})$	$\varepsilon_e=\frac{l_1-l_o}{l_o}$ $\varepsilon_t=ln(1+\varepsilon_e)$	-
η	$\frac{1}{3}$	$\frac{1}{3}+\sqrt{2}\ln(1+\frac{a_0}{2R})$	$\frac{\sqrt{3}}{3}(1+2\ln(1+\frac{t}{4R}))$	$-\frac{1}{3}$	$\frac{\sigma_h}{\sigma_{eq}}=\frac{\text{sign}(\sigma)}{\sqrt{3}+12(\frac{\tau}{\sigma})^2}$
θ	1 [8]	1 / -1 (when compression) [8]	0 [8]	-1 [8]	From 0 to ±1 [112]

Figure 48 presents elastic FE results in terms of stress distribution in the butterfly specimen for four loading angle values, $\alpha = 90°$ (pure tension), $\alpha = 30°, 60°$ (both combined tension and shear) and $\alpha = 0°$ (pure shear) right at the deformation beginning (elastic domain). The basic materials properties applied are listed on Table 16.

Table 17 lists the analytical expressions used in this research for stress distribution in the minimal cross section, as well the stress triaxiality and lode angle. Using these analytical expressions, the local stresses and strains in the elastic regime, can be calculated and therefore, allowing the yield points evaluation.

3.3.5 Dynamic Mechanical Analysis (DMA) Specimens

According to the ISO 6721-1, the dimensions of the specimens shall be as required by the equipment for the DMA test mode. It must have uniform size or shape and are ordinarily analysed in rectangular form [74]. DMA specimens of uniform dimensions were cut from the butterfly specimen shoulders, illustrated in red areas in Figure 49 (1). Care was taken to ensure that specimen edges were parallel and flat after cutting, a light sand paper sheet, 600 grit, was used when necessary to remove any machining burrs or surface inconsistencies. The overall dimensions of the DMA specimen are shown in Figure 49 (2).

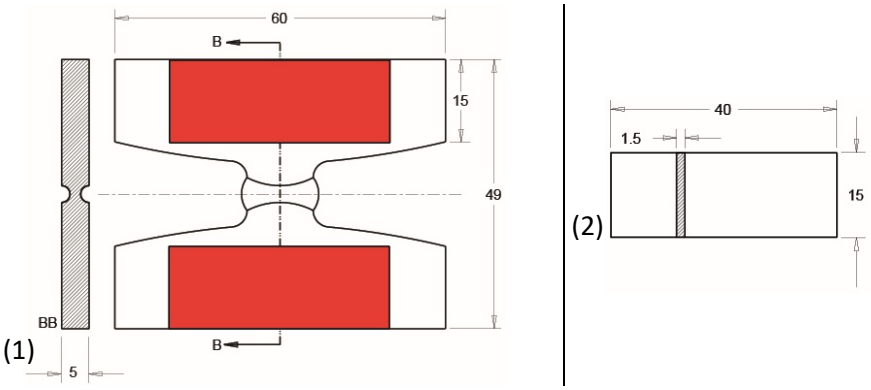


Figure 49 – (1) Locations of butterfly specimen from which the specimens were cut; (2) DMA specimen shape. Dimensions in mm.

3.3.6 Specimen for Differential Scanning Calorimetry (DSC) Experiments

Specimens for DSC experiments were machined from the butterfly specimen shoulders (extracted from the same localization of DMA specimens). The overall dimensions are shown in Figure 50. Those specimens were used to investigated the effect of strain/deformation on DSC, behaviour of the material. Thus, virgin/injected and deformed specimens, were tested by DSC. DSC does not require a specimen with a well-defined geometry. The test specimens are cut, with an appropriate mean, in the form of solid granulates small enough to fit in an aluminium DSC container.

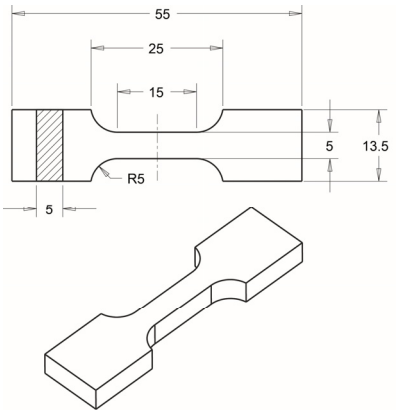


Figure 50 – Specimen for differential scanning calorimetry (DSC). Dimensions in mm.

3.4 Arcan Apparatus

For the present biaxial experiments, it was designed and manufactured an arcan apparatus (Figure 51 (1)). The designed arcan apparatus is a modification based on the work by Doyoyo and Wierzbicki [96], which in turn is based on the original specimen presented by Arcan et al. [94]. The loading apparatus consists of two pairs of plane semi-circular loading steel plates and the butterfly specimen placed in between. The array of pin holes locations on the outer edge of the loading plates provides a range of biaxial loading angles α. The biaxial loading angle can be varied in steps of 15° from 0° to 90°. They correspond, to shear (0°) (Figure 51 (2)), combined of tension/compression and shear load with varying proportions (15° to 75°) and pure tensile/compression (90°) (Figure 51 (3)) loading conditions. With the increase of loading angle from 0° to 90°, the proportion of the tensile force increases and no shear force is present in the 90° position.

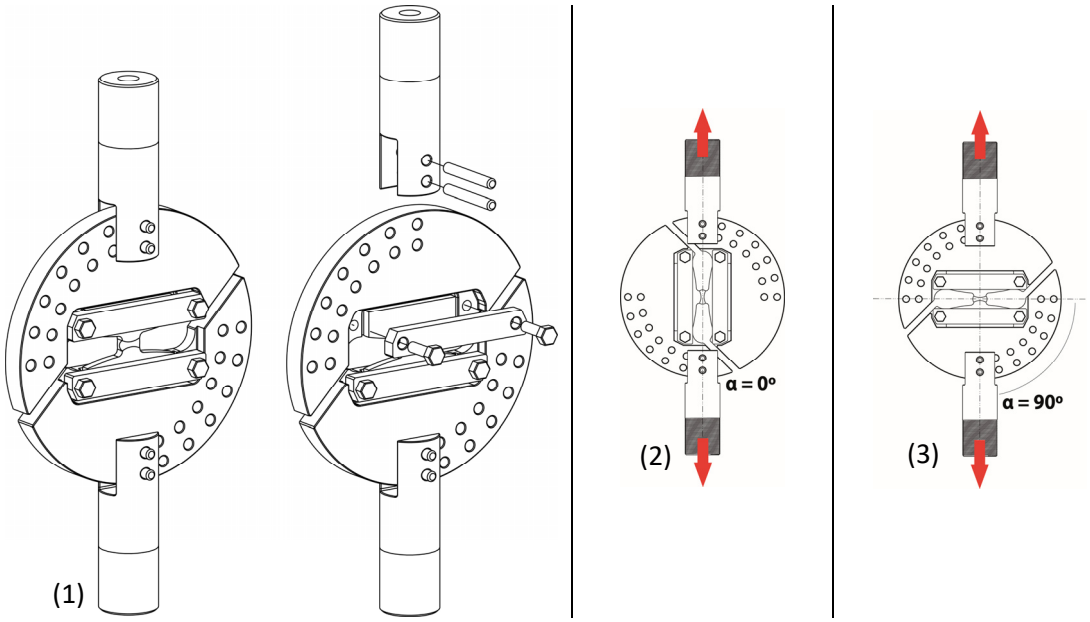


Figure 51 – (1) Designed arcan apparatus with the butterfly specimen, (2) α = 0° (pure shear) and (3) α = 90° (pure tension/compression).

The butterfly specimen connects the two semi-circular loading plates. Two removable clamps positioned the butterfly specimen in the symmetry plane of the arcan apparatus. Two screws at each side provided sufficient clamping pressure. The plates are connected to a universal testing machine by intermediate grips (at the top and bottom) via loading pins. The four pins, two in opposite side, prevents any rotation or misalignment either vertical or horizontal during the biaxial loading. The out-of-plane is avoided. Since plates, grips and butterfly specimen are aligned along the loading axis of the universal testing machine, the measurement of the vertical force is not influenced. (Detailed technical drawings can be found in Appendix 8.1.1).

The designed experimental set-up controls the localization of deformation gradients, which are highest in the central gauge section of the butterfly specimen and measures all forces acting on the specimen; also subjects the significant section of a butterfly specimen to a near uniform stress-strain and a homogeneous deformation field.

Two modifications were made in arcan apparatus for temperature testing: (1) As the fixture setup of Instron 3367 loading machine was different from servohydraulic MTS 810 universal testing machine a new design for intermediate grips (at the top and bottom) were developed and (2) Due to temperature increases the material softens and flows more easily, therefore four clamps were designed in order to provide an extra clamping pressure, avoiding any specimen displacement (Figure 52). (Detailed technical drawings can be found in Appendix 8.1.2).

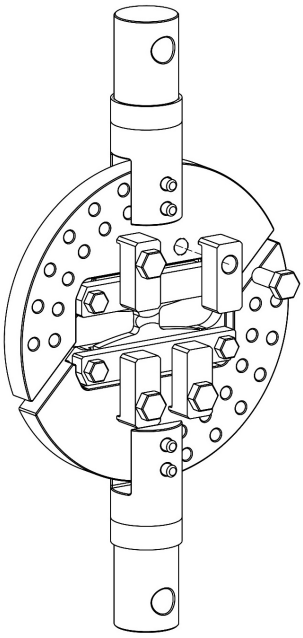


Figure 52 – Modifications in arcan apparatus for temperature testing.

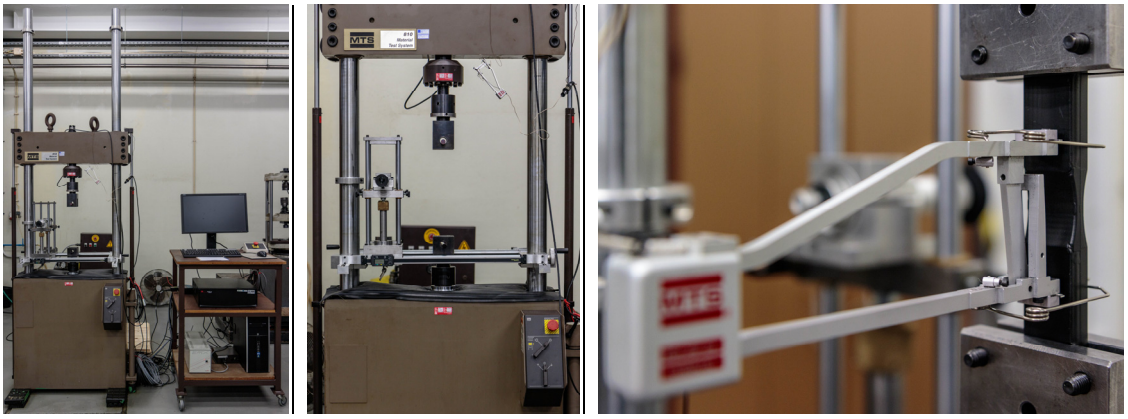
3.5 Testing Machines, Testing Matrix and Testing Conditions

The standard environment at which the tests were performed was: air temperature of 21 °C (deviation ± 2 °C) and relative humidity of 55% (deviation ± 10 %) at room temperature (RT), also was the same environment at which all specimens were conditioned. In all processes, cautions

to avoid exposing the specimens to any aggressive environment, such as high temperatures, UV light, chemicals and humidity extremes, were taken in consideration. The shape of specimens during deformation were recorded by a Canon 7D Mark II digital camera with a canon 17-55mm EF-S f2.8 IS USM lens.

3.5.1 Mechanical Tests at Room Temperature (RT)

The experimental results should reflect the material behavior but might depend largely on the test set-up and specimen behavior. The RT mechanical tests were carried out on a servohydraulic MTS 810 universal testing machine (MTS Systems Corporation), with a 10KN load cell (Figure 53 (1)). In order to compare the yield responses obtained from a series of tension/compression and biaxial loading (pure shear, combined shear and tension/compression, pure tension/ compression), different crosshead speeds of 1, 20 and 200 mm/min, were tested.



(1) (1) (2)

Figure 53 – (1) Servohydraulic MTS 810 universal testing machine and (2) MTS 634.25 axial extensometer.

The displacement measurements were performed by a MTS 634.25 axial extensometer with a gauge length of 50 mm (Figure 53 (2)) in all tensile tests, whereas for compression and biaxial tests the displacement measurements were delivered by the MTS 810 internal displacement transducer. Both displacement and force were recorded by data acquisition at an appropriate frequency (depending on crosshead speed). The specifications of the MTS 810 universal testing machine can be found in Table 18, and in Table 19, the specification of MTS 634.25 axial extensometer, are presented.

Table 18 - MTS 810 universal testing machine specifications [147].

Parameters	Units	MTS 810
Maximum Force	KN	100
Available Actuator	KN	10, 25, 50, 100
Max. Vertical Test Space	mm	1625

Table 19 - MTS 634.25 axial extensometer specifications [148].

Parameters	Units	MTS 634.25
Gauge Length	mm	50.00 ±0.05
Maximum Travel	mm	0 to 25
Maximum Strain	%	0 to 50

Tension/compression tests: To study the yield behaviour of HDPE, PP and PA 6 under tension conditions dumbbell specimens, flat notched specimens and cylindrical notched specimens, were used. The specimens were clamped at both ends of the MTS 810. One end was fixed while the other was displaced at a pre-defined constant crosshead speed.

Cylindrical notched and unnotched, were tested under compression. Friction between loading steel platen of the testing machine and specimens was minimized by applying a lubricant to the contact surfaces. To minimize the incidence of specimen shearing during the compression, care was taken to ensure the cylinder ends were smooth and parallel.

Table 20 - Total number of tensile tests.

Material	Testing Speed (mm/min)	Specimen Type		
		Dumbbell	Flat Notched Radius= 30 and Radius= 5	Cylindrical Notched Radius= 30 and Radius= 5
HDPE	1	5	5 + 5	5 + 5
	20	5	5 + 5	5 + 5
	200	5	5 + 5	5 + 5
PP	1	5	5 + 5	5 + 5
	20	5	5 + 5	5 + 5
	200	5	5 + 5	5 + 5
PA 6	1	5	5 + 5	5 + 5
	20	5	5 + 5	5 + 5
	200	5	5 + 5	5 + 5
		Total: 45	**Total: 90**	**Total: 90**

Table 21 - Total number of compression tests.

Material	Testing Speed (mm/min)	Specimen Type	
		Cylindrical	Notched
HDPE	1	5	5
	20	5	5
	200	5	5
PP	1	5	5
	20	5	5
	200	5	5
PA 6	1	5	5
	20	5	5
	200	5	5
		Total: 45	**Total: 45**

The width and thickness or the diameter in cylindrical specimens were measured with a sliding caliper prior to the testing. In general, five repetitions were performed for each specimen, geometry and material, also the force displacement curves were checked for repeatability of the experiments results. The total number of specimens used are depicted in Table 20, for tensile tests, and in Table 21 for compression tests.

Biaxial loading tests: Positive and negative vertical constant speeds were performed on the butterfly specimens at four different loading angles, α = 0°, 30°, 60° and 90° (Figure 54) at different crosshead speeds (1, 20 and 200 mm/min) until the entire gauge section failed, corresponding to a sudden drop in the applied force. By varying the biaxial loading angle and the strain rates, HDPE, PP and PA are subjected to different stress states. The total number of butterfly specimens used in positive vertical displacement tests are depicted in Table 22. The same amount of butterfly specimens, were used in negative vertical displacement tests, with exception to the loading angle α= 0° (pure shear) (Table 23). In this situation, performing the tests in positive or negative speeds yields the same (loading type – shear). Therefore, a total of 315 = 180 (Tensile) + 135 (Compression) butterfly specimens, were tested.

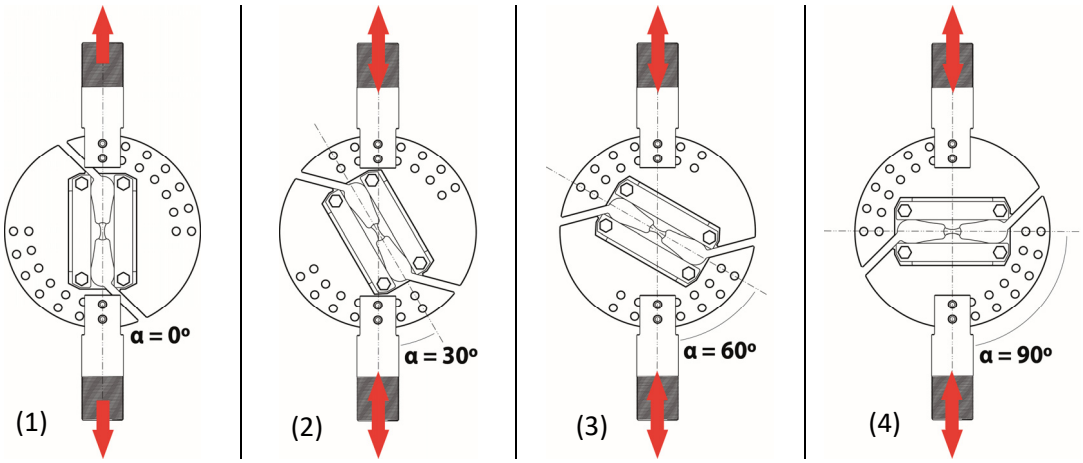


Figure 54 – Butterfly specimen at four different loading angles, (1) α = 0° (pure shear), (2) and (3) α = 30°, 60° (both combined shear and tension/ compression) and (4) α = 90° (pure tension/ compression).

Table 22 - Total number of butterfly specimens used in combined tensile/shear loading.

Material	Testing Speed (mm/min)	Number of butterfly specimens			
		α= 0°	α= 30°	α= 60°	α= 90°
HDPE	1	5	5	5	5
	20	5	5	5	5
	200	5	5	5	5
PP	1	5	5	5	5
	20	5	5	5	5
	200	5	5	5	5
PA 6	1	5	5	5	5
	20	5	5	5	5
	200	5	5	5	5
		Total: 180 Butterfly Specimens			

Table 23 - Total number of butterfly specimens used in combined compression/shear loading.

Material	Testing Speed (mm/min)	Number of butterfly specimens		
		α= 30°	α= 60°	α= 90°
HDPE	1	5	5	5
	20	5	5	5
	200	5	5	5
PP	1	5	5	5
	20	5	5	5
	200	5	5	5
PA 6	1	5	5	5
	20	5	5	5
	200	5	5	5
		Total: 135 Butterfly Specimens		

3.5.2 Mechanical Tests at 50 °C (Constant Temperature)

The behaviour of HDPE, PP and PA 6 at constant temperature of 50 °C was investigated. The loading force was transmitted to the butterfly specimen through arcan apparatus, which was placed inside Instron environmental chamber (temperature rating from -150 °C to +350 °C) and attached to an Instron 3367 loading machine (Figure 55) [149]. The loading force and displacement were continuously measured by internal devices of Instron 3367. The specifications of the Instron 3367 universal testing machine can be found in Table 24.

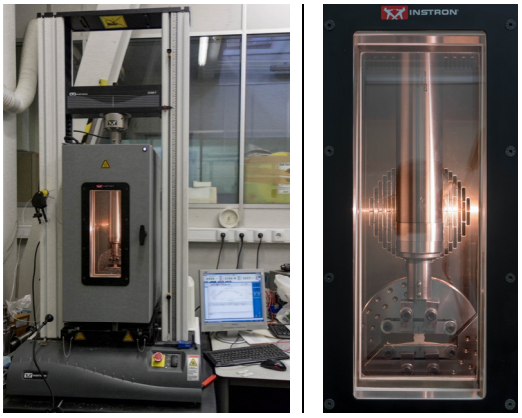


Figure 55 - Instron environmental chamber and Instron 3367 loading machine.

Table 24 - Instron 3367 universal testing machine specifications [149].

Parameters	Units	Instron 3367
Load Force Capacity	KN	30
Max. Speed	mm/min	500
Max. vertical test space	mm	1193

The methodology for testing at elevated temperatures was similar to that at ambient conditions. Four different loading angles, α = 0°, 30°, 60° and 90°, were applied in the butterfly specimens (Figure 54) at different crosshead speeds (1 and 200 mm/min). The tests were performed after the specimen stabilizing in the chamber for 20 minutes at the required temperature (50 °C) in order to obtain sufficiently constant cross-sectional temperature (assure thermal equilibrium). The total number of butterfly specimens used in positive vertical displacement tests are depicted in Table 25. As above mentioned, for negative vertical displacement α= 90° (pure shear) loading angle is equal to α= 90° in tensile loading, therefore it is excluded, which gives a total of 72 (Tensile) + 54 (Compression) tests.

Table 25 - Total number of butterfly specimens used in combined tensile/shear loading.

Material	Testing Speed (mm/min)	Number of butterfly specimens			
		α= 0°	**α= 30°**	**α= 60°**	**α= 90°**
HDPE	1	3	3	3	3
	200	3	3	3	3
PP	1	3	3	3	3
	200	3	3	3	3
PA 6	1	3	3	3	3
	200	3	3	3	3
		Total: 72 Butterfly Specimens			

3.5.3 Differential Scanning Calorimetry (DSC)

The HDPE, PP, PA 6 materials were characterized using a TA Instruments DSC Q20 (Figure 56 (1)) on approximately 8 to 10 mg of material. The test specimens were in form of solid granulates small enough to fit in an aluminium DSC pan hermetically sealed by a lid. Specific heat capacity was calculated from two measurements, sample measurement and empty run.

Some aspects of the DSC scan, as the exact location of glass transition temperature, are somewhat dependent on the imposed heating rate. Therefore, care must be taken in choosing a heating rate and a compromise should always be sought between a fast rate that would cause non-uniform heating of the sample and a very slow rate that could cause ageing of the sample in the DSC pan. For that purpose, the tests were performed between -80 °C and 250 °C and at a heating rate of 10 °C /min to determine the heat of fusion (enthalpy ΔH_f), the degree of crystallinity, melting temperature (T_m) and glass transition temperature (T_g) of the materials. The heat of fusion was calculated by integrating the area under the differential scanning calorimetry endotherm peak.

DSC tests, were also performed on pre-strained material by tensile tests. The tensile tests on the designed specimens for DSC experiments were performed at room temperature and at a crosshead speed of 1 mm/min on servohydraulic MTS 810 universal testing machine. Two true strains were defined: 0.5 and 1 for each specimen. The specimens were then unloaded to zero force and a cut of the material from the deformed region, was performed for DSC. At this point, the DSC results were used to investigate the effect of deformation on the tested material crystallinity.



(1) (2)

Figure 56 – (1) DSC. TA Instruments DSC Q20 and (2) DMA. TA instruments model Q800.

The most relevant characteristics of the DSC equipment can be found in Table 26. In Table 27 are depicted the machine-parameters used in the DSC analyses. The reproducibility of the measurements was verified by achieving a second run. The total number of DSC tests are depicted in Table 28.

Table 26 - Machine Specifications – DSC Q20 [150].

Parameters	Units	DSC Qdsc20
Temperature Range	°C	-180 to 725
Temperature Accuracy	°C	± 0.1
Temperature Precision	°C	± 0.05
Measuring Range	mW	± 350

Table 27- Parameters used in DSC analyses.

			Values From Literature [76].		
Material	**Temperature Range (°C)**	**Heating Rate (°C/min)**	**Glass Transition (T_g)**	**Melting Temperature (T_m)**	**Degree of Crystallinity (%)**
HDPE	-80 to +250	10	-100°C, -60°C	130°C to 137°C	35 to 90
PP			-20°C	168°C to 175°C	40 to 70
PA 6			50°C	215°C to 220°C	50

Table 28 - Total number of DSC tests.

Material	Virgin Specimen	Strained Material	
		True Strain 0.5	True Strain 1
HDPE	2	2	2
PP	2	2	2
PA 6	2	2	2

3.5.4 Dynamic Mechanical Analysis (DMA)

The DMA equipment from TA instruments, model Q800 (Figure 56 (2)) was calibrated before the tests. The most relevant characteristics of the equipment can be found in Table 29. The viscoelastic spectrum, storage modulus E', loss modulus E'' and loss factor tan (δ) $(d = E''/E')$ were evaluated using a simple cantilever beam system with strain amplitudes of 0.5 % in the linear viscoelastic range of the materials. The number of tested specimens for each material, were two. Three single frequencies were applied (0.1, 1 and 10 Hz) at a heating rate of 2 °C/min. The tests were performed with a temperature gradient ranging from room temperature of ± 30 °C to a temperature lower than the melting temperature for each material in order to prevent any damage in the testing machine. Table 30 depicts the machine-parameters used in the DMA analyses. Figure 57 shows the DMA experimental framework.

Table 29 – DMA Machine Specifications – DMA Q800 [151].

Parameters	Units	DMA Q800
Maximum Force	N	18
Strain Resolution	-	0.00001
Frequency Range	Hz	0.01 to 200
Temperature Range	°C	-150 to 600
Heating Rate	°C/mm	0.1 to 20

Table 30 – Parameters used in DMA analyses.

Material	Frequency (Hz)	Strain (%)	Temperature (°C)	Heating Rate (°C/min)
HDPE	0.1, 1 and 10	0.5	RT to +110	2
PP			RT to +140	
PA 6			RT to +190	

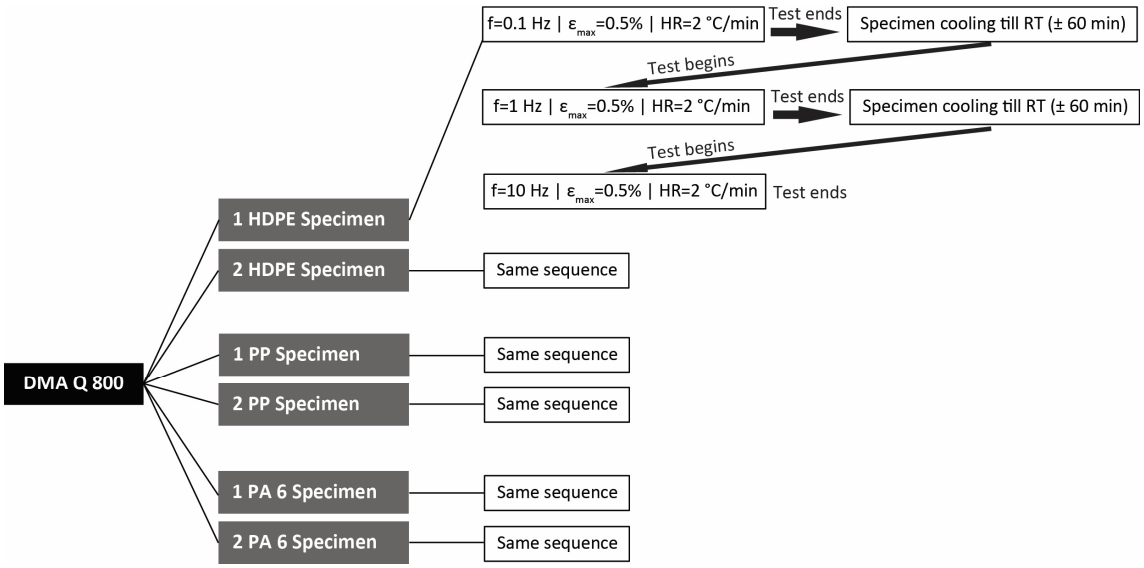


Figure 57 – DMA experimental framework.

3.5.5 Scanning Electron Microscopy (SEM)

The fracture surface on HDPE, PP and PA 6 butterfly specimens were examined on a scanning electron microscope (SEM). The surface fracture observations only included, one butterfly specimen for three biaxial loading angles, $\alpha = 0°$, 30°, and 90° at crosshead speed of 200 mm/min, at room temperature 21 °C ± 2 °C and constant temperature of 50 °C. For a better understanding, the total number of SEM observations on butterfly specimens are depicted in Table 31.

Table 31 - Total number of butterfly specimens used in SEM observations.

Material	**Crosshead Speed (mm/min)**	**Number of Butterfly Specimens**					
		Room Temperature 21 °C ± 2 °C			Constant Temperature of 50 °C		
		α= 0°	**α= 30°**	**α= 90°**	**α= 0°**	**α= 30°**	**α= 90°**
HDPE	200	1	1	1	1	1	1
PP		1	1	1	1	1	1
PA 6		1	1	1	1	1	1
		Total: 18 Butterfly Specimens					

Fracture surfaces of HDPE, PP and PA 6 flat notched and cylindrical notched specimens with notch radii of *R* = 30 mm and *R* = 5 mm tested at crosshead speed of 200 mm/min and at room temperature, were also examined by SEM. Table 32 depicts the total number of SEM observations for flat and cylindrical notched specimens.

Table 32 - Total number of flat and cylindrical notched specimens used in SEM observations.

Material	**Crosshead Speed (mm/min)**	**Number of Specimens**			
		Flat Notched Specimen		Cylindrical Notched Specimen	
		Radius 5	**Radius 30**	**Radius 5**	**Radius 30**
HDPE	200	1	1	1	1
PP		1	1	1	1
PA 6		1	1	1	1
		Total: 12 Butterfly Specimens			

The SEM observations were performed by an SEM microscope FEI Quanta 400FEG ESEM (Figure 58) with a nominal resolution of <2 nm. The secondary electrons (SE) mode allowed a detailed examination of the semi crystalline structure. The intensity of the digitized micrographs is defined on a 256 greyscale [152]. The specimens were fixed with double coated carbon tape which, also allows the dissipation of the electron beam charge and heat. All specimens were coated with silver before scanning with SEM using Jeol, IFC 1600 coating machine. The specimens were observed under different magnifications.

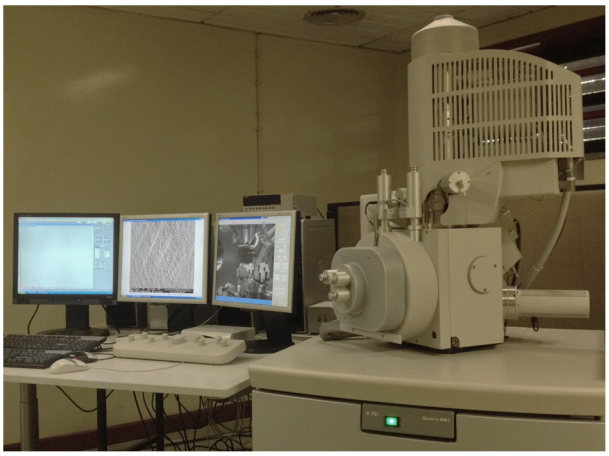


Figure 58 - SEM instrument FEI Quanta 400FEG ESEM.

Butterfly specimens fracture to be characterized by scanning electron microscopy (SEM) were treated according to the following protocol: (1) shoulder laterals were cut, (2) shoulder height was reduced to half and was finely polished and (4) fractured surface was coated with a thin silver layer to enhance their conductivity. For flat and cylindrical notched specimens, the same protocol was followed, however in these particular cases the main body were cut almost until the begin of notch radii in order to fit on the SEM stage.

4 Experimental Results and Discussion

Mechanical properties are one of the primary criteria to meet for engineering applications. Since the discovery of polymers, there have been a large number of studies on their mechanical properties. Most of the fundamental works were carried out based on polyethylene, polypropylene and polyamide 6. However, the mechanical properties of polymers are still not fully understood because they are tightly related with their complex microstructure and loading conditions.

When a tensile or compressive load is applied to a specimen, the properties of the material can be quantified by the analyses of load-displacement behaviour. For polymers, the load-displacement behaviour is sensitive to testing temperature and crosshead speed, due to the viscous nature of the polymers. Young's modulus, load and displacement at yield load, and load and displacement at fracture point are some important indicators of the mechanical behaviour.

The mechanical response of high-density polyethylene, polypropylene and polyamide 6, were examined under different stress states. In order to compare the yield load, temperature responses and neck propagation (strain localization) a series of biaxial loading tests (pure shear, combined shear and tension/compression, pure tension/compression) at different crosshead speeds of 1, 20 and 200 mm/min, were performed at room temperature and at temperature of 50 °C.

In order to investigate a wider range of stress states, tensile tests were performed on dumbbell, flat notched and cylindrical notched specimens with different notch radii. In addition, compression tests on cylindrical and cylindrical notched specimens, were included in the research program. Various additional analysis techniques were used to characterize the thermal properties and crystallinity, using differential scanning calorimetry and dynamical mechanical analysis.

ISO 527-1, defines the yield stress as the first stress at which an increase in strain occurs without an increase in stress [66]. As a convention in this monograph, and hereinafter, from the load displacement curves the yield load is considered as the first maximum force at which an increase in displacement occurs without an increase in load, when noticeable.

4.1 High-Density Polyethylene (HDPE)

HDPE is composed of ordered crystalline and amorphous regions, being of great technological interest as they combine the strength of purely crystalline materials with the strain hardening of fully amorphous polymers. Deformation mechanisms of HDPE are always accompanied by changes in the microscopic structure of the material that result in an alteration of specimen properties during deformation. Establishing a link between the underlying micro structure and mechanical properties behaviour is one of the major challenges in polymer's science.

4.1.1 Tensile Tests at Room Temperature

Tensile test is probably the most common type and widely used mechanical test. From laboratory tests on dumbbell, flat notched and cylindrical notched specimens, information about the material behaviour is disclosed. Three different crosshead speeds of 1, 20 and 200 mm/min, were used. As mentioned in section: 3.5 Testing Machines, Testing Matrix and Testing Conditions the standard environment in which the tests were performed, was: air temperature of 21 °C (deviation ± 2 °C) and relative humidity of 55% (deviation ± 10 %) at room temperature.

The mechanical tests were carried out on a servohydraulic MTS 810 universal testing machine. The applied force was recorded by servohydraulic MTS 810, whereas the deformation was monitored by MTS 634.25 axial extensometer axial extensometer and recorded by a Canon 7D Mark II digital camera with a canon 17-55mm EF-S f2.8 IS USM lens. Five tests were performed for each specimen geometry and crosshead speeds.

The load-displacement curves of HDPE drawn at three crosshead speeds are displayed in Figures 59 and 60, for each specimen geometry. The load-displacement responses were compared to ensure repeatability of the results. The scatter between the tests batches was relatively small. It is shown that the three specimen geometries exhibit, two distinct features, first the yield load in the lowest speed reaches a maximum corresponding displacement value at higher displacements. At lower crosshead speed and displacements, the polymer macromolecules have the time necessary to induce an orderly alignment just enough to accept the increase in deformation. At higher crosshead speed, increases both the propensity of the material to form a clear and higher yield load at lower displacement values. It is also clear the reduction of ductility as the crosshead speed increases exhibiting the material a more brittle behaviour.

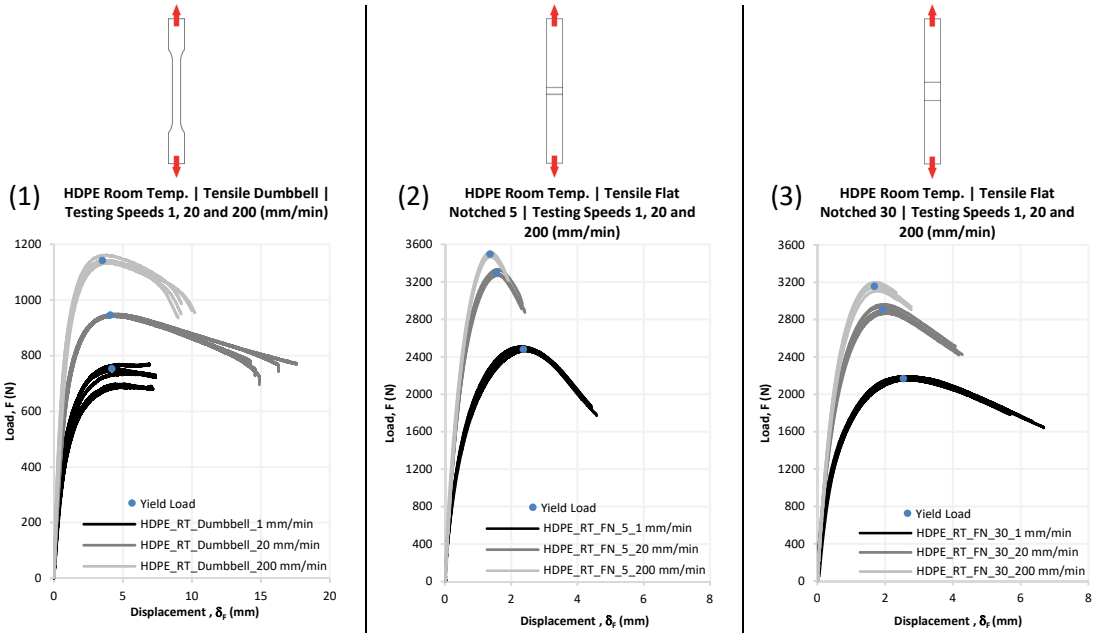


Figure 59 – Tensile load-displacement curves of (1) Dumbbell, (2) flat notched 5 and (3) flat notched 30 specimens (HDPE, Room Temperature).

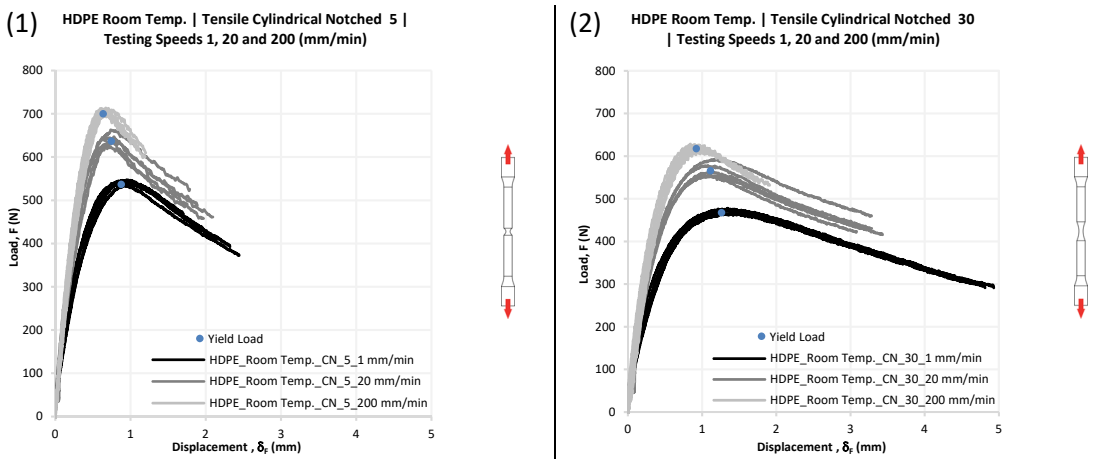


Figure 60 - Tensile load-displacement curves of (1) cylindrical notched 5 and (2) cylindrical notched 30 specimens (HDPE, Room Temperature).

Tables 33, 34, 35, 36 and 37 shows sequential images and corresponding load and displacement values for the HDPE specimens at three deformation stages: virgin or unloaded, yield load or first maximum force and the interrupted test point. From values analysis, is observed an increase on the yield load, by about 57% (from 730.4 N to 1144.6 N) for uniaxial tension of dumbbell, 40% (from 2485.3 N to 3488.8 N) for flat notched 5, 46% (from 2174.1 N to 3164.5 N) for flat notched 30, 30% (from 543.9 N to 707.1 N) for cylindrical notched 5 and 31% (from 474.4 N to 619.3 N) for cylindrical notched 30, when testing speeds increased from 1 mm/min to 200 mm/min.

Note: These tests were stopped after some deformation because the maximum travel of the extensometer was 25 mm, which was insufficient to fracture some HDPE specimen geometries. Therefore, none of these specimens were deformed until complete fracture.

Tensile test results on cylindrical notched specimens (Figure 60) indicate that the presence of notch altered the load-displacement behaviour. The results show changes in the load-displacement data due to the presence of two different notch radii: R 30 and R 5, despite the same minimum cross section. Also, this behaviour can be observed on flat notched specimens (Figure 59). The yield load increases with decreasing the specimen notch radii (increasing the stress triaxiality), whereas the corresponding displacement ductility decreases.

This behaviour might be attributed to the notch strengthening effect where the notch under tension produces radial and circumferential stresses in addition to the axial stress. These additional stresses could inhibit lamellar rotation toward axial direction; also alter the force acting on the crystalline lamellae, thereby altering their ability to participate in slip processes and delaying the onset of plastic deformation [143]. The plastic behaviour exhibits no displacement hardening.

Table 33 – Load and displacement values for dumbbell specimen at selected deformation stages (all values are averaged) (HDPE).

Testing Speed (mm/min)	**Yield Load**		**Interrupted Test**	
	Load, F (N)	Displ., δ_F (mm)	Load, F (N)	Displ., δ_F (mm)
1	730.4	5.3	682.9	7.1
20	948.1	4.5	750.1	15.3
200	1144.6	3.8	852.7	10.1

Table 34 – Deformation patterns and corresponding load and displacement values for flat notched 5 specimens at three deformation stages (all values are averaged) (HDPE).

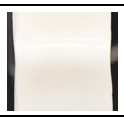
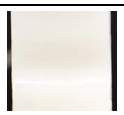
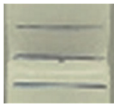
Testing Speed (mm/min)	**Virgin specimen**		**Yield Load**			**Interrupted Test**		
	Displ., δ_{0F} (mm)	Image	Load, F (N)	Displ., δ_F (mm)	Image	Load, F (N)	Displ., δ_F (mm)	Image
1	0		2485.3	2.4		1866.9	4.4	
20	0		3301.8	1.6		2977.1	2.3	
200	0		3488.8	1.4	-	3198.9	1.9	

Table 35 – Deformation patterns and corresponding load and displacement values for flat notched 30 specimens at three deformation stages (all values are averaged) (HDPE).

Testing Speed (mm/min)	**Virgin specimen**		**Yield Load**			**Interrupted Test**		
	Displ., δ_{0F} (mm)	Image	Load, F (N)	Displ., δ_F (mm)	Image	Load, F (N)	Displ., δ_F (mm)	Image
1	0		2174.1	2.6		1706.6	6.2	
20	0		2924.2	1.9		1393.1	9.1	
200	0		3164.5	1.7		3022.9	2.5	

Table 36 – Deformation patterns and corresponding load and displacement values for cylindrical notched 5 specimens at three deformation stages (all values are averaged) (HDPE).

Testing Speed (mm/min)	**Virgin specimen**		**Yield Load**			**Interrupted Test**		
	Displ., δ_{0F} (mm)	Image	Load, F (N)	Displ., δ_F (mm)	Image	Load, F (N)	Displ., δ_F (mm)	Image
1	0		543.9	0.9		410.3	2.2	
20	0		643.9	0.7		484.2	1.9	
200	0		707.1	0.6		571.8	1.3	

Table 37 – Deformation patterns and corresponding load and displacement values for cylindrical notched 30 specimens at three deformation stages (all values are averaged) (HDPE).

Testing Speed (mm/min)	**Virgin specimen**		**Yield Load**			**Interrupted Test**		
	Displ., δ_{0F} (mm)	Image	Load, F (N)	Displ., δ_F (mm)	Image	Load, F (N)	Displ., δ_F (mm)	Image
1	0		474.4	1.3		316.7	4.3	
20	0		572.2	1.2		431.0	3.3	
200	0		619.3	1.1		532.6	1.9	

The notch strengthening effect on cylindrical notched specimens can be observed from the sequential images from Table 36 and 37. It is verified that loading induces deformation along both radial and longitudinal directions in the notch. At deformation beginning, a so-called ‘‘renotching” phenomenon can be observed (at yield load) due to deformation localisation within the deformed shape emanating from the initial notched area. The “renotching” phenomenon is similar to the necking process. While the displacement increases, the notched area extends longitudinally, the notch radius becomes larger while the neck is stretched. This is called a “denotching” phenomenon. Due to this renotching/denotching effects and following Bridgman formula the stress triaxiality is expected to respectively, increase (renotching) and decrease (denotching) [145].

At above the yield load it was observed that the HDPE specimens gradually started to whiten, with the exception of dumbbell specimen. As the plastic deformation continued, the stress whitening became clearer and sets the shape changes (dilatation). Therefore, a neck started to form at the same location as onset of stress whitening. This characteristic was clearly noticeable among cylindrical notched specimens R 5 and R 30 (see the sequential figures on Table 36 and 37). Along with the stress whitening zone, the neck propagated through the notched section of the specimen during the deformation. Plastic dilation in polymers can be assumed to be related to damage. Such damage can be microvoids that grow from local irregularities of the molecular structure [43, 48, 153].

It was shown by Dasari et al. [154], using atomic force microscopy (AFM) that during uniaxial tensile deformation of HDPE, the transition from the initial spherulitic structure by plastic deformation to the final fibrillar structure involves the destruction of the lamellae, alignment and orientation of structure by longitudinal sliding motion of fibrils/microfibrils. Brady and Thomas [155] summarizes the deformation of HDPE, in sequential order, as following: the stressed spherulitic lamellae shear into crystal blocks via chain unfolding, tilt and slip within lamellae and longitudinal slip at mosaic block interfaces; the blocks rotate such that the molecular chains align along the local principal stress direction; the crystal blocks thickness decrease in width by chain slip and unfolding until microfibrils of alternating crystal and amorphous regions are formed. Each lamellar stack forms numerous micronecks once the yield stress is reached. Each microneck in turn is associated with the formation of a microfibril morphology.

Possible multiphase layer structure with oriented crystalline morphology along the cross-section perpendicular to the melt flow, might be included in the responses reported in this study. Also, during the deformation process and with increasing the crosshead speed may lead to an increase in temperature producing a thermal softening of the material, which was not quantified. It should be apparent that the faster the crosshead speed, the less time for heat transfer, hence the more important the adiabatic effects, are. Also, the higher the experimental temperature, the smaller is the value of the plastic work input to the specimen and hence the lower the temperature rise under heating. For future work developments it is suggested to underline the importance of understanding the effects of thermomechanical behaviour during polymer deformations.

Chou et al. [156] measured temperature increasing during mechanical deformation of four polymers, in which PP and PA 6 are included. The polymers were tested in compression for six strain rates ranging from 0.0004/s to 1000/s at 22 °C (RT). Temperature rise developed during deformation was measured using a thermocouple. PA 6 and PP at lower strain, at yield stress, the temperature increase in the specimens was 6 °C for a strain rate of 1250/s and 2 °C for a strain rate of 1500/s, respectively, whereas at maximum strain (20%) the increase in temperature was 16 °C for PA 6 and 12 °C for PP.

Arruda et al. [157] have investigated the effects of strain rate on the plastic response of semi crystalline polymers. In their studies, uniaxial compression of polymethylmethacrylate (PMMA) was tested over a range of low strain rates, from -0.01/s and -0.1/s at RT. Temperature change was monitored through a single unfocused infrared detector element. They found that the

temperature increase during the test can cause thermal softening, and thus have effects on the stress-strain behaviour. The greater influence of temperature on the stress-strain behaviour was at intermediate and large strains in which for a strain rate of -0.1/s the specimen had a maximum temperature increment of 40 °C

The thermomechanical behaviour of polyamide 12 (PA 12) was studied for uniaxial monotonic loading tests performed on ISO 527 specimens, by Wattrisse et al. [158]. A specialised electronic system was performed to get a simultaneous recording of speckle and infrared images. A combined treatment of kinematics and thermal data then allowed the temperature of material surface elements to be tracked and local energy balances to be constructed. Both calorimetric and kinematic measurements indicate that the specimen softening is associated with a progressive localization of heat sources and strain-rates.

The temperature effect is therefore not regarded as important for the tension or compression test results, because the yield response and elastic domain have been selected as the focus of this research.

4.1.2 Combined Tensile/Shear Tests at Room Temperature

Biaxial loading situations happen in several applications. It is therefore crucial to understand the stress behaviour of the material under combined biaxial loadings. In this section a set of proportional biaxial loading tests in positive vertical (tensile/shear) constant speeds performed on butterfly specimen at RT, are presented and discussed. The experimental details are summarized as follows:

- Crosshead speeds of 1, 20 and 200 mm/min,
- Standard environment: air temperature of 21 °C (deviation ± 2 °C) and relative humidity of 55% (deviation ± 10 %),
- The mechanical tests were carried out on a servohydraulic MTS 810 universal testing machine,
- The applied force (F) and displacement (δ_F) were recorded by servohydraulic MTS 810 universal testing machine,
- The deformation was recorded by a Canon 7D Mark II digital camera with a canon 17-55mm EF-S f2.8 IS USM lens,
- Five tests were performed for each loading angles, α = 0°, 30°, 60°, and 90° and crosshead speeds,
- The basic results of the tests are presented in terms of load vs displacement curves,
- Tests were performed until the specimen fracture.

Figure 61 shows the results when a positive vertical displacement is applied during biaxial loading. At RT and for all loading angles, the corresponding load-displacement behaviour shows the expected increase in initial yield force with increase in crosshead speed. It can be observed that the load-displacement curves almost do not intersect each other; the higher the loading angle (from α = 0° to 90°), the higher the load required to deform the specimens, is. The general

shape of all curves, seems to be homothetic, for each biaxial loading angle exhibiting remarkably similar intrinsic behaviour.

The initial linear elastic response is followed by a nonlinear evolution, this nonlinearity increasing with applied crosshead speed. At the peak load denotes the onset of stress whitening at the central section of the butterfly specimens. Whitening and crazing may reveal that some formation of numerous microvoids (cavities) are taking place in the centre of a specimen shortly before yielding. With deformation, independently of the loading angle, near fracture point, the crazes, which are bridged by fibrils, open up and fracture occurs upon the failure of these fibrils, without causing cracking and global failure of the butterfly specimens.

For loading angles of $\alpha = 90°$ and $\alpha = 60°$, the mechanical response looks like to that obtained in above experiments for flat notched and cylindrical notched specimens. At $\alpha = 0°$, pure shear, the material behaviour is completely different, the yield displacement is increased and there is large deformation (strain hardening) which means more ductile behaviour.

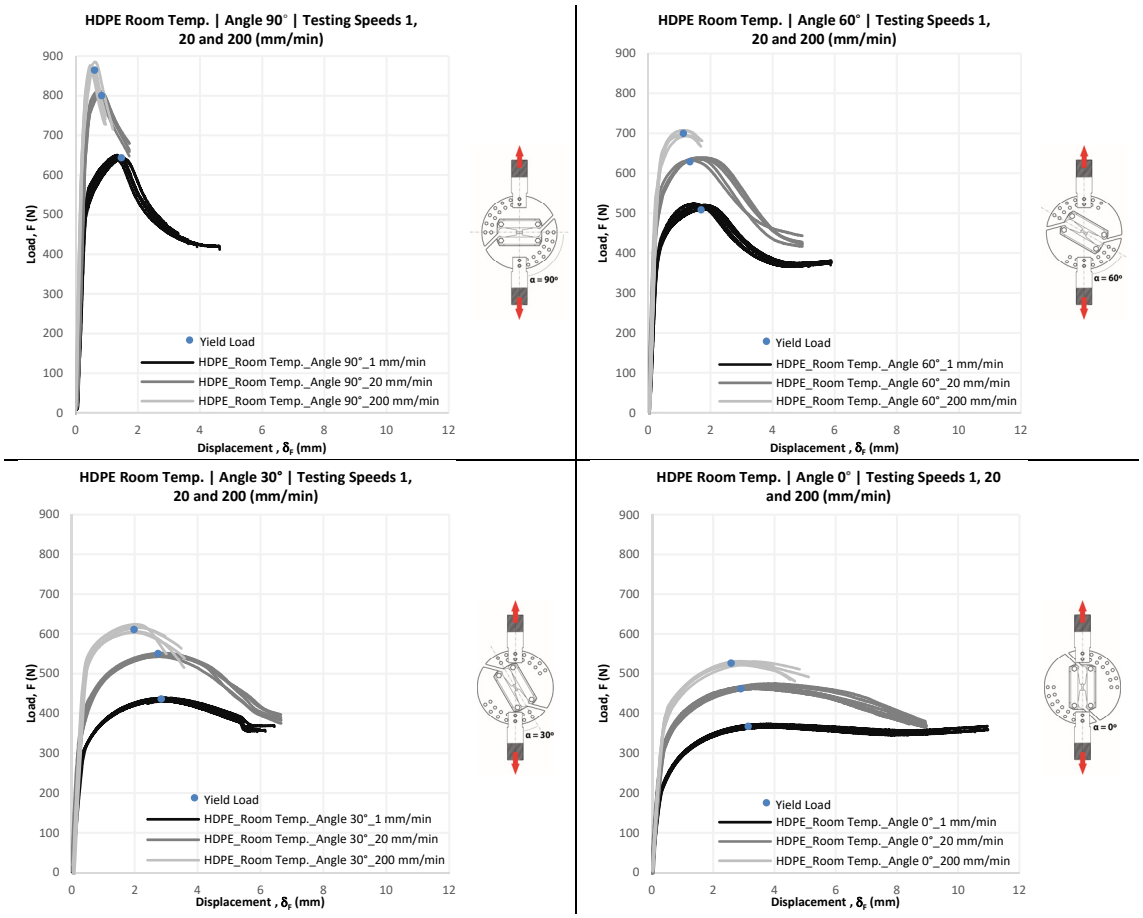


Figure 61 - Load-displacement curves for HDPE resulting from combined tensile/shear loading at RT: influence of crosshead speeds for each loading angle.

From Figure 62, changing the biaxial loading angle from $\alpha = 0°$ to 90° and fixing the crosshead speed, the load-displacement curves and yield loads shifts to higher values, whereas the displacement decreases. The simple, physical explanation of this phenomenon is that HDPE become more difficult to deform when the molecules get closer to an aligned, stretched

conformation, this situation happens when the loading angle for butterfly specimens is α = 90°, pure tensile [160].

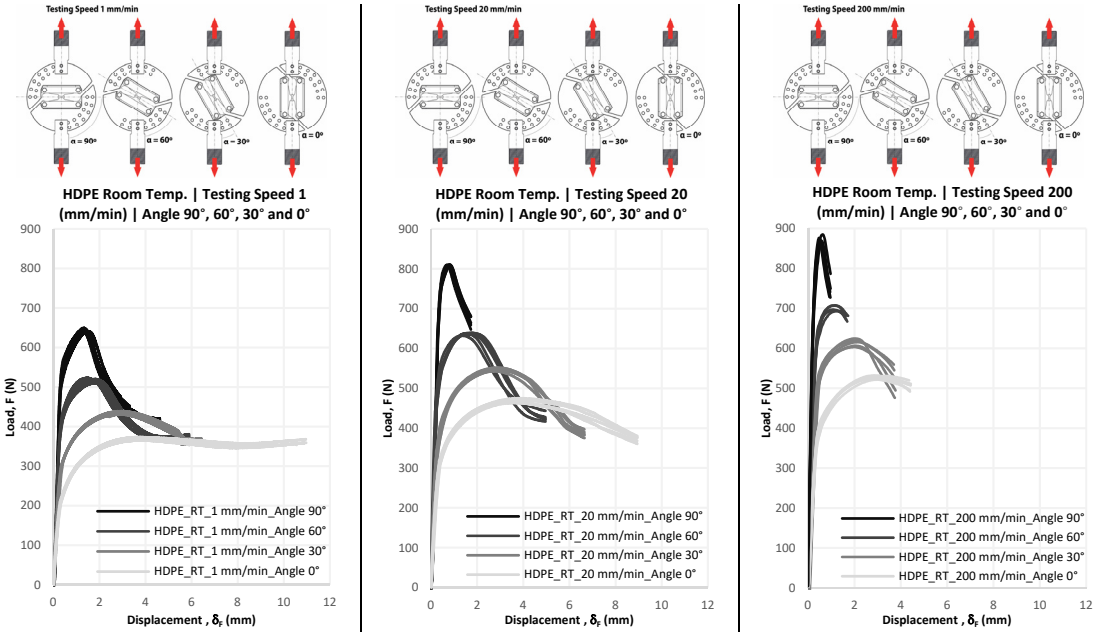


Figure 62 - Load-displacement curves for HDPE resulting for combined tensile/shear loading at RT: effect of loading angle for given crosshead speeds.

Tables 38, 39, 40 and 41 show sequential deformation images and corresponding load and displacement values for the HDPE specimens at three deformation stages: virgin or unloaded, yield load or first maximum force and fracture point. From values analysis on yield load at crosshead speeds of 1 mm/min to 200 mm/min, is observed an increase on the yield load values by about 37% (from 642.2 N to 876.9 N) for loading angle α = 90°, 35% (from 520.2 N to 699.7 N) for loading angle α = 60°, 41% (from 435.8 N to 614.3 N) for loading angle α = 30° and 43% (from 369.9 N to 527.5 N) for loading angle α = 0°.

Table 38 – Deformation patterns and corresponding load and displacement values for butterfly specimens loaded at α = 90° (pure tension) at RT (all values are averaged) (HDPE).

Testing Speed (mm/min)	**Virgin specimen**		**Yield Load**			**Fracture Point**		
	Displ., δ_{0F} (mm)	Image	Load, F (N)	Displ., δ_F (mm)	Image	Load, F (N)	Displ., δ_F (mm)	Image
1	0		642.2	1.4		432.2	3.8	
20	0		809.4	0.8		642.0	1.9	
200	0		876.9	0.6		594.8	1.5	

Table 39 - Deformation patterns and corresponding load and displacement values for butterfly specimens loaded at α = 60° (combined tension/shear) at RT (all values are averaged) (HDPE).

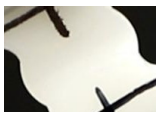
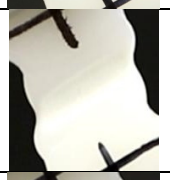
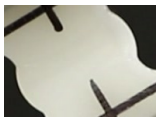
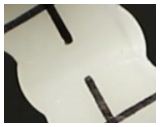
Testing Speed (mm/min)	**Virgin specimen**		**Yield Load**			**Fracture Point**		
	Displ., δ_{0F} (mm)	Image	Load, F (N)	Displ., δ_F (mm)	Image	Load, F (N)	Displ., δ_F (mm)	Image
1	0		520.2	1.9		370.7	5.6	
20	0		549.4	1.7		494.1	4.7	
200	0		699.7	1.1		628.6	2.1	

Table 40 - Deformation patterns and corresponding load and displacement values for butterfly specimens loaded at α = 30° (combined tension/shear) at RT (all values are averaged) (HDPE).

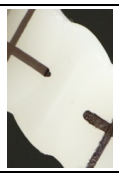
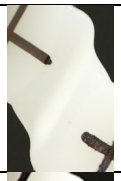
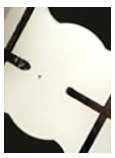
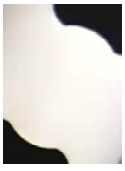
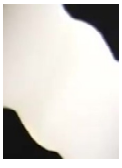
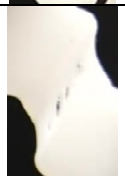
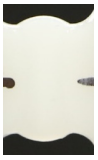
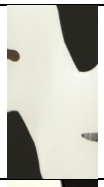
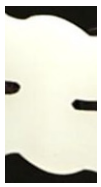
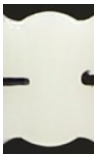
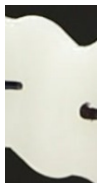
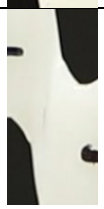
Testing Speed (mm/min)	**Virgin specimen**		**Yield Load**			**Fracture Point**		
	Displ., δ_{0F} (mm)	Image	Load, F (N)	Displ., δ_F (mm)	Image	Load, F (N)	Displ., δ_F (mm)	Image
1	0		435.8	2.9		359.8	6.2	
20	0		549.4	2.7		396.1	6.2	
200	0		614.3	2.1		507.5	3.9	

Table 41 - Deformation patterns and corresponding load and displacement values for butterfly specimens loaded at α = 0° (pure shear) at RT (all values are averaged) (HDPE).

Testing Speed (mm/min)	**Virgin specimen**		**Yield Load**			**Fracture Point**		
	Displ., δ_{0F} (mm)	Image	Load, F (N)	Displ., δ_F (mm)	Image	Load, F (N)	Displ., δ_F (mm)	Image
1	0		369.9	3.6		360.7	10.6	
20	0		469.8	3.5		367.4	9.1	
200	0		527.5	2.8		486.8	5.1	

A careful examination of the fractured specimens for each loading angle, indicates that cracks initiate at the centre of the gauge section in all the cases. However, it is difficult to determine directly from the experiments whether fracture starts from the middle thickness of the cross section or from the surface.

Possible molecular orientation (anisotropic), such as shish-kebab or stacked lamellae structures, due to melt-processing on the gauge section of butterfly specimen, might be included in the responses reported in this study. The consequence of a preferred molecular orientation in a specific direction is that might lead to a distinct anisotropy in mechanical properties, such as the increasing of the yield load [159].

Also, the microstructure deformation mechanisms during biaxial loading conditions might be in accordance with the research work performed by Zhou and Wilkes [160]. In their research the mechanical properties and the associated plastically deformed morphologies of high density polyethylene films were investigated by tensile testing, WAXS and TEM. Uniaxially oriented films, both with and without row-nucleated structure were deformed at three angles, 0°, 45° and 90°, with respect to the original machine (extrusion) direction. It was shown that lamellar separation, lamellar shear and lamellar break-up were the dominant initial deformation mechanisms for the respective 0°, 45° and 90° deformations. As a result, the 45° and 90° deformations generated a final microfibril morphology oriented along the stretch direction, while the 0° deformation resulted in broken (mosaic) blocks of crystalline lamellae.

Considering the work reported above and the present work, the microstructure deformation mechanisms during biaxial loading might be:

- At $\alpha = 90°$ (pure tension deformation) lamellar separation causes crystalline lamellae to "open-up" or splay, and this results in the strain whitening. As the deformation proceeded, the crystalline lamellae have to be deformed to generate higher strains, and this promotes the yielding. Chain slip might be the dominant deformation mode for the crystalline phase. The slip of the crystalline phase also might causes the large degree of strain hardening [160].

- At $\alpha = 60°$ and $30°$ (combined tension/shear deformation) the dominate deformation mode at the early stage of the deformation might be the interlamellar shear. Also, this corresponded to an intermediate observed yield load and displacements, as compared to the deformations at the $\alpha = 90°$ and $\alpha = 0°$ orientations. To accommodate the lamellae shear, chain slip, either fine or course, takes place through the sliding of tie molecules and this corresponds to the yielding of the crystalline phase. In the process of yielding, lamellar rotation occurred as a result of lamellar shear and/or chain slip, and the re-orientation of polymer chains towards the loading direction. At this stage of the deformation, crystalline lamellae began to break up due to the competitive constraint between lamellar shear and chain slip. The break-up of the crystalline lamellae is essentially a cold-drawing process by chain slip within the crystalline lamellae, as in contrast to the pull-out of chains as in the case of $\alpha = 0°$ deformation [160].

- At $\alpha = 0°$ (pure shear deformation) the crystalline lamellae is perpendicular to the direction of the load, the deformation on the level of the crystalline lamellae and amorphous layers, via lamellar separation, lamellar shear and lamellar rotation, is significantly limited. At $\alpha = 0°$ the crystalline phase and the amorphous phase are deformed in parallel. Therefore, the specimens yielded sharply after a small amount of elastic deformation of the crystalline phase and amorphous phase and what followed is the localized break-up of the crystalline lamellae, by transverse slip in the crystal. During the break-up process, polymer chains are pulled-out of the crystalline lamellae and realigned parallel to the load, which is perpendicular to the original molecular induced direction [160].

4.1.3 Combined Tensile/Shear Tests at Temperature of 50°C

Biaxial loading tests were also performed with butterfly specimens at constant temperature of 50 °C. The experimental details are summarized hereafter:

- Crosshead speeds of 1 and 200 mm/min, were used,
- Instron environmental chamber at constant temperature of 50 °C,
- A minimum of 20 minutes to stabilize the specimens after the testing oven temperature, was allowed and before loading,
- The mechanical tests were carried out on a Instron 3367 loading machine,
- The applied force (F) and displacement (δ_F) were recorded by Instron 3367 software,
- Three tests were performed for each loading angles, of $\alpha = 0°$, $30°$, $60°$, and $90°$ and crosshead speeds,
- The results of the tests are presented in terms of load vs displacement,
- Tests were performed until the specimen fracture.

Figure 63 compares the load-displacement results from biaxial loading at RT with corresponding results in the temperature of 50 °C. A decrease in the yield load or an increase yield load displacement, is observed with an increase in temperature and a decrease in the crosshead speed. Temperature and strain rate have a clear influence on mechanical properties of HDPE. The displacement at failure also increases with an increase of temperature.

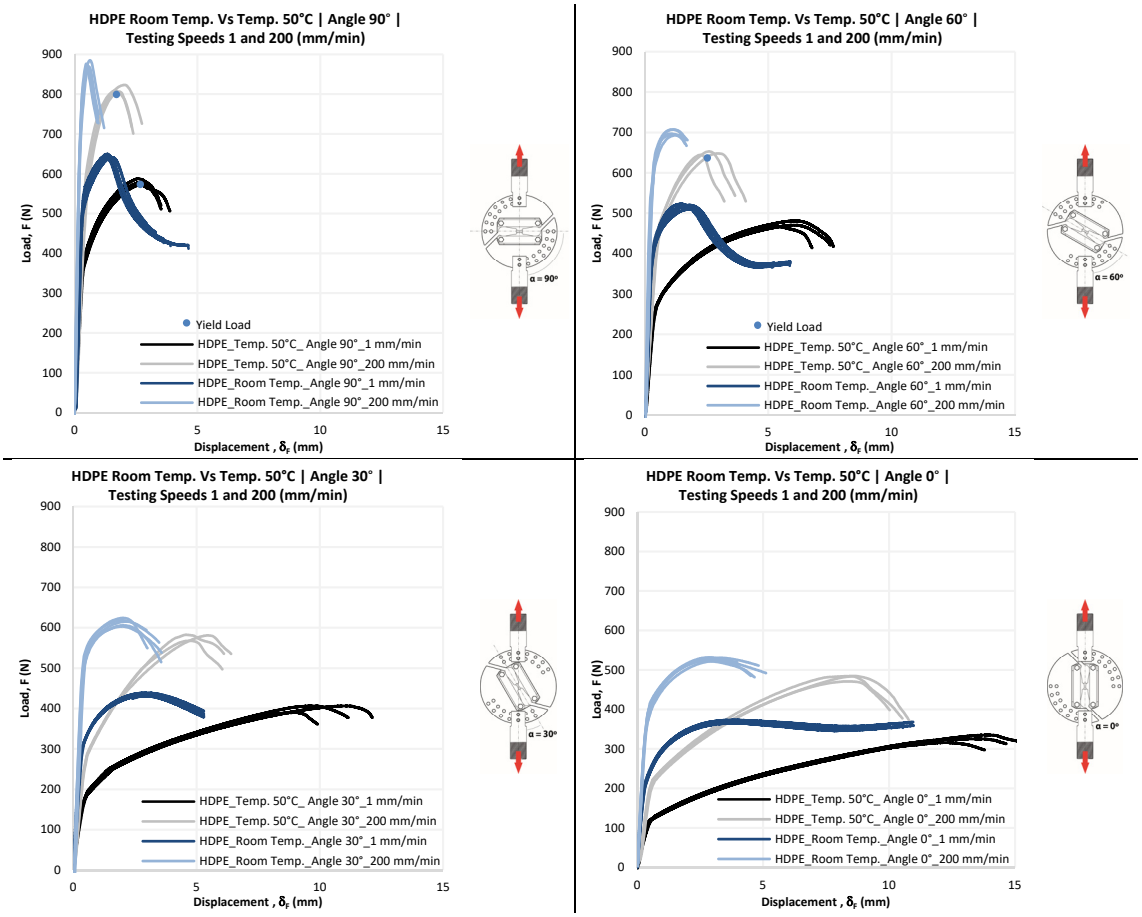


Figure 63 – Load-displacement curves for HDPE resulting from combined tension/shear loading at RT and 50 °C: influence of crosshead speeds for each loading angle.

Changing the biaxial loading angle from $\alpha = 0°$ to 90° and fixing the crosshead speed (Figure 64), similar mechanical behaviour as those obtained at room temperature are displayed, however at lower loads and higher displacements. At higher temperatures the chain mobility increases in the crystalline phase and raise the possibility for the shear deformation of crystals. Decreasing the loading angle, the load-displacement curves and yield load shift to higher values, whereas the limit displacement decreases. The simple, physical explanation of this phenomenon is that HDPE become more difficult to deform when the molecules are closely aligned with loading, leading to stretched conformation, this situation happens when the loading angle for butterfly specimens is $\alpha = 90°$ (pure tensile).

Stress whitening was observed in the gauge section of HDPE butterfly specimen. The occurrence of stress whitening in HDPE was found to be dependent upon the temperature and strain rate. From the experimental load-displacement curves, can be clearly seen that the yield load only

can be determined in some situations, which is by side with temperature a characteristic for ductile polymers. There is no single point at which the material starts to yield (null slope), instead the yielding is spread within a finite region, without pronounced yield load. As mentioned before possible multiphase layer structure with oriented crystalline morphology along the cross-section perpendicular to the melt flow, might be included in the responses reported in this study. Plausible explanations for the microstructure deformation mechanisms during biaxial loading are depicted in 4.1.2 Combined Tensile/Shear Behaviour at Room Temp.

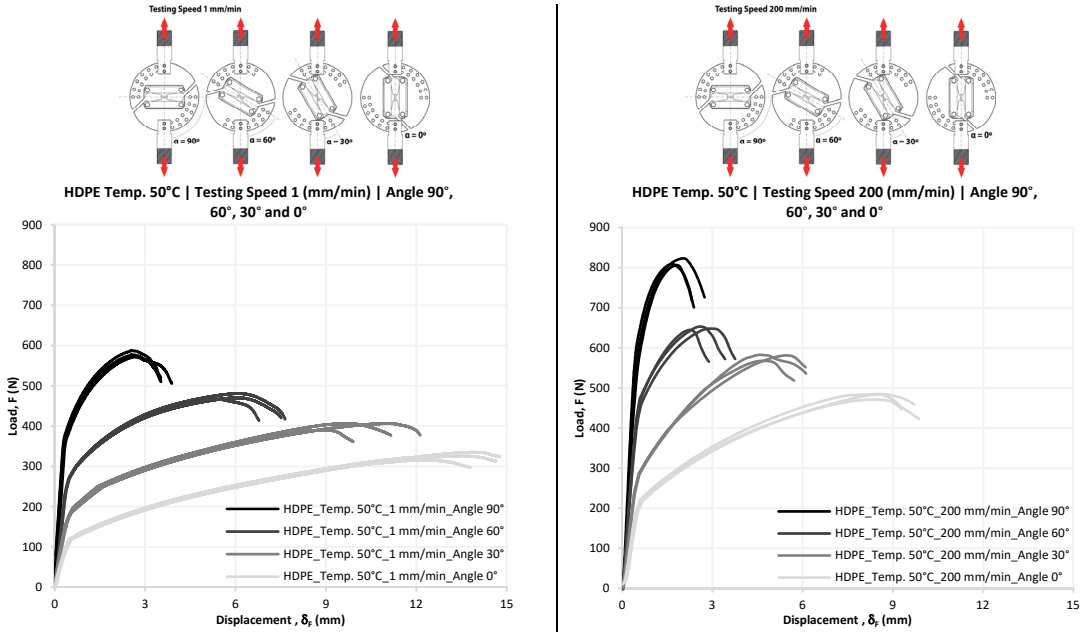


Figure 64 – Load-displacement curves for HDPE resulting for combined tensile/shear loading at temperature of 50 °C: influence of resulting in combined tension/shear for given crosshead speeds.

Tables 42, 43, 44 and 45 show typical failure images and notable load and displacement values for the HDPE specimens. At crosshead speed of 1 mm/min, an increase from RT to 50 °C, resulted in a 12% decrease in the yield load (from 642.2 N to 574.9 N) at α = 90° and at crosshead speed of 200 mm/min, resulted in a 9% decrease in the yield load (from 876.9 N to 807.9 N) at α = 90°. Note that, for the tests performed at constant temperature of 50 °C, at 1 mm/min and loading angle α = 60°, 30° and 0° no clear yield load can be identified as the material hardens without reaching a maximal force.

Table 42 – Fracture appearance and corresponding load and displacement values for butterfly specimen at α = 90° (pure tension) at 50 °C (all values are averaged) (HDPE).

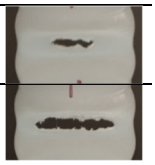
Testing Speed (mm/min)	**Yield Load**		**Fracture Point**		
	Load, F (N)	Displ., δ_F (mm)	Load, F (N)	Displ., δ_F (mm)	Image
1	574.9	2.6	508.5	3.7	
200	807.9	1.7	704.2	2.3	

Table 43 - Fracture appearance and corresponding load and displacement values for butterfly specimen at α = 60° (combined tension/shear) at 50 °C (all values are averaged) (HDPE).

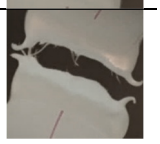
Testing Speed (mm/min)	**Yield Load**		**Fracture Point**		
	Load, F (N)	Displ., δ_F (mm)	Load, F (N)	Displ., δ_F (mm)	Image
1	-	-	466.4	7.6	
200	723.2	3.1	522.6	4.5	

Table 44 - Fracture appearance and corresponding load and displacement values for butterfly specimen at α = 30° (combined tension/shear) at 50 °C (all values are averaged) (HDPE).

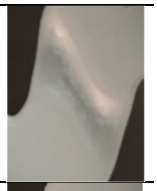
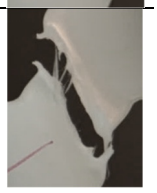
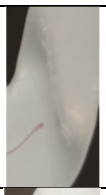
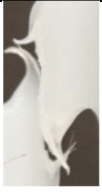
Testing Speed (mm/min)	**Fracture Point**		
	Load, F (N)	Displ., δ_F (mm)	Image
1	471.7	12.8	
200	547.6	7.1	

Table 45 - Fracture appearance and corresponding load and displacement values for butterfly specimen at α = 0° (pure shear) at 50 °C (all values are averaged) (HDPE).

Testing Speed (mm/min)	**Fracture Point**		
	Load, F (N)	Displ., δ_F (mm)	Image
1	425.4	15.1	
200	454.9	10.4	

4.1.4 Compression Tests at Room Temperature

Compression tests were performed on cylindrical and cylindrical notched specimens. The experimental details are summarized hereafter:

- Crosshead speeds of 1, 20 and 200 mm/min,
- Air temperature of 21 °C (deviation ± 2 °C) and relative humidity of 55% (deviation ± 10 %),
- Tests carried out on a servohydraulic MTS 810 universal testing machine,
- Applied force (F) and displacement (δ_F) recorded by servohydraulic MTS 810 universal testing machine,
- The deformation was recorded by a Canon 7D Mark II digital camera with a canon 17-55mm EF-S f2.8 IS USM lens,
- Five tests performed for each specimen geometry and crosshead speeds,
- Results of the tests are presented in terms of load vs displacement curves.

The compression load-displacement curves of HDPE at three crosshead speeds are presented in Figure 65, for each specimen geometry. From the experimental load-displacement curves, it can be seen that the yield load cannot be specifically determined, because there is no single point at which the material starts to yield. The response is initially linear for all curves before it bends to a lower slope at longitudinal displacement around δ_F = 0.9 mm and increases with the crosshead speed. Beyond this point, a progressive plastic strain hardening is observed. This can be related to the modification of microstructure with deformation. The observed macroscopic strain hardening in compression is associated to a planar molecular orientation process [5]. The initial elastic deformation of both geometries leads to compaction of the specimen. The onset of barrelling, due to friction is highlighted with a red dot. After this point the stress state is no longer purely uniaxial. The onset of barrelling is somewhat unclear since it appeared gradually. However, the first clear sign of barrelling was observed when the beginning of curves bends started.

As regard the notched specimens, compression leads to a significant change in notch geometry after yielding. Therefore, only linear and limited nonlinear response is presented in Figure 65 (2).

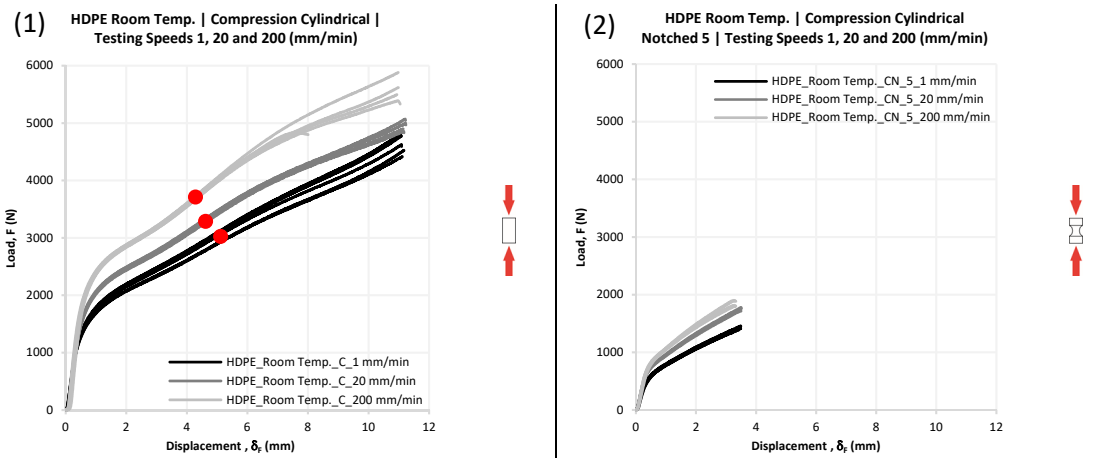


Figure 65 - Compression load-displacement curves of (1) cylindrical and (2) cylindrical notched specimens.

A sequence of images of cylindrical and cylindrical notched specimens at different stages during compression, are shown in Tables 46 and 47. From the sequential figures on cylindrical specimens it can be seen that barrelling effect started after some deformation. This is due to friction between the steel platens at the top and bottom surfaces of the specimens, which cannot be totally removed even with the use of Teflon sheets and lubricant. Even though barrelling effect in compression, the data provided by these tests are considered suitable for the purpose of evaluation of yield response which is the main focus of this research.

Table 46 – Deformation pattern and corresponding load and displacement values for cylindrical specimen at three deformation stages (all values are averaged) (HDPE).

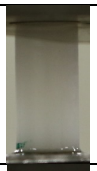
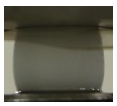
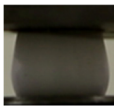
Testing Speed (mm/min)	**Virgin specimen**		**Barrelling Onset**			**Interrupted Test**		
	Displ., δ_{0F} (mm)	Image	Load, F (N)	Displ., δ_F (mm)	Image	Load, F (N)	Displ., δ_F (mm)	Image
1	0		3184.9	5.3		4802.4	11.1	
20	0		3409.1	4.9		4911.2	11.1	
200	0		3948.0	4.8		5751.8	11.1	

Table 47 – Deformation pattern and corresponding load and displacement values for cylindrical notched specimen at two deformation stages (all values are averaged) (HDPE).

Testing Speed (mm/min)	**Virgin specimen**		**Interrupted Test**		
	Displ., δ_{0F} (mm)	Image	Load, F (N)	Displ., δ_F (mm)	Image
1	0		1416.4	3.5	
20	0		1763.4	3.5	
200	0		1835.4	3.5	

For future improvements in compression tests, the friction between the specimen and the compression platens should be further reduced. Van Melick et al. [161] reduced the friction by using a PTFE tape (3M 5480, PTFE skived film tape) and the surface between compression platens and tape was lubricated by a soap–water mixture. They report, during the compression test no buckling of the specimen was observed for true strains up to -1.5, indicating that the friction was sufficiently reduced. Also, Rastogi et al. [162] minimize any friction between the specimens and the platens by using a thin film of Teflon, lubricated with extra soap–water mixture, placed between the platens and the specimen, providing uniform deformation to a very large strains. Also, the possibility of conducting the test by successive loading/unloading can improve the tribological condition, by removing the friction conditions.

4.1.5 Combined Compression/Shear Tests at Room Temperature

Biaxial loading tests were performed on butterfly specimen at room temperature in a negative (compressive) vertical displacement. The experimental details are depicted hereafter:

- Crosshead speeds of 1, 20 and 200 mm/min,
- Standard environment: air temperature of 21 °C (deviation ± 2 °C) and relative humidity of 55% (deviation ± 10 %),
- Mechanical tests carried out on a servohydraulic MTS 810 universal testing machine,
- Applied force (F) and displacement (δ_F) recorded by servohydraulic MTS 810 universal testing machine,
- Deformation recorded by a Canon 7D Mark II digital camera with a canon 17-55mm EF-S f2.8 IS USM lens,
- Five tests are performed for each loading angles, α = 0°, 30° and 60° and crosshead speeds,
- Results of the tests presented in terms of load vs displacement curves.

Experimentally measured curves for biaxial loading under, α = 90°, 60°, 60° and 0° are shown in Figures 66 and 67. All experimental results show an initially linear force-displacement response followed by a nonlinear regime until the test is interrupted due to limitation of the maximum travel allowed by the arcan apparatus, in negative vertical direction. The negative vertical loads and displacements were converted into positive values. From Figure 67 is observed, that changing the biaxial loading angle from α = 90° to 0° and fixing the crosshead speed, the load-displacement curves shift to lower values.

For the deformation till 1 mm it is visible a transition from linear to nonlinear behaviour, but the load continues to increase in the nonlinear domain. Strain rate effects are clearly visible with load increasing with testing speed increasing. Also, as the loading progresses from compression to pure shear one can realize a load reduction, with the highest load reduction between α = 90° to 60°.

As mention before possible multiphase layer structure with oriented crystalline morphology along the cross-section perpendicular to the melt flow, might be included in the responses reported in this study. Plausible explanations for the microstructure deformation mechanisms during biaxial loading are depicted in 4.1.2 Combined Tensile/Shear Behaviour at Room Temp.

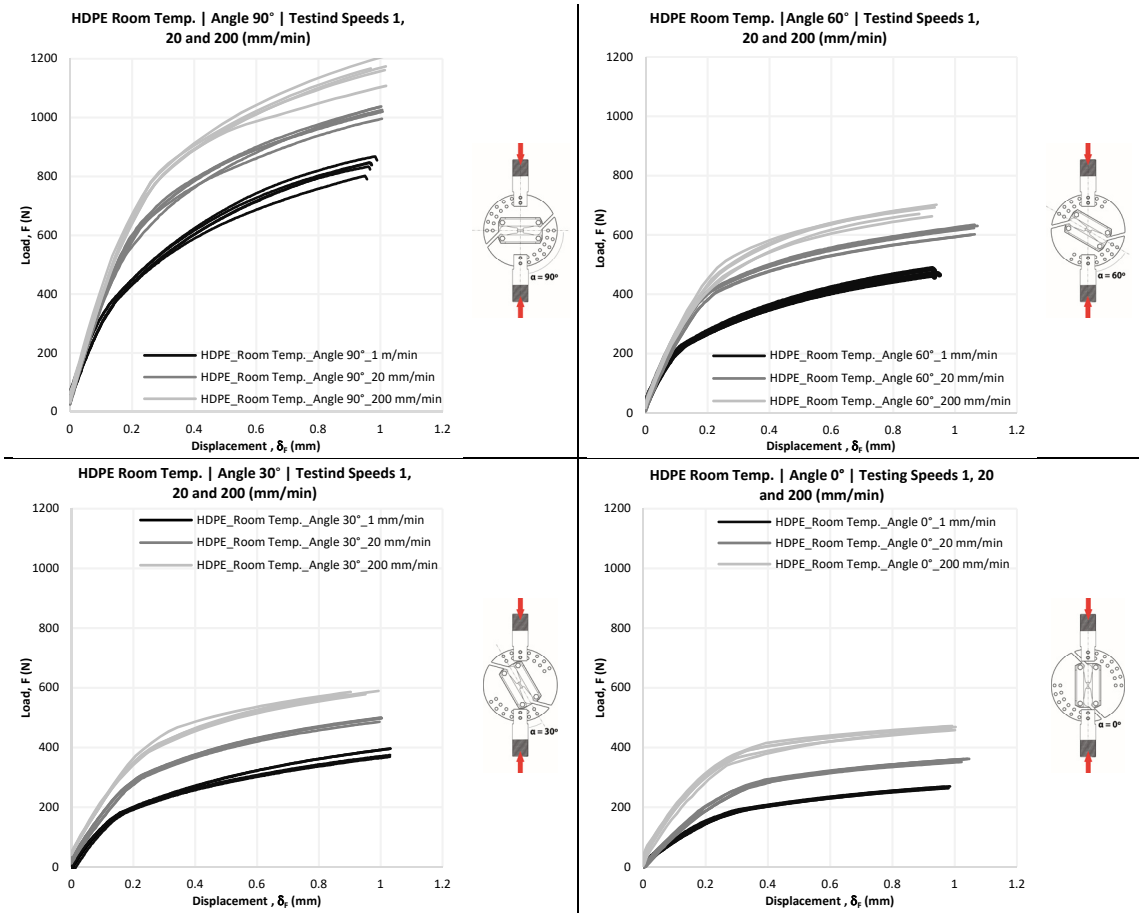


Figure 66 - Load-displacement curves during biaxial loading for negative vertical displacement, for a given loading angle (α = 90°, 60°, 30°, and 0°) and distinct crosshead speeds of 1, 20 and 200 mm/min, at RT.

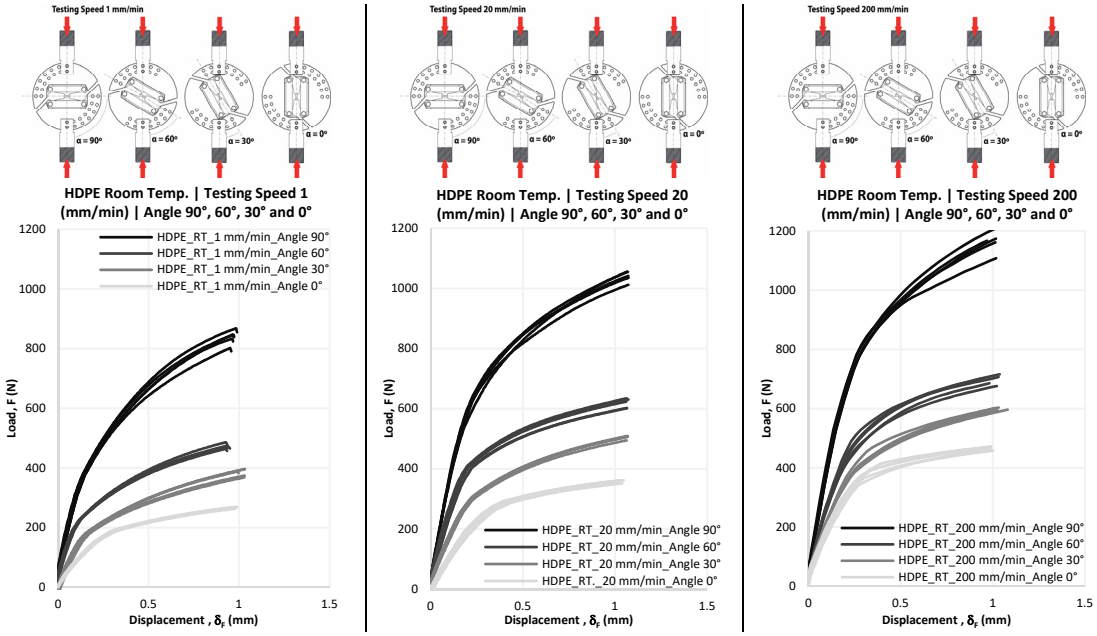


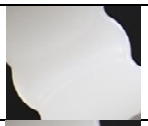
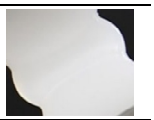
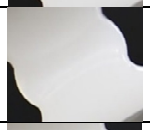
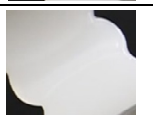
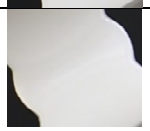
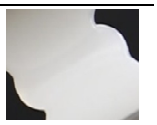
Figure 67 - Load-displacement curves for negative vertical displacement at RT, for a given crosshead speed and distinct loading angles (α = 90°, 60°, 30°, and 0°).

Tables 48, 49, 50 and 51 shows sequential images of the deformation behaviour and corresponding load and displacement values for the HDPE specimens at two deformation stages: virgin or unloaded material and interrupted test conditions (δ_F = 1mm) at crosshead speeds of 1 mm/min, 20 mm/min and 200 mm/min. It is observed an increase in load values, due to the increasing of loading speed from 1 to 200 mm/min by about 38% (from 846.6N to 1168.6 N) for loading angle α = 90°, 49% (from 462.6 N to 690.3N) for loading angle α = 60°, 51% (from 389.7 N to 586.7 N) for loading angle α = 30° and 55% (from 299.7 N to 463.8 N) for loading angle α = 0°.

Table 48 – Deformation patterns and corresponding load and displacement values for butterfly specimen at α = 90° (pure compression) at RT (all values are averaged) (HDPE).

Testing Speed (mm/min)	**Virgin specimen**		**Interrupted Test**		
	Displ., δ_{0F} (mm)	Image	Load, F (N)	Displ., δ_F (mm)	Image
1	0		846.6	1.0	
20	0		1032.7	1.0	
200	0		1168.6	1.0	

Table 49 – Deformation patterns and corresponding load and displacement values for butterfly specimen at α = 60° (combined compression/shear) at RT (all values are averaged) (HDPE).

Testing Speed (mm/min)	**Virgin specimen**		**Interrupted Test**		
	Displ., δ_{0F} (mm)	Image	Load, F (N)	Displ., δ_F (mm)	Image
1	0		462.6	1.0	
20	0		605.6	1.0	
200	0		690.3	1.0	

The strain rate effects are increasing with loading biaxiality changing from pure compression to pure shear.

Table 50 – Deformation patterns and corresponding load and displacement values for butterfly specimen at α = 30° (combined compression/shear) and RT (all values are averaged) (HDPE).

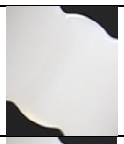
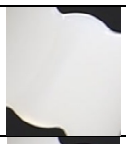
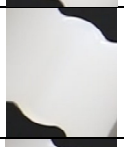
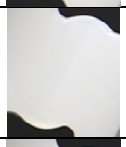
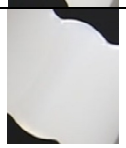
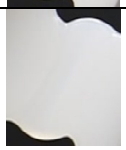
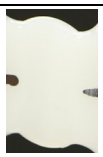
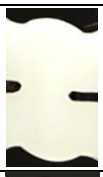
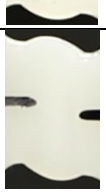
Testing Speed (mm/min)	**Virgin specimen**		**Interrupted Test**		
	Displ., δ_{0F} (mm)	Image	Load, F (N)	Displ., δ_F (mm)	Image
1	0		389.7	1.0	
20	0		485.4	1.0	
200	0		586.7	1.0	

Table 51 – Deformation patterns and corresponding load and displacement values for butterfly specimen at α = 0° (pure shear) at RT (all values are averaged) (HDPE).

Testing Speed (mm/min)	**Virgin specimen**		**Interrupted Test**		
	Displ., δ_{0F} (mm)	Image	Load, F (N)	Displ., δ_F (mm)	Image
1	0		299.7	1.0	
20	0		389.2	1.0	
200	0		463.8	1.0	

4.1.6 Combined Compression/Shear Tests at Temperature of 50°C

Combined compression/shear tests were performed on butterfly specimens at a constant temperature of 50 °C. The experimental details are summarized as followed:

- Crosshead speeds of 1 and 200 mm/min,
- Instron environmental chamber at constant temperature of 50 °C,
- A minimum of 20 minutes was allowed to elapse after the oven air temperature had equilibrated before loading testing,
- Mechanical tests carried out on a Instron 3367 loading machine,
- Applied force (F) and displacement (δ_F) recorded by Instron 3367 software,

- Three tests performed for each loading angles, α = 0°, 30° and 60° and crosshead speeds,
- Results of the tests are presented in terms of load vs displacement curves.

Load-displacement curves (α = 90°, 60°, 30°, and 0°) for a negative vertical displacement (combined compression/shear), crosshead speeds of 1 and 200 mm/min at room temperature and constant temperature of 50 °C are given in Figure 68 and 69. As expected the load-displacement curves are found to decrease (reduce strength) with an increasing temperature and decreasing crosshead speed. The following conclusions are drawn:

- At constant temperature of 50 °C the load grows with the crosshead speed. For a given crosshead speed, the load decreases with temperature.
- Changing the biaxial loading angle from α = 90° to 0° at constant temperature of 50 °C, load-displacement curves decreases.

As mention before possible multiphase layer structure with oriented crystalline morphology along the cross-section perpendicular to the melt flow, might be included in the responses reported in this study. Plausible explanations for the microstructure deformation mechanisms during biaxial loading are depicted in 4.1.2 Combined Tensile/Shear Behaviour at Room Temp.

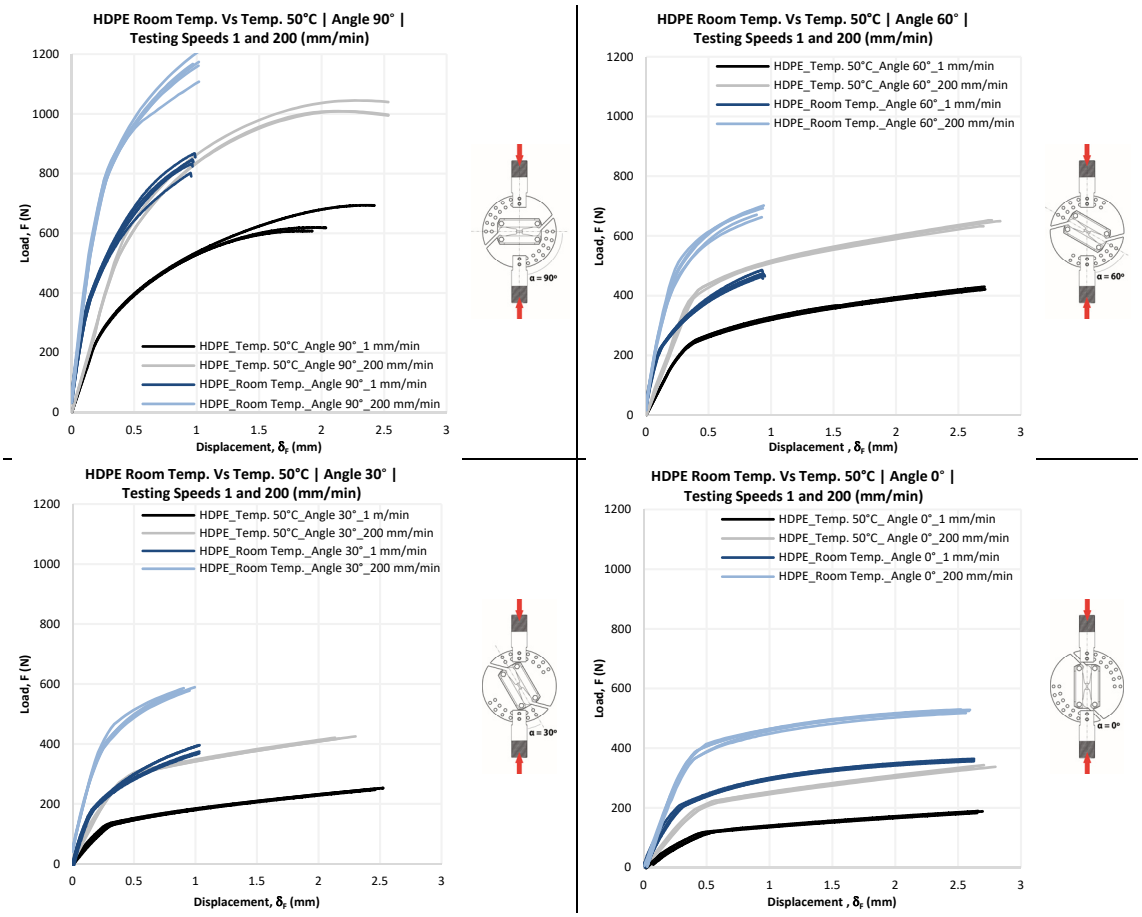


Figure 68 – Load-displacement curves during biaxial loading (α = 90°, 60°, 30°, and 0°) under a negative vertical displacement and room temperature or constant temperature of 50 °C.

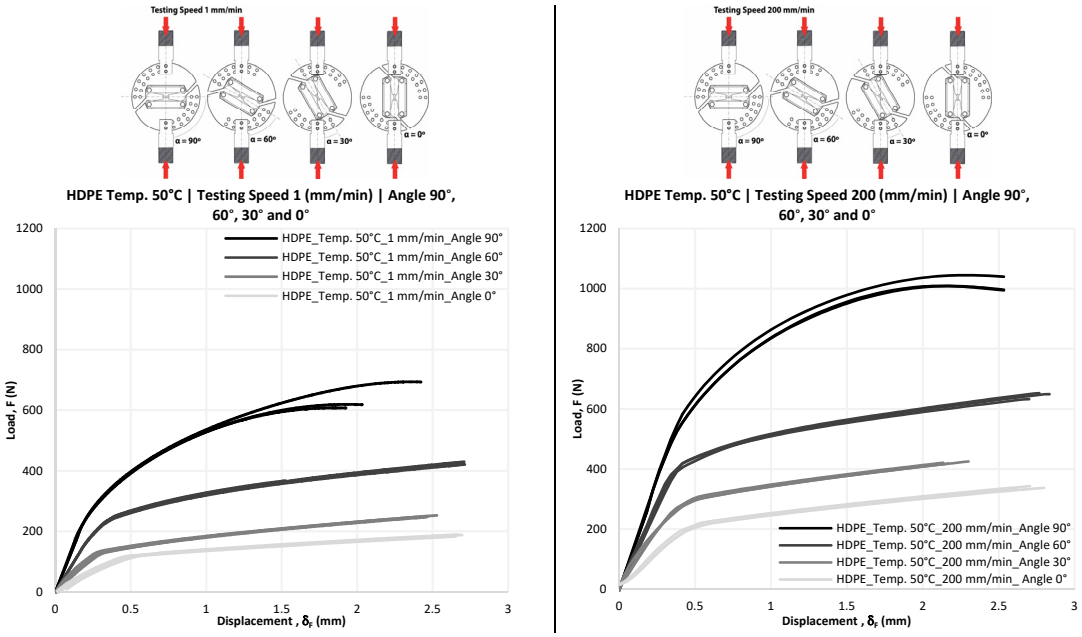


Figure 69 – Load-displacement curves in a negative vertical displacement under constant temperature of 50 °C. Effects of loading angles for fixed crosshead speed.

Tables 52, 53, 54 and 55 shows some characteristics load and displacement values for the HDPE specimens tested at 50 °C and combined compression/shear.

Table 52 – Fracture appearance and corresponding load and displacement values for butterfly specimen at α = 90° (pure compression) at 50 °C (all values are averaged) (HDPE).

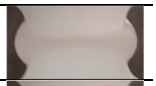
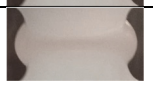
Testing Speed (mm/min)	**Interrupted Test**		
	Load, F (N)	Displ., δ_F (mm)	Image
1	656.1	2.2	
200	1019.8	2.5	

Table 53 – Fracture appearance and corresponding load and displacement values for butterfly specimen loaded at α = 60° (combined compression/shear) at 50 °C (all values are averaged).

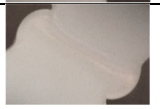
Testing Speed (mm/min)	**Interrupted Test**		
	Load, F (N)	Displ., δ_F (mm)	Image
1	425.5	2.7	
200	640.9	2.8	

Table 54 – Deformation pattern and corresponding load and displacement values for butterfly specimen loaded at α = 30° (combined compression/shear) at 50 °C (all values are averaged).

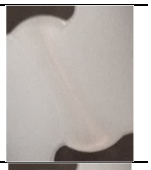
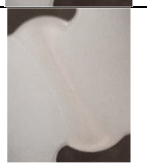
Testing Speed (mm/min)	**Interrupted Test**		
	Load, F (N)	Displ., δ_F (mm)	Image
1	251.6	2.5	
200	423.3	2.3	

Table 55 – Characteristic load and displacement values for butterfly specimens loaded at α = 0°, (pure shear) at 50 °C (all values are averaged) (HDPE).

Testing Speed (mm/min)	**Interrupted Test**	
	Load, F (N)	Displ., δ_F (mm)
1	193.7	2.7
200	353.9	2.8

4.1.7 Differential Scanning Calorimetry (DSC)

DSC tests were performed on solid granulates of HDPE. The experimental details are summarized hereafter:

- 8 to 10 mg of material, used,
- Tests were performed between -80 °C and 250 °C
- Heating rate of 10 °C /min
- The reproducibility of the measurements verified by a second run.

Figure 70, shows the DSC curves for the HDPE. The DSC curves show that the melting peak occurs at 139.2°C and at 140°C, respectively, which correspond to an endothermic transition (the transition absorbs heat). The heat of fusion (Enthalpy) using the average area under the combined peaks was 161.4 J/g. The heat of fusion of a reference fully crystalline polyethylene was assumed equal to 293 J/g [76]. This leads to a level of crystallinity of 55.1% (Table 56). These values are in accordance with data sheet from Hitachi High-Tech Science Corporation [163].

Note that according to ISO 11357, the fusion enthalpy is based on a virtual baseline, which is defined as imaginary straight line drawn through a reaction and/or transition zone assuming the heat of reaction and/or transition to be zero, which connects the peak onset and the peak end [77].

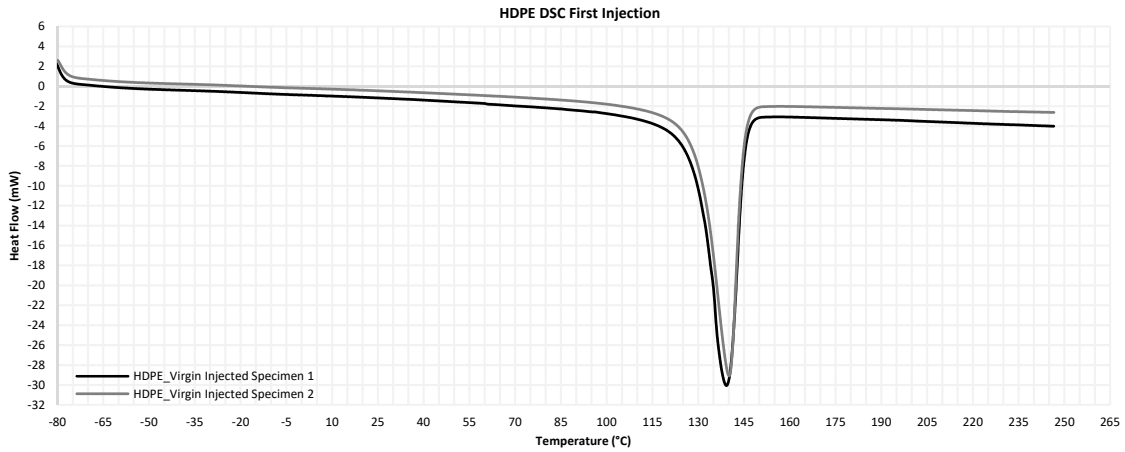


Figure 70 – DSC curves for HDPE virgin/injected material.

Table 56 - Thermal properties and crystallinity of HDPE determined by DSC, injected material.

	Units	Specimens	
		Virgin Injected Specimen 1	**Virgin Injected Specimen 2**
Enthalpy (ΔH_f)	J/g	162.9	160
Average	J/g	161.4	
Melting Temperature (T_m)	°C	139.2	140
Average	°C	139.6	
Enthalpy of Perfect Polymer Crystal (ΔH^0_f)	J/g	293 [76]	
Crystallinity	%	55.6	54.6
Average	%	55.1	

Tensile test specimens of HDPE were deformed in tension to two different elongations. The specimens were thereafter split in two at the middle of gauge section (Figure 71 (2)). Small pieces containing these cross sections were cut out and investigated in differential scanning calorimetry. The level of crystallinity was then compared with the different elongations and virgin material. The intention of the study is to investigate if there is any change in material crystallinity due to deformation. Tensile tests were performed on specimens for DSC. The experimental details are depicted hereafter:

- Crosshead speeds of 1 mm/min,
- Air temperature of 21 °C (deviation ± 2 °C) and relative humidity of 55% (deviation ± 10 %),
- Mechanical tests carried out on a servohydraulic MTS 810 universal testing machine,
- Applied force (F) and displacement (δ_F) recorded by Servohydraulic MTS 810 universal testing machine
- DSC experimental procedure similar as above described.

Figure 71 (1) shows the effects on DSC curves deformed specimens at true strain of 0.5 and 1 in uniaxial tension at same crosshead speed of 1 mm/min and temperature. The DSC data of the deformed specimens present a small increase of the average crystallinity. It changes from 55.1%

to 56.1% and 57.6%, respectively from virgin material to deformed specimens with 0.5 and 1 (Table 57). Beyond yield load, the increase in crystallinity can be referred to the chain alignment that occurs during specimen deformation. However, the change in crystallinity was only marginal. The DSC records does not reveal the state change in the material, besides the melting of material.

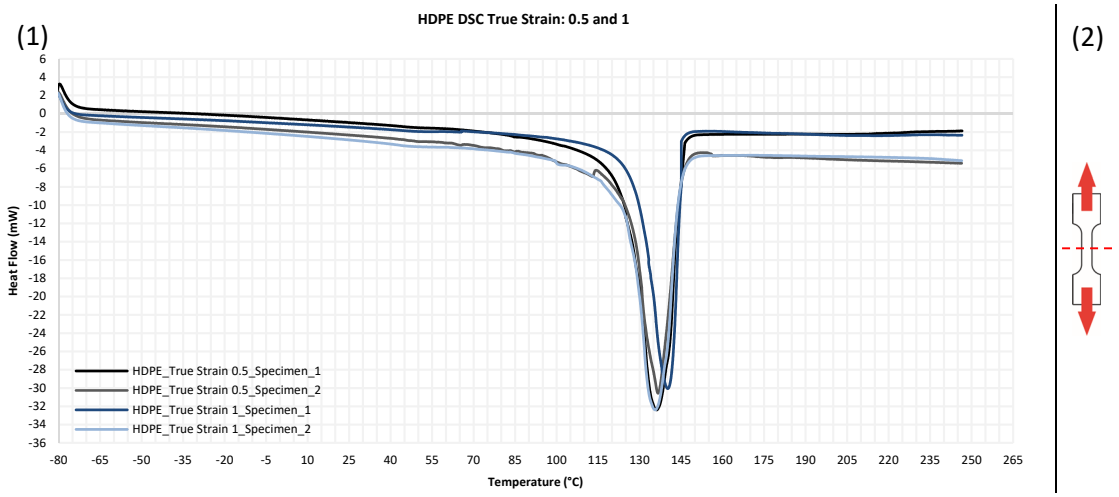


Figure 71 - (1) DSC curves for HDPE at true strains of 0.5 and 1, (2) red dashed line is the longitudinal section investigated in the DSC.

Table 57 – Influence of deformation on thermal properties and crystallinity of HDPE determined by DSC, deformed specimens.

	Units	Specimens			
		True Strain 0.5_1	**True Strain 0.5_2**	**True Strain 1_1**	**True Strain 1_2**
Enthalpy (ΔH_f)	J/g	165.3	163.2	169.9	167.8
Average	J/g	164.3		168.9	
Melting Temperature (T_m)	°C	136.2	136.6	140.1	135.7
Average	°C	136.4		137.9	
Enthalpy of Perfect Polymer Crystal (ΔH^0_f)	J/g	293[76]			
Crystallinity	%	56.4	55.7	58	57.3
Average	%	56.1		57.6	

4.1.8 Dynamic Mechanical Analysis (DMA)

DMA test were performed on rectangular specimens with the following dimensions: 40 mm×15 mm×1.8 mm. The experimental details are depicted hereafter:

- Frequencies tested: 0.1, 1 and 10 Hz
- Strain amplitude: 0.5 %
- Tests performed from room temperature to 110 °C
- Heating rate of 2 °C /min

- The reproducibility of the measurements was verified by a second run.

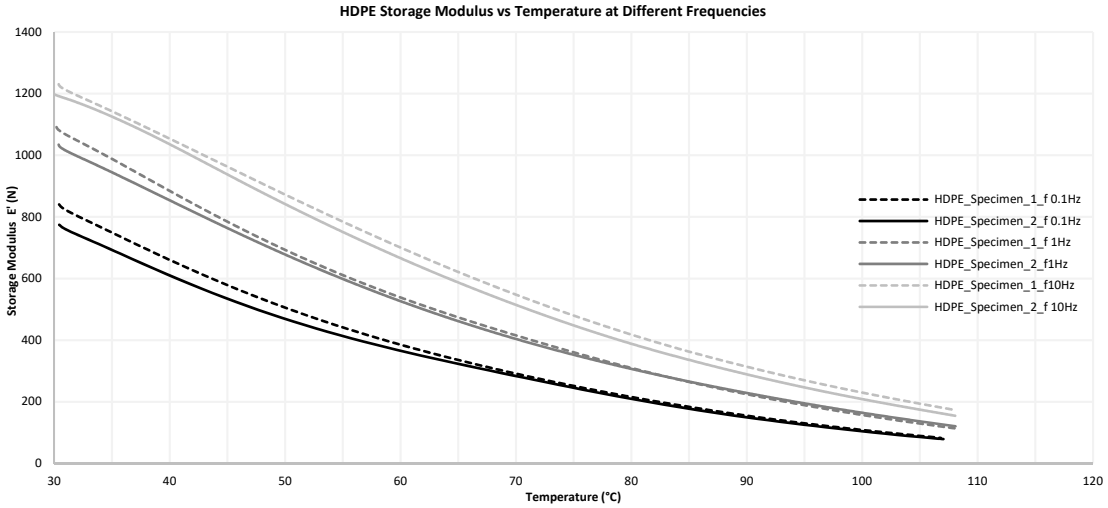


Figure 72 – Results of DMA experiments: the storage modulus (*E'*) as function of temperature (°*C*) and frequency for HDPE.

The DMA results for storage modulus (*E'*) as function of temperature (°*C*) and frequency effects of HDPE is given in Figure 72. The HDPE exhibits the dynamic mechanical response which is characteristic for a thermoplastic material. At room temperature the storage modulus is relatively high, ranging from 750 N to 754 N for frequency 0.1 Hz, 820 N to 841 N for frequency 1 Hz and 1040 N to 1090 N for frequency 10 Hz and with increasing temperature, this modulus gradually reduces. The decrease in storage modulus is observed, since here the polymer chains are progressively being in full segmental mobility and their state changes from glassy-rubbery to rubbery flow. There is no noticeable transition in material behaviour since HDPE is in rubbery state in the tested range. HDPE glass transition temperature occurs between -100 °C to -60 °C [76].

4.2 Polypropylene (PP)

Semi crystalline polymers are being increasingly used in structural components ranging from aerospace applications to a variety of automobile components, due to their properties such as lower density and higher yield strains, when compared to metals. In addition, one of the most interesting characteristics of semi crystalline polymers is that complicated shapes can be easily fabricated using processes such as injection moulding.

Mechanical behaviour of PP is highly dependent on strain rate, temperature and loading modes. Thus, the assessment of the strain rate, temperature and combined loading modes effects in mechanical properties of PP is a main concern in the design of engineering structures. In the fallowing section the results of various mechanical tests performed on PP are presented and discussed.

4.2.1 Tensile Tests at Room Temperature

Tensile tests were performed on dumbbell, flat notched and cylindrical notched specimens at RT. The experimental details were already summarized in section: 4.1.1 Tensile Tests at Room Temperature (HDPE). These tests were performed until the fracture, with exception of dumbbell specimen, which exhibit higher deformation than the limit displacement of axial extensometer.

Tensile deformation of PP involves the micro structural evolution of both the crystalline and the amorphous phases. It is established that the nature of crystalline phase determines the small deformation properties via crystallographic fine slips, intralamellar block slips and/or interlamellar slips and stack rotation, whereas the amorphous network dominates deformation behaviour at larger displacements upon further stretching. The transition associated with the onset of fragmentation and beginning of fibril formation is marked by a strain softening followed by a strain hardening, which is determined by the interplay between the stability of crystalline blocks and the state of entangled amorphous network [4, 41, 42].

The load-displacement curves obtained at different crosshead speeds for PP specimens with different geometries, are depicted in Figures 73 and 74. The three specimen geometries exhibit similar behaviour. Initially, the deformation is linear with the load increasing proportionally with displacement. There is then a nonlinear region prior to yield load followed by yield, where the force reaches a maximum. The corresponding yield displacement decrease with the crosshead speed increasing, with exception to cylindrical notched 5 specimens, which the displacement value is very similar for the three crosshead displacements.

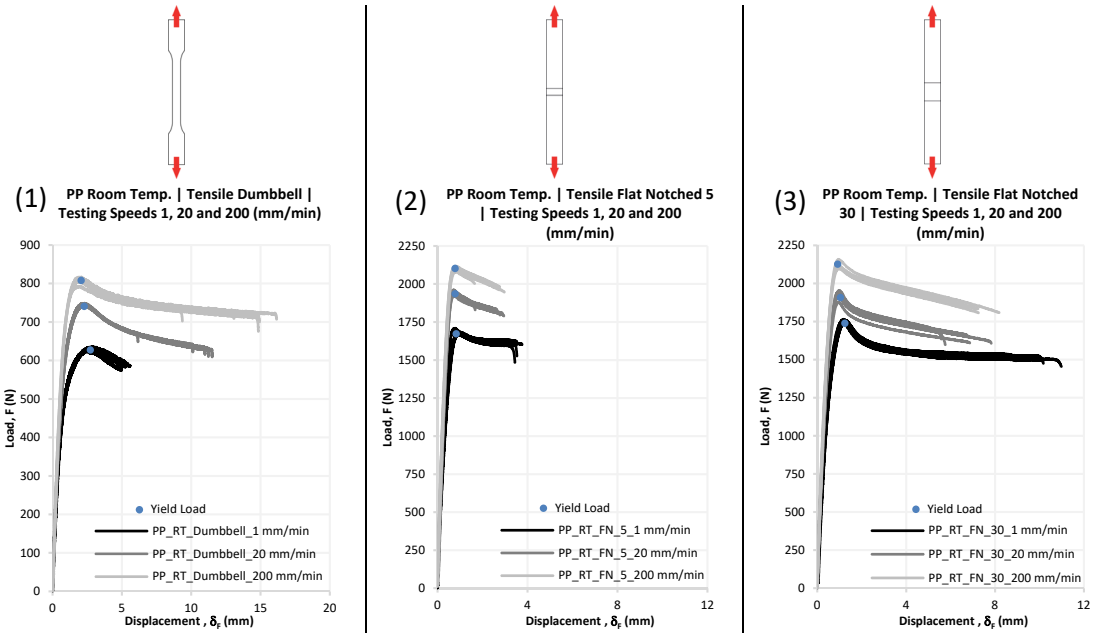


Figure 73 – Tensile load-displacement curves of (1) Dumbbell, (2) flat notched 5 and (3) flat notched 30 specimens (PP, Room Temperature).

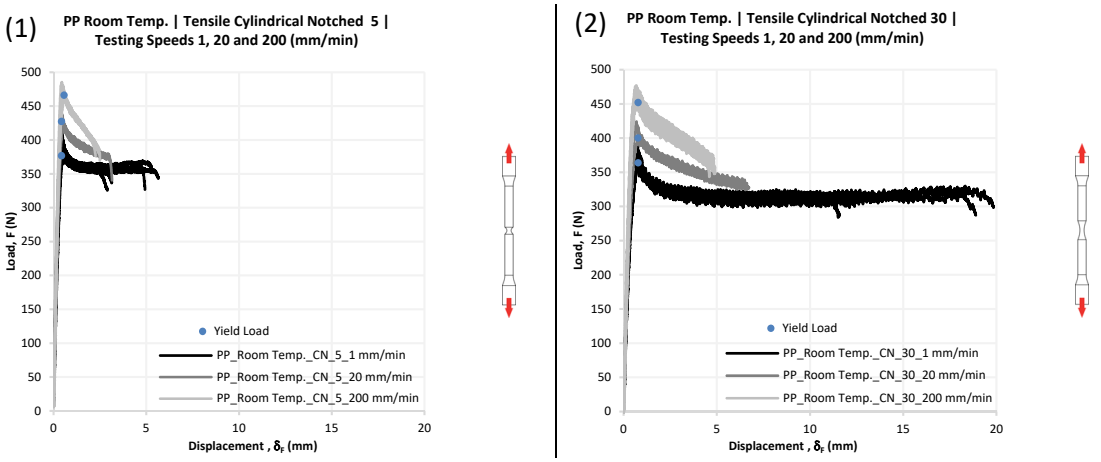


Figure 74 - Tensile load-displacement curves of (1) cylindrical notched 5 and (2) cylindrical notched 30 specimens (PP, Room Temperature).

After yield, the force is observed (Figures 73 and 74) to decrease with increasing displacement. In PP, the strain softening causes localisation of plastic strain, which cannot be sufficiently stabilised due to the low value of strain hardening, which at crosshead speeds higher than 1 mm/min are almost neglected. Only at crosshead speed of 1 mm/min, the plastic behaviour exhibits a nearly zero strain hardening. With ongoing deformation, localisation grows to extremes, resulting in void nucleation, craze formation and catastrophic failure.

At higher crosshead speed the yield occurs for higher force values, whereas for lower crosshead speeds the deformation is slight higher. By decreasing the crosshead speed allows more time for the polymer chains to rearrange towards a less oriented state, also allows more time for the chain segments to engage in an increased amount of entanglement slippage and therefore increase the hardening effect. Higher crosshead speeds reduce the degree of chain relaxation, resulting in more preferred orientation, yielding lower displacement values and consequent shift to brittle behaviour [59].

Tables 58, 59, 60, 61 and 62 shows sequential images and corresponding load and displacement values for the PP specimens at three deformation stages: virgin or unloaded, yield load or first maximum force and the interrupted test/fracture point. From values analysis on tables is observed an increase on the yield load by about 27% (from 631.7 N to 803.4 N) for uniaxial tension of dumbbell, 25% (from 1676.6 N to 2096.0 N) for flat notched 5, 21% (from 1752.7 N to 2128.8 N) for flat notched 30, 22% (from 387.1 N to 474.2 N) for cylindrical notched 5 and 22% (from 384.6 N to 468.7 N) for cylindrical notched 30, when testing speeds increased from 1 mm/min to 200 mm/min.

As the displacement increases, after yield load the force drop and the stress whitening is detected indicating the beginning of the neck formation, with the exception of dumbbell specimen. As the plastic deformation continued, the stress whitening became clearer and sets the shape changes (dilatation). In cylindrical notched specimens, where this effect is more pronounced, it is observed along with the stress whitening zone, that the neck propagated through the notched section of the specimen during the deformation (see the sequential figures on Table 61 and 62).

Table 58 – Load and displacement values for dumbbell specimen at selected deformation stages (all values are averaged) (PP).

Testing Speed (mm/min)	**Yield Load**		**Interrupted Test**	
	Load, F (N)	Displ., δ_F (mm)	Load, F (N)	Displ., δ_F (mm)
1	631.7	2.6	581.9	5.3
20	747.5	2.3	629.1	9.1
200	803.4	1.9	720.8	11.9

Table 59 – Deformation patterns and corresponding load and displacement values for flat notched 5 specimens at three deformation stages (all values are averaged) (PP).

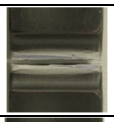
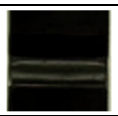
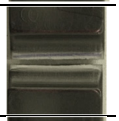
Testing Speed (mm/min)	**Virgin specimen**		**Yield Load**			**Fracture Point**		
	Displ., δ_{0F} (mm)	Image	Load, F (N)	Displ., δ_F (mm)	Image	Load, F (N)	Displ., δ_F (mm)	Image
1	0		1676.6	0.9		1574.9	3.6	
20	0		1969.3	0.7		1827.6	2.6	
200	0		2096.0	0.7		1971.1	2.4	

Table 60 – Deformation patterns and corresponding load and displacement values for flat notched 30 specimens at three deformation stages (all values are averaged) (PP).

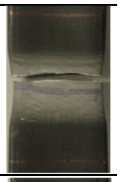
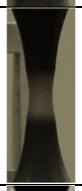
Testing Speed (mm/min)	**Virgin specimen**		**Yield Load**			**Fracture Point**		
	Displ., δ_{0F} (mm)	Image	Load, F (N)	Displ., δ_F (mm)	Image	Load, F (N)	Displ., δ_F (mm)	Image
1	0		1752.7	1.2		1390.7	10.1	
20	0		1909.1	1.1		1609.5	6.9	
200	0		2128.8	1.0		1821.2	6.5	

Table 61 – Deformation patterns and corresponding load and displacement values for cylindrical notched 5 specimens at three deformation stages (all values are averaged) (PP).

Testing Speed (mm/min)	**Virgin specimen**		**Yield Load**			**Fracture Point**		
	Displ., δ_{0F} (mm)	Image	Load, F (N)	Displ., δ_F (mm)	Image	Load, F (N)	Displ., δ_F (mm)	Image
1	0		387.1	0.5		340.1	3.8	
20	0		431.6	0.5		364.4	3.0	
200	0		474.2	0.5		376.8	2.4	

Table 62 – Deformation patterns and corresponding load and displacement values for cylindrical notched 30 specimens at three deformation stages (all values are averaged) (PP).

Testing Speed (mm/min)	**Virgin specimen**		**Yield Load**			**Fracture Point**		
	Displ., δ_{0F} (mm)	Image	Load, F (N)	Displ., δ_F (mm)	Image	Load, F (N)	Displ., δ_F (mm)	Image
1	0		384.6	0.8		291.1	14.3	
20	0		422.5	0.7		309.1	6.6	
200	0		468.7	0.7		348.7	4.8	

It is important to highlight that in this set of experiments on PP the presence of notch with different radii did not produce significant alterations in the yield load value, when compared with a fixed crosshead speed. For example, for flat notched specimens at crosshead speed of 200 mm/min, the yield load values are: 2096 N and 2128.8 N, respectively for R 5 and R 30. However, the same does not apply to the displacement values, which for a fixed crosshead value increases with higher radii value.

Load-displacement curves for PP cylindrical notched specimens are presented in Figure 74. Distinct behaviour can be delineated from that curves plots, (1) linear elastic, (2) yield load (first maximum force), (3) continuation of yielding (sharp drop in load) and (3) strain hardening region (almost constant and parallel to the displacement axis). The maximum displacement achieved

was for crosshead speed of 1 mm/min. For higher crosshead speeds, the load decreases monotonically till fracture. From the figures on Table 60 and 61 it is shown that the plastic deformation was localized at notch root and well-developed. As the displacement increases, after yield load the stress whitening is detected indicating the beginning of the neck formation. The strain whitened region spread over the entire gauge section.

4.2.2 Combined Tensile/Shear Tests at Room Temperature

Combined tension/shear loading tests were performed on butterfly specimens at room temperature. The experimental details are summarized in section: 4.1.2 Combined Tensile/Shear Behaviour at Room Temperature (HDPE). Tests were performed until the fracture.

Figures 75 and 76 shows the results when a positive vertical displacement is applied resulting in combined tension/shear loading. It can be observed that the load-displacement curves do not intersect each other. Higher the loading angle, higher is the load required to deform the specimens. The general shape of all curves, seems to be exhibit, for each biaxial loading angle remarkably similar intrinsic behaviours. The initial linear elastic response is followed by a nonlinear evolution. The yielding onset generally corresponds to stress whitening at the central gauge section (see the sequential figures on Table 63, 64, 65 and 66).

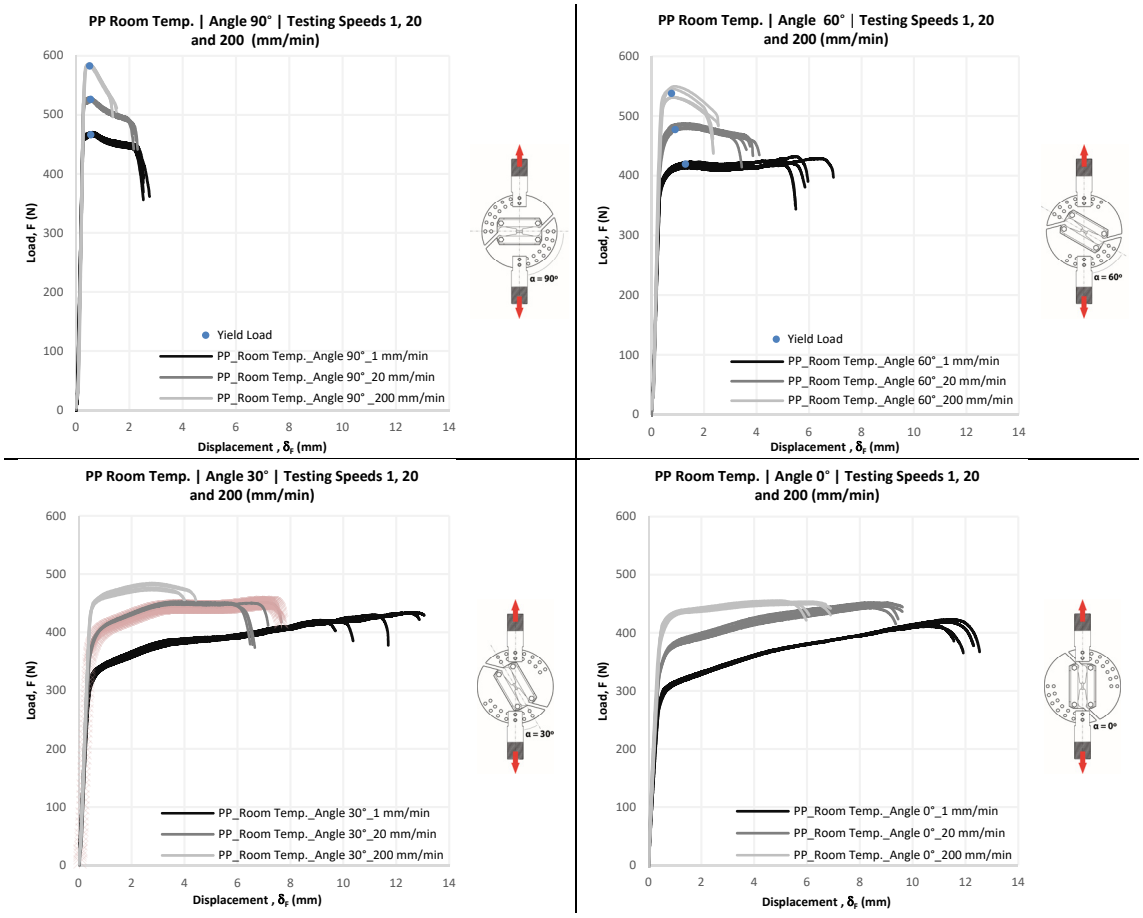


Figure 75 - Load-displacement curves for PP resulting from combined tension/shear loading at RT: influence of crosshead speeds for each loading angle.

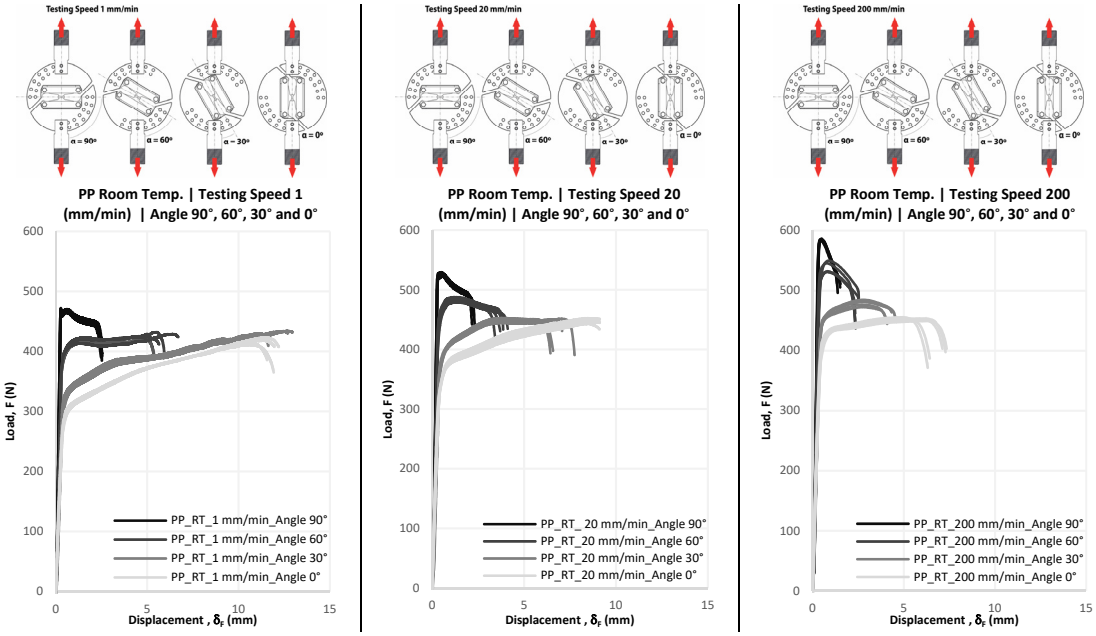


Figure 76 - Load-displacement curves for PP resulting for combined tensile/shear loading at RT: effect of loading angle for given crosshead speeds.

The load-displacement curves shift to higher load values with increase of crosshead speed. The main differences between this loading angles in their post-yield behaviour, are: (1) the drop of the load with biaxial loading angle are found maximum for the loading angle $\alpha = 0°$ (pure shear) and minimum for $\alpha = 90°$ (pure tension), (2) the plastic stiffness decreases with increasing of crosshead speed in all loading angles, (3) the yield load is only noticeable at loading angles of $\alpha = 90°$ and $\alpha = 60°$ and (4) at loading angle $\alpha = 0°$ the displacement achieves the maximum values. The crosshead speed and loading angle "after yielding" plays a key role in the macroscopic deformation behaviour and determines whether the material behaves as brittle or ductile.

Tables 63, 64, 65 and 66 show sequential images and corresponding load and displacement values for the PP specimens at three deformation stages: virgin or unloaded, yield load or first maximum force and fracture point. From values analysis on yield load at crosshead speeds of 1 mm/min and 200 mm/min, it is observed an increase on the yield load values by about 24% (from 470.7 N to 583.3 N) for loading angle $\alpha = 90°$ and 26% (from 421.1 N to 531.5 N) for loading angle $\alpha = 60°$. For loading angle of $\alpha = 30°$ and 0° the yield load is not noticeable, as specified in standard ISO 527-1by a local load peak. During the plastic deformation process crack formation defects, so-called crazes, appear in the gauge section of butterfly specimen, near fracture point. With increasing load, the crazes, which are bridged by fibrils, open up and macroscopic fracture occurs upon the failure of these fibrils.

Table 63 – Deformation patterns and corresponding load and displacement values for butterfly specimens loaded at α = 90° (pure tension) at RT (all values are averaged) (PP).

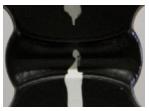
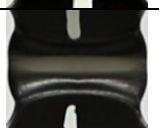
Testing Speed (mm/min)	**Virgin specimen**		**Yield Load**			**Fracture Point**		
	Displ., δ_{0F} (mm)	Image	Load, F (N)	Displ., δ_F (mm)	Image	Load, F (N)	Displ., δ_F (mm)	Image
1	0		470.7	0.5		411.2	2.5	
20	0		528.8	0.5		455.3	2.2	
200	0		583.3	0.5		515.9	1.3	

Table 64 - Deformation patterns and corresponding load and displacement values for butterfly specimens loaded at α = 60° (combined tension/shear) and RT (all values are averaged) (PP).

Testing Speed (mm/min)	**Virgin specimen**		**Yield Load**			**Fracture Point**		
	Displ., δ_{0F} (mm)	Image	Load, F (N)	Displ., δ_F (mm)	Image	Load, F (N)	Displ., δ_F (mm)	Image
1	0		421.1	1.6		405.9	5.6	
20	0		484.1	1.3		418.1	3.8	
200	0		531.5	0.8		461.2	2.4	

Table 65 - Deformation patterns and corresponding load and displacement values for butterfly specimens loaded at α = 30° (combined tension/shear) at RT (all values are averaged) (PP).

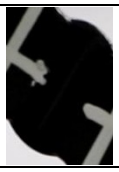
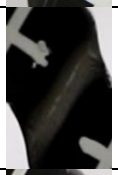
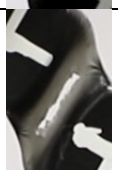
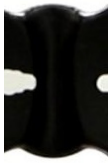
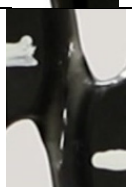
Testing Speed (mm/min)	**Virgin specimen**		**Fracture Point**		
	Displ., δ_{0F} (mm)	Image	Load, F (N)	Displ., δ_F (mm)	Image
1	0		424.6	11.7	
20	0		444.8	6.8	
200	0		460.9	4.3	

Table 66 - Deformation patterns and corresponding load and displacement values for butterfly specimens loaded at α = 0° (pure shear) and RT (all values are averaged) (PP).

Testing Speed (mm/min)	**Virgin specimen**		**Fracture Point**		
	Displ., δ_{0F} (mm)	Image	Load, F (N)	Displ., δ_F (mm)	Image
1	0		412.0	11.3	
20	0		439.9	9.5	
200	0		435.0	6.5	

It is expected a processing-induced molecular orientation on the mechanical response of PP. In the injection moulding processing, the polymer chains in the crystalline domains are oriented towards the main injection direction, whereas the chains in the amorphous domains are stretched along this same direction. The flow induced during melt-processing causes the polymer molecules to stretch and orient in the direction of flow [164]. An important

consequence of a preferred molecular orientation in a specific direction is that it leads to anisotropy in mechanical properties, such as in the yield load [159].

Van Erp et al. [159] observed that for injection moulding, substantially different failure modes may be found within a single polymer product, covering the full range from brittle to ductile. Dumbbell specimens of PP with a gauge section of 22 mm and width of 5mm, were cut at four different locations. Two specimens are perpendicular to the flow direction, one close to the gate and one at the end of the flow path. The other two specimens were cut, one in flow direction and another one at an angle of 45° with respect to the flow direction. Also found that, the ratio between the times-to-failure upon application of a constant load parallel (flow direction) and perpendicular to the injection direction can be as large as 500 within a single product of polypropylene.

Possible microstructure deformation mechanisms during biaxial loading are depicted in section 4.1.2 Combined Tensile/Shear Behaviour at Room Temperature, concerned with HDPE polymer.

4.2.3 Combined Tensile/Shear Test at Temperature of 50°C

Biaxial loading tests were performed on butterfly specimen at constant temperature of 50 °C. The experimental details are summarized in section: 4.1.3 Combined Tensile/Shear Tests at Temperature of 50°C (HDPE). Tests were performed until the fracture.

The observed effects of temperature and crosshead speed at the yield load and load-displacement curves during biaxial loading show the expected tendencies: decreasing crosshead speed and increasing temperature generally result in lowering of the load needed to reach a given displacement. Therefore, the yield load shows an explicit dependency on temperature and crosshead speed. Similar conclusions on temperature dependence were obtained by Hartmann et al. [165], who performed uniaxial tension tests to the yield load on polypropylene dumbbell specimens as a function of temperature from 22 to 143°C at a strain rate of 2 /min. From this study it was shown that yield stress decreases with the increase of temperature and the yield strain reaches a maximum value at the temperature around 60 °C to 70 °C.

Figures 77 and 78, presents the plots of load versus displacement for room temperature and 50 °C. The following conclusions are drawn:

- At constant temperature of 50 °C the strength increases with the crosshead speed. For a given crosshead speed, the strength decreases with temperature,
- Growth of temperature and reduction in crosshead speed lead to transition from brittle to ductile fracture of specimens,
- As a general view, the displacements at failure are similar in load-displacement curves at room temperature and at temperature of 50 °C.
- Changing the biaxial loading angle from $\alpha = 90°$ to 0° at temperature of 50 °C decreases the yield loads and increases the displacement at failure.
- Stress whitening is observed in the gauge section of PP butterfly specimen, shortly before yielding.

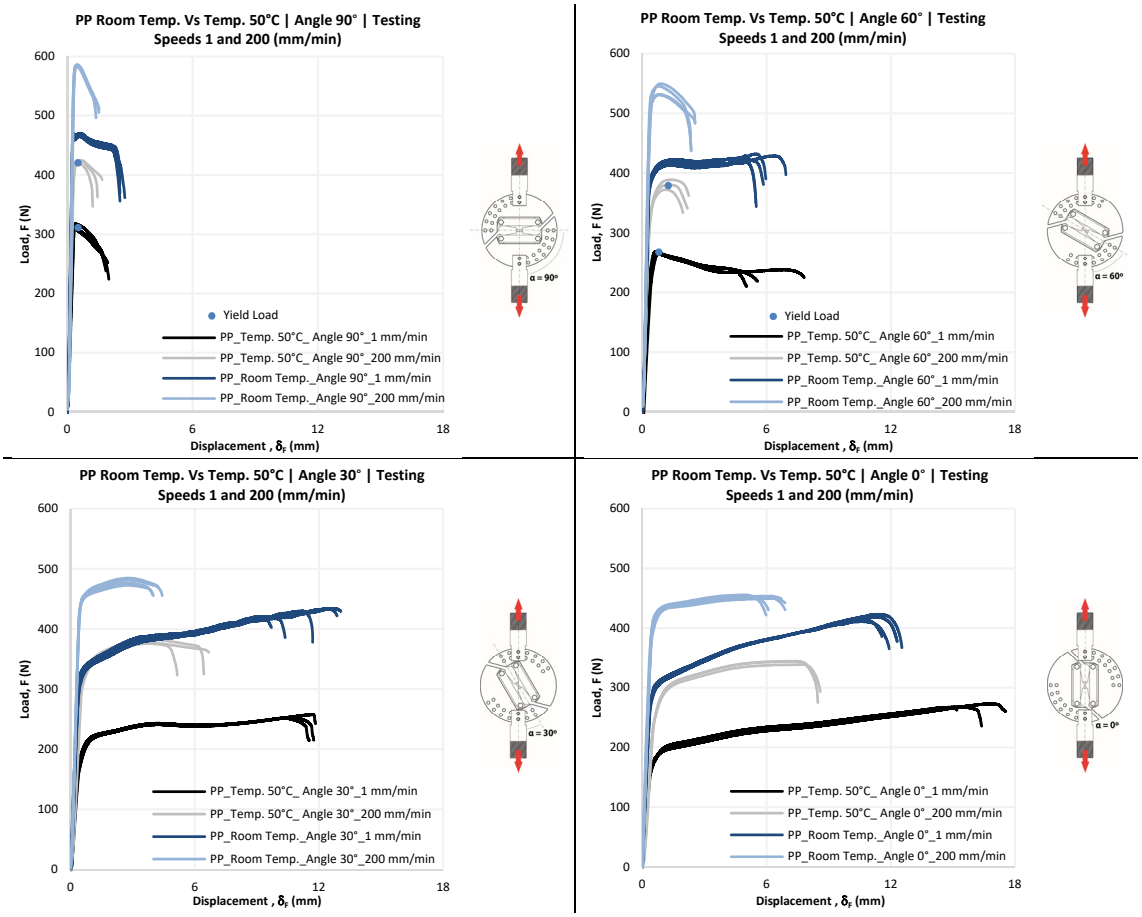


Figure 77 – Load-displacement curves for PP resulting from combined tension/shear loading at RT and 50 °C: influence of crosshead speeds for each loading angle.

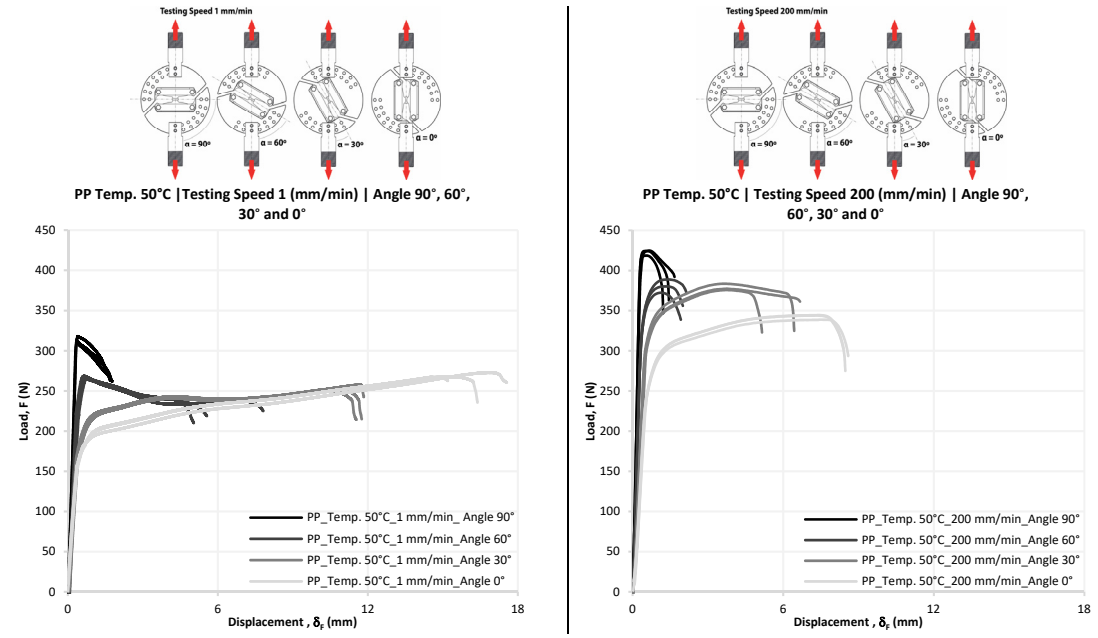


Figure 78 – Load-displacement curves for PP resulting for combined tensile/shear loading at temperature of 50 °C: influence of resulting in combined tension/shear for given crosshead speeds.

Tables 67, 68, 69 and 70 summarize reference values of loads and displacements for the PP butterfly specimens at three deformation stages: virgin or unloaded, yield load or first maximum force and fracture point. At crosshead speed of 1 mm/min, an increase in temperature from room temperature to 50 °C, resulted in a 49% decrease in the yield load (from 470.7 N to 315.7 N) at α = 90° and 57% decrease in the yield load (from 421.1 N to 267.6 N) at α = 60°.

At crosshead speed of 200 mm/min, an increase in temperature from room temperature to 50 °C, resulted in a 39% decrease in the yield load (from 583.3 N to 421.6 N) at α = 90° and 41% decrease in the yield load (from 531.5 N to 376.3 N) at α = 60°. Note that, for the tests performed at 50 °C and loading angles α = 30° and 0°, no clear yield load can be identified as the material show progressive hardening without reaching the first local peak force.

As mention before, possible multiphase layer structure with oriented crystalline morphology along the cross-section perpendicular to the melt flow, might be included in the responses reported in this study. Plausible explanation for the microstructure deformation mechanisms during biaxial loading are depicted in 4.1.2 Biaxial Tension at Room Temperature. Plausible explanations for the microstructure deformation mechanisms during biaxial loading are included in section 4.1.2 Combined Tensile/Shear Behaviour at Room Temperature, For HDPE material which is expected to be extensive to PP.

Table 67 - Fracture appearance and corresponding load and displacement values for butterfly specimen at α = 90° (pure tension) at 50 °C (all values are averaged) (PP).

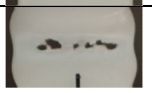
Testing Speed (mm/min)	**Yield Load**			**Fracture Point**		
	Load, F (N)	Displ., δ_F (mm)	Image	Load, F (N)	Displ., δ_F (mm)	Image
1	315.7	0.5	-	262.4	1.7	
200	421.6	0.5	-	354.9	1.3	

Table 68 - Fracture appearance and corresponding load and displacement values for butterfly specimen at α = 60° (combined tension/shear) at 50 °C (all values are averaged) (PP).

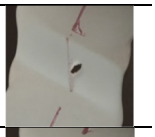
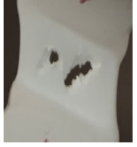
Testing Speed (mm/min)	**Yield Load**			**Fracture Point**		
	Load, F (N)	Displ., δ_F (mm)	Image	Load, F (N)	Displ., δ_F (mm)	Image
1	267.6	0.7	-	217.7	6.4	
200	376.3	1.2	-	279.3	2.3	

Table 69 - Fracture appearance and corresponding load and displacement values for butterfly specimen at α = 30° (combined tension/shear) at 50 °C (all values are averaged) (PP).

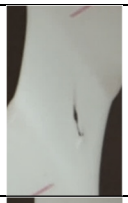
Testing Speed (mm/min)	**Fracture Point**		
	Load, F (N)	Displ., δ_F (mm)	Image
1	231.6	11.6	
200	355.1	6.6	

Table 70 - Fracture appearance and corresponding load and displacement values for butterfly specimen at α = 0° (pure shear) at 50 °C (all values are averaged) (PP).

Testing Speed (mm/min)	**Fracture Point**		
	Load, F (N)	Displ., δ_F (mm)	Image
1	260.6	16.3	
200	293.3	8.5	

4.2.4 Compression Tests at Room Temperature

Uniaxial compression tests were performed on cylindrical and cylindrical notched specimens. The experimental details are summarized in section: 4.1.4 Compression Tests at Room Temperature (HDPE).

Figure 79 presents the load-displacement curves of (1) cylindrical and (2) cylindrical notched specimens at RT for three crosshead speeds. The first observation is that the load-displacement curves shift to higher strength values with an increasing crosshead speed. On effect, an increase of crosshead speed will decrease the molecular mobility of the polymer chains, making the material less susceptive to deform.

The second observation is show in Figure 79 (1) about cylindrical specimens, the compressive curve can be roughly divided into four different domains: (1) the initial linear elastic deformation region, where the force almost linearly increases with the compressive load, (2) the transition domain from elastic to plastic deformation zone, where the force grows nonlinearly with displacement, (3) the plastic plateau, where the force remains nearly constant with displacement and (4) the strain hardening region, where the stress increases fast with displacement due to densification of the specimen.

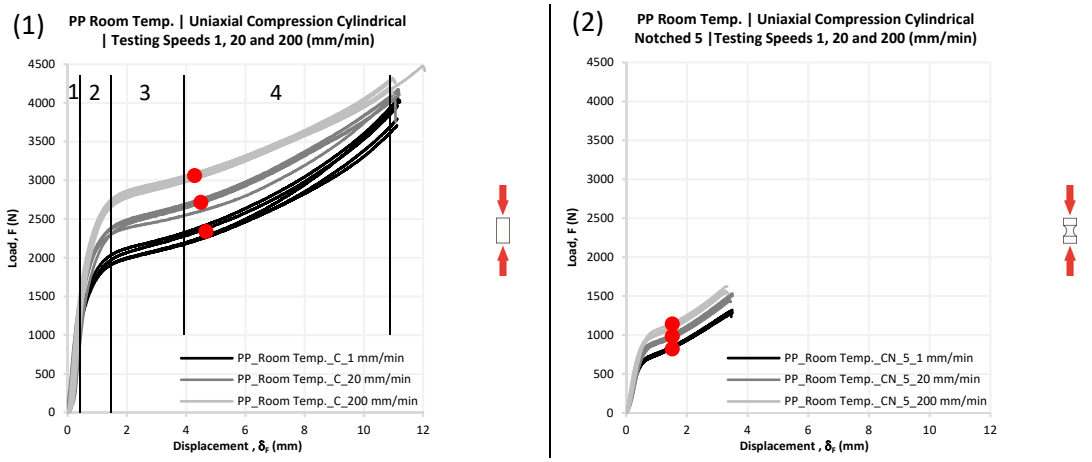


Figure 79 - Compression load-displacement curves of (1) cylindrical and (2) cylindrical notched specimens.

From the load-displacement curves it can be seen that the yield load cannot be objectively determined, since there is no single point at which the material starts to yield. The onset of barrelling is highlighted with a red circle in the graphs.

During the deformation process and with increasing the crosshead speed, heating effect on plastic domain, may be developed. The increase in temperature might be recognized at large plastic deformations and at high values for crosshead speeds due to internal material dissipation/friction and low thermal diffusivities of semi crystalline polymers. Effects of temperature are expected to be significant for high strain rate testing, yet still dependent on polymer type.

A sequence of images of cylindrical and cylindrical notched specimens at different stages of the compression tests, are shown in Tables 71 and 72. From the pictures of the deformation patterns of cylindrical specimens, it can be seen the barrelling deformation effect due to friction.

Table 71 - Deformation pattern and corresponding load and displacement values for cylindrical specimen at three deformation stages (all values are averaged) (PP).

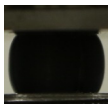
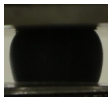
Testing Speed (mm/min)	**Virgin specimen**		**Barrelling Onset**			**Interrupted Test**		
	Displ., δ_{0F} (mm)	Image	Load, F (N)	Displ., δ_F (mm)	Image	Load, F (N)	Displ., δ_F (mm)	Image
1	0		2380.3	4.5		4008.4	11.1	
20	0		2714.2	4.4		4082.6	11.1	
200	0		3048.2	4.2		4267.5	11.1	

Table 72 – Deformation pattern and corresponding load and displacement values for cylindrical notched specimen at two deformation stages (all values are averaged) (PP).

Testing Speed (mm/min)	**Virgin specimen**		**Barrelling Onset**			**Interrupted Test**		
	Displ., δ_{0F} (mm)	Image	Load, F (N)	Displ., δ_F (mm)	Image	Load, F (N)	Displ., δ_F (mm)	Image
1	0		883.3	1.7		1285.5	3.5	
20	0		969.6	1.7		1464.5	3.5	
200	0		1132.8	1.7		1551.4	3.5	

4.2.5 Combined Compression/Shear Tests at Room Temperature

Combined compression/shear tests were performed on butterfly specimens of PP at room temperature. The experimental details are summarized in section: 4.1.5 Combined Compression/Shear Tests at Room Temperature (HDPE). Experimentally measured curves for biaxial loading under, α = 90°, 60°, 60° and 0° are shown in Figures 80 and 81.

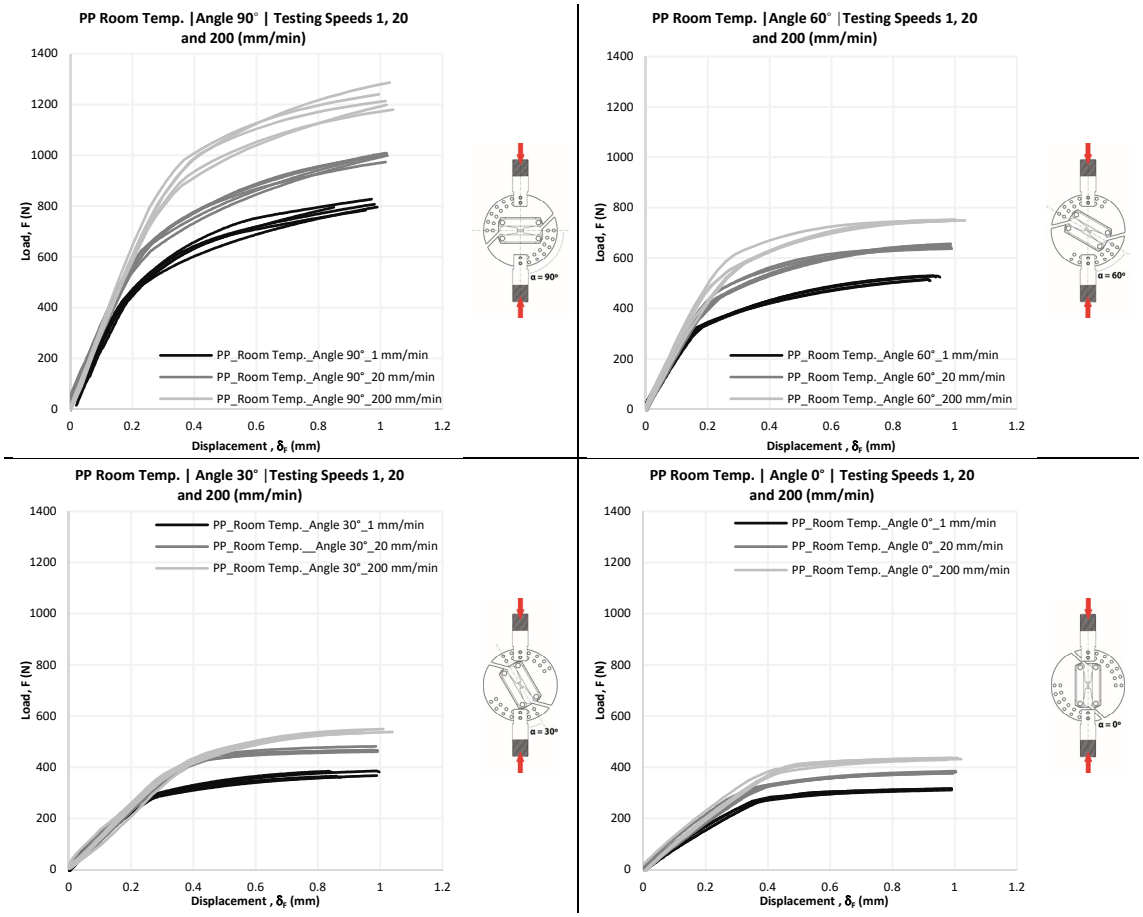


Figure 80 - Load-displacement curves for PP resulting from combined compression/shear loading at RT: influence of crosshead speeds for each loading angle.

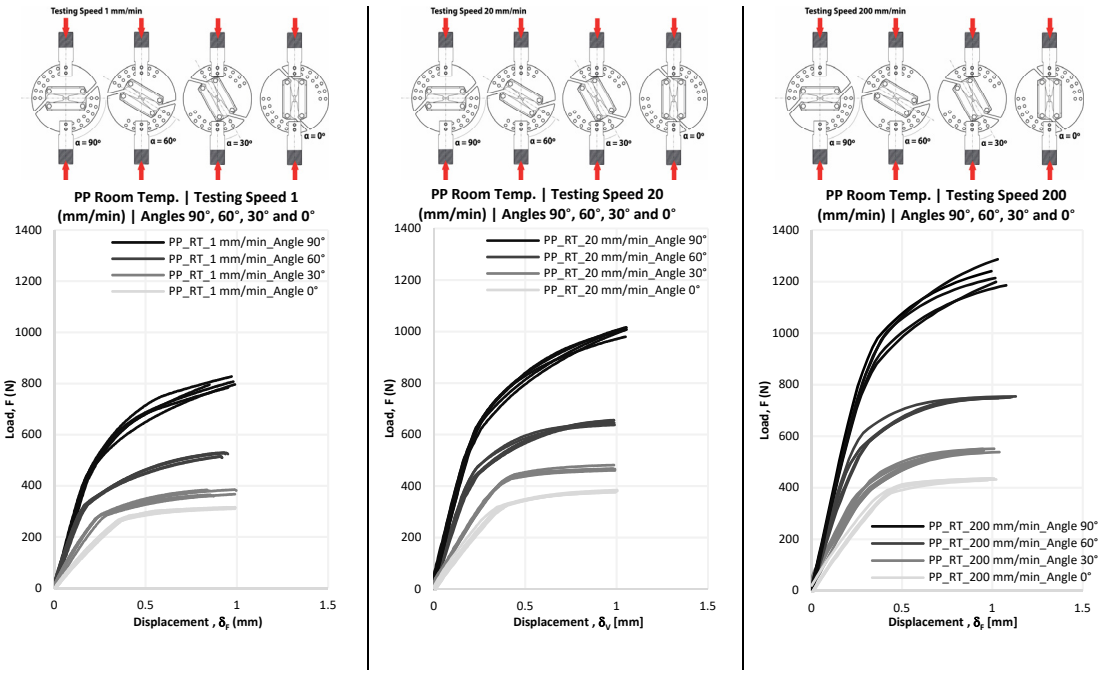


Figure 81 - Load-displacement curves for PP resulting for combined compression/shear loading at RT: effect of loading angle for given crosshead speeds.

All experimental results show an initially linear force-displacement response followed by a nonlinear regime until the test is interrupted due to limitation of the maximum travel allowed by the arcan apparatus, in negative vertical direction. For the deformation till 1 mm it is visible a transition from linear to nonlinear behaviour, but the load continues to increase in the nonlinear domain. Strain rate effects are clearly visible with load increasing with testing speed increasing in Figure 80.

Regarding the results for combined shear and compression given in Figure 81 (negative vertical loads and displacements were converted into positive values) it can be observed that the initial stiffness of the curves decrease with the decreasing loading angle and are minimum for the loading angle $\alpha = 0°$ (pure shear). The displacement and loads corresponding to the elastic-plastic transition (yielding at the central gauge section) are highly dependent on the loading angle. Lower the loading angle (from $\alpha = 90°$ to 0°), lower is the load required to deform the specimens. From the load-displacement curves, it can be seen that the yield load cannot be locally determined, since there is no single point at which the material starts to yield. Instead, a transition yielding is observed.

Tables 73, 74, 75 and 76 show some images of the specimens gauge section and corresponding load and displacement values for the PP specimens at different deformation stages: virgin or unloaded and interrupted test.

Table 73 - Deformation patterns and corresponding load and displacement values for butterfly specimen at $\alpha = 90°$ (pure compression) at RT (all values are averaged) (PP).

Testing Speed (mm/min)	**Virgin specimen**		**Interrupted Test**		
	Displ., δ_{0F} (mm)	Image	Load, F (N)	Displ., δ_F (mm)	Image
1	0		805.7	1.0	
20	0		1001.3	1.0	
200	0		1222.3	1.0	

Table 74 - Deformation patterns and corresponding load and displacement values for butterfly specimen at $\alpha = 60°$ (combined shear/compression) at RT (all values are averaged) (PP).

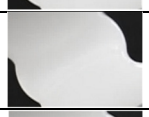
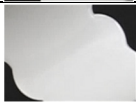
Testing Speed (mm/min)	**Virgin specimen**		**Interrupted Test**		
	Displ., δ_{0F} (mm)	Image	Load, F (N)	Displ., δ_F (mm)	Image
1	0		528.3	1.0	
20	0		650.7	1.0	
200	0		751.4	1.0	

Table 75 - Deformation patterns and corresponding load and displacement values for butterfly specimen at α = 30° (combined shear/compression) at RT (all values are averaged) (PP).

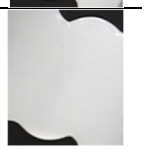
Testing Speed (mm/min)	**Virgin specimen**		**Interrupted Test**		
	Displ., δ_{0F} (mm)	Image	Load, F (N)	Displ., δ_F (mm)	Image
1	0		334.2	1.0	
20	0		464.8	1.0	
200	0		544.2	1.0	

Table 76 - Deformation patterns and corresponding load and displacement values for butterfly specimen at α = 0° (pure shear) at RT (all values are averaged) (PP).

Testing Speed (mm/min)	**Virgin specimen**		**Interrupted Test**		
	Displ., δ_{0F} (mm)	Image	Load, F (N)	Displ., δ_F (mm)	Image
1	0		315.3	1.0	
20	0		382.7	1.0	
200	0		434.7	1.0	

As mention before possible multiphase layer structure with oriented crystalline morphology along the cross-section perpendicular to the melt flow, might be included in the responses reported in this study. Plausible explanations for the microstructure deformation mechanisms during biaxial loading are depicted in 4.1.2 Combined Tensile/Shear Behaviour at Room Temp.

4.2.6 Combined Compression/Shear Tests at Temperature of 50°C

Biaxial loading tests were performed on butterfly specimen at constant temperature of 50 °C. The experimental details are summarized in section: 4.1.6 Combined Compression/Shear Tests at Temperature of 50°C (HDPE).

Load-displacement curves corresponding to the combined compression/shear loading (α = 90°, 60°, 30°, and 0°) for crosshead speeds of 1 and 200 mm/min at room temperature and temperature of 50 °C are presented in Figure 82 and 83. As expected, the load-displacement curves shift down with an increasing temperature and decreasing the crosshead speed. The following conclusions are drawn:

- At constant temperature of 50 °C, the load increases with the crosshead speed. In a given crosshead speed, the load decreases with temperature.
- Changing the loading angle from α = 90° to 0° at constant temperature of 50 °C, load-displacement curves shifts downward.

Plausible explanations for the microstructure deformation mechanisms during biaxial loading are depicted in 4.1.2 Combined Tensile/Shear Behaviour at Room Temperature.

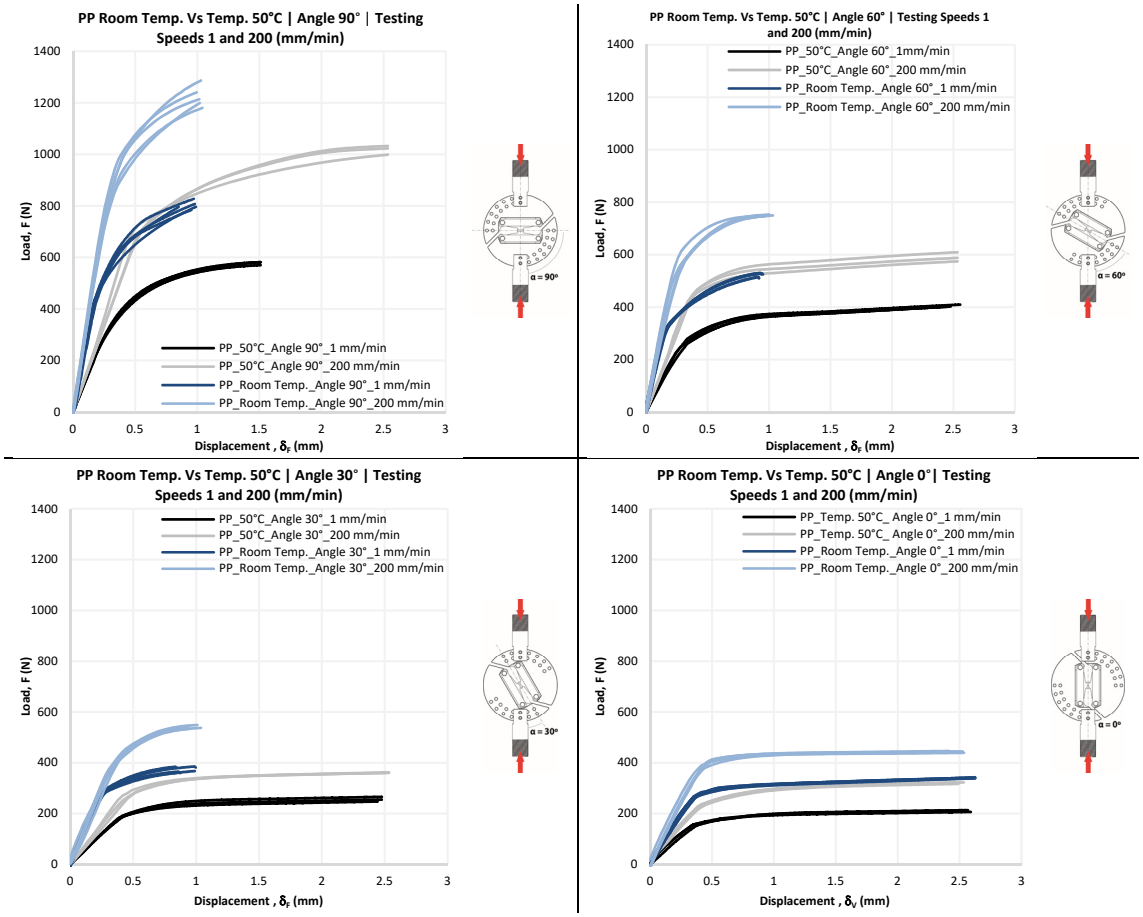


Figure 82 – Load-displacement curves for PP resulting from combined compression/shear loading at RT and 50 °C: influence of crosshead speeds for each loading angle.

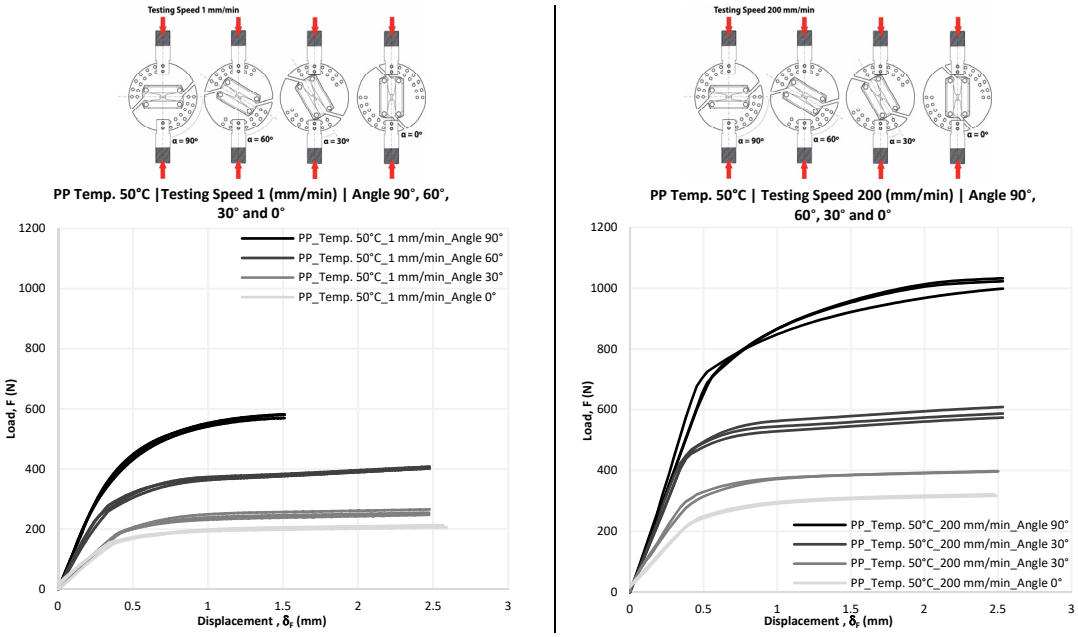


Figure 83 – Load-displacement curves for PP resulting for combined compression/shear loading at 50 °C: effect of loading angle for given crosshead speeds.

Tables 77, 78, 79 and 80 show load and displacement values for the PP specimens at final deformation stage with corresponding deformation appearance. Tests were interrupted without being observed material failure.

Table 77 – Deformation pattern and corresponding load and displacement values for butterfly specimen at α = 90° (pure compression) at 50 °C (all values are averaged) (PP).

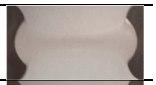
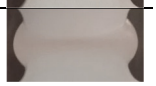
Testing Speed (mm/min)	**Interrupted Test**		
	Load, F (N)	Displ., δ_F (mm)	Image
1	575.5	1.5	
200	1017.1	2.5	

Table 78 - Deformation pattern and corresponding load and displacement values for butterfly specimen at α = 60° (combined compression/shear) at 50 °C (all values are averaged) (PP).

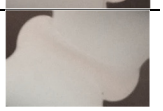
Testing Speed (mm/min)	**Interrupted Test**		
	Load, F (N)	Displ., δ_F (mm)	Image
1	404.8	2.5	
200	589.9	2.5	

Table 79 - Deformation pattern and corresponding load and displacement values for butterfly specimen at α = 30° (combined compression/shear) at 50 °C (all values are averaged) (PP).

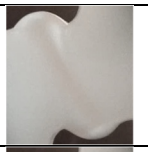
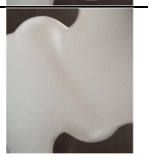
Testing Speed (mm/min)	**Interrupted Test**		
	Load, F (N)	Displ., δ_F (mm)	Image
1	256.3	2.5	
200	360.9	2.5	

Table 80 - Deformation pattern and corresponding load and displacement values for butterfly specimen at α = 0° (pure shear) at 50 °C (all values are averaged) (PP).

Testing Speed (mm/min)	**Interrupted Test**	
	Load, F (N)	Displ., δ_F (mm)
1	129.2	2.6
200	319.9	2.6

4.2.7 Differential Scanning Calorimetry (DSC)

DSC tests were performed on solid granulates of PP. The experimental details are depicted hereafter: The experimental details are summarized in section: 4.1.7 Differential Scanning Calorimetry (DSC) (HDPE).

DSC scans were performed on solid granulates, which were organized in to three groups, corresponding to: virgin injected specimens (Figure 84) and deformed specimens (Figure 85) with true strain of 0.5 and 1. In the virgin material (Table 81), DSC scan exhibits an endothermic peak at 170.7 °C (average value), an average enthalpy (ΔH_f) of 84.3 J/g and crystallinity percentage of 40.4%. The melting temperature and percentage of crystallinity are in agreement with the work of Lei et al. [166]. A melting heat of 209 J/g [76] have been reported for completely crystallized polypropylene. The ratio of the melting heat of the sample and the melting heat of the completely crystallized polypropylene was used to calculate the degree of crystallization.

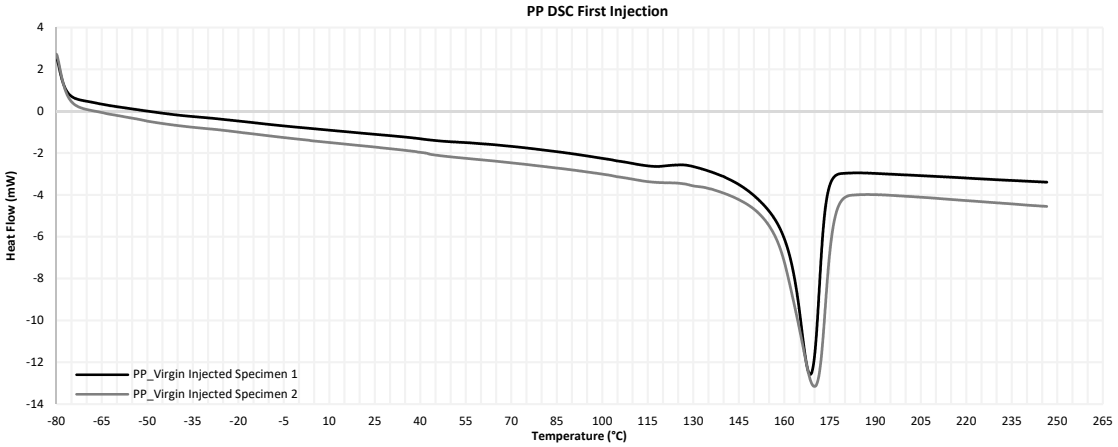


Figure 84 – DSC curves for PP virgin/injected material.

Table 81 – Thermal properties and crystallinity of PP determined by DSC, virgin material.

	Units	Specimens	
		Virgin Injected Specimen 1	**Virgin Injected Specimen 2**
Enthalpy (ΔH_f)	J/g	85.5	83.2
Average	J/g	84.3	
Melting Temperature (T_m)	°C	168.5	172.8
Average	°C	170.7	
Enthalpy of Perfect Polymer Crystal (ΔH^0_f)	J/g	209 [76]	
Crystallinity	%	40.9	39.8
Average	%	40.4	

The solid granulates extracted from middle section of deformed specimens at true strain of 0.5 and 1, crosshead speed of 1 mm/min and room temperature, both show an endothermic peak at 171.5 °C, an average enthalpy (ΔH_f) content of 87.2 J/g and 82.1 J/g, crystallinity percentage of 41.7% and 39.3%, respectively (Table 82). From these results it can be concluded that the percentage crystallinity slight increased by 1.2 % at true strain of 0.5 and decreases by 1.2% at true strain of 1, relatively to the virgin values. At true strain of 0.5, beyond yield load, the increase in deformed specimen crystallinity can be referred to the chain alignment that occurs during specimen deformation.

At large deformation, in the uniaxial tension of semi crystalline polymers, several deformation stages are present. These stages involving tie molecule stretching, crystalline lamellar rotation and alignment, fine slip, course slip, fragmentation of lamellae, and finally chain alignment with further destruction of lamellae. These events can result in a decrease in crystallinity due to tensile deformation. These mechanisms might explain the current changes in the relative crystallinity of deformed PP specimens compared with virgin specimens. This results are in accordance with the research work of Fouad [143]. Furthermore, at large displacements near fracture point the plastic deformation of semi crystalline polymers has also been considered as a decrystallization process, defined as mechanically induced destruction of crystalline lamellae

(unfolding) [160]. It appears that, at least for PP, yielding at or near room temperature is basically controlled by crystal plasticity processes while, for large post-yielding deformations, decrystallization are involved.

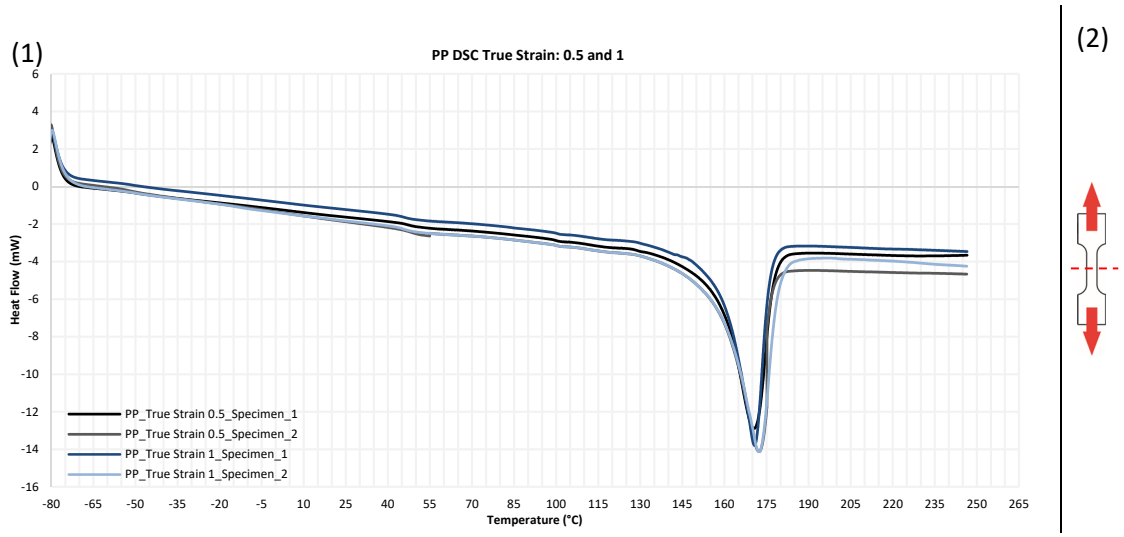


Figure 85 - (1) DSC curves for PP at true strains of 0.5 and 1, (2) red dashed line is the longitudinal section investigated in the DSC.

Table 82 - Thermal properties and crystallinity of PP determined by DSC, deformed specimens.

	Units	Specimens			
		True Strain 0.5_1	**True Strain 0.5_2**	**True Strain 1_1**	**True Strain 1_2**
Enthalpy (ΔH_f)	J/g	87.8	86.7	81.8	82.3
Average	J/g	87.2		82.1	
Melting Temperature (T_m)	°C	170.5	172.4	170.7	172.4
Average	°C	171.5		171.5	
Enthalpy of Perfect Polymer Crystal (ΔH^0_f)	J/g	209[76]			
Crystallinity	%	42.0	41.5	39.2	39.4
Average	%	41.7		39.3	

4.2.8 Dynamic Mechanical Analysis (DMA)

DMA tests were performed on rectangular specimens with the following dimensions: 40 mm×15 mm×1.8 mm of PA 6. The experimental details are summarized in section: 4.1.8 Dynamic Mechanical Analysis (DMA) (HDPE).

The DMA results for storage modulus (*E'*) as function of temperature (°*C*) and frequency is given in Figure 86 for PP. The DMA curves shifts to higher values as the test frequency increases. The PP exhibit the dynamic mechanical response which is characteristic of a thermoplastic material. At room temperature the storage modulus is relatively high, ranging from 780 N to 820 N for frequency 0.1 Hz, 1040 N to 1080 N for frequency 1 Hz and 1200 N to 1240 N for frequency 10

Hz and with increasing temperature, this modulus gradually reduces to the rubbery flow. The loss factor tan (δ) as function of temperature it was not taken into account due to PP glass transition temperature (T_g) ranges between -20 °C and 0 °C [76].

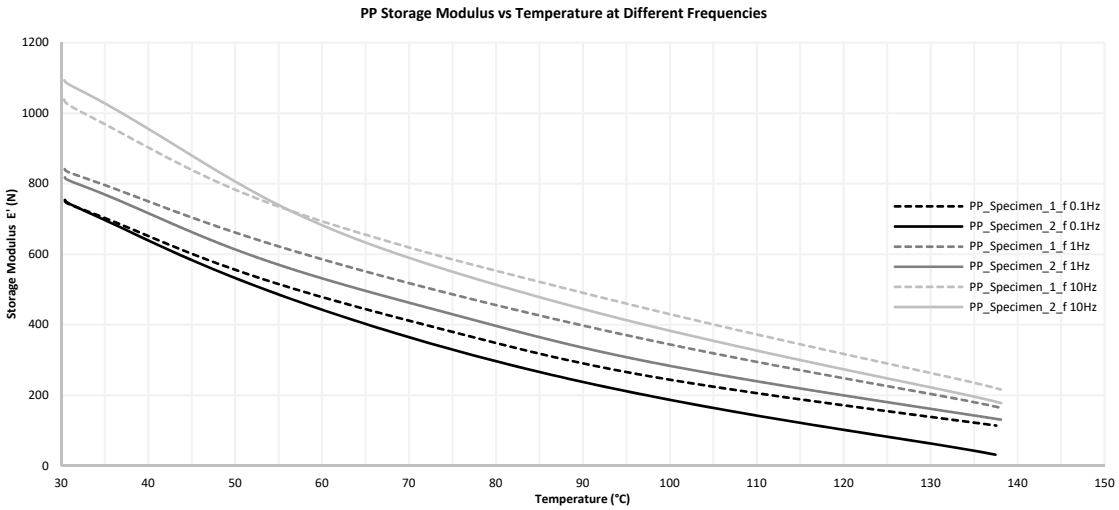


Figure 86 – Results of DMA experiments; the storage modulus (E') as function of temperature (°C) for and frequency effects on PP.

4.3 Polyamide 6 (PA 6)

The deformation behaviour of Polyamide 6 (PA 6) based on load-displacement curves is complex because of highly inhomogeneous nature of plastic deformation, in particular hardening and necking. The propagation of neck along the longitudinal direction strongly influences the physical and structural properties of PA 6, which makes a comparison between different polymeric materials difficult [167].

The deformation mechanisms and the mechanical properties of PA 6 are highly strain rate and temperature dependent. Therefore, the yielding and post yielding behaviour of PA 6 is highly sensitive to strain rate, and the test loads generally increase with increasing crosshead speeds. Strain rate, further influence the fracture toughness of material. Also, the extent of PA 6 dependency on strain rate is also influenced by temperature. Generally, for PA 6 the deformation levels increase with temperature [167].

4.3.1 Tensile Tests at Room Temperature

Tensile tests were performed on dumbbell, flat notched and cylindrical notched specimens at room temperature. The experimental details were already summarized in section: 4.1.1 Tensile Tests at Room Temperature (HDPE). Tests were performed until the fracture, with exception of dumbbell and cylindrical notched 30 specimens, because the maximum travel of the extensometer was 25 mm, which was insufficient to reach fracture of the specimen.

Figures 87 and 88 show the load-displacement curves, obtained for constant crosshead speeds of 1, 20 and 200 mm/min. For the flat notched and cylindrical notched specimens, there is a pronounced effect, when decreasing the crosshead speed, which remarkably lowers the yield load. Dumbbell specimens did not exhibit a load drop at yield load. Also, for each notch radius, it can be observed that the higher the crosshead speed, the higher is the peak load. Moreover, the smaller the notch radius (the higher the stress triaxiality), the higher is the peak load and the lower is the displacement at failure.

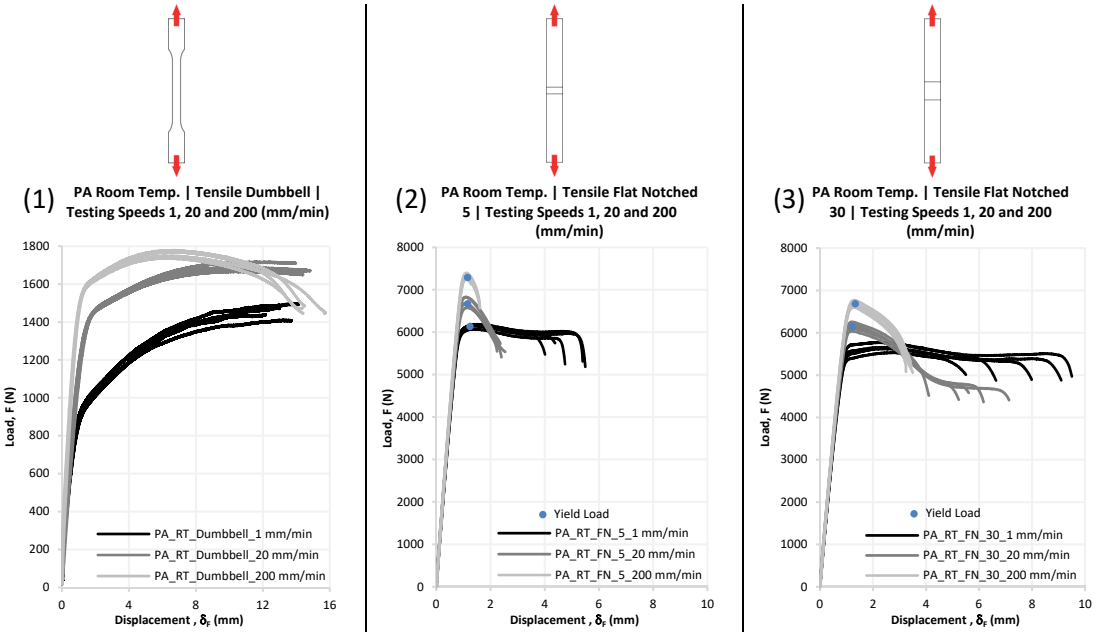


Figure 87 - Tensile load-displacement curves of (1) dumbbell, (2) flat notched 5 and (3) flat notched 30 specimens (PA 6, Room Temperature).

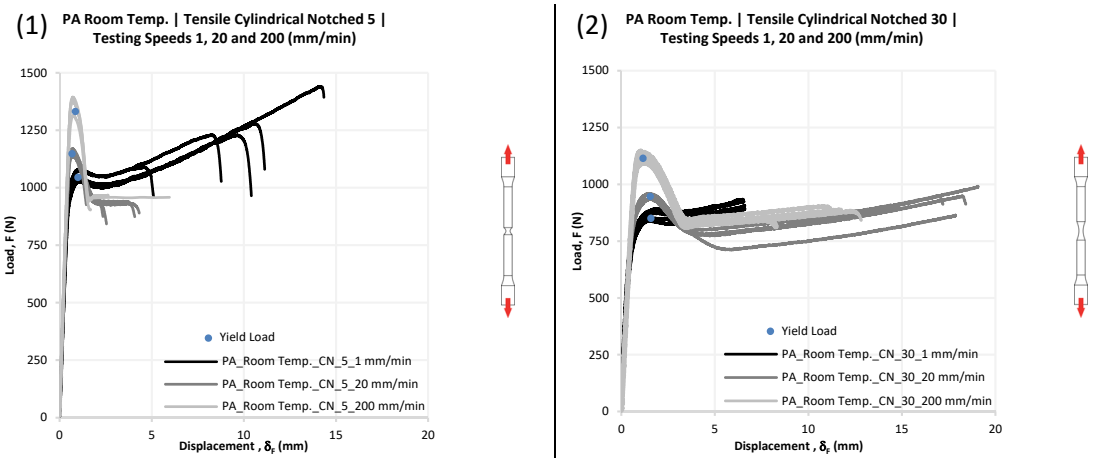


Figure 88 - Tensile load-displacement curves of (1) cylindrical notched 5 and (2) cylindrical notched 30 specimens (PA 6, Room Temperature).

Deformation of semi crystalline polymers is always accompanied by changes in the microscopic structure that result in an alteration of specimen properties during deformation. From load-

displacement curves of PA 6 (Figures 87 and 88) it is observed two transition points: from elastic to plastic and from plastic to rupture. At elastic domain the deformation process might be associated to the onset of isolated inter- and intralamellar slip processes and the deformation is recoverable. At plastic domain the deformation process can be related to the slip and tilting of crystalline lamellar chains, and orientation of crystal blocks. This corresponds to moderate hardening displacements. Then, once the spherulite microstructure has been destroyed and transformed into a fibrillar microstructure, deformation continues by destruction of the lamellar morphology [145].

At the yield load, as the displacement increases the stress whitening and shape changes are detected probably due to crazing that can be attributed to microvoids. The stress whitening was not observed in dumbbell specimen deformation. During tensile tests whitening occurs first homogeneously all along the gauge length of the specimen, then it is localised around the necked zone after the maximum loading. Craze structure consists of porosity and oriented hard fibrils. During craze development might be induced both material softening due to void growth and pressure sensitivity related to volume change [168]. Also, thermal softening might be included in the responses reported in this study, specially at high crosshead speed, due to sharp decrease observed in the load-displacement curves, depicted in Figures 87 and 88.

Focusing in Figure 88 on the cylindrical notched 5 and 30 specimens, the PA 6 load-displacement response during tensile loading can be examined. The highly nonlinear response of PA 6 is clearly illustrated. After the initial elastic response and the rollover to yield load, the stress whitening and significant softening is followed by a progressive plastic strain hardening, which is nearly zero for crosshead speed of 20 and 200 mm/min. The softening increases with crosshead speed. The beginning of the softening coincides with the pre-neck (quick cross-section reduction) (see deformation patterns on Tables 86 and 87). The macroscopic strain hardening is related to the stretching of chains in the amorphous phase and to the fragmentation of crystallites leading to the formation of a fibrillar microstructure [169].

Tables 83, 84, 85, 86 and 87 show sequential images of deformation patterns evolution and corresponding load and displacement values for the PA 6 specimens at three deformation stages: virgin or unloaded, yield load or first force peak and the interrupted test/fracture point. From the analyses of results it is observed an increase on the yield load by about 19% (from 6178.3 N to 7338.2 N) for flat notched 5, 29% (from 1067.4 N to 1380.6 N) for cylindrical notched 5 and 30% (from 867.9N to 1131.8 N) for cylindrical notched 30, when testing speeds increased from 1 mm/min to 200 mm/min. For dumbbell specimens and flat notched 5 at lowest crosshead speed the yield load are not associated to local peak load.

Table 83 – Load and displacement values for dumbbell specimen at selected deformation stages (all values are averaged) (PA 6).

Testing Speed (mm/min)	**Interrupted Test**	
	Load, F (N)	Displ., δ_F (mm)
1	1446.3	14.3
20	1686.4	14.7
200	1461.2	14.9

Table 84 – Deformation patterns and corresponding load and displacement values for flat notched 5 specimens at three deformation stages (all values are averaged) (PA 6).

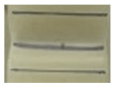
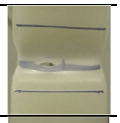
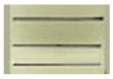
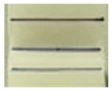
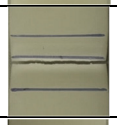
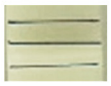
Testing Speed (mm/min)	**Virgin specimen**		**Yield Load**			**Fracture Point**		
	Displ., δ_{0F} (mm)	Image	Load, F (N)	Displ., δ_F (mm)	Image	Load, F (N)	Displ., δ_F (mm)	Image
1	0		6178.3	1.5		5395.4	4.7	
20	0		6754.9	1.1		5586.9	2.3	
200	0		7338.2	1.1		6589,2	1.6	

Table 85 – Deformation patterns and corresponding load and displacement values for flat notched 30 specimens at three deformation stages (all values are averaged) (PA 6).

Testing Speed (mm/min)	**Virgin specimen**		**Yield Load**			**Fracture Point**		
	Displ., δ_{0F} (mm)	Image	Load, F (N)	Displ., δ_F (mm)	Image	Load, F (N)	Displ., δ_F (mm)	Image
1	0		-	-	-	4909.3	8.4	
20	0		6152.4	1.3		4465.7	5.6	
200	0		6634.3	1.3		5193.9	3.3	

Table 86 – Deformation patterns and corresponding load and displacement values for cylindrical notched 5 specimens at three deformation stages (all values are averaged) (PA 6).

Testing Speed (mm/min)	**Virgin specimen**		**Yield Load**			**Fracture Point**		
	Displ., δ_{0F} (mm)	Image	Load, F (N)	Displ., δ_F (mm)	Image	Load, F (N)	Displ., δ_F (mm)	Image
1	0		1067.4	1.1		1232.3	9.2	
20	0		1144.2	0.7		901.1	3.6	
200	0		1380.6	0.7		1012.1	2.0	

Table 87 – Deformation patterns and corresponding load and displacement values for cylindrical notched 30 specimens at three deformation stages (all values are averaged) (PA 6).

Testing Speed (mm/min)	**Virgin specimen**		**Yield Load**			**Interrupted Test**		
	Displ., δ_{0F} (mm)	Image	Load, F (N)	Displ., δ_F (mm)	Image	Load, F (N)	Displ., δ_F (mm)	Image
1	0		867.9	1.7		914.6	6.6	
20	0		938.1	1.5		878.7	16.3	
200	0		1131.8	1.1		950.6	18.8	

To sum up the tensile tests on notched specimens indicated that the presence of notches altered the yield load and displacements. The results show significant changes in the load-displacement curves due to the presence of notches with different geometries. All cylindrical and flat notched specimens show a progressive increase in the yield load and decrease in the displacement with decreasing the specimen notch radii. For example, the yield load for flat and cylindrical notched specimens at crosshead speed of 200 mm/min increases by 10.6% (from 6634.3 N to 7338.2 N) 22% (from 1131.8 N to 1380.6 N) for notched R 30 to R 5, respectively.

These results can be attributed to the relatively larger stress triaxiality that makes the specimen's deformation more difficult and hence, more stress is needed to reach the same strain. Therefore, the larger stress triaxiality the higher fracture driving forces, which results in the fracture of the specimen at a lower strain. Also, the triaxial state of stress reduces the tested material chain alignment which is remarked during the tensile test [143].

4.3.2 Combined Tensile/Shear Tests at Room Temperature

Combined tension/shear loading tests were performed on butterfly specimens at room temperature. The experimental details are summarized in section: 4.1.2 Combined Tensile/Shear Behaviour at Room Temperature (HDPE). Tests were performed until the fracture.

Figures 89 and 90 show the results when a positive vertical displacement is applied is applied in Arcan grips generating combined tension/shear loading. It can be observed that the load-displacement curves overlap each other, for high plastic strains. Higher the loading angle (from α = 0° to 90°), higher is the load required to deform the specimens. Increasing the crosshead

speed reduces the time for molecular rearrangements, however the polymer behaviour at large displacements are almost the same – the load-displacement curves beyond the yield load, becomes coincident for all loading rates. This mechanical behaviour might indicate that there is an thermal softening associated with a progressive localization of heat sources at high crosshead speed as observed by Wattrisse et al. [158]. The initial linear elastic response is followed by a nonlinear evolution, the peak load denotes the onset of stress whitening at the central section (see the sequential figures on Tables 88, 89, 90 and 91).

The load-displacement curves shift to high strength values with increasing of crosshead speed. The main differences between these different loading rates are found in their post-yield behaviour: (1) the drop of the load are found maximum for the loading angle of $\alpha = 0°$, pure shear and minimum for $\alpha = 90°$, pure tension, (2) the equality of displacement with increasing of crosshead speed in all loading angles (there are slight differences), (3) the yield load is only noticeable at loading angles of $\alpha = 90°$ and $\alpha = 60°$ (4) at loading angle $\alpha = 0°$ the displacement at failure achieves the maximum values. The crosshead speed and loading angle plays a key role in the macroscopic "after yielding" deformation behaviour and determines whether a material behaves like brittle or ductile. Possible microstructure deformation mechanisms during biaxial loading are depicted in section 4.1.2 Combined Tensile/Shear Behaviour at Room Temperature, concerned with HDPE polymer.

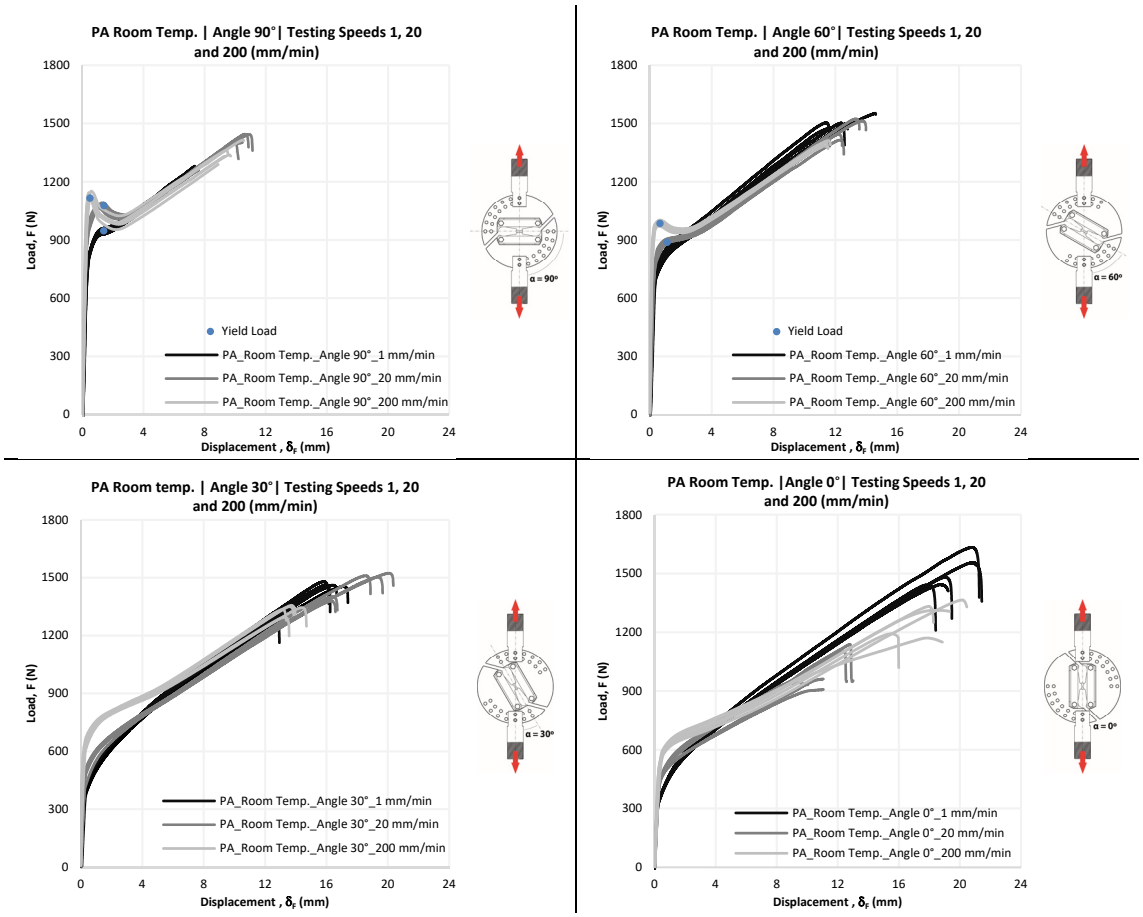


Figure 89 - Load-displacement curves for PA 6 resulting from combined tension/shear loading at RT: influence of crosshead speeds for each loading angle.

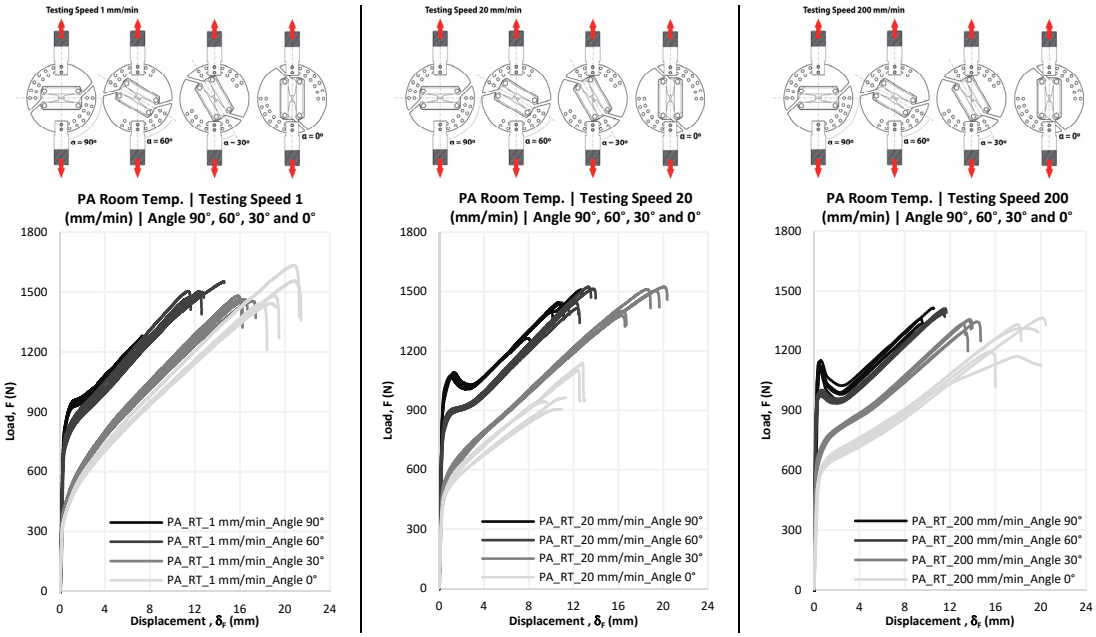


Figure 90 - Load-displacement curves for PA 6 resulting for combined tensile/shear loading at RT: effect of loading angle for given crosshead speeds.

Tables 88, 89, 90 and 91 show sequential images of the deformation patterns of gauge length and corresponding load and displacement values for PA 6 specimens at three deformation stages: virgin or unloaded, yield load or first peak force and fracture point. From values analysis on yield load at crosshead speeds of 1 mm/min, 20 mm/min and 200 mm/min, it is observed an increase on the yield load values by about 19% (from 952.4 N to 1131.3 N) for loading angle α = 90° and for crosshead speeds of 20 mm/min to 200 mm/min at loading angle α = 60° there is an increase of about 9% (from 907.4 N to 992.3 N). For loading angle of α = 30° and 0° the yield load is not clearly noticeable.

Table 88 - Deformation patterns and corresponding load and displacement values for butterfly specimens loaded at α = 90° (pure tension) at RT (all values are averaged) (PA 6).

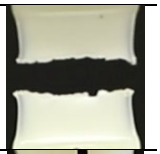
Testing Speed (mm/min)	**Virgin specimen**		**Yield Load**			**Fracture Point**		
	Displ., δ_{0F} (mm)	Image	Load, F (N)	Displ., δ_F (mm)	Image	Load, F (N)	Displ., δ_F (mm)	Image
1	0		952.4	1.3		1251.3	7.1	
20	0		1081.5	1.2		1454,5	11.2	
200	0		1131.3	0.5		1351.7	9.7	

Table 89 - Deformation patterns and corresponding load and displacement values for butterfly specimens loaded at α = 60° (combined tension/shear) and RT (all values are averaged) (PA 6).

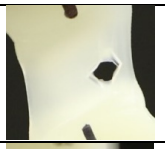
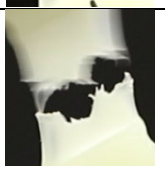
Testing Speed (mm/min)	**Virgin specimen**		**Yield Load**			**Fracture Point**		
	Displ., δ_{0F} (mm)	Image	Load, F (N)	Displ., δ_F (mm)	Image	Load, F (N)	Displ., δ_F (mm)	Image
1	0		-	-	-	1514.3	12.9	
20	0		907.4	1.4		1484.7	12.9	
200	0		992.3	0.6		1401.6	11.4	

Table 90 - Deformation patterns and corresponding load and displacement values for butterfly specimens loaded at α = 30° (combined tension/shear) and RT (all values are averaged) (PA 6).

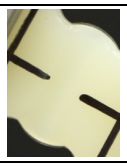
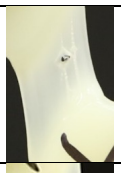
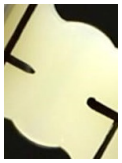
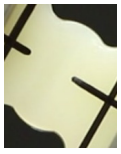
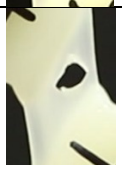
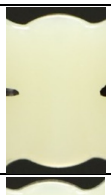
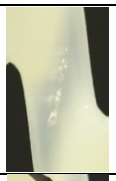
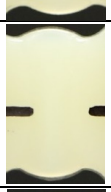
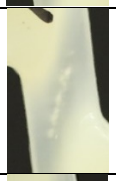
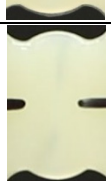
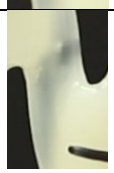
Testing Speed (mm/min)	**Virgin specimen**		**Fracture Point**		
	Displ., δ_{0F} (mm)	Image	Load, F (N)	Displ., δ_F (mm)	Image
1	0		1395.4	15.1	
20	0		1466.9	18.7	
200	0		1324.4	13.4	

Table 91 - Deformation patterns and corresponding load and displacement values for butterfly specimens loaded at α = 0° (pure shear) and RT (all values are averaged) (PA 6).

Testing Speed (mm/min)	**Virgin specimen**		**Fracture Point**		
	Displ., δ_{0F} (mm)	Image	Load, F (N)	Displ., δ_F (mm)	Image
1	0		1472.6	19.2	
20	0		1118.7	12.6	
200	0		1260.1	16.9	

4.3.3 Combined Tensile/Shear Test at Temperature of 50°C

Biaxial loading tests were performed on butterfly specimen at constant temperature of 50 °C. The experimental details are summarized in section: 4.1.3 Combined Tensile/Shear Tests at Temperature of 50°C (HDPE). Tests were performed until the fracture. Figures 91 and 92, present the load versus displacement curves and compares the RT behaviour with the corresponding behaviour at 50 °C. The following conclusions are drawn:

- At constant temperature of 50 °C the load grows in the yield region with the crosshead speed. For a given crosshead speed, the load decreases with temperature. Similar mechanical behaviour were found on studies on Nylon 6.6 using dumbbell specimens tested for temperatures from 21 °C to 200 °C, at a strain rate of 2 mm/min, by Hartmann et al. [170]. This research shown that yield stress decreases with the increase of temperature and the yield strain reaches a maximum value at the temperature of 160 °C.
- Growth of temperature and reduction in crosshead speed lead to transition from brittle to ductile fracture of specimens.
- As general view the displacements at failure are greater at room temperature than at temperature of 50 °C.
- Changing the loading angle from α = 90° to 0° at constant temperature of 50 °C load-displacement curves reveals lower strength, increasing ductility.
- Stress whitening was observed in the gauge section of PA 6 butterfly specimen, shortly before yielding with microvoids appear in the specimen's centre. With increasing deformation, the microvoids change their size, density, and orientation becoming elongated parallel to deformation.

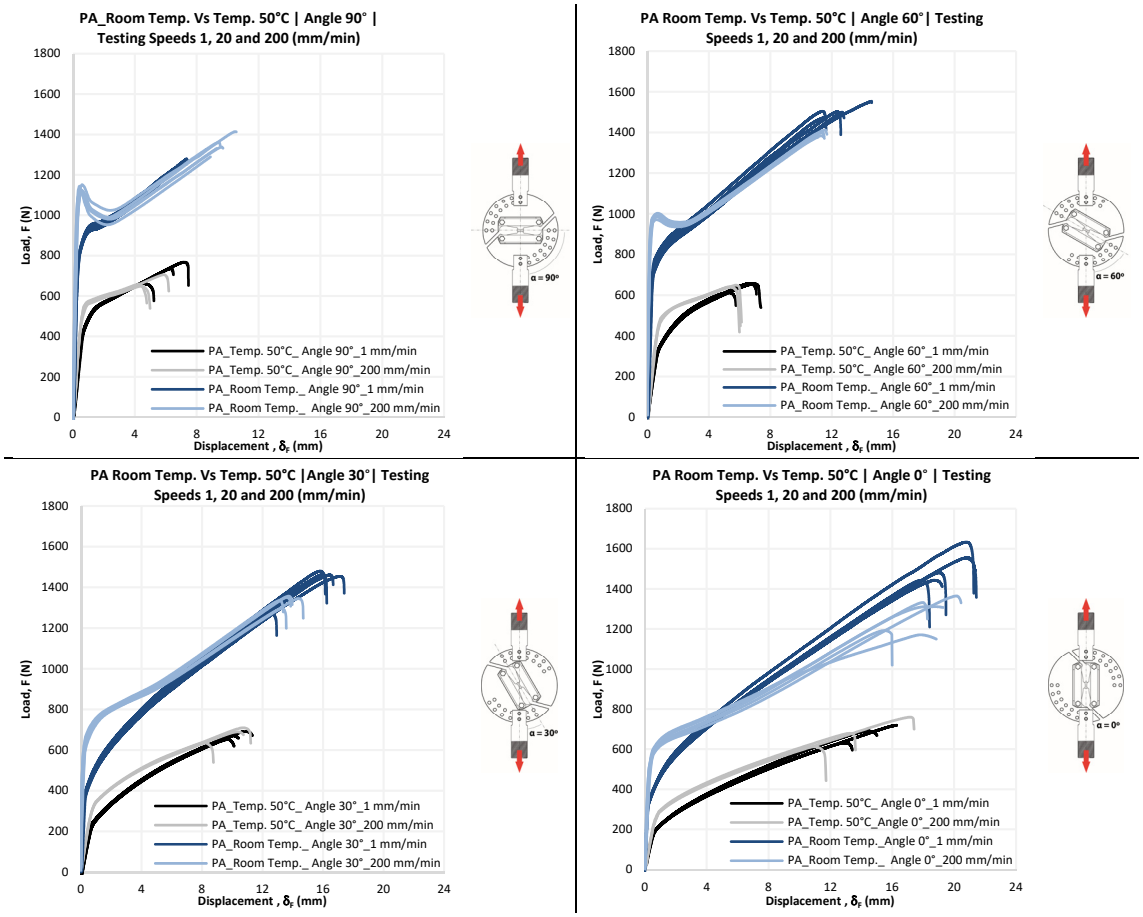


Figure 91 – Load-displacement curves for PA 6 resulting from combined tension/shear loading at RT and 50 °C: influence of crosshead speeds for each loading angle.

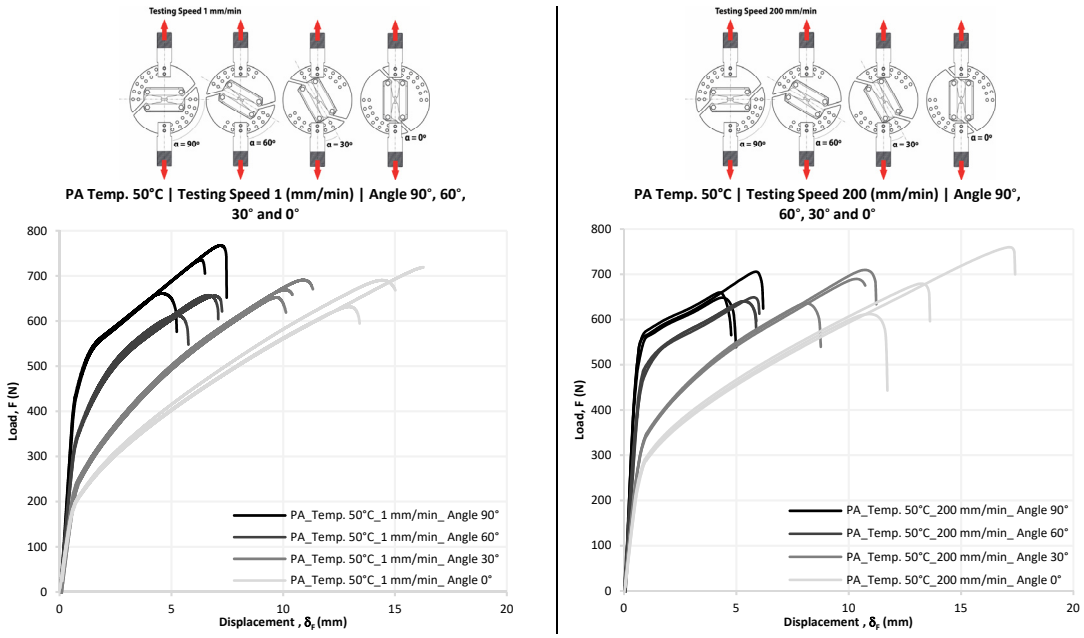


Figure 92 - Load-displacement curves for PA 6 resulting for combined tensile/shear loading at 50 °C: influence of resulting in combined tension/shear for given crosshead speeds.

Tables 92, 93, 94 and 95 show sequential images illustrating deformation failure patterns and corresponding load and displacement values for the tested PA 6. Note that, for the tests performed at constant temperature of 50 °C the yield load was not noticeable, as the material progressively yields without reaching a local force peak.

Table 92 - Fracture appearance and corresponding load and displacement values for butterfly specimen at α = 90° (pure tension) at 50 °C (all values are averaged) (PA 6).

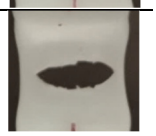
Testing Speed (mm/min)	**Fracture Point**		
	Load, F (N)	Displ., δ_F (mm)	Image
1	712.8	6.3	
200	637.8	4.6	

Table 93 - Fracture appearance and corresponding load and displacement values for butterfly specimen at α = 60° (combined tension/shear) at 50 °C (all values are averaged) (PA 6).

Testing Speed (mm/min)	**Fracture Point**		
	Load, F (N)	Displ., δ_F (mm)	Image
1	632.7	6.2	
200	636.3	5.7	

Table 94 - Fracture appearance and corresponding load and displacement values for butterfly specimen at α = 30° (combined tension/shear) at 50 °C (all values are averaged) (PA 6).

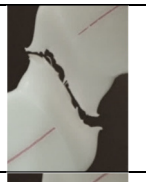
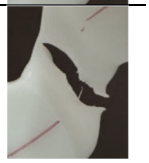
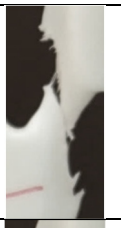
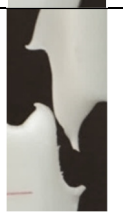
Testing Speed (mm/min)	**Fracture Point**		
	Load, F (N)	Displ., δ_F (mm)	Image
1	665.1	10.6	
200	660.1	9.6	

Table 95 - Fracture appearance and corresponding load and displacement values for butterfly specimen at $\alpha = 0°$ (pure shear) at 50 °C (all values are averaged) (PA 6).

Testing Speed (mm/min)	**Fracture Point**		
	Load, F (N)	Displ., δ_F (mm)	Image
1	645.3	14.8	
200	712.0	15.5	

4.3.4 Compression Tests at Room Temperature

The effects of the deformation rate on the load-displacement curves and on the yield behaviour was investigated by compression tests. In the compression test the localisation phenomena like crazing and necking are absent. Uniaxial compression tests were performed on cylindrical and cylindrical notched. The experimental details are summarized in section: 4.1.4 Compression Tests at Room Temperature (HDPE).

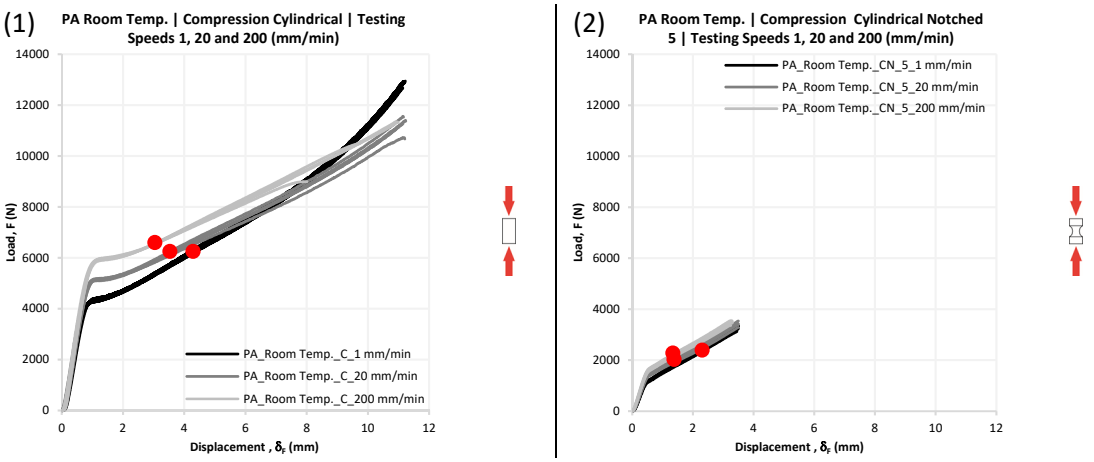


Figure 93 - Compression load-displacement curves of (1) cylindrical and (2) cylindrical notched specimens.

The observations of the compressive behaviour of cylindrical specimens (Figure 93 (1)) of all tested specimens shows an increase in the material strength for increasing crosshead speed. Three domains can be identified on cylindrical specimen. The first domain correspond to low deformation level showing a quite good linearity between imposed displacement and load. In the end of this domain the material starts to yield and reaches a plateau, which is referred as

the second domain. The plateau covers a quite small region. Roughly, starts at displacement about 1 mm to 2 mm, depending on crosshead speed. The plateau ends when the load starts to increase progressively, going into third domain. The later can be characterized by a fairly large deformation range and a very large increase in the load.

In the first domain, the applied load is expected to cause soft changes on the morphology without modifying the configuration of amorphous and crystalline components as well as the interactions among themselves. These interactions are stressed and reach higher energetic states as the load increases, but without losing the original feature. The linearity between applied load and displacement can be observed. After a displacement of 1 mm the relative positions among internal components are expected to be altered due to overload. Activation energy for plastic deformation is attained and the material begins to yield. After the transition, higher deformation levels suggest a new microstructure settling. The resistance to plastic deformation might be correlated to the strength of all interactions inside of material. The third domain starts when the compression reaches a certain high value, the concentration of applied load on the remaining crystalline particles is unavoidable.

As above mentioned, during the deformation process and with increasing crosshead speed, heating generated by deformation may lead to a effect on plastic domain. The increase in temperature might be recognized at large deformations and at high values for crosshead speed, due to the slope of the curve less pronounced for 1 mm/min than for 200 mm/min. A sequence of images about deformation evolution of cylindrical and cylindrical notched specimens at different stages during compression, are shown in Tables 96 and 97. From the sequential figures on cylindrical specimen it can be seen barrelling effect near becoming clear after some deformation. The onset of barrelling is highlighted with a red dot in Figure 93.

Table 96 – Deformation pattern and corresponding load and displacement values for cylindrical specimen at three deformation stages (all values are averaged) (PA 6).

Testing Speed (mm/min)	**Virgin specimen**		**Barrelling Onset**			**Interrupted Test**		
	Displ., δ_{0F} (mm)	Image	Load, F (N)	Displ., δ_F (mm)	Image	Load, F (N)	Displ., δ_F (mm)	Image
1	0		6251.0	4.2		12909.1	11.2	
20	0		6227.3	3.7		11023.9	11.2	
200	0		6757.4	3.4		11270.3	10.9	

Table 97 – Deformation pattern and corresponding load and displacement values for cylindrical notched specimen at two deformation stages (all values are averaged) (PA 6).

Testing Speed (mm/min)	**Virgin specimen**		**Barrelling Onset**			**Interrupted Test**		
	Displ., δ_{0F} (mm)	Image	Load, F (N)	Displ., δ_F (mm)	Image	Load, F (N)	Displ., δ_F (mm)	Image
1	0		2411.4	2.2		3284.9	3.5	
20	0		2051.0	1.6		3347.7	3.5	
200	0		2250.9	1.6		3365.2	3.2	

4.3.5 Combined Compression/Shear Tests at Room Temperature

Combined compression/shear tests were performed on butterfly specimens of PA 6 at room temperature using arcan apparatus. The experimental details are summarized in section: 4.1.5 Combined Compression/Shear Tests at Room Temperature (HDPE).

In the results for combined compression/shear given in Figure 94 and 95 (negative vertical loads and displacements were converted into positive values) it is observed that the slope of the curves in elastic regime decreases with the loading angle reduction being minimum for $\alpha = 0°$. Moreover, the curves reach a peak load, beyond which the load drops (displacements between 0.18 and 0.22 mm). The peak load can be associated to the onset of buckling at the central section. Higher the loading angle, higher is the load required to deform the specimens. From the load-displacement curves it can be seen that the yield load cannot be specifically determined, there is no single point at which the material starts to yield, instead a smooth yield region is visible.

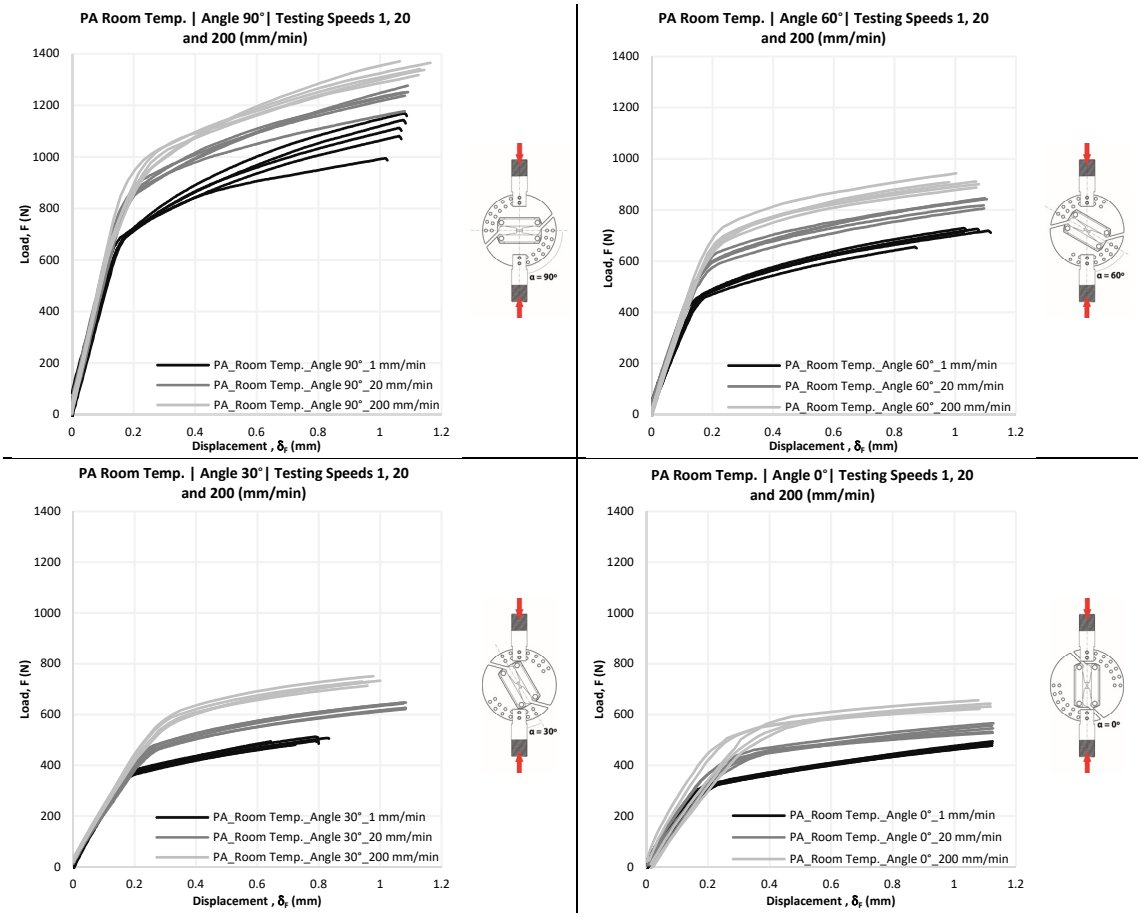


Figure 94 - Load-displacement curves for PA 6 resulting from combined compression/shear loading at RT: influence of crosshead speeds for each loading angle.

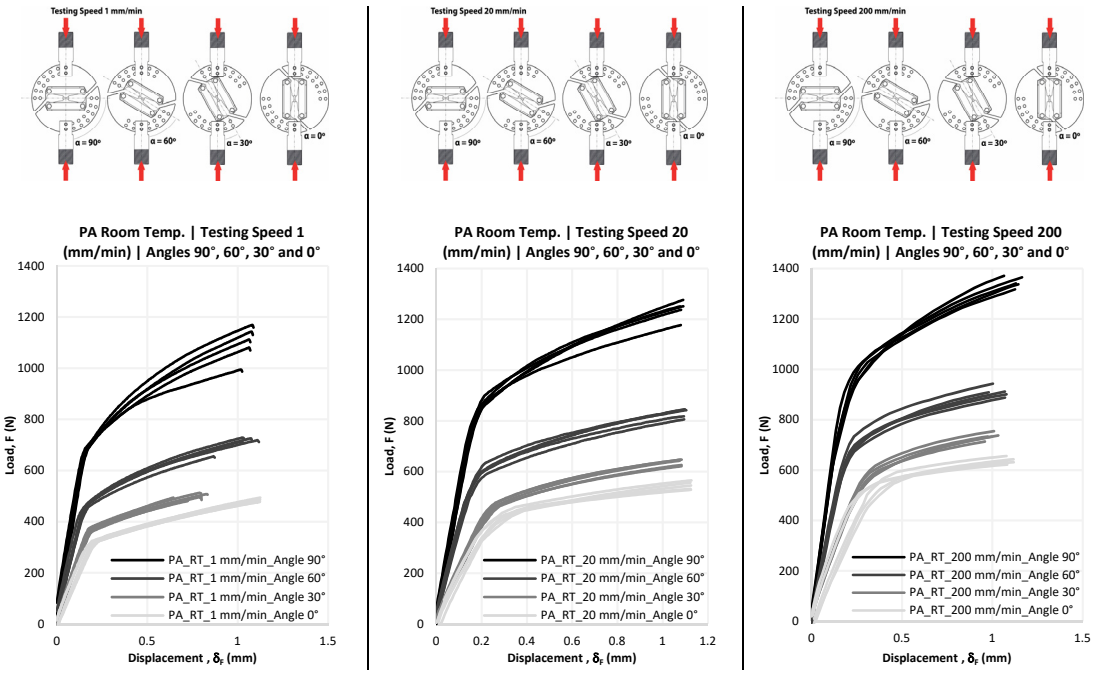


Figure 95 - Load-displacement curves for PA 6 resulting for combined compression/shear loading at RT: effect of loading angle for given crosshead speeds.

Tables 98, 99, 100 and 101 show sequential images of the deformation of gauge section and corresponding load displacement values for the PA 6 specimens at distinct deformation stages: virgin or unloaded and point of test interruption due to excess deformation without fracture.

Table 98 - Deformation patterns and corresponding load and displacement values for butterfly specimen at $\alpha = 90°$ (pure compression) at RT (all values are averaged) (PA 6).

Testing Speed (mm/min)	**Virgin specimen**		**Interrupted Test**		
	Displ., δ_{0F} (mm)	Image	Load, F (N)	Displ., δ_F (mm)	Image
1	0		1144.3	1.1	
20	0		1267.1	1.1	
200	0		131.2	1.1	

Table 99 - Deformation patterns and corresponding load and displacement values for butterfly specimen at $\alpha = 60°$ (combined compression/shear) at RT (all values are averaged) (PA 6).

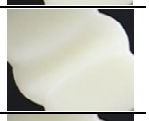
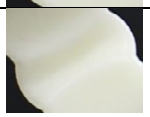
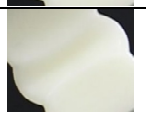
Testing Speed (mm/min)	**Virgin specimen**		**Interrupted Test**		
	Displ., δ_{0F} (mm)	Image	Load, F (N)	Displ., δ_F (mm)	Image
1	0		713.9	1.1	
20	0		831.5	1.1	
200	0		922.8	1.1	

Table 100 - Deformation patterns and corresponding load and displacement values for butterfly specimen at $\alpha = 30°$ (combined compression/shear) at RT (all values are averaged) (PA 6).

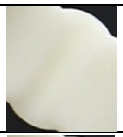
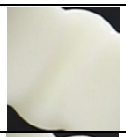
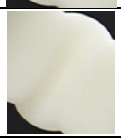
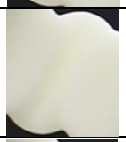
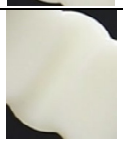
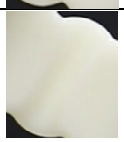
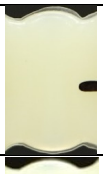
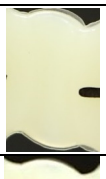
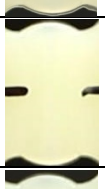
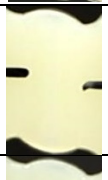
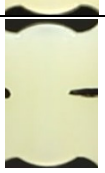
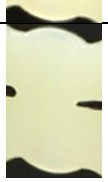
Testing Speed (mm/min)	**Virgin specimen**		**Interrupted Test**		
	Displ., δ_{0F} (mm)	Image	Load, F (N)	Displ., δ_F (mm)	Image
1	0		424.0	0.7	
20	0		626.2	1.1	
200	0		711.8	1.1	

Table 101 - Deformation patterns and corresponding load and displacement values for butterfly specimen at α = 0° (pure shear) at RT (all values are averaged) (PA 6).

Testing Speed (mm/min)	**Virgin specimen**		**Interrupted Test**		
	Displ., δ_{0F} (mm)	Image	Load, F (N)	Displ., δ_F (mm)	Image
1	0		480.5	1.1	
20	0		549.4	1.1	
200	0		646.7	1.1	

4.3.6 Combined Compression/Shear Tests at Temperature of 50°C

Biaxial loading tests were performed on butterfly specimen at constant temperature of 50 °C. The experimental details are summarized in section: 4.1.6 Combined Compression/Shear Tests at Temperature of 50°C (HDPE).

The load-displacement curves during combined loading (α = 90°, 60°, 30°, and 0°) and crosshead speeds of 1 and 200 mm/min at room temperature and temperature of 50 °C are given in Figure 96 and 97. As expected the load-displacement curves are found to shift down with an increasing temperature and decreasing crosshead speed. The following conclusions are drawn:

- At constant temperature of 50 °C the strength grows with the crosshead speed. For a given crosshead speed, the load decreases with temperature,
- Changing the loading angle from α = 90° to 0° at constant temperature of 50 °C the load-displacement curves shift down in the sense of reducing strength.

Plausible explanations for the microstructure deformation mechanisms during biaxial loading are depicted in 4.1.2 Combined Tensile/Shear Behaviour at Room Temperature.

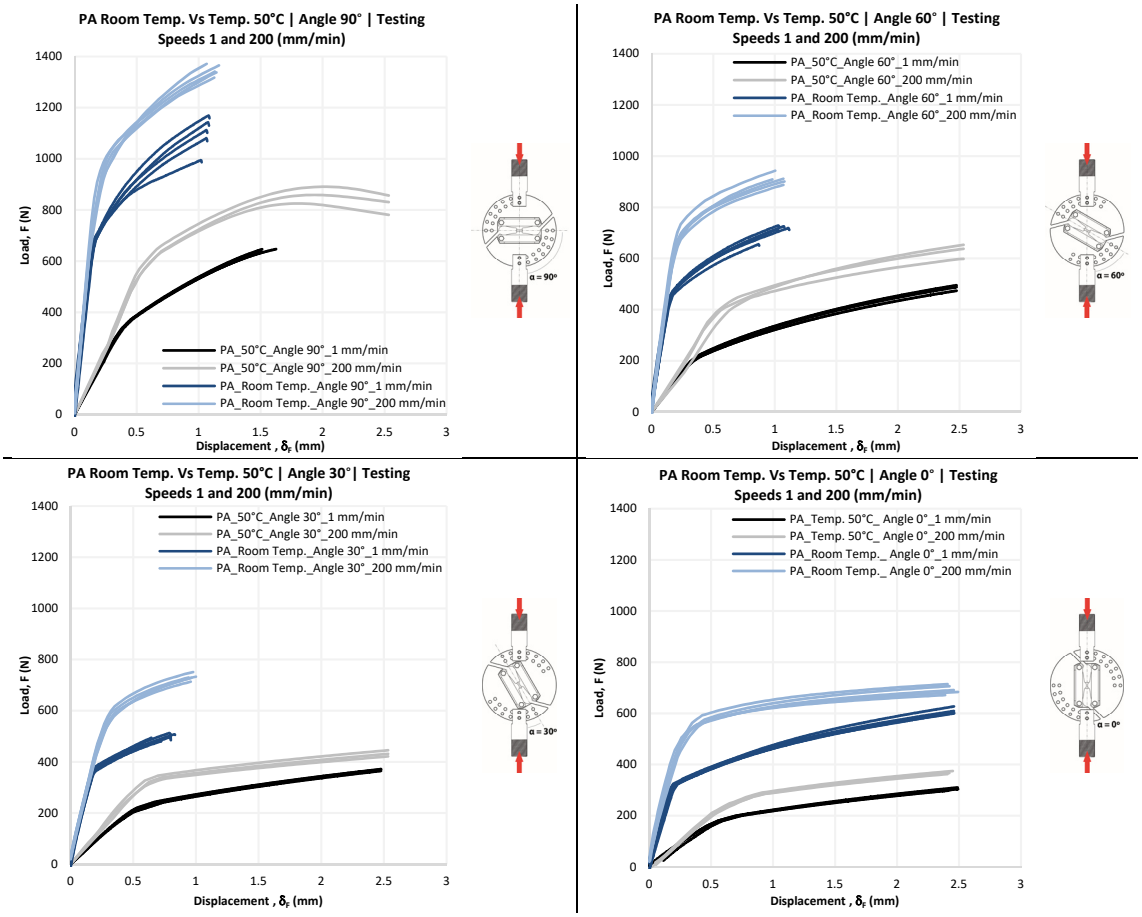


Figure 96 – Load-displacement curves for PA 6 resulting from combined compression/shear loading at RT and 50 °C: influence of crosshead speeds for each loading angle.

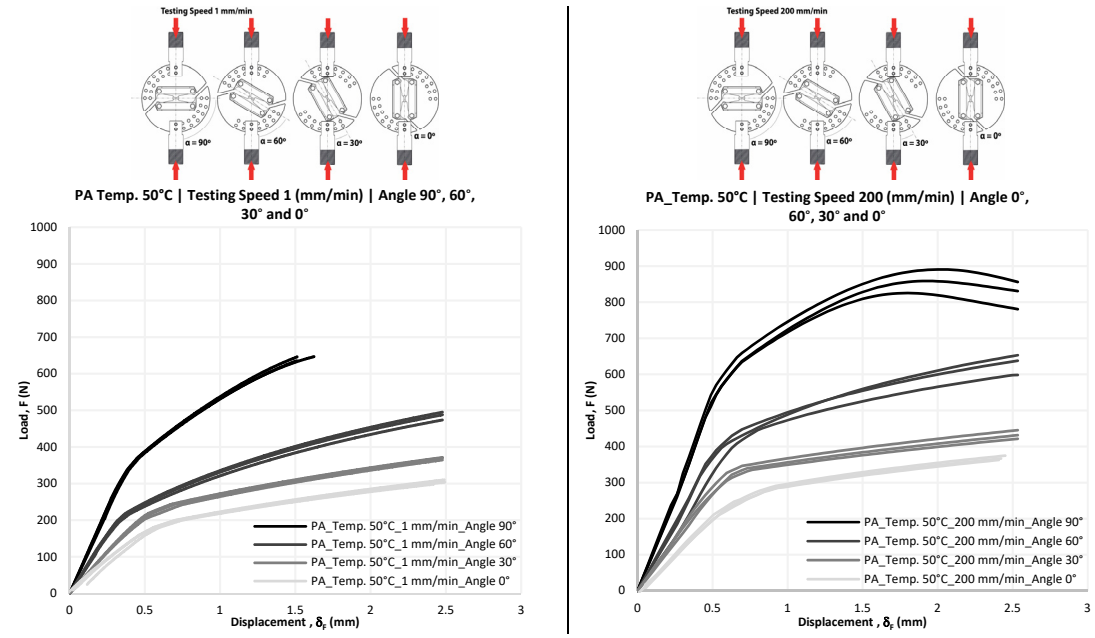


Figure 97 – Load-displacement curves for PA 6 resulting for combined compression/shear loading at 50 °C: effect of loading angle for given crosshead speeds.

Tables 102, 103, 104 and 105 show sequential images of final deformation gauge section and corresponding load and displacement values for the PA 6 butterfly specimens.

Table 102 - Deformation pattern and corresponding load and displacement values for butterfly specimen at α = 90° (pure compression) at 50 °C (all values are averaged) (PA 6).

Testing Speed (mm/min)	**Interrupted Test**		
	Load, F (N)	Displ., δ_F (mm)	Image
1	634.4	1.5	
200	841.5	2.5	

Table 103 - Deformation pattern and corresponding load and displacement values for butterfly specimen at α = 60° (combined compression/shear) at 50 °C (all values are averaged) (PA 6).

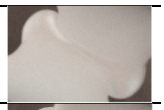
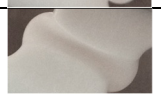
Testing Speed (mm/min)	**Interrupted Test**		
	Load, F (N)	Displ., δ_F (mm)	Image
1	495.8	2.5	
200	625.5	2.5	

Table 104 – Deformation pattern and corresponding load and displacement values for butterfly specimen at α = 30° (combined compression/shear) at 50 °C (all values are averaged) (PA 6).

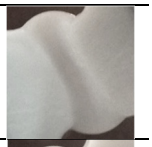
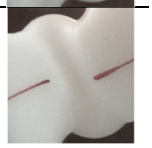
Testing Speed (mm/min)	**Interrupted Test**		
	Load, F (N)	Displ., δ_F (mm)	Image
1	336.3	2.5	
200	395.9	2.5	

Table 105 - Deformation pattern and corresponding load and displacement values for butterfly specimen at α = 0° (pure shear) at 50 °C (all values are averaged) (PA 6).

Testing Speed (mm/min)	**Interrupted Test**		
	Load, F (N)	Displ., δ_F (mm)	Image
1	318.2	2.5	-
200	370.9	2.5	-

4.3.7 Differential Scanning Calorimetry (DSC)

DSC test were performed using samples of PA 6. The experimental details are depicted hereafter: The experimental details are summarized in section: 4.1.7 Differential Scanning Calorimetry (DSC) (HDPE).

DSC scans were performed on solid granulates from virgin material as well as with specimens that were deformed under uniaxial tension at different true strain. The DSC results enable the assessment of the percent crystallinity content, the glass transition temperature and melting temperature. Figure 98 show DSC curves for the PA 6 virgin material results and Figure 99 depicts DSC curves for PA 6 true strains 0.5 and 1. Both figures shows the variation of heat flow into the specimens as a function of increasing temperature, at a constant heating rate of 10°C/min.

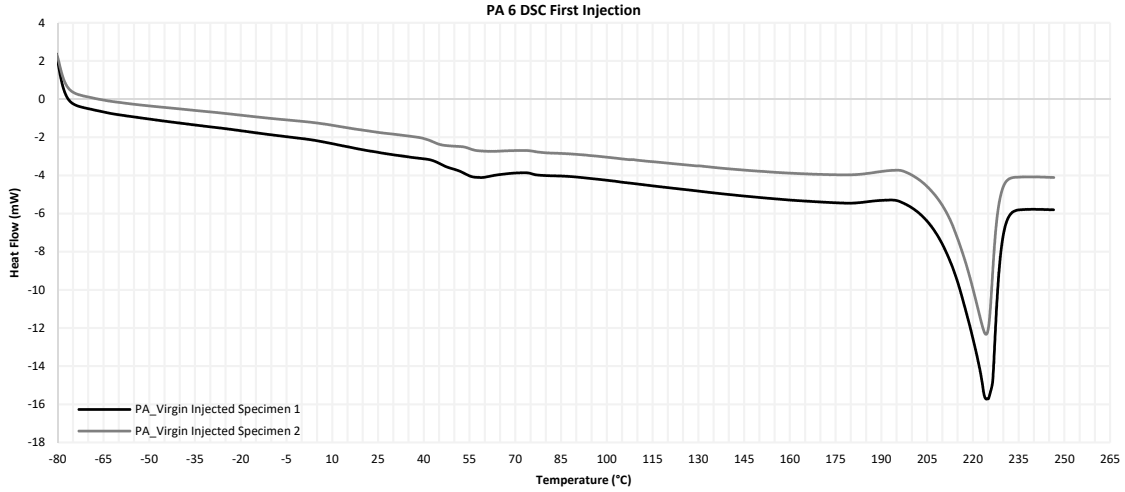


Figure 98 – DSC curves for PA 6 virgin/injected material.

At that particular heating rate, the T_g is observed at approximately 54± 2 °C, in all situations. The T_g exhibit a smooth enthalpic transition and manifests as endothermic. It is observed from the DSC scans in Figure 98, that as the temperature is increased beyond T_g the crystals begin to melt at an approximate temperature of 195 ± 2°C. The melting of the crystals manifests itself as a wide endotherm whose peak is approximately at 227.4°C and its Enthalpy (ΔH_f) is equal to 90.6 J/g (Table 106). The heat of fusion of fully crystalline PA 6 was taken was 188 J/g [76], which corresponded to a level of crystallinity of 48,2% .

Table 106 - Thermal properties and crystallinity of PA 6 determined by DSC, virgin material.

	Units	Specimens	
		Virgin Injected Specimen 1	**Virgin Injected Specimen 2**
Enthalpy (ΔH_f)	J/g	89.4	91.8
Average	J/g	90.6	
Melting Temperature (T_m)	°C	227.5	227.2
Average	°C	227.4	
Enthalpy of Perfect Polymer Crystal (ΔH^0_f)	J/g	188[76]	
Crystallinity	%	47.6	48.8
Average	%	48.2	
Glass Transition (T_g)	°C	55.7	-
Average	°C	55.7	

Figure 99 show the effects on DSC curves of the different levels of imparted strain at the same crosshead speed of 1 mm/min and at room temperature for specimens strained under uniaxial tension. It is observed that, not only are lower the onset temperatures of the endotherms, as the melting endotherm areas of the specimen strained to 0.5 and 1 do not change considerably, which are bigger than 90.6 J/g (virgin specimen) about 92.3 J/g and 95.9 J/g, respectively (Table 107). At true strain of 0.5 and at 1, the decrease in deformed specimen crystallinity can be referred to the decrystallization process.

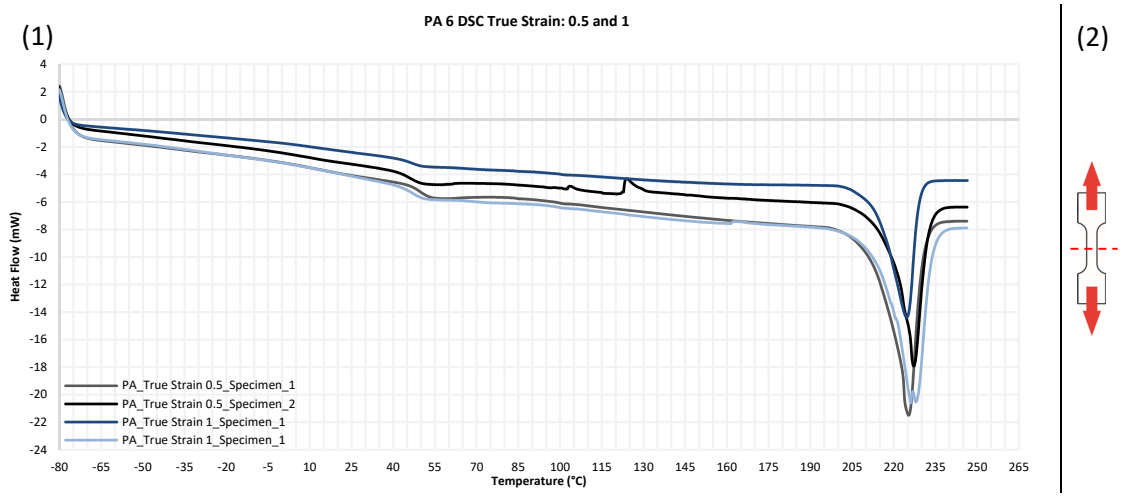


Figure 99 - (1) DSC curves for PA 6 at true strains of 0.5 and 1, (2) red dashed line is the longitudinal section investigated in the DSC.

Table 107 - Thermal properties and crystallinity of PA 6 determined by DSC, deformed specimens.

	Units	Specimens			
		True Strain 0.5_1	**True Strain 0.5_2**	**True Strain 1_1**	**True Strain 1_2**
Enthalpy (ΔH_f)	J/g	92.3	92.2	95	96.7
Average	J/g	92.3		95.9	
Melting Temperature (T_m)	°C	225.3	227.2	224.6	226
Average	°C	226.2		225.3	
Enthalpy of Perfect Polymer Crystal (ΔH^0_f)	J/g	188[76]			
Crystallinity	%	49.1	49	50.5	51.4
Average	%	49.1		47.2	
Glass Transition (T_g)	°C	54.8	52.4	51.8	51.2
Average	°C	53.6		51.5	

4.3.8 Dynamic Mechanical Analysis (DMA)

DMA tests were performed on rectangular specimens with the following dimensions: 40 mm×15 mm×1.8 mm of PA 6. The experimental details are summarized in section: 4.1.8 Dynamic Mechanical Analysis (DMA) (HDPE).

DMA is commonly employed to determine and analyse the viscoelastic properties of polymers. The α transition is featured with a more significant change of tan (δ) value and is recognized as the glass transition. The DMA results for PA 6 are given in Figures 100 and 101. The storage modulus (*E'*) as function of the temperature (°*C*) and frequency is shown in Figure 100. The storage modulus increases with increasing the frequency. Taking into account the modulus behaviour, for frequencies 1 and 10 Hz, three regions can be distinguished in the obtained diagram: the glassy (1), the glass transition (2) and the rubbery (3) regions.

For PA 6 at room temperature the storage modulus ranges from 750 N to 870 N for frequency of 0.1 Hz, 1550 N to 1570 N for frequency of 1 Hz and 1770 N to 1820 N for frequency of 10 Hz and with increasing temperature, this modulus gradually is reduced. At the glass transition temperature (T_g) a sharp decrease in storage modulus is observed, since here the polymer chains obtain full segmental mobility and their state changes from glassy to rubbery, where crystals are known to yield readily, and an influence of the tie molecules on the network is considered to be absent [39].

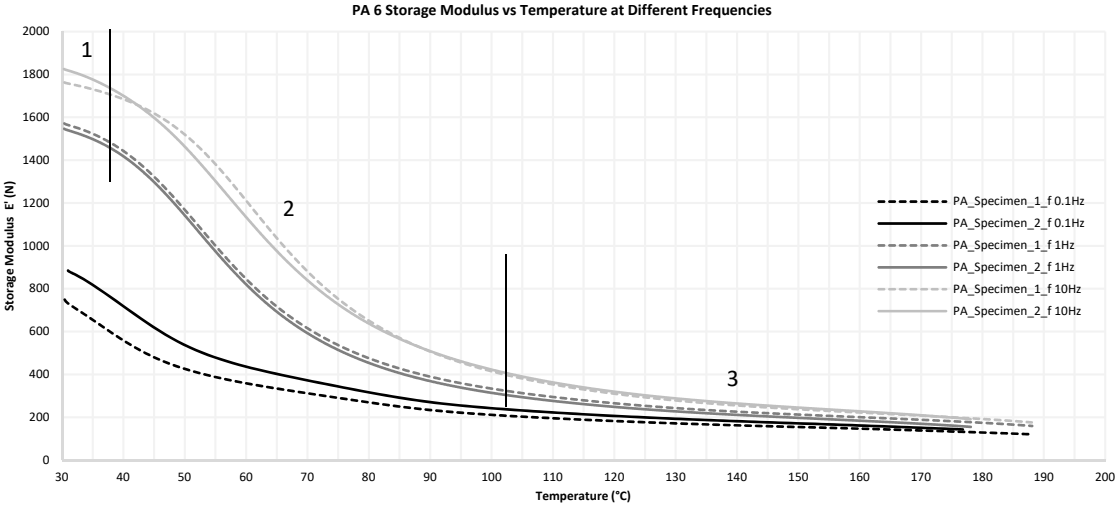


Figure 100 – Results of DMA experiments; the storage modulus (E') as function of temperature (°C) and frequency effects on PA 6.

For each frequency, the loss factor tan (δ) shows a peak close to glass transition temperature, indicating that the contribution of the viscous portion (loss modulus E'') to the dynamic response is relatively high in this temperature range (Figure 101). The glass transition temperature increases with increasing of frequency, ranging from 49 °C for 0.1 Hz, 67 °C for 1 Hz and 75 °C for 10 Hz.

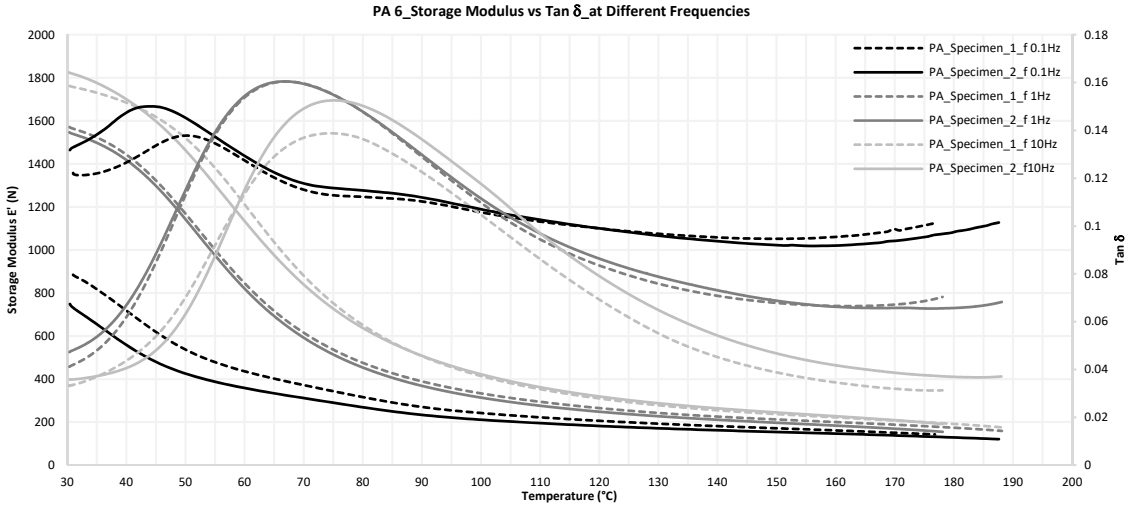


Figure 101 – Results of DMA experiments; the storage modulus (E') and loss factor, tan (δ) as function of temperature (°C) on PA 6.

4.4 Discussion and Concluding Remarks

Large number of tests were carried out to achieve basic information about the mechanical properties of HDPE, PP and PA 6. The mechanical responses, were examined under different stress states. Despite belonging to semi crystalline polymers with crystallinity percentage from

DSC scans of 55.1%, 40.4% and 48.2%, respectively for HDPE, PP and PA 6, their mechanical behaviour is somewhat different.

4.4.1 Tensile Tests at Room Temperature - HDPE, PP and PA 6

From laboratory tests on dumbbell, flat notched and cylindrical notched specimens, information about the material behaviour is disclosed. Three different crosshead speeds of 1, 20 and 200 mm/min at RT, were used. From the experimental test, one can conclude that:

- The yield load in the lowest testing speed occurs at higher displacements. At lower crosshead speed and displacements, the polymer macromolecules have the time necessary to induce an orderly alignment just enough to accept the increase in deformation; also allows more time for the chain segments to engage in an increased amount of entanglement slippage and therefore increase the hardening effect. Higher crosshead speeds reduce the degree of chain relaxation, resulting in more preferred orientation, yielding lower displacement values and consequent shift to brittle behaviour [59].

- At higher crosshead speed, increases both the propensity of the material to form a clear and higher yield load at lower displacement values. It is also clear the reduction of ductility as the crosshead speed increases exhibiting the material a more brittle behaviour.

- For tensile test results on notched specimens, the yield load increases with decreasing the specimen notch radii (increasing the stress triaxiality), whereas the corresponding displacement ductility decreases. This behaviour might be attributed to the notch strengthening effect where the notch under uniaxial tension produces radial and circumferential stresses in addition to the axial stress and hence, more stress is needed to reach the same strain. Therefore, the larger stress triaxiality the higher fracture driving forces, which results in the fracture of the specimen at a lower strain. These additional stresses could inhibit lamellar rotation toward axial direction; also alter the force acting on the crystalline lamellae, thereby altering their ability to participate in slip processes and delaying the onset of plastic deformation [143].

- It was observed that the HDPE, PP and PA 6 notched specimens gradually started to whiten, near yield load. As the plastic deformation continued, the stress whitening became clearer and sets the shape changes (dilatation). Plastic dilation and whitening in polymers can be assumed to be related to damage. Such damage can assume the form of microvoids that grow from local irregularities of the molecular structure [43, 48, 153]. With ongoing deformation, localisation grows to extremes, resulting in void nucleation, craze formation and catastrophic failure.

- Possible multiphase layer structure with oriented crystalline morphology, such as shish-kebab or stacked lamellae structures, along the cross-section perpendicular to the melt flow, might be included in the responses reported in this study, due to injection mould production. The consequence of a preferred molecular orientation in a specific direction is that might lead to a distinct anisotropy in mechanical properties, such as the increasing of the yield load [159].

- During the deformation process and with increasing crosshead speed, an increase in temperature producing a thermal softening of the material is likely to occur, despite not

quantified/measured during this work. It should be apparent that the faster the crosshead speed, the less time for heat transfer, hence the more important the adiabatic effects are.

- Arruda et al. [157] have investigated the effects of strain rate on the plastic response of semi crystalline polymers. They reported that the greater influence of temperature on the stress-strain behaviour was at intermediate and large strains in which for a strain rate of 0.1/s the specimen had a maximum temperature increment of 40 °C.

- It is important to highlight that experiments on PP, the presence of notch with different radii did not produce significant alterations in the yield point values, for fixed crosshead speed. For example, for flat notched specimens at crosshead speed of 200 mm/min, the yield loads values were: 2096 N and 2128.8 N, respectively for R 5 and R 30. However, the same does not apply to the displacement values, which for a fixed crosshead value increases with higher notch radii values.

4.4.2 Combined Tensile/Shear and Compression/Shear Tests - HDPE, PP and PA 6

In order to compare the mechanical responses, a series of biaxial loading (pure shear, combined shear and tension/compression, pure tension/compression) at different crosshead speeds of 1, 20 and 200 mm/min, were performed on a butterfly specimen at room temperature and temperature of 50 °C.

Combined Tensile/Shear at Room Temperature:

- The microstructure deformation mechanisms during biaxial loading conditions might be in accordance with the research work performed by Zhou and Wilkes [160]. In their research, oriented films, both with and without row-nucleated structure were deformed at three angles, 0°, 45° and 90°, with respect to the original machine (extrusion) direction. It was shown that lamellar separation, lamellar shear and lamellar break-up were the dominant initial deformation mechanisms for the respective 0°, 45° and 90° deformations. As a result, the 45° and 90° deformations generated a final microfibril morphology oriented along the stretch direction, while the 0° deformation resulted in broken (mosaic) blocks of crystalline lamellae.

- At RT the drop of the load with biaxial loading angle are found minimum for the loading angle $\alpha = 0°$ (pure shear) and maximum for $\alpha = 90°$ (pure tension);

- The plastic stiffness decreases with increasing of crosshead speed in all loading angles;

- The crosshead speed and loading angle “after yielding” plays a key role in the macroscopic deformation behaviour and determines whether the material behaves as brittle or ductile;

- Whitening and crazing, are observed and may reveal that some formation of numerous microvoids (cavities) are taking place in the centre of a specimen shortly before yielding;

- In PA 6 the load-displacement curves beyond the yield point, becomes coincident for all loading rates. This mechanical behaviour might indicate that there is an thermal softening associated

with a progressive localization of heat sources at high crosshead speed as observed by Wattrisse et al. [158].

Combined Tensile/Shear at High Temperature:

- Decreasing crosshead speed and increasing temperature generally result in lowering of the load needed to reach a given displacement. Therefore, the yield load shows an explicit dependency on temperature and crosshead speed. At higher temperatures the chain mobility increases in the crystalline phase and raise the possibility for the shear deformation of crystals.

- Growth of temperature and reduction in crosshead speed lead to a more ductile behaviour.

- Changing the loading angle from $\alpha = 90°$ (pure tension) to 0° (pure shear) at temperature of 50 °C, results in load-displacement curves with lower strength and increased ductility.

- Stress whitening is observed in the gauge section of butterfly specimens, shortly before yielding. The stress whitening in HDPE, PP and PA 6 were found to be dependent upon the temperature and strain rate.

Combined Compression/Shear at Room Temperature:

- All experimental results show an initially linear force-displacement response followed by a nonlinear regime until the test is interrupted due to limitation of the maximum travel allowed by the arcan apparatus, in negative vertical direction.

- Strain rate effects are clearly visible with load increasing as testing speed increases. Also, as the loading progresses from compression to pure shear one can realize a load reduction. Higher the loading angle, higher is the load required to deform the specimens.

Combined Compression/Shear at High Temperature:

- The load-displacement curves are found to decrease (reduce strength) with an increasing temperature and decreasing crosshead speed.

- At temperature of 50 °C the load grows with the crosshead speed. For a given crosshead speed, the load decreases with temperature.

- Changing the biaxial loading angle from $\alpha = 90°$ to 0° at constant temperature of 50 °C, load-displacement curves decreases.

4.4.3 Compression Tests at Room Temperature - HDPE, PP and PA 6

In addition, compression tests on cylindrical and cylindrical notched specimens, were included in the research program.

- The compressive behaviour of all tested specimens shows an increase in the material strength for increasing crosshead speed. On effect, an increase of crosshead speed will decrease the molecular mobility of the polymer chains, making the material less susceptive to deform.

- In compression tests the barrelling effect started after some deformation, due to friction between the steel platens at the top and bottom surfaces of the specimens. Even though barrelling effect in compression, the data provided by these tests are considered suitable for the purpose of evaluation of yield response which is the main focus of this research.

4.4.4 DSC and DMA - HDPE, PP and PA 6

Various additional analysis techniques were used to characterize the thermal properties and crystallinity, using differential scanning calorimetry and dynamical mechanical analysis.

DSC:

DSC scans were performed on solid granulates from virgin material as well as with specimens that were deformed (true strain 0.5 and 1) under uniaxial tension at different true strain. The intention of the study is to investigate if there is any change in material crystallinity due to deformation. The DSC results of the percent crystallinity content, the glass transition temperature and melting temperature, are summarized in Table 108.

Table 108 – Principal thermal properties of HDPE, PP and PA 6 determined by DSC, virgin material and deformed.

	Units	HDPE	PP	PA 6
Virgin Material Crystallinity	%	55.1	40.4	48.2
Virgin Material Glass Transition (T_g)	°C	-	-	55.7
Virgin Material Melting Temperature (T_m)	°C	139.6	170.7	227.4
True Strain 0.5_1 Crystallinity	%	56.1	41.7	49.1
True Strain 0.5_1 Glass Transition (T_g)	°C	-	-	53.6
True Strain 0.5_1 Melting Temperature (T_m)	°C	136.4	171.5	226.2
True Strain 1_1 Crystallinity	%	57.6	39.3	47.2
True Strain 1_1 Glass Transition (T_g)	°C	-	-	51.5
True Strain 1_1 Melting Temperature (T_m)	°C	137.9	171.5	225.3

- In HDPE the increase in crystallinity can be referred to the molecular chain alignment that occurs during specimen deformation.

- In PP the percentage crystallinity slight increased by 1.2 % at true strain of 0.5 and decreases by 1.2% at true strain of 1, relatively to the virgin values. At true strain of 0.5, beyond yield point,

the increase in deformed specimen crystallinity can be referred to the chain alignment that occurs during specimen deformation. At true strain 1, the decrystallization process, defined as mechanically induced destruction of crystalline lamellae (unfolding) [160], might be the cause for crystallinity decrease.

- PA 6 at true strain of 0.5 and at 1, the decrease in deformed specimen crystallinity can be referred to the decrystallization process.

DMA:

DMA test were performed on rectangular specimens with the following dimensions: 40 mm×15 mm×1.8 mm.

- HDPE at room temperature the storage modulus is relatively high, ranging from 750 N to 754 N for frequency 0.1 Hz, 820 N to 841 N for frequency 1 Hz and 1040 N to 1090 N for frequency 10 Hz and with increasing temperature, this modulus gradually reduces.

- The decrease in storage modulus is observed, since here the polymer chains are progressively being in full segmental mobility and their state changes from glassy-rubbery to rubbery flow.

- Concerning the HDPE, there is no noticeable transition in material behaviour since HDPE is in rubbery state in the tested range. HDPE glass transition temperature occurs between -100 °C to -60 °C [76].

- PP DMA curves shifts to higher values as the test frequency increases. At room temperature the storage modulus is relatively high, ranging from 780 N to 820 N for frequency 0.1 Hz, 1040 N to 1080 N for frequency 1 Hz and 1200 N to 1240 N for frequency 10 Hz and with increasing temperature, this modulus gradually reduces to the rubbery flow.

- The loss factor tan (δ) as function of temperature did not showed sensitive transition due to PP glass transition temperature (T_g) ranging between -20 °C and 0 °C [76], which is out of the testing range.

- For PA 6 the storage modulus increases with increasing the frequency. At room temperature the storage modulus ranges from 750 N to 870 N for frequency of 0.1 Hz, 1550 N to 1570 N for frequency of 1 Hz and 1770 N to 1820 N for frequency of 10 Hz and with increasing temperature, this modulus gradually is reduced.

- At the glass transition temperature (T_g) a sharp decrease in storage modulus is observed, since here the polymer chains obtain full segmental mobility and their state changes from glassy to rubbery, where crystals are known to yield readily, and an influence of the tie molecules on the network is considered to be absent [39].

- The glass transition temperature increases with increasing of frequency, ranging from 49 °C (in accordance with DSC results) for 0.1 Hz, 67 °C for 1 Hz and 75 °C for 10 Hz.

4.4.5 HDPE, PP, PA 6 Mechanical Behaviour Discussion

The mechanical response of HDPE, PP and PA 6, were compared under different stress states and loading angle conditions. Three different crosshead speeds of 1, 20 and 200 mm/min at RT, were used. The load-displacement curves results for different loading conditions are presented in Figures 102 and 103. It is noteworthy that the load displacement curves were already presented and commented in previous chapters, however new insights are explored, here.

The mechanical responses, were examined under different stress states. Despite belonging to semi crystalline polymers with crystallinity percentage from DSC scans of 55.1%, 40.4% and 48.2%, respectively for HDPE, PP and PA 6, and different T_g temperatures their mechanical behaviour is somewhat different. These differences might be either due to their unique and different thermal softening, molecular structure or manufacturing process.

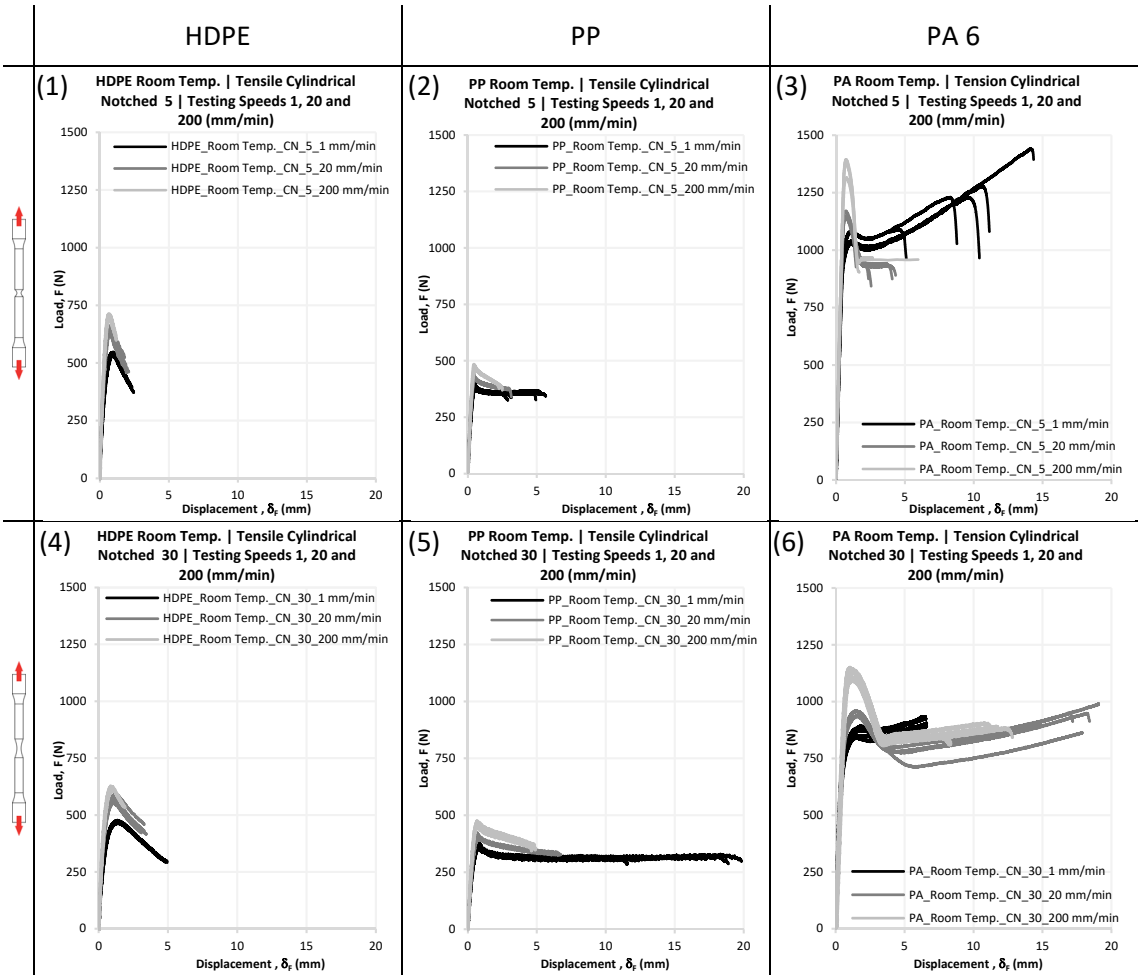


Figure 102 – Tensile load-displacement curves of cylindrical notched R 5 for: (1) HDPE, (2) PP and (3) PA 6; and cylindrical notched R 30 for: (4) HDPE, (5) PP and (6) PA 6 at RT.

PA 6 mechanical responses (Figures 102 and 103) at RT, are characterized by yield, softening and hardening. As the crosshead speed increases from 1 mm/min to 200 mm/min, the corresponding load-displacement curves show the expected increase in initial yield load. However, as the specimens are inelastically strained, the material is observed to soften,

probably due to temperature rising. At crosshead speed of 200 mm/min, the test requires approximately 1 s to 2 s and nearly adiabatic conditions exist due to insufficient time for significant heat transfer to occur. The remarkable softening of the material is observed after yield load due to combined result of strain softening and thermal softening. The softening ends where the load-displacement response is observed to level off even though the temperature in the specimen might continue to rise. This aspect of the observed behaviour is the result of the competing effects of continued thermal softening and commencing strain hardening which is occurring due to the evolution of chain orientation with plastic stretch [157]. Much of the observed effects of the increased crosshead speed on the post yield response of PA 6, was observed by Arruda et al. [157] on polymethylmethacrylate (PMMA).

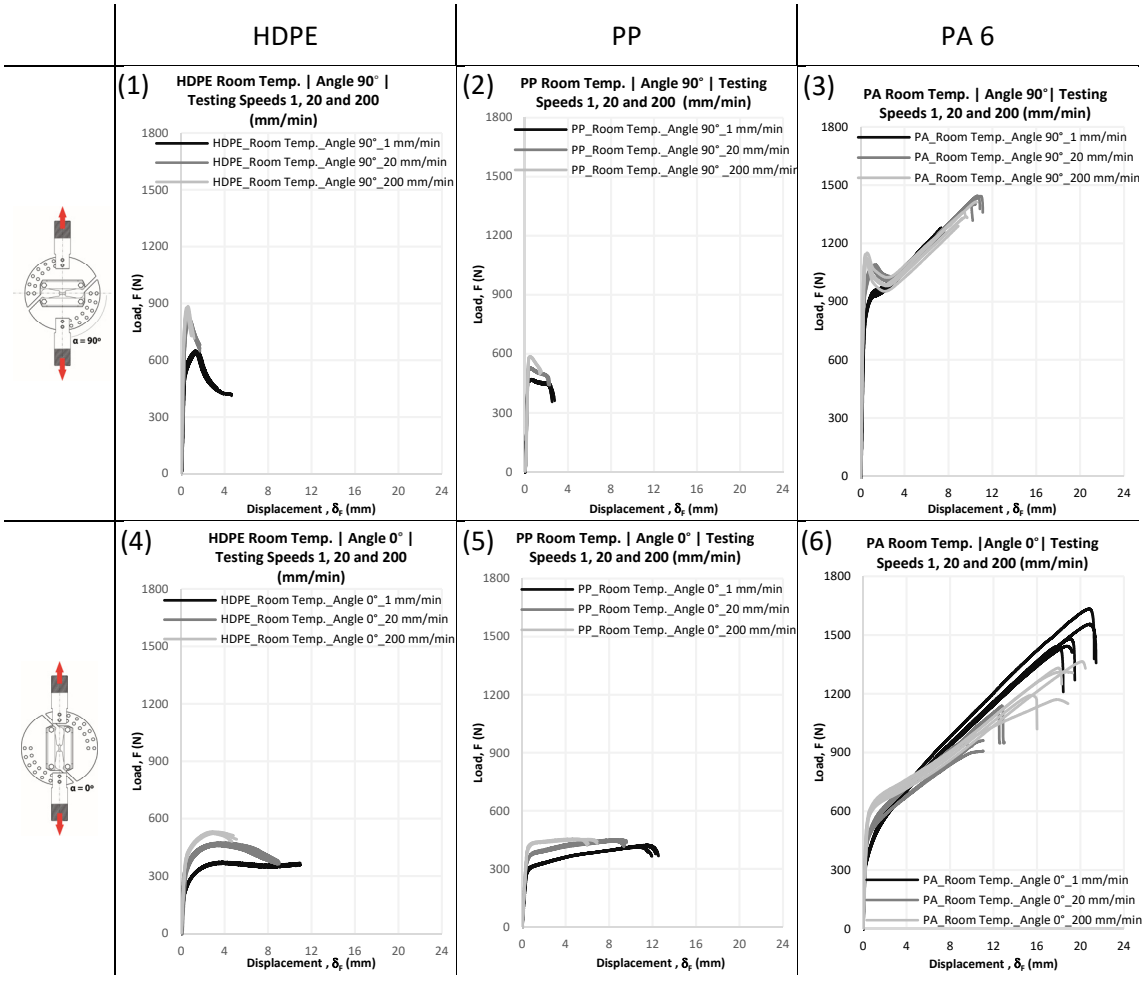


Figure 103 – Load-displacement curves resulting from tensile loading on: (1) HDPE, (2) PP and (3); and shear loading on: (4) HDPE, (5) PP and (6) PA 6 at RT.

However, at temperature of 50°C the softening behaviour it is not observed in Figure 91, considering the same loading angle. As the glass temperature of PA 6 ranges between 49 °C (DMA) to 56 °C (DSC); at RT the imposed deformations might induce the change of material state, from glassy to glassy-rubbery (glass transition temperature) by increasing its internal temperature. As the internal temperature increases, PA 6 passes through glass transition, above which it softens. The glass transition marks the onset of extensive molecular motion which is

reflected in marked changes in properties, such as volume and stiffness. The material may be more easily deformed and become ductile [4]. On the other hand at temperature of 50°C, PA 6 is already in its glass temperature state, although possible increase of internal material temperature due to deformation there is no change of state.

As a general rule, however, semi crystalline polymers are used at temperatures between glass transition temperature and a practical softening temperature which lies above T_g and below T_m, these are the cases of HDPE and PP. In Figures 102 and 103, although the different stress states, loading angle conditions, the general shape of all curves for each material and test, seems to exhibit remarkably similar intrinsic behaviours, when compared with increase crosshead speed. At higher crosshead speed, increases the propensity of material to soften, however it is not so pronounced as in PA 6. It seems that in semi crystalline polymers used at temperatures above T_g becomes more stables.

Relatively to the molecular structure, HDPE has a long linear chain (lower degree of branching), therefore has stronger intermolecular forces. HDPE is chemically the closest in structure to PP, therefore similarities in load-displacement curves, are observed. However HDPE exhibits better mechanical properties [127].

Possible multiphase layer structure with oriented crystalline morphology along the cross-section perpendicular to the melt flow, might be included in the responses reported in this study, due to injection mould manufacturing process. Investigations on injection-moulding specimens of semi crystalline polymers, have shown a multiphase layer structure along the cross-section perpendicular to the melt flow. The morphology of these multiphase layers is strongly dependent on processing temperatures, flow rate, pressure and have different thicknesses along flow direction [26, 27]. Schrauwen et al. [26] identified four structural layers: a skin layer (A), a transition layer (B), a shear layer (C) and an isotropic core (D). Stern et al. [34] showed that the elastic modulus of a polypropylene depends not only on the degree of crystallinity but also on the crystalline orientation and the crystal thickness.

5 Fracture Surface Analysis

The morphologies and mechanisms of fracture of high-density polyethylene (HDPE), polypropylene (PP) and polyamide 6 (PA 6) are investigated experimentally under different stress states, by the use of a scanning electron microscope (SEM). Fracture morphologies were investigated from a series of specimens tested under combined tension/shear loading at three different loading angles (α = 0°, 30° and 90°) at room temperature (RT) and 50 °C. In addition, the effects of notch profile radii (stress triaxiality) on HDPE, PP and PA 6 fracture behaviour have been studied at RT. In order to accomplish these task, flat and cylindrical notched specimens with different curvature radii, were used.

Specimens geometries were carefully designed to achieve various loading conditions and allowing to explore initial stress triaxialities ranged from 0 in pure shear loading (α = 0°) to a maximum of 0.84 for flat notched specimen with Radius of 5. The fracture surfaces are analysed with emphasis on the relation between loading angles and temperature on combined loading, and notch effects on notched specimens.

5.1 Triaxiality and Temperature

The brittle failure of semi crystalline polymers sets significant limits to engineering polymers. The state of stress, such as the one included by the presence of notches, is one factor that controls the occurrence of extended yielding or brittle failure, even though such polymers behaves as ductile under tensile tests over wide temperature and strain-rate ranges [171]. Many experimental results have shown that the material's fracture changes under different loading conditions. Among different damage mechanisms, the stress triaxiality, has been recognize as one of the most important fracture controlling factor [8]. Bridgman [172] conducted experiments on a variety of metallic alloys discovering that a rise in stress triaxiality results in a corresponding increase in damage nucleation and growth. The location of high hydrostatic stress is thought to favour craze initiation. Crazing happens due to the nucleation of microvoids in regions of stress concentrations, normal to the maximum principal stress. These voids do not coalesce to form cracks (as in metals) since highly stretched molecular chains, or fibrils, stabilize this process to create crazes, thus craze consists of a web of interpenetrating voids and polymer fibrils [173].

In the current experimental investigation, different stress triaxiality levels are induced by different notch radii in tensile specimens. The smaller the notch radius, the higher the stress triaxiality is. The triaxial stress state effects on fracture morphology were examined by means of tests using cylindrical and flat notched specimens with different curvature radii in order to set different triaxial stress states in the median cross-section, from 0.39 for the cylindrical notched specimen with radius of 30 to 0.84 for the flat notched specimens with radius of 5. In addition, for combined loading performed with butterfly specimens the stress triaxialities ranged from 0 to 0.58, being those specimens also analysed by SEM. Table 109 summarizes the values of stress triaxiality for all tested specimens.

Note: The stress triaxiality analytical formulas and a detailed explanation on how the triaxiality values were calculated, are depicted in section 3.3 Specimens Geometry. These triaxialities values corresponds to the initial deformation state and not the final failure state where the material can suffer significant geometric changes due to plastic deformation.

Table 109 – Summary of stress triaxialities, whose fracture surfaces were observed by SEM.

Specimens	R 5	R 30	α = 0°	α = 30°	α = 90°
Cylindrical	0.64	0.39	-	-	-
Flat	0.84	0.62	-	-	-
Butterfly	-	-	0	0.19	0.58

Polymers have a quite significant level of change in physical properties over a relatively small change in temperature, which are largely determined by their molecular structure and the resulting bonds. Tijssens et al. [174] showed the importance that temperature plays in crazing of amorphous polymers. Elongation at failure typically increases when the temperature increases and polymer behaves in a much more viscous manner. At relatively low temperatures, the craze damaging mechanisms widens very rapidly. The breakdown will occur faster, thus behaviour becomes more brittle. At higher temperatures a more spread-out craze zone will develop. Since a craze widens slower as temperature increases, more crazes tend to be initiated.

5.2 Analysis of Flat Notched Specimens Fracture Morphologies under Tension at Stress Triaxialities: 0.62 to 0.84

All flat notched specimens made of HDPE, PP and PA 6, experienced full section fracture under tension at crosshead speed of 200 mm/min. Fracture surfaces of representative specimens are displayed in Figures 105 and 106. Extensive SEM micrographs of flat notched specimens fracture morphologies for the three semi crystalline polymers, can be found in Appendix 8.2.1.

Qualitative SEM observations of HDPE fracture surfaces at several magnifications for flat notched specimens *R* 5 and *R* 30 show the formation of an oriented texture of fibrous surface at the centre with a number of longer fibrils. At the centre, due to the higher stress triaxiality, occurs the initial fracture, while at the near surface the fracture surface becomes more inhomogeneous, because is the last region to fracture. It is believed that cavitation at centre, due to numerous voids (“cavities”) and crazing near surface are the dominant modes of deformation. Cavitation might precede crazing due to the formation of microfibrils of oriented chains that span around the faces of the voids.

Studies on the development and growth of crazes in thermoplastic materials have indicated that crazing involves alignment, merging, and splitting of microfibrils and nucleation of micro-voids [167]. The difference between crazes and cavities, is that the last one do not have an internal structure, thus are unable to transfer stress [59]. The presence of fibrous surface with fibrils pulled out in the fracture surface is an indicator of ductility. It is observed that rising the stress triaxiality, the fracture becomes more brittle and homogeneous, with less formation propensity of longer fibrous surface and more voids content.

Dasari et al. [175] observed on their experiments on ethylene - propylene copolymers, wedge shaped micro-cracks parallel to the tensile direction on the surface of the deformed specimen. During tensile straining the edges multiplied and the plastic flow around the edges led to their separation from the surrounding matrix leading to fibrillation type of fracture (Figure 104). An illustration of this is presented in Figure 106, column HDPE at central and extremities near surface, due to high radius the material flows more extensively, besides that multiplication of wedges, crazing also occurred.

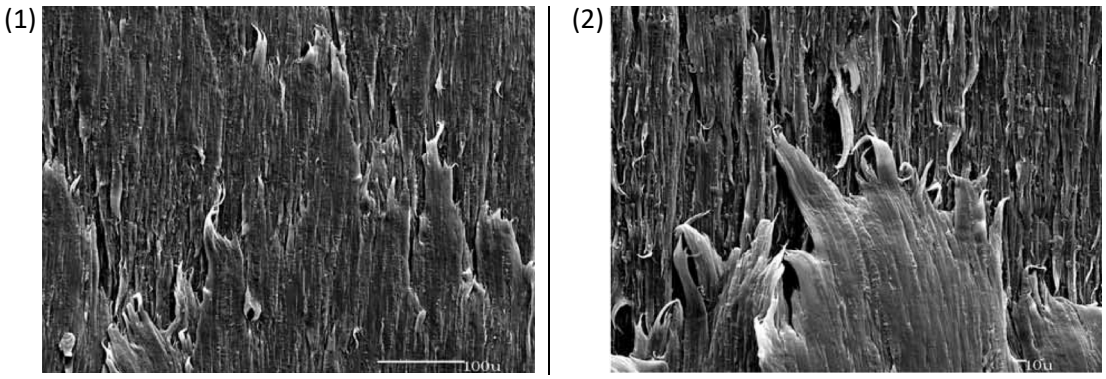


Figure 104 – SEM of tensile deformed long chain ethylene - propylene copolymers, showing the fibrillation type of fracture, during tensile straining [175].

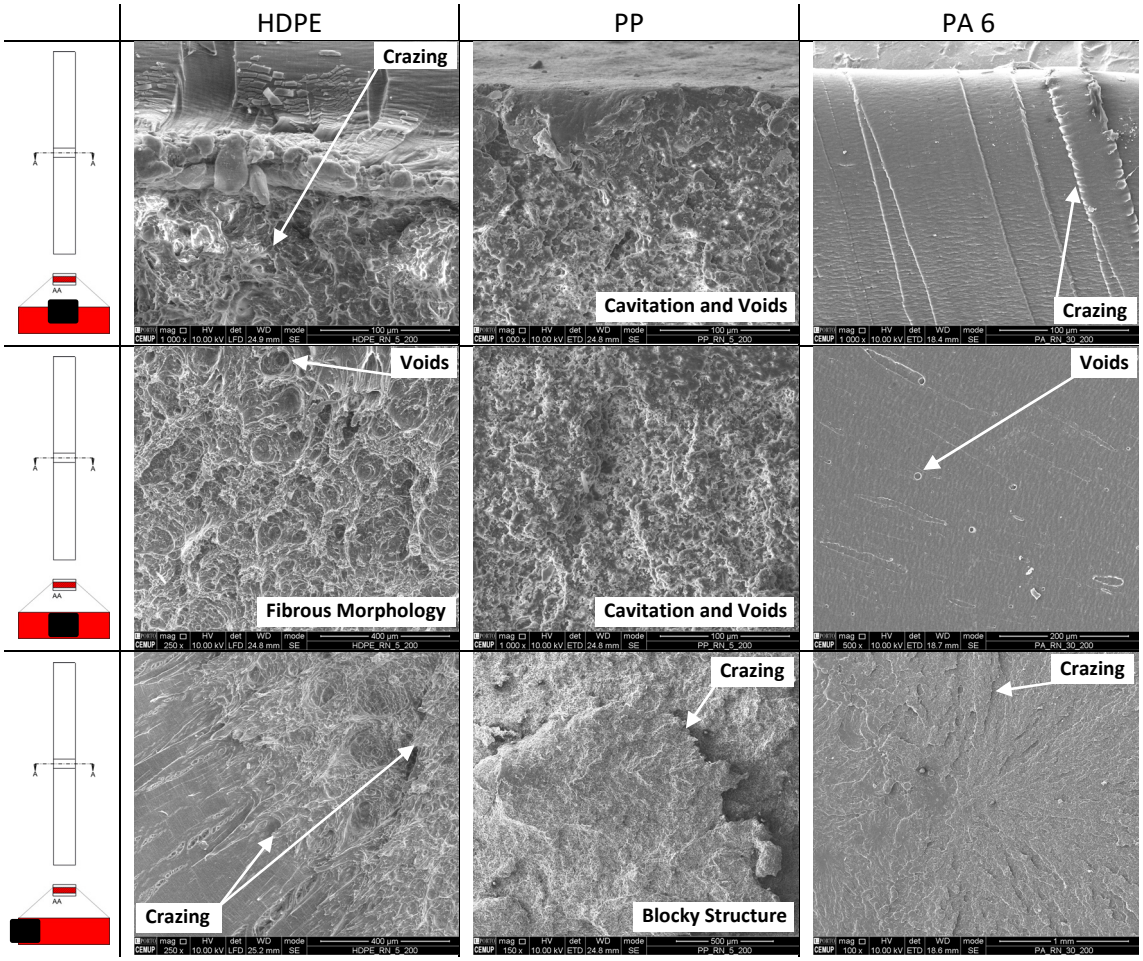


Figure 105 – SEM fracture surfaces for flat notched specimens with *R 5*, for HDPE, PP and PA 6. Note that in the first column the geometry of specimen and fracture surface location are indicated by the black square.

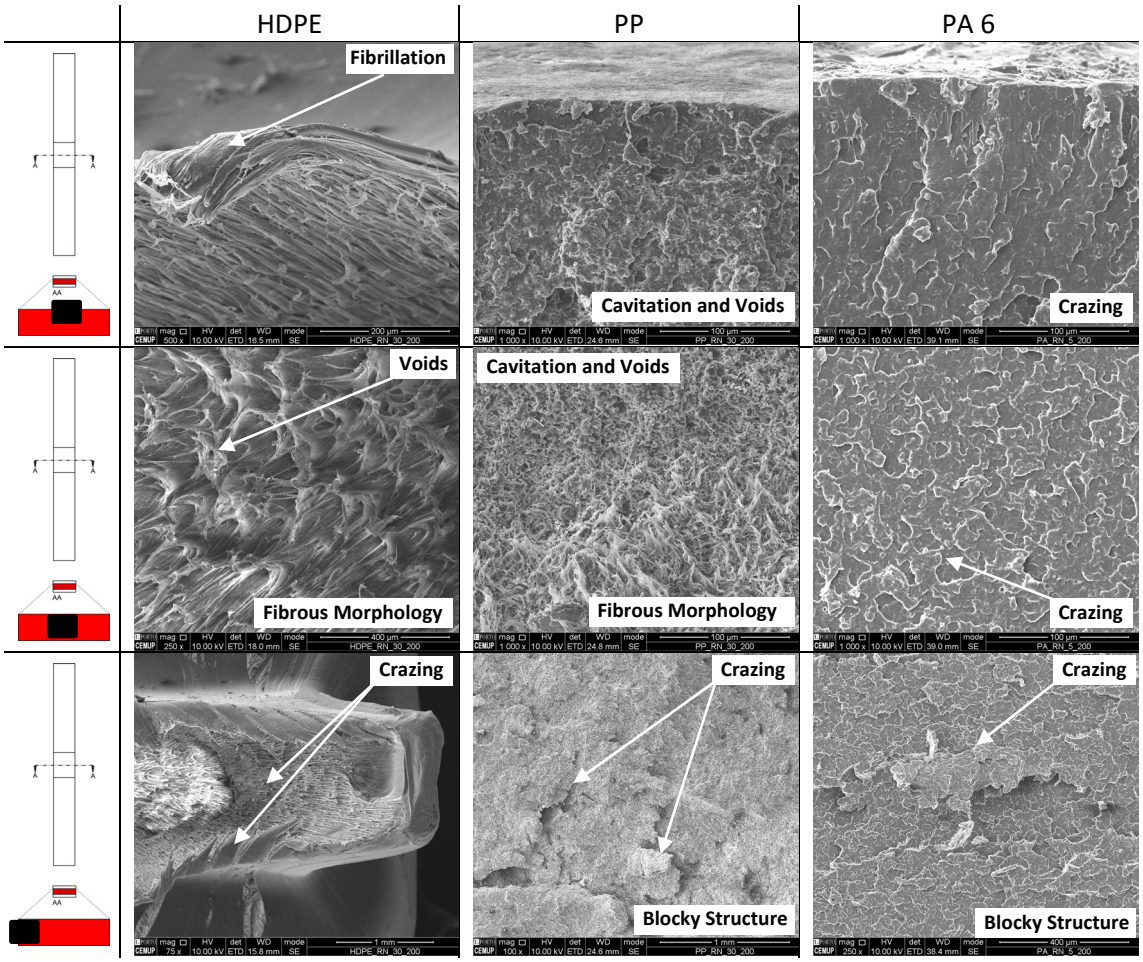


Figure 106 – SEM fracture surfaces for flat notched specimens with *R 30*, for HDPE, PP and PA 6. Note that in the first column the geometry of specimen and fracture surface location are indicated by the black square.

SEM micrographs of PP exhibits rough surface patterns in fracture region, for *R 5*. The predominantly brittle failure, cavitation and voids, are detected. Cavitation is the formation of voids (cavities) inside amorphous phase during deformation. It is often a precursor to brittle fracture or crazing and a common phenomenon in semi crystalline polymers [61]. In PP flat notched specimens with *R 30*, it is observed a mix of rough surface (cavitation and voids) with fibrous surface, in central region-fracture. In the extremities of flat notched specimen *R 30*, the surface acquires a more inhomogeneous morphology, due to low stress triaxiality which causes the material flows more extensively. A number of discontinuities or jumps in the fracture process leading to a blocky structure is observed. Considering that the inherent stress concentration is expected to be high in the mid thickness region, a stable crack nucleates and propagates through wedge and craze containing regions that grow inward from the surface leading to a blocky structure [167]. Brittle and crazing, are the two modes of fracture, observed for both notch radii. The effect of stress triaxiality, slightly modifies the fracture surface and influence the void growth and size.

It is observed from SEM micrographs of PA 6, clearly different surface fractures, when compared with HDPE or PP. The fracture surface *R 5* is smooth at the centre with some voids content and slight rough at the extremities, the last region to fracture, whereas the surface *R* 30 is rough, with a very fine mesh and absence of fibrils formation. Some blocks structures are observed at near surface. Both fracture morphologies are an indicator of brittleness. Crazing and brittle fracture are the dominant modes of failure, even though in PA 6 *R 5* the brittle fracture is smooth, occasionally spherical voids were observed, probably due to high stress triaxiality which induces the void formation [145]. Also, crazing mode of fracture occurred at some distance away from the centre.

Even with the same specimen geometries, the fracture surface show different morphologies. The fracture surface is slightly rough for PA 6 *R 30*, more heterogeneous for PP and filament like structure for HDPE.

5.3 Analysis of Cylindrical Notched Specimens Fracture Morphologies under Tension at Stress Triaxialities: 0.39 to 0.64

To explore the underlying fracture mechanisms under tension at crosshead speed of 200 mm/min, SEM images were taken for the fracture surfaces of cylindrical notched specimens made of HDPE, PP and PA 6. Fracture surfaces of representative specimens with two different notch radii, are displayed in Figures 107 and 108. Extensive SEM micrographs of cylindrical notched fracture morphologies for HDPE, PP and PA 6, can be found in Appendix 8.2.2.

Laiarinandrasana et al. [145] discussed the effect of temperature, crosshead speed and stress triaxiality on the fracture of Polyvinylidene Fluoride (PVDF), a semi crystalline polymer. To this end, tensile tests were performed on cylindrical notched specimens. It was reported more ductile fracture behaviour for specimens with larger notch radii (lower triaxialities), while increasing the stress triaxiality ratio (decreasing the notch radius) or increasing strain rate seems to favour the brittle fracture. This is in accordance with the experience from the present study. The HDPE and PA 6 cylindrical notched specimen, in particular the cylindrical geometry, with *R 30* were too ductile to complete fracture, while the specimens with *R 5* were able to fully fracture the cross section in a brittle manner. The effect of stress triaxiality on fracture surface of PP, are minimum, however with increase of notch radii seems to lead to a more ductile behaviour.

SEM micrographs of cylindrical notched specimens with notch *R 5* of HDPE identified two fracture morphologies: brittle fracture, where crack growth is supposed to be rapid and brittle/ductile fracture with some microfibrils content near surface, due to crazing fracture mechanism. The central fracture surface is less uneven than the fracture close to the material surface because the stress concentration is higher in the centre, probably from where the cracks nucleates and propagates. For *R* 30 a uniform fibrillar structure over the cross section is visible, indicating that the fracture was ductile in nature, exhibiting enhanced ductility. The uniform fibrillar structure might be indicating that the surface layer had failed after void nucleation and multiple formation of microfibrils.

At peripherical and central region microfibrils with knobs or nodules with a smooth rounded surface like features probably formed by the relaxation of hot material, is observed. Similar features were found in research work performed by Brough et al. [176] on scanning electron micrographs of HDPE fracture surfaces. It is observed a large peeling skin for notched *R 5* specimen. The stress triaxiality rules the fracture morphology, which becomes more ductile with large fibril formation at low stress triaxiality (notched *R 30*), on the other hand becomes more brittle with increasing the stress triaxiality (notched *R 5*).

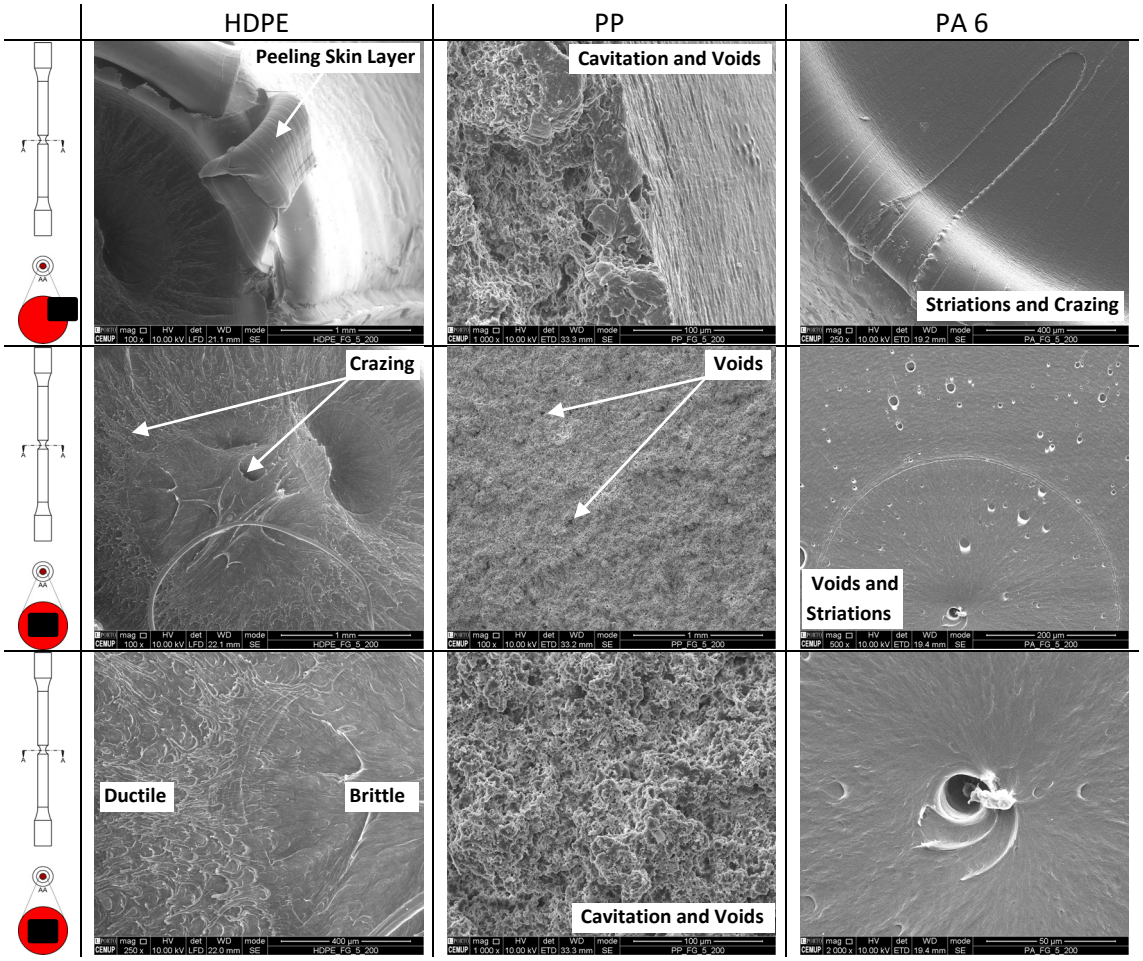


Figure 107 - SEM fracture surfaces for cylindrical notched specimens with *R 5*, for HDPE, PP and PA 6. Note that in the first column the geometry of specimen and fracture surface location are indicated by the black square.

The fracture surface of PP for notch radii *R* 5 exhibits a uniform fracture aspect, predominantly with rough surface, dominated by brittle fracture (cavitation and voids). Absence of fibrils formation, are verified. In the case of the notch *R* 30 there is a fibrillar structure, pulled out from the background surface, at the central fracture surface, which is consequence of low stress triaxiality. The fracture becomes more ductile. Similar to fracture morphology observation on PP Flat notched, also with cylindrical notched specimens, the effect of stress triaxiality slightly modifies the fracture surface and influence the void growth and size.

Contrasting with the fracture surface of HDPE and PP, PA 6 features an “smooth surface” with radial striations and also some disperse cavitation/voids are detected in both notched radii 5 and 30. The absence of fibril formation is an indication of brittle fracture. The voids distribution density is higher at the specimen centre and decreases toward the specimen border. By comparing the two radii, the voids amount and size decreases with notch radius increase (lower stress triaxiality ratio). Similar features on the mechanisms of void growth on cylindrical notched specimens were observed by Laiarinandrasana et al. [145]. In notched radii 5 the dominant mode of deformation near surface, was crazing.

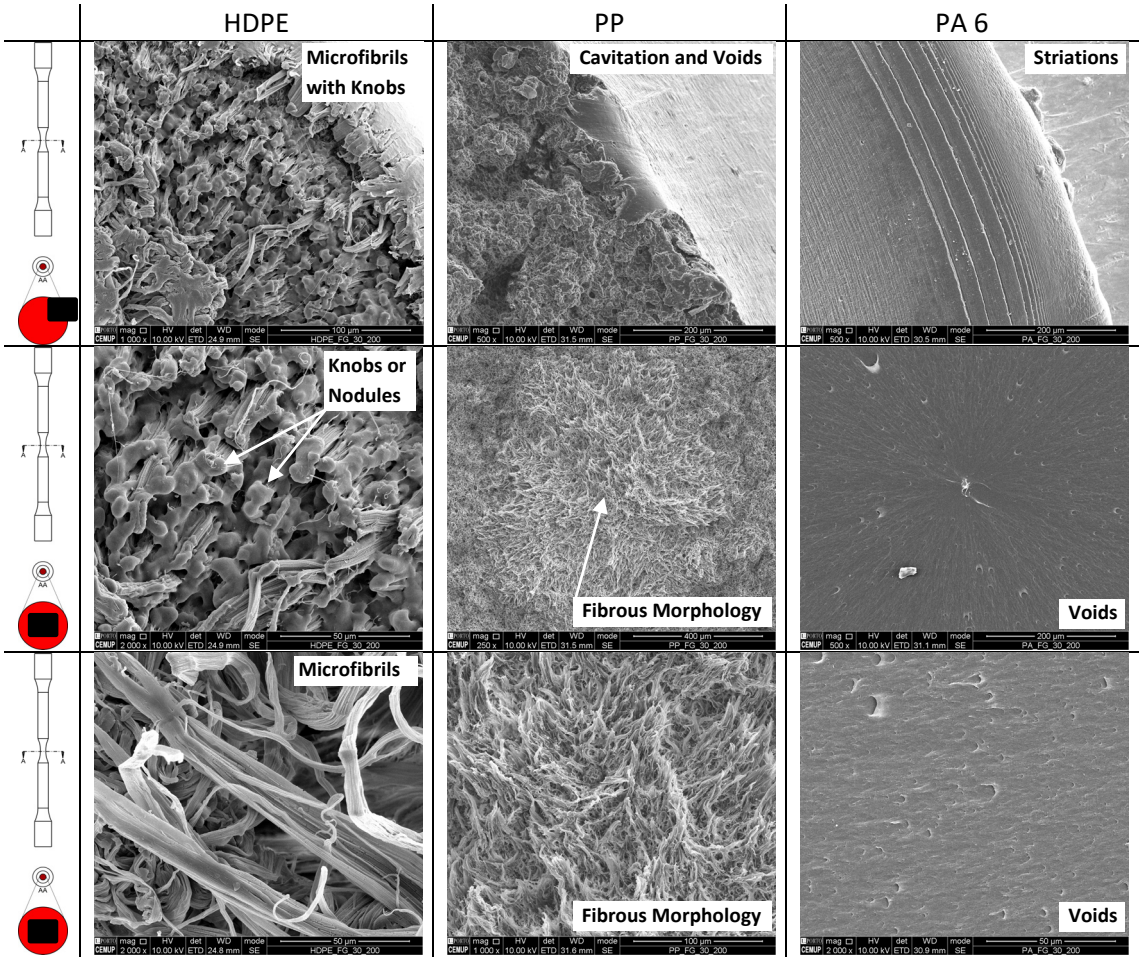


Figure 108 - SEM fracture surfaces for cylindrical notched specimens with *R 30*, for HDPE, PP and PA 6. Note that in the first column the geometry of specimen and fracture surface location are indicated by the black square.

An impression from comparing the fracture surfaces and the two radii of HDPE and PP specimens is that a higher radius caused a rougher fracture surface with higher fibril formation. Therefore, the presence of notches (triaxial state of stress) might change the fracture mechanism of the tested material from ductile (low stress triaxiality) to brittle (high stress triaxiality) mechanism. It was also noted that some kind of a thin skin layer was formed around the fracture surface of specimens, such as in HDPE.

5.4 Analysis of Combined Tensile/Shear Loading Fracture Morphologies at Stress Triaxialities: 0 to 0.58

Fracture morphologies under different loading angles of HDPE, PP and PA 6 butterfly specimens were investigated with SEM. Due to the three loading angles (α = 90°, 30°, and 0°) applied to the butterfly specimen at crosshead speed 200 mm/min and at two temperatures: room temperature and temperature of 50 °C, distinct fracture morphologies are generated for each material. In appendix 8.2.3 a comprehensive presentation of the corresponding SEM micrographs, can be found.

5.4.1 Pure Tension (α = 90°) – Stress Triaxiality: 0.58

To explore the underlying fracture mechanisms under α = 90° (pure tension) at room temperature and at temperature of 50 °C, for HDPE, PP and PA 6 SEM images were taken from the fracture surfaces and are presented in Figures 109 and 110.

Room Temperature: The fracture morphology exhibits different modes of deformation, for α = 90°, pure tension at moderated stress triaxiality and at room temperature. For HDPE, the plastic deformation occurs predominantly by a combination of crazing in the fracture surface centre and fibrillation/Crazing type of fracture in the surface extremities, which is the last region to fracture. Also, a multiphase layer structure – “peeling skin layer” are shown in peripheric central region-fracture. The fractured skin layer behaves as a “peeling skin layer” and takes a form of high oriented fibrils or as massive craze and tearing [167].

Considering that the inherent stress concentration is expected to be high in the middle section, crack nucleates and propagates through wedges. Fracture surface exhibit two main characteristics: ductile fracture associated with crazing at the centre from which fracture initiates. Then, a transition area appears showing fibrillation type of fracture, associated with an extensive plastic flow, where crack growth is supposed to be rapid and last region of fracture. In the case of PP, the surface morphology, displays an irregular surface with high void and cavitation content, which becomes rather rough and uneven at extremities; similar morphology was already observed on PP flat and cylindrical notched specimens. Brittle failure, is the predominant fracture characteristic.

A high inhomogeneous multiphase structure is exhibited by PA 6. From SEMs, It is observed that near surface the fracture takes a form of massive craze and tearing crazing. Dasari et al. [175] defined crazing and tearing, based on their observations made on in iPP-L and HDPE fracture surfaces, as the initially crazes formation on the surface, with increase in strain, a crack nucleates and propagates inward through an array of crazes resulting tearing. The core region with high irregular fracture surface, is characterized mainly by crazes and brittle failure. SEM micrographs at low magnification shows crazing and tearing in the region away from the centre of the fracture surface. It appears that the fracture initiated near the core of the butterfly specimen, and propagated outwards breaking through the crazed surface on both sides and extremities (resulting in tearing of the crazed region) at approximately the same position long the length of

the bar. Also, at longitudinal near surface are observed inward growth of crazes from all the sides.

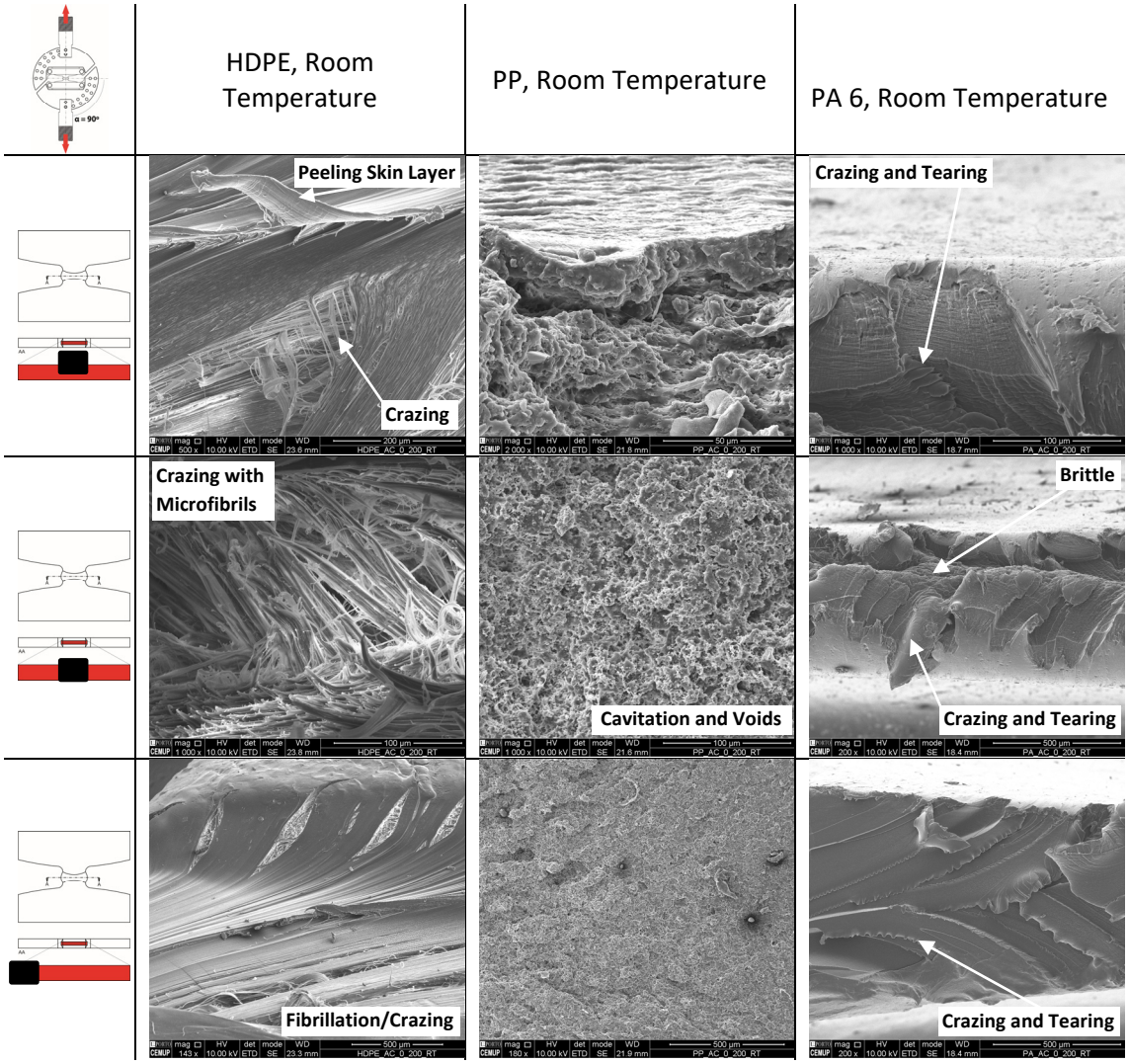


Figure 109 - SEM images of butterfly specimens fractured for tensile loading at room temperature for HDPE, PP and PA 6. In the first column the geometry of specimen and fracture surface location are indicated by the black square.

Temperature of 50 °C: SEM images are also taken at a temperature of 50 °C. In general mode with increase in temperature, the fracture becomes more homogenous, the extent of craze region decreases and the ductile area/surface increases. In the case of HDPE, at central region, the fracture surface is reduced, becoming narrower, suggesting that was the last region to fracture. However, the fracture surface is more homogeneous. Also, it is observed, crazing and tearing with microfibrils formation and slope surfaces.

High magnification of PP fracture surface, shows irregular surface with high void content, also at fracture extremities are observed large voids surrounded by fibrils. The fracture surface of PP does not undergo with major changes, with increasing the temperature. Even though the brittle failure is dominant, there is some evidence of ductile pulling of microfibrils around the voids at

the edges. The “peeling skin layer” is observed in both HDPE and PP in peripheric central region-fracture.

At a temperature of 50 °C, PA 6 exhibits a fracture surface completely different from that obtained under room temperature. The fracture surface becomes more ductile with fibril formation at central region and more inhomogeneous at the extremities (the last region to fracture), with massive crazing and tearing formation.

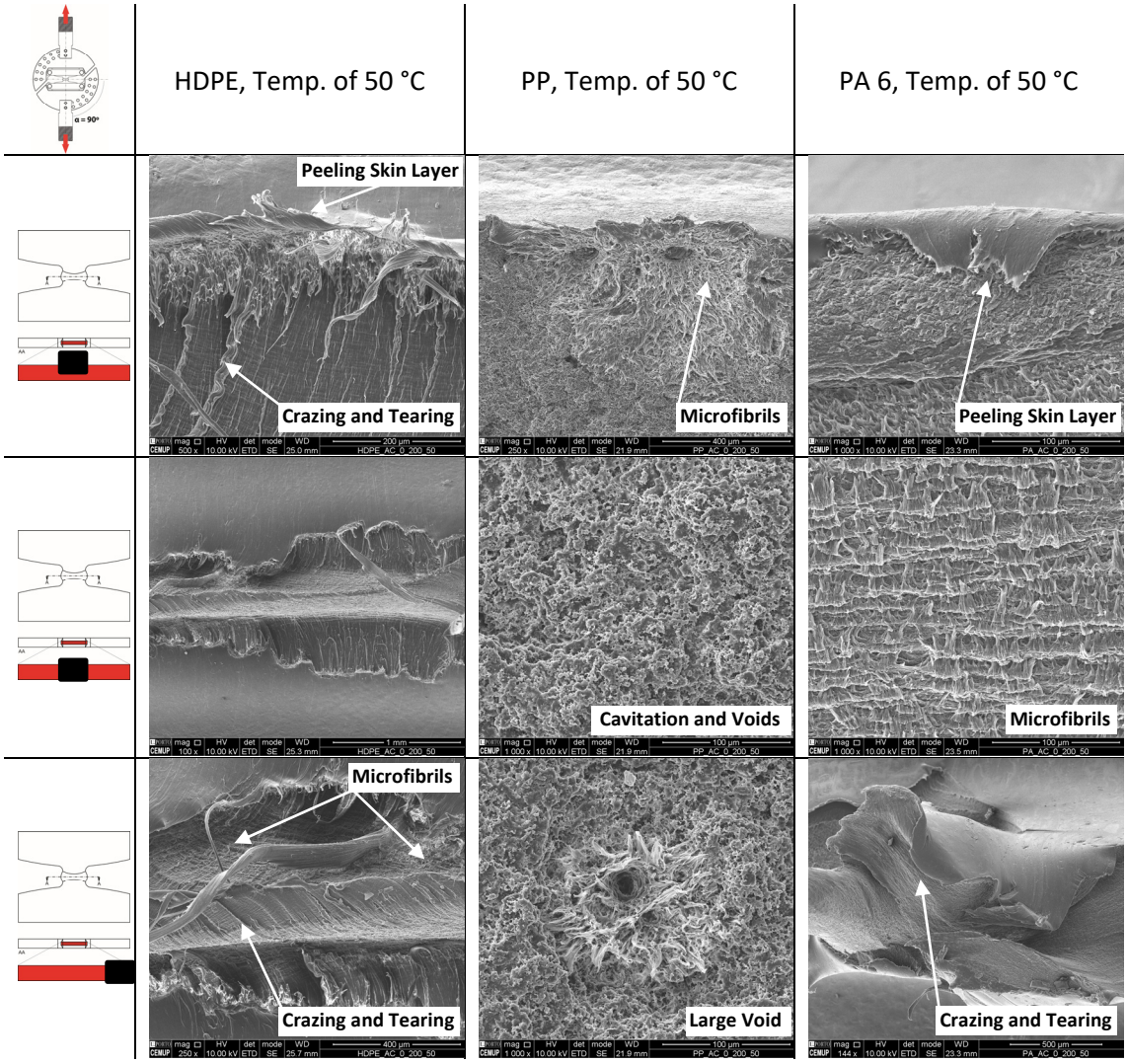


Figure 110 - SEM images of butterfly specimens fractured for tensile loading at temperature of 50 °C for HDPE, PP and PA 6. In the first column the geometry of specimen and fracture surface location are indicated by the black square.

5.4.2 Combined Tension/Shear (α = 30°) – Stress Triaxiality: 0.19

SEM images of fracture mechanisms under combined tension/shear (α = 30°), in a positive vertical displacement at room temperature and at temperature of 50 °C, for HDPE, PP and PA 6, are displayed in Figures 111 and 113.

Room Temperature: At room temperature, brittle fracture associated with large voids and cavitation, crazing and tearing associated to the combined tension/shear loading, with ductile pulling of microfibrils in the regions away from the centre of the fracture surface are the dominant plastic deformation for HDPE. In the central fracture surface of HDPE, the two large ellipsoidal voids, surround by oriented fibrils morphology, are visible. The formation of elliptically shaped voids would be either due to plastically deformation inside amorphous phase or a pre-existing defect or even because the combined tension/shear loading (ellipse major axis in the shear direction). The fracture initiated in the centre and propagated outwards towards the surface, where the fracture surface is characterized by crazing and tearing.

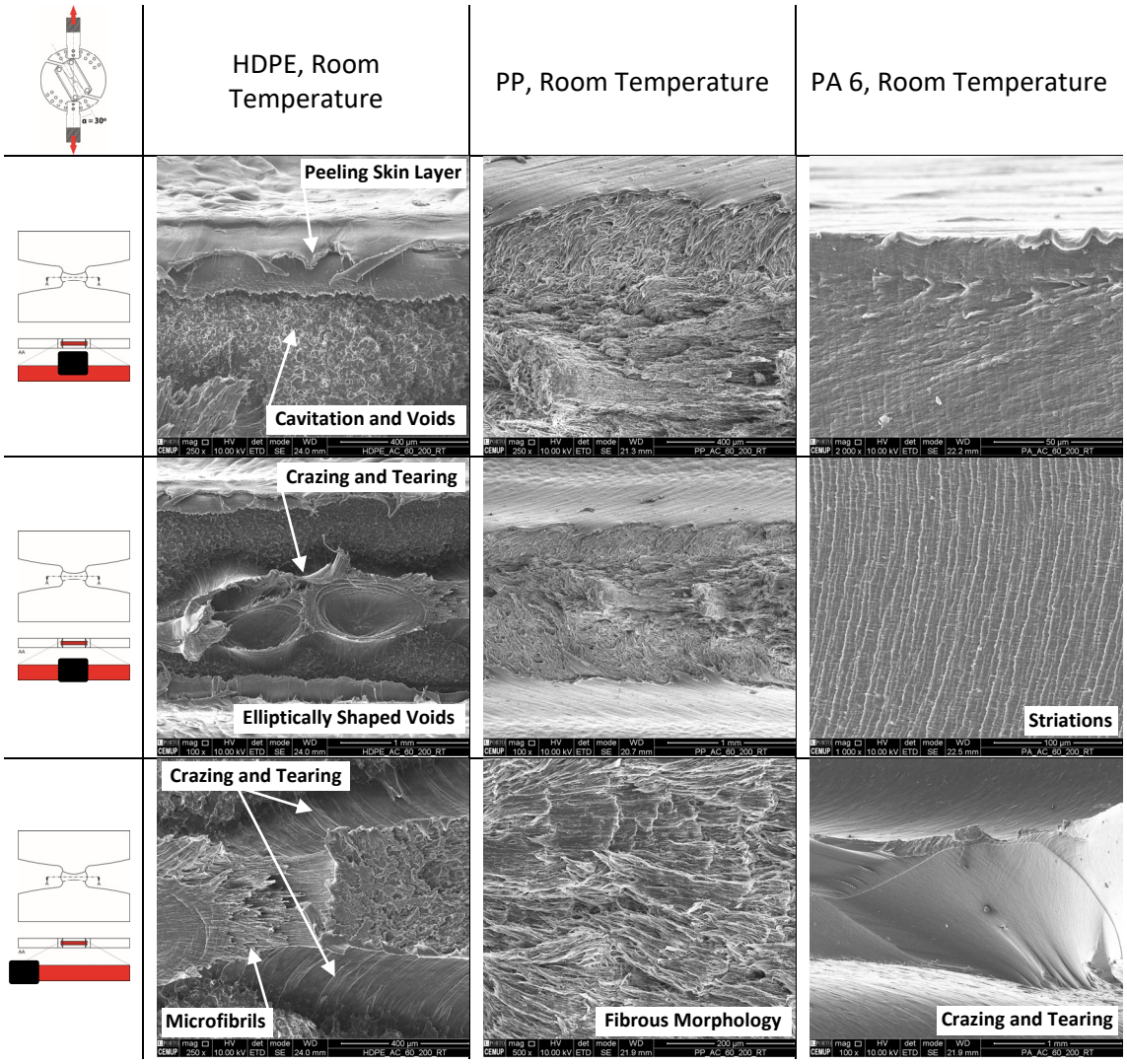


Figure 111 - SEM images of butterfly specimens fractured for combined tensile/shear loading α = 30° at room temperature for HDPE, PP and PA 6. In the first column the geometry of specimen and fracture surface location are indicated by the black square.

SEM micrographs of PP in the peripheric-central region, show oriented fibrils with the direction of loading (α = 30°), exhibiting high deformation before failure (ductile failure). The inner layer shows a more ductile behaviour than at (α = 90°) and is observed at the ends knobs or nodules that might be caused by thermal softening (Figure 112 (1)). The fracture initiated in the outer

layer and propagated inwards towards the centre, this justifies the presence of fibrous morphology elongations at centre; compared with near surface. Thus, the centre of the fracture surface is characterized by extensive plastic flow around and inhomogeneous morphology.

From, PA 6 SEM micrographs, it is clear a brittle failure. At central fracture region, all surfaces are covered with a very fine mesh of striation configuration. High magnifications (Figure 112 (2)) show material pulled out from the fracture surface, by crazing and tearing. SEM micrographs shows crazing and tearing at the fracture surface end. The striations are result of successive crack propagation on failures. The striations are perpendicular to the shear loading.

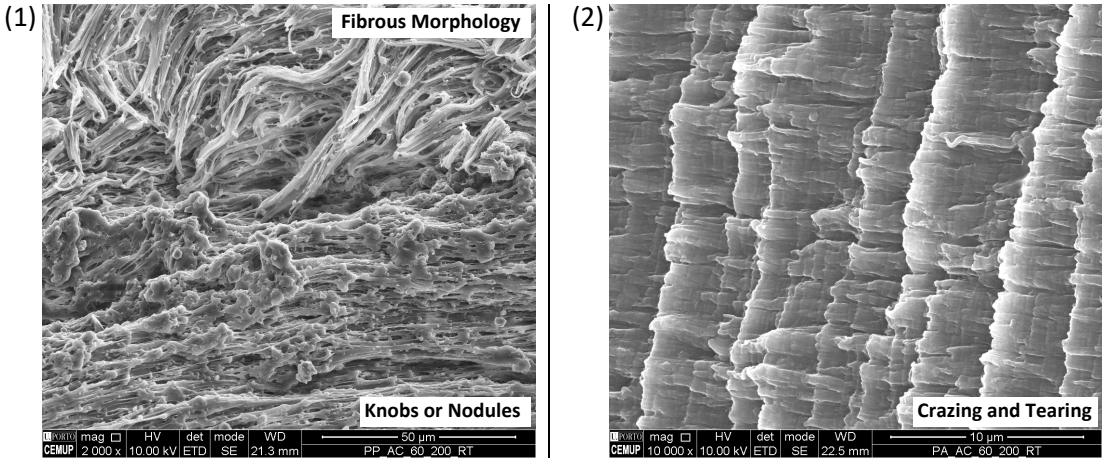


Figure 112 – High magnifications (1) PP peripheric-central region and (2) PA 6, central fracture region.

Temperature of 50 °C: At a temperature of 50 °C, HDPE fracture surface becomes more regular, more homogeneous at the centre. Crazing and tearing as well as peeling skin layer, are observed. The main fracture feature is the central slope formation, propagated through the fracture length. Similar geometry was obtained for $\alpha = 90°$. Although, crazing characterizes the ductile behaviour of a material, the central slope formation is considered to represent enhanced ductility (or plastic flow), consistent with decrease in fracture area.

With temperature increase the fracture surface of PP exhibits, an irregular surface with microfibrils formation. The area fraction of fibrous morphology is increased with increase of temperature, with respected to RT. Large amount of deformation all over the area with a number of longer fibrils and large voids, also some evidence of thermal softening, are observed at fracture extremities.

PA 6 SEM micrographs shows microfibrillar failure in the mid-thickness regions of the fracture surface versus craze embrittlement (brittle mode of failure due to high crosshead speed and temperature). The fracture surface becomes more rough and irregular, with increasing the temperature. At extremities, the fracture surface shows high inhomogeneous surface. At this region, the fracture surface is characterized by crazing and tearing. Generally, in a tensile test, one expects high hydrostatic stress to be in the centre of the specimen and may well be the reason for the brittle fracture feature in the centre and more ductile in the longitudinal extremes.

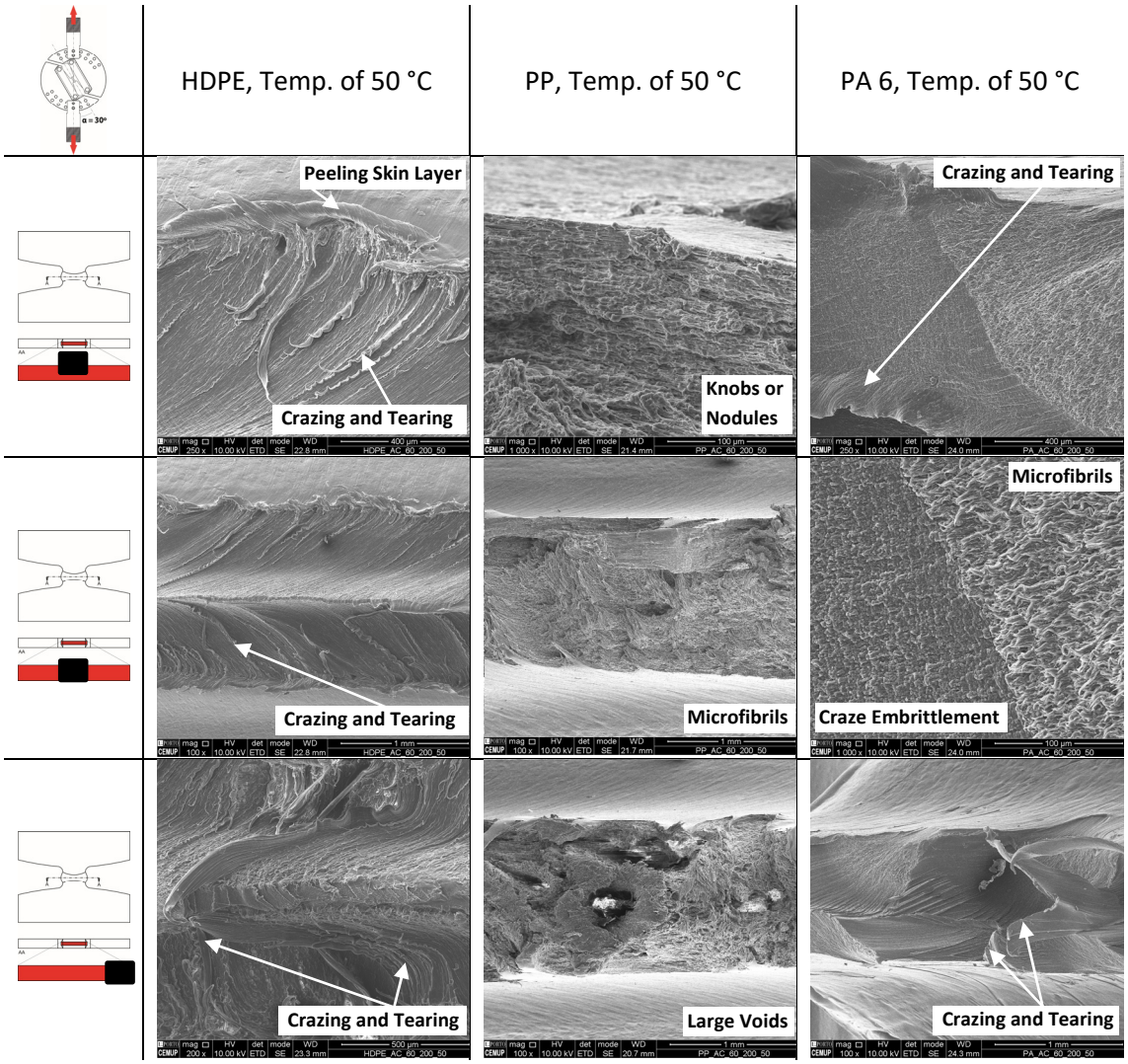


Figure 113 - SEM images of butterfly specimens fractured for combined tensile/shear loading α = 30° at temperature of 50 °C for HDPE, PP and PA 6. In the first column the geometry of specimen and fracture surface location are indicated by the black square.

5.4.3 Pure Shear (α = 0°) – Stress Triaxiality: 0

SEM images of fracture mechanisms under pure shear at room temperature and at temperature of 50 °C, for HDPE, PP and PA 6, are depicted in Figures 114 and 115.

Room Temperature: From SEM images at room temperature of HDPE and PP is observed that the fracture surface exhibit predominantly ductile failure with crazing and tearing, fibril formation associated with the shear loading. Pure shear leaves a relatively smooth fracture surface and orientated geometry. For PP, the fracture surface generated is particularly “clean” with a smooth surface in a form of waved structures, with fibril formation, along the shear stress direction, whereas in the case of HDPE displays a regular surface with almost geometric triangular patterns at the specimen centre. In side fracture surface is observed the fibrils formation and alignment. The symmetry suggests that the fracture starts near surface and

propagates inwards through the crazed surface on both sides (resulting in tearing of the crazed region) at approximately the same position along the length of the bar.

PA 6 is the exception; SEM micrographs shows a considerable plastic deformation and inhomogeneous morphology with significant localized deformation in the form of crazing tearing at the extremities and at the centre. At high magnification at central region, textured fracture surfaces are observed, with some fibrils formation and crazing tearing formation. At extremity SEM micrographs shows some amount of microbuckling leading to a corrugated appearance in the regions away from the centre of the fracture surface.

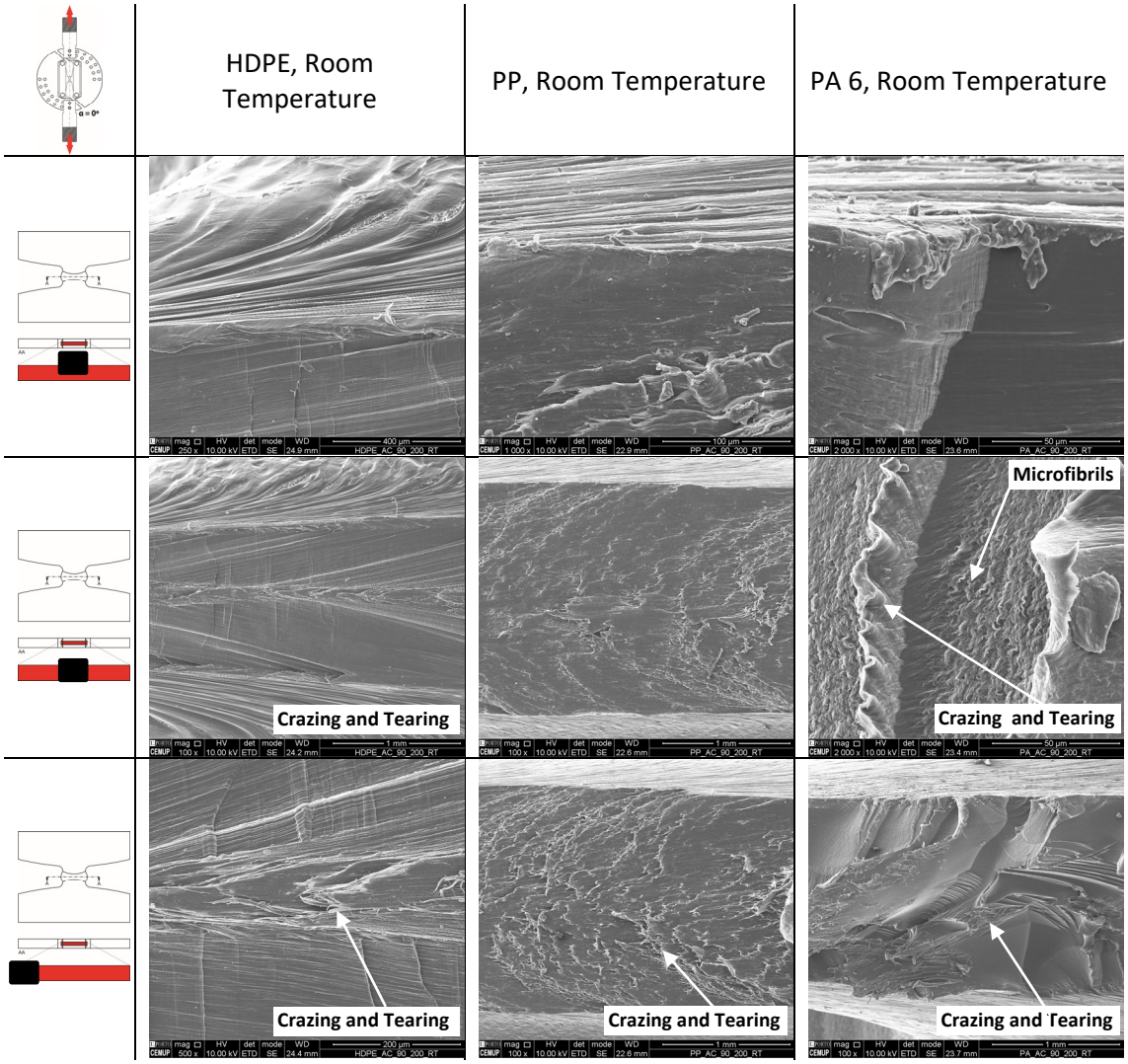


Figure 114 - SEM images of butterfly specimens fractured for shear loading at room temperature for HDPE, PP and PA 6. In the first column the geometry of specimen and fracture surface location are indicated by the black square.

Temperature of 50 °C: SEM images are also taken at a temperature of 50 °C. At higher temperatures the polymer behaves in a much more viscous manner and the crazes widens very rapidly. The fracture surface seems to appear less rough and more homogeneous in the case of PP and PA 6. For HDPE, the regular surface with almost geometric triangular patterns, are

elongated along the shear stress direction. HDPE fracture surfaces at RT and 50 °C have the geometric patterns, however in 50 °C, at near surface appears a large number of microfibrils, indicating a continued plastically deformation as decohesion of crazing occurred. The dominant fracture is crazing, as well as for PP. PP fracture surface extremities shows large areas covered with striations, also several edge discontinuities are included with attendant fibrils (Figure 116). The fracture surface is similar with RT.

In the shear deformation of PA 6 at 50 °C three fracture morphologies are identified: brittle with ductile pulling of microfibrils, crazing and shearing. The area fraction of brittle failure decreased with increase in temperature with consequent increase in ductile fracture.

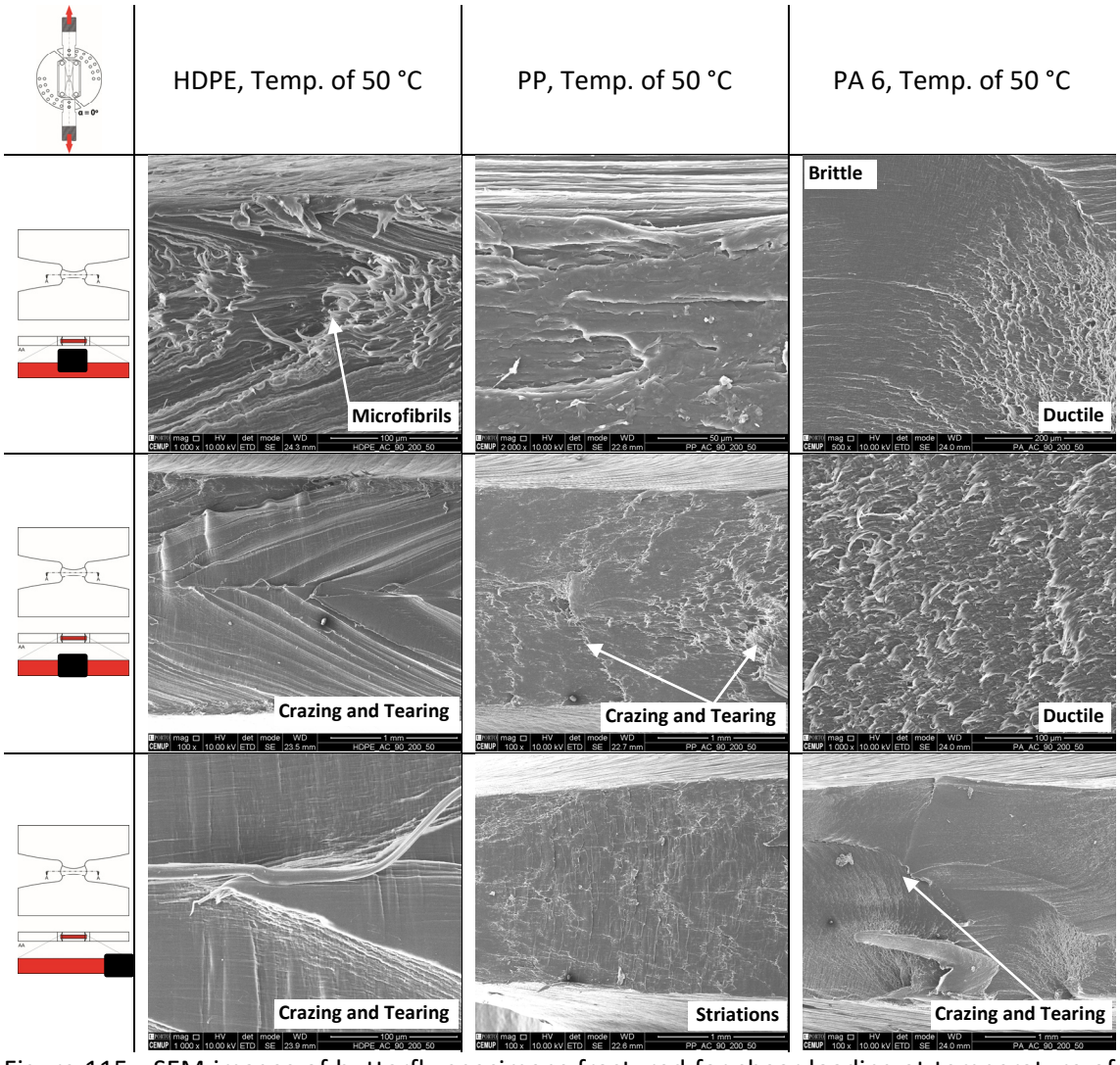


Figure 115 - SEM images of butterfly specimens fractured for shear loading at temperature of 50 °C for HDPE, PP and PA 6. In the first column the geometry of specimen and fracture surface location are indicated by the black square.

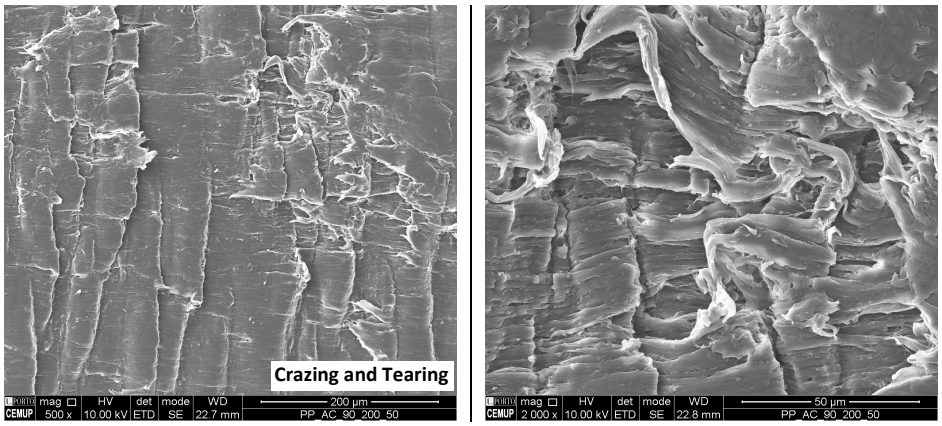


Figure 116 – High magnification of PP fracture surface at extremities.

5.5 Discussion and Concluding Remarks

SEM has the capability of providing valuable information about the morphologies and fracture mechanisms of HDPE, PP and PA 6. As expected, SEM fracture morphologies of HDPE, PP and PA 6, revealed that the formation of cavities or cracks depends on the particular internal morphology of polymer, such as molecular structure, molecular weight, distribution and experimental factors, such as loading rate, temperature and stress triaxiality imposed by specimens with different notches geometries.

5.5.1 Flat and Cylindrical Notched Specimens

The mechanisms of plastic deformation of semi crystalline polymers, are composed by highly oriented microfibrils (stack of lamellae), organized into fibril bundles. Shear or tension will be the main deformation modes of stack of lamellae, depending on its orientation with respect to the principal stress direction. Most of the plastic deformation is taken up by the amorphous regions, which are entangled networks attached to the adjacent crystalline lamellae through tie molecules [30, 34, 59].

During further deformation the tie molecules are stretched leading to strong tensions and transfer locally elastic stresses to the lamellae. Stress relief can occur in two ways, through cavitation within the amorphous network and/or through crystal plastic deformation. Slip on certain preferred lattice planes, chain unfolding, and/or crystal breakup, are the principal modes of crystal lamellae deformation. The competition between the straining (amorphous regions) and breakdown (crystalline regions) gives rise to different regimes: fibrillated shear and cavitation [30, 34, 59].

Fibrillated shear occurs if both amorphous and crystalline regions which are affected similarly by the drawing process, giving rise to brittle or to ductile failure. Brittle failure is highly localized and resembles fracture by crazing. Cavitation of the amorphous regions occurs preferentially if the crystalline lamellae are stronger than amorphous phase [30, 34, 59]. It is assumed that the

fracture toughness of semi crystalline polymers is controlled by mechanisms such as crazing, void and cavitation formation [59], all mechanisms were observed and described in this chapter.

One of the major factors controlling the occurrence of yielding or brittle fracture is the state of stress, such as the one included by the presence of notches. Therefore, different stress triaxiality levels were induced by different notch radii in tensile specimens at RT and crosshead speed of 200 mm/min. All flat specimens experienced full section fracture. The smaller the notch radius, the higher the stress triaxiality is. The fracture morphologies on flat notched specimens were studied in detail. HDPE and PP were deformed at temperature above the glass transition. Above glass transition, the macromolecules in the amorphous phase have more mobility and elongations to failure typically increases. The main results are illustrated in Figures 117 and 118, and are summarized, as follows:

- SEM fracture morphologies of HDPE, PP and PA 6, reveals that the fracture morphologies are highly dependent on stress states. Lower stress triaxiality is a synonymous of ductile fracture. Flat notched specimen *R* 5 and *R* 30 show the formation of an oriented texture of fibrous surface, which increases with decrease of notched radii (low triaxiality) (Figure 117);

- It is observed that rising the stress triaxiality, the fracture becomes more brittle and homogeneous, with less formation propensity of longer fibrous surface and more voids content (Figures 117 and 118);

- Qualitative SEM observations of HDPE, PP and PA 6, fracture surfaces of flat and cylindrical notched specimens depict inhomogeneous morphology. Mechanisms such as crazing, void and cavitation formation, are observed. In the same surface two or more mechanisms, are found. These means that the stress at surface is no equal and is maximum at centre, where the fracture normally begins (Figures 105, 106, 107 and 108);

- Laiarinandrasana et al. [145], states that high values of stress triaxiality influence void growth and brittle failure. These observations are in agreement with current experimental investigation results. Voids are larger next to the specimen axis, where the stress triaxiality ratio is high, see Figure 118, column PA 6, and its distribution density is higher at the specimen centre and decreases toward the specimen border. By comparing the two radii, the voids amount and size decreases with notch radius increase (lower stress triaxiality ratio);

- SEM micrographs of PP exhibit predominantly brittle failure, cavitation and voids. Although the different stress triaxialities imposed by different specimen's geometries and notches, the fracture surfaces morphologies slight modifies (Figures 117 and 118). This feature might be attributed to the internal morphology of polymer;

- In HDPE cylindrical *R 30* at peripherical and central region microfibrils with knobs or nodules with a smooth rounded surface like features probably formed by the relaxation of hot material, is observed in Figure 118. Similar features were found in research work performed by Brough et al. [176] on scanning electron micrographs of HDPE fracture surfaces. Also, this supports the conclusions of Chou et al. [156] and Arruda et al. [157] that heating occurs during deformation.

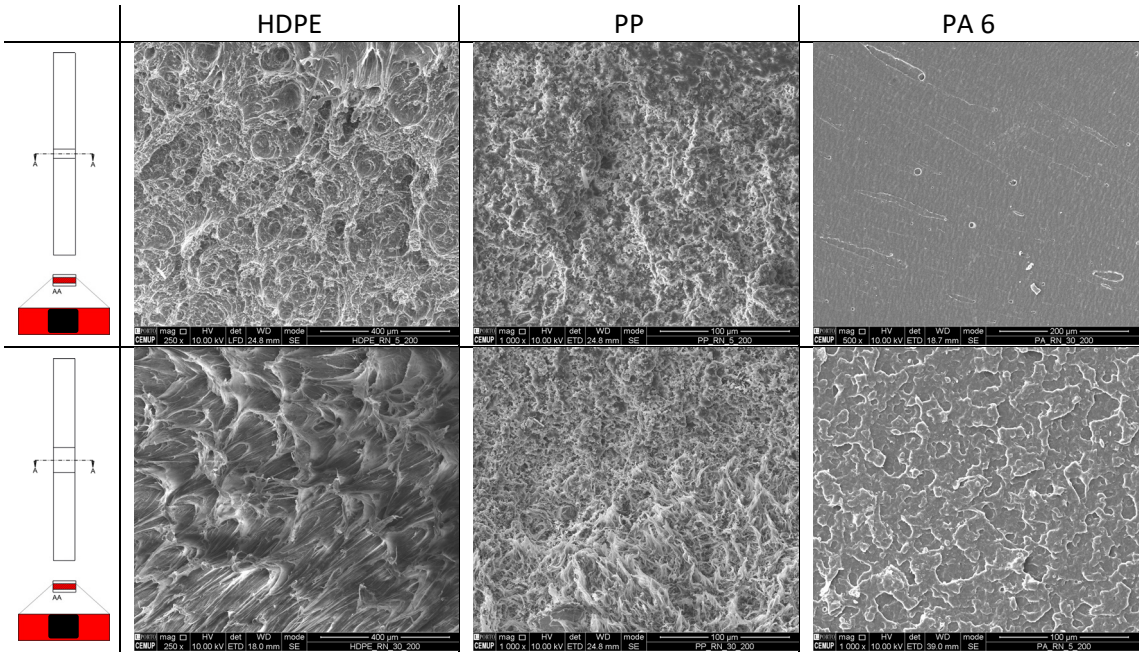


Figure 117 - SEM fracture surfaces for flat notched specimens with *R 5* and *R 30*, for HDPE, PP and PA 6 at central localization.

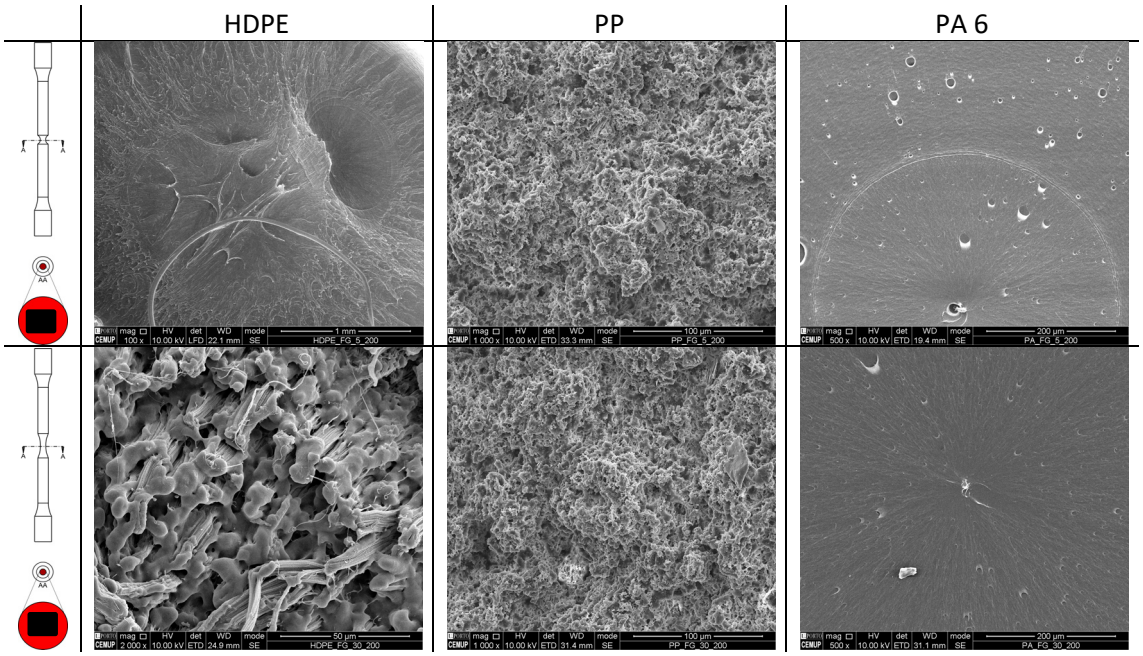


Figure 118 - SEM fracture surfaces for cylindrical notched specimens with *R 5* and *R 30*, for HDPE, PP and PA 6 at central localization.

Note that SEM micrographs were already used in this thesis, however are displayed in different mode.

5.5.2 Combined Tensile/Shear Loading Fracture Morphologies

Pure Tension: Beyond the state of stress, combined tensile/shear loading, also influence the fracture morphology. Figures 119, 120 and 121 summarizes SEM micrographs for combined tensile/shear loading fracture morphologies at room temperature and at temperature of 50 °C, for HDPE, PP and PA 6. The microstructure deformation mechanisms during biaxial loading at α = 90° tension were already above described. The main observations on SEM micrographs are in Figure 119 and are summarized hereafter:

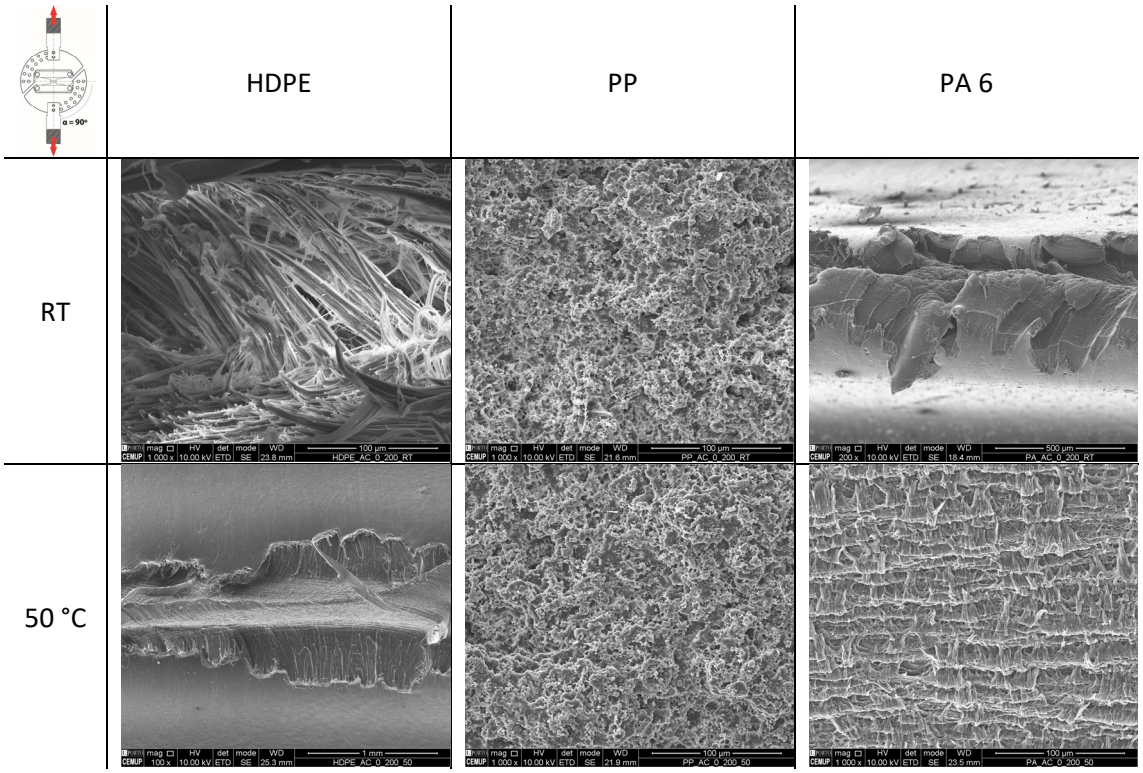


Figure 119 - SEM images of butterfly specimens fractured for tensile loading at room temperature for HDPE, PP and PA 6 at central localization.

- The fracture morphology exhibits different modes of deformation, for α = 90°, pure tension at moderated stress triaxiality and at room temperature. Mechanisms such as crazing, void and cavitation formation, are observed. Two or more mechanisms are predominant and fracture morphology are inhomogeneous;

- The inherent stress concentration is expected to be high in the middle section, thus crack nucleates and propagates through wedges;

- The surface morphology of PP displays a rough and uneven surface with high void and cavitation content, in both temperature, RT and at 50 °C. Similar morphology was already observed on PP flat and cylindrical notched specimens;

- In general mode with increase in temperature, the fracture becomes more homogenous, the extent of craze region decreases and the ductile area/surface increases. In the case of HDPE, at central region, the fracture surface is reduced, becoming narrower, suggesting that was the last

region to fracture. PA 6 acquires a fracture surface completely different from that obtained with room temperature. With increasing temperature the fracture surface becomes more ductile with fibril formation at central region.

Combined Tensile/Shear: As already referred in 4.1.2 Combined Tensile/Shear Tests at Room Temperature and at temperature of 50 °C, the microstructure deformation mechanisms during combined loading at $\alpha = 30°$ might be in accordance with the research work performed by Zhou and Wilkes [160]. Zhou and Wilkes [160] describes that in the the process of yielding, lamellar rotation occurred as a result of lamellar shear and/or chain slip, and the reorientation of polymer chains towards loading direction. At this stage of the deformation, crystalline lamellae began to break up owing to the competitive constraint between lamellar shear and chain slip. The break-up of the crystalline lamellae is essentially a cold-drawing process by chain slip within the crystalline lamellae.

The main observations on SEM micrographs for combined tensile/shear loading, $\alpha = 30°$, fracture morphologies at room temperature and at temperature of 50 °C at central region, for HDPE, PP and PA 6, are summarized in Figure 120.

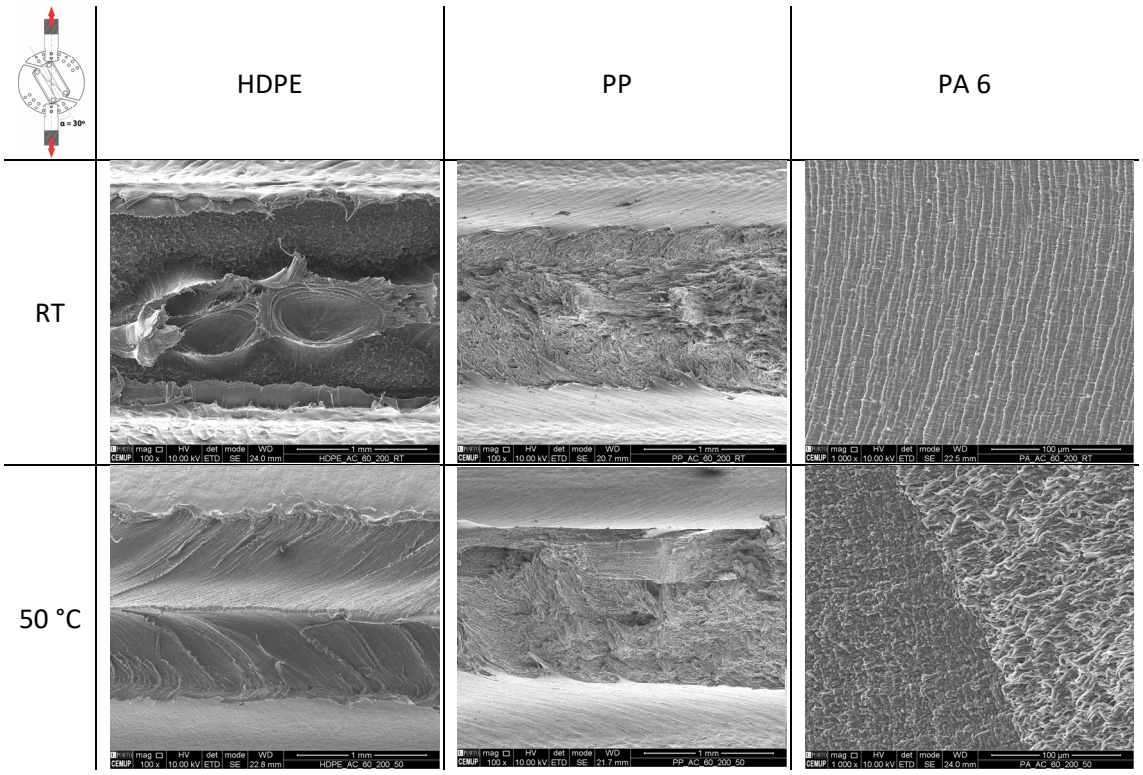


Figure 120 - SEM images of butterfly specimens fractured for combined tensile/shear loading at room temperature and at temperature of 50 °C for HDPE, PP and PA 6 at central localization.

- It is observed a fracture morphology oriented towards loading direction, such as in the case of PP, which at RT or at temperature of 50 °C shows oriented fibrils with the direction of loading ($\alpha = 30°$), exhibiting high deformation before failure (ductile failure). The inner layer shows a more ductile behaviour than at $\alpha = 90°$;

- Diferent fracture morfologies are observed, when compared with $\alpha = 90°$. The fracture becomes more ductile and less homogeneous, with more formation propensity of longer fibrous surface;

- Also, with temperature increase, the fracture becomes more homogenous.

Pure Shear: Zhou and Wilkes [160] also describes the microstructure deformation mechanisms during shear. It is referred that lamellar break-up is the dominant deformation mechanisms. During the break-up process, polymer chains are pulled-out of the crystalline lamellae and realigned parallel to the load, which is perpendicular to the original molecular induced direction, this might explain the fracture morphologies obtained for shear loading (Figure 121).

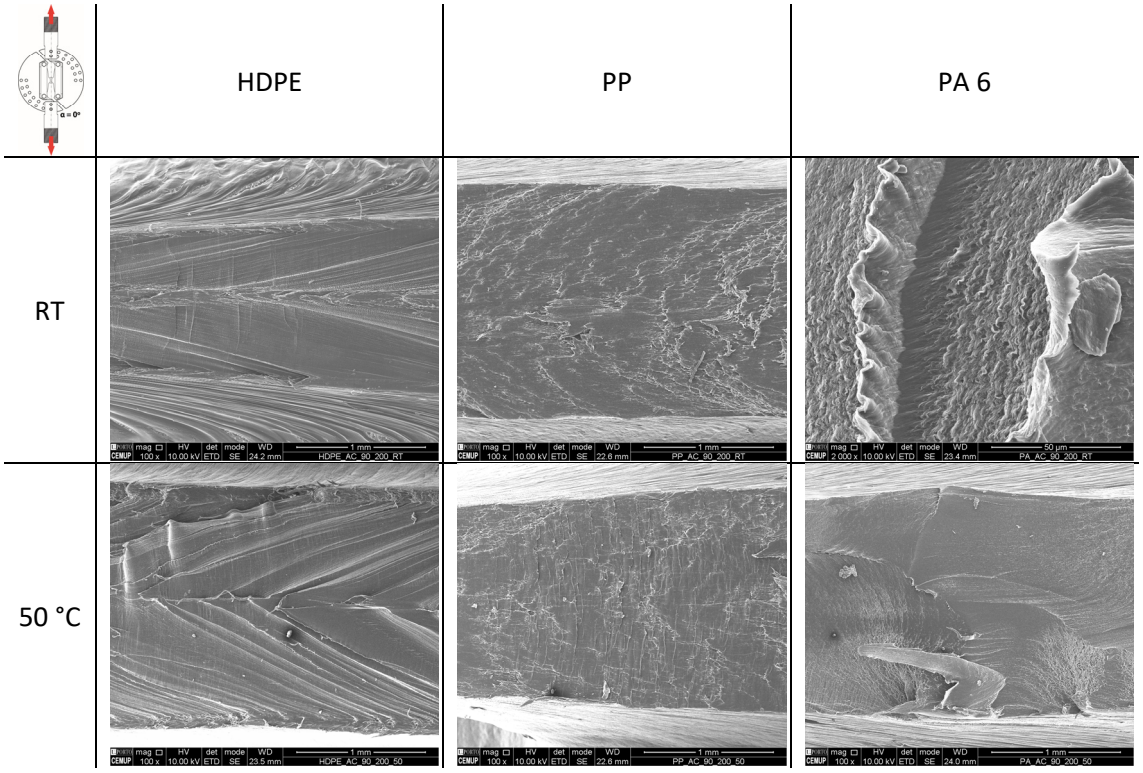


Figure 121 - SEM images of butterfly specimens fractured for shear loading at room temperature for HDPE, PP and PA 6 at central localization.

SEM images of fracture mechanisms under pure shear at RT and at temperature of 50 °C, for HDPE, PP and PA 6, shown:

- From SEM images at room temperature of HDPE and PP is observed that the fracture surfaces exhibit predominantly ductile failure with crazing and tearing, fibril formation associated with the shear loading, whereas PA 6 exhibits a considerable plastic deformation and inhomogeneous morphology;

-Pure shear leaves a relatively smooth fracture surface and orientated geometry. In general, is observed that the fibrils are oriented to the shear direction;

- With temperature increase, the fracture becomes more homogenous in the case of PA 6 and slight inhomogeneous for PP and PA 6.

6 Plasticity Model Calibration and Verification – Drucker-Prager and von Mises

The deformation of semi crystalline polymers commonly involves large plastic deformations, with high gradients of plastic stress and strain. Their mechanical response is, in general, sensitive to strain rate and temperature and are often regarded as pressure sensitive materials; a higher yield strength in compression than in tension is commonly observed. Semi crystalline polymers exhibit viscoelasticity, initial viscoplasticity and subsequent strain hardening.

The aim of this chapter is to assess the predictive ability of two yield criterions and to calibrate the plasticity models Drucker-Prager and von Mises yield criteria based on the mechanical experimental results measured under different stress sates and different crosshead speed of three semi crystalline polymers – HDPE, PP and PA 6. The plasticity models calibration and verification were performed through numerical simulation of all tests using Abaqus.

von Mises assumes that the hydrostatic pressure and the third invariant of the deviatoric stress have no effect on plastic yielding. However, this criteria cannot accurately predict the behaviour of HDPE, PP and PA 6, as yielding in these materials is sensitive to hydrostatic and to deviatoric stresses. The effect of hydrostatic pressure can be found in the difference observed between the tensile and compressive yield stresses, also in tests performed in notched specimens. As a consequence, pressure dependent plasticity theory is more appropriate in this case. In this context, the Drucker-Prager yield criterion is widely used for polymeric materials and is applied in this research in order to describe the yield behaviour of polymers [177].

The data requirements for a finite element analysis depend on the choice of the model used to describe the deformation behaviour of the polymer. The nonlinear material response was modelled using isotropic hardening with a von Mises yield criterion, and with a Drucker-Prager yield criterion. The true stress versus plastic strain data from the tensile test on dumbbell specimen, with stress triaxiality η = 1/3 and Lode angle parameter $\overline{\theta} = 1$, was used as input for the hardening curve, d parameter.

The tensile test on dumbbell was selected to extract the true stress versus plastic strain behaviour of material, instead of compressive test, which is the more standard for polymers, because the main concern, in this thesis is the analysis of initial yielding. At initial yielding it is reasonable to assume that the tensile test still enable to capture the behaviour of the material. At that point it can be assumed that the cross-sectional area of specimen remains constant (the area reduction is uniform over the gauge section) and the true strain is approximately constant and could be calculated from the measured relative displacement. For larger deformations more sophisticated experimental equipments are necessary in order to ensure that the specimens are tested at constant true strain. Also, in compression tests, homogeneous compression is difficult to achieve for vary large reduction because of the effect of friction between the ends of the specimen and the flat platens, and the associated "barreling" of specimens.

The elastic modulus behaviour and the Drucker-Prager plasticity model parameters, β which is the slope of the linear yield surface in the *p*–*q* stress plane, were determined as functions of the true stress-strain results obtained by the mechanical tests on five different specimens geometries: tensile tests on dumbbell and cylindrical notched, and compression tests on cylindrical unnotched and cylindrical notched specimens.

The aim of calibrating the material constitutive models, is to assess by means of numerical simulation the predictive ability of both criteria on other stress states: biaxial loading experimental results (pure shear, combined shear and tension/compression, pure tension/compression) performed on butterfly specimen and tensile experiments on flat notched specimens, by comparing the experimental load-displacement curves with the numerical simulation. The stress triaxiality and Lode angle parameter for each geometry are initially determined. The effects of stress triaxiality and Lode angle parameter on the plastic domain behaviour of HDPE, PP and PA 6 are discussed.

Each specimen or loading condition represents a specific stress state, which can be defined with two set of parameters, stress triaxiality η and Lode angle $\overline{\theta}$ parameter. The initial covered stress states by the investigated sets of specimens geometries, are depicted in Figure 122.

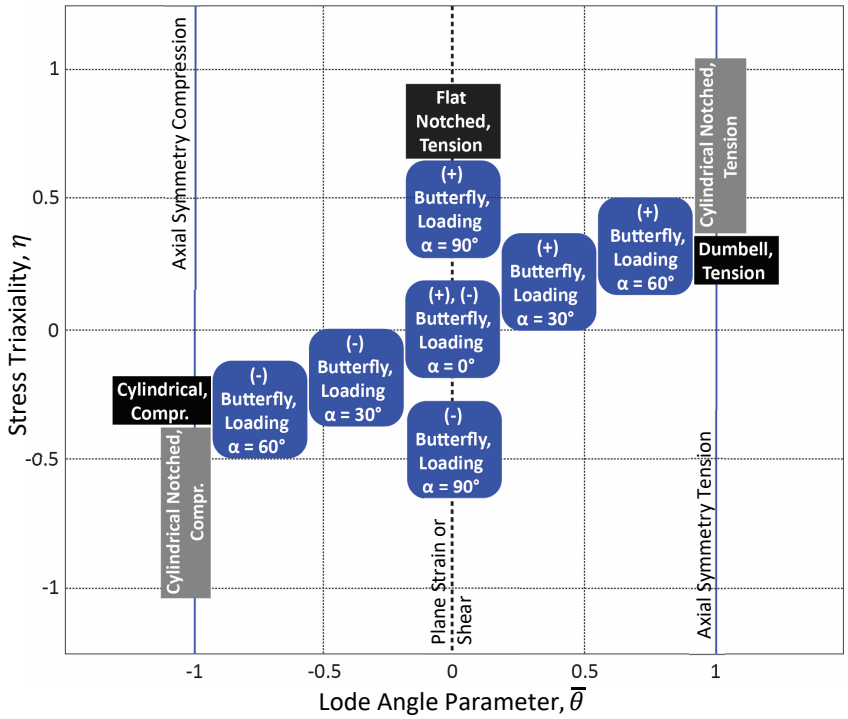


Figure 122 – Initial loading conditions of the specimens geometries in the plane of stress triaxiality and Lode angle parameter [8, 112].

Fourteen different tests on HDPE, PP and PA 6 semi crystalline polymers were performed, covering an initial wide range of stress triaxialities $-0.64 < \eta < 0.84$ and initial Lode angle parameter $-1 < \overline{\theta} < 1$.

- Tensile tests: dumbbell, flat and cylindrical notched specimens with radius 5 and 30,

- Combined tensile/shear tests: Butterfly specimens, loading angles of α = 90°, α = 60°, α = 30° and α = 0°,

- Compression: cylindrical unnotched and cylindrical notched, radius 5 specimens,

- Combined compression/shear tests: butterfly specimens, loading angles of α = 90°, α = 60° and α = 30°.

Tensile tests on dumbbell and cylindrical notched as well as compression tests are used for calibrations while the other tests are used for validation.

By introducing on flat and cylindrical specimens different notch radii, a range of stress triaxiality at constant Lode angle parameter, of $\overline{\theta} = 0$ and $\overline{\theta} = 1$, is obtained enabling the analysis of each parameter independently. Decreasing the notch radius increases the stress triaxiality value. It should be noted that those specimens cover the range of high stress triaxiality. On the other hand, the butterfly tests, cover a wide range of stress triaxiality and Lode angle parameter with a single specimen geometry (Figure 122), by suitably changing orientation of the specimen with respect of the loading direction different combination of tension, shear and compression, can be obtained [112]. The approximate range of stress triaxiality and Lode angle parameter covered by butterfly tests is depicted in Figure 122. Compression tests are often performed to investigate the negative range of stress triaxiality and Lode angle parameter.

6.1 Drucker-Prager and von Mises Calibration and Verification - High-Density Polyethylene (HDPE)

6.1.1 Yield Stress Determination

The material transition from the elastic to the plastic state is called yielding. Depending on the stress-strain curve shape, the yield stress of semi crystalline polymers can be defined by several methods [178]. As mentioned before, ISO 527-1, defines the yield stress as the first stress at which an increase in strain occurs without an increase in stress [66]. However, the mechanical response of HDPE, PP and PA 6 does not systematically present an intrinsic yield stress drop for the different loading conditions.

In such case, the yield stress might be determined by the “Considère construction” or by “two tangent intersection method”, which is in essence, somewhat arbitrary. The strain off-set method inspired by the convention adopted for metallic materials is satisfactory for metals, where there is a clear distinction between elastic recoverable deformation and plastic irrecoverable deformation, but in polymers the distinction is not so straightforward [178].

Alternatively, the stress level at which yielding occurs can be determined from the deviation of the linear elastic response [5]. An example of the procedure used is shown in Figure 123. A trendline is applied in excel with $R^2 = 0.99$ (almost a straight line) covering the elastic range. The closer to 1, the more reliable the trendline, is. The points where the straight line diverge from the true stress-strain curves are the yield stress. This was the methodology adopted in this work, for the yield stress determination for all examined stress-strain curves.

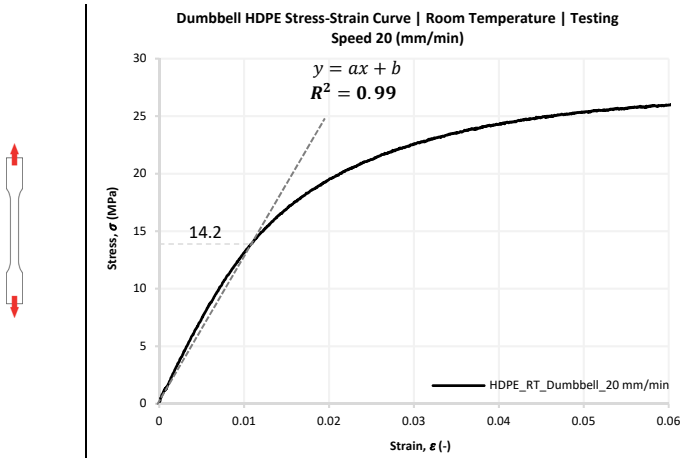


Figure 123 – Yield stress determination, example of procedure used for tensile test on dumbbell with crosshead speed of 20 mm/min. The value 14.2 MPa (σ_{ZZ}) is depicted in Table 110 in tensile dumbbell column.

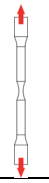
6.1.2 Numerical Calibration

A Drucker-Prager (with higher yield stress in compression than in tension) and a von Mises (same yield stress in compression and tension) yield criterion models, were used. In order to calibrate the material models for numerical simulations with finite element code Abaqus, the average values of stress, as well as the average values of the elastic modulus from the tensile tests on dumbbell, cylindrical notched and compression tests on cylindrical unnotched and cylindrical notched specimens with respective standard deviation together with the coefficient of variation are calculated. The respective values are tabulated in Table 110, for each crosshead speed.

Just a reminder: five tests were performed for each specimen geometry and crosshead speed to ensure the reproducibility. At 1 mm/min, the elastic modulus ranged from 1059 to 1070 MPa, exhibiting a standard deviation of 4.1 MPa. The standard deviation for 20 and 200 mm/min was similar 4.8 and 4.6 MPa, respectively.

The displacement measurements were obtained with MTS 634.25 axial extensometer in all tensile tests, whereas for compression and biaxial tests the displacement measurements were obtained from the MTS 810 as well as the Force. For cylindrical notched specimens, two measurement methods were performed: one with the extensometer and other using digital image, for local measurements in the specimen's gauge section. Therefore, for each image captured there is an associated load. The true stress-strain curves for all specimen geometries, were obtained from analytical formulas, depicted in section 3.3 Specimens Geometry and are resumed in Table 17. With the knowledge of this analytical expressions, the local stresses and strains in the elastic regime, were calculated and therefore, allowed the yield stress and elastic modulus to be extracted.

Table 110 - Elastic Modulus, stress components in tension and compression on yield at room temperature for HDPE.

					
	Tensile Dumbbell	Tensile Cylindrical Notched R 30	Tensile Cylindrical Notched R 5	Compression Cylindrical	Compression Cylindrical Notched R 5
REF	T_Dumbbell	T_CN_R30	T_CN_R5	C_C	C_CN_R5
1 mm/min					
σ_{zz} (MPa)	9.9	10.1	10.3	13.8	14.3
σ_{yy} (MPa)	0	0.4	1.8	0	0.5
σ_{xx} (MPa)	0	0.4	1.8	0	0.5
Elastic Modulus, *E* (MPa)	1059	1070	1061	1060	1060
Average, *E* (MPa)	1062				
Standard Deviation, *E*	4.1				
Coefficient of Variation, *E*	0.4%				
20 mm/min					
σ_{zz} (MPa)	14.2	14.4	14.6	18.2	18.9
σ_{yy} (MPa)	0	0.6	2.6	0	0.7
σ_{xx} (MPa)	0	0.6	2.6	0	0.7
Elastic Modulus, *E* (MPa)	1354	1357	1354	1359	1362
Average, *E* (MPa)	1357				
Standard Deviation, *E*	4.8				
Coefficient of Variation, *E*	0.4%				
200 mm/min					
σ_{zz} (MPa)	19.3	19.2	19.6	21.2	23.4
σ_{yy} (MPa)	0	0.8	3.5	0	0.9
σ_{xx} (MPa)	0	0.8	3.5	0	0.9
Elastic Modulus, *E* (MPa)	1477	1479	1467	1470	1465
Average, *E* (MPa)	1472				
Standard Deviation, *E*	4.6				
Coefficient of Variation, *E*	0.3%				

The true stress-strain curves for each specimen geometry and crosshead speed are shown in Figure 124. Multiple tested specimens were performed for each specimen geometry, but only a single representative true stress-strain curve for each specimen geometries is plotted, for a fixed crosshead speed.

From Figure 124, it is observed that the deformation of HDPE is very sensitive to hydrostatic pressure. In particular, the effect of pressure can be seen in the difference observed between stress-strain curves in tensile tests (HDPE_RT_T_CN_R5; HDPE_RT_T_CN_R5; HDPE_RT_T_ Dumbbell) and compression tests (HDPE_RT_C_CN_R5; HDPE_RT_C_CR), higher yield stress values, which are associated with a positive and negative pressure, respectively. Also, the effect of notched radii on the hydrostatic pressure, is observed. By decreasing the notched radius, increases the hydrostatic pressure and stress triaxiality, as well as the stress-strain curves reveals higher strength. It has been experimentally observed by several authors that the molecular mobility is reduced by the hydrostatic pressure, which might be a factor for the increase strength of the material [143]. Moreover, at higher crosshead speeds, the yield stress increases, for all specimen geometries.

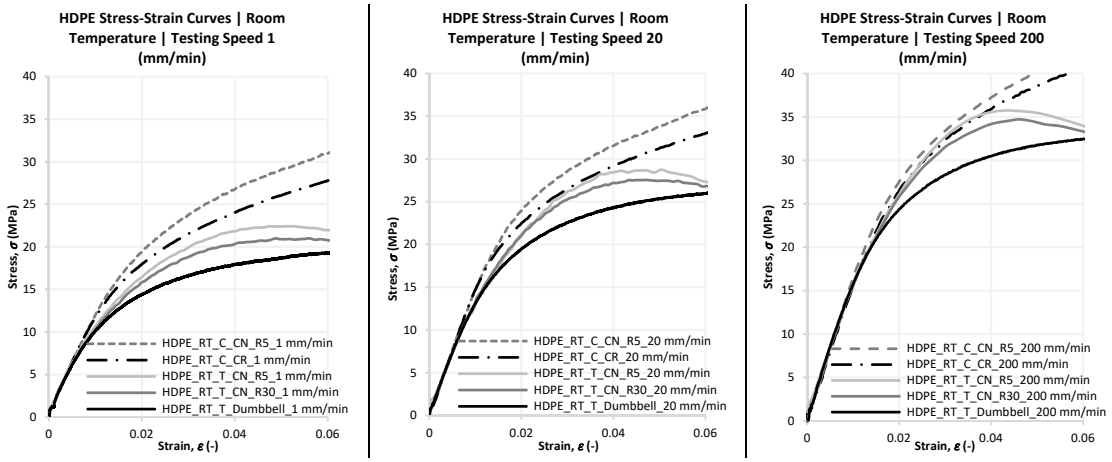


Figure 124 –True stress-strain curves for all 5 specimens geometries, for each crosshead speed. Only one curve is displayed for each specimen geometry and crosshead speed.

In this study, the plastic deformation is modelled by the Drucker-Prager plasticity model parameters, β which is the slope of the linear yield surface in the *p–q* stress plane, also known as friction angle, was identified through mechanical experimental results on tensile tests on dumbbell, cylindrical notched and compression tests on cylindrical and notched specimens, whereas the isotropic hardening, d was determined from tensile tests on dumbbell results. The hydrostatic pressure, p (hydrostatic pressure p is defined as $p = -\sigma_h$) and von Mises equivalent stress, q of Table 111, are plotted in Figure 125 (1), in order to determine the Drucker-Prager friction angle β. The two invariants, hydrostatic pressure, p and von Mises equivalent stress, q were obtained from analytical formulas, depicted in section 2.7.1, equations 2.19 and 2.20.

It is observed that the yield points corresponding to the tensile and compression results lie on the same straight line. The three lines are almost parallel, where with the increase of crosshead speed the higher is the (*p*-*q*) relation, illustrating the strain-rate sensitivity (hardening) of the

HDPE, while the friction angles β are 25°, 21° and 14°, respectively for crosshead speed 1, 20, 200 mm/min.

Table 111 - The von Mises equivalent stress (q) and hydrostatic pressure (p), are displayed.

	Tensile Dumbbell	Tensile Cylindrical Notched R 30	Tensile Cylindrical Notched R 5	Compression Cylindrical	Compression Cylindrical Notched R 5
1 mm/min					
q	9.9	8.5	9.7	13.8	13.8
p	-3.3	-4.7	-3.6	4.6	5.1
20 mm/min					
q	14.2	12.7	13.8	18.2	18.1
p	-4.7	-6.1	-5.2	6.1	6.8
200 mm/min					
q	19.3	17.0	18.8	21.2	22.4
p	-6.4	-8.3	-7.0	7.1	8.4

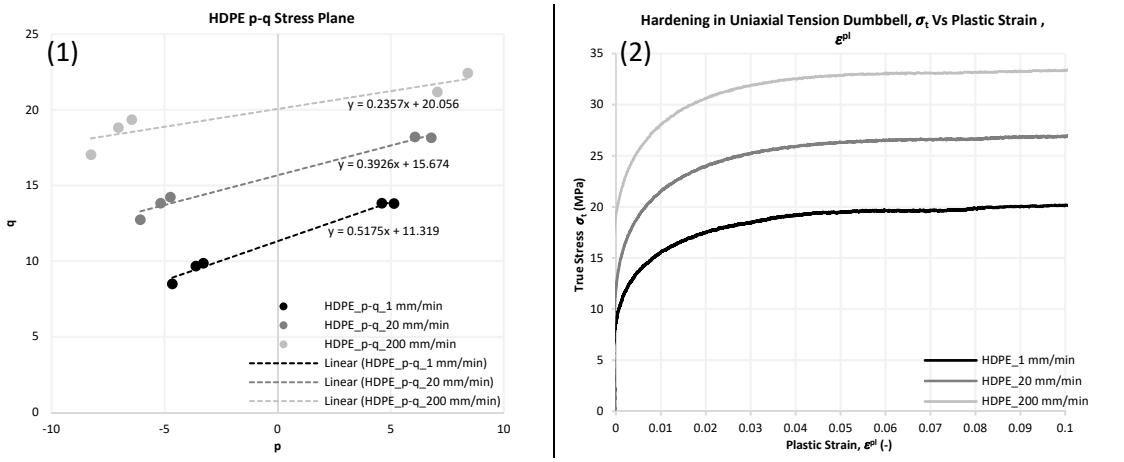


Figure 125 - (1) The equivalent stress and pressure of Table 111 are plotted. (2) Hardening curves for 1, 20 and 200 mm/min crosshead speed.

The yield behaviour of plastics depends on strain rate so, for maximum accuracy in predictions, hardening curves were determined over a range of strain rates. Determination of the hardening evolution, which is the plastic part of the true-strain curves of dumbbell: the true stress (σ_t) versus true plastic strain (ε_t) data from the tensile test on tensile dumbbell specimen, was used as input for the hardening curve, d parameter (the elastic strain part is ignored). In this step, only the data point before specimen necking can be used because the equations are valid only up to necking initiation. By using Hooke's law, the true plastic strain is obtained by:

$$True\ Plastic\ Strain\ \varepsilon_t^{pl} = \varepsilon_t - \frac{\sigma_t}{E}. \tag{6.1}$$

Here, ε_t^{pl} is the true plastic strain or equivalent plastic strain and E is the elastic modulus. The true stress-equivalent plastic strain curves are presented in Figure 125 (2). The strain hardening behaviour was only determined up to an equivalent plastic strain of 10% from a tensile dumbbell

experiment, due to the onset of necking. The hardening curves were introduced into Abaqus with eleven data points for equivalent plastic strains in Drucker-Prager and von Mises yield criterion Table 112.

Table 112 – Drucker Prager hardening in tension points for HDPE.

	Plastic Strain	**Yield Stress at 1 mm/min**	**Yield Stress at 20 mm/min**	**Yield Stress at 200 mm/min**
1	0	8.67	11.93	19.70
2	0.01	15.55	21.52	28.07
3	0.02	17.44	23.85	30.67
4	0.03	18.40	25.17	32.91
5	0.04	19.15	25.89	32.50
6	0.05	19.45	26.31	32.86
7	0.06	19.62	26.49	33.07
8	0.07	19.66	26.62	33.11
9	0.08	19.79	26.69	33.20
10	0.09	19.82	26.73	33.29
11	0.1	19.91	26.82	33.38

Numerical Simulation Parameters:

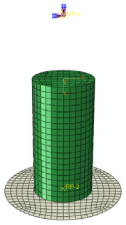
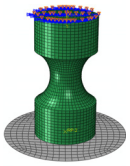
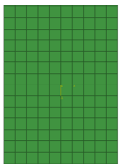
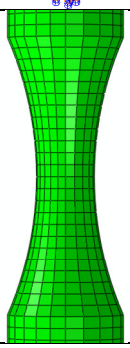
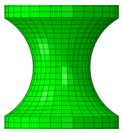
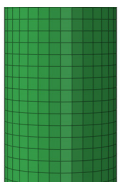
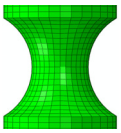
- Analyses type and mesh properties: numerical simulations were performed with the commercial finite element code Abaqus explicit version 6.16. ABAQUS three-dimensional reduced integration, eight-node linear solid element C3D8R with reduced integration, was used to construct the mesh. A finer and uniform mesh was generated in all specimen's geometry. As an example, for the Dumbbell: a total of 110080 C3D8R elements, connected by 113665 nodes, was used to construct the 3D model. The mesh models, element type, element shape, geometric order, number of elements and nodes for each specimen, are shown on Table 114.

- Material properties: Elastic-plastic material models were assigned, considering the material as isotropic and homogeneous. The simulations were carried out employing basic material properties, such as elastic model with elastic modulus, poisson's ratios and mass density. The basic materials properties for 1, 20 and 200 mm/min crosshead speeds are listed on Table 113. The poisson ratio and mass density were taken from literature [76], while the elastic modulus was taken from the true stress-strain curves defined by means of the deviation of the linear elastic response. Also, the identified parameters of Drucker-Prager plasticity model β and d, isotropic hardening (Table 112), were introduced into Abaqus. The d, parameter was assigned to both models, Drucker-Prager and von Mises.

Table 113 - Basic material properties assigned.

Testing Speed (mm/min)	**Elastic Modulus (MPa)**	**Poisson's Ratio** [76]	**Mass Density (g/cm³)** [76]
1	1062	0.4	0.964
20	1357		
200	1472		

Table 114 - Mesh models, element type, element shape, geometric order, number of elements and nodes.

	Tensile Dumbbell	**Tensile Cylindrical Notched R 30**	**Tensile Cylindrical Notched R 5**	**Compression Cylindrical Unnotched**	**Compression Cylindrical Notched R 5**
Meshed Model					
Meshed Detail - Center					
Element Type	C3D8R - the C3D8 element with reduced integration	C3D8R - the C3D8 element with reduced integration	C3D8R - the C3D8 element with reduced integration	C3D8R - the C3D8 element with reduced integration	C3D8R - the C3D8 element with reduced integration
Element Shape	Hexahedral	Hexahedral	Hexahedral	Hexahedral	Hexahedral
Geometric Order	Linear	Linear	Linear	Linear	Linear
Elements	110080	123648	122880	Specimen: 8920 / Base: 384	Specimen: 10520 / Base: 384
Nodes	113665	126140	129745	Specimen: 9373 / Base: 418	Specimen: 12051 / Base: 418

- Boundary conditions: The finite element simulation of the tensile tests was performed with the same boundary and loading conditions as the experimental reference. The bottom face of the specimens was constrained from moving in the vertical direction, while a vertical displacement was applied to the upper face, which simulates the movement of the crosshead. The clamped part of the specimen was omitted. A surface-to-surface contact with friction was introduced to model the interaction between the platen and the specimen in the compression of the cylindrical and cylindrical notched R 5, due to unknown friction coefficient (μ) between specimens and the platform of the testing machine. The friction coefficient is adjusted iteratively in the simulation to make the final deformed shape of specimens agree with the experimental results. The friction coefficient (μ) of 0.2 was used, which makes the load-displacement curves

agree well with the experimental ones. Also, the compression platens were modelled as rigid bodies employing R3D4 element type with 384 elements and 417 nodes. The bottom plate is fully fixed, and the upper plate is where displacement was applied.

Numerical Simulation Results:

The following simulations aim to check whether the material parameters, determined above, can reproduce the response of the tensile and compression tests. 3D finite element models with the same dimensions and geometries of experimental tests are used.

Numerical and experimental load-displacement responses are compared for three different crosshead speeds and specimen geometries (Figures 126 to 127). The solid lines represent numerical results while the dashed lines represent the results from the experimental tests (five tests). The numerical simulation captures the initial elastic range, however the post-elastic response is overestimated for notched specimens. For dumbbell and compression (unnotched specimen) simulations the results essentially matched the experimental results, whereas the peak force is well captured, with both Drucker-Prager and von Mises models. The best correlation is with Drucker-Prager yield criterion, even though there is a clear overestimation of the force in the post-elastic response, for notched specimens. The overestimation increases with the crosshead speed. Essentially von Mises is a pressure independent yield criterion. However, most polymers have a different behaviour in tension and compression. To take that aspect into account a pressure dependent criterion needs to be assumed, which happens with Drucker-Prager model.

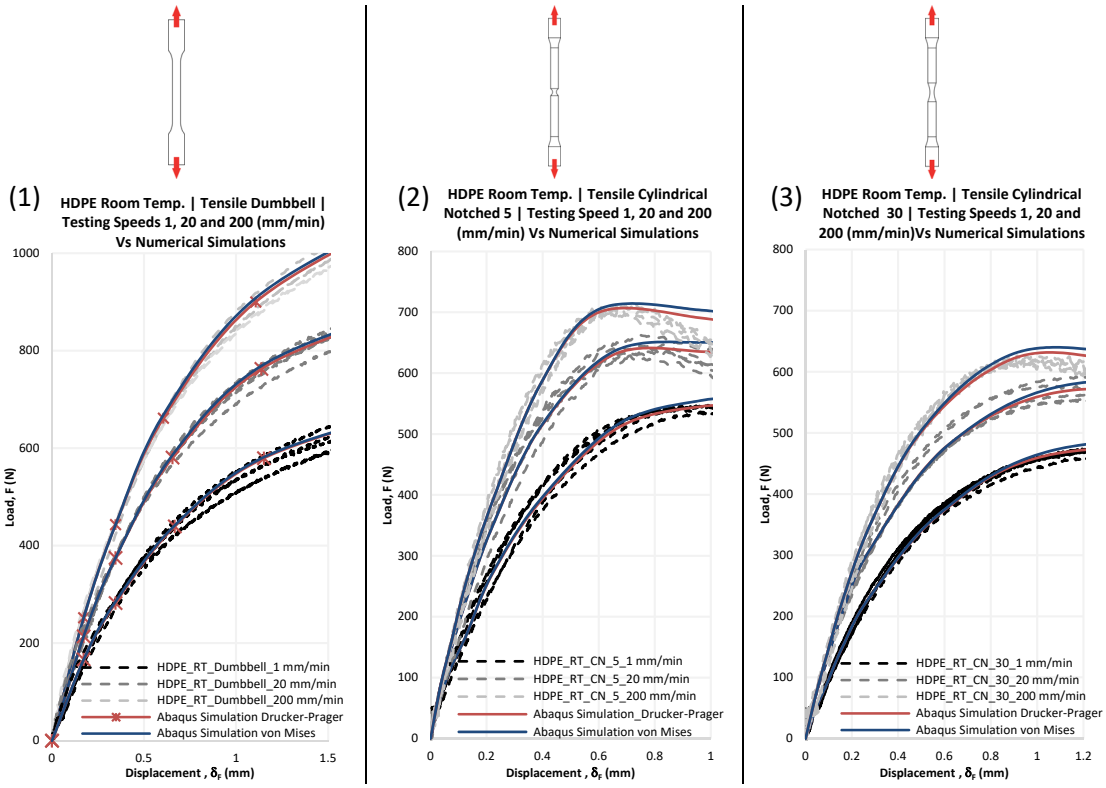


Figure 126 – Comparison of the numerical simulations with experimental results. Tensile load-displacement curves of (1) Dumbbell, (2) cylindrical notched 5 and (3) cylindrical notched 30 specimens (HDPE, Room Temperature).

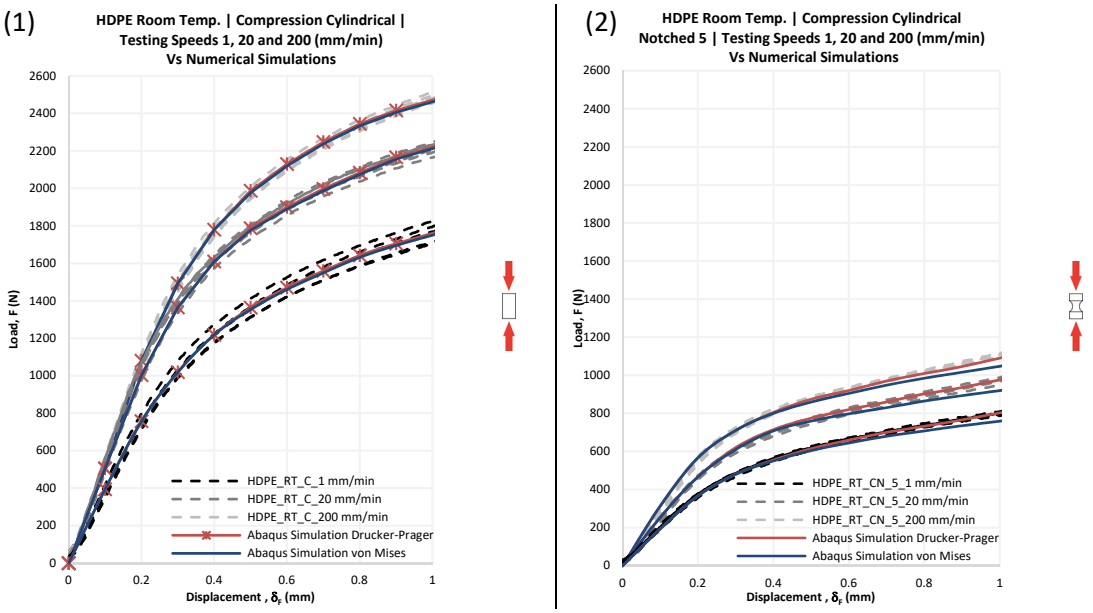


Figure 127 - Comparison of the numerical simulations with experimental results. Compression load-displacement curves of (1) cylindrical and (2) cylindrical notched specimens (HDPE, Room Temperature).

6.1.3 Numerical Verification

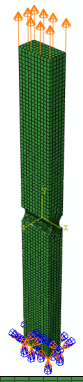
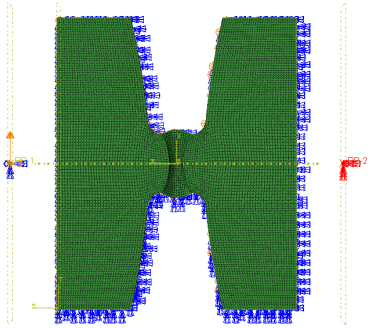
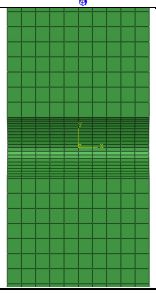
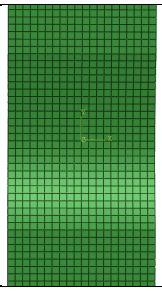
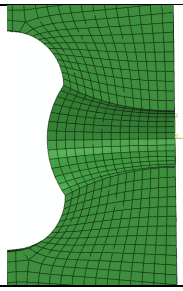
In order to assess the calibrated Drucker-Prager and von Mises yield criteria, the numerical simulations of flat notched specimens and of combined tensile/shear and compression/shear performed on butterfly specimens, were compared with the experimental load-displacement curves.

Numerical Simulation Parameters:

- Analyses type and mesh properties: Finite element analyses were performed using a general-purpose finite element code, Abaqus version 6.16. 3-D quadratic linear elements C3D8R and C3D20R were adopted in the simulation, where C3D8R is an eight-node linear brick element with reduced-integration points and C3D20R is a twenty-node linear brick element reduced-integration. The C3D8R and C3D20R elements, were chosen because the C3D8R is a first order element, while the C3D20R is a second order element. Second order elements provide higher accuracy for problems that do not involve complex contact conditions, impact, or severe element distortions and capture stress concentrations more effectively, however the drawback is that they are computationally more expensive than first-order elements [179].

- The finite element mesh of the flat notched specimens consisted of 121183 and 132257 eight-node linear brick element, C3D8R, respectively for radius 5 and 30, and the finite element mesh of butterfly model consisted of 1357123 twenty-node hexahedral element, C3D20R. Due to the symmetry of the butterfly specimen in the x-y plane, only half of the specimen was generated and the required boundary conditions were applied to simulate this symmetry plane. The mesh models, element type, element shape, geometric order, number of elements and nodes for each FE model, are shown on Table 115.

Table 115- Mesh models, element type, element shape, geometric order, number of elements and nodes.

	Tensile Flat Notched 5	**Tensile Flat Notched 30**	**Biaxial Tension / Compression Angle 90° | 1/2 Butterfly Specimen**
Meshed Model			
Meshed Detail - Center			
Element Type	C3D8R - the C3D8 element with reduced integration	C3D8R - the C3D8 element with reduced integration	C3D20R – 20 node quadratic brick, reduced integration
Element Shape	Hexahedral	Hexahedral	Hexahedral
Geometric Order	Linear	Linear	Quadratic
Elements	115350	126320	181200
Nodes	121183	132257	1357123

- Material properties: The elastic-plastic material models, Drucker-Prager plasticity model and von Mises model were assigned with the basic materials properties listed on Table 113 and on Table 112, for isotropic hardening. The Drucker-Prager plasticity model, was selected in Abaqus with the identified parameter, β friction angles, obtained in section 6.1.2 Numerical Calibration.

- Boundary conditions: For numerical simulations of flat notched, the bottom face of the specimen was constrained from moving in the vertical direction while a vertical displacement was applied to the upper face. The clamped part of the specimen was omitted. In the case of biaxial loading, the lateral shoulder surfaces of the butterfly specimen model were constrained, the lateral bottom was prevented from moving, whilst the vertical displacement was applied to the upper lateral surface (Figure 128). Exploiting the symmetry of the specimen geometry, only half of its thickness is used. Note that the arcan apparatus was assumed to be sufficiently stiff and was not modelled in the numerical simulations. In addition, the boundary conditions at the grips are applied to shoulders of the butterfly specimen, this is why the lateral shoulder surfaces of the butterfly specimen model were constrained (all surface in red).

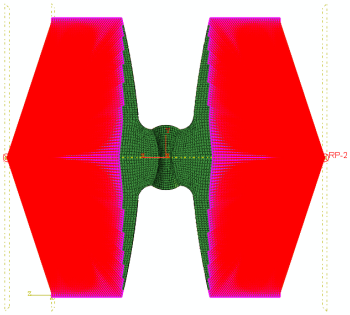


Figure 128 – Butterfly model, boundary constrains.

Numerical Simulation Results:

The predictions obtained by the calibrated criteria together with experimental tests on flat notched and biaxial loading on butterfly specimens are compared. The comparison of the experimental and numerical load-displacement curves, are presented in Figures 129 to 131. The solid lines represent numerical results while the dashed lines represent the results from the experimental tests (five tests). In general, it can be seen that the experimental results for the load-displacement curves have a close agreement with the results obtained with Abaqus simulation in the elastic range. They give the best correlation with Drucker-Prager yield criterion, which is pressure-sensitive criteria. Nevertheless, it is observed that after the post-elastic response there is an overestimation of the force. For cylindrical and flat notched results the initial response is reasonably well captured. However, we see a clear overestimation of the force in the plastic domain, with increasing of crosshead speed.

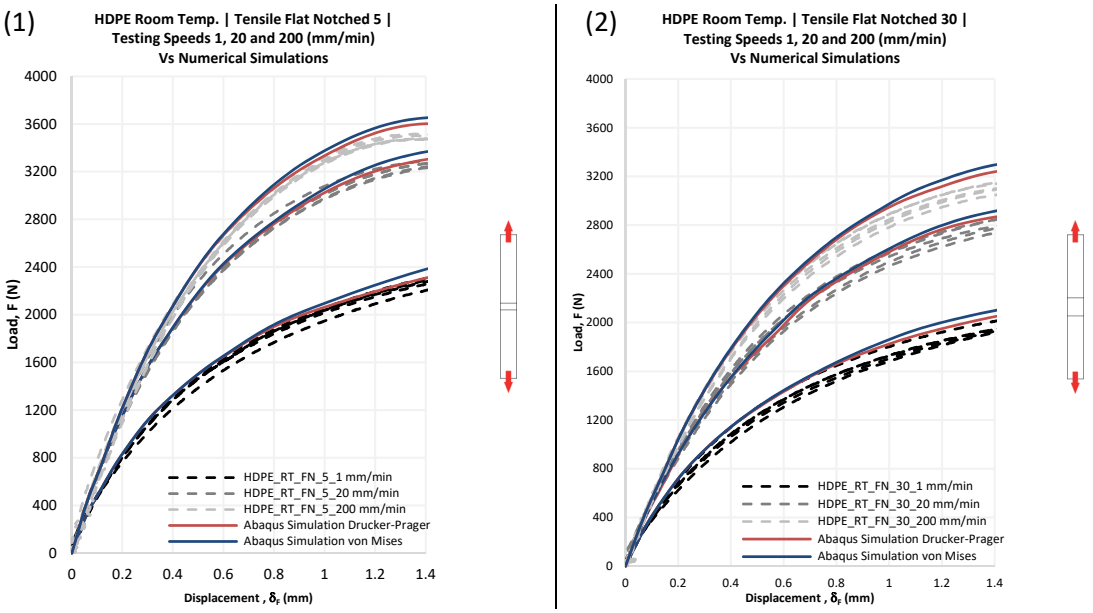


Figure 129 – Comparison of the numerical simulations with experimental results. Tensile load-displacement curves of (1) flat notched 5 and (2) flat notched 30 specimens (HDPE, Room Temperature).

Numerical simulations of the deformation of combined tensile/compression/shear on butterfly specimens are carried out to check whether the material parameters determined in section 6.1.2 Numerical Calibration are able to capture a more complex stress state. Load-displacement curves from the simulations are compared with those from the experimental tests. Thus, the capability of the Drucker-Prager and von Mises yield criterion models to capture the material response is explored through nonlinear finite element analyses of the combined experimental tests presented in section 4.1.2 Combined Tensile/Shear and 4.1.5 Combined Compression/Shear.

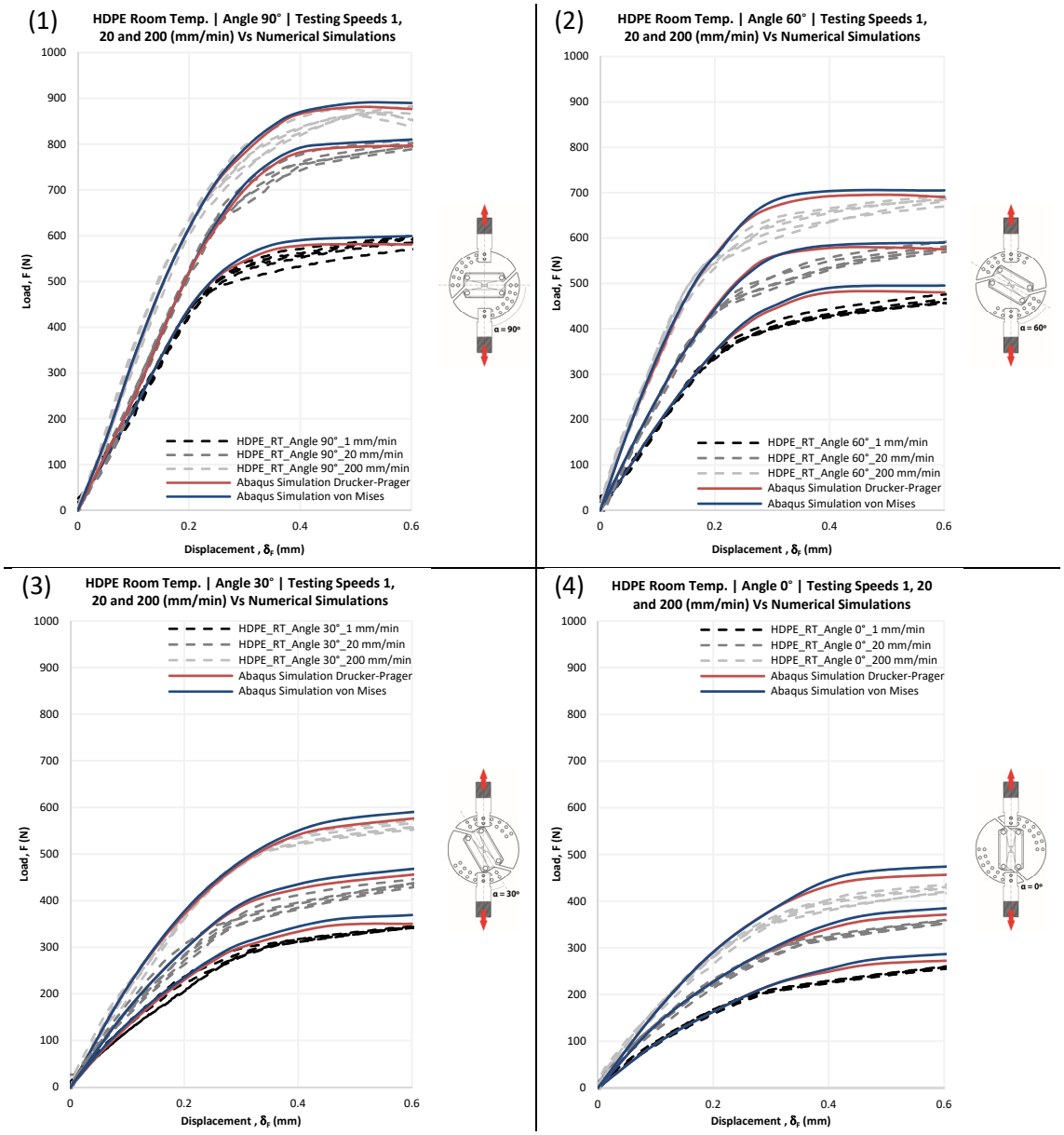


Figure 130 - Comparison of the numerical simulations with experimental results. Load-displacement curves for HDPE resulting from combined tensile/shear loading at RT. Loading angles: (1) α = 90°, (2) α = 60°, (3) α = 30° and (4) α = 0°.

The load-displacement curves from the numerical simulations of combined tensile/shear are compared with results from experiments in Figures 130. The initial response is reasonably well

predicted, within the elastic domain. As it has been observed, the Drucker-Prager yield criterion provides a closer agreement with the plastic deformation, however the post-elastic response is overestimated and the best correlation is for a loading angle α =90°, which corresponds to pure tension. For intermediate loading angles α = 60° and α = 30°, also in pure shear (α =0°) there is an overestimation of the force.

Figure 131 shows the results from the simulations together with the tests results of combined compression/shear. Drucker-Prager and von Mises yield criterion are capable of predicting the main features of the loading response. It can be seen, that for loading angles α = 60° to 30° at crosshead of 20 and 200 mm/min there is an underestimation and overestimation, respectively in the force values. The force predicted from the simulation is somewhat higher than the experimental results. However, for loading angle α = 90° there is a good agreement between numerical simulation and experimental test. The plastic deformation it is better predicted with Drucker-Prager yield criterion. Therefore, it is possible to concluded along as the stress state is close to the calibrated stress state, the yield criterions are able to predict the load-displacement response.

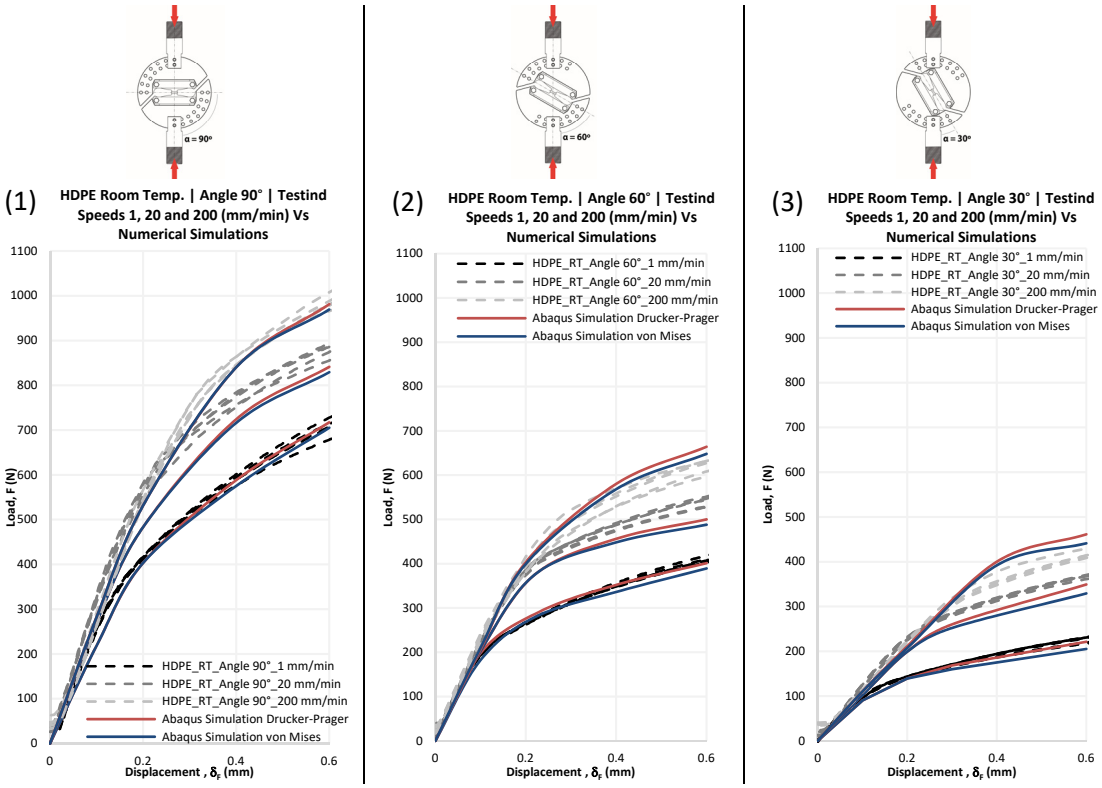


Figure 131 - Comparison of the numerical simulations with experimental results. Load-displacement curves for HDPE resulting from combined compression/shear loading at RT. Loading angles: (1) α = 90°, (2) α = 60° and (3) α = 30°.

Although the von Mises yield criterion is able to give an acceptable prediction of the mechanical response, it does not take into account the effect of the hydrostatic stress on the yield surface, depending only on the second invariant of the deviatoric stress tensor. Studies showed that the mechanical response of polymers is sensitive to hydrostatic stresses [88, 142, 145]. This can

easily be observed from the differences on mechanical experimental results on tensile and compression tests plotted in Figure 125 (1) or in the difference between stress-strain curves in tensile tests and compression tests in Figure 124, where the yield stress is found to be higher in compression. Also, the effect of notched radii on the hydrostatic pressure, is observed. By decreasing the notched radius, increases the hydrostatic pressure and stress triaxiality, as well as the stress-strain curves reveals higher strength. In more general terms it can be stated that the yield stress changes with the hydrostatic stress component. As a consequence of the commonly observed difference between the yield stress in tension and compression, material models with a pressure sensitive yield criterion are employed. However, Drucker-Prager yield criterion, even including the hydrostatic stress parameter and the isotropic hardening, determined from tensile dumbbell test, cannot predict accurately the load-displacement responses in some tests. Even though it allows a more precise prediction of deformation, than von Mises yield criterion it is still an isotropic criterion. The effect of Lode angle was not taken into account. Some studies however showed that the mechanical response of polymers is sensitive also to Lode angle parameter [180]. Thus, the Lode angle parameter effect should also be taken into account in the description of the plastic behaviour. For a more general approach, elastic and plastic anisotropy should be employed.

6.1.4 Drucker-Pager Model - Stress Triaxiality and Lode Angle Parameter

It is very difficult or even impossible to determine individual components of stress and strain at a particular location directly from physical experiments, which is possible through numerical simulation analysis. The correlation of the experimental and numerical results with Drucker-Prager model at crosshead speed of 1 mm/min essentially matches in terms of the load-displacement response. With the more accurate load-displacement responses, the local quantities obtained from simulations are believed to reasonably represent the real values.

Fracture ductility is understood as the ability of a material to accept large amount of deformation prior to fracture. In this section, the stress triaxiality and Lode angle parameter obtained with Drucker-Pager model for a crosshead speed of 1 mm/min and at plastic domain (not at fracture) of each specimen, are collected. From some experimental tests, at fracture initiation, characterized by a significant load drop in the load-displacement curves, a larger scatter is observed. Also, this type of sudden drop in force level did not occur in compression tests and fracture onset was not observed. Thus the displacement between the yield load and fracture point (plastic domain) was selected, in which the strain and corresponding stress states, are determined.

For some specimen geometries and loading conditions, namely notched and butterfly specimens, the fracture initiation location can be observed at the centre of the gauge section, during the experimental tests. However, it is difficult to determine directly from the experiments, whether the fracture initiates at the centre or at the outside surface of the specimen cross-section. In the present study, with the plastic strain and stress triaxiality evolution, it is possible to have a clue of the fracture location. Therefore, it is assumed that fracture initiates at the location with the highest stress triaxiality and plastic strain values.

The displacement in the model and experiment are correlated based upon the equivalent plastic strain. Table 116 lists the displacements for each specimen geometry, from where the components of stress triaxiality and Lode angle parameter and equivalent plastic strain, were determined. The displacements were taken from the load-displacement charts in Figures 126, 127, 129, 130 and 131. When the numerical simulation reaches the experimental displacement, for each specimen, the corresponding stress components and the equivalent plastic strain at the centre and at the outside surface, are extracted from the numerical model.

Table 116 – Displacements from where the stress triaxiality , Lode angle parameter and equivalent plastic strain were determined.

	Tensile Dumbbell	Tensile Cylindrical Notched R 5	Tensile Cylindrical Notched R 30	Compression Cylindrical Unnotched and Notched	Tensile Flat Notched R 5 and R 30	Butterfly – all loading angles
Displa. (mm)	1.5	1	1.2	1	1.4	0.6

Figure 132, illustrates the sites from where the stress triaxiality, Lode angle parameter and equivalent plastic strain, were collected. The evolution of the stress triaxiality and the Lode angle parameter with respect to plastic strain at the centre and at the outside surface are illustrated in Figures 133 and 134, respectively.

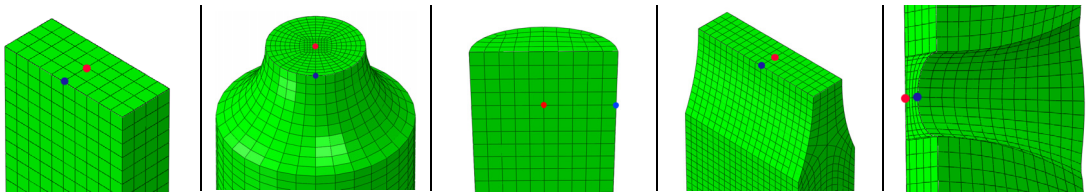


Figure 132 – Locations from where the strain and corresponding stress states were extracted, for each specimen geometry. Red dot, centre and blue dot, outside surface.

In Figures 133 (1) and 134 (1) the plastic strain and stress triaxiality at centre and at the outside surface, are shown. Generally, numerical simulations show that there is variation of the stress triaxiality and equivalent plastic strain along the cross section and the location of the maximum plastic strain and maximum stress triaxiality in the specimens are coincident for the investigated tests and are located at the centre of the specimen. It is found that the stress triaxiality increases with the equivalent plastic strain, the exception being for combined tension/shear $\alpha = 30°$, which decreases.

The stress triaxiality and Lode angle parameter values obtained from numerical simulations and initial stress triaxiality values calculated from analytical formulas, resumed in Table 17 are summarized in Tables 117 and 118.

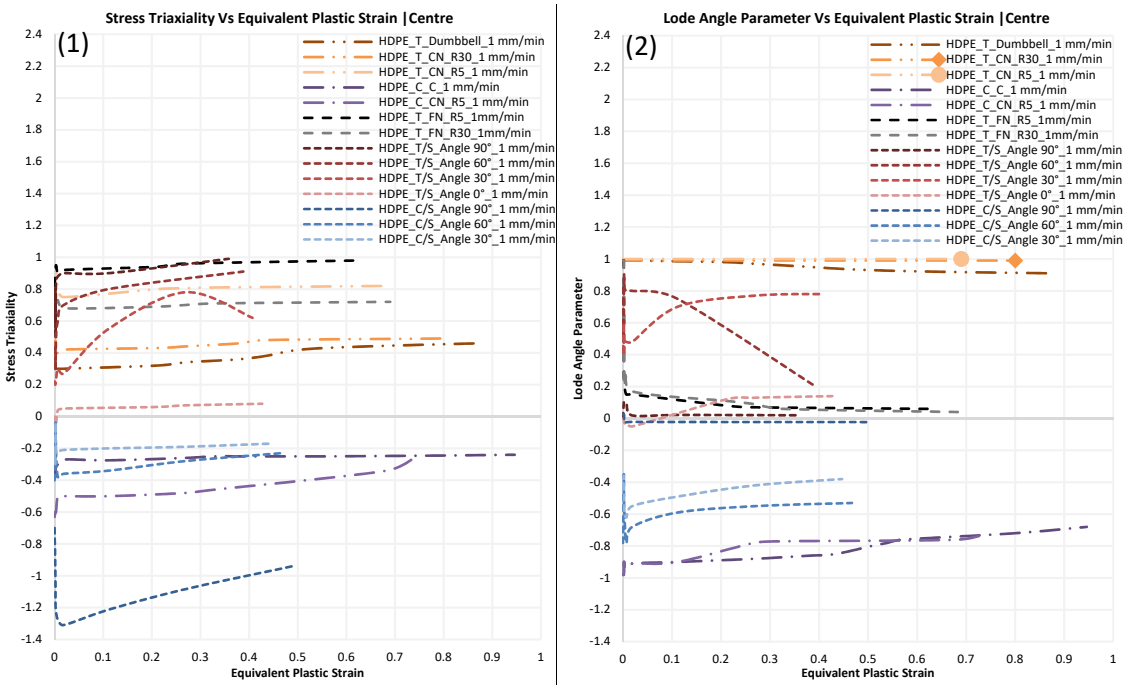


Figure 133 - Evolution of the (1) stress triaxiality and (2) Lode angle parameter with respect to plastic strain at centre, for all specimens geometries in study.

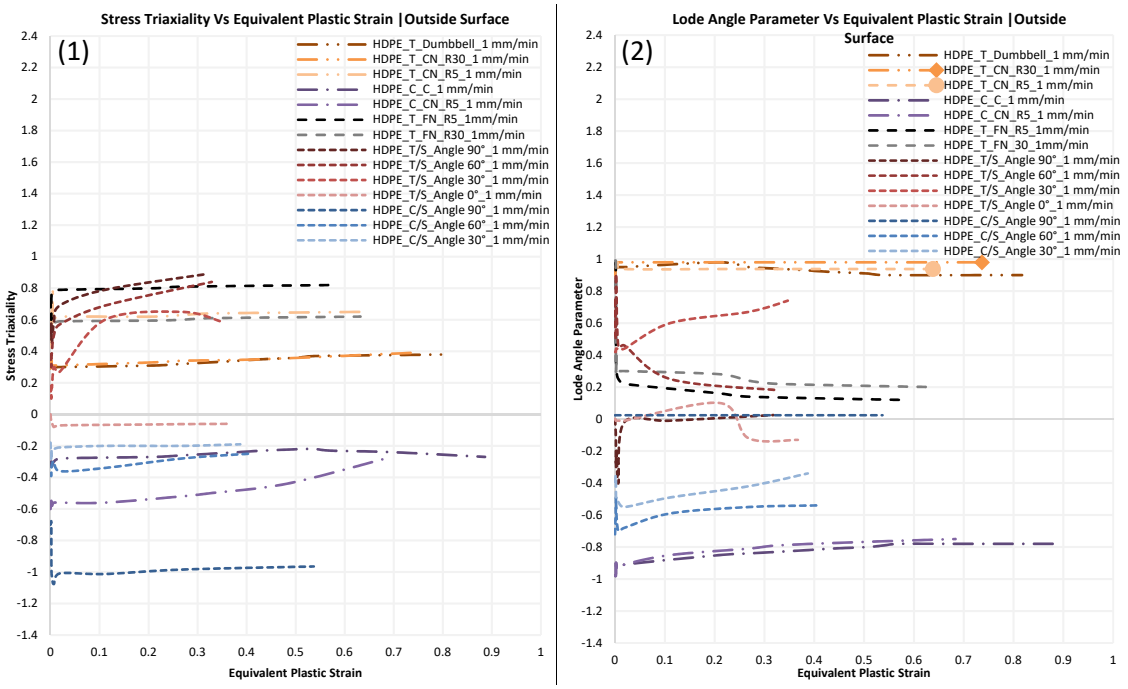


Figure 134 - Evolution of the (1) stress triaxiality and (2) Lode angle parameter with respect to plastic strain at outside surface, for all specimens geometries in study.

Table 117 - Stress triaxiality and Lode angle parameter values obtained from numerical simulations. The initial stress triaxiality values calculated from the analytical formulas are listed in the second column.

		Numerical Simulation | Calibration							
		Centre				**Outside Surface**			
Specimen Description	**Analytical Formulas, η_0**	η_0	θ_0	η_f	θ_f	η_0	θ_0	η_f	θ_f
Tension									
Dumbbell, 1 mm/min	1/3	0.33	0.95	0.46	0.91	0.33	0.96	0.38	0.90
Cylindrical R 5, 1 mm/min	0.64	0.61	0.99	0.82	0.99	0.52	0.95	0.65	0.94
Cylindrical R 30, 1 mm/min	0.39	0.36	0.99	0.52	0.98	0.29	0.9	0.39	0.98
Compression									
Cylindrical, 1 mm/min	- 1/3	-0.34	-0.98	-0.24	-0.68	-0.33	-0.98	-0.27	-0.70
Cylindrical R 5, 1 mm/min	- 0.64	-0.63	-0.99	-0.25	-0.72	-0.6	-0.99	-0.28	-0.75

Table 118 - Stress triaxiality and Lode angle parameter values obtained from numerical simulations. The initial stress triaxiality values calculated from the analytical formulas are listed in the second column.

		Numerical Simulation | Verification							
		Centre				**Outside Surface**			
Specimen Description	**Analytical Formulas, η_0**	η_0	θ_0	η_f	θ_f	η_0	θ_0	η_f	θ_f
Tension									
Flat R 5, 1 mm/min	0.84	0.82	0.99	0.98	0.06	0.73	0.98	0.82	0.12
Flat R 30, 1 mm/min	0.62	0.60	0.99	0.72	0.04	0.52	0.99	0.62	0.2
Combined Tensile/Shear									
α = 90°	0.58	0.60	0.07	0.99	0.02	0.52	0.02	0.89	0.03
α = 60°	0.38	0.43	0.82	0.91	0.21	0.38	0.74	0.84	0.18
α = 30°	0.19	0.22	0.42	0.62	0.78	0.18	0.42	0.59	0.74
α = 0°	0	0.01	0.02	0.08	0.14	0.01	0.01	-0.06	-0.13
Combined Compression/Shear									
α = 90°	-0.58	-0.70	-0.03	-0.93	-0.02	-0.52	0.02	-0.96	0.03
α = 60°	-0.38	-0.40	-0.78	-0.23	-0.53	-0.38	-0.72	-0.25	-0.54
α = 30°	-0.19	-0.23	-0.44	-0.17	-0.38	-0.18	-0.39	-0.19	-0.34

Ognedal [88], in her investigation on tensile cylindrical notched specimens made of HDPE and PVC, found that the stress triaxiality varies with the radial distance from the centre axis of specimen and has the highest stress triaxiality at the centre. The radial distributions of the stress triaxiality in the different specimens were found from finite element simulations. Similar results are observed for HDPE cylindrical notched specimens. The strain gradient through the thickness

is small (the difference of strain between the middle of thickness and surface is less than 4%), however, the difference of the stress triaxiality is not negligible and in fact is about 20% for cylindrical R 5 in tension (Table 117) between the centre and the outside surface. Therefore, the fracture initiation can be assumed to initiate at the centre of specimens. Flat notched specimens, also presents higher values of stress triaxiality and equivalent plastic strain at the centre. For notched specimens, decreasing the notch radius the stress triaxiality values increases and the difference between the initial and final values are higher at centre.

For combined tensile/shear loading angles for α = 0° shear and α = 30°, also in compression cylindrical notched and unnotched, the difference in the stress triaxiality at the centre and at the outside surface is not significant. For these situations, the locations with higher equivalent plastic strain, which is at the centre, determines the localization of the possible fracture initiation. For loading angle α = 60° and α = 90° the location with the highest stress triaxiality and plastic strain is at the centre. For combined compression/shear loading angle α = 90° the stress triaxiality is slightly higher at the centre, whereas the plastic strain is higher on the outside surface. For this loading angle fracture is assumed to initiate at outside surface. Except for combined tensile/shear loading angles of α = 90°, α = 60° and α = 30° and combined compression/shear α = 90° performed on butterfly specimens, the stress triaxiality shows a slightly increasing trend through deformation. In the above exceptions the stress triaxiality increases rapidly at the beginning and then slightly increases in a linear manner. The maximum difference of stress triaxiality between the beginning and the end of deformation at centre is around 52,7% for α = 60° combined tensile/shear (Table 118). Also the numerical simulation reveals that the stress triaxiality values at beginning and at outside surface are lower than the values obtained for the centre for tensile, whereas for compression the initial stress triaxiality values are higher at outside surface.

It should be noted that the Lode angle parameter has a constant value ($\overline{\theta} = 1$) during loading, of cylindrical notched specimens and the stress triaxiality varies with the notch radius (Figures 133 (2) and 134 (2)). The smaller the notch radius is, the higher the stress triaxiality is. In the case of flat notched, the Lode angle parameter converges very quickly to ($\overline{\theta} = 0$) and remains constant through the loading to fracture, while the stress triaxiality value is different for specimens having different groove radius. For combined tensile/shear loading α = 0° (pure shear) performed on butterfly specimens, the stress triaxiality and Lode angle parameter remain close to zero and for combined tensile/shear loading α = 60° the Lode angle parameter decreases from 0.82 to 0.21. There is a significant fluctuation on the Lode angle parameter. On the loading path, the material starts with a near axisymmetric tension ($\overline{\theta} = 0.82$) and transforms to a near tensile shear ($\overline{\theta} = 0.21$). Note that it is observed a nearly constant Lode angle parameter of, $\overline{\theta} = 0$, for combined loading angle α = 90°.

Tables 117 and 118, analytical solutions for initial values of stress triaxiality are compared to the numerical results. The comparison shows reasonable good agreement between analytical and numerical solutions for the values at the centre of the specimens. The existence of some differences is mainly due to the fact that the analytical solution is based on the average value of the whole cross-section.

The stress triaxiality and Lode angle parameter space is covered with several different type of specimens and loading conditions. Each specimen is assumed to represent a single point in the space of stress triaxiality and Lode angle parameter. For all tests, the stress triaxiality and Lode angle parameter values are plotted in Figure 135. It is observed that tensile cylindrical notched stay on the line corresponding to axial symmetry ($\overline{\theta} = 1$), flat notched is in the state of plane strain ($\overline{\theta} = 0$) as well as butterfly at loading angle of α = 90° in both loadings: tension and compression. The point with the coordinates (0, 0) represents pure shear and is given by butterfly specimen at loading angle of α = 0°. Points between $\overline{\theta} = \pm 1$ and $\overline{\theta} = 0$ corresponds to compression on cylindrical unnotched and notched specimens and combined loading angles of α = 30° and α = 60°. A reduction of the stress triaxiality and Lode angle parameter space for outside surface results, is observed.

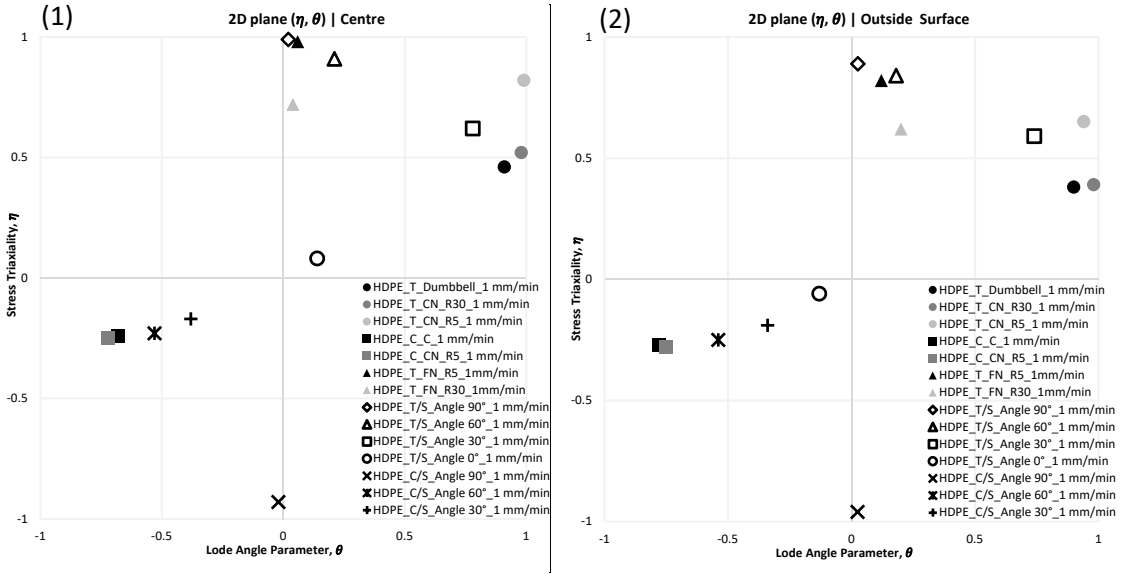


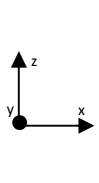
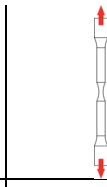
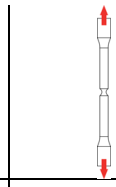
Figure 135 - Effect of stress triaxiality and Lode angle parameter on the equivalent plastic strain of HDPE based on the experimental and numerical results. (1) At centre and (2) at outside surface.

6.2 Drucker-Prager and von Mises Calibration and Verification - Polypropylene (PP).

A series of tests including tensile tests, combined tensile/shear tests, compression tests, combined compression/shear tests on PP (Figure 122) providing the evolution of the stress state variables, stress triaxiality and Lode angle parameter with respect to plastic strain, were carried out. Following the procedures described in previous section, in this section the same strategy will be applied for PP. The experimental load-displacement responses discussed in section 4.2 Polypropylene (PP) are used as reference for the numerical simulations. Numerical simulations are carried out with a von Mises yield criterion, and with a Drucker-Prager yield criterion to determine the numerical load-displacement responses. Nevertheless, the von Mises plasticity model does not take the hydrostatic pressure nor the Lode angle parameter into account. A relative good correlation between the experiments and numerical simulations was achieved, with Drucker-Prager yield criterion from which the two stress state parameters, stress triaxiality and Lode angle parameter, were extracted.

6.2.1 Numerical Calibration

Table 119 – Elastic Modulus, yield loci, stress components in tension and compression at room temperature for PP

					
	Tensile Dumbbell	Tensile Cylindrical Notched R 30	Tensile Cylindrical Notched R 5	Compression Cylindrical	Compression Cylindrical Notched R 5
REF	T_Dumbbell	T_CN_R30	T_CN_R5	C_CR	C_CN_R5
1 mm/min					
σ_{zz} (MPa)	13.6	13.7	13.9	17.6	18.3
σ_{yy} (MPa)	0	0.5	3.2	0	0.7
σ_{xx} (MPa)	0	0.5	3.2	0	0.7
Elastic Modulus, *E* (MPa)	1140	1144	1142	1152	1150
Average, *E* (MPa)	1146				
Standard Deviation, *E*	6.7				
Coefficient of Variation, *E*	0.6%				
20 mm/min					
σ_{zz} (MPa)	17.3	17.5	17.9	21.3	22.1
σ_{yy} (MPa)	0	0.7	3.2	0	0.9
σ_{xx} (MPa)	0	0.7	3.2	0	0.9
Elastic Modulus, *E* (MPa)	1269	1266	1268	1274	1263
Average, *E* (MPa)	1268				
Standard Deviation, *E*	6.0				
Coefficient of Variation, *E*	0.5%				
200 mm/min					
σ_{zz} (MPa)	20.8	21.7	22.4	25.3	26.1
σ_{yy} (MPa)	0	0.9	4.0	0	1.2
σ_{xx} (MPa)	0	0.9	4.0	0	1.2
Elastic Modulus, *E* (MPa)	1373	1359	1365	1368	1356
Average, *E* (MPa)	1364				
Standard Deviation, *E*	5.3				
Coefficient of Variation, *E*	0.4%				

Experimental investigations give information about the physical nature of the material. However, in the experimental measurements it is not possible to perform direct measurements at local material points such as in the specimens middle gauge section. Therefore, numerical simulations are required to reveal the physical information in conjunction with experiments. Drucker-Prager and von Mises yield criterion models, were used.

The property requirements for von Mises and Drucker-Prager models are: (1) elastic modulus, poisson's ratios and mass density as well as (2) tensile hardening curves $\sigma_t(\varepsilon_t^{pl})$, while for Drucker-Prager adds the parameters, β, which is the slope of the linear yield surface in the *p–q* stress plane, also known as the hydrostatic stress sensitivity parameter.

Table 119, depicts the average values of stress and elastic modulus of tensile tests on dumbbell, cylindrical notched and compression tests on cylindrical unnotched and cylindrical notched specimens, as well as the average values of the elastic modulus and respective standard deviation and coefficient of variation for PP, for each crosshead speed. The average values of stresses and elastic modulus are used to calibrate the material models for numerical simulations with finite element code Abaqus. A detailed description on the way of determining the true stress-strain curves of all specimen geometries is described in section 3.3 Specimens Geometry and summarized in Table 17. With the knowledge of this analytical expressions, the local stresses and strains in the elastic domain, were calculated and therefore, allowed the yield stress and elastic modulus to be extracted. The stress level at which yielding occurs was determined from the deviation of the linear elastic response, (see section: 6.1.1 Yield Stress Determination).

The true stress-strain curves of each specimen geometries and crosshead speed are shown in Figure 136. Multiple tested specimens were performed for each specimen geometry, but only a single representative true stress-strain curve for each specimen geometries is depicted, for a fixed crosshead speed. In the triaxial test, strength of the material is found to increase with the increasing confining pressure (lower notched radius). Also, the effect of pressure can be seen in the difference observed between stress-strain curves in tension and compression. The notched radius and loading rate influence the stress-strain behaviour of PP. It is observed a post yield stress softening and hardening behaviour on tensile tests.

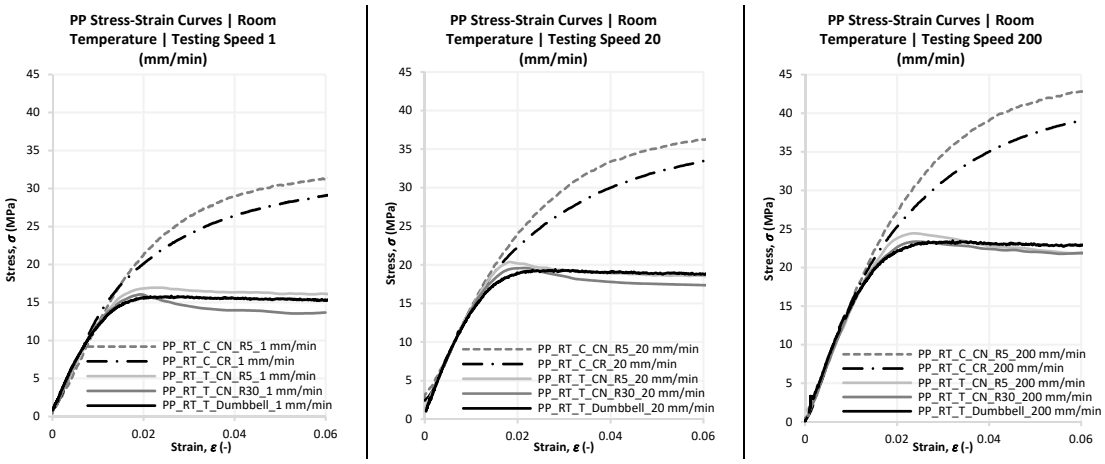


Figure 136 –True stress-strain curves for all 5 specimens geometries, for each crosshead speed. Only one curve is displayed for each specimen geometry and crosshead speed.

Table 120, are tabulated the two invariants, hydrostatic pressure, p and von Mises equivalent stress, q which were obtained from analytical formulas, depicted in section 2.7.1, equations 2.19 and 2.20. They were calculated based on the values of stress on tensile tests on dumbbell, cylindrical notched and compression tests on cylindrical and notched specimens, on Table 119. The p and q data of Table 120, are plotted in Figure 137 (1), in order to determine the Drucker-Prager friction angle β.

Table 120 - The von Mises equivalent stress (q) and hydrostatic pressure (p), are displayed.

	Tensile Dumbbell	Tensile Cylindrical Notched R 30	Tensile Cylindrical Notched R 5	Compression Cylindrical	Compression Cylindrical Notched R 5
1 mm/min					
q	13.6	11.2	13.2	17.6	17.6
p	-4.5	-6.1	-4.9	5.9	6.6
20 mm/min					
q	17.3	15.5	16.8	21.3	21.2
p	-5.8	-7.6	-6.3	7.1	8.0
200 mm/min					
q	20.8	19.2	20.8	25.3	24.9
p	-6.9	-9.6	-7.8	8.4	9.5

It is observed that the yield points corresponding to the tension and compression results lie on the same straight line. The three lines are almost parallel, where with the increase of crosshead speed the higher is the (*p*-*q*) relation, illustrating the strain-rate sensitivity (hardening) of the PP, while the friction angle β is 22°, 18° and 15 °, respectively for crosshead speed 1, 20, 200 mm/min. The difference between the yielding in tension and that in compression are due to hydrostatic pressure.

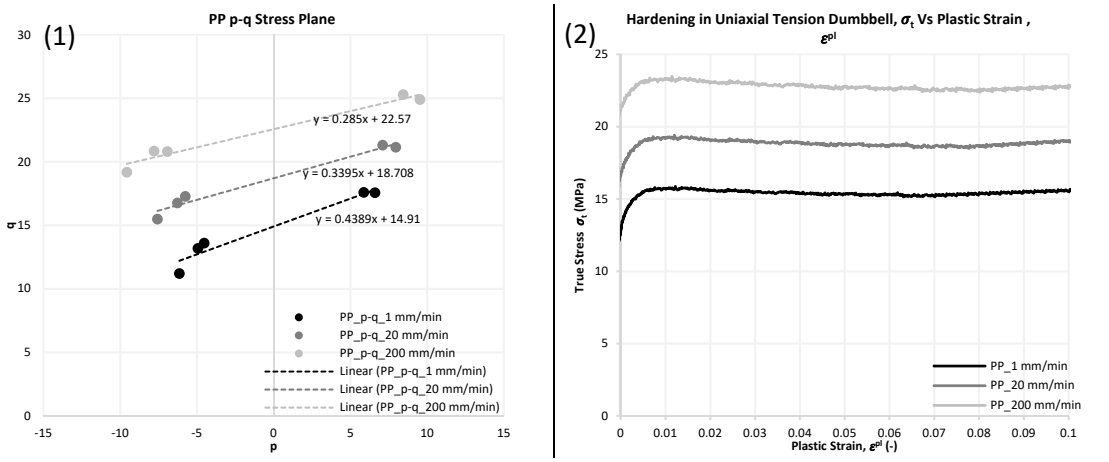


Figure 137 - (1) The equivalent stresses and pressures of Table 120 are plotted. (2) Hardening curves for 1, 20 and 200 mm/min crosshead speed.

The true stress-equivalent plastic strain curves are presented in Figure 137 (2). The strain hardening behaviour was only determined up to an equivalent plastic strain of 10% from a tensile dumbbell experiment, due to the onset of necking and by using the equation 6.1 in section 6.1.2. The hardening curves were introduced into Abaqus with eleven data points for

equivalent plastic strain in Drucker-Prager and von Mises yield criterion, which are listed in Table 121.

Table 121 – Drucker Prager hardening in tension, points for PP.

	Plastic Strain	Yield Stress at 1 mm/min	Yield Stress at 20 mm/min	Yield Stress at 200 mm/min
1	0	12.62	16.65	21.19
2	0.01	15.75	19.24	23.35
3	0.02	15.57	19.01	23.12
4	0.03	15.41	18.85	22.98
5	0.04	15.39	18.79	22.86
6	0.05	15.36	18.75	22.75
7	0.06	15.27	18.61	22.63
8	0.07	15.26	18.60	22.44
9	0.08	15.25	18.59	22.40
10	0.09	15.41	18.75	22.68
11	0.1	15.53	19.97	22.72

Numerical Simulation Parameters:

In section 6.1.2, all the information about numerical simulation parameters such as the mesh models, element type, element shape, geometric order, number of elements and nodes as well as boundary conditions are described and the same are used hereinafter. Numerical simulations were performed with the commercial finite element code Abaqus explicit version 6.16.

Elastic-plastic material models were assigned to the specimens, considering the material as isotropic and homogeneous. The simulations were carried out employing basic materials properties. The basic materials properties for 1, 20 and 200 mm/min crosshead speeds are listed on Table 122. The poisson ratio and mass density were taken from literature [76], while the elastic modulus was taken from the true stress-strain curves defined by means of the deviation of the linear elastic response. The friction angle β, parameter was assigned into Drucker-Prager model, while the eleven data points for equivalent plastic strain (Table 121) were assigned in both, Drucker-Prager and von Mises.

Table 122 - Basic material properties assigned.

Testing Speed (mm/min)	Elastic Modulus (MPa)	Poisson's Ratio [76]	Mass Density (g/cm^3) [76]
1	1146	0.38	0.905
20	1268		
200	1364		

Numerical Simulation Results:

The following simulations aim to check whether the material parameters, determined above, can reproduce the response of the tensile and compression tests of PP, presented in sections 4.2.1 and 4.2.4. Thus, the capability of the Drucker-Prager and von Mises yield criterion models

are explored. 3D finite element models with the same dimensions and geometries of experimental tests are used. In the following, load-displacement curves from the numerical simulations will be presented together with experimental results and compared (Figures 138 and 139). The solid lines represent numerical results while the dashed lines represent the results from the experimental tests (five tests).

Similar with HDPE results, the response of dumbbell and compression (unnotched specimen) simulations seems to be well captured by both finite element models and the results are in close agreement with the experimental results. For cylindrical notched specimens, on the other hand, the numerical simulation captures well the initial elastic range, however the post-elastic response is overestimated. It is seen that it is predicted higher maximum force level for specimens with smaller notch radius and the softening behaviour in the experimental test is not captured by both numerical simulations. Even though the best correlation is with Drucker-Prager yield criterion. The mismatched in load displacement curves increases with the crosshead speed.

It is shown that the parameters of the von Mises model with isotropic hardening rule, determined from tensile dumbbell test, cannot predict correctly the load-displacement responses in the notched specimens. The reason for that is the notched specimens are subjected to higher hydrostatic pressure than the cylindrical unnotched or in dumbbell. Thus, Drucker-Prager model with the hydrostatic-pressure and isotropic hardening, brings a better correlation with test results, however the notched cylindrical simulations still over-predict the load-displacement curves.

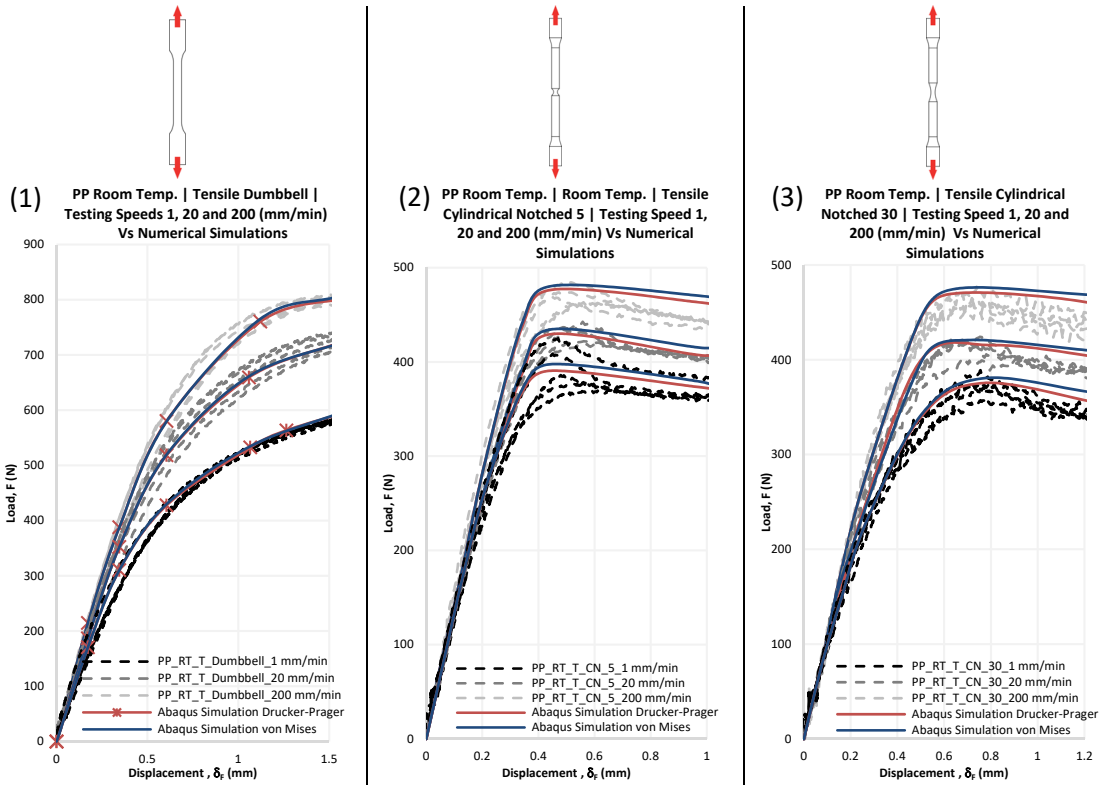


Figure 138 – Comparison of the numerical simulations with experimental results. Tensile load-displacement curves of (1) Dumbbell, (2) cylindrical notched 5 and (3) cylindrical notched 30 specimens (PP, Room Temperature).

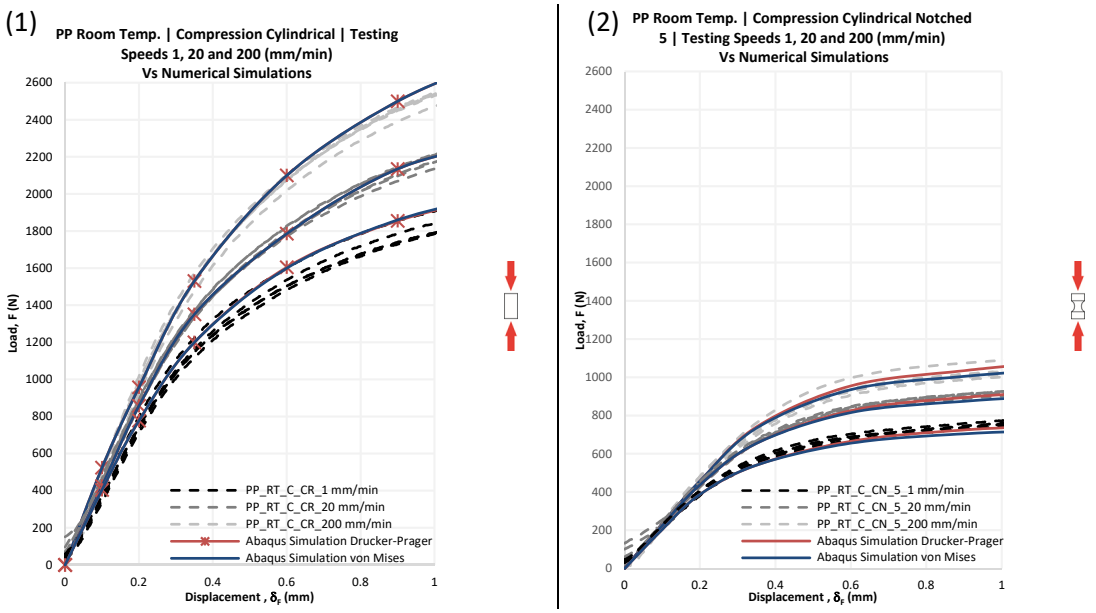


Figure 139 - Comparison of the numerical simulations with experimental results. Compression load-displacement curves of (1) cylindrical and (2) cylindrical notched specimens (PP, Room Temperature).

6.2.2 Numerical Verification

In sections 4.2.1, 4.2.2 and 4.2.5, experimental tensile tests have been performed on flat notched specimens with two notches of different sizes, combined tension/shear and combined compression/shear, and were examined and analysed. This section is concerned with how the material models Drucker-Prager and von Mises yield criterion represent the triaxial stress states and combined stress states, from the above experimental program. The numerical simulations were compared with the with the experimental results to check the agreement.

Numerical Simulation Parameters:

In section 6.1.3 Numerical Verification, all information about numerical simulation parameters such as the mesh models, element type, element shape, geometric order, number of elements and nodes as well as the boundary conditions is described and the same are used hereinafter.

Material properties: The elastic-plastic material models, Drucker-Prager plasticity model and von Mises model were assigned with the basic materials properties listed on Table 122, and with the eleven data points for equivalent plastic strain on Table 121, for isotropic hardening. The Drucker-Prager plasticity model, was introduced into Abaqus with the identified parameter, β friction angles, 22°, 18° and 15 °, respectively for crosshead speed 1, 20, 200 mm/min. The slope of the linear yield surfaces are plotted in Figure 137 (1).

Numerical Simulation Results:

The finite element results using von Mises yield function and Drucker-Prager yield function are compared to the experimental results in Figures 140 to 142. The solid lines represent numerical results while the dashed lines represent the results from the experimental tests (five tests). The

load-displacement curves from simulations and experimental tests are plotted in Figure 140 for flat notched specimens. It ca be observed that the experimental results for the load-displacement curves are fitted by Abaqus simulation in the elastic range. However, there is an overestimation of the force in the post-elastic response, which increases with the development of the plastic domain and with increasing of crosshead speed. The best correlation is with Drucker-Prager yield criterion. Even though Drucker-Prager yield criterion is linearly dependent on hydrostatic stress, it did not match accurately in the post-elastic response.

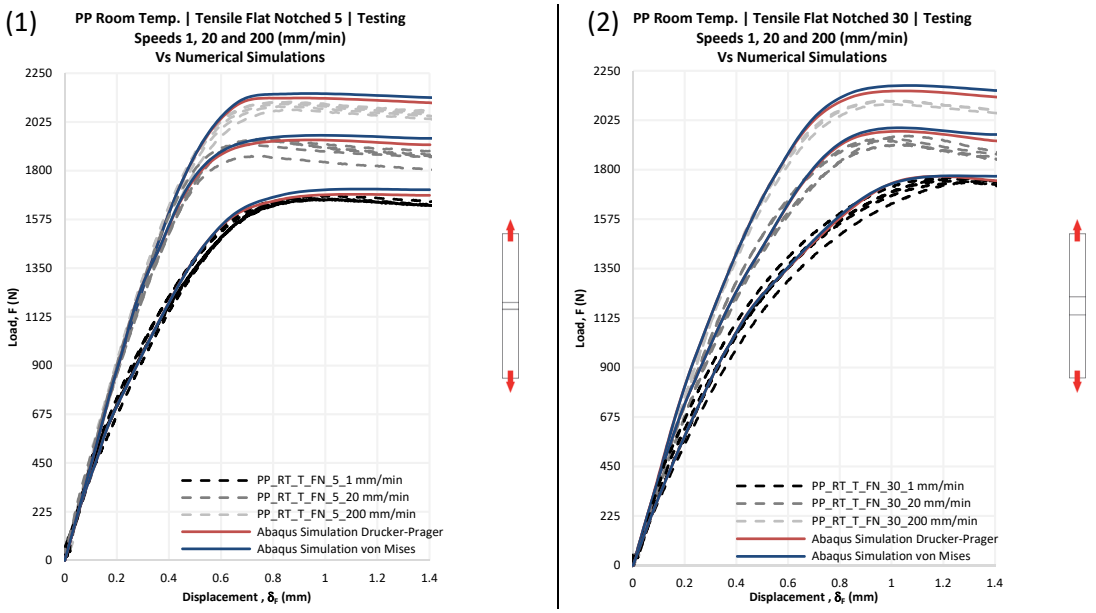


Figure 140 – Comparison of the numerical simulations with experimental results. Tensile load-displacement curves of (2) flat notched 5 and (3) flat notched 30 specimens (PP, Room Temperature).

The load-displacement curves from the numerical simulations of combined tensile/shear and combined compression/shear are compared with results from experiments in Figures 141 and 142. The initial responses are reasonably well predicted. Drucker-Prager yield criterion captures better the plastic deformation, however the post-elastic response is overestimated. For combined tensile/shear the best agreement between numerical and experimental results is with loading angle α =90°, pure tension, although the softening behaviour is not captured. Decreasing the loading angle, α =90° to α =0° increases the overestimation.

In combined compression/shear It is observed that Drucker-Prager and von Mises yield criterion are capable of predicting the main features of the loading response. It can be seen, that the worst result occurs for a loading angle α = 30° at 20 mm/min.

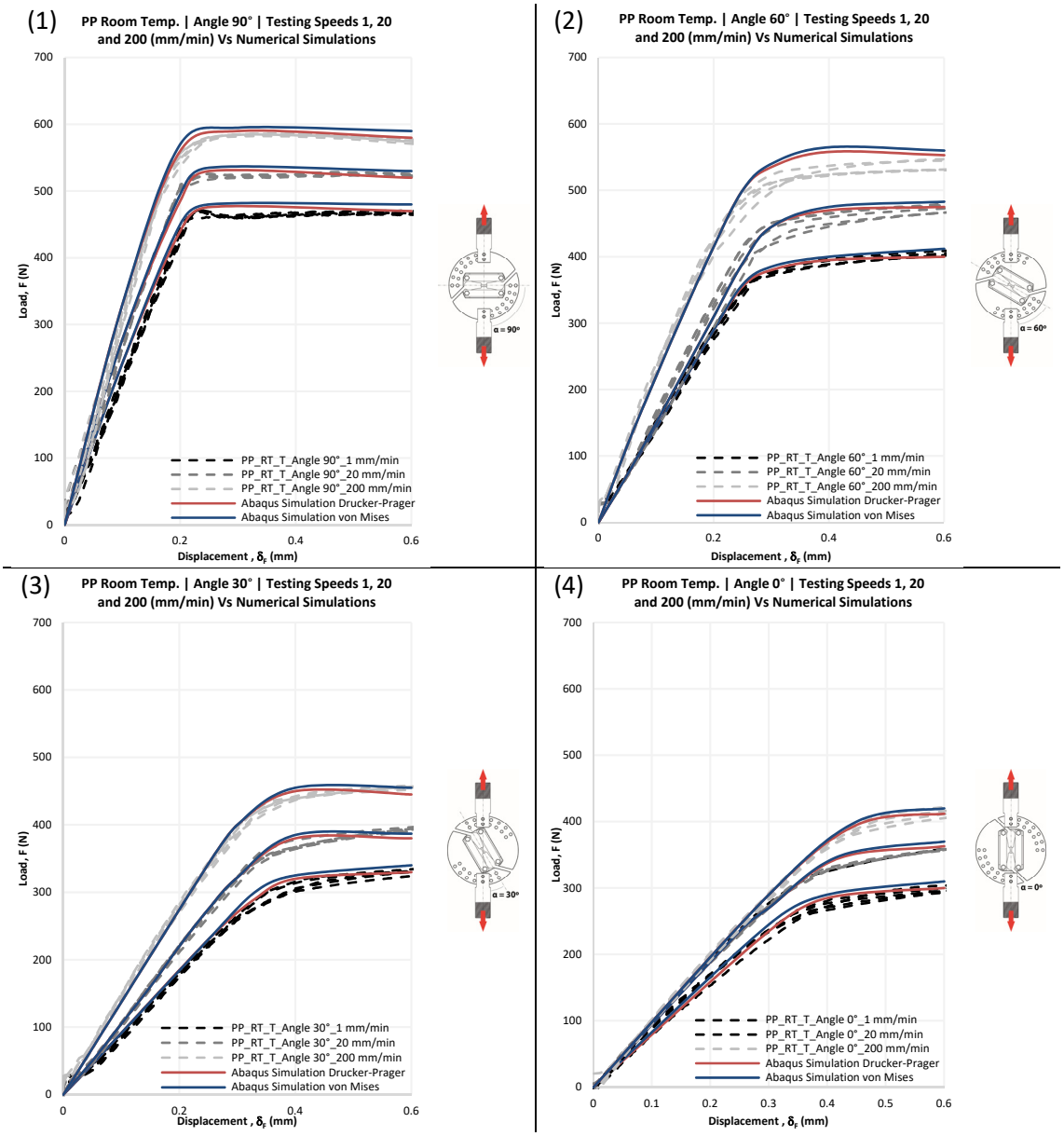


Figure 141 - Comparison of the numerical simulations with experimental results. Load-displacement curves for PP resulting from combined tensile/shear loading at RT. Loading angles: (1) $\alpha = 90°$, (2) $\alpha = 60°$, (3) $\alpha = 30°$ and (4) $\alpha = 0°$.

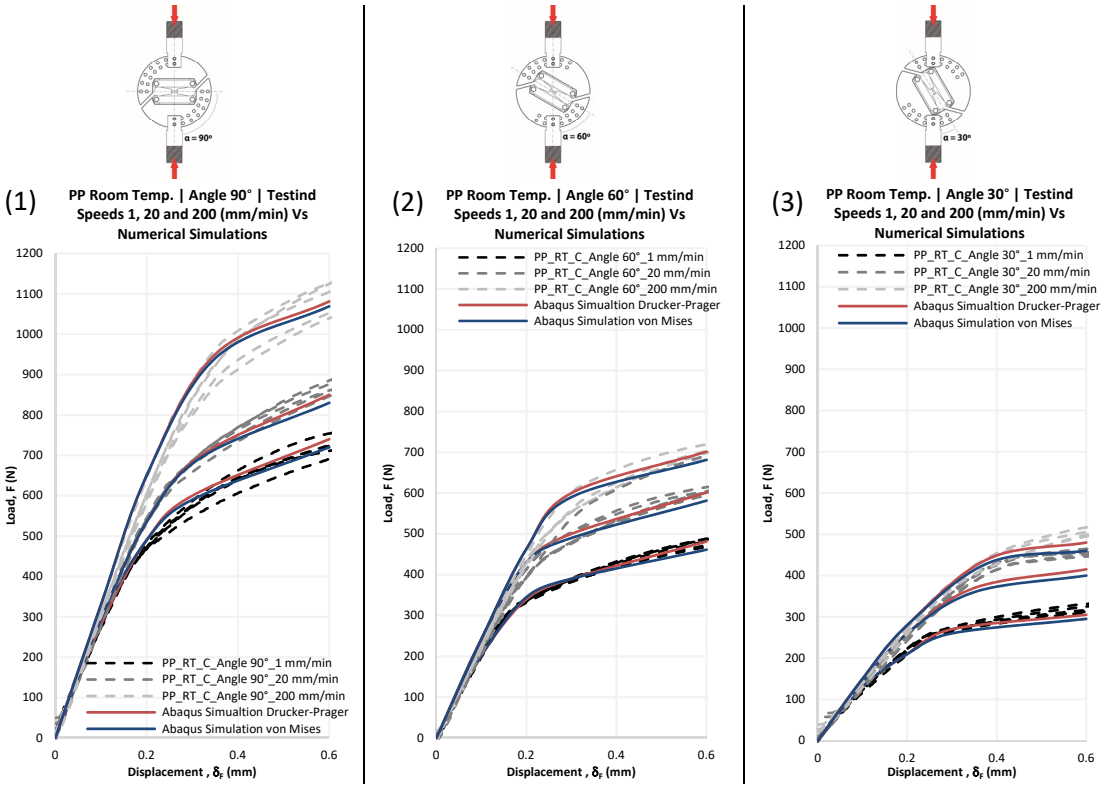


Figure 142 - Comparison of the numerical simulations with experimental results. Load-displacement curves for PP resulting from combined compression/shear loading at RT. Loading angles: (1) α = 90°, (2) α = 60° and (3) α = 30°.

This section has shown that the material models Drucker-Prager and von Mises yield criterion with parameters calibrated from tensile and compression tests are capable of describing the behaviour and the main features of the loading response of PP under triaxial (flat notched) and combined stress states (combined tension or compression/shear). However it was observed that the von Mises yield function overpredicts the experimental load-displacement response in the post-yield response and even though Drucker-Prager yield criterion is linearly dependent on hydrostatic stress, it did not match accurately with the experimental load-displacement curves in the post-yield. Nevertheless, after the post-elastic range, the Drucker-Prager yield function was consistently more accurate than the von Mises yield function.

The cylindrical notched, flat notched and butterfly specimens, develop a larger hydrostatic stress than unnotched specimens such as dumbbell. Therefore the differences between the von Mises and Drucker-Prager yield criteria were much smaller for plane stress conditions, such as tensile dumbbell and compression cylindrical. The post-elastic overprediction between experimental and numerical results in notched specimens indicate that isotropic hardening, d and/or the friction angle, β when coupled with the Drucker-Prager yield function, are not enough to describe adequately the load-displacement behaviour of PP. Thus, the Lode angle parameter effect should also be taken into account in the description of the plastic behaviour. Even though, the yield behaviour of PP is more accurately modelled using a yield function that includes a hydrostatic stress term.

6.2.3 Drucker-Pager Model - Stress Triaxiality and Lode Angle Parameter

The evolution of the stress state variables, stress triaxiality and Lode angle parameter with respect to plastic strain, was obtained by comparing experimental results at crosshead speed of 1 mm/min with numerical simulations with Drucker-Prager. Since at crosshead speed of 1 mm/min, the correlation of the experimental and numerical results is almost perfect in terms of the load-displacement relation for all cases considered in this study, it is reasonable to study the evolution of the stress state variables with respect to plastic strain at centre and at outside surface obtained from numerical simulations. With the more accurate load-displacement responses, the local quantities obtained from simulations are believed to reasonably represent the real values.

The procedure is briefly described and was the following: (1) perform a series of experimental tests and obtain load-displacement responses, (2) experimental results were used to calibrate the models, (3) by setting up the parameters for models calibration, the numerical simulations were performed, (4) matching by correlation the displacement from tests with the displacement from numerical simulations the stress components, are obtained (5) with the simulation time of displacement the equivalent plastic strain is extracted, also by correlation.

For some specimen geometries and loading conditions, namely notched and butterfly specimens, the fracture initiation location can be observed at the centre of the gauge section, during the experimental tests. However, it is difficult to determine directly from the experiments, whether fracture initiates in the centre or in the outside surface of the specimen cross-section. In the present study, with the equivalent plastic strain and stress triaxiality results, it is possible to have a clue of the fracture location. Therefore, it is assumed that the fracture initiates at the location with highest stress triaxiality and plastic strain values.

The displacement in the model and experiment are correlated based upon the equivalent plastic strain. Table 116 lists the displacements for each specimen geometry, from where the components of stress triaxiality and Lode angle parameter and equivalent plastic strain, are determined. Figure 132, illustrates the sites from where the stress triaxiality, Lode angle parameter and equivalent plastic strain, were collected.

The numerical simulations provide the values of stress state variables (stress triaxiality and Lode angle parameter) and strain components and also load-displacement responses. The loading paths are determined in terms of stress triaxiality, Lode angle and equivalent plastic strain at the centre and at the outside surface of specimens are shown in Figures 143 and 144, respectively.

Numerical simulations show that there is variation of the stress triaxiality and equivalent plastic strain along the cross section and the location of the maximum plastic strain and maximum stress triaxiality in the specimens are coincident for the investigated tests and are located at the centre of the specimen.

The stress triaxiality and Lode angle parameter values obtained from numerical simulations and initial stress triaxiality values calculated from analytical formulas, listed in Table 17 are summarized in Tables 123 and 124.

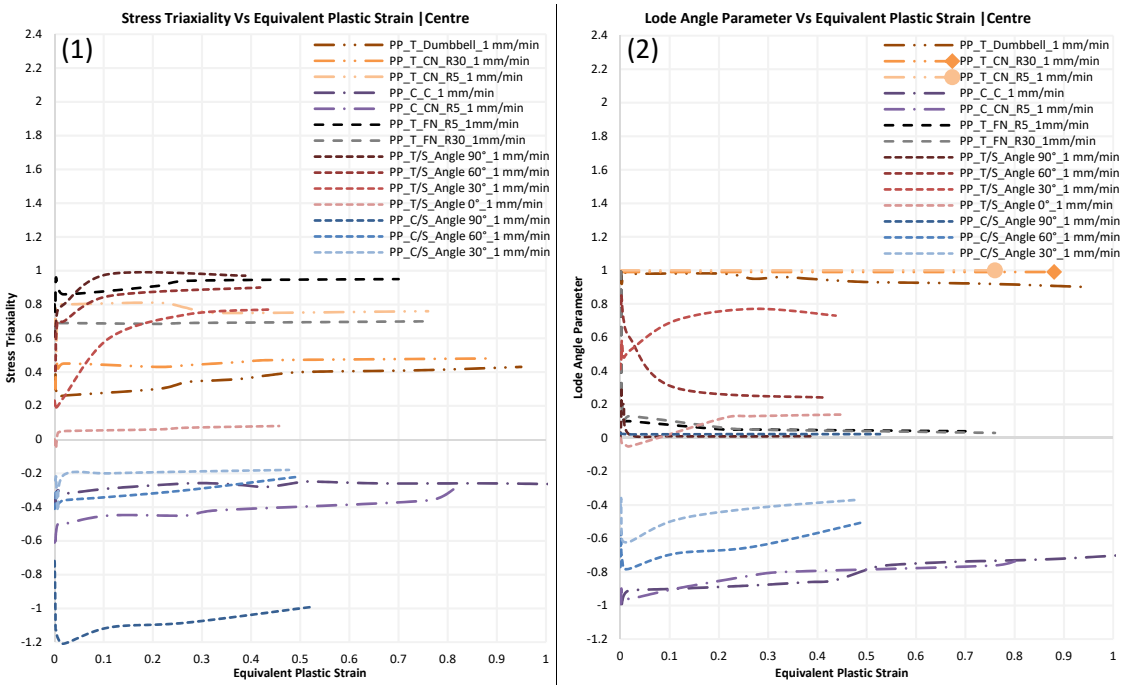


Figure 143 - Evolution of the (1) stress triaxiality and (2) Lode angle parameter with respect to plastic strain at centre, for all specimens geometries in study.

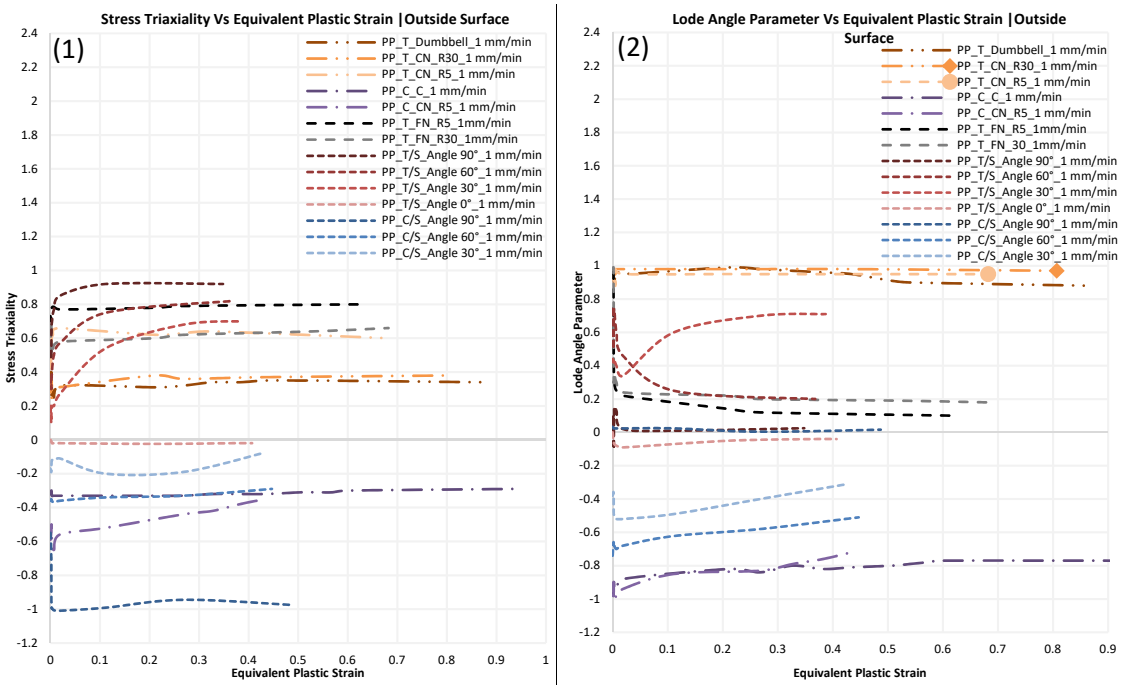


Figure 144 - Evolution of the (1) stress triaxiality and (2) Lode angle parameter with respect to plastic strain at outside surface, for all specimens geometries in study.

Table 123 - Stress triaxiality and Lode angle parameter values obtained from numerical simulations. The initial stress triaxiality values calculated from the analytical formulas are listed in the second column.

		Numerical Simulation | Calibration							
		Centre				**Outside Surface**			
Specimen Description	**Analytical Formulas, η_0**	η_0	θ_0	η_f	θ_f	η_0	θ_0	η_f	θ_f
Tension									
Dumbbell, 1 mm/min	1/3	0.32	0.93	0.43	0.9	0.3	0.98	0.34	0.88
Cylindrical R 5, 1 mm/min	0.64	0.6	0.99	0.79	0.99	0.53	0.96	0.6	0.95
Cylindrical R 30, 1 mm/min	0.39	0.34	0.99	0.5	0.99	0.28	0.93	0.38	0.97
Compression									
Cylindrical, 1 mm/min	- 1/3	-0.36	-0.99	-0.27	-0.67	-0.32	-0.97	-0.29	-0.77
Cylindrical R 5, 1 mm/min	- 0.64	-0.61	-0.99	-0.29	-0.7	-0.59	-0.98	-0.35	-0.72

Table 124 - Stress triaxiality and Lode angle parameter values obtained from numerical simulations. The initial stress triaxiality values calculated from the analytical formulas are listed in the second column.

		Numerical Simulation | Verification							
		Centre				**Outside Surface**			
Specimen Description	**Analytical Formulas, η_0**	η_0	θ_0	η_f	θ_f	η_0	θ_0	η_f	θ_f
Tension									
Flat R 5, 1 mm/min	0.84	0.8	0.99	0.95	0.04	0.73	0.97	0.8	0.1
Flat R 30, 1 mm/min	0.62	0.62	0.99	0.71	0.03	0.5	0.98	0.66	0.18
Combined Tensile/Shear									
α = 90°	0.58	0.61	0.01	0.97	0.01	0.52	0.01	0.92	0.03
α = 60°	0.38	0.41	0.81	0.9	0.24	0.37	0.74	0.82	0.2
α = 30°	0.19	0.23	0.41	0.77	0.73	0.20	0.44	0.70	0.71
α = 0°	0	0.02	0.02	-0.02	-0.04	0.01	0.02	-0.03	-0.08
Combined Compression/Shear									
α = 90°	-0.58	-0.72	-0.03	-0.99	-0.02	-0.55	0.03	-0.97	0.02
α = 60°	-0.38	-0.41	-0.77	-0.22	-0.5	-0.36	-0.74	-0.29	-0.51
α = 30°	-0.19	-0.24	-0.43	-0.14	-0.37	-0.17	-0.38	-0.18	-0.31

Generally, the stress triaxiality during the entire deformation is not constant and it is found that it increases with the equivalent plastic strain. The stress triaxiality changes significantly, especially in combined tension/shear loading angles α = 90°, α = 60° and α = 30° or in combined compression/shear α = 90°. In tensile tests on the cylindrical and flat notched specimens, the

stress triaxiality is approximately constant and is 0.79 and 0.5, respectively for the Radii 5 and 30. At pure shear, loading angle α = 0° the stress-triaxiality is near zero.

In Figures 143 and 144 it is possible to observe that the observed that equivalent plastic strain and stress triaxiality values are higher at the centre of the specimens than at the outside surface for the entire deformation process, thus fracture probably initiates from the centre and propagates towards the outer surface. This is the case of cylindrical notched specimens in which the stress triaxiality varies with the radial distance from the centre axis of specimen and has the highest stress triaxiality at the centre. Similar observations for cylindrical notched specimens where obtained by Alves and Jonas [181] in their investigation on mild steel axisymmetric notched specimens. The numerical simulations showed that the stress triaxiality is highest at the middle of the minimum cross-section of the notched specimens, a region where failure initiates, regardless of the notch radius. Flat notched specimens, also present higher values of stress triaxiality and equivalent plastic strain at the centre. For notched specimens, decreasing the notch radius, the stress triaxiality values increases and the difference between the initial and final values is higher at centre. The stress triaxiality for all geometries at the outside surface location shows a slightly increasing trend through deformation since this is a free surface.

For combined tensile/shear loading angles α = 0°, combined compression/shear loading angle α = 30° and α = 90°, and also in compression cylindrical unnotched, the difference in the stress triaxiality at the centre and at the outside surface is not significant. For these situations, the locations with higher equivalent plastic strain, which is at the centre determine the localization of the possible fracture initiation. The maximum difference of stress triaxiality between the beginning and the end of deformation at centre is around 70% for α = 30° combined tensile/shear (Table 124). Also the numerical simulation reveals that the stress triaxiality values at beginning and at the outside surface are lower than the values obtained for the centre for tensile, whereas for compression the initial stress triaxiality values are higher at the outside surface.

As expected the Lode angle parameter has a constant value ($\overline{\theta} = 1$), for cylindrical notched specimens, through loading. In the case of flat notched the Lode angle parameter converges very quickly to ($\overline{\theta} = 0$) and remains constant through the loading to fracture. For combined tensile/shear loading α = 0° (pure shear) performed on butterfly specimens, the Lode angle parameter remains close to zero and combined tensile/shear loading α = 60° the Lode angle parameter decreases from 0.81 to 0.24. There is a significant fluctuation on the loading path for the Lode angle parameter. The material starts with a near axisymmetric tension ($\overline{\theta} = 0.81$) and transforms to a near tensile shear ($\overline{\theta} = 0.24$).

The comparison between the analytical solution and the numerical results for the initial stress triaxiality in Tables 123 and 124 shows a reasonable good agreement. The existence of some differences is mainly due to the fact that the analytical solution is based on the average value of the whole cross-section. Figure 145, shows the plotted results of Tables 123 and 124 on the plane ($\eta, \overline{\theta}$) which uniquely characterizes the stress state. Although all specimens are under tensile, compression or combined loading, the stress state variables are quite different, because different specimens geometries generates different stress states. It is understandable that the stress triaxiality increases with the deformation and is not the same for all specimens. It is

observed that the tensile cylindrical notched stays on the line corresponding to axial symmetry ($\overline{\theta} = 1$), flat notched is in the state of plane strain ($\overline{\theta} = 0$) as well as butterfly at loading angle of α = 90° in both loadings: tension and compression. The point with the coordinates (0, 0) represents pure shear and is given by butterfly specimen at loading angle of α = 0°. Points between $\overline{\theta} = \pm 1$ and $\overline{\theta} = 0$ correspond to compression on cylindrical unnotched and notched specimens and combined loading angles of α = 30° and α = 60°.

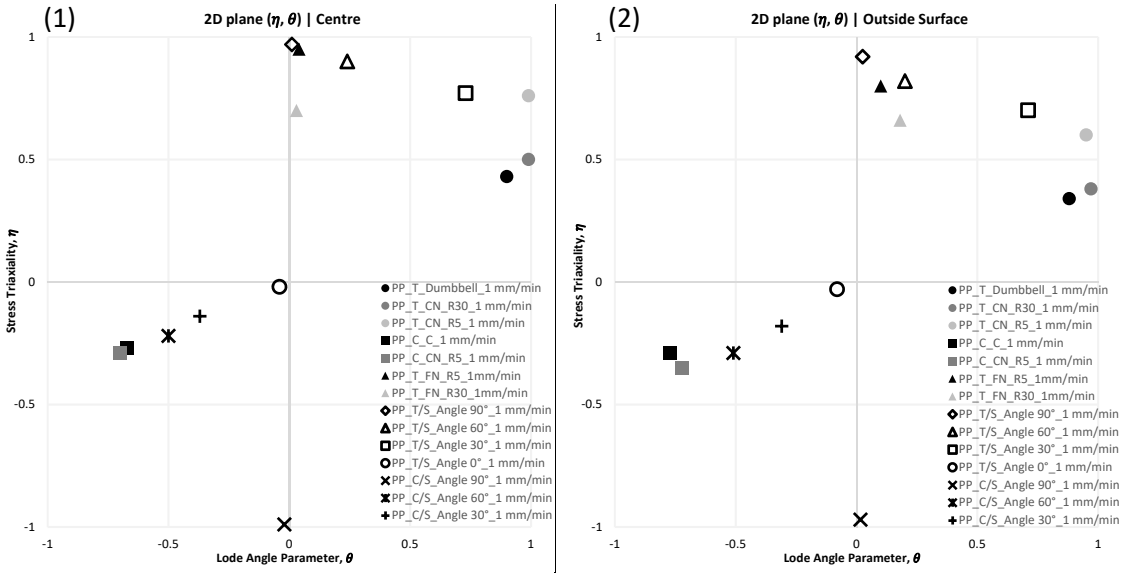


Figure 145 - Effects of stress triaxiality and Lode angle parameter on the equivalent plastic strain of PP based on the experimental and numerical results. (1) At centre and (2) at outside surface.

6.3 Drucker-Prager and von Mises Calibration and Verification - Polyamide 6 (PA 6).

The same procedures as well as the same strategy are applied for PA 6. Mechanical tests under different stress states were designed and conducted. The load-displacement curves for PA 6 are discussed in section 4.3 Polyamide (PA 6). Numerical simulations are carried out with a von Mises yield criterion, and with a Drucker-Prager yield criterion to determine the numerical load-displacement responses. Numerical simulations are carried out using ABAQUS in order to compare load-displacement responses. The accuracy of the numerical simulation was checked against available experimental data. The evolution of stress triaxiality and Lode angle parameter with equivalent plastic strain are also extracted from Drucker-Prager yield criterion, which accounts for the hydrostatic pressure. The results show strong stress state dependency on the plastic behaviour, which can be described by the combination of stress triaxiality and Lode angle parameter. Good correlation between the numerical simulations and the experimental results is achieved for crosshead speed of 1 mm/min.

6.3.1 Numerical Calibration

Table 125, depicts the average values for the stress and elastic modulus of tensile tests on dumbbell and cylindrical notched, and compression tests on cylindrical unnotched and

cylindrical notched specimens, as well as the average values of the elastic modulus and respective standard deviation and coefficient of variation for PA 6, for each crosshead speed.

Table 125 – Elastic Modulus, yield loci, stress components in tension and compression at room temperature for PA 6.

					
	Tensile Dumbbell	Tensile Cylindrical Notched R 30	Tensile Cylindrical Notched R 5	Compression Cylindrical	Compression Cylindrical Notched R 5
REF	T_Dumbbell	T_CN_R30	T_CN_R5	C_CR	C_CN_R5
1 mm/min					
σ_{zz} (MPa)	43.0	46.6	47.2	50.0	53.9
σ_{yy} (MPa)	0	1.5	8.4	0	9.5
σ_{xx} (MPa)	0	1.5	8.4	0	9.5
Elastic Modulus, *E* (MPa)	2085	2092	2079	2078	2082
Average, *E* (MPa)	2083				
Standard Deviation, *E*	5.4				
Coefficient of Variation, *E*	0.3%				
20 mm/min					
σ_{zz} (MPa)	54.0	55,8	57.5	60.2	63.4
σ_{yy} (MPa)	0	2.2	10.2	0	11.2
σ_{xx} (MPa)	0	2.2	10.2	0	11.2
Elastic Modulus, *E* (MPa)	2236	2243	2237	2240	2240
Average, *E* (MPa)	2240				
Standard Deviation, *E*	3.7				
Coefficient of Variation, *E*	0.2%				
200 mm/min					
σ_{zz} (MPa)	63.2	63,6	65.4	68.9	70.7
σ_{yy} (MPa)	0	2.5	11.6	0	12.5
σ_{xx} (MPa)	0	2.5	11.6	0	12.5
Elastic Modulus, *E* (MPa)	2370	2379	2383	2373	2370
Average, *E* (MPa)	2375				
Standard Deviation, *E*	5.8				
Coefficient of Variation, *E*	0.2%				

The true stress-strain curves for all specimen geometries, were obtained from analytical formulas, depicted in section 3.3 Specimens Geometry and summarized in Table 17. With the knowledge of this analytical expressions, the local stresses and strains in the elastic regime, were calculated and therefore, allowed the yield stress and elastic modulus to be extracted. The stress level at which yielding occurs was determined from the deviation of the linear elastic response, (see section: 6.1.1 Yield Stress Determination). The average values of stresses and elastic modulus are used to calibrate the material models for numerical simulations with finite element code Abaqus.

Multiple tested specimens were used for each specimen geometry, but only a single representative true stress-strain curve for each specimen geometry and crosshead speed are plotted in Figure 146. The effect of hydrostatic pressure can be seen from the difference observed between stress-strain curves in tensile tests and compression tests (higher yield stress values). The yield strength in tension is smaller than in compression and this behaviour shows the effect of the first stress invariant on the yield strength of this material (hydrostatic pressure). Also, the stress-strain curves reveal higher yield strength, due to notched radius, which increases the hydrostatic pressure and stress triaxiality. It is observed a post yield stress softening on tensile tests, namely on cylindrical notched specimens at high crosshead speeds.

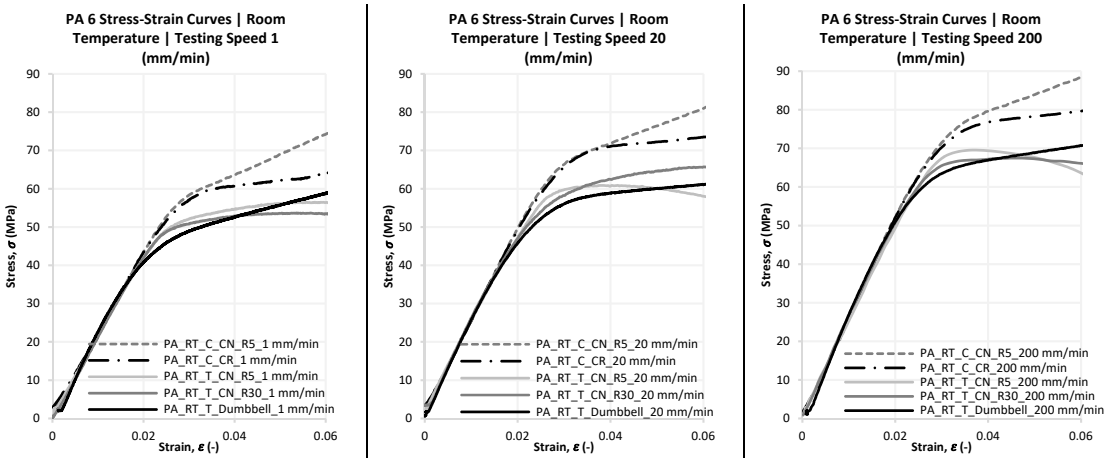


Figure 146 –True stress-strain curves for all 5 specimens geometries. Only one curve is displayed for each specimen geometry and crosshead speed.

The input properties requirements for von Mises and Drucker-Prager models are: (1) elastic modulus, poisson's ratios and mass density as well as (2) tensile hardening curves $\sigma_t(\varepsilon_t^{pl})$, while for Drucker-Prager adds the parameters, β, which is the slope of the linear yield surface in the *p–q* stress plane, also known as the hydrostatic stress sensitivity parameter.

Table 126, lists the two invariants, hydrostatic pressure, p and von Mises equivalent stress, q which were obtained from analytical formulas, described in section 2.7.1, equations 2.19 and 2.20. They were calculated based on the values of stress on tensile tests of dumbbell, cylindrical notched and compression tests on cylindrical and notched specimens, on Table 125. The p and q data of Table 126, are plotted in Figure 147 (1), in order to determine the Drucker-Prager parameter, β.

Table 126 - The von Mises equivalent stress (q) and hydrostatic pressure (p), are displayed.

	Tensile Dumbbell	Tensile Cylindrical Notched R 30	Tensile Cylindrical Notched R 5	Compression Cylindrical	Compression Cylindrical Notched R 5
1 mm/min					
q	43.0	38.8	45.2	50.0	49.3
p	-14.3	-21.3	-16.5	16.7	21.0
20 mm/min					
q	54.0	47.4	53.7	60.2	58.2
p	-18.0	-26.0	-20.1	20.1	24.6
200 mm/min					
q	63.2	55.8	61.1	68.9	64.2
p	-21.1	-29.2	-22.9	23.0	27.9

It is observed that the yield points corresponding to the tension and compression results lie on the same straight line. The three lines are almost parallel, where with the increase of crosshead speed the higher is the curve (*p*-*q*), illustrating the strain-rate sensitivity (hardening) of the PA 6, while the friction angle β is 11°, 10° and 8 °, respectively for crosshead speed 1, 20, 200 mm/min. The difference between the yielding in tension and that in compression are due to hydrostatic pressure.

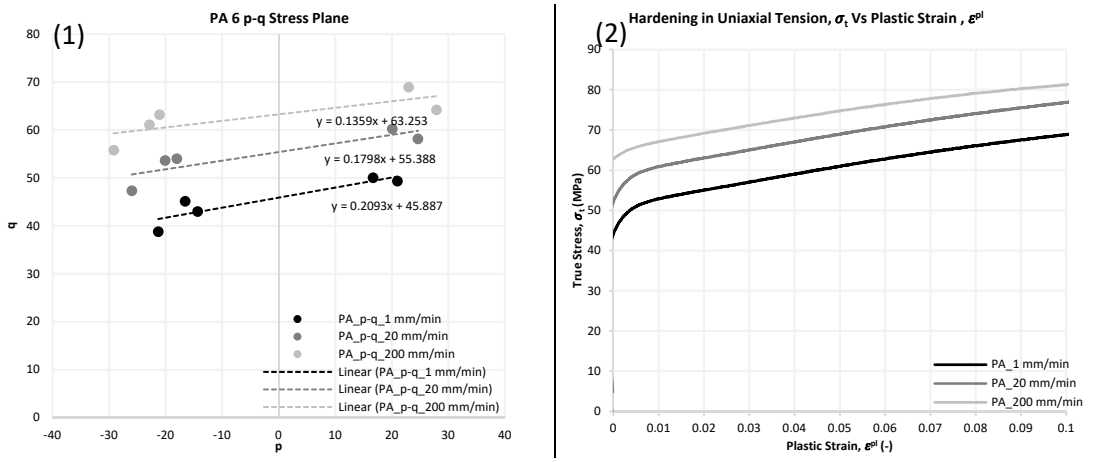


Figure 147 - (1) The equivalent stresses and pressures of Table 126 are plotted. (2) Hardening curves for 1, 20 and 200 mm/min crosshead speed.

The true stress-equivalent plastic strain curves are presented in Figure 147 (2). The strain hardening behaviour was only determined up to an equivalent plastic strain of 10% from a tensile dumbbell experiment, due to the onset of necking and by using the equation 6.1 in section 6.1.2. The hardening curves were introduced into Abaqus with eleven data points for equivalent plastic strains in Drucker-Prager and von Mises yield criterions Table 127.

Table 127 – Drucker Prager hardening in tension, points for PA 6.

	Plastic Strain	Yield Stress at 1 mm/min	Yield Stress at 20 mm/min	Yield Stress at 200 mm/min
1	0	44.39	51.28	63.36
2	0.01	53.35	60.79	67.40
3	0.02	55.01	62.86	69.36
4	0.03	56.80	64.86	71.36
5	0.04	59.01	66.93	73.01
6	0.05	60.74	69.08	74.80
7	0.06	62.86	70.59	76.33
8	0.07	64.57	72.27	77.69
9	0.08	65.96	74.01	78.97
10	0.09	67.46	75.51	80.14
11	0.1	68.57	76.49	81.19

Numerical Simulation Parameters:

In section 6.1.2 Numerical Calibration, all the information about numerical simulation parameters such as the mesh models, element type, element shape, geometric order, number of elements and nodes and boundary conditions are described and the same are used hereinafter.

Elastic-plastic material models were assigned to the specimens, considering the material as isotropic and homogeneous. The simulations were carried out employing basic material properties. The basic materials properties for 1, 20 and 200 mm/min crosshead speeds are listed on Table 128. The poisson ratio and mass density were taken from literature [76], while the elastic modulus was taken from the true stress-strain curves defined by means of the deviation of the linear elastic response. The friction angle β, parameter was assigned to Drucker-Prager model, while the eleven data points for equivalent plastic strain (Table 127) were assigned to both, Drucker-Prager and von Mises.

Table 128 - Basic material properties assigned.

Testing Speed (mm/min)	Elastic Modulus (MPa)	Poisson's Ratio [76]	Mass Density (g/cm^3) [76]
1	2083	0.3	1.13
20	2240		
200	2375		

Numerical Simulation Results:

Numerical simulations were run with the parameters obtained with the calibration presented above. The aim is to check whether the material parameters, determined above, can reproduce the response of the tensile and compression tests of PA 6, presented in sections 4.3.1 and 4.3.4. 3D finite element models with the same dimensions and geometries of experimental tests are used. The finite element results using a von Mises yield criterion and a Drucker-Prager yield criterion are compared to the experimental results (Figures 148 to 149). The solid lines represent

numerical results while the dashed lines represent the results from the experimental tests (five tests).

The results from the numerical simulations of dumbbell and compression (unnotched specimen) essentially matches the experimental results, whereas for notched specimens the von Mises and Drucker-Prager yield functions overpredict the load-displacement experimental curves in the post-elastic range. Although, the best correlation is with Drucker-Prager. Therefore, the Drucker-Prager yield function is more accurate than the von Mises yield function.

The notched specimens develops a larger hydrostatic stress than dumbbell or than cylindrical unnotched specimens. Thus, the differences between the von Mises and Drucker-Prager yield criteria are much smaller for dumbbell and cylindrical unnotched specimens and larger for notched specimens because von Mises yield criterion assumes that the hydrostatic pressure has no effect on plastic yielding, overestimating the plastic behaviour [113].

Strength-differential, which is the difference between compressive and tensile strength of a material at a given strain, appears to be adequately handled using the Drucker-Prager yield function. Even though there is a clear overestimation of the force, for notched specimens. Like HDPE and PP the yield strength of PA 6 in compression is greater than in tension. In addition the best correlation between experimental and numerical results indicates that isotropic hardening, when coupled with the Drucker-Prager yield function, describes better the strain hardening of PA 6, because von Mises is a pressure independent yield criterion.

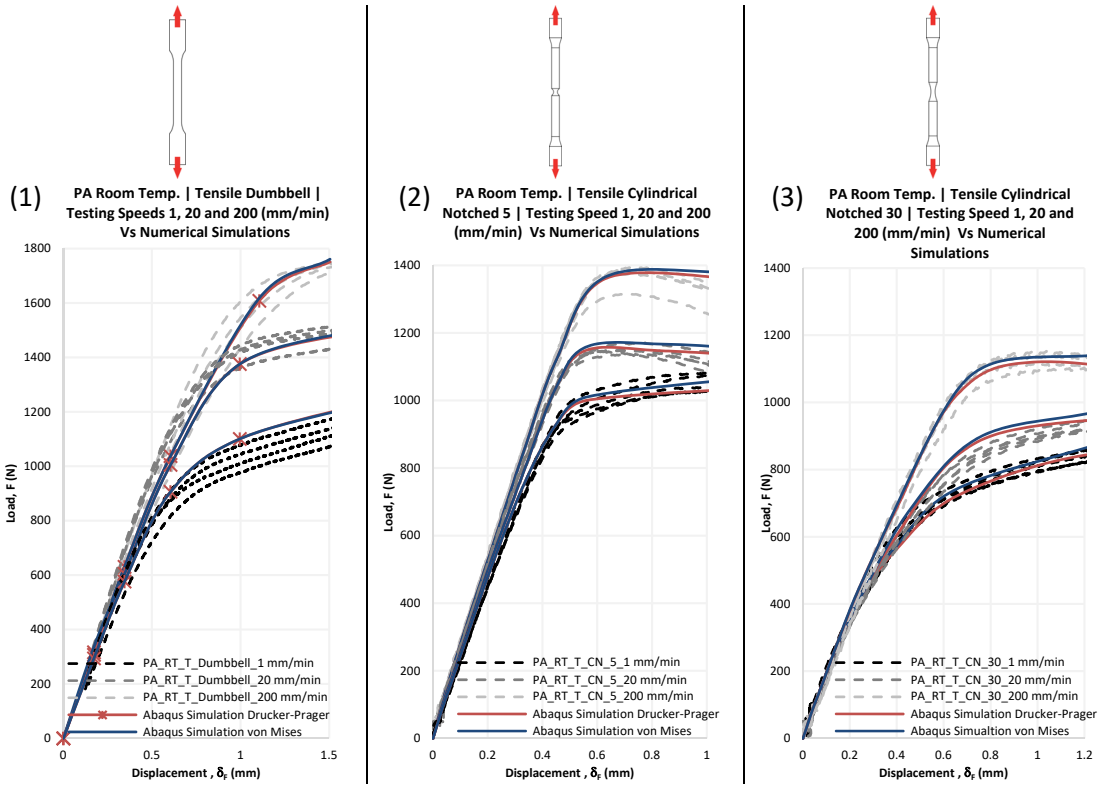


Figure 148 – Comparison of the numerical simulations with experimental results. Tensile load-displacement curves of (1) Dumbbell, (2) cylindrical notched 5 and (3) cylindrical notched 30 specimens (PA 6, Room Temperature).

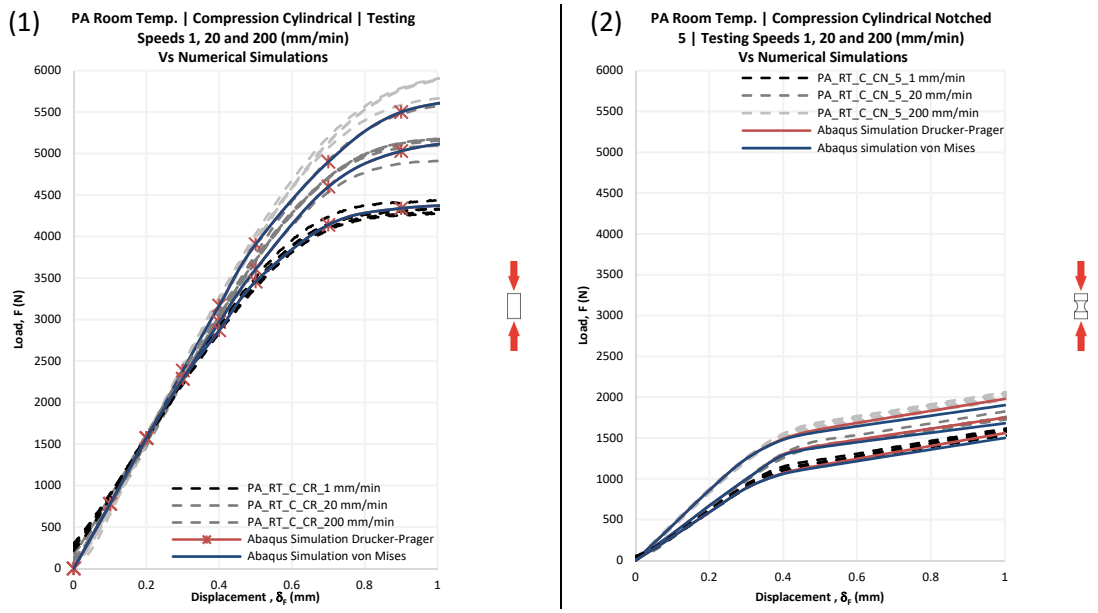


Figure 149 - Comparison of the numerical simulations with experimental results. Compression load-displacement curves of (1) cylindrical and (2) cylindrical notched specimens (PA 6, Room Temperature).

6.3.2 Numerical Verification

In order to validate the calibrated Drucker-Prager and von Mises yield criteria, the numerical simulations of flat notched specimens and of combined tensile/shear and compression/shear performed on butterfly specimens, were compared with the experimental load-displacement curves, analysed in sections 4.3.1, 4.3.2 and 4.3.5.

Numerical Simulation Parameters:

In section 6.1.3 Numerical Verification, all the information about numerical simulation parameters such as the mesh models, element type, element shape, geometric order, number of elements and nodes as well as the boundary conditions are described and the same are used hereinafter.

Material properties: The elastic-plastic material models, Drucker-Prager plasticity model and von Mises model were assigned with the basic materials properties listed on Table 128, and with the eleven data points for equivalent plastic strain on Table 127, for isotropic hardening. The Drucker-Prager plasticity model, was introduced into Abaqus with the identified parameter, β friction angles, 11°, 10° and 8 °, respectively for crosshead speed 1, 20, 200 mm/min.

Numerical Simulation Results:

The results from the experimental tests were compared with the results from numerical simulations employing the von Mises and Drucker-Prager yield criterion models. The comparison of the experimental and numerical load-displacement curves is shown in Figures 150 to 152. The solid lines represent numerical results while the dashed lines represent the results from the experimental tests (five tests).

The purpose of this comparison is the validation of the numerical calibration criteria together with the assessment of the criteria for experimental tests on flat notched and combined loading on butterfly specimens to identify to which extent the calibrated models, with the isotropic hardening determined from tensile dumbbell test and Drucker-Prager plasticity model parameter, β (friction angle), captured the mechanical behaviour.

Figure 150, displays the load-displacement curves from simulations and experimental for flat notched. Like it was observed with the HDPE an PP numerical results, for PA 6 the numerical simulation captures the initial elastic range, however the post-elastic response is overestimated for notched specimens. In spite of the overestimation, the best correlation is with the Drucker-Prager yield criterion.

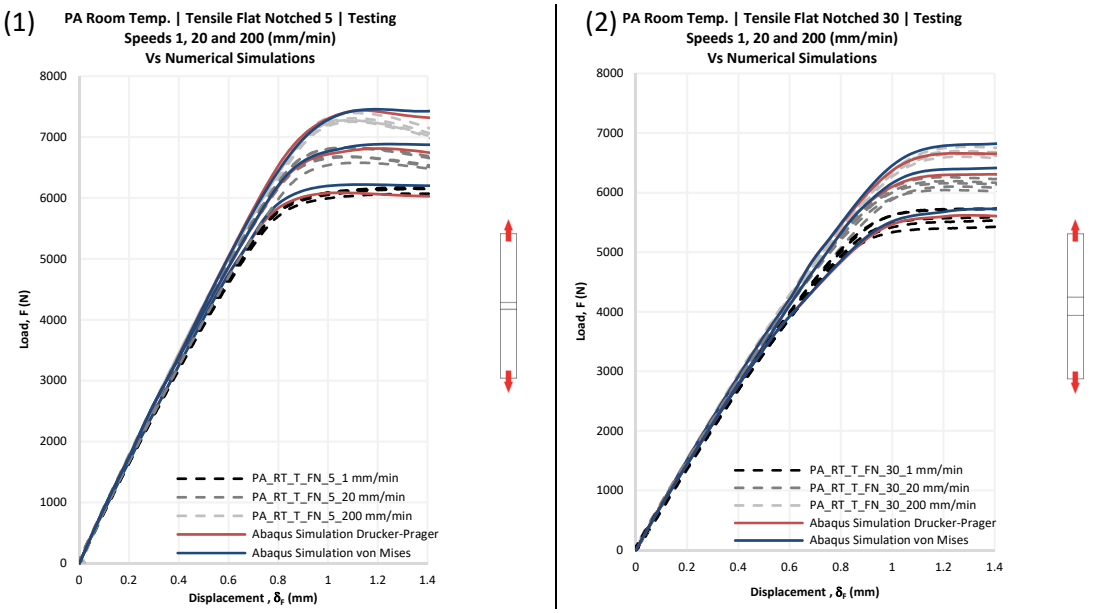


Figure 150 – Comparison of the numerical simulations with experimental results. Tensile load-displacement curves of (2) flat notched 5 and (3) flat notched 30 specimens (PA 6, Room Temperature).

Numerical simulations of the deformation of combined tensile/compression/shear on butterfly specimens, in Figures 151 and 152, show that the experimental tests are generally well reproduced by the numerical simulations as well as the initial responses are reasonable well predicted. Drucker-Prager yield criterion is consistently more accurate than the von Mises yield function, due to its linearly dependence with the hydrostatic stress. Both yield criterions, predict that the load-displacement responses increases with the loading angle (α =0° to α =90°) and crosshead speed.

However, there is an overprediction on the load-displacement curves, which is larger with increasing crosshead speed. The numerical model predicts the expected behaviour of combined Tensile/Shear and Compression/Shear, which is: (1) higher the loading angle, higher is the load required to deform the specimens and (2) the load-displacement curves shift to higher load values with increasing of crosshead speed.

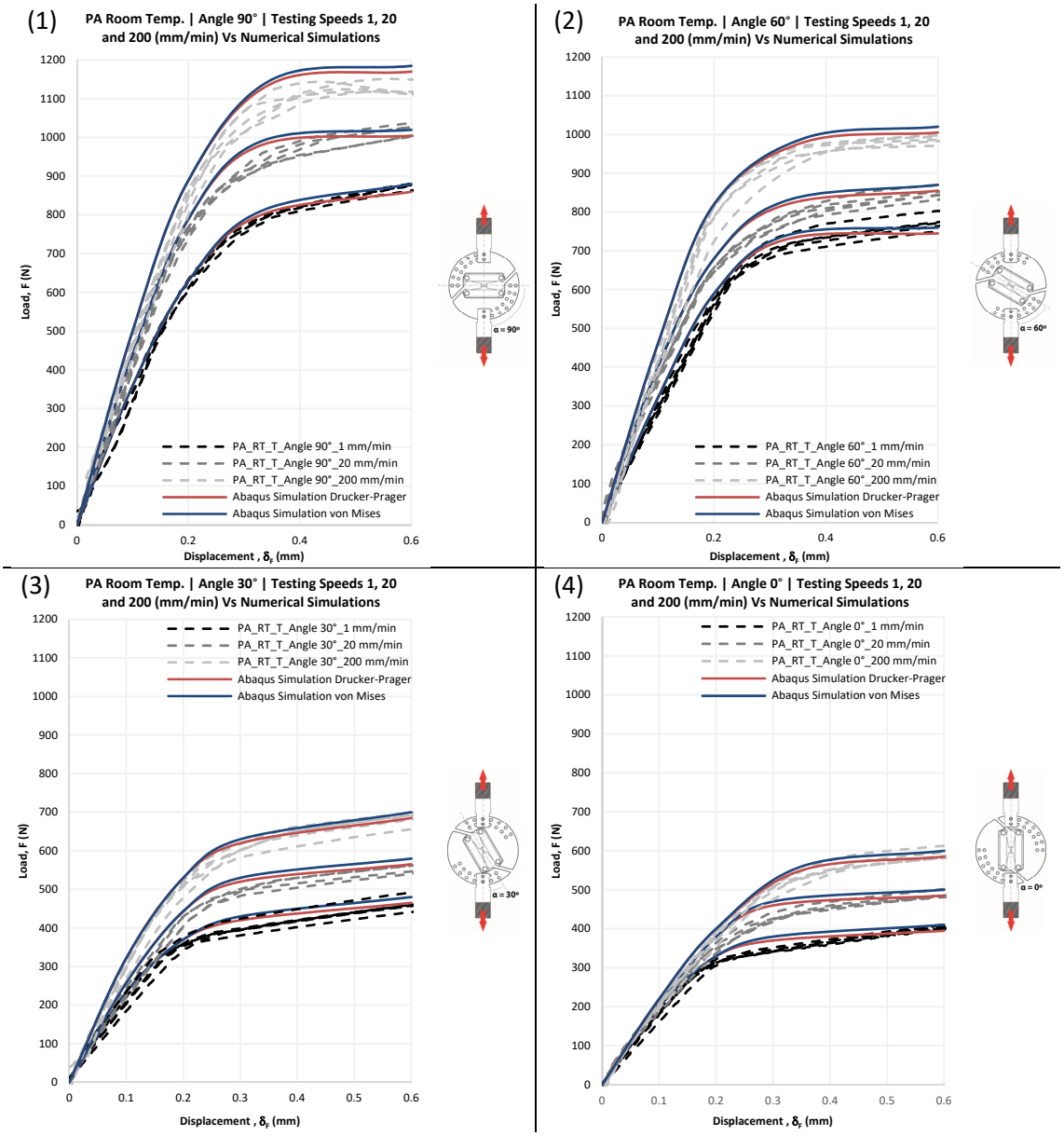


Figure 151 - Comparison of the numerical simulations with experimental results. Load-displacement curves for PA 6 resulting from combined tensile/shear loading at RT. Loading angles: (1) α = 90°, (2) α = 60°, (3) α = 30° and (4) α = 0°.

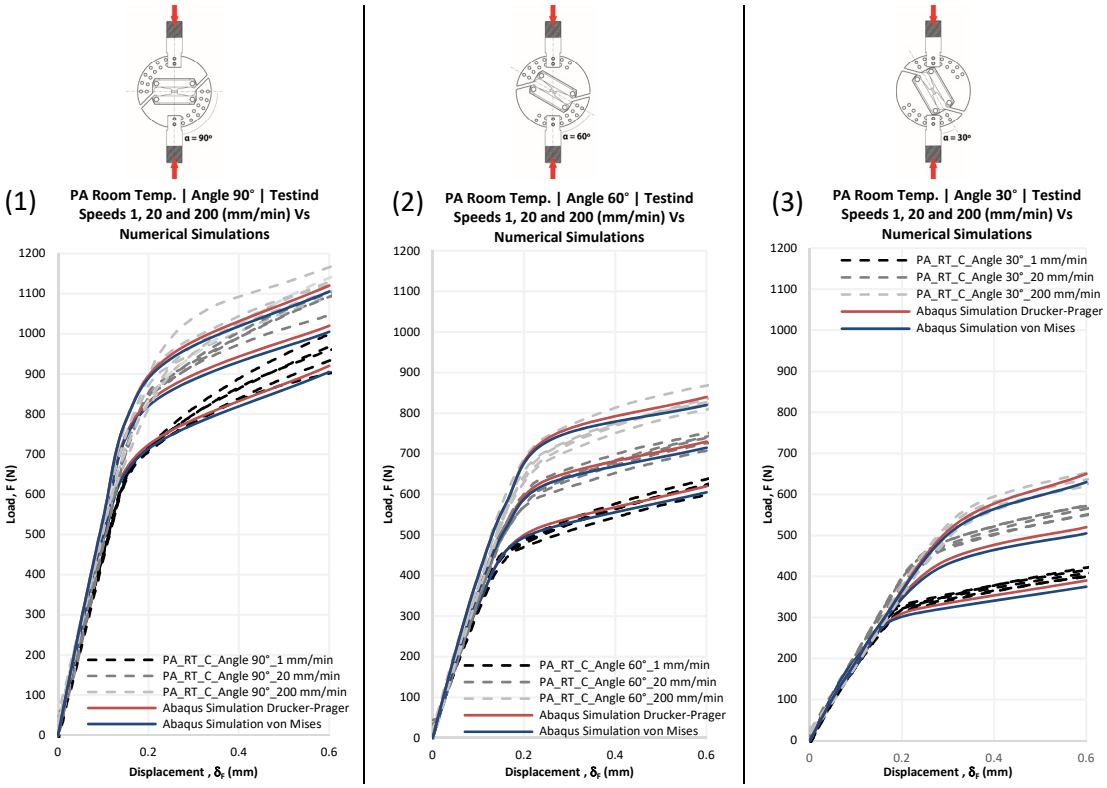


Figure 152 - Comparison of the numerical simulations with experimental results. Load-displacement curves for PA 6 resulting from combined compression/shear loading at RT. Loading angles: (1) α = 90°, (2) α = 60° and (3) α = 30°.

6.3.3 Drucker-Pager Model - Stress Triaxiality and Lode Angle Parameter

A good correlation was obtained between the numerical simulations and the experimental tests in terms of global load-displacement response with the Drucker-Prager yield criterion at crosshead of 1 mm/min. The numerical simulations provide exact values of stress state variables and strain components and also load displacement responses. By comparing the tests with simulation, one can determine the magnitude of the equivalent strain at the determined point as well as the evolution of the stress state variables, stress triaxiality and the Lode angle parameter. The relationship between displacement and equivalent plastic strain can be obtained from the numerical simulation for each specimen case. Table 116 lists the displacements for each specimen geometry, from where the corresponding stress components and the equivalent plastic strain at the centre and at the outside surface, are extracted. Figure 132, illustrates the sites from where the stress triaxiality, Lode angle parameter and equivalent plastic strain, were collected.

The evolution of the stress state variables, stress triaxiality and Lode angle parameter with respect to plastic strain, obtained with Drucker-Prager plasticity model at centre and at outside surface for all specimens are presented in Figures 153 and 154.

In the present study, with the equivalent plastic strain and stress triaxiality results, it is possible to have an informed guess of the fracture location. If it is assumed that specimens fails at the centre, then the effective equivalent plastic strain and stress triaxiality show their highest values.

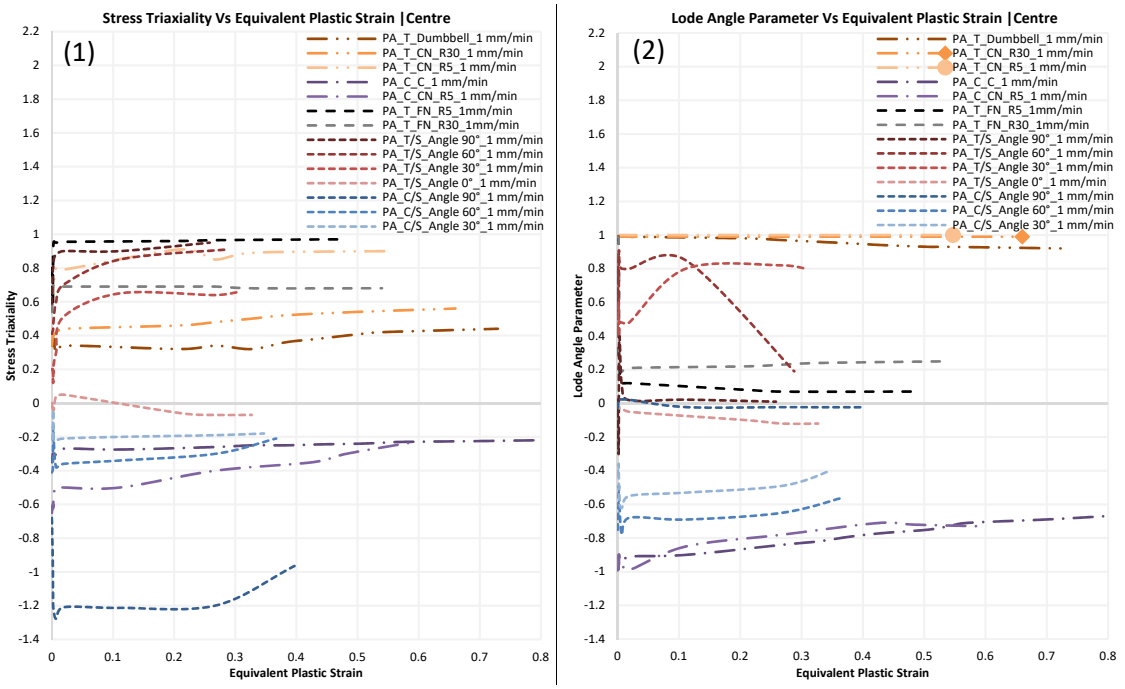


Figure 153 - Evolution of the (1) stress triaxiality and (2) Lode angle parameter with respect to plastic strain at centre, for all specimens geometries in study.

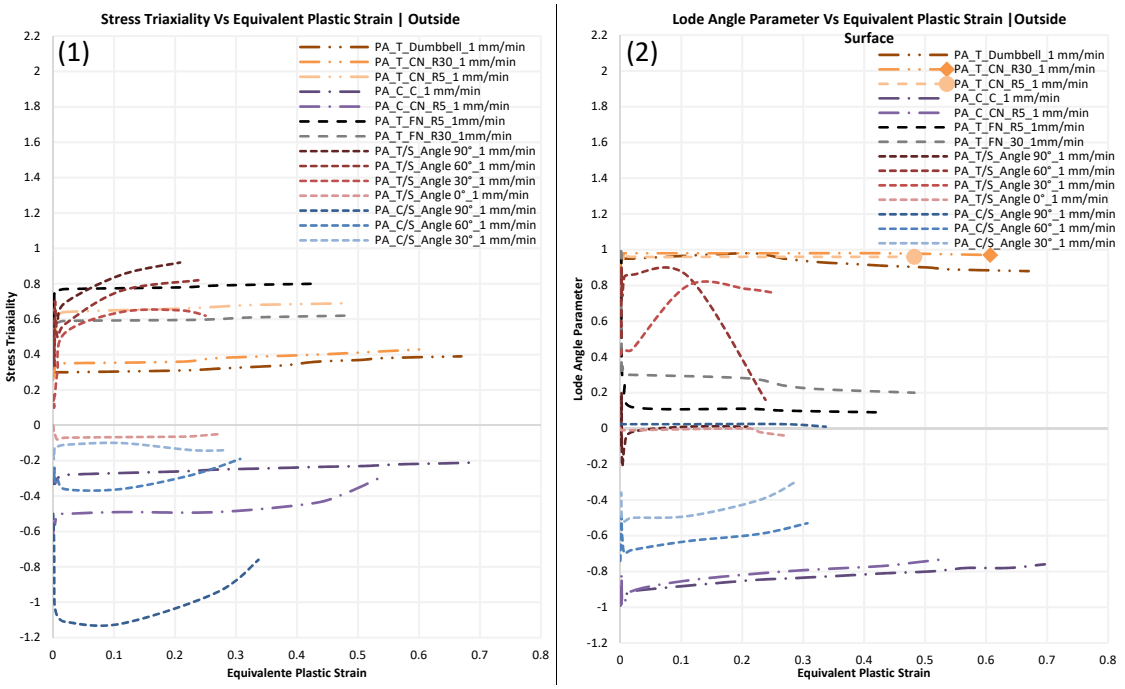


Figure 154 - Evolution of the (1) stress triaxiality and (2) Lode angle parameter with respect to plastic strain at outside surface, for all specimens geometries in study.

The stress triaxiality and Lode angle parameter values obtained from numerical simulations and initial stress triaxiality values calculated from analytical formulas, listed in Table 17 are summarized in Tables 129 and 130.

Table 129 - Stress triaxiality and Lode angle parameter values obtained from numerical simulations. The initial stress triaxiality values calculated from the analytical formulas are listed in the second column.

		Numerical Simulation | Calibration							
		Centre				**Outside Surface**			
Specimen Description	**Analytical Formulas, η_0**	η_0	θ_0	η_f	θ_f	η_0	θ_0	η_f	θ_f
Tension									
Dumbbell, 1 mm/min	1/3	0.34	0.97	0.4	0.92	0.33	0.98	0.39	0.88
Cylindrical R 5, 1 mm/min	0.64	0.63	0.99	0.9	0.99	0.5	0.98	0.69	0.96
Cylindrical R 30, 1 mm/min	0.39	0.40	0.99	0.62	0.99	0.26	0.9	0.43	0.97
Compression									
Cylindrical, 1 mm/min	- 1/3	-0.35	-0.98	-0.22	-0.65	-0.33	-0.99	-0.23	-0.76
Cylindrical R 5, 1 mm/min	- 0.64	-0.65	-0.99	-0.23	-0.67	-0.61	-0.99	-0. 3	-0.73

Table 130 - Stress triaxiality and Lode angle parameter values obtained from numerical simulations. The initial stress triaxiality values calculated from the analytical formulas are listed in the second column.

		Numerical Simulation | Verification							
		Centre				**Outside Surface**			
Specimen Description	**Analytical Formulas, η_0**	η_0	θ_0	η_f	θ_f	η_0	θ_0	η_f	θ_f
Tension									
Flat R 5, 1 mm/min	0.84	0.8	0.99	0.97	0.07	0.71	0.97	0.8	0.09
Flat R 30, 1 mm/min	0.62	0.62	0.99	0.73	0.02	0.54	0.99	0.68	0.25
Combined Tensile/Shear									
α = 90°	0.58	0.59	0.02	0.95	0.01	0.5	0.02	0.92	0.01
α = 60°	0.38	0.41	0.81	0.91	0.19	0.36	0.72	0.82	0.16
α = 30°	0.19	0.20	0.44	0.66	0.8	0.17	0.41	0.62	0.76
α = 0°	0	0.03	0.1	-0.07	-0.12	0.02	0.03	-0.05	-0.04
Combined Compression/Shear									
α = 90°	-0.58	-0.68	-0.02	-0.96	-0.02	-0.5	0.02	-0.76	0.01
α = 60°	-0.38	-0.41	-0.75	-0.21	-0.56	-0.28	-0.74	-0.19	-0.53
α = 30°	-0.19	-0.21	-0.43	-0.18	-0.4	-0.16	-0.37	-0.16	-0.3

From Figures 153 and 154, it is observed that there is variation of the stress triaxiality and equivalent plastic strain along the cross section and the location of the maximum equivalent plastic strain and maximum stress triaxiality in the specimens is located at the centre. Also, the stress triaxiality shows an increasing trend through deformation.

As can be observed, the tensile cylindrical and flat notched specimens have a similar loading path for the stress triaxiality. The initial stress triaxiality for both types of specimens increases with decreasing of the notch radius. For smaller notched radius (R 5) the stress triaxiality in the initial stages of plastic deformation, shows a higher increase than notched radius R 30.

On the contrary, the dumbbell shows a steady increase in the stress triaxiality as the equivalent plastic strain increases. The stress triaxiality changes significantly, especially in combined tension/shear loading angles, such as for α = 90°, or in combined compression/shear for the same loading angle. At pure shear, loading angle α = 0° the stress-triaxiality is near zero. The comparison between analytical solution and numerical results for initial stress triaxiality in Tables 123 and 124 shows a reasonable good agreement.

Studies of ductile fracture in metals, by Needleman and Tvergaard [182] shown that the failure site for the axisymmetric specimens is located always on the longitudinal axis of symmetry because the triaxiality is highest there, regardless of the value of the plastic strain. This conclusion is a numerical confirmation of the experimental observation of Mackenzie et al. [183] and matches with the current experimental results, for cylindrical notched specimens. Thus fracture probably initiates from the centre and propagates towards the outer surface.

For the cylindrical notched specimens, the Lode angle parameter has a constant value ($\overline{\theta} = 1$) during loading, which indicates that the material is under axisymmetric tension during the entire loading process. In the case of flat notched, the Lode angle parameter converges very quickly to ($\overline{\theta} = 0$) and remains constant through the loading to fracture, which suggests a plane strain state during the entire loading.

For combined tensile/shear loading α = 0° (pure shear) performed on butterfly specimens, the Lode angle parameter remains close to zero and for combined tensile/shear loading α = 60° and α = 30° there is a significant fluctuation on the loading path for the Lode angle parameter. The material starts with a near axisymmetric tension and transforms to a near tensile, for α = 60°. In pure tension/compression, α = 90° it is observed a nearly constant Lode angle parameter of, $\overline{\theta} = 0$. For combined compression/shear loading angles α = 30° and α = 60° some fluctuation throughout the loading is observed.

From the numerical simulations combined with experiment results, one can also obtain the loading conditions in the plane of stress triaxiality and the Lode angle parameter, as shown in Figure 155. Details about the data points can be found in Tables 129 and 130. Different specimen geometries allows to generate different stress states. It is understandable that the stress triaxiality increases with the deformation and is not the same for all specimens.

It is observed that the tensile cylindrical notched stays on the line corresponding to axial symmetry ($\overline{\theta} = 1$), the flat notched is in the state of plane strain ($\overline{\theta} = 0$) as well as butterfly at loading angle of α = 90° in both loadings: tension and compression. By introducing on flat and cylindrical specimens different notch radii, a range of stress triaxiality at constant Lode angle parameter, of $\overline{\theta} = 0$ and $\overline{\theta} = 1$, it is possible to analyse the influence of each parameter independently. It is observed that decreasing the notch radius increases the stress triaxiality value.

Combined loading tension or compression/shear cover a wide range of the stress triaxiality and Lode angle parameters. The point with the coordinates (0, 0) represents pure shear and is given by butterfly specimen at a loading angle of $\alpha = 0°$. Points between $\overline{\theta} = \pm 1$ and $\overline{\theta} = 0$ correspond to compression on cylindrical unnotched and notched specimens and combined loading angles of $\alpha = 30°$ and $\alpha = 60°$. Compression tests are often performed to investigate the negative range of stress triaxiality and Lode angle parameter.

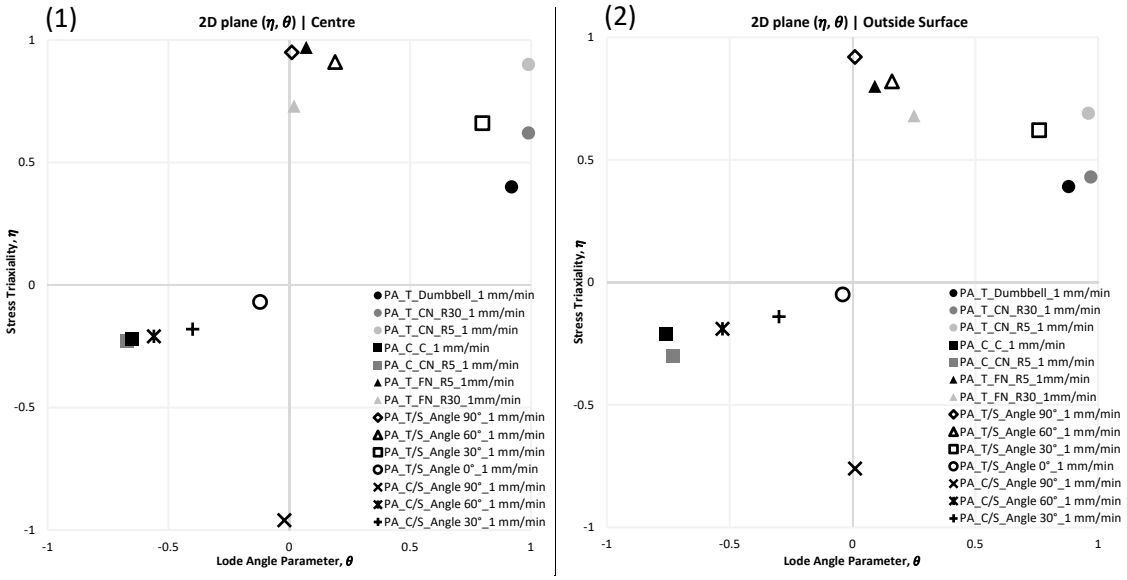


Figure 155 – Effects of stress triaxiality and Lode angle parameter on the equivalent plastic strain of PA 6 based on the experimental and numerical results. (1) At centre and (2) at outside surface.

6.4 Discussion and Concluding Remarks

The deformation of semi crystalline polymers commonly involves large plastic deformations, polymers are pressure sensitive materials with a higher yield strength in compression than in tension, are sensitive to strain rate and temperature, some polymers have a stress softening behaviour after the yield limit, while others experience monotonic hardening.

Finite element analysis use elastic-plastic models to describe the nonlinear, large strain behaviour of inelastic materials. Although not developed for plastics materials, these models can be used to simulate their deformation. The accuracy of predictions will depend on the suitability of the model for the polymer being studied and the accuracy achieved in the determination of model parameters [184].

The aim of this chapter was to assess the predictive ability of two yield criterions and to calibrate the plasticity models Drucker-Prager and von Mises yield criteria based on the mechanical experimental results measured under different stress sates and different crosshead speed for three semi crystalline polymers - HDPE, PP and PA 6. The plasticity models calibration and verification were performed through numerical simulation of all tests using Abaqus. The stress triaxiality and lode angle results at plastic domain (not at fracture) of each specimen are collected and analysed.

3D finite element models with the same dimensions and geometries of experimental tests are used. The data required to calibrate the material models for numerical simulations, was:

- The elastic modulus behaviour and the Drucker-Prager plasticity model parameters, β which is the slope of the linear yield surface in the *p–t* stress plane, were determined as functions of the true stress-strain results obtained by the mechanical tests on five different specimens geometries: tensile tests on dumbbell and cylindrical notched, and compression tests on cylindrical unnotched and cylindrical notched specimens. Poisson's ratio and mass density were taken for literature.

- The nonlinear material response was modelled using isotropic hardening with a von Mises yield criterion, and with a Drucker-Prager yield criterion. The true stress versus plastic strain data from the tensile test on dumbbell specimen, with stress triaxiality η = 1/3 and Lode angle parameter $\overline{\theta} = 1$, was used as input for the hardening curve $\sigma_t(\varepsilon_t^{pl})$.

The results of the numerical simulation on HDPE, PP and PA 6 show that, both Drucker-Prager and von Mises models capture the initial elastic range, however the post-elastic response is overestimated for notched specimens and combined loading on butterfly. For unnotched specimens, tensile dumbbell and compression cylindrical, the numerical simulations results essentially matched the experimental results, whereas the peak force is well captured, with both Drucker-Prager and von Mises models. The cylindrical and flat notched specimens, develop a larger hydrostatic stress than unnotched specimens such as dumbbell. Therefore the differences between the von Mises and Drucker-Prager yield criteria are much smaller for plane stress conditions, such as tensile dumbbell and compression cylindrical.

For triaxial and combined stress, the best correlation is obtained with Drucker-Prager yield criterion, however it cannot predict accurately the load-displacement responses in some tests, even including the hydrostatic stress parameter and the isotropic hardening. Nevertheless, it allows a more precise prediction of deformation, than von Mises yield criterion. Essentially the elastic-plastic model based on the von Mises yield criterion neglects the influence of the hydrostatic component of stress on yield behaviour (same response in tension and compression), although this behaviour is pronounced in polymeric materials. The linear Drucker-Prager model is more accurate for polymers than the von Mises model since it accounts with the influence of the hydrostatic component of stress on yield behaviour.

The effect of Lode angle was not properly explored in the Drucker-Prager yield model calibration. Some studies however showed that the mechanical response of polymers is sensitive also to Lode angle parameter [180]. Thus, the Lode angle parameter effect should also be taken into account in the description of the plastic behaviour, for a better accuracy in the results.

The correlation of the experimental and numerical results with Drucker-Prager model at crosshead speed of 1 mm/min essentially matches in terms of load-displacement response for all tests, which allow to study the evolution of the stress state variables, stress triaxiality and Lode angle parameter with respect to plastic strain at centre and outside surface.

A wide range on the stress triaxiality and Lode angle parameter was covered with the proposed experimental program. For most of the tests, numerical simulations shows that there is variation

of the stress triaxiality and equivalent plastic strain along the cross section and the location of the maximum plastic strain and maximum stress triaxiality in the specimens are located at the centre. Thus fracture probably initiates from the centre and propagates towards the outer surface.

The Lode angle parameter has a constant value through deformation to fracture for the set of cylindrical notched specimens ($\overline{\theta} = 1$) and for the set of flat notched specimens it converges quickly to $\overline{\theta} = 0$ at the beginning of the deformation. However the stress triaxiality value is not constant through loading, it increases with notched radii. It is verified that decreasing the notched radii, the higher difference of stress triaxiality between the beginning and end of deformation, due to increasing the stress triaxiality.

For combined tensile/shear loading α = 0° (pure shear) performed on butterfly specimens, the stress triaxiality and Lode angle parameter remain close to zero, while for combined tensile/shear loading α = 60° there is a significant fluctuation on the loading path for the Lode angle parameter. It is observed a nearly constant Lode angle parameter of, $\overline{\theta} = 0$, for combined loading angle α = 90°.

Different specimens geometries generates different stress state as different loading conditions, such as tensile, compression or combined. It is understandable that the stress triaxiality increases with the deformation and is not the same for all specimens. Each specimen is assumed to represent a single point in the space of stress triaxiality and Lode angle parameter. Tensile cylindrical notched stay on the line corresponding to axial symmetry $(\overline{\theta} = 1)$, flat notched is in the state of plane strain $(\overline{\theta} = 0)$ as well as butterfly at loading angle of α = 90° in both situation: tension and compression. The point with the coordinates (0, 0) represents pure shear and is given by butterfly specimen at loading angle of α = 0°. Points between $\overline{\theta} = \pm 1$ and $\overline{\theta} = 0$ corresponds to compression on cylindrical unnotched and notched specimens and combined loading angles of α = 30° and α = 60°.

There is a reduction area, on the plane (η, θ) when compared the stress state, at centre and outside surface. The biaxial loading performed on butterfly specimens, shows that it is possible to investigate the stress triaxiality and Lode angle parameter for different stress states with a single specimen geometry by changing the loading angle.

7 Conclusions and Future Studies

The mechanical response of High-Density Polyethylene (HDPE), Polypropylene (PP) and Polyamide 6 (PA 6) were studied. Different specimens geometries, including more conventional specimens such as dumbbell for uniaxial tension and cylindrical unnotched for uniaxial compression tests, were examined. In order to investigate a wider range of stress states, cylindrical and flat notched specimens with different curvature radii and butterfly specimens, which allow biaxial loading tests (pure shear, combined shear and tension/compression, pure tension/compression) using the Arcan testing Apparatus , were adopted to study the yield stress, elastic modulus, the stress triaxiality and Lode angle parameter effects on the plastic domain behaviour, mainly on initial yielding behaviour.

Also, various complementary analysis techniques were used to characterize the thermal properties and crystallinity degree using Differential Scanning Calorimetry (DSC) and viscoelastic properties using Dynamical Mechanical Analysis (DMA).

The fracture surface of flat and cylindrical notched, as well as butterfly (combined tensile/shear) specimens were investigated with SEM. The effect of stress state and temperature on the fracture surface was investigated.

In the domain of isotropic constitutive modelling, the capabilities of the von Mises and Drucker-Prager yield models were investigated. The experimental load-displacement curves were compared with the numerical simulation. While the von Mises is only sensitive to the second invariant of the stress tensor, the Drucker-Prager yield model shows also dependency on the first and third invariants of the stress tensor. The stress triaxiality and Lode angle parameter evolution were evaluated along with the equivalent plastic strain.

7.1 Conclusions: Chapter 4 Experimental Results and Discussion

Despite belonging to semi crystalline polymers with crystallinity percentage from DSC scans of 55.1%, 40.4% and 48.2%, respectively for HDPE, PP and PA 6, their mechanical behaviour are somewhat different and still not fully understood because they are tightly related with their complex microstructure and loading conditions.

Tensile Tests at Room Temperature - HDPE, PP and PA 6:

- The yield load in the lowest testing speed occurs at higher displacements, because the polymer macromolecules have the time necessary to induce an orderly alignment; also allows more time for the chain segments to engage in an increased amount of entanglement slippage and therefore increase the hardening effect.

- At higher crosshead speed, increases both the propensity of the material to form a clear and higher yield load at lower displacement values and the material exhibits a more brittle behaviour.

- Higher crosshead speeds reduce the degree of chain relaxation, resulting in more preferred orientation, yielding lower displacement values and consequent shift to brittle behaviour.

- In tensile tests of notched specimens, the yield load increases with decreasing the specimen notch radii (increasing the stress triaxiality), while the corresponding displacement decreases.

- It was observed that the HDPE, PP and PA 6 notched specimens gradually started to whiten, near the yield load. As the plastic deformation continued, the stress whitening became clearer and sets the shape changes (dilatation).

Combined Tensile or Compression/Shear at Room Temperature and at 50°C:

- At RT the drop of the load with the biaxial loading angle attains a maximum value for the loading angle $\alpha = 0°$ (pure shear) and minimum for $\alpha = 90°$ (pure tension). The higher the loading angle, higher is the load required to deform the specimens;

- The load-displacement curves shift to higher load values with increase of crosshead speed;

- The plastic stiffness decreases with increasing of crosshead speed for all loading angles;

- The crosshead speed and loading angle "after yielding" play a key role in the macroscopic deformation behaviour and determine whether the material behaves as brittle or ductile;

- Whitening and crazing, are observed and may reveal that the formation of numerous microvoids (cavities) is taking place in the centre of a specimen shortly before yielding;

- In PA 6 the load-displacement curves beyond the yield point, become coincident for all loading rates. This mechanical behaviour might indicate that there is a thermal softening associated with a progressive localization of heat sources at high crosshead speed as observed by Wattrisse et al. [158].

- Decreasing crosshead speed and increasing temperature results in lowering of the load needed to reach a given displacement. Therefore, the yield load shows an explicit dependency on temperature and crosshead speed.

Compression Tests at Room Temperature - HDPE, PP and PA 6:

- The compressive behaviour of all tested specimens shows an increase in the material strength for increasing crosshead speed. On effect, an increase of crosshead speed will decrease the molecular mobility of the polymer chains, making the material less susceptive to deform.

DSC - HDPE, PP and PA 6:

- In HDPE the increase in crystallinity can be referred to the molecular chain alignment that occurs during specimen deformation (55.1%, 56.1% and 57.6%, respectively virgin material, true strain 0.5 and 1).

- In PP the percentage crystallinity (40.4%, 41.7% and 39.3%, respectively virgin material, true strain 0.5 and 1) slight increased by 1.2 % at true strain of 0.5 and decreases by 1.2% at true strain of 1, relatively to the virgin values. At true strain of 0.5, beyond yield point, the increase

in deformed specimen crystallinity can be referred to the chain alignment that occurs during specimen deformation. At true strain 1, the decrystallization process, defined as mechanically induced destruction of crystalline lamellae (unfolding), might be the cause for crystallinity decrease.

- PA 6 at true strain of 0.5 and at 1, the decrease in deformed specimen crystallinity can be referred to the decrystallization process (49.1% and 47.2%, respectively, true strain 0.5 and 1). The virgin material crystallinity is 48.2%.

- Melting Temperature (T_m) ranged between 136°C and 140°C for HDPE; 170°C and 172°C for PP and 225°C and 227°C for PA 6, for the three situations: virgin material, deformed at true strain 0.5 and 1.

- The glass temperature, T_g, of PA 6 was 54± 2 °C. For HDPE and PP the glass transition were not detected since they are expected to be negative.

DMA - HDPE, PP and PA 6:

- HDPE at room temperature the storage modulus is relatively high, ranging from 750 N to 754 N for frequency 0.1 Hz, 820 N to 841 N for frequency 1 Hz and 1040 N to 1090 N for frequency 10 Hz and with increasing temperature, this modulus gradually reduces.

- PP DMA curves shift to higher values as the test frequency increases. At room temperature, the storage modulus is relatively high, ranging from 780 N to 820 N for frequency of 0.1 Hz, 1040 N to 1080 N for frequency of 1 Hz and 1200 N to 1240 N for frequency of 10 Hz and with increasing temperature, this modulus gradually reduces to the rubbery flow.

- For PA 6 the storage modulus increases with increasing frequency. At room temperature the storage modulus ranges from 750 N to 870 N for frequency of 0.1 Hz, 1550 N to 1570 N for frequency of 1 Hz and 1770 N to 1820 N for frequency of 10 Hz and with increasing temperature, this modulus gradually is reduced.

- At the glass transition temperature (T_g) a sharp decrease in storage modulus is observed, since here the polymer chains obtain full segmental mobility and their state changes from glassy to rubbery, where crystals are known to yield readily, and an influence of the tie molecules on the network is considered to be absent [39].

- The glass transition temperature increases with increasing frequency, ranging from 49 °C (in accordance with DSC results) for 0.1 Hz, 67 °C for 1 Hz and 75 °C for 10 Hz.

HDPE, PP, PA 6 Mechanical Behaviour Discussion:

- PA 6 mechanical responses at RT, are characterized by yield, softening and hardening. Increasing the crosshead speed to 200 mm/min, the material is observed to soften, probably due to temperature rising.

- However, at a temperature of 50°C the softening behaviour it is not observed, considering the same loading angle. As the glass temperature of PA 6 ranges between 49 °C (DMA) to 56 °C (DSC); at RT the imposed deformations might induce the change of material state, from glassy

to glassy-rubbery (glass transition temperature) by increasing its internal temperature. As the internal temperature increases, PA 6 passes through glass transition, above which it softens.

- On the other hand at temperature of 50°C, PA 6 is already in its glass temperature state, although possible increase of internal material temperature due to deformation there is no change of state.

- As a general rule, semi crystalline polymers are used at temperatures between glass transition temperature and a practical softening temperature which lies above T_g and below T_m, these are the cases of HDPE and PP. Although the different stress states, loading angle conditions, the general shape of all curves for each material and test, seem to exhibit remarkably similar intrinsic behaviours, when compared with increased crosshead speed.

7.2 Conclusions: Chapter 5 Fracture Surface Analysis

As expected, SEM fracture morphologies of HDPE, PP and PA 6, revealed that the formation of cavities or cracks depends on the particular internal morphology of polymer, such as molecular structure, molecular weight, distribution and experimental factors, such as, temperature and stress triaxiality imposed by specimens with different notches geometries.

Flat and Cylindrical Notched Specimens:

- It is assumed that the fracture toughness of semi crystalline polymers is controlled by mechanisms such as crazing, void and cavitation formation. One of the major factors controlling the occurrence of yielding or brittle fracture is the state of stress, such as the one included by the presence of notches.

- SEM fracture morphologies of HDPE, PP and PA 6, reveal that the fracture morphologies are highly dependent on stress states. Lower stress triaxiality is a synonymous of ductile fracture. Flat notched specimen *R* 5 and *R* 30 show the formation of an oriented texture of fibrous surface, which increases with decrease of notched radii (low triaxiality).

- It is observed that rising the stress triaxiality, fracture becomes more brittle and homogeneous, with less formation propensity of longer fibrous surface and more voids content.

- Qualitative SEM observations of HDPE, PP and PA 6, fracture surfaces of flat and cylindrical notched specimens depict inhomogeneous morphology. Mechanisms such as crazing, void and cavitation formation, are observed. In the same surface two or more mechanisms, are found. This means that the stress across fracture surface is not equal and is maximum at centre, where the fracture normally begins (large triaxiality).

- SEM micrographs of PP exhibit predominantly brittle failure, cavitation and voids. Although the different stress triaxialities imposed by different specimen's geometries and notches, the fracture surfaces morphologies slight modifies. This feature might be attributed to the internal morphology of polymer.

- In HDPE cylindrical *R 30* at peripherical and central region microfibrils with knobs or nodules with a smooth rounded surface like features probably formed by the relaxation of hot material, was observed. Similar features were found in research work performed by Brough et al. [176] on scanning electron micrographs of HDPE fracture surfaces. Also, this supports the conclusions of Chou et al. [156] and Arruda et al. [157] that heating occurs during deformation.

Combined Tensile/Shear Loading Fracture Morphologies:

Pure Tension: Beyond the state of stress, combined tensile/shear loading, also influence the fracture morphology. The microstructure deformation mechanisms during biaxial loading at α = 90° tension, at room temperature and at temperature of 50 °C, for HDPE, PP and PA 6, are:

- The fracture morphology exhibits different modes of deformation, for α = 90°, pure tension at moderated stress triaxiality and at room temperature. Mechanisms such as crazing, void and cavitation formation, are observed. Two or more mechanisms are predominant and fracture morphology are inhomogeneous.

- In general, with the increase in temperature, fracture becomes more homogenous, the extent of craze region decreases and the ductile area/surface increases. In the case of HDPE, at the central region, the fracture surface is reduced, becoming narrower, suggesting that was the last region to fracture. PA 6 acquires a fracture surface completely different from that obtained with room temperature. With increasing temperature the fracture surface becomes more ductile with fibril formation at central region.

Combined Tensile/Shear: The main observations on SEM micrographs for combined tensile/shear loading, α = 30°, fracture morphologies at room temperature and at temperature of 50 °C, for HDPE, PP and PA 6, are:

- It is observed a fracture morphology oriented towards the loading direction, such as in the case of PP, which at RT or at temperature of 50 °C shows oriented fibrils with the direction of loading (α = 30°), exhibiting high deformation before failure (ductile failure). The inner layer shows a more ductile behaviour than at α = 90°.

- Diferent fracture morfologies are observed, when compared with α = 90°. The fracture becomes more ductile and less homogeneous, with more formation propensity of longer fibrous surface. Also, with the temperature increase, fracture becomes more homogenous.

Pure Shear: SEM images of fracture mechanisms under pure shear, α = 0°, at RT and at temperature of 50 °C, for HDPE, PP and PA 6, show:

- From SEM images at room temperature of HDPE and PP is observed that the fracture surfaces exhibit predominantly ductile failure with crazing and tearing, fibril formation associated with the shear loading, whereas PA 6 exhibits a considerable plastic deformation and inhomogeneous morphology.

-Pure shear leaves a relatively smooth fracture surface and orientated geometry. In general, it is observed that the fibrils are oriented towards the shear direction.

7.3 Conclusions: Chapter 6 Plasticity Model Calibration and Verification – Drucker-Prager and von Mises

- The results of numerical simulation with HDPE, PP and PA 6 show that, both Drucker-Prager and von Mises models capture the initial elastic range, however the post-elastic response is overestimated for notched specimens and combined loading on butterfly.

- For unnotched specimens, tensile dumbbell and compression cylindrical, the numerical simulations results essentially matched the experimental results, whereas the peak force is well captured, with both Drucker-Prager and von Mises models. The cylindrical and flat notched specimens, develop a larger hydrostatic stress than unnotched specimens such as dumbbell. Therefore the differences between the von Mises and Drucker-Prager yield criteria are much smaller for plane stress conditions, such as tensile dumbbell and compression cylindrical.

- For triaxial and combined stress, the best correlation is with the Drucker-Prager yield criterion, that however cannot predict accurately the load-displacement responses in some tests, even including the hydrostatic stress parameter and the isotropic hardening. Even though it allows a more precise prediction of deformation, than von Mises yield criterion.

- The effect of Lode angle was not taken into account. Deviations observed in the predicted and experimental results obtained with the Drucker-Prager yield model are very likely attributed to third invariant stress tensor effects not properly explored in the Drucker-Prager yield model calibration. Also, some studies however showed that the mechanical response of polymers is sensitive also to Lode angle parameter [180]. Thus, the Lode angle parameter effect should also be taken into account in the description of the plastic behaviour, for a better accuracy in the results.

- For most tests, numerical simulations show that there is variation of the stress triaxiality and equivalent plastic strain along the cross section and the location of the maximum plastic strain and maximum stress triaxiality in the specimens are located at the centre. Thus the yielding probably initiates from the centre and propagates towards the outer surface.

- The Lode angle parameter has a constant value through deformation to fracture for the set of cylindrical notched specimens ($\overline{\theta} = 1$) and for the set of flat notched specimens it converges quickly to $\overline{\theta} = 0$ at the beginning of the deformation. However, the stress triaxiality value is not constant through loading and increases with notched radii. It is verified that decreasing the notch radii, the higher difference of stress triaxiality between the beginning and end of deformation, due to increasing the stress triaxiality.

- Each specimen is assumed to represent a single point in the space of stress triaxiality and Lode angle parameter. The biaxial loading performed on butterfly specimens, shown that it is possible to investigate the stress triaxiality and Lode angle parameter for different stress states with a single specimen geometry by changing the loading angle.

7.4 Future Studies

Concerning the experimental work and for improvements in compression tests, it is recommended to reduce the friction between the specimen and the compression platen, for instance by using some PTFE-film. Moreover, the volume change during deformation should be investigated as well as quantified the increase in temperature, with increasing the crosshead speed. It should be apparent that the faster the crosshead speed, the less time for heat transfer, hence the more important the adiabatic effects, which might produce a thermal softening of the material. The use of thermographic cameras in future tests with polymers is recommended since these materials are very sensitive to small temperature changes.

Use of 3D Digital Image Correlation to monitor the local yielding of the material for the tested geometries adopted in this work is also recommended to provide data for direct identification of constitutive models.

Addressing the stress-drop or even the yield stress or the very beginning of strain hardening, it would been interesting to study compressed or tensioned specimens in a scanning electron microscope (SEM) to see whether any signs of damage could be observed at the microscopic level.

Developments of new constitutive model is probably is the next step. The deformation of thermoplastic polymers commonly involves large elastic and plastic deformations. From the extensive experimental data, it can be concluded that the behaviour of HDPE, PP and PA 6 is complex due to its strong dependency on strain-rate, stress triaxiality (pressure) and temperature. The materials studied also experience the stress triaxiality pressure-dependent yield strength. It means that the yield strength of HDPE, PP and PA 6 increases as the pressure increases which results in a higher yield strength in compression compared to the one in tension. Therefore, the predictive modelling of their behaviour requires complex mathematical formulations due to those dependencies. The modelling of the plastic behaviour of the materials till failure is a task that needs to be addressed in future works.

Finally this kind of study should be extended to higher strain rate loading regimes which are very important for applications.

8 Appendix

8.1 Arcan Apparatus

8.1.1 Arcan Apparatus Technical Drawings - All Details and Dimensions

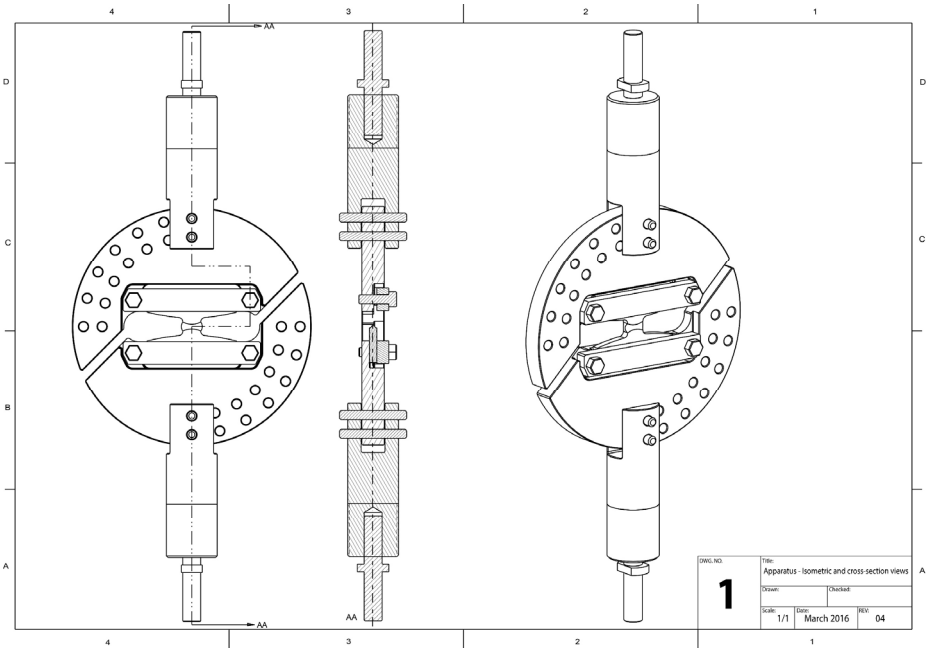


Figure 156 - Designed Arcan Apparatus – isometric and orthogonal views.

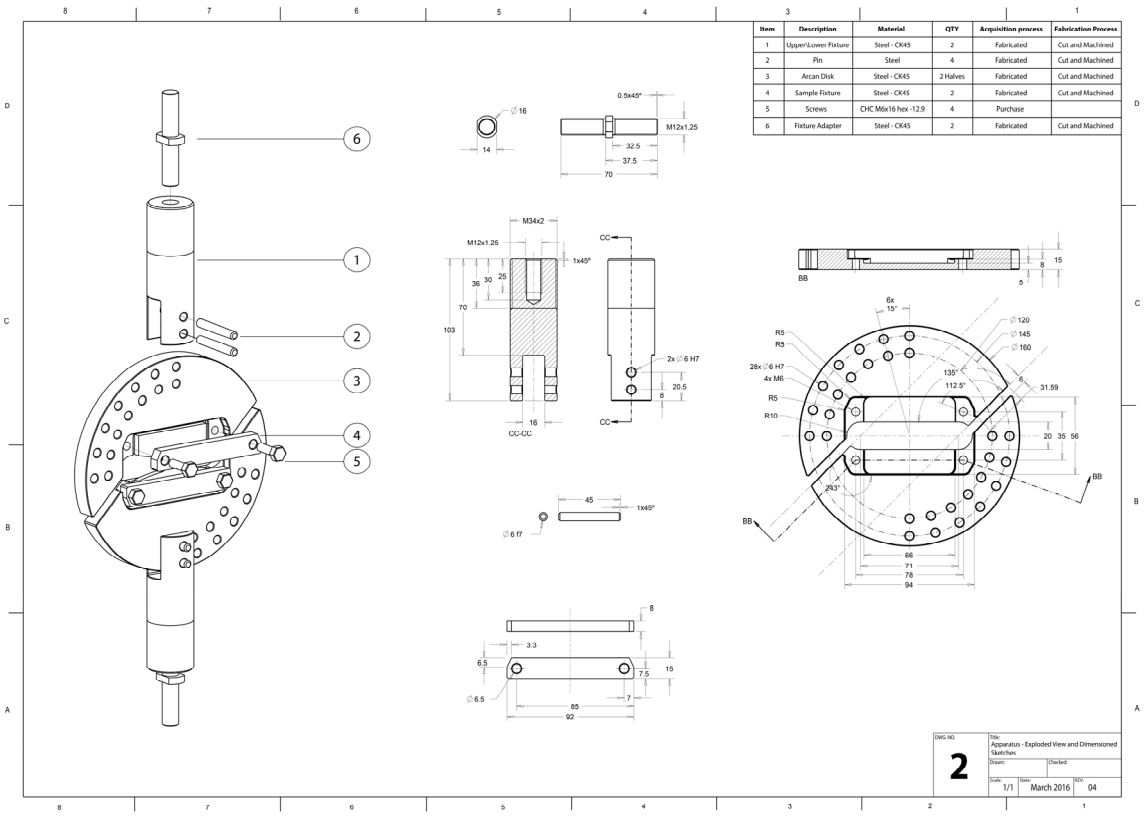


Figure 157 - Designed Arcan Apparatus – exploded view and dimensions of components.

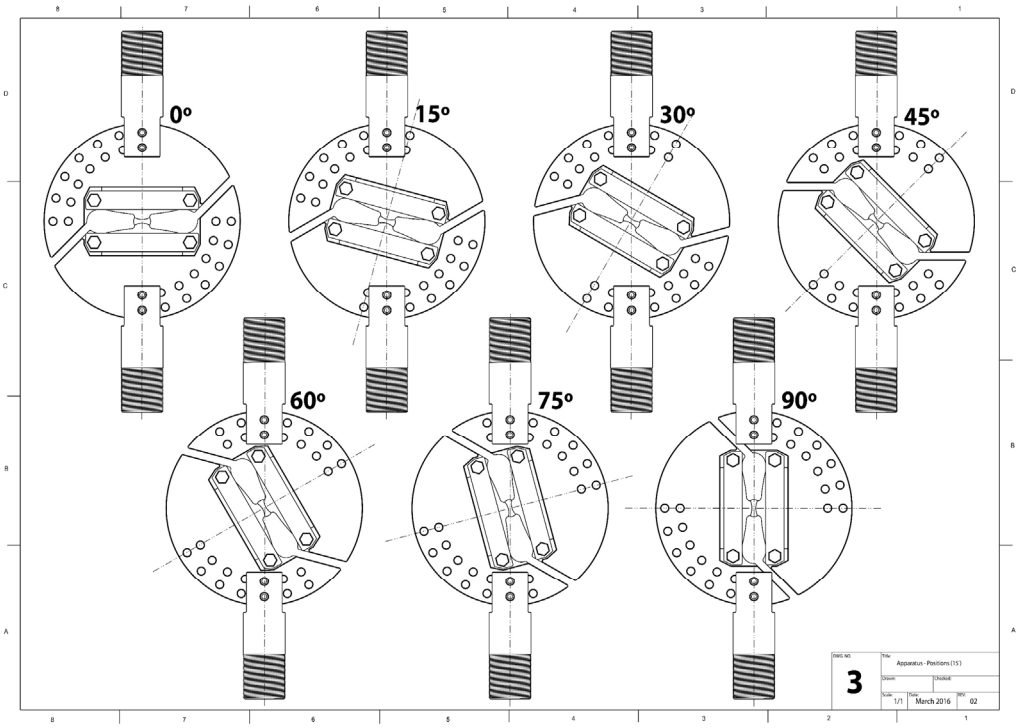


Figure 158 - Designed Arcan Apparatus - range of biaxial loading angles (α = 0°: shear; α = 90°: tension/compression).

8.1.2 Arcan Apparatus Modifications - Technical Drawings

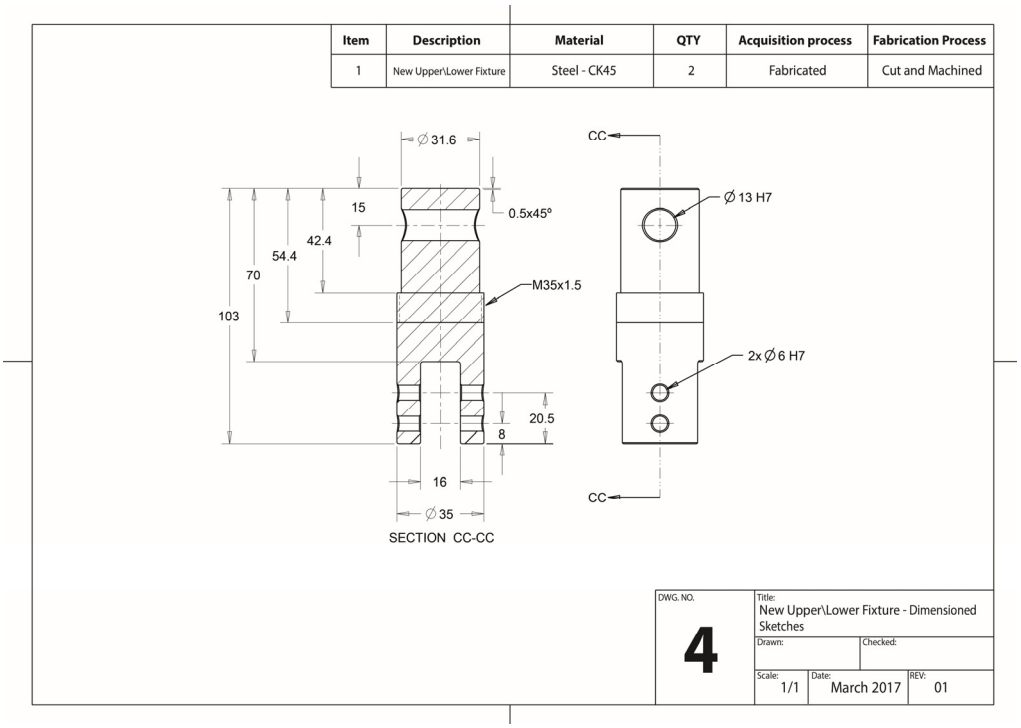


Figure 159 - Arcan Apparatus Modifications - intermediate grips modification to avoid rotation of specimens gripping.

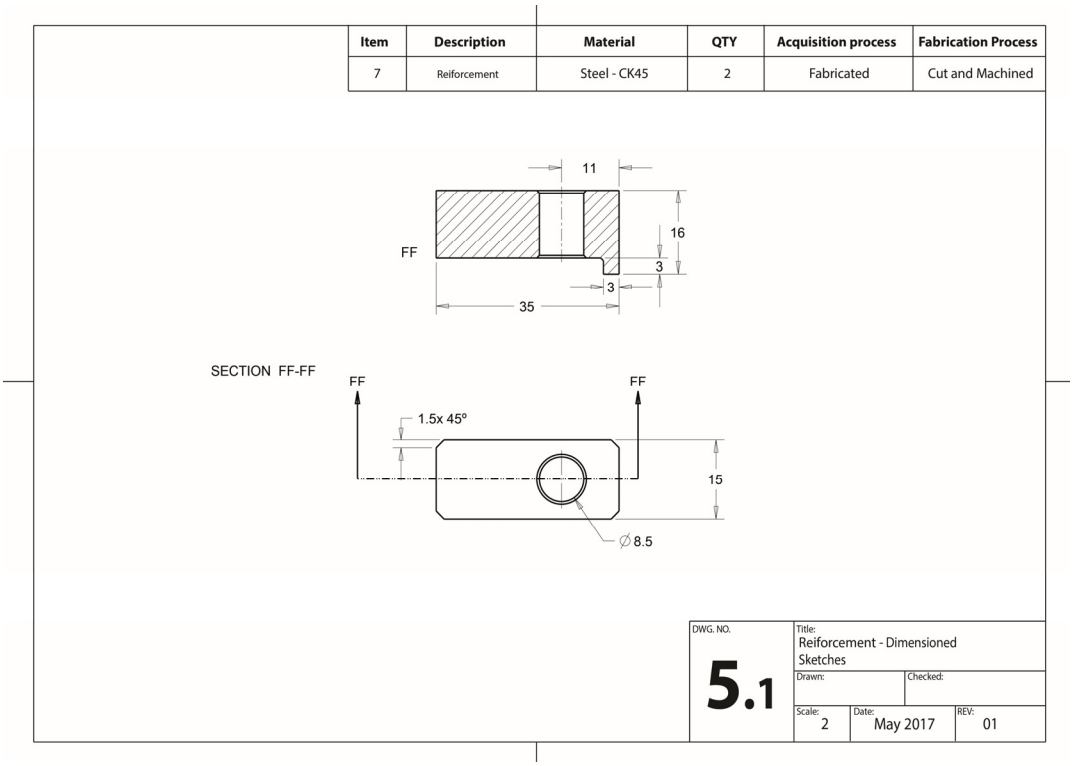


Figure 160 - Arcan Apparatus Modifications - designed specimen extra-clamping device.

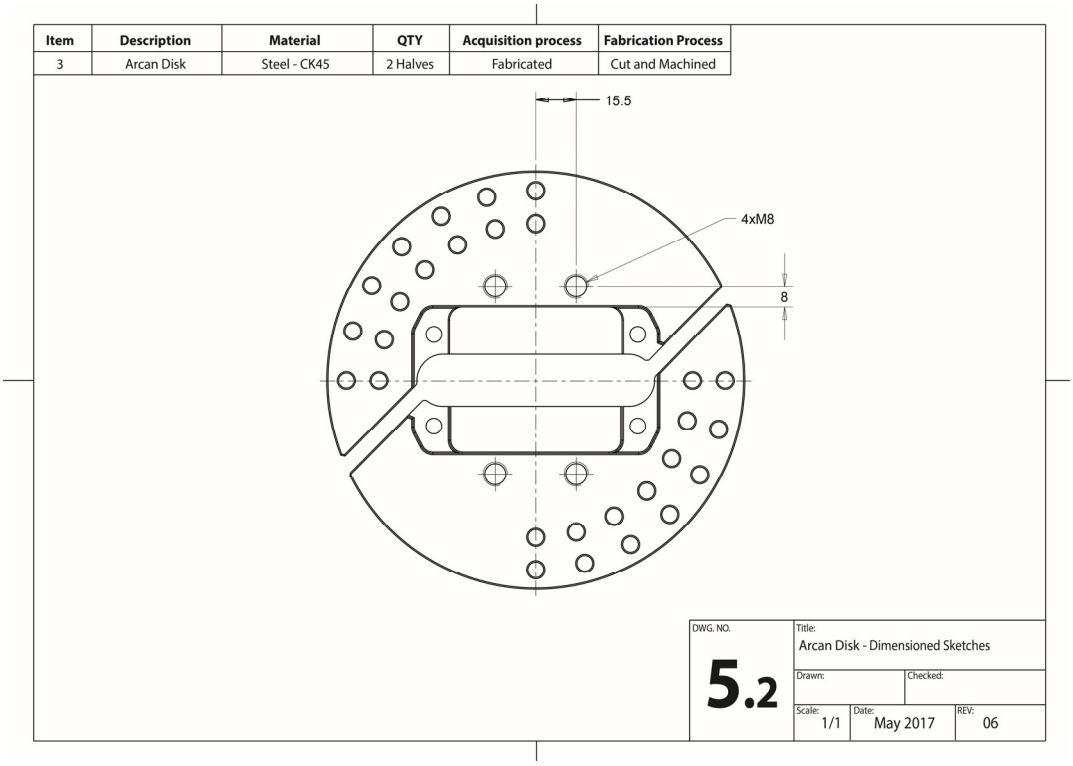
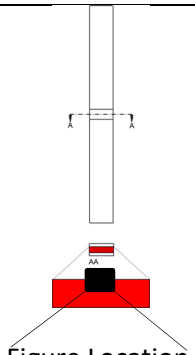
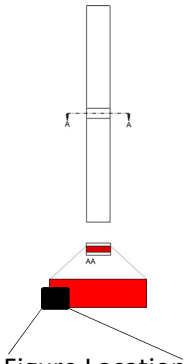


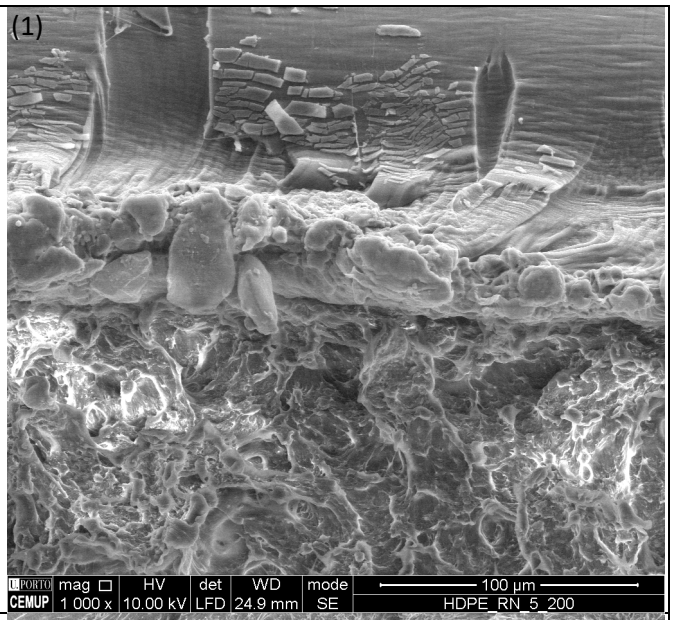
Figure 161 - Arcan Apparatus Modifications – extra drilled holes for extra specimen clamps.

8.2 All SEM Micrographs

8.2.1 All SEM Micrographs – Flat Notched Specimens – HDPE, PP and PA 6

Note that in the first column the geometry of specimen and fracture surface location are indicated by the black square.

HDPE, Fracture Surface	
- Room temperature 21 °C ± 2 °C, - Tensile test, - Crosshead speed: 200 mm/min, - Flat notched radius 5.	
	
	
SEM micrographs. (1) Skin layer. Inhomogeneous multiphase structure. (2) Low magnification. Brittle Vs ductile failure.	



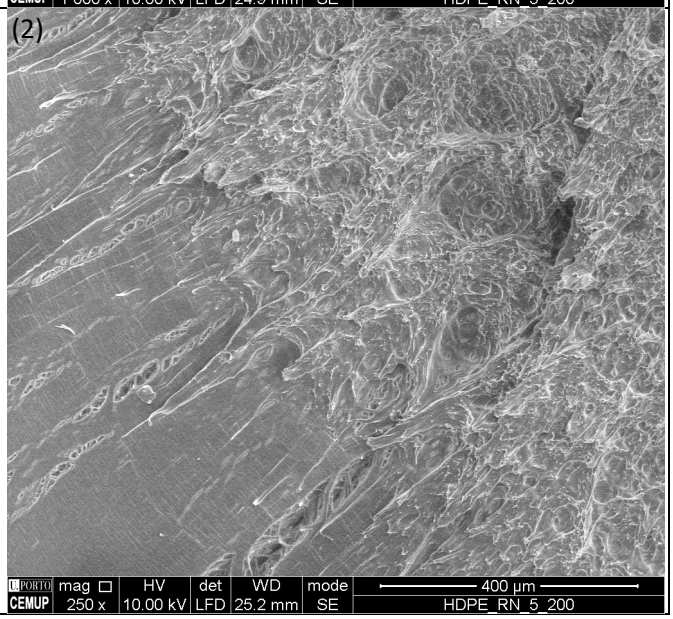
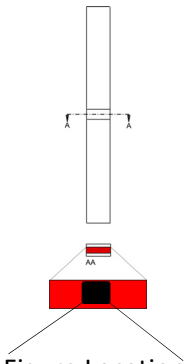


Figure 162 – SEM fracture surfaces for flat notched specimens with *R 5* for HDPE at RT. Localization: near surface.

HDPE, Fracture Surface	
- Room temperature 21 °C ± 2 °C, - Tensile test, - Crosshead speed: 200 mm/min, - Flat notched radius 5.	
	
SEM micrographs. (1) Overall view of central fracture surface, at low magnification. Large amount of small deformations all over the surface with a number of longer fibrils. (2) High magnification. Fibrils pulled out from a background of deformed material.	

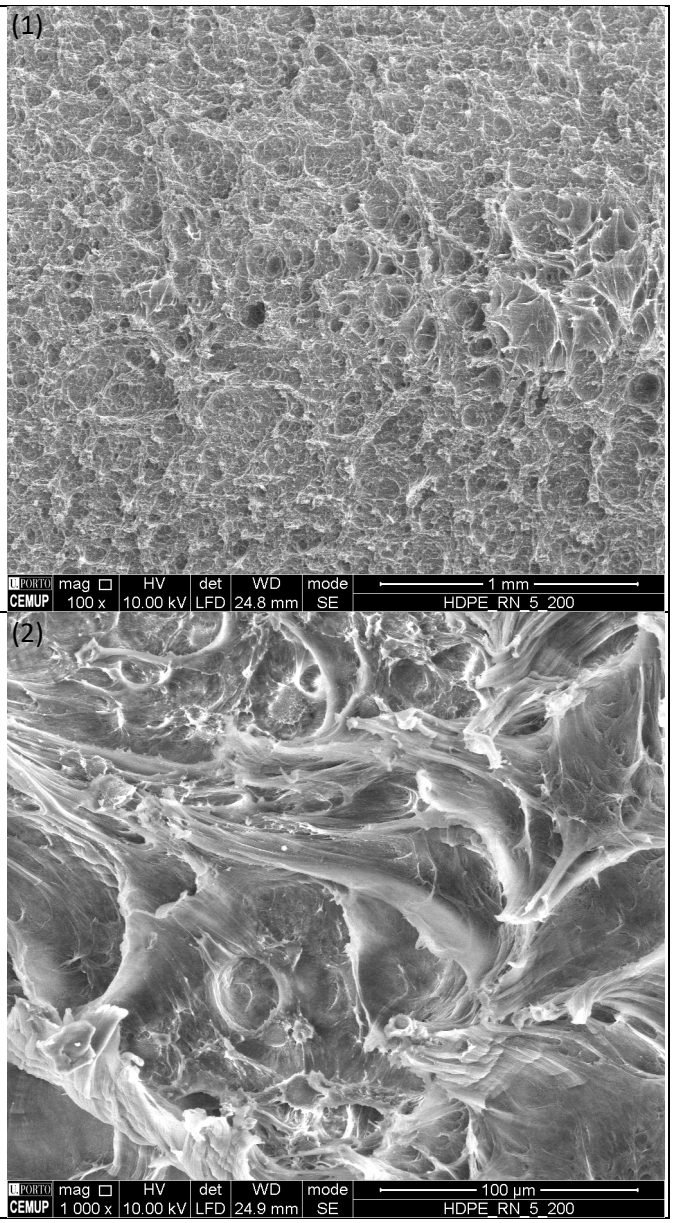
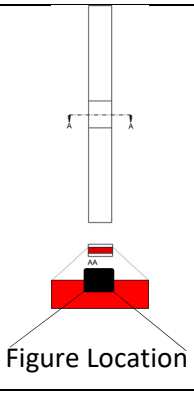
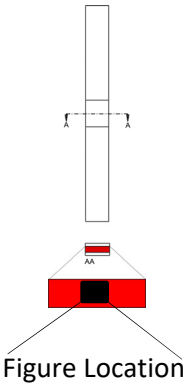
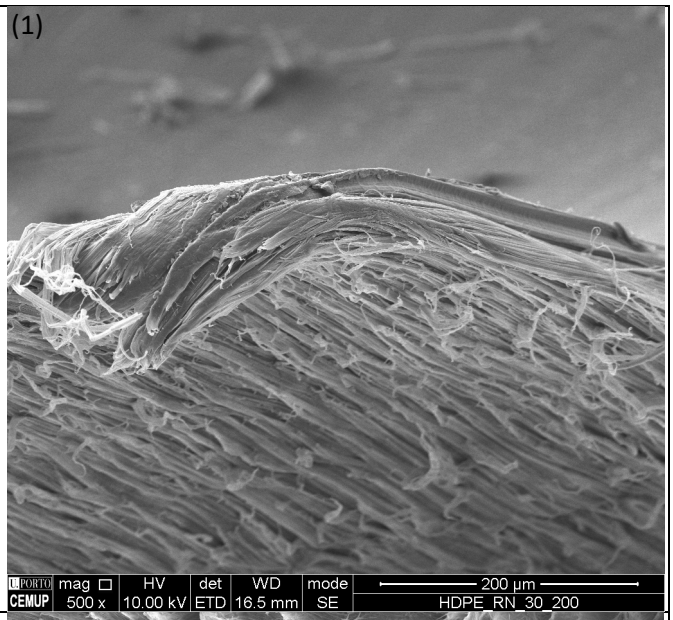
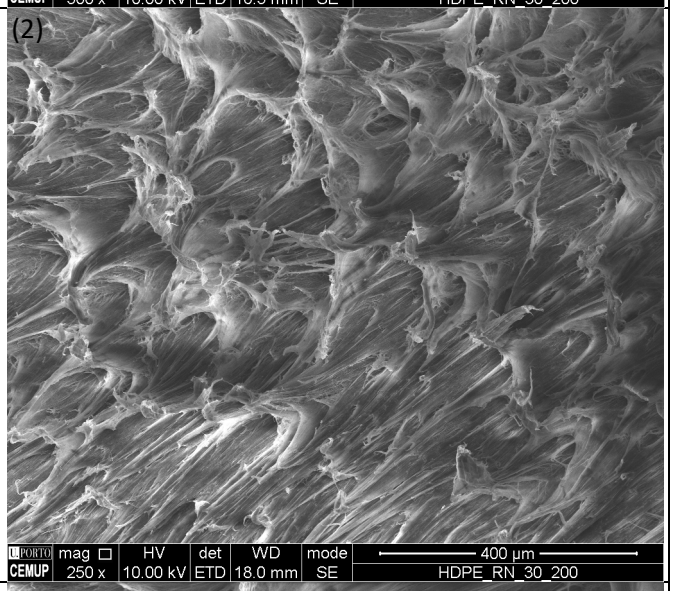


Figure 163 – SEM fracture surfaces for flat notched specimens with *R 5* for HDPE at RT. Localization: central.

HDPE, Fracture Surface	
- Room temperature 21 °C ± 2 °C, - Tensile test, - Crosshead speed: 200 mm/min, - Flat notched radius 30.	
	 Figure Location
	 Figure Location
SEM micrographs. (1) “Peeling skin layer” with large amount of fibrils. (2) and (3) Fibrils pulled out, some of them starting from points of apparent discontinuity in the progress of the crack in central region-fracture.	





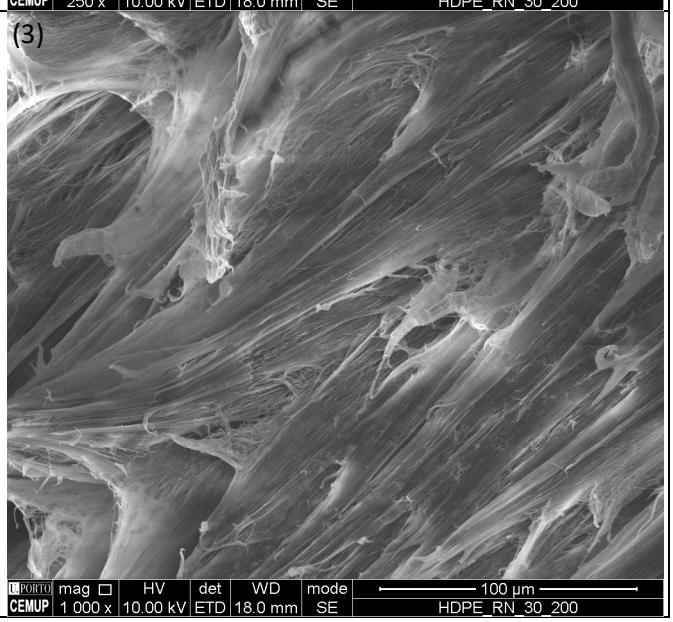


Figure 164 – SEM fracture surfaces for flat notched specimens with *R 30* for HDPE at RT. Localization: central and near surface.

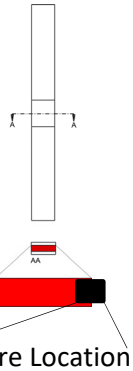
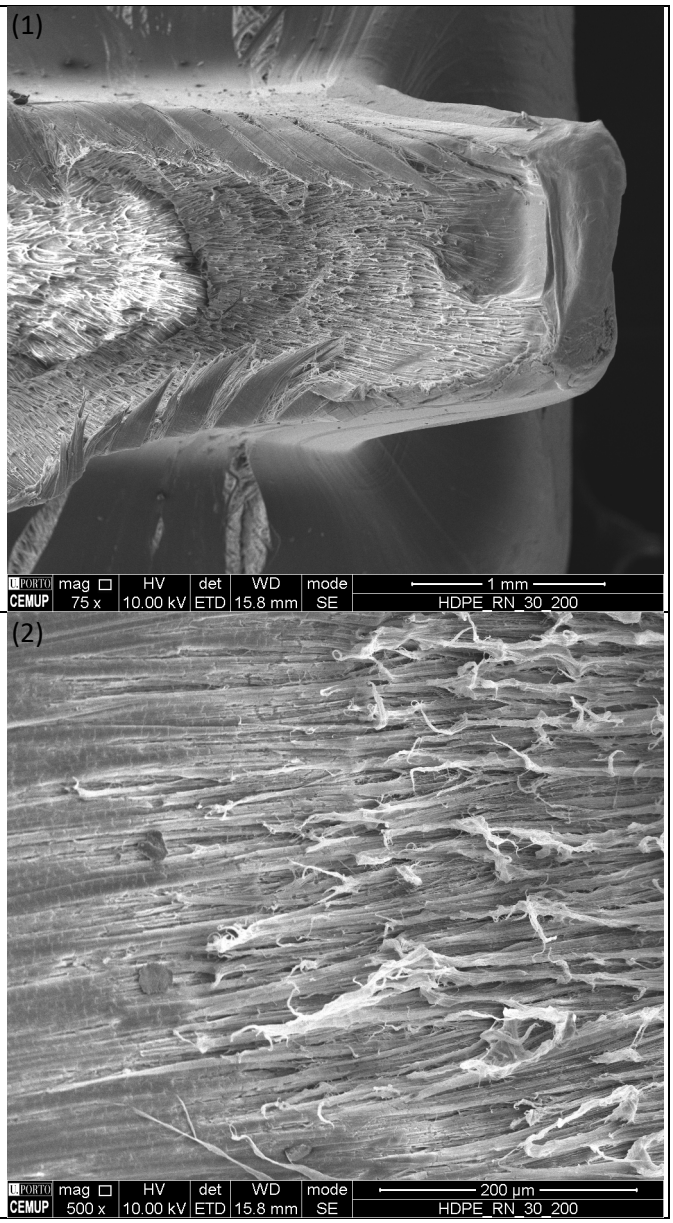
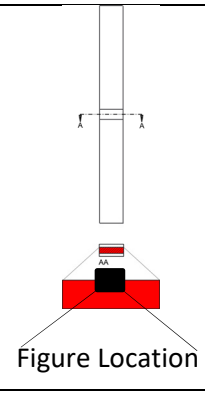
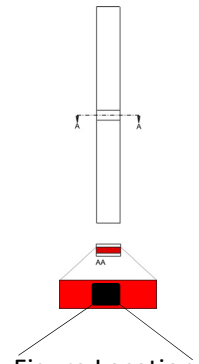
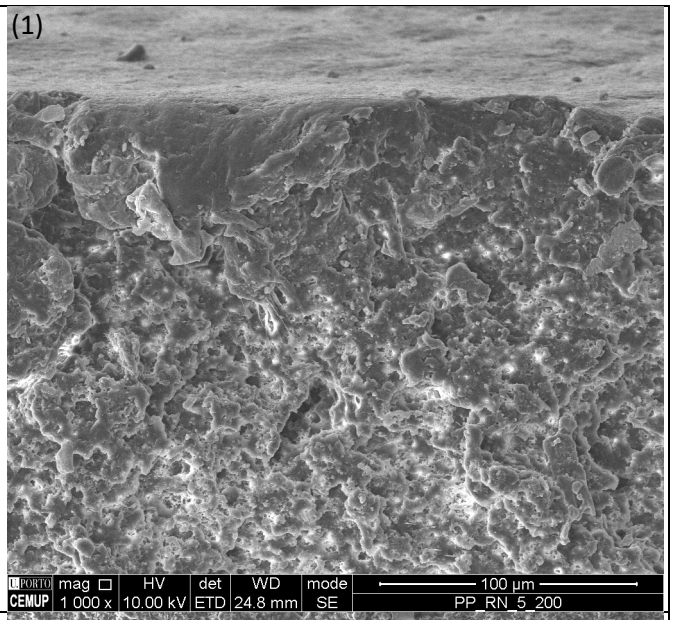
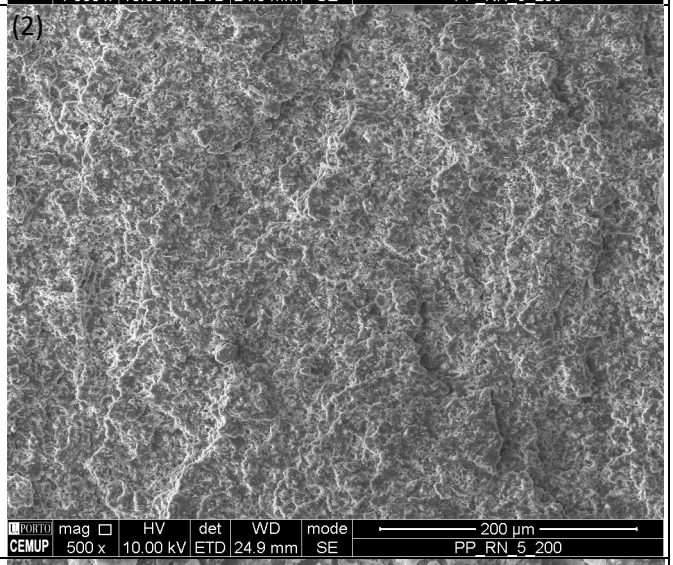
HDPE, Fracture Surface	
- Room temperature 21 °C ± 2 °C, - Tensile test, - Crosshead speed: 200 mm/min, - Flat notched radius 30.	
	
SEM micrographs. (1) View of the extreme right fracture surface at low magnification, shows an inhomogeneous fracture (2) High magnification view of a craze in a form of fibrils. It was the last region to fracture.	

Figure 165 – SEM fracture surfaces for flat notched specimens with *R 30* for HDPE at RT. Localization: near surface.

PP, Fracture Surface	
- Room temperature 21 °C ± 2 °C, - Tensile test, - Crosshead speed: 200 mm/min, - Flat notched radius 5.	
	
	
SEM micrographs. (1) and (2) at low magnifications, exhibiting surface patterns in fracture region. (3) At high magnification, the fracture surface exhibits the predominantly brittle failure characteristics also cavitation and voids, are detected.	





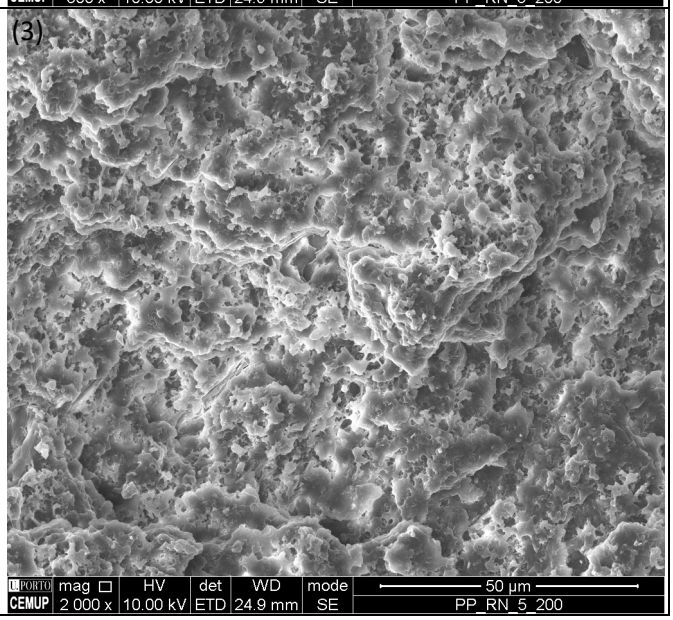


Figure 166 – SEM fracture surfaces for flat notched specimens with *R 5* for PP at RT. Localization: central and near surface.

PP, Fracture Surface	
- Room temperature 21 °C ± 2 °C, - Tensile test, - Crosshead speed: 200 mm/min, - Flat notched radius 30.	
	Figure Location
	Figure Location
SEM micrographs (1), (2) and (3) shows similar fracture surface characteristics than the previous. However, the roughness fracture surface seems to increases with increase of notched radius. (3) At centre, an amount of fibrils is depicted.	

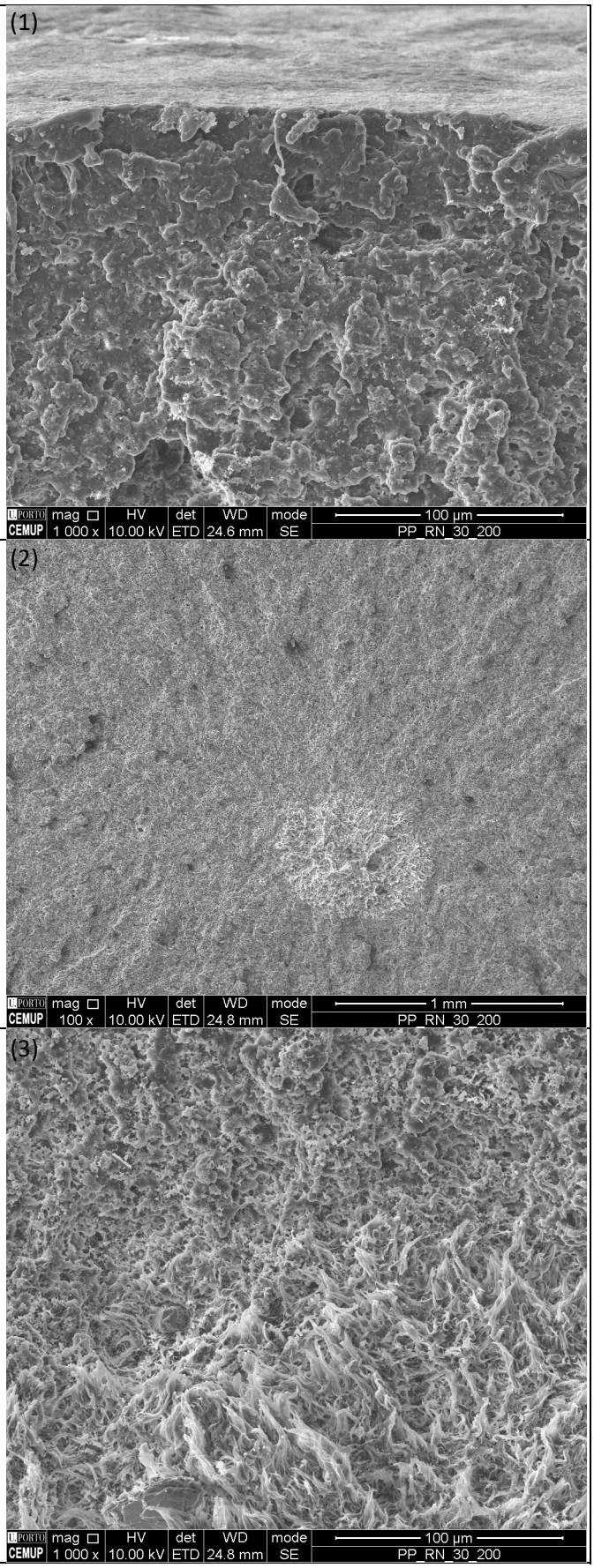
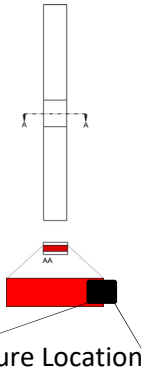


Figure 167 – SEM fracture surfaces for flat notched specimens with *R 30* for PP at RT. Localization: central and near surface.

PP, Fracture Surface	
- Room temperature 21 °C ± 2 °C, - Tensile test, - Crosshead speed: 200 mm/min, - Flat notched radius 30.	
	
SEM micrographs. At (1) low and (2) high magnification is included a number of discontinuities or jumps in the fracture process leading to a blocky structure. (2) A very fine mesh of deformed polymer, is observed.	

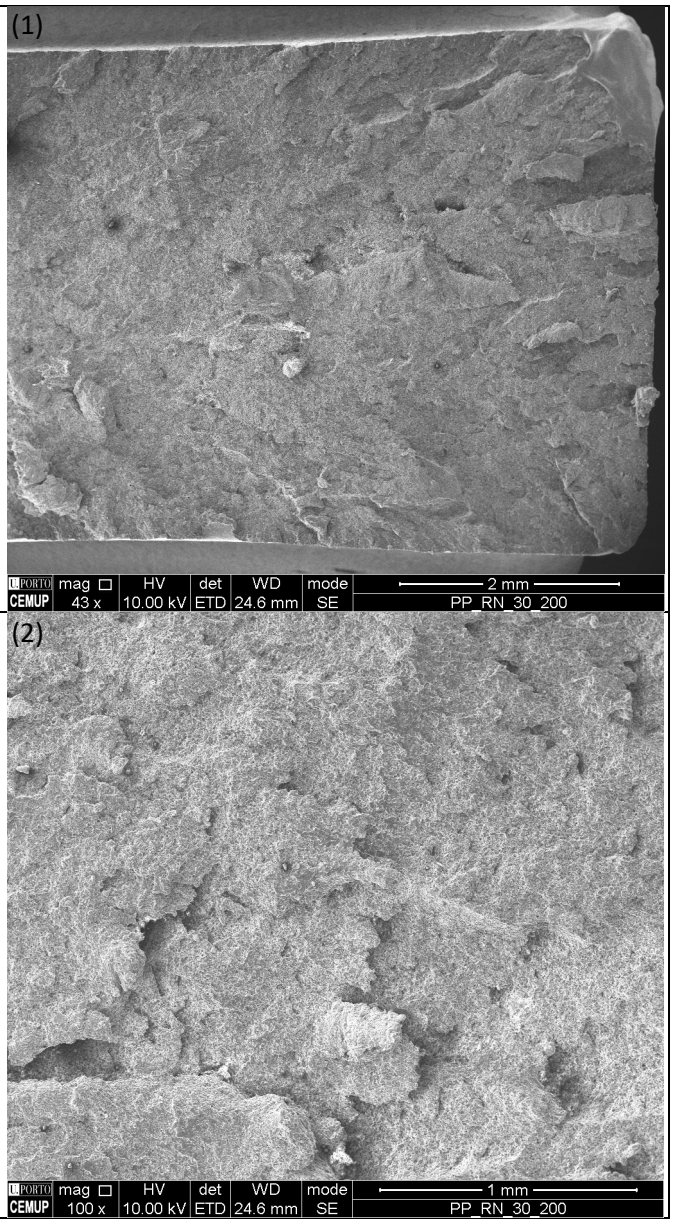
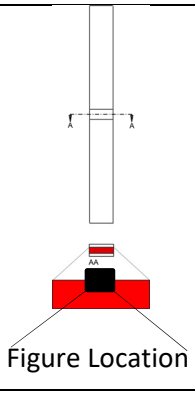
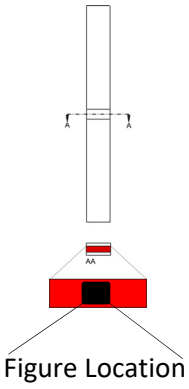
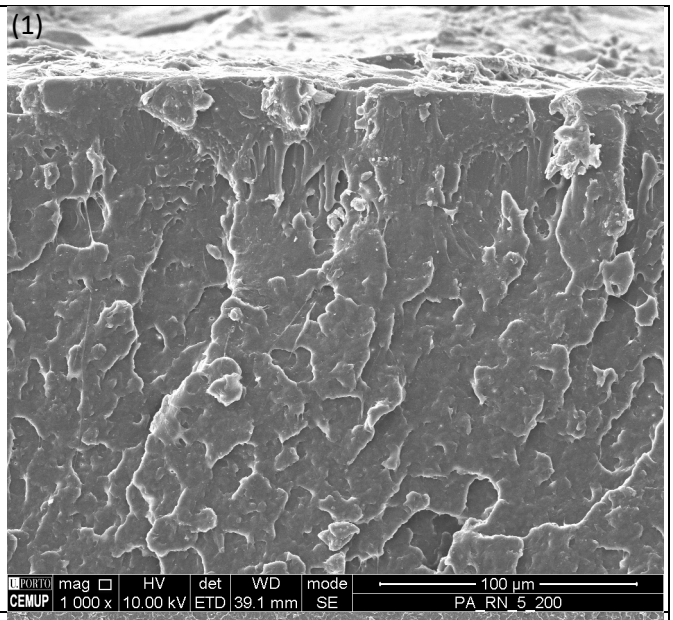
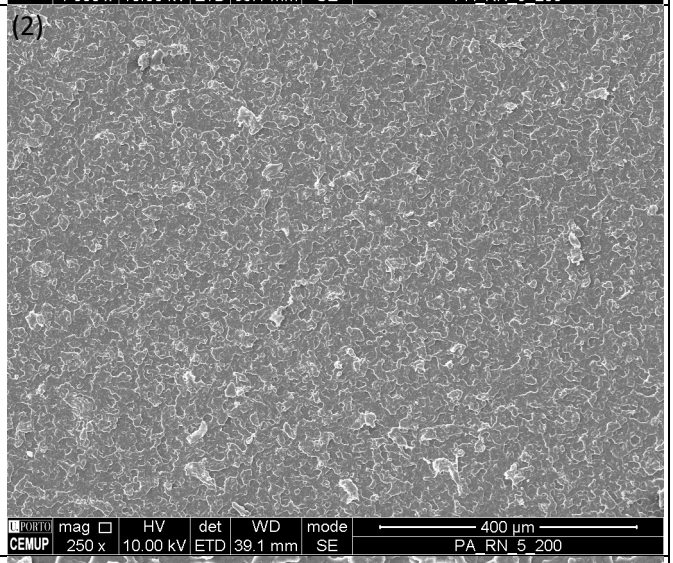


Figure 168 – SEM fracture surfaces for flat notched specimens with *R 30* for PP at RT. Localization: near surface.

PA 6, Fracture Surface	
- Room temperature 21 °C ± 2 °C, - Tensile test, - Crosshead speed: 200 mm/min, - Flat notched radius 5.	
	
	
SEM micrographs (1), (2) and (3) shows that fracture surface is covered with a very fine mesh of deformed polymer. Brittle fracture and absence of fibrils formation, are verified.	





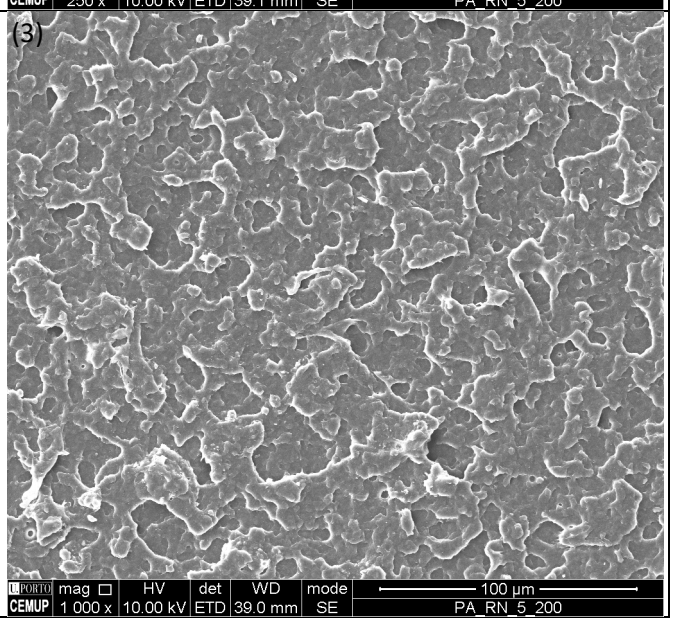
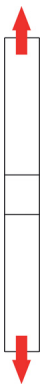
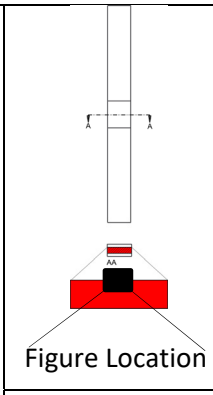
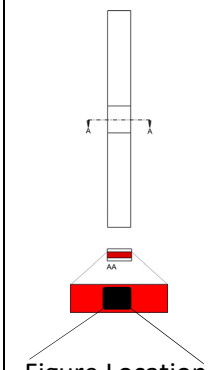
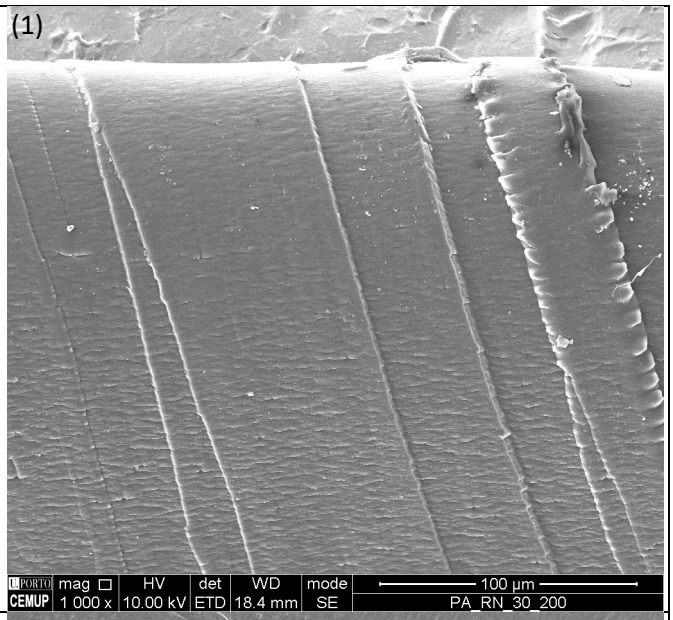


Figure 169 – SEM fracture surfaces for flat notched specimens with *R 5* for PA 6 at RT. Localization: central and near surface.

PA 6, Fracture Surface	
- Room temperature 21 °C ± 2 °C, - Tensile test, - Crosshead speed: 200 mm/min, - Flat notched radius 30.	
	 Figure Location
	 Figure Location
SEM micrographs. (1) Crazing tearing. (2) and (3) smooth surface with some voids content at the centre.	





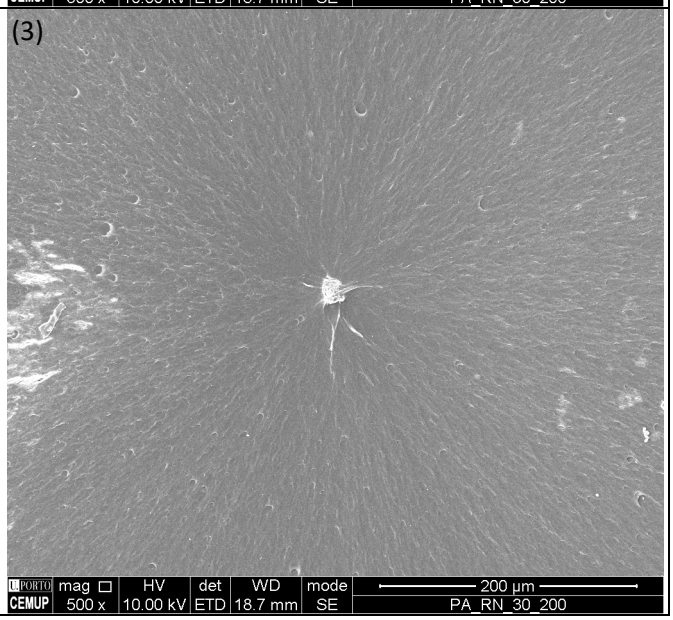
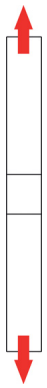
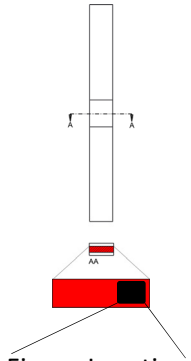


Figure 170 – SEM fracture surfaces for flat notched specimens with *R 30* for PA 6 at RT. Localization: central and near surface.

PA 6, Fracture Surface	
- Room temperature 21 °C ± 2 °C, - Tensile test, - Crosshead speed: 200 mm/min, - Flat notched radius 30.	
	
SEM micrographs. (1) Low and (2) high magnification shows rough surface at extremity. It was the last region to fracture.	

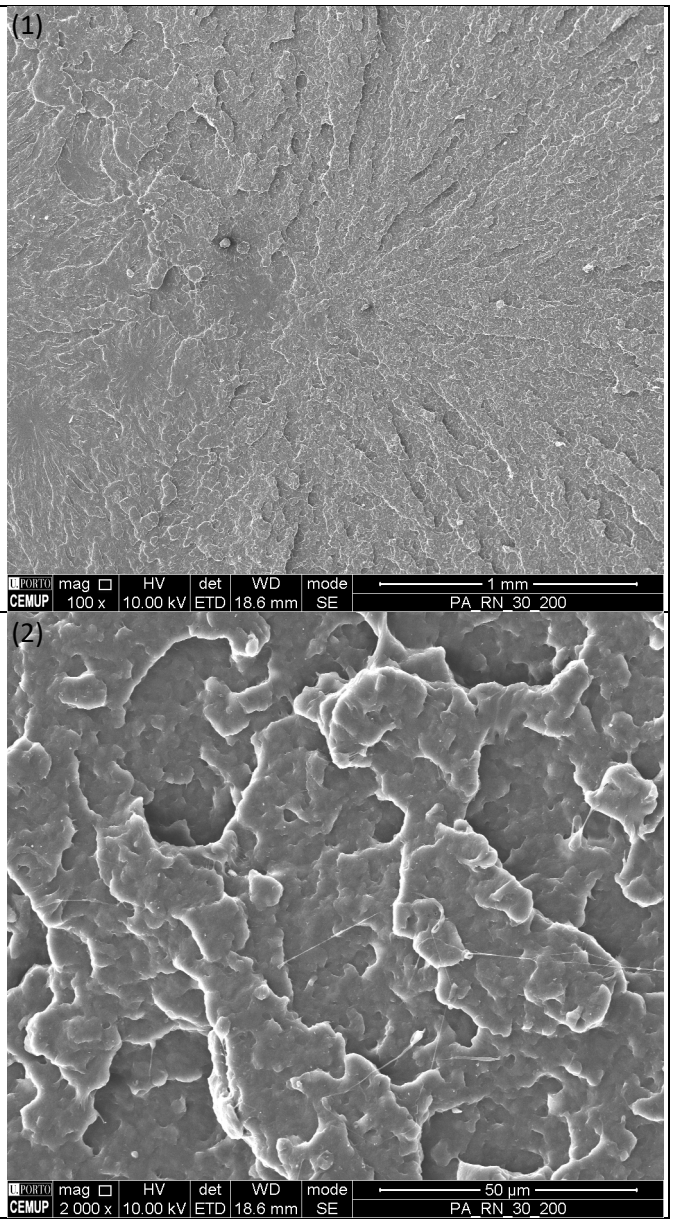
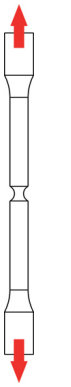
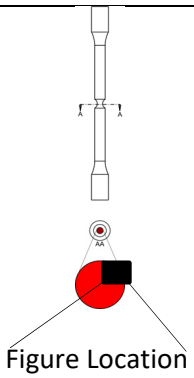
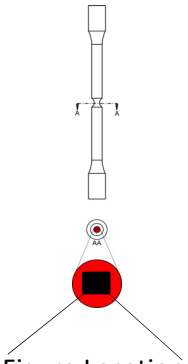
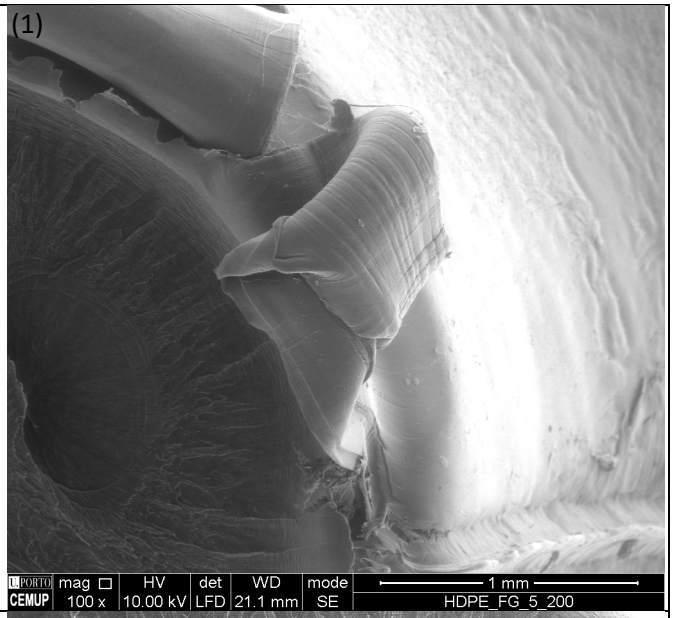


Figure 171 – SEM fracture surfaces for flat notched specimens with *R 30* for PA 6 at RT. Localization: near surface.

8.2.2 All Micrographs – Cylindrical Notched Specimens – HDPE, PP and PA 6

HDPE, Fracture Surface	
- Room temperature 21 °C ± 2 °C, - Tensile test, - Crosshead speed: 200 mm/min, - Cylindrical notched radius 5.	
	 
SEMs (1) and (2) at low magnifications, shows some microfibrils content near surface, due to crazing fracture mechanism. (1) Large “peeling skin surface”.	



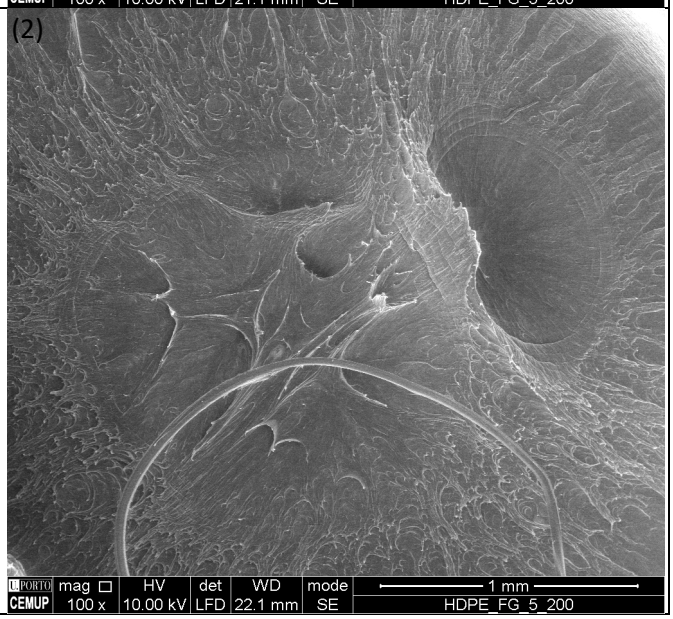
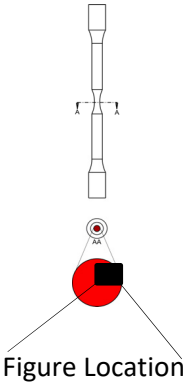
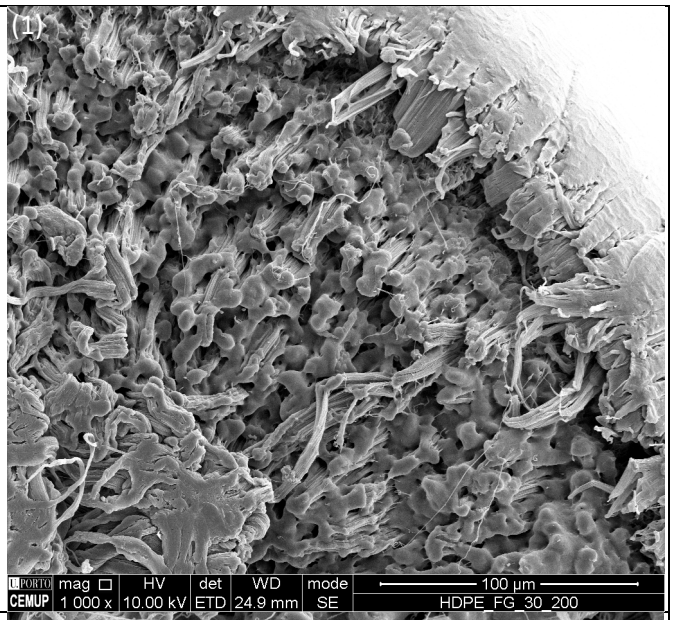


Figure 172 – SEM fracture surfaces for cylindrical notched specimens with *R 5* for HDPE at RT. Localization: central and near surface.

HDPE, Fracture Surface	
- Room temperature 21 °C ± 2 °C, - Tensile test, - Crosshead speed: 200 mm/min, - Cylindrical notched radius 30.	
	
SEMs are shown at three levels of magnification. (1) one quarter view. Large amount of short fibrils at periphery and long fibrils at centre. (2) High magnification. Fibrils with knobs or nodules with a smooth rounded surface. (3) High magnification. Long fibrils at centre.	



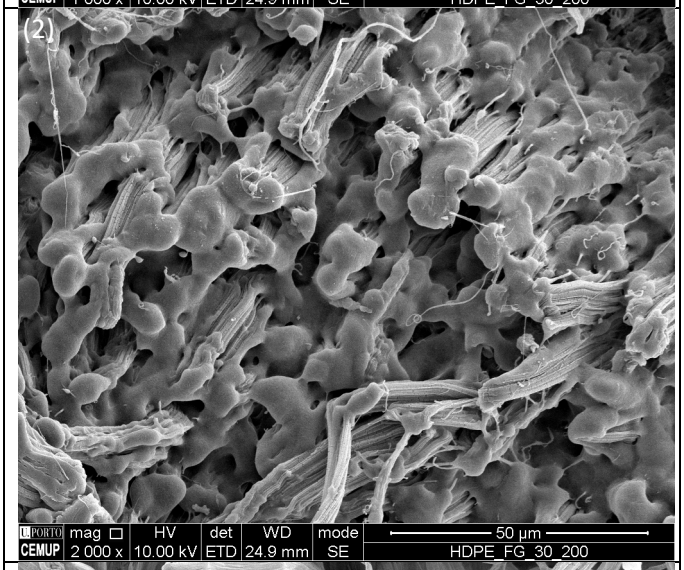
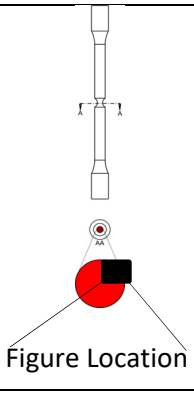
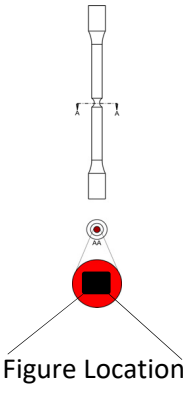
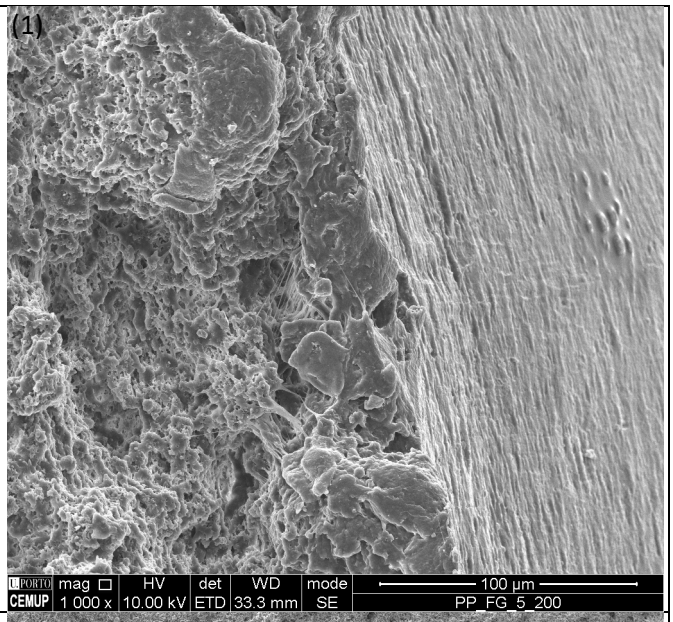
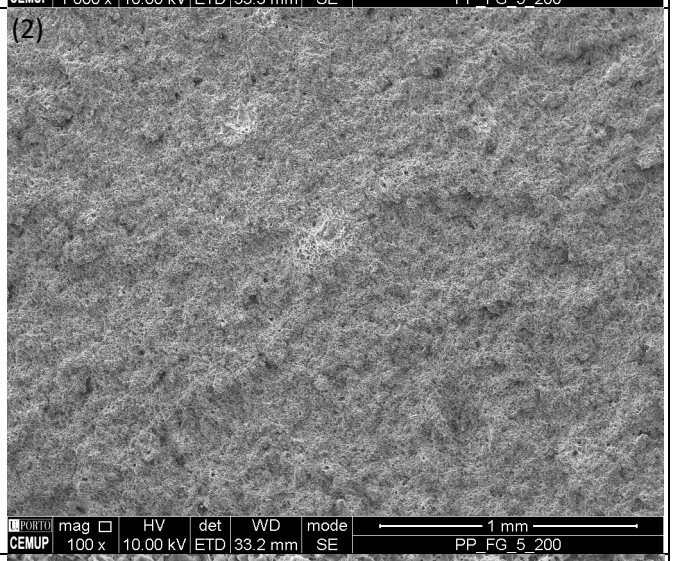




Figure 173 – SEM fracture surfaces for cylindrical notched specimens with *R 30* for HDPE at RT. Localization: near surface.

PP, Fracture Surface	
- Room temperature 21 °C ± 2 °C, - Tensile test, - Crosshead speed: 200 mm/min, - Cylindrical notched radius 5.	
	
	
SEM micrographs. (1), (2) and (3) shows that surfaces are covered with a rough mesh of deformed polymer. Brittle fracture and absence of fibrils formation, are verified.	





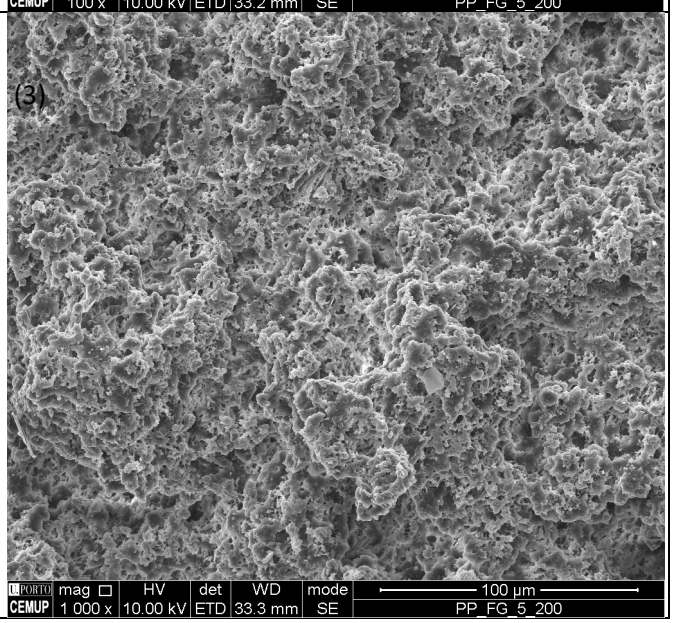
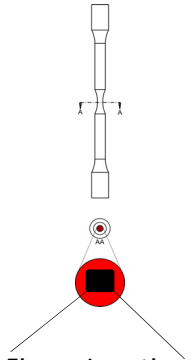


Figure 174 – SEM fracture surfaces for cylindrical notched specimens with *R 5* for PP at RT. Localization: central and near surface.

PP, Fracture Surface	
- Room temperature 21 °C ± 2 °C, - Tensile test, - Crosshead speed: 200 mm/min, - Cylindrical notched radius 30.	
	
SEM micrographs. (1) By comparing the two radii, the roughness surface increases with notch radius and in the fracture surface extremities. (2) Fibrils pulled out from the centre region surface. (3) High magnification of a rough surface.	

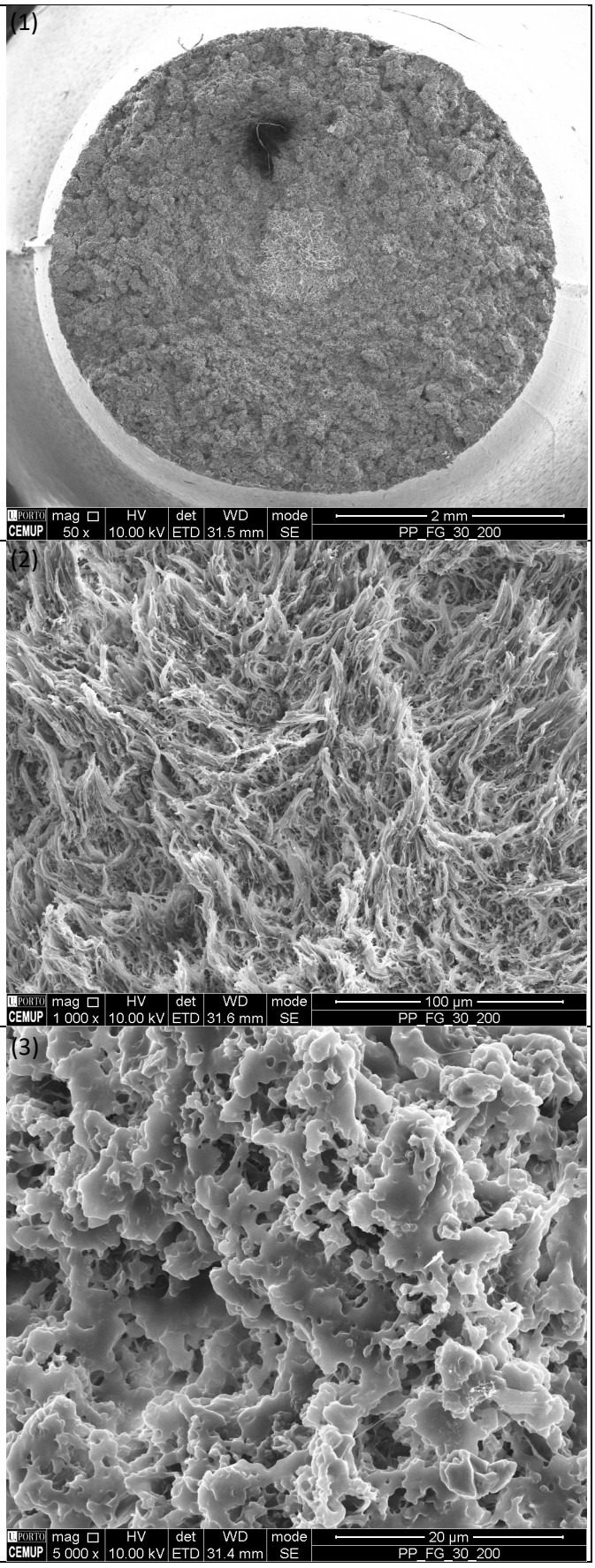
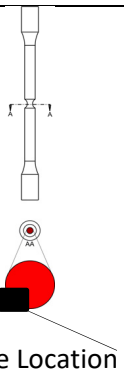
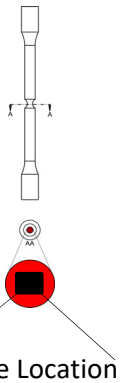
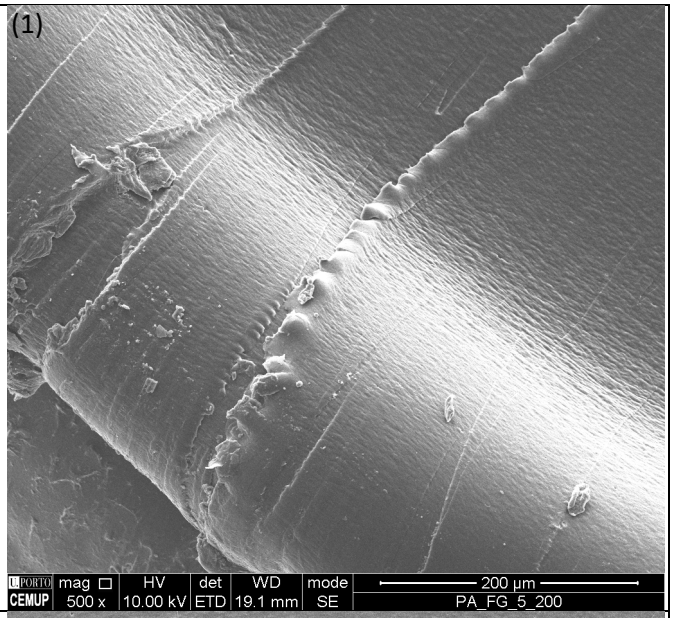


Figure 175 – SEM fracture surfaces for cylindrical notched specimens with *R 30* for PP at RT. Localization: central.

PA 6, Fracture Surface	
- Room temperature 21 °C ± 2 °C, - Tensile test, - Crosshead speed: 200 mm/min, - Cylindrical notched radius 5.	
	 Figure Location
	 Figure Location
SEM micrographs. (1) Crazing tearing. (2) Smooth fracture surfaces with voids dispersed in the fracture surface. Radial striations, are observed.	



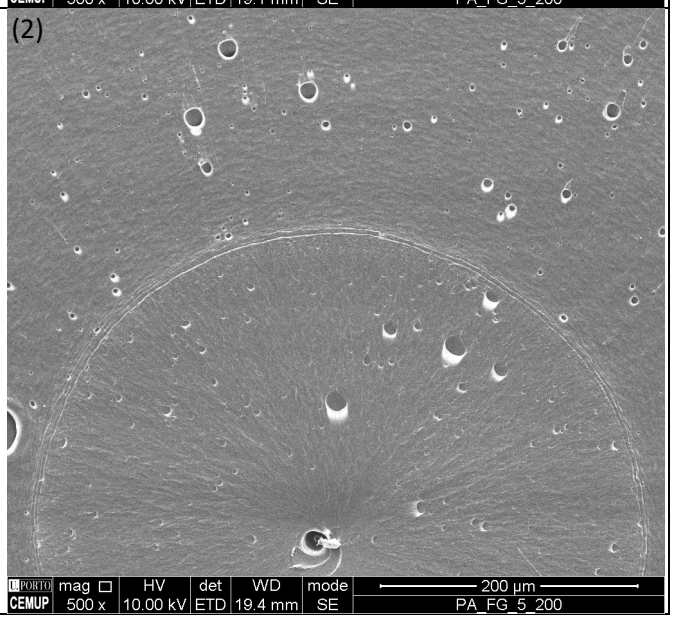


Figure 176 – SEM fracture surfaces for cylindrical notched specimens with *R 5* for PA 6 at RT. Localization: central and near surface.

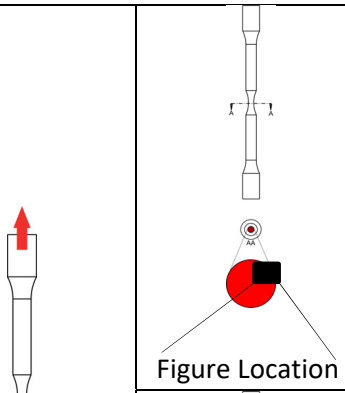
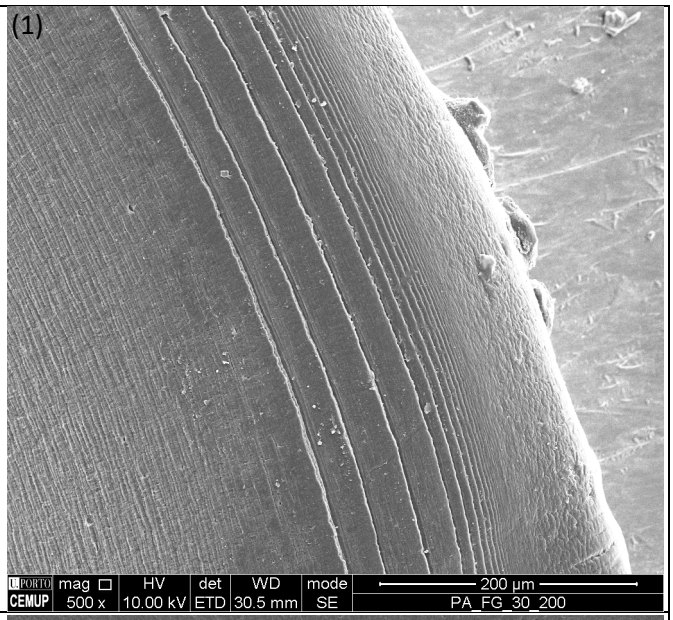
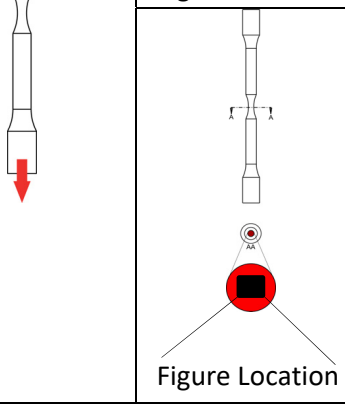
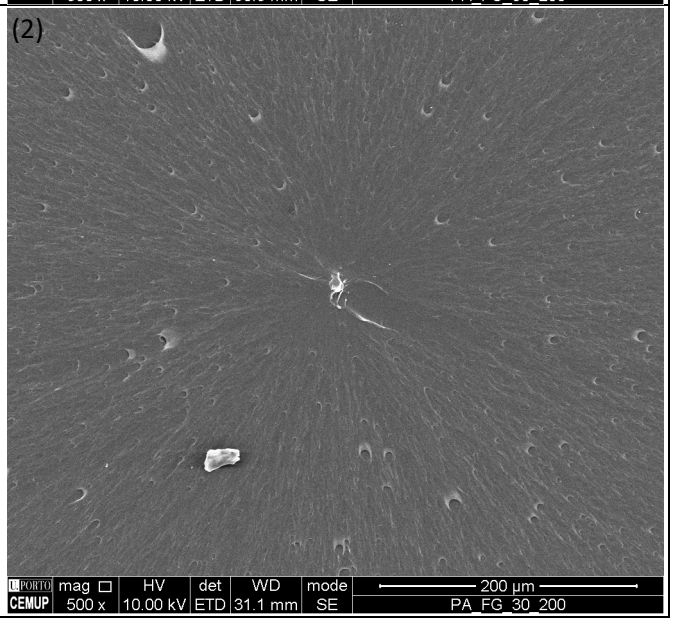
PA 6, Fracture Surface	
- Room temperature 21 °C ± 2 °C, - Tensile test, - Crosshead speed: 200 mm/min, - Cylindrical notched radius 30.	
	
	
SEM micrographs. (1) Radial striations at extremity. (2) Smooth surface. By comparing the two radii, voids amount decreases with notch radius (lower stress triaxiality ratio).	

Figure 177 – SEM fracture surfaces for cylindrical notched specimens with *R 30* for PA 6 at RT. Localization: central and near surface.

8.2.3 All SEM Micrographs –Butterfly Specimens – HDPE, PP and PA 6

Pure Tension at Room Temperature - HDPE

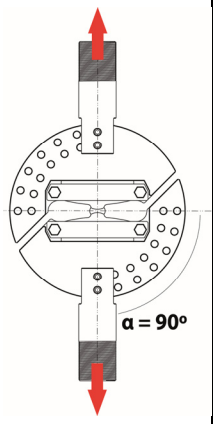
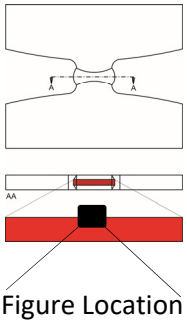
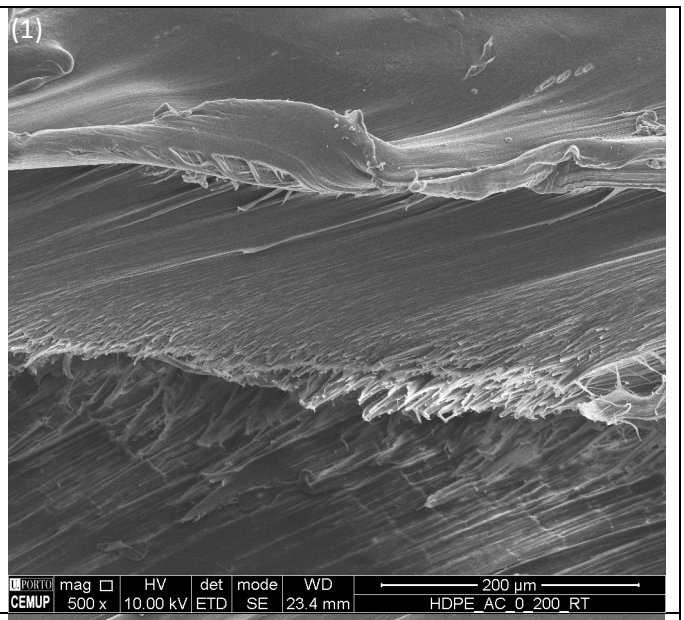
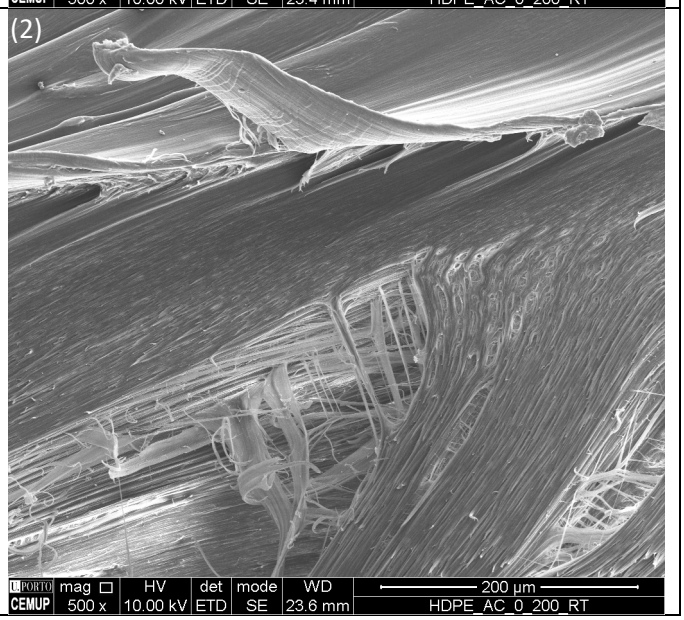
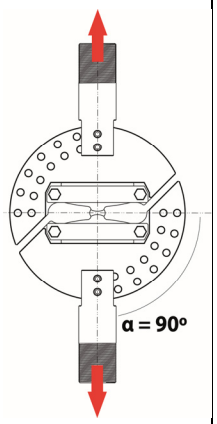
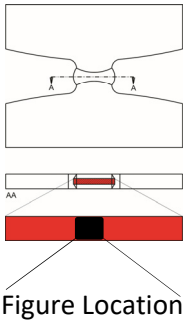
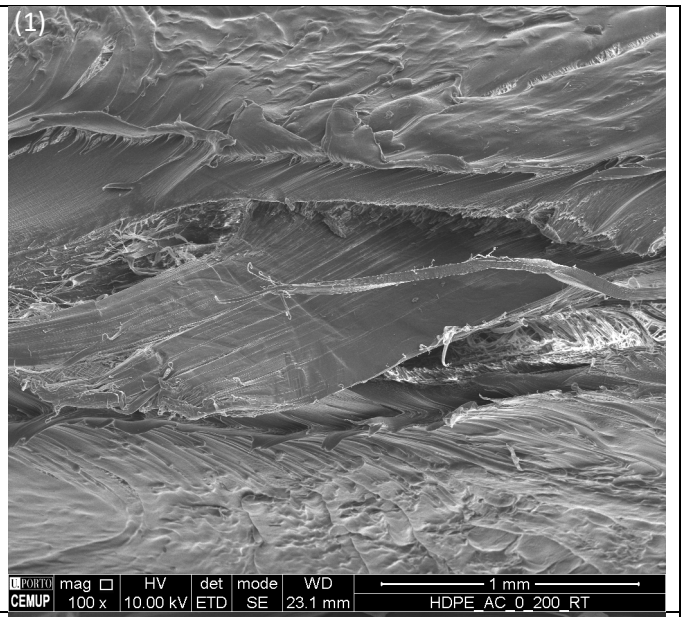
HDPE, Fracture Surface	
- Room temperature 21 °C ± 2 °C, - Pure tension, - Crosshead speed: 200 mm/min.	
  Figure Location	 
SEM micrographs. (1) Multiphase layer structure and “peeling skin layer”, is observed. (2) Fibrillar craze with different geometries (slow crack).	

Figure 178 - SEM images of butterfly specimens fractured for tensile loading at RT for HDPE. Localization: near surface.

HDPE, Fracture Surface	
- Room temperature 21 °C ± 2 °C, - Pure tension, - Crosshead speed: 200 mm/min.	
  Figure Location	
SEM micrographs. (1) Low magnification at central region-fracture. Inhomogeneous fracture morphology (2) High magnification view of a craze in a form of fibrils.	



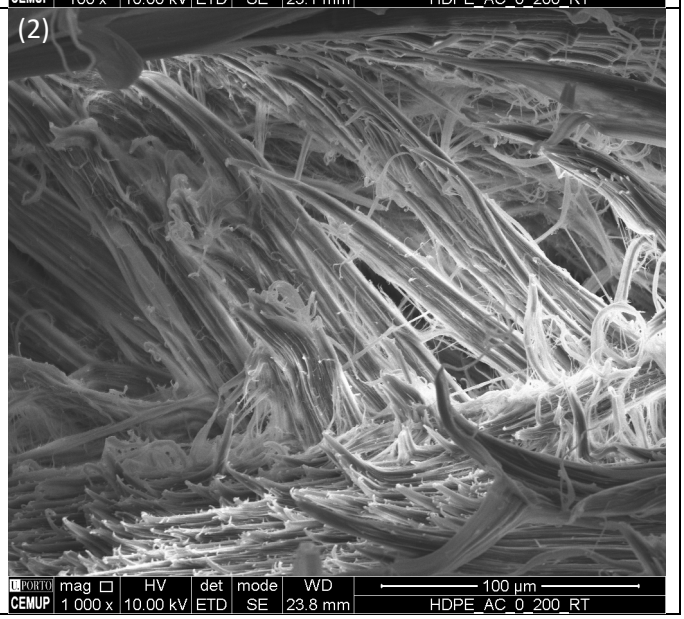


Figure 179 - SEM images of butterfly specimens fractured for tensile loading at RT for HDPE. Localization: central.

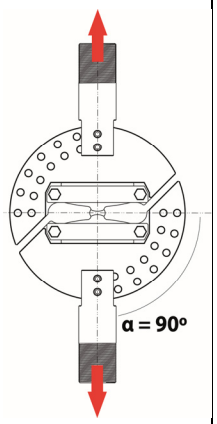
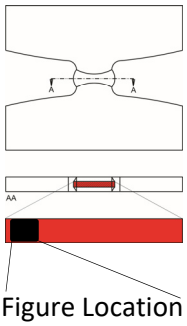
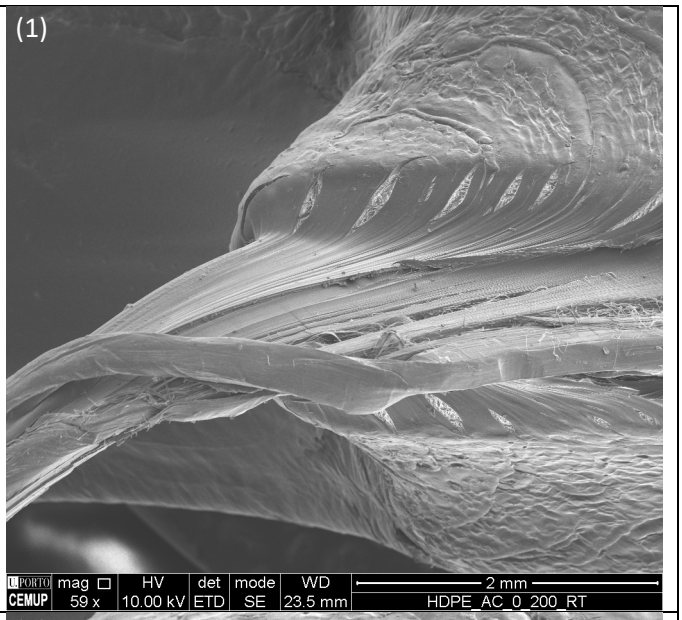
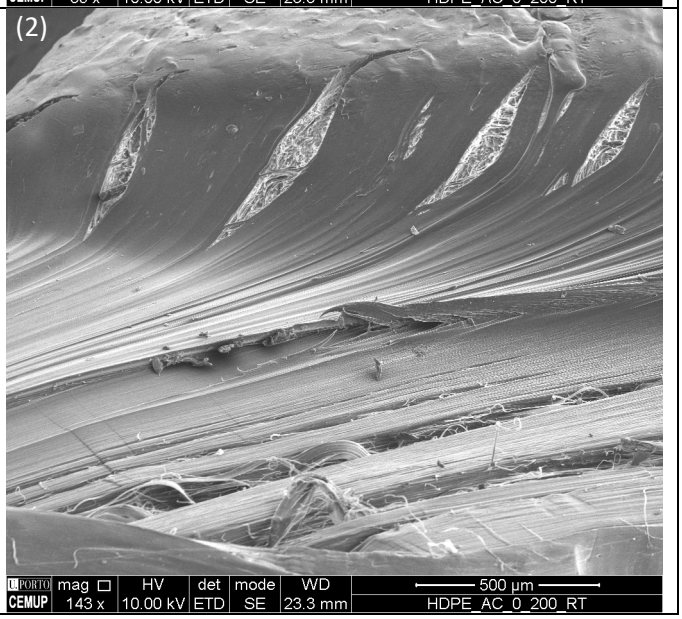
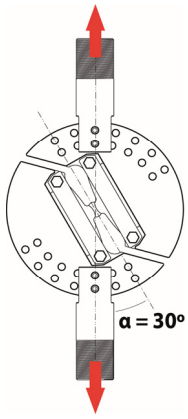
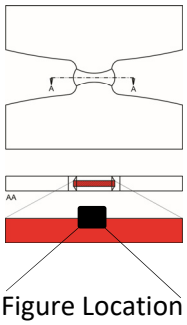
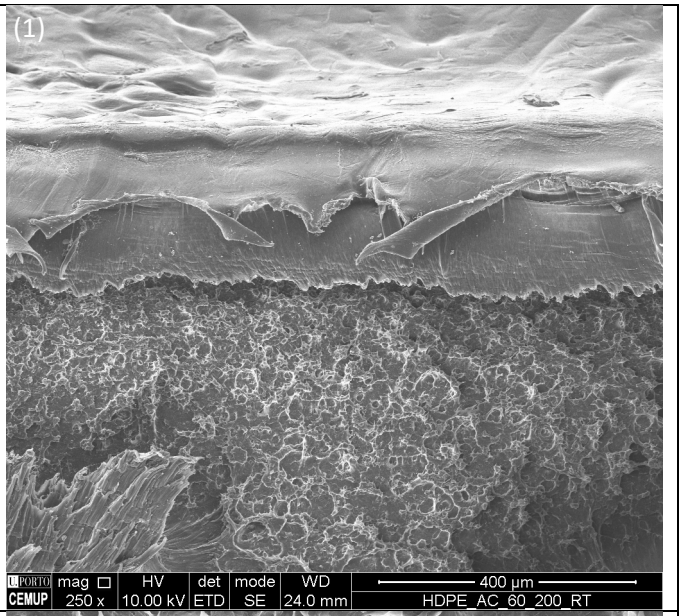
HDPE, Fracture Surface	
- Room temperature 21 °C ± 2 °C, - Pure tension, - Crosshead speed: 200 mm/min.	
  Figure Location	 
SEM micrographs. (1) and (2) Region, away from the fracture centre. Oriented crazing tearing morphology. It was the last region to fracture.	

Figure 180 - SEM images of butterfly specimens fractured for tensile loading at RT for HDPE. Localization: near surface.

Combined Tensile/Shear at Room Temperature - HDPE

HDPE, Fracture Surface	
- Room temperature 21 °C ± 2 °C, - Combined tensile/shear, - Crosshead speed: 200 mm/min.	
	
SEM micrographs. (1) Low and (2) high magnifications, exhibiting surface patterns in fracture region. The predominantly brittle failure also cavitation and voids, are detected.	



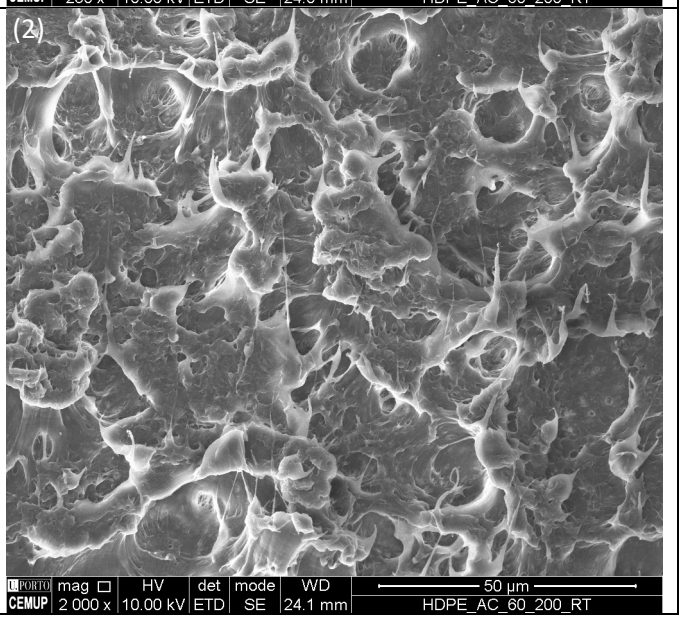
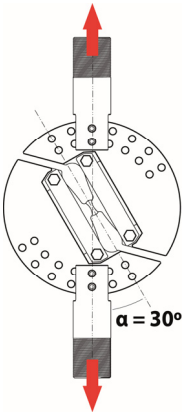
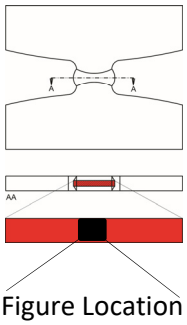
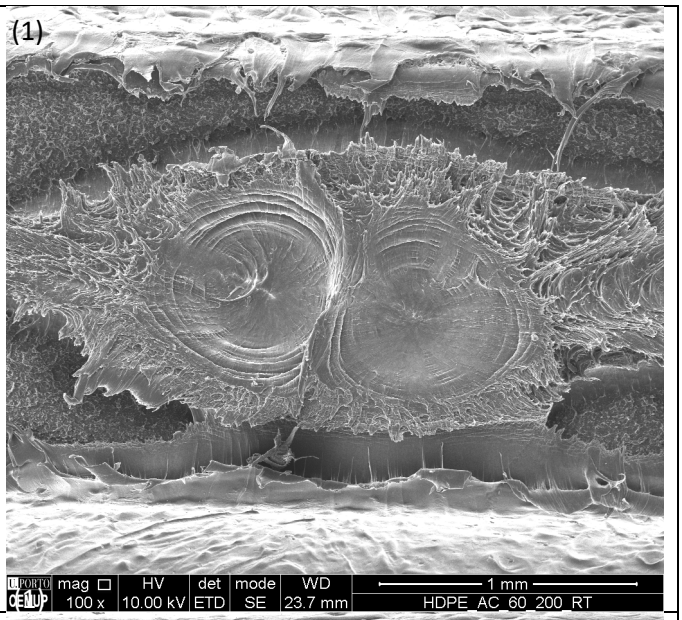
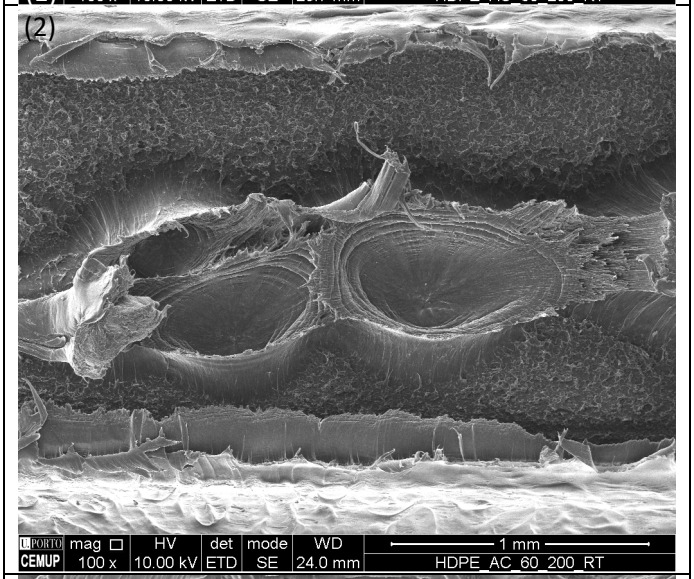


Figure 181 - SEM images of butterfly specimens fractured for combined tension/shear loading α = 30° at RT for HDPE. Localization: near surface.

HDPE, Fracture Surface	
- Room temperature 21 °C ± 2 °C, - Combined tensile/shear, - Crosshead speed: 200 mm/min.	
	 Figure Location
SEM micrographs in central fracture region. Voids surrounded by oriented fibrils morphology is observed in (1) and (2). (3) The voids are in ellipsoids of revolution. The formation of elliptically shaped voids would be either due to plastically deformation inside amorphous phase or a pre-existing defect.	





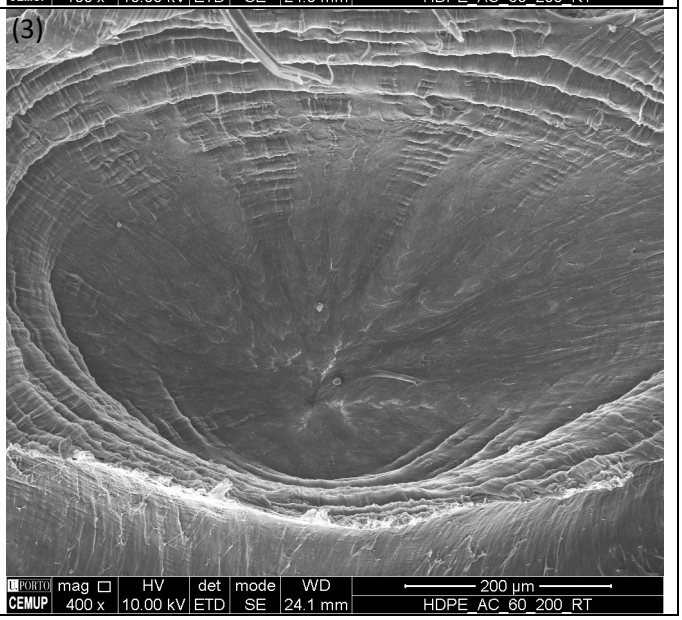


Figure 182 - SEM images of butterfly specimens fractured for combined tension/shear loading α = 30° at RT for HDPE. Localization: central.

Pure Shear at Room Temperature - HDPE

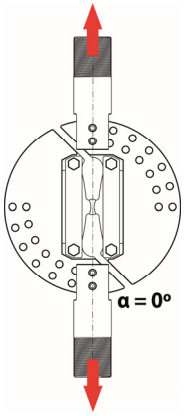
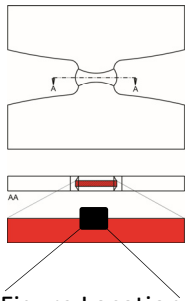
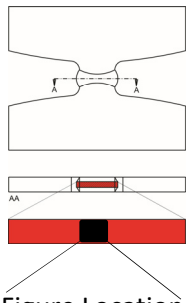
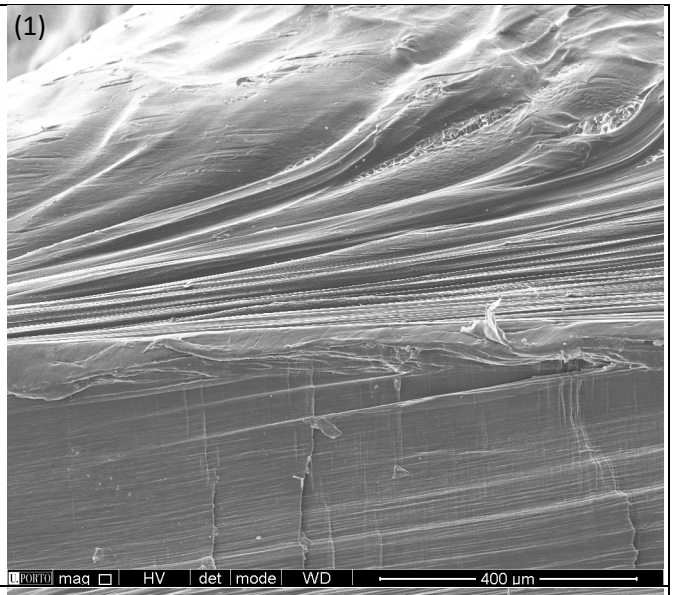
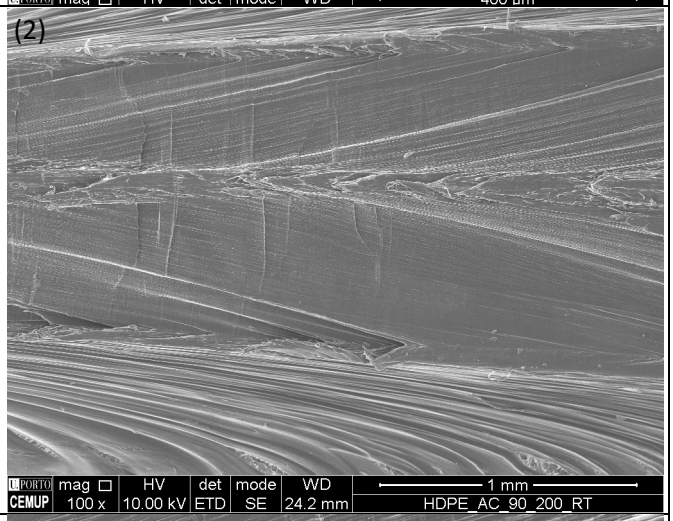
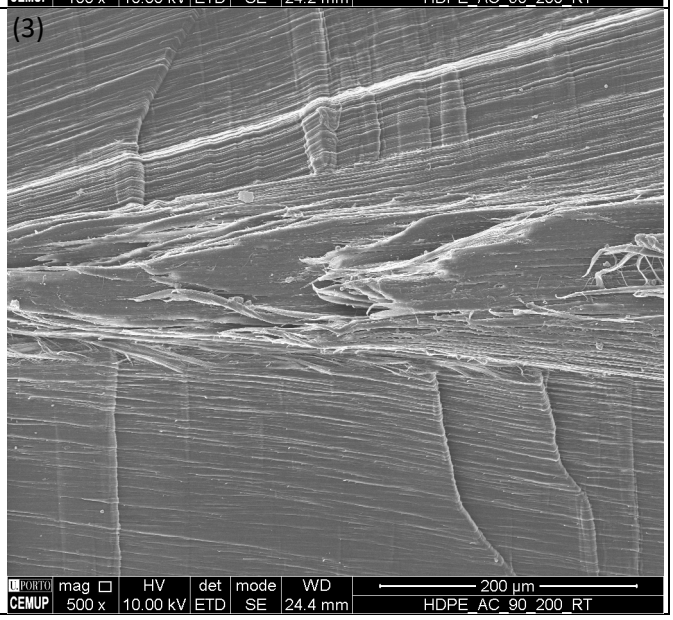
HDPE, Fracture Surface	
- Room temperature 21 °C ± 2 °C, - Pure shear, - Crosshead speed: 200 mm/min.	
	 
SEM micrographs. (1) Low magnification peripheric to central region. Fibrils alignment, are observed. (2) Low and (3) high magnifications, exhibiting the predominantly ductile failure with crazing tearing and fibril formation associated with the shear transformation. Pure shear leaves a relatively smooth fracture surface and orientated geometry.	  

Figure 183 - SEM images of butterfly specimens fractured for shear loading at RT for HDPE. Localization: central and near surface.

Pure Tension at Temperature of 50°C - HDPE

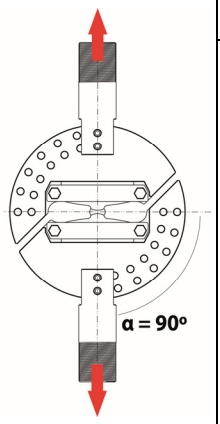
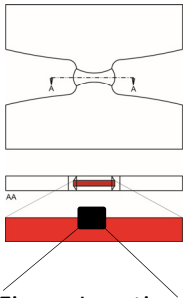
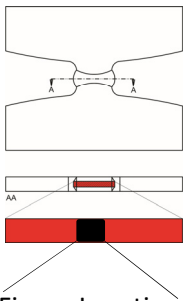
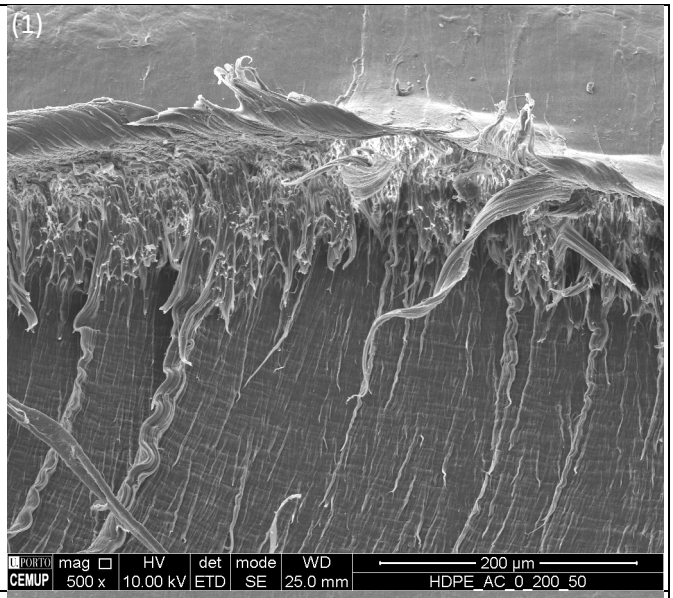
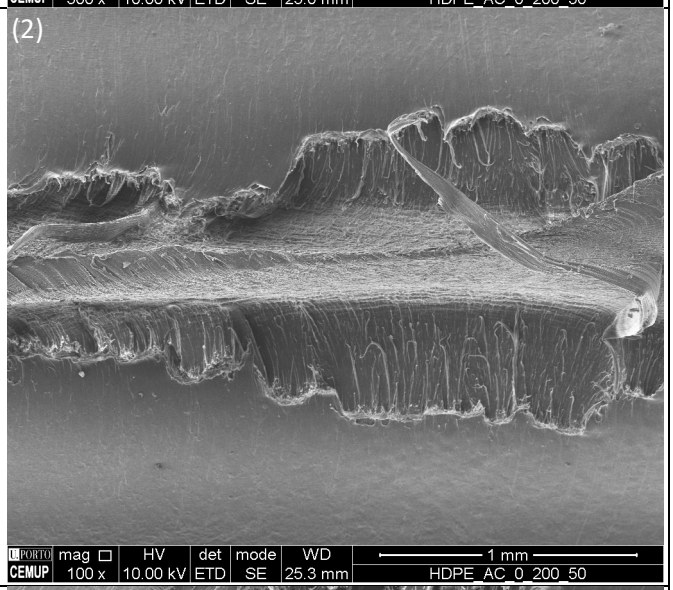
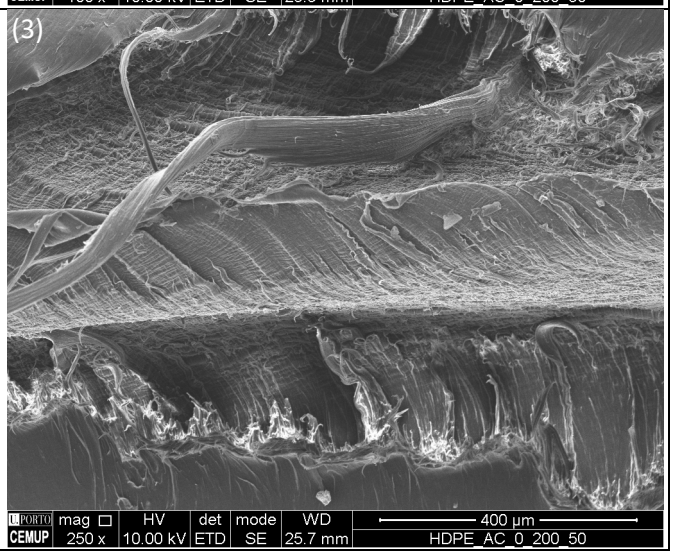
HDPE, Fracture Surface	
- Temperature of 50 °C, - Pure tension, - Crosshead speed: 200 mm/min.	
	 
SEM micrographs. (1) Peripheric central region. “Skin peeling” takes a form of crazing tearing. In the transition regions from skin layer to core region there is a heavily fibrillation region. (2) Low and (3) high magnifications, exhibiting an inhomogeneous fracture. Crazing tearing, fibrils formation and slope surfaces, are observed.	  

Figure 184 - SEM images of butterfly specimens fractured for tensile loading at temperature of 50 °C for HDPE. Localization: central and near surface.

Combined Shear/Tension at Temperature of 50°C – HDPE

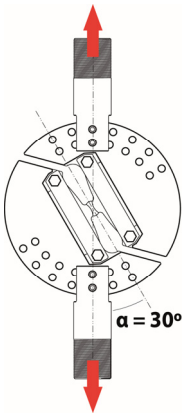
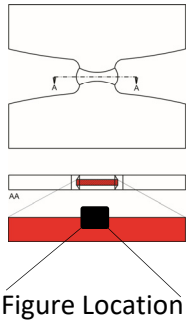
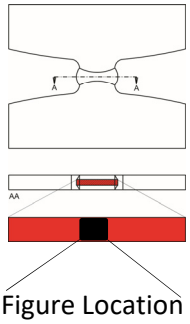
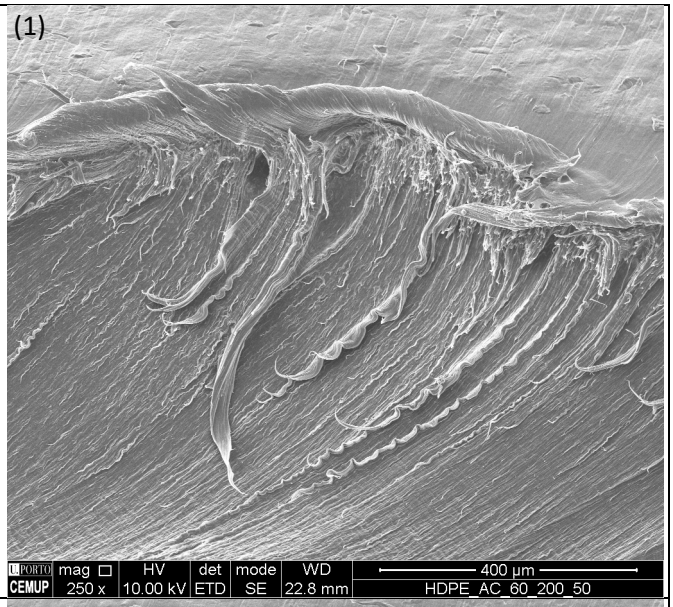
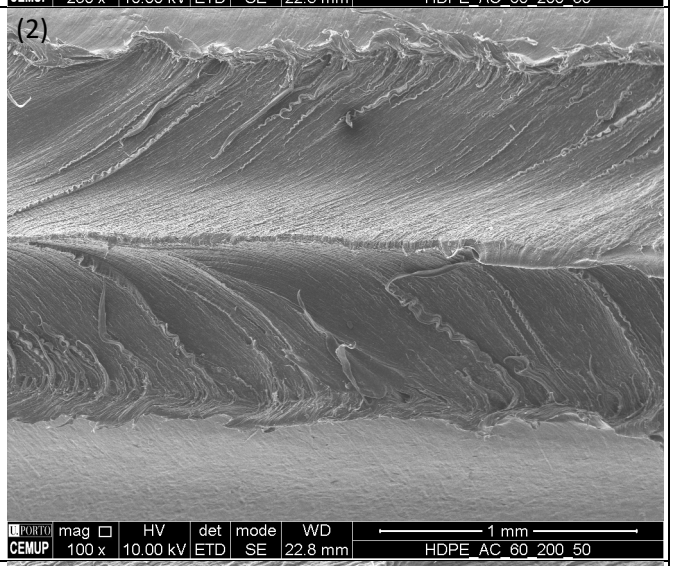
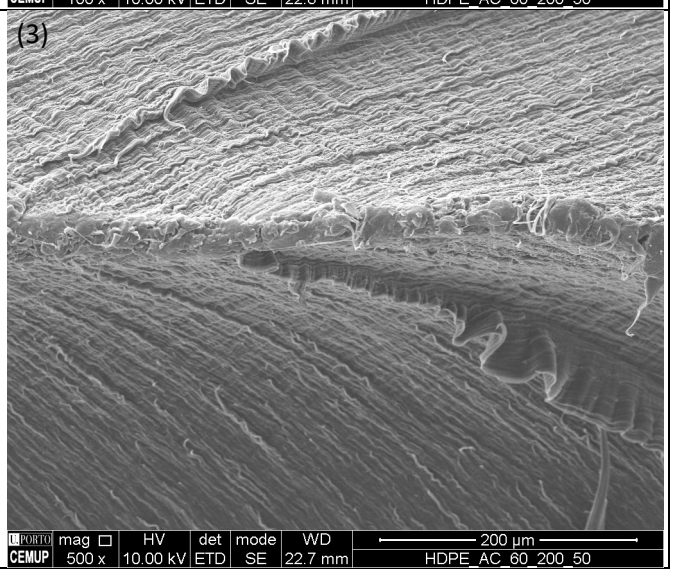
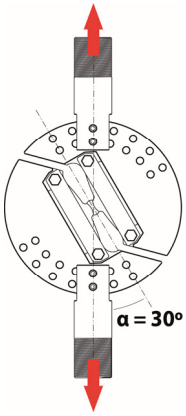
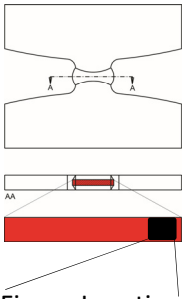
HDPE, Fracture Surface	
- Temperature of 50 °C, - Combined tensile/shear, - Crosshead speed: 200 mm/min.	
	 
SEM micrographs. (1) Peripheric central region. Crazing tearing, fibrils region (transition layer) and a more regular ductile fracture surface. (2) and (3) The dominant characteristic is a central slope in the longitudinal direction with fibril formation and crazing tearing associate to the combined shear/tension.	  

Figure 185 - SEM images of butterfly specimens fractured for combined tension/shear loading α = 30° at temperature of 50 °C for HDPE. Localization: central and near surface.

HDPE, Fracture Surface	
- Temperature of 50 °C, - Combined tensile/shear, - Crosshead speed: 200 mm/min.	
	
SEM micrographs. Crazing tearing and fibrils morphologies in the regions away from the mid-regions of the fracture surface. (2) and (3) Central slope. Crazing/tearing	

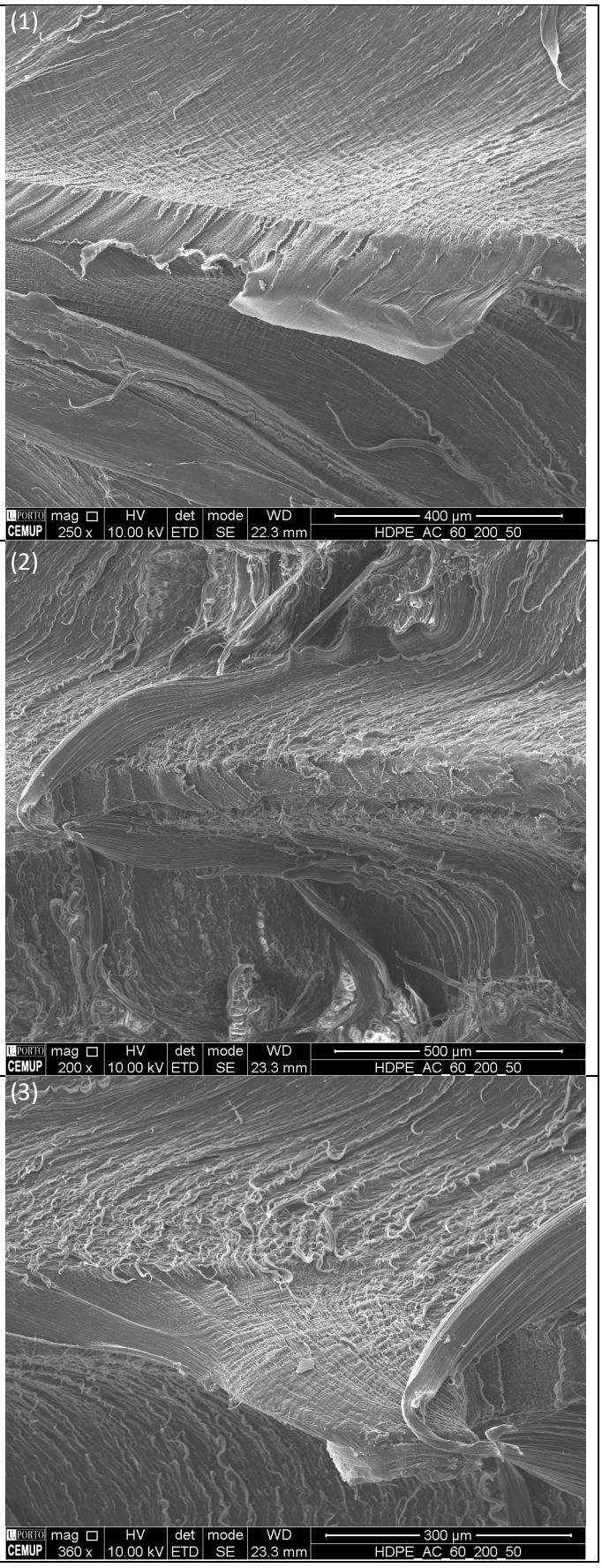


Figure 186 - SEM images of butterfly specimens fractured for combined tension/shear loading α = 30° at temperature of 50 °C for HDPE. Localization: near surface.

Pure Shear at Temperature of 50°C – HDPE

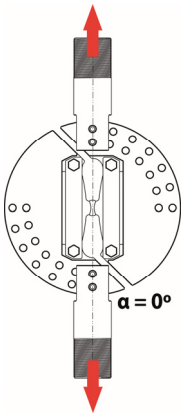
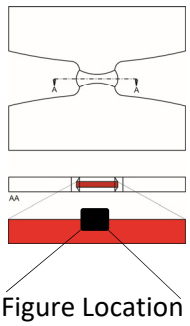
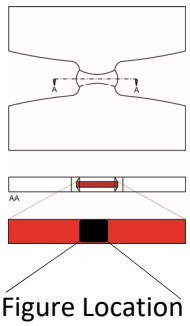
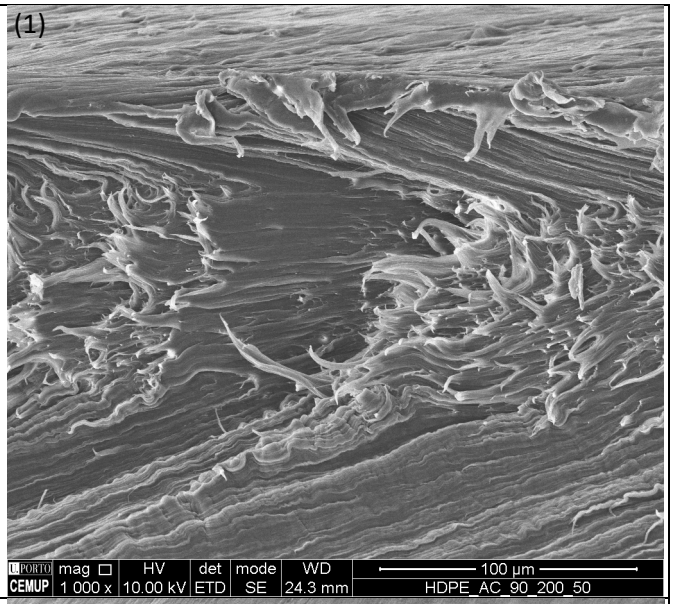
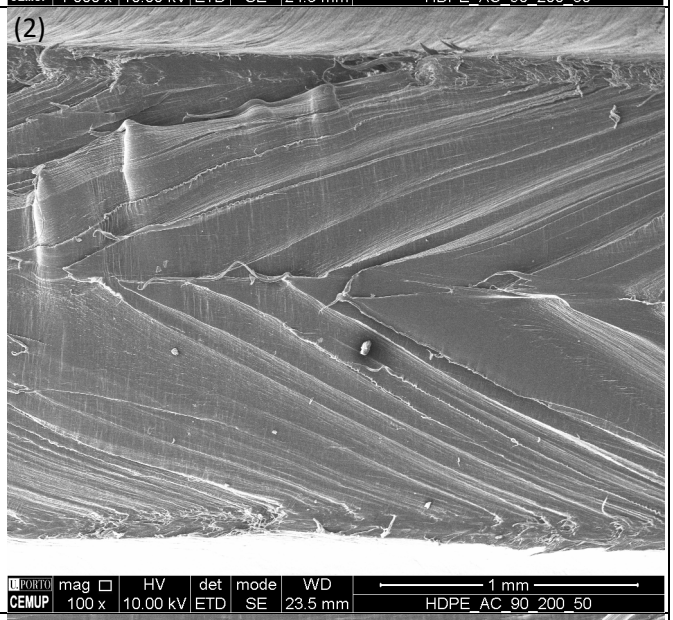
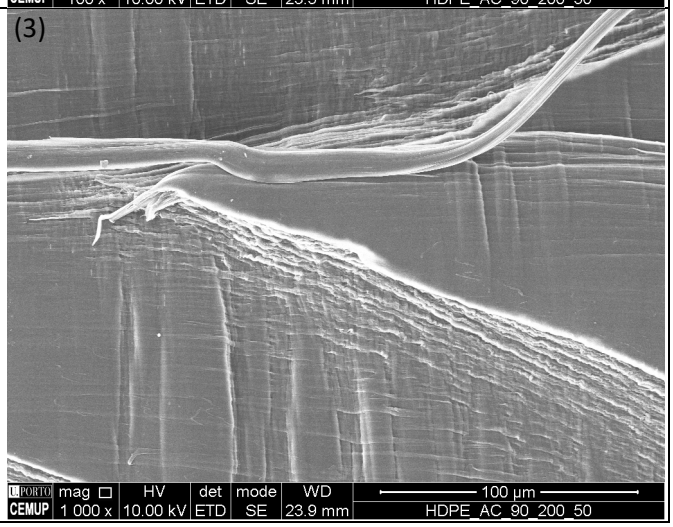
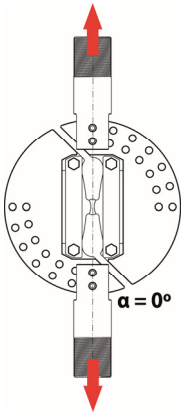
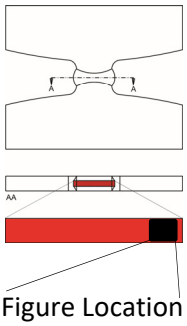
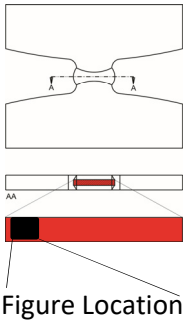
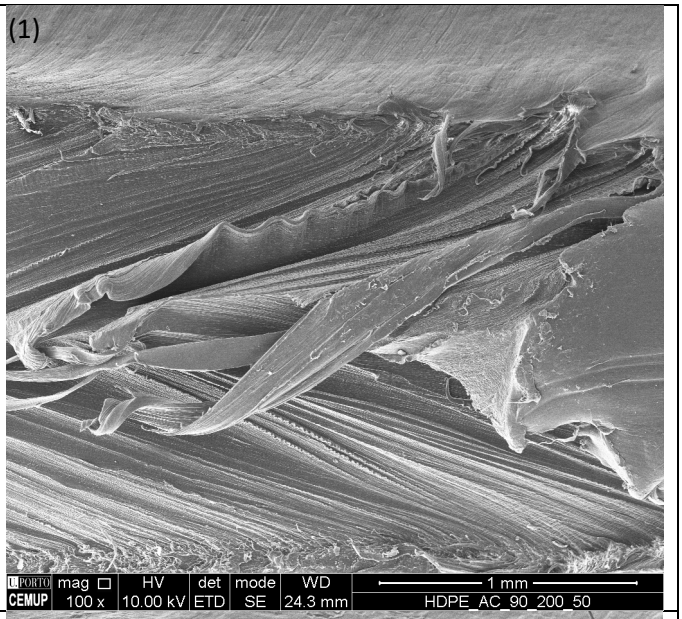
HDPE, Fracture Surface	
- Temperature of 50 °C, - Pure shear, - Crosshead speed: 200 mm/min.	
	 
SEM micrographs. (1) Peripheric central region. “Peeling skin layer” takes a form of fibrils as well as in the core region. (2) Regular surface with almost geometric triangular patterns. (3) Low magnification, crazing tearing in triangular form.	  

Figure 187 - SEM images of butterfly specimens fractured for shear loading at temperature of 50 °C for HDPE. Localization: near surface and central.

HDPE, Fracture Surface	
- Temperature of 50 °C, - Pure shear, - Crosshead speed: 200 mm/min.	
	 
SEM micrographs. (1) and (2) Crazing tearing in the regions away from the centre of the fracture surface.	



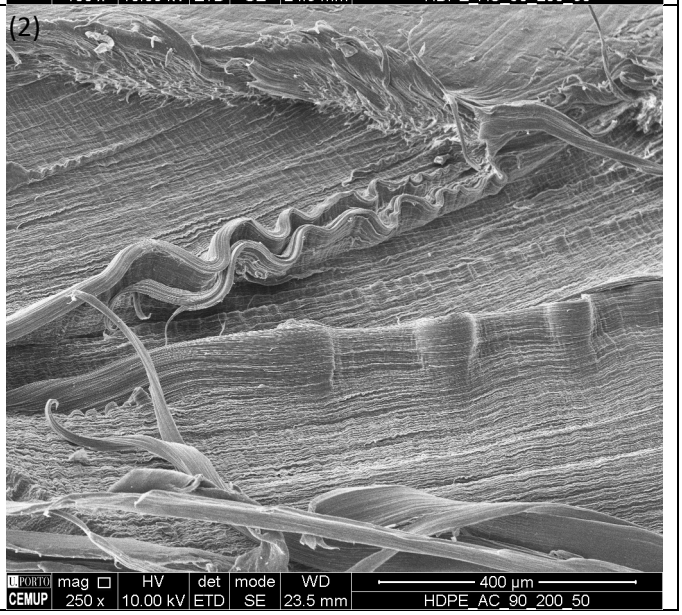


Figure 188 - SEM images of butterfly specimens fractured for shear loading at temperature of 50 °C for HDPE. Localization: near surface.

Pure Tension at Room Temperature – PP

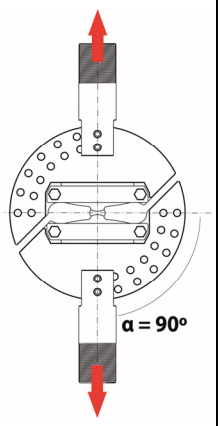
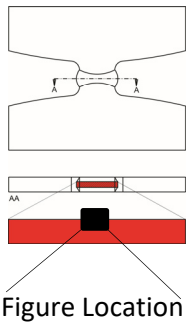
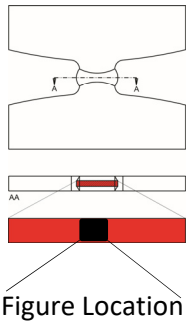
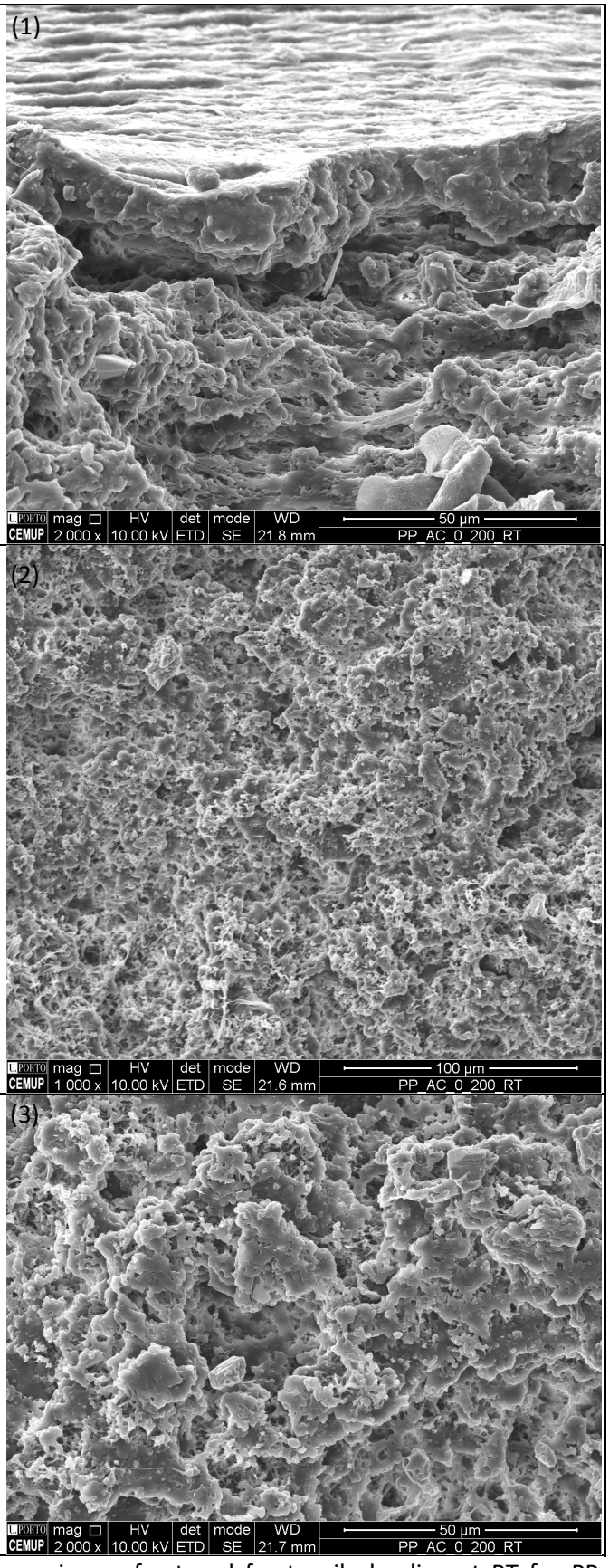
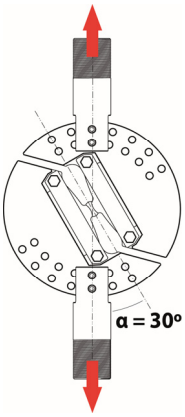
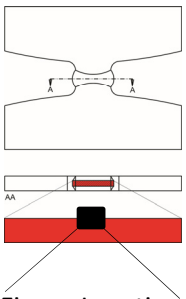
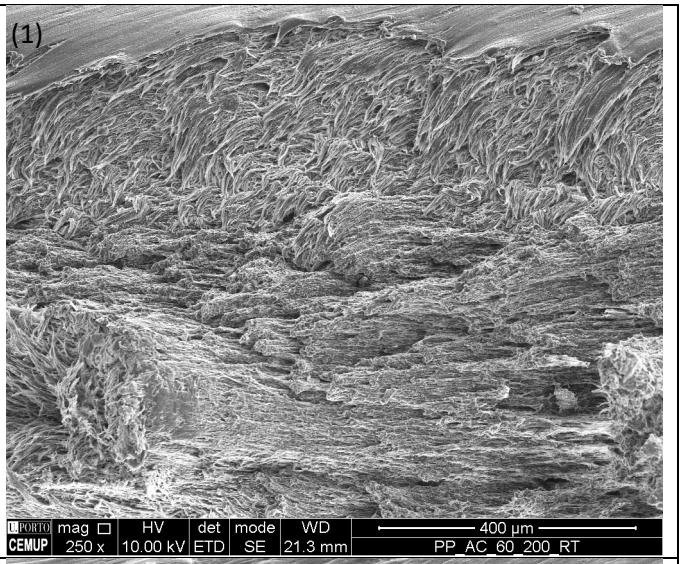
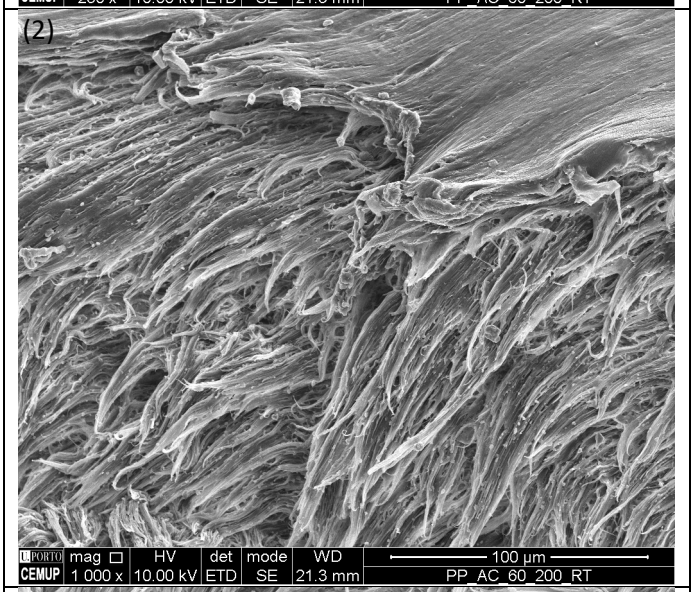
PP, Fracture Surface	
- Room temperature 21 °C ± 2 °C, - Pure tension, - Crosshead speed: 200 mm/min.	
	 
SEM micrographs. Multiphase layer structure. (1) Skin layer and core region. (2) and (3) Central fracture region. Irregular surface with high void content.	

Figure 189 - SEM images of butterfly specimens fractured for tensile loading at RT for PP. Localization: near surface and central.

Combined Shear/Tension at Room Temperature – PP

PP, Fracture Surface
- Room temperature 21 °C ± 2 °C, - Combined tensile/shear, - Crosshead speed: 200 mm/min.
  Figure Location
SEM micrographs. (1) and (2) Oriented fibrils on the outer layer structure, indicating high deformation before fail (ductile failure). (3) Inner layer shows a less ductile behaviour. It is observed at the ends knobs or nodules, which might be caused by thermal softening.





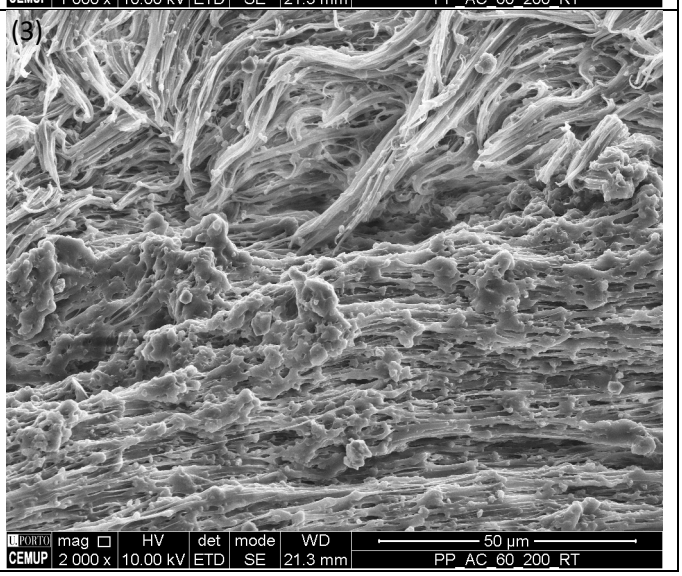
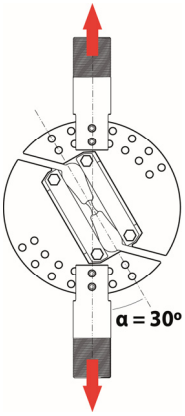
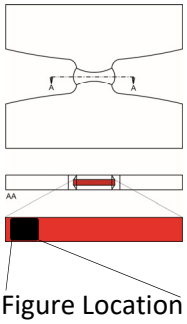
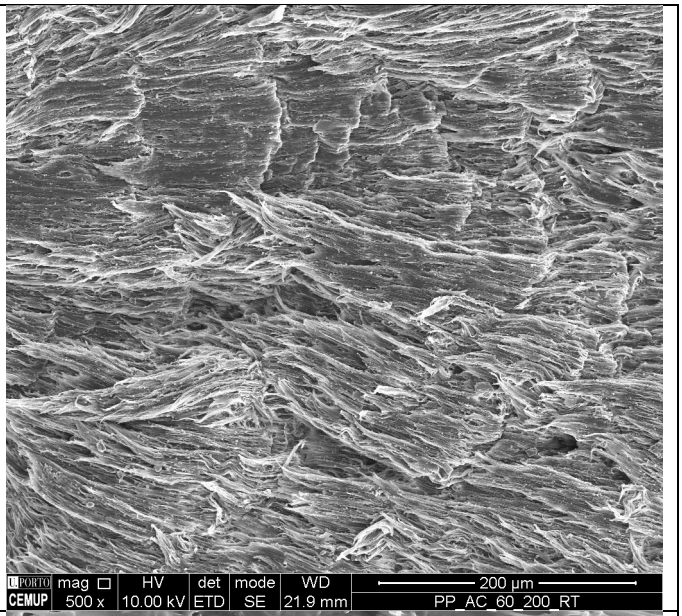
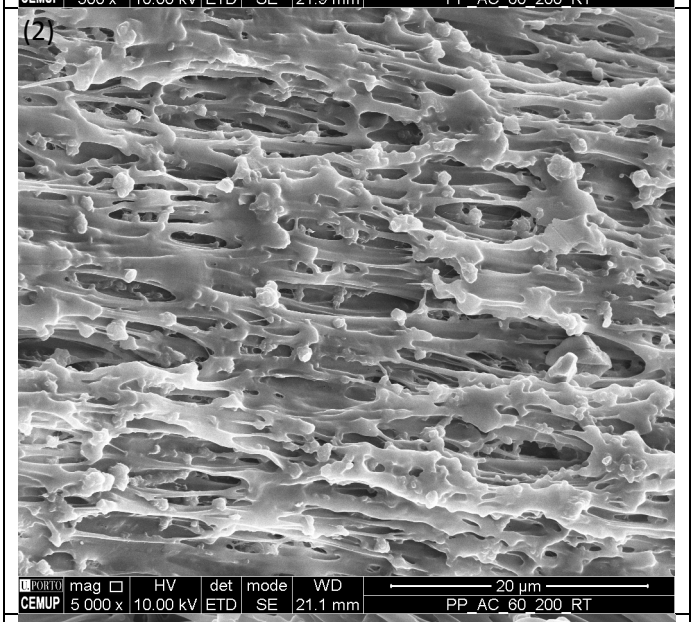


Figure 190 - SEM images of butterfly specimens fractured for combined tension/shear loading α = 30° at RT for PP. Localization: near surface.

PP, Fracture Surface	
- Room temperature 21 °C ± 2 °C, - Combined shear/tension, - Crosshead speed: 200 mm/min.	
	
SEM micrographs. (1) Fibrillar failure with high void content. (2) and (3) The elongated voids are a result of the fibrous morphology. On fibrils ends there are a large number of knobs or nodules with a smooth rounded surface.	





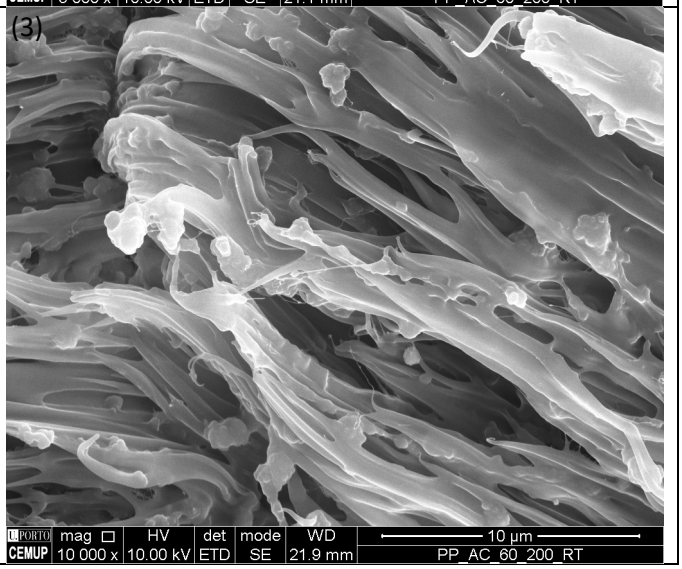
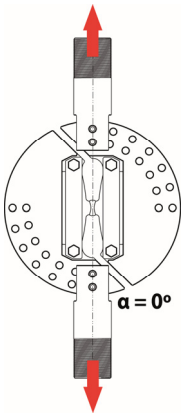
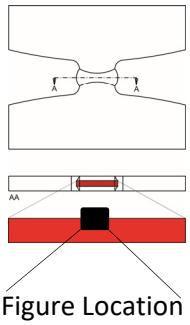
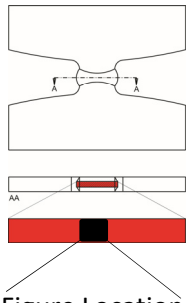


Figure 191 - SEM images of butterfly specimens fractured for combined tension/shear loading α = 30° at RT for PP. Localization: near surface.

Pure Shear at Room Temperature – PP

PP, Fracture Surface	
- Room temperature 21 °C ± 2 °C, - Pure shear, - Crosshead speed: 200 mm/min.	
	 
SEM micrographs. (1), (2) and (3) Ductile fracture with crazing tearing morphology associated with pure shear fracture mode.	

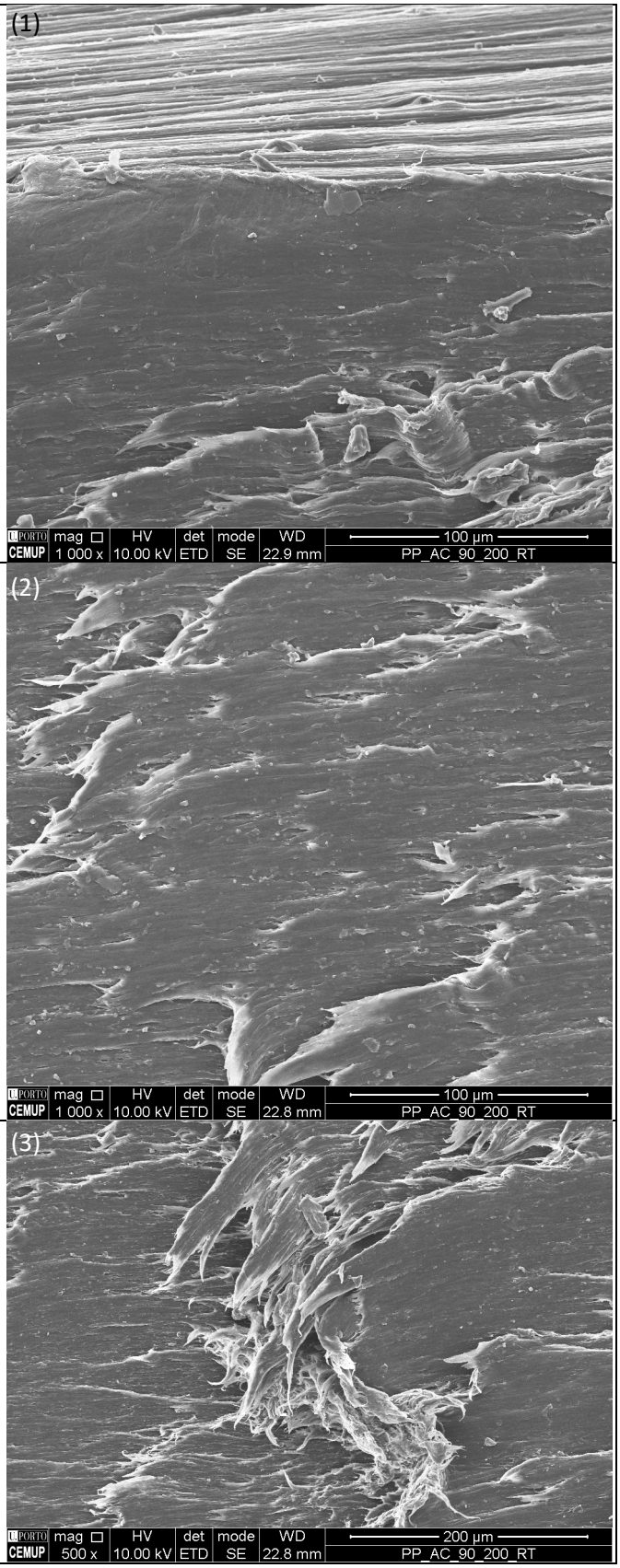
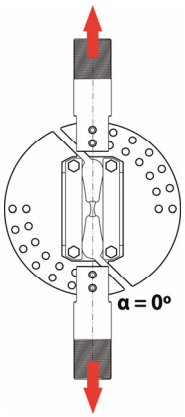
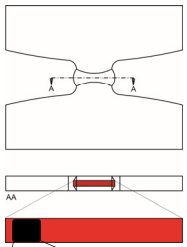


Figure 192 - SEM images of butterfly specimens fractured for combined shear loading at RT for PP. Localization: near surface and central.

PP, Fracture Surface	
- Room temperature 21 °C ± 2 °C, - Pure shear, - Crosshead speed: 200 mm/min.	
  Figure Location	
SEM micrographs. (1), (2) and (3) Wedge central region, are characterized by crazing tearing. Fibrils aligned and grouped in a network that leads to ductile fracture.	

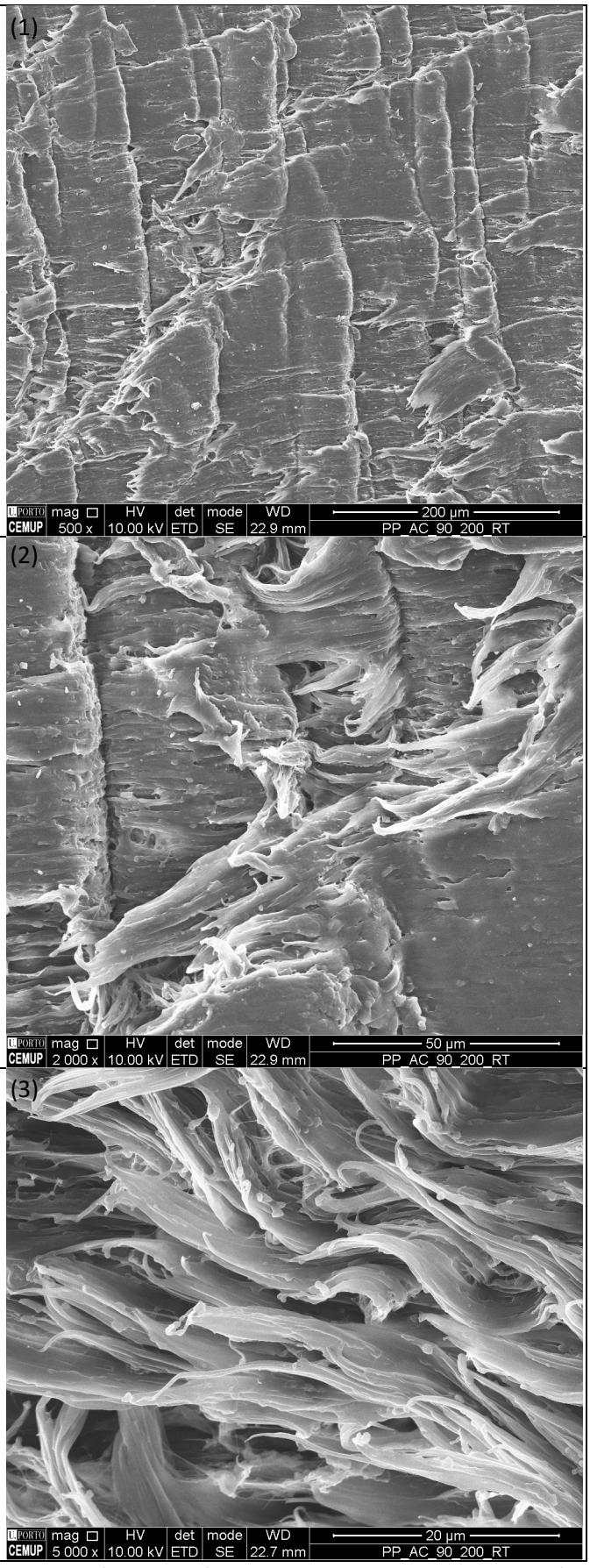
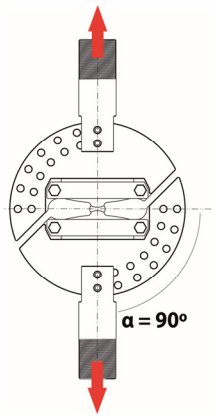
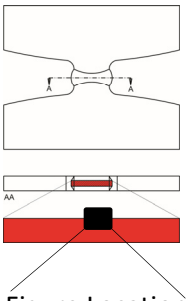
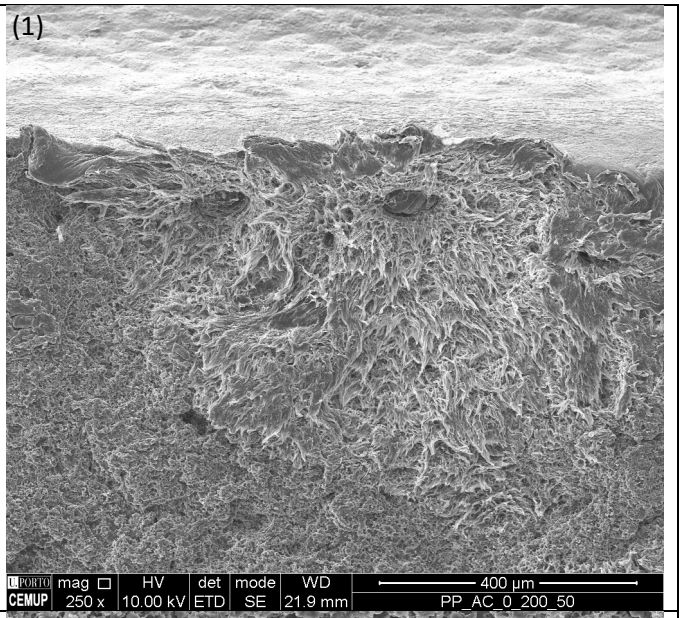


Figure 193 - SEM images of butterfly specimens fractured for combined shear loading at RT for PP. Localization: near surface.

Pure Tension at Temperature of 50°C – PP

PP, Fracture Surface	
- Temperature of 50 °C, - Pure tension, - Crosshead speed: 200 mm/min,	
	 Figure Location
SEM micrographs. (1) low and (2) high magnification shows irregular surface with high void content. Voids with larger dimensions are surrounded by fibrils.	



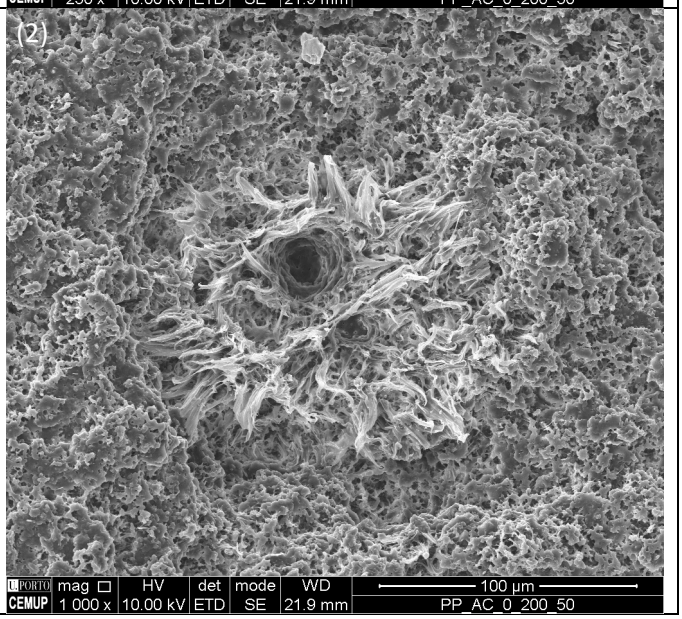


Figure 194 - SEM images of butterfly specimens fractured for tensile loading at temperature of 50 °C for PP. Localization: near surface.

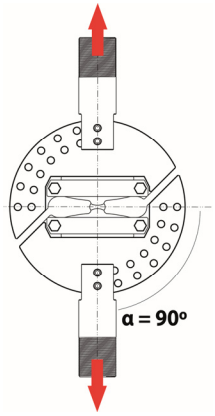
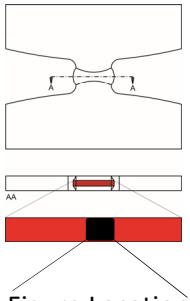
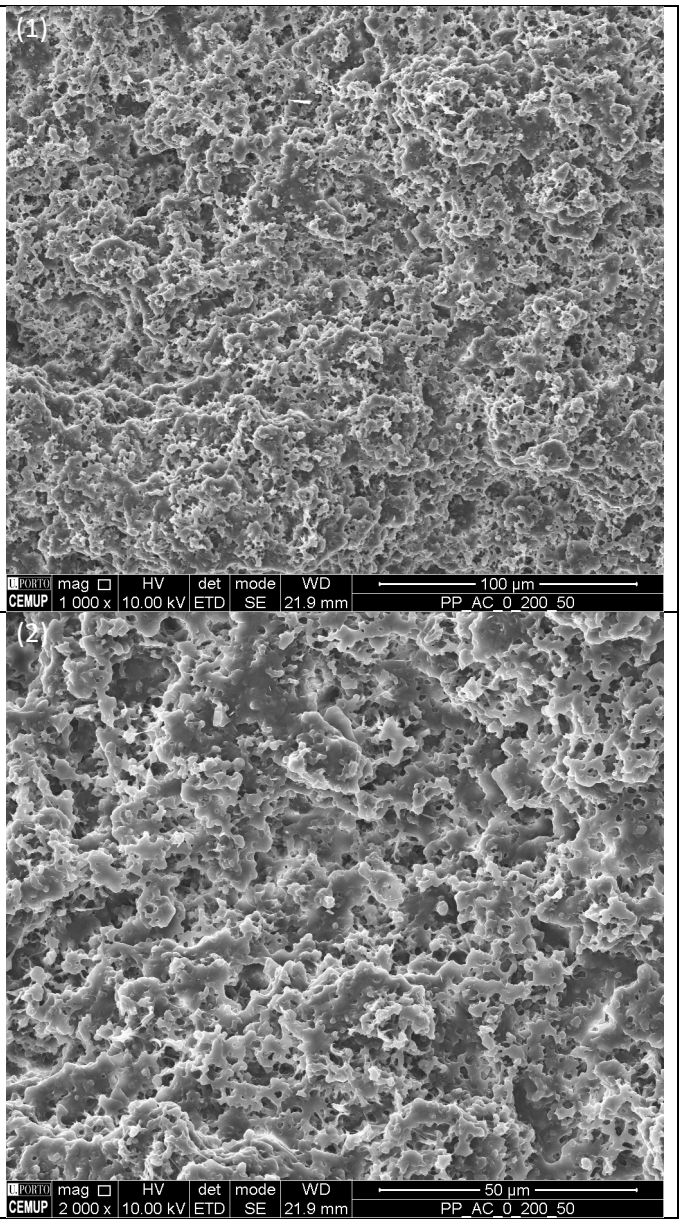
PP, Fracture Surface	
- Temperature of 50 °C, - Pure tension, - Crosshead speed: 200 mm/min.	
 	
SEM micrographs. (1) and (2) Central fracture region. Irregular surface with high void content.	

Figure 195 - SEM images of butterfly specimens fractured for tensile loading at temperature of 50 °C for PP. Localization: central.

Combined Shear/Tension at Temperature of 50°C – PP

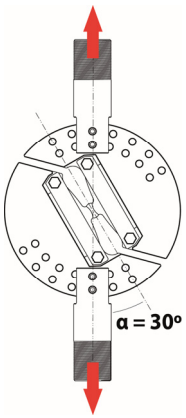
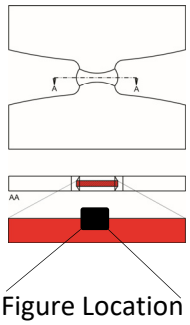
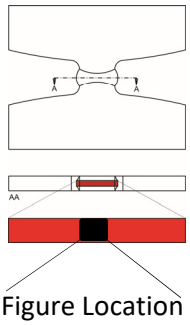
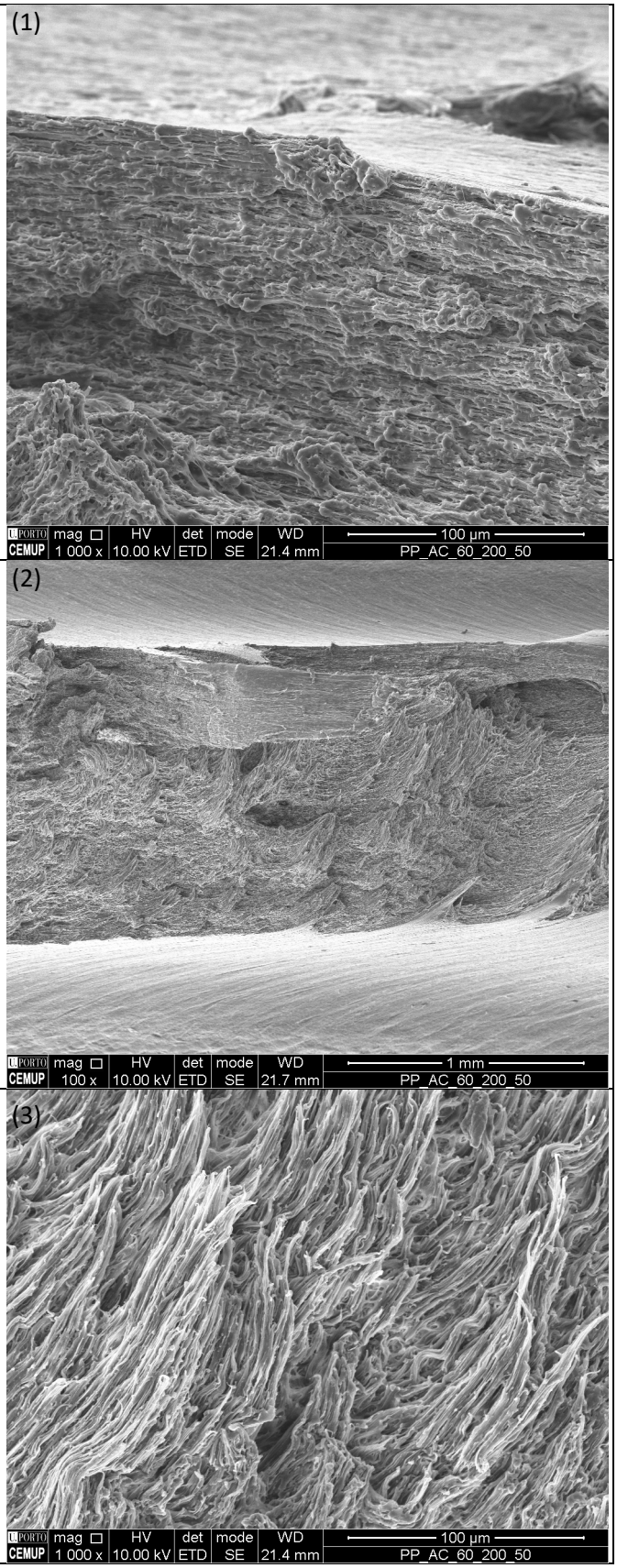
PP, Fracture Surface	
- Temperature of 50 °C, - Combined shear/tension, - Crosshead speed: 200 mm/min.	
	 
SEM micrographs. (1) No skin layer is noticeable. Irregular surface with high voids content. Scanning electron micrograph at: (2) low and (3) high magnifications. Fibrillation (fibrillation is defined as ductile drawing of fibrils with enhanced plastic flow) [175].	

Figure 196 - SEM images of butterfly specimens fractured for combined tension/shear loading α = 30° at temperature of 50 °C for PP. Localization: central.

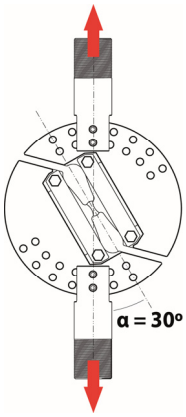
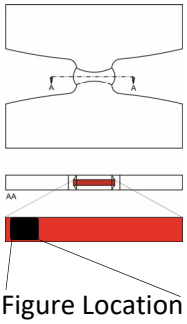
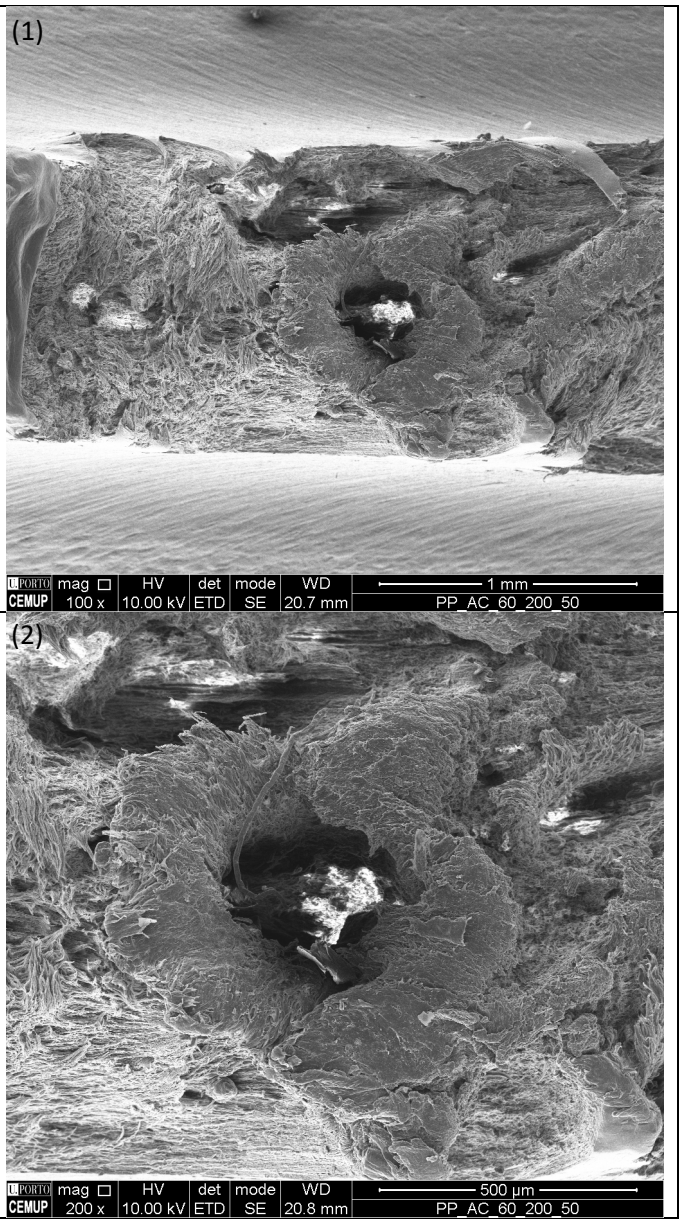
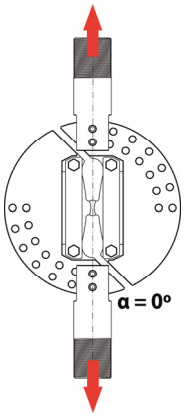
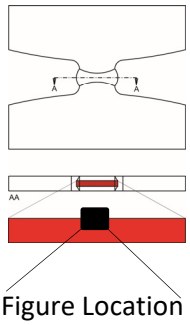
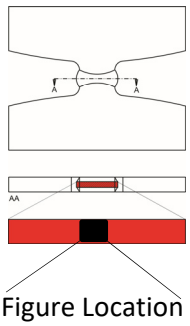
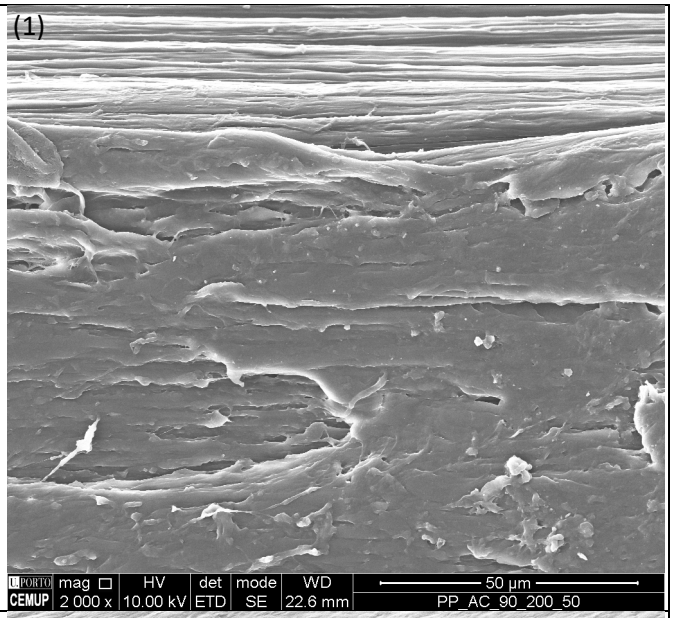
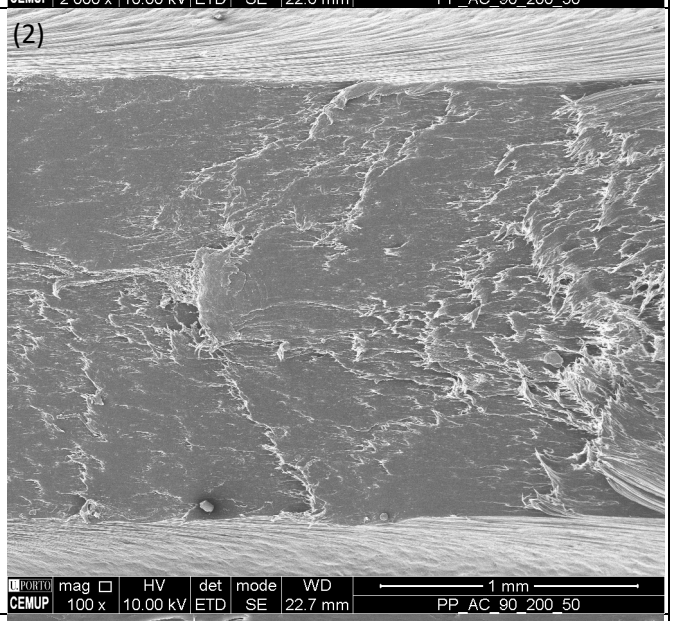
PP, Fracture Surface	
- Temperature of 50 °C, - Combined shear/tension, - Crosshead speed: 200 mm/min.	
 	
(1) and (2) SEMs are shown at two levels of magnification. On top show an overall view of the left fracture surface. There is a large amount of deformation all over the area with a number of longer fibrils and voids content. At high magnification shows a detailed void geometry.	

Figure 197 - SEM images of butterfly specimens fractured for combined tension/shear loading α = 30° at temperature of 50 °C for PP. Localization: near surface.

Pure Shear at Temperature of 50°C – PP

PP, Fracture Surface	
- Temperature of 50 °C, - Pure shear, - Crosshead speed: 200 mm/min.	
	 
SEM micrographs. (1), (2) and (3) Ductile fracture with fibril formation associated with crazing tearing.	





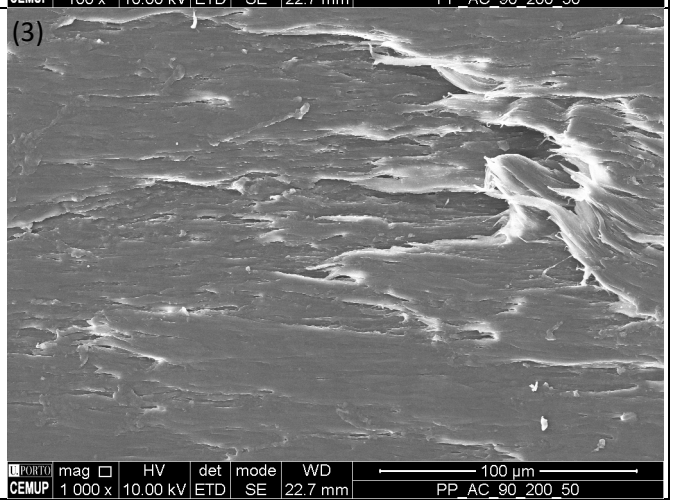
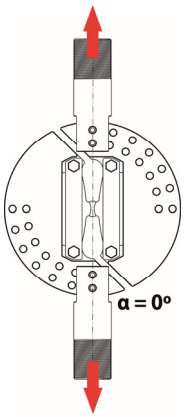
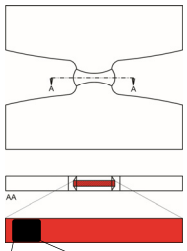
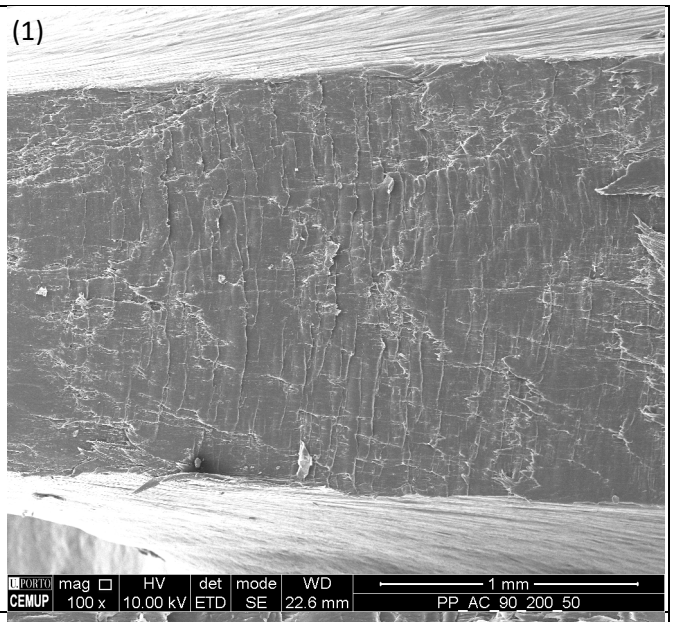
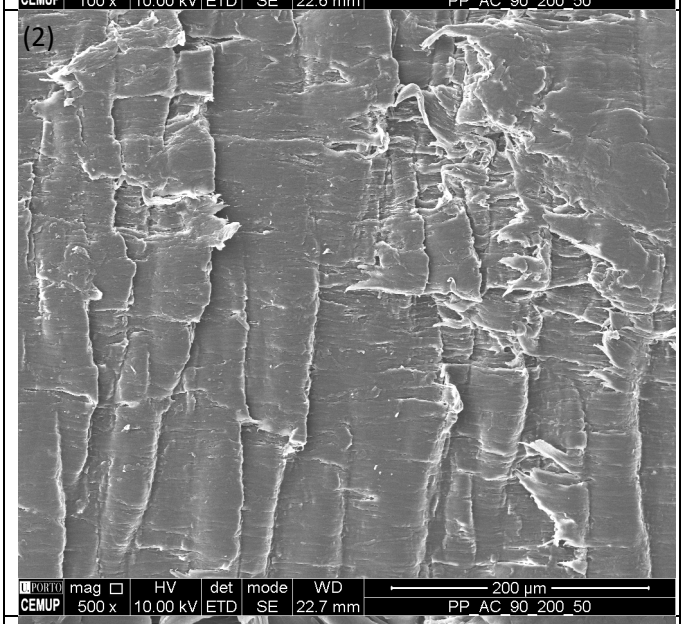


Figure 198 - SEM images of butterfly specimens fractured for shear loading at temperature of 50 °C for PP. Localization: centre.

PP, Fracture Surface	
- Constant temperature of 50 °C, - Positive vertical displacement, - Crosshead speed: 200 mm/min.	
 	
SEMs are shown at three levels of magnification. Large areas covered with striations are shown, also several edge discontinuities are included with attendant fibrils (detailed in higher magnification).	





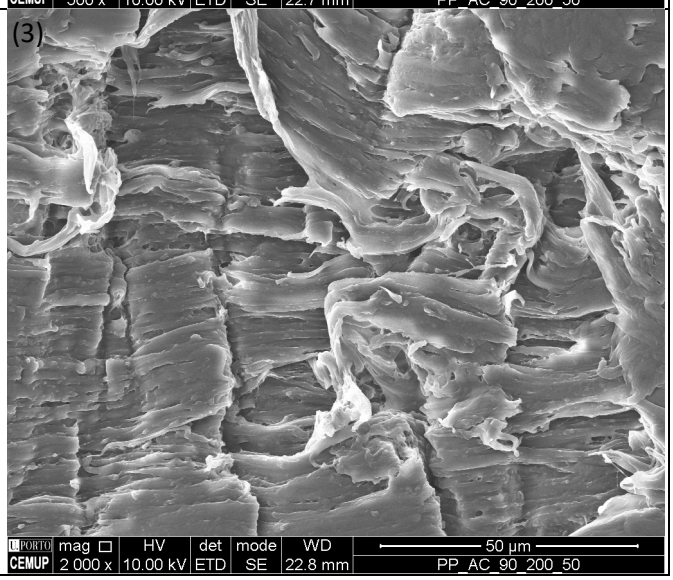


Figure 199 - SEM images of butterfly specimens fractured for shear loading at temperature of 50 °C for PP. Localization: near surface.

Pure Tension at Room Temperature – PA 6

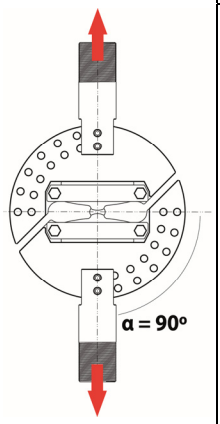
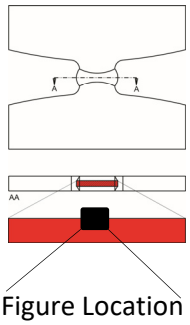
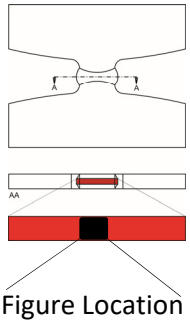
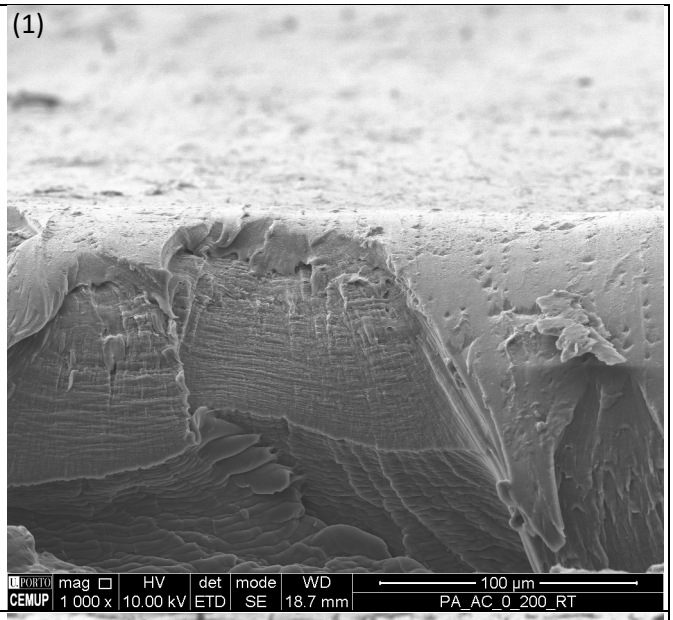
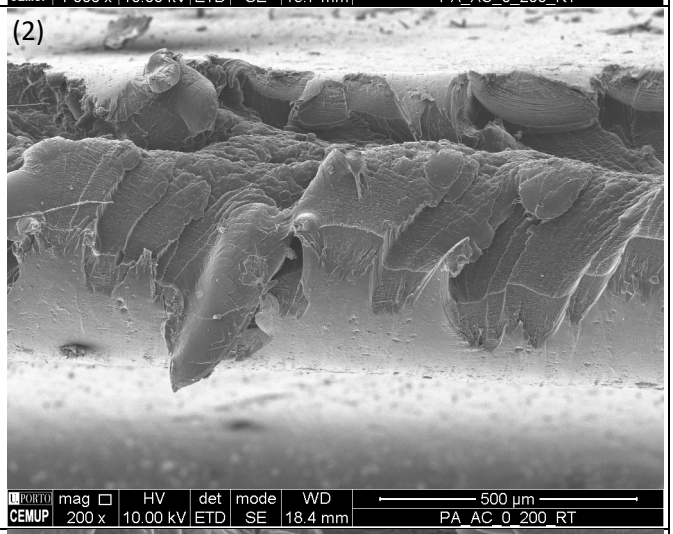
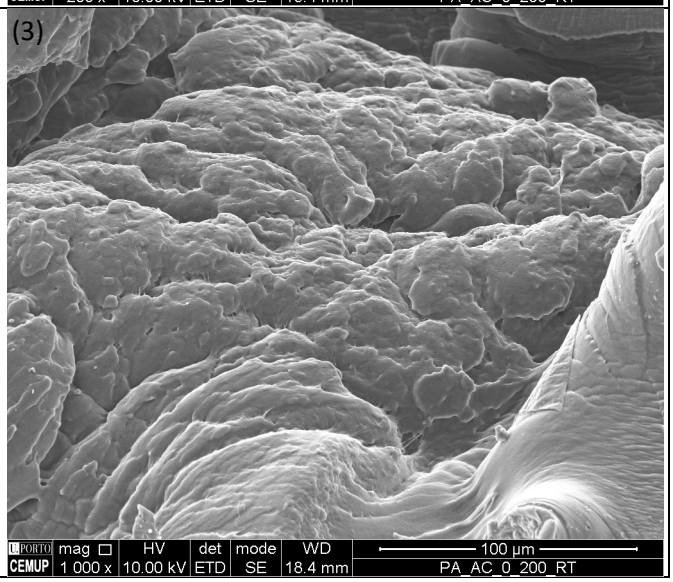
PA 6, Fracture Surface	
- Room temperature 21 °C ± 2 °C, - Pure tension, - Crosshead speed: 200 mm/min.	
	 
SEMs are shown a high inhomogeneous fracture surface. (1) Skin layer takes a form of crazing tearing. (2) Central region with irregular fracture surface, characterized mainly by crazes and (3) brittle failure.	  

Figure 200 - SEM images of butterfly specimens fractured for tensile loading at RT for PA 6. Localization: near surface and central.

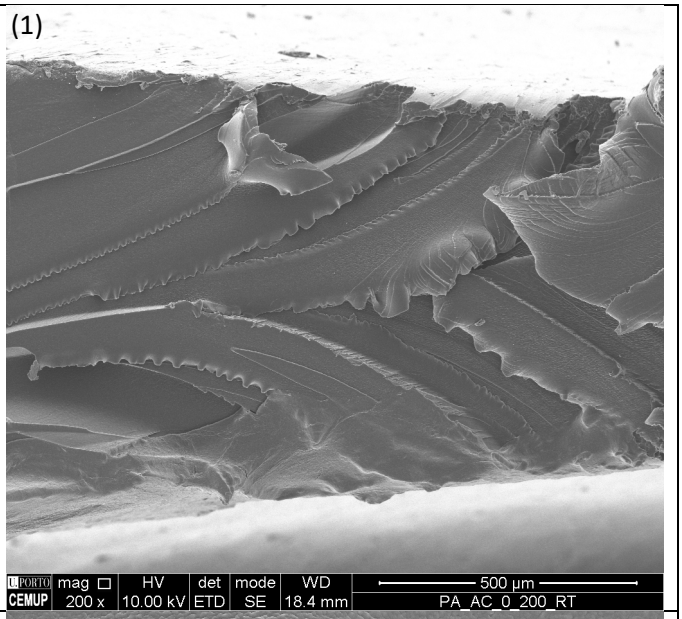
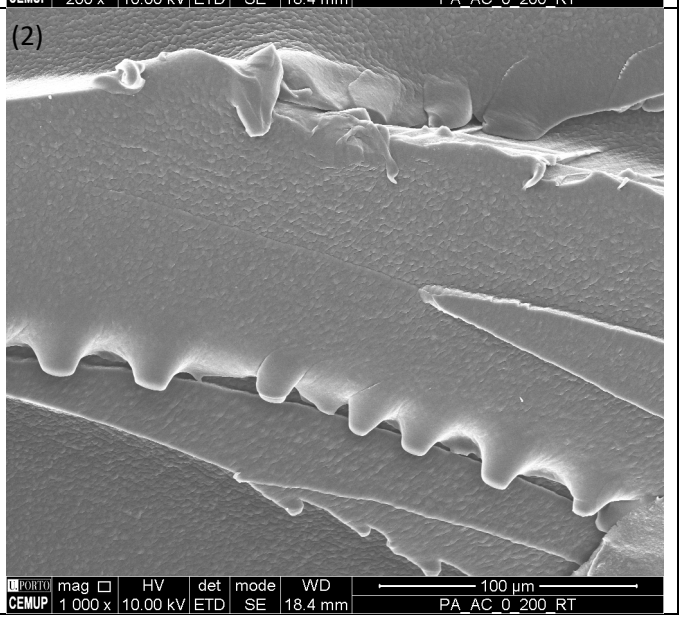
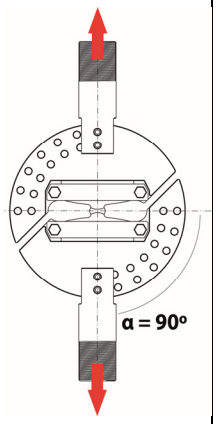
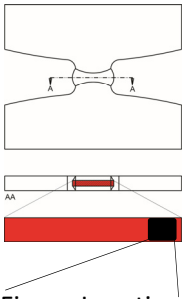
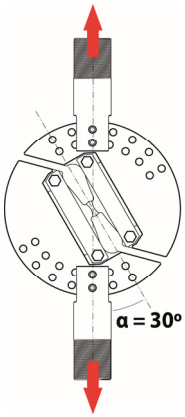
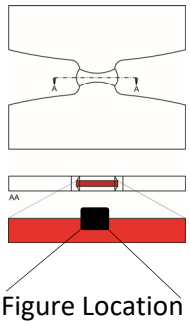
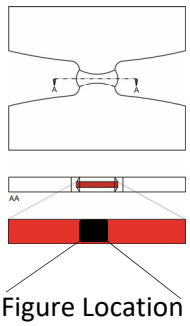
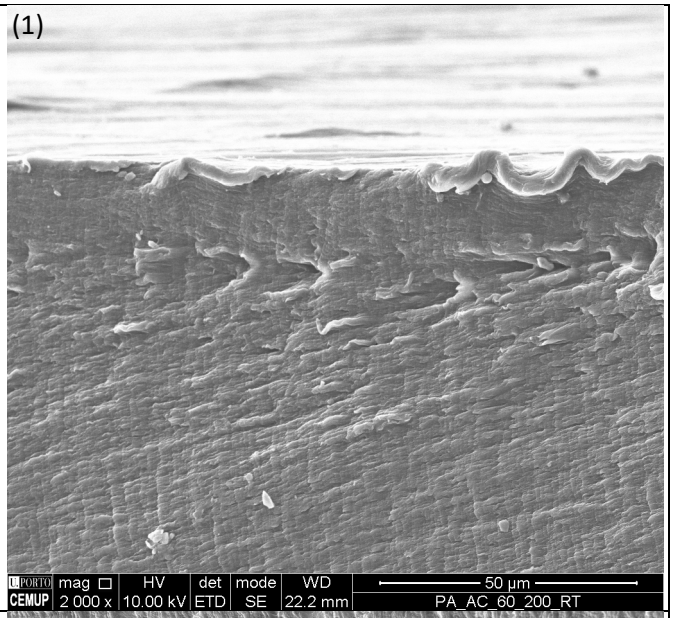
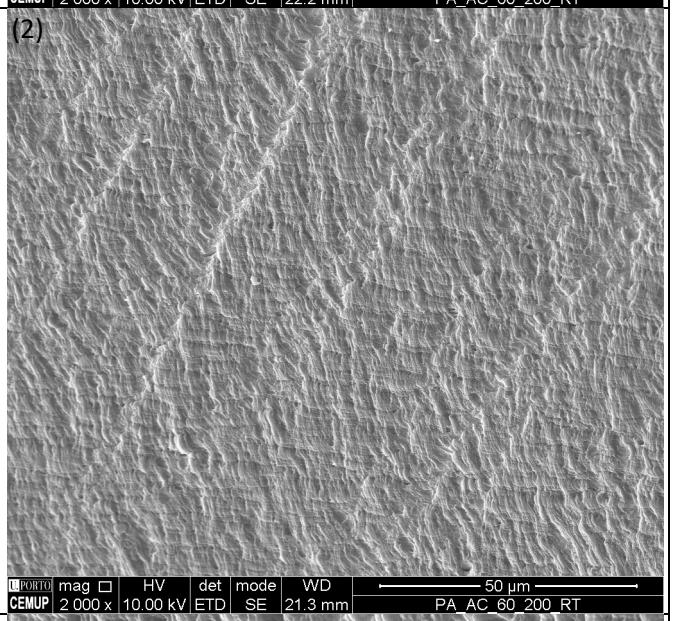
PA 6, Fracture Surface	(1) 
- Room temperature 21 °C ± 2 °C, - Pure tension, - Crosshead speed: 200 mm/min.	(2) 
 	
SEM micrographs. (1) Low and (2) high magnification shows crazing tearing in the region away from the centre of the fracture surface.	

Figure 201 - SEM images of butterfly specimens fractured for tensile loading at RT for PA 6. Localization: near surface.

Combined Shear/Tension at Room Temperature – PA 6

PA 6, Fracture Surface	
- Room temperature 21 °C ± 2 °C, - Combined shear/tension, - Crosshead speed: 200 mm/min.	
	 
Figure 135 – SEM micrographs. Brittle failure. All the surfaces are covered with a very fine mesh of deformed polymer.	





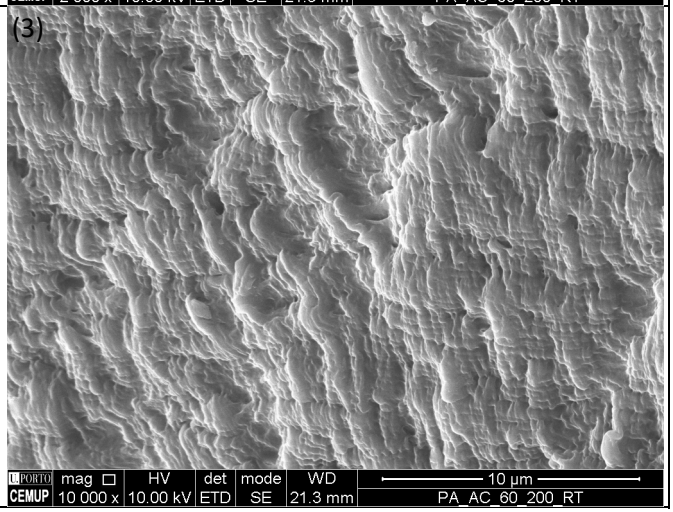
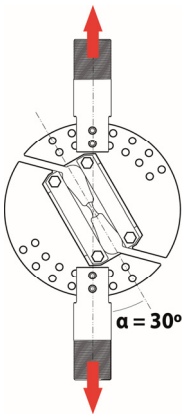
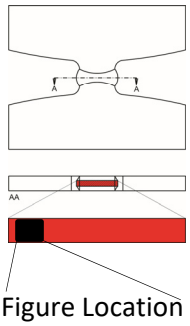
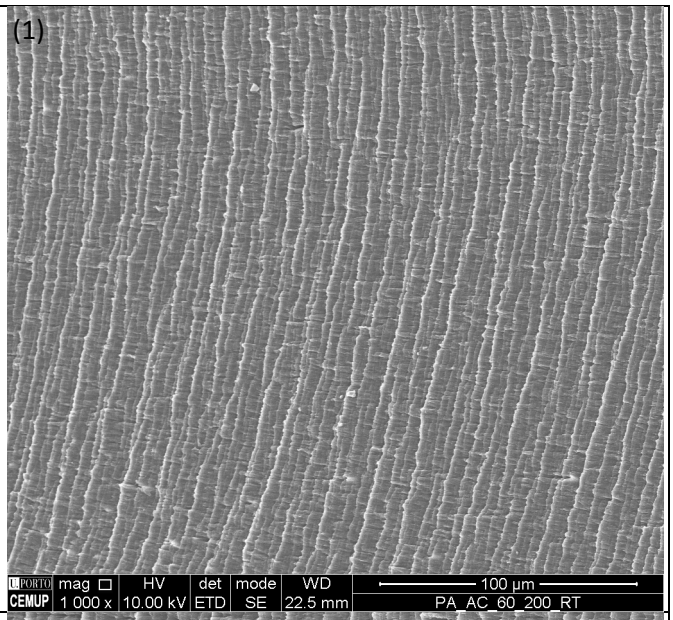
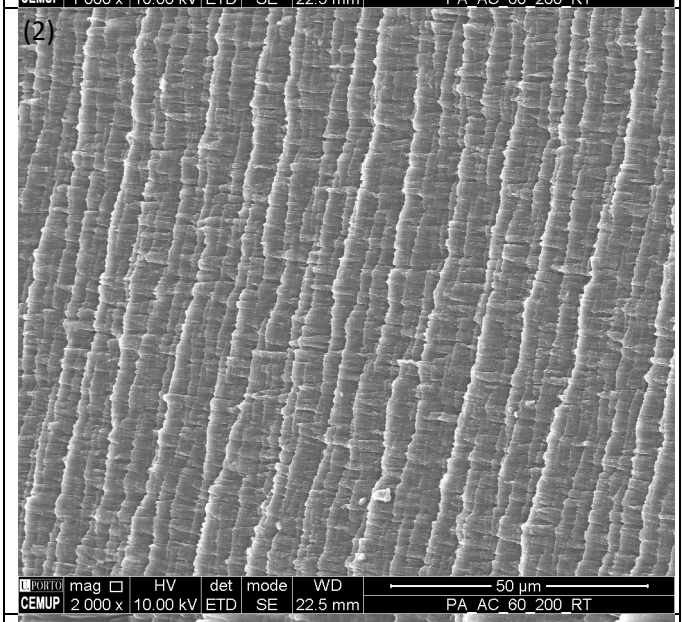


Figure 202 - SEM images of butterfly specimens fractured for combined tension/shear loading α = 30° at RT for PA 6. Localization: near surface and centre.

PA 6, Fracture Surface	
- Room temperature 21 °C ± 2 °C, - Combined shear/tension, - Crosshead speed: 200 mm/min.	
	
SEM micrographs. (1) and (2) The surface fracture has a striation configuration. (2) At high magnifications show material pulled out from the fracture surface.	





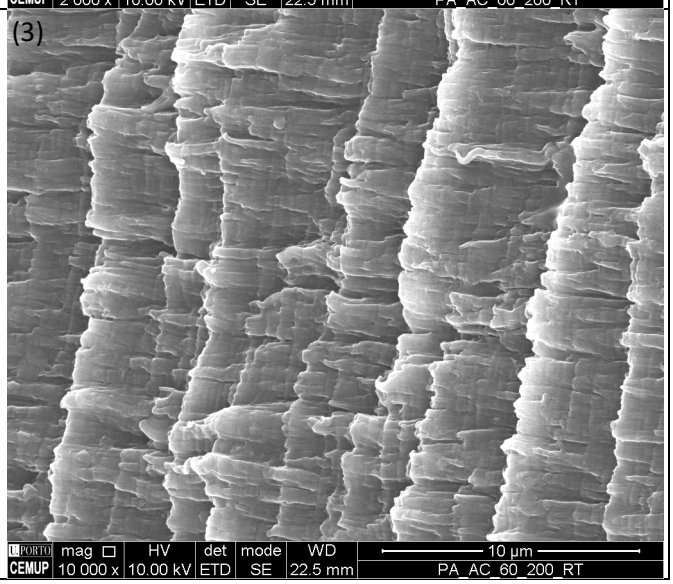
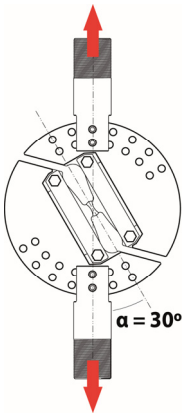
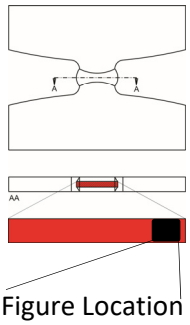


Figure 203 - SEM images of butterfly specimens fractured for combined tension/shear loading α = 30° at RT for PA 6. Localization: near surface.

PA 6, Fracture Surface	
- Room temperature 21 °C ± 2 °C, - Combined shear/tension, - Crosshead speed: 200 mm/min.	
  Figure Location	
SEM micrographs. (1) and (2) SEM micrographs shows crazing tearing morphology.	

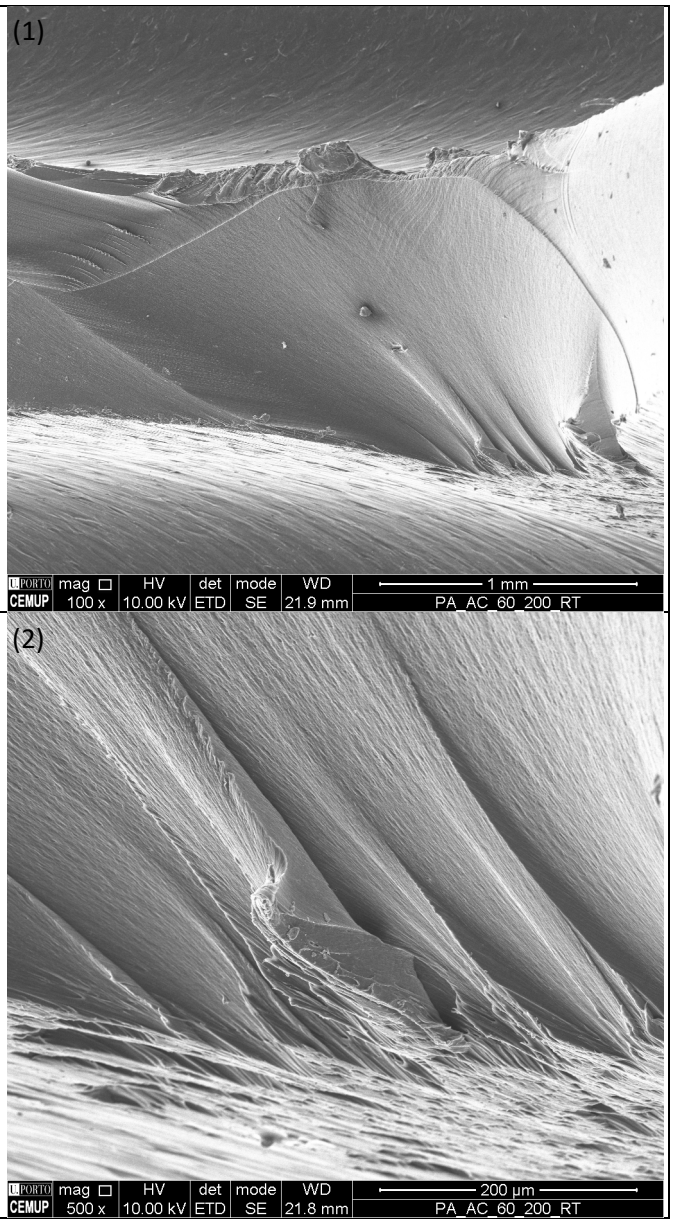


Figure 204 - SEM images of butterfly specimens fractured for combined tension/shear loading α = 30° at RT for PA 6. Localization: near surface.

Pure Shear at Room Temperature – PA 6

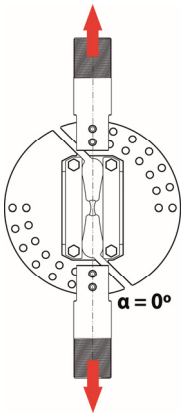
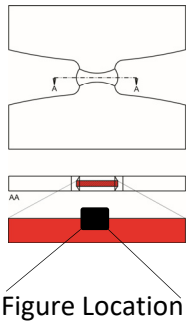
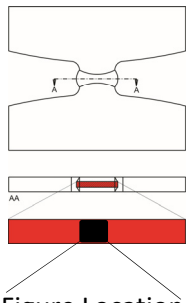
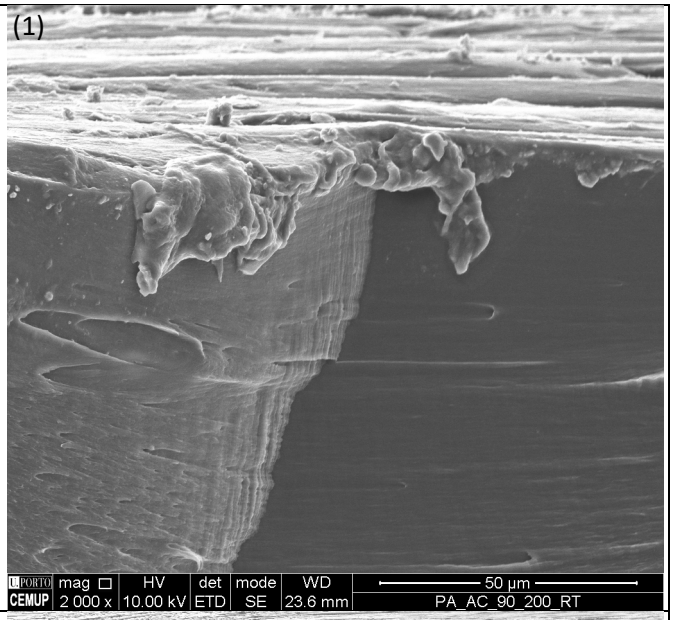
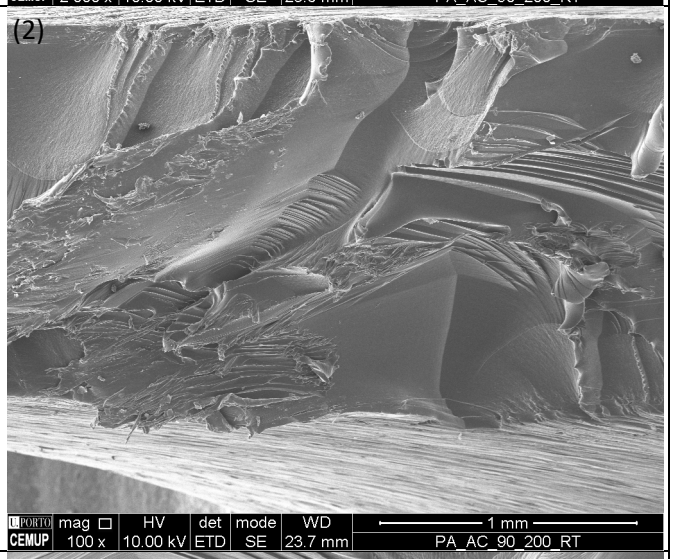
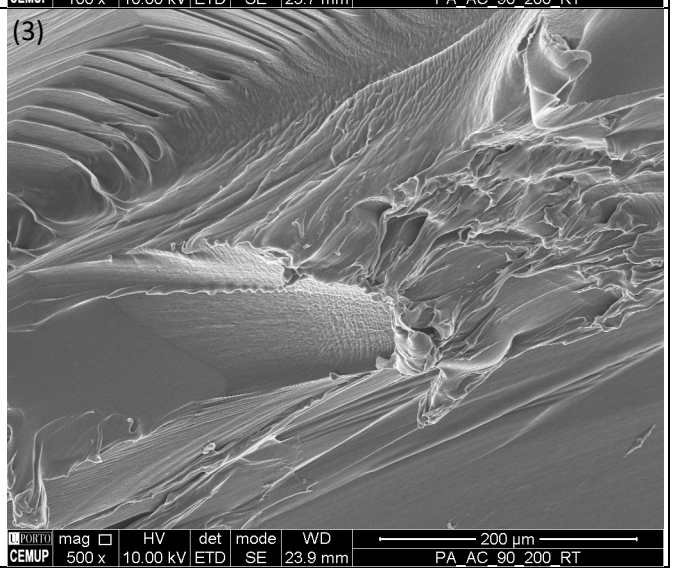
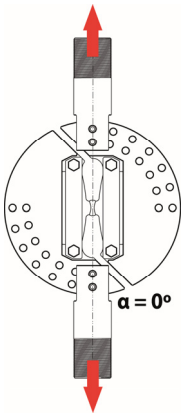
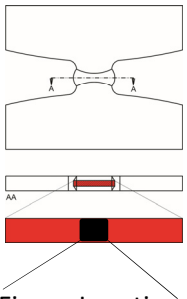
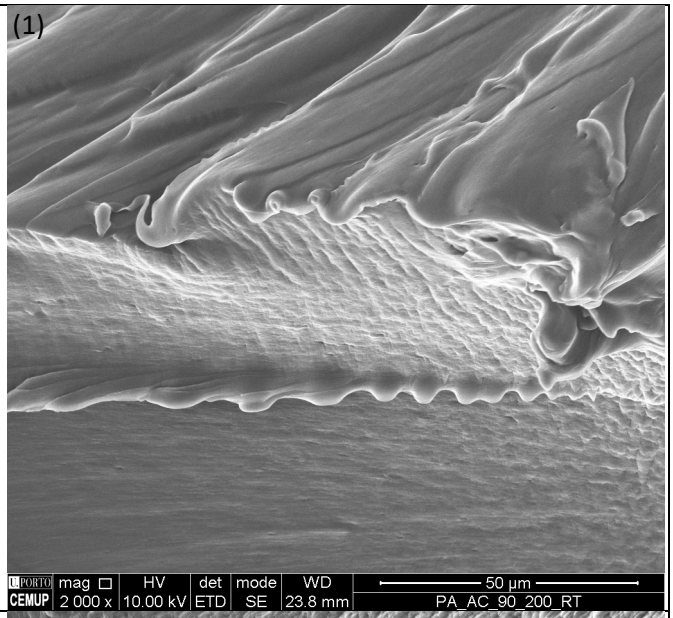
PA 6, Fracture Surface	
- Room temperature 21 °C ± 2 °C, - Pure shear, - Crosshead speed: 200 mm/min.	
	 
(1), (2) and (3) SEM micrographs shows a considerable plastic deformation and inhomogeneous morphology at fracture centre. There are a mix between crazing tearing and brittle fracture.	  

Figure 205 - SEM images of butterfly specimens fractured for shear loading at RT for PA 6. Localization: near surface and centre.

PA 6, Fracture Surface	
- Room temperature 21 °C ± 2 °C, - Pure shear, - Crosshead speed: 200 mm/min.	
	
SEM micrographs at High magnification shows (1) brittle failure Vs crazing tearing and (2) Brittle failure.	



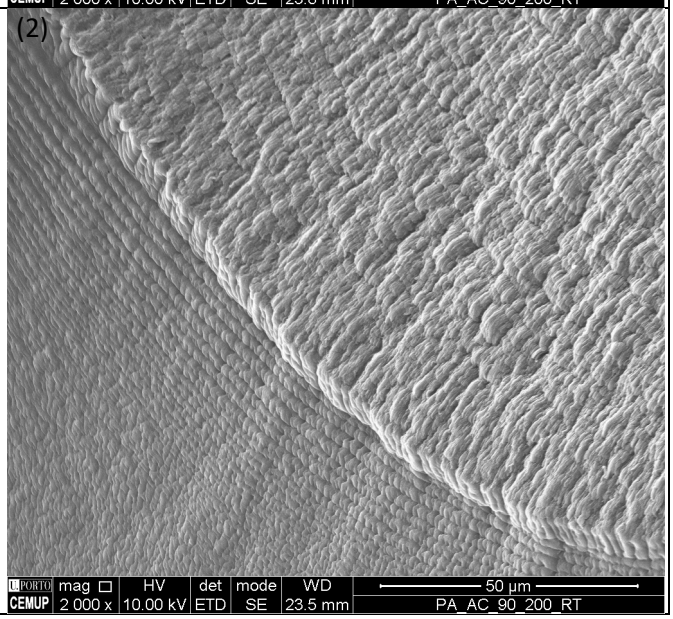
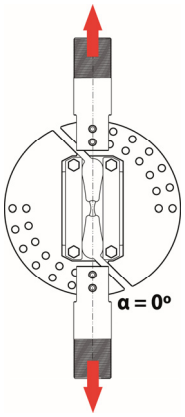
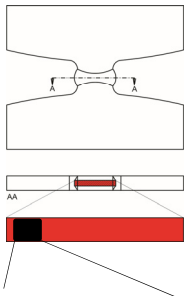


Figure 206 - SEM images of butterfly specimens fractured for shear loading at RT for PA 6. Localization: centre.

PA 6, Fracture Surface	
- Room temperature 21 °C ± 2 °C, - Pure shear, - Crosshead speed: 200 mm/min.	
 	
SEM micrographs (1) shows some amount of crazing tearing leading to a corrugated appearance in the regions away from the centre of the fracture surface. (2) High magnification - crazing tearing.	

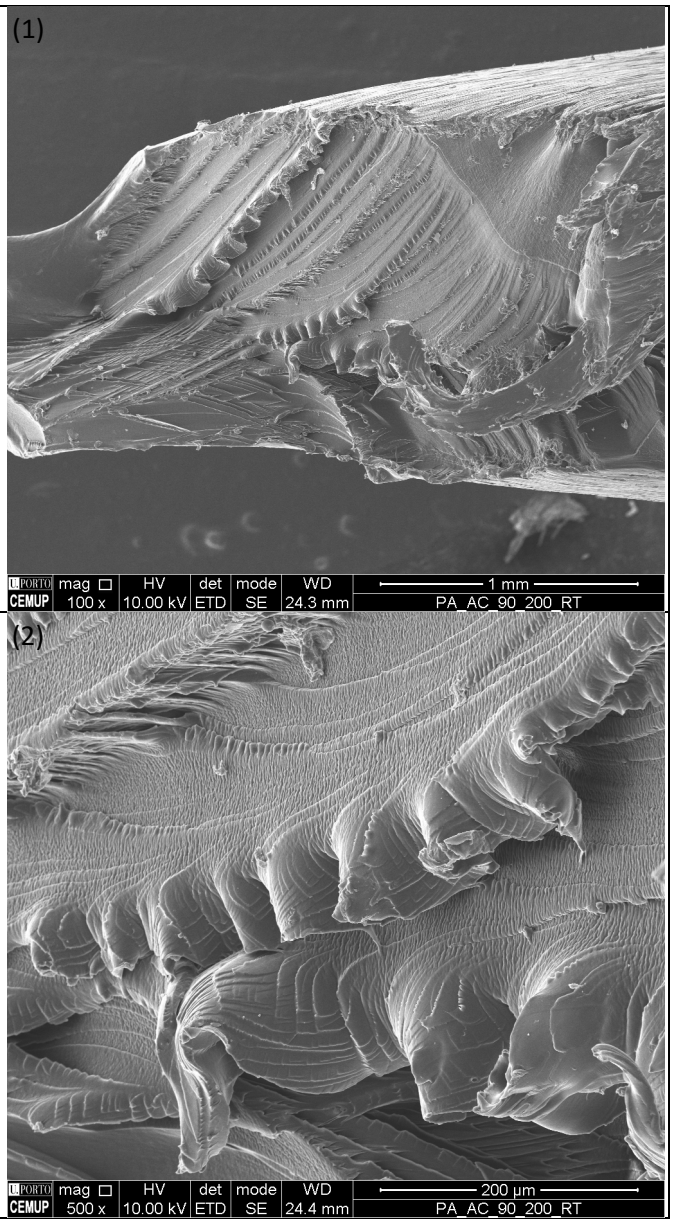


Figure 207 - SEM images of butterfly specimens fractured for shear loading at RT for PA 6. Localization: near surface.

Pure Tension at Temperature of 50°C – PA 6

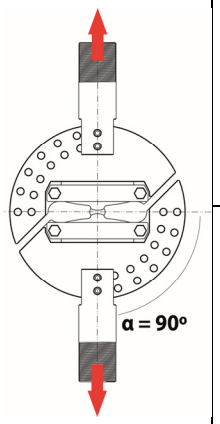
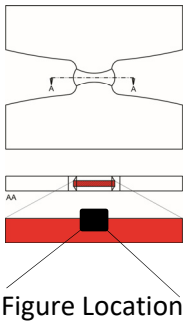
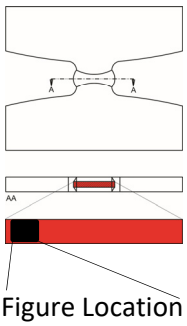
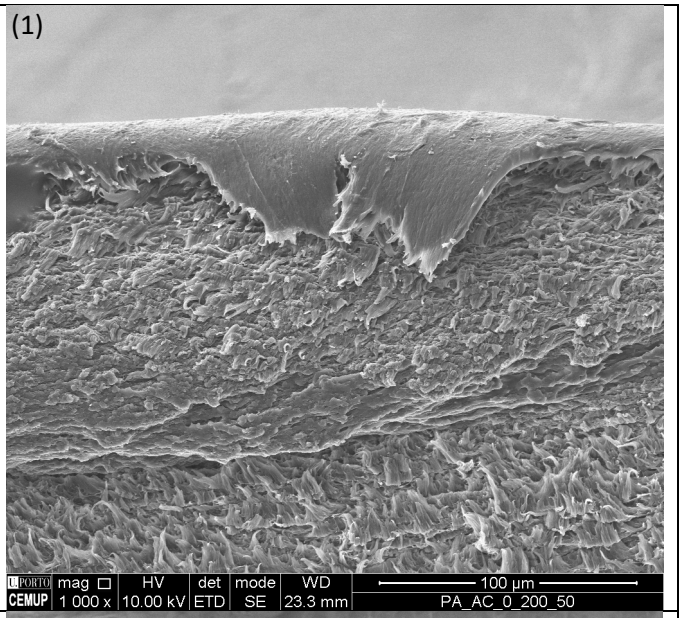
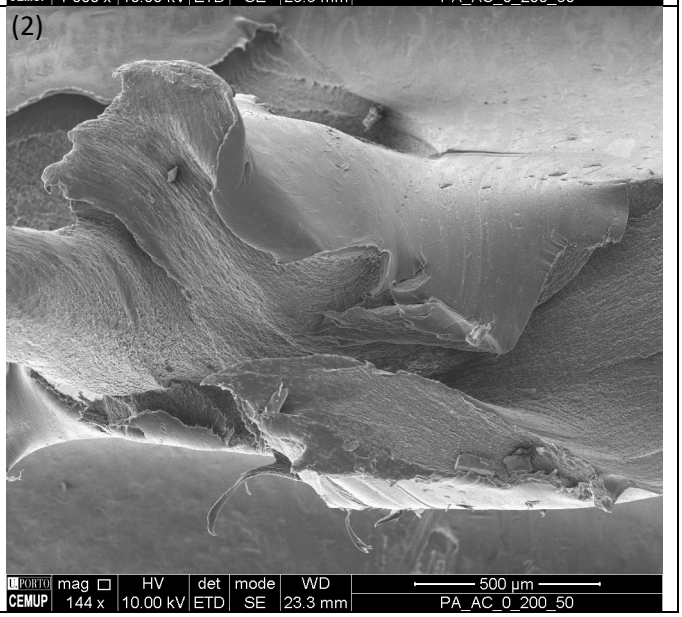
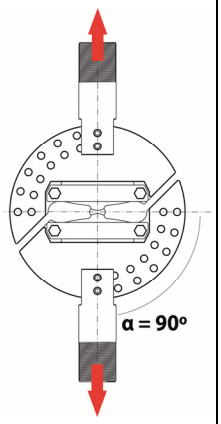
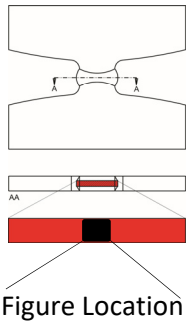
PA 6, Fracture Surface	
- Temperature of 50 °C, - Pure tension, - Crosshead speed: 200 mm/min.	
  	 
SEM micrographs (1) shows “peeling skin layer” and a more regular surface at core than at the ends. (2) Crazing tearing.	

Figure 208 - SEM images of butterfly specimens fractured for tensile loading at temperature of 50 °C for PA 6. Localization: near surface.

PA 6, Fracture Surface	
- Temperature of 50 °C, - Pure tension, - Crosshead speed: 200 mm/min.	
  Figure Location	
SEM micrographs shows at (1) and at (2) large amount of fibrils formation.	

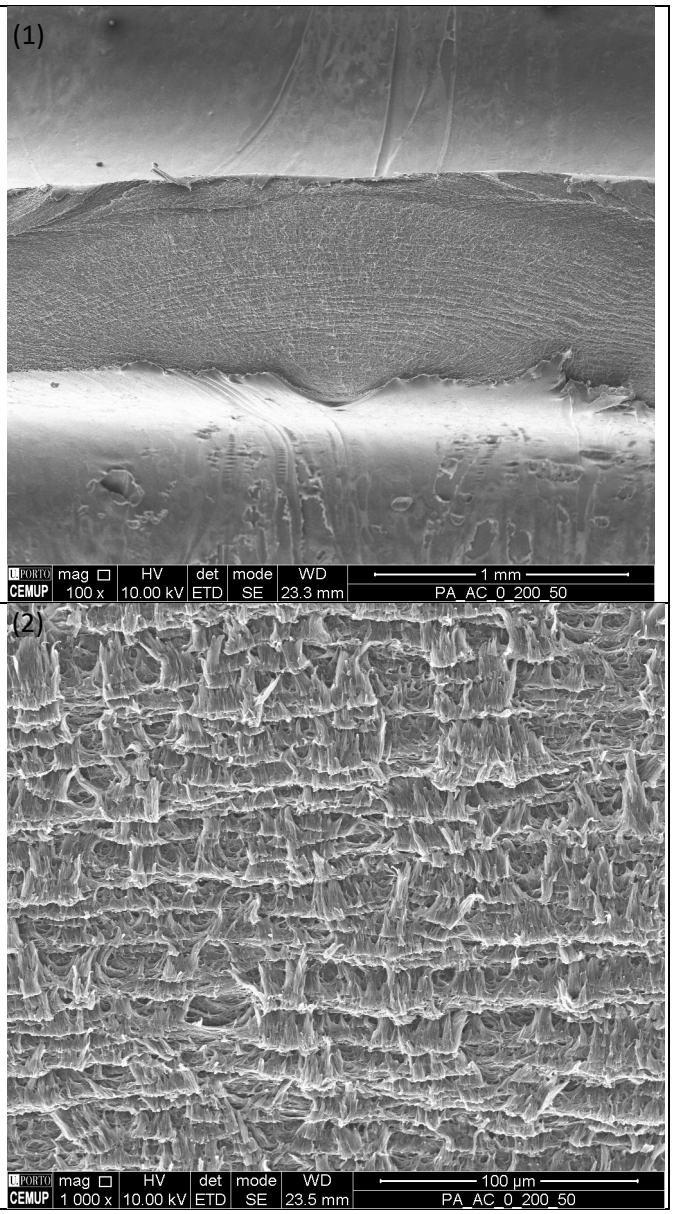
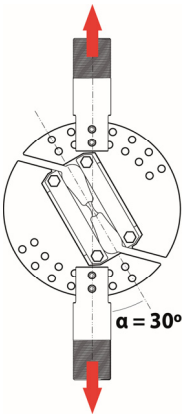
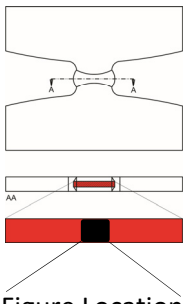
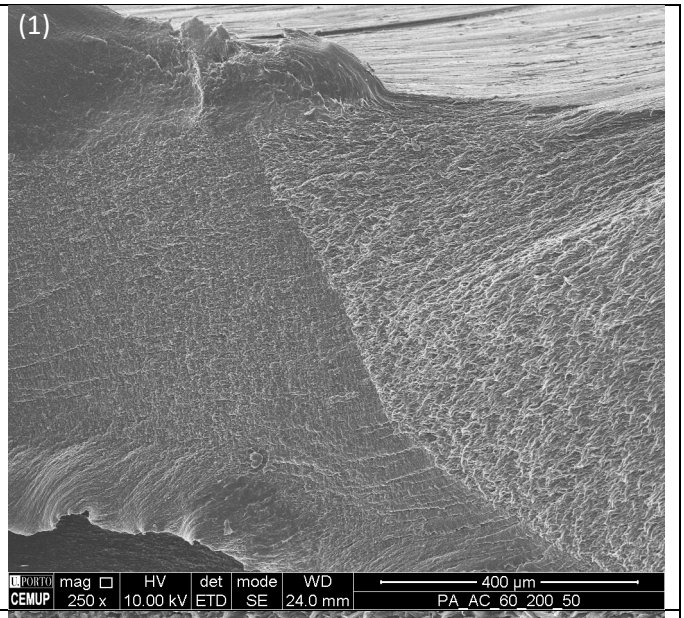


Figure 209 - SEM images of butterfly specimens fractured for tensile loading at temperature of 50 °C for PA 6. Localization: centre.

Combined Shear/Tension at Temperature of 50°C – PA 6

PA 6, Fracture Surface	
- Temperature of 50 °C, - Combined shear/tension, - Crosshead speed: 200 mm/min.	
	
SEM micrographs. (1) and (2) Fibrillar failure in the mid-thickness regions of the fracture surface Vs craze embrittlement (brittle mode of failure due to high crosshead speed).	



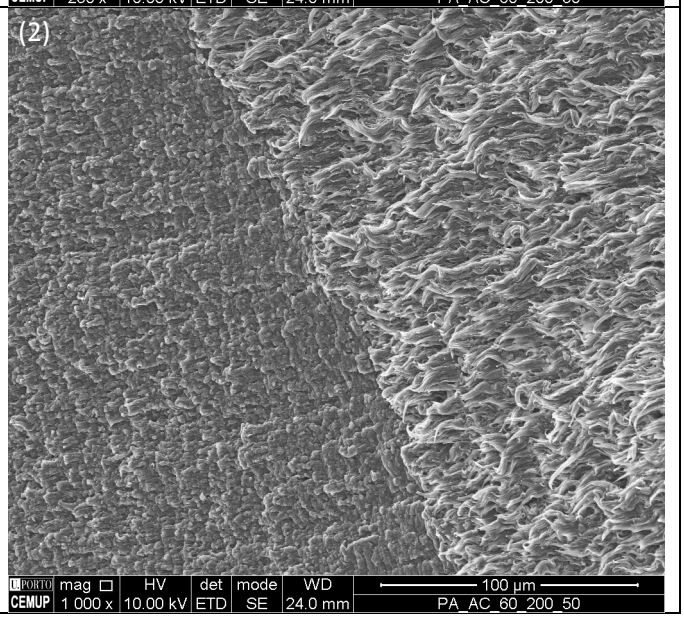
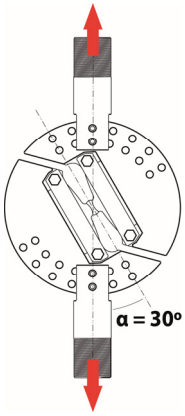
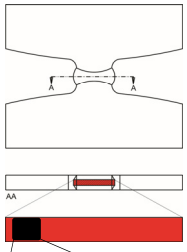
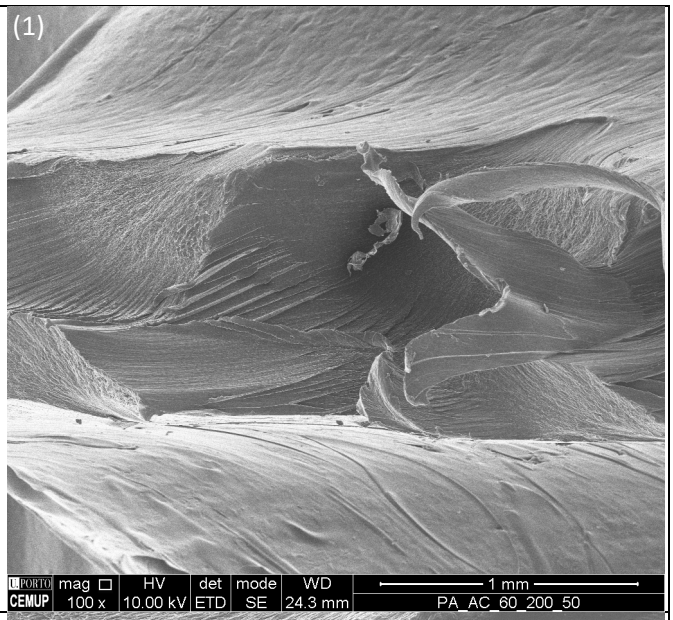
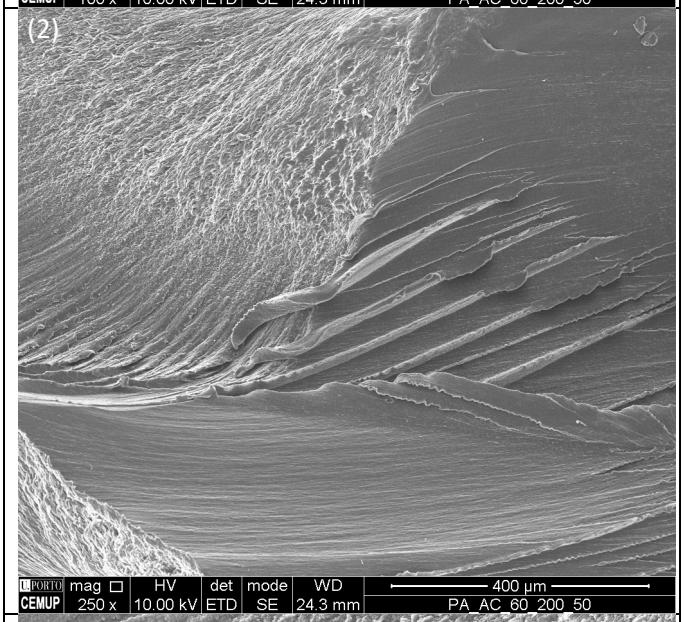


Figure 210 - SEM images of butterfly specimens fractured for combined tension/shear loading α = 30° at temperature of 50 °C for PA 6. Localization: centre.

PA 6, Fracture Surface	
- Temperature of 50 °C, - Combined shear/tension, - Crosshead speed: 200 mm/min.	
  Figure Location	
SEM micrographs. (1), (2) and (3) shows high inhomogeneous surface. Fracture surface is characterized by crazing tearing, brittle fracture and ductile pulling of fibrils.	





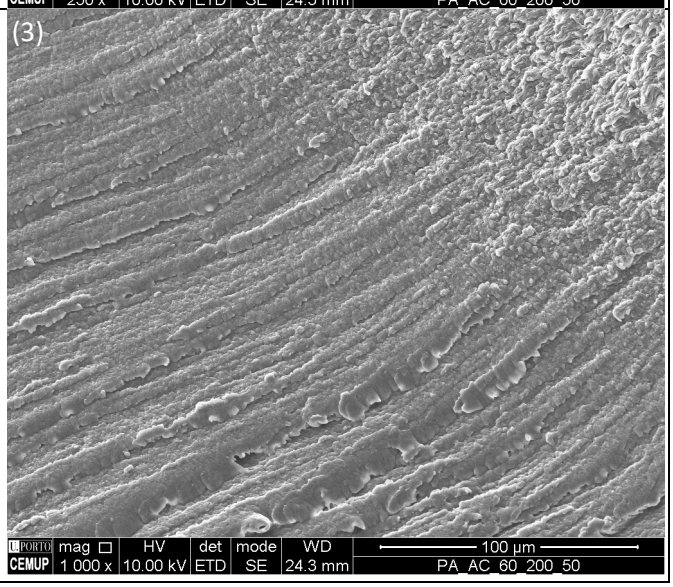
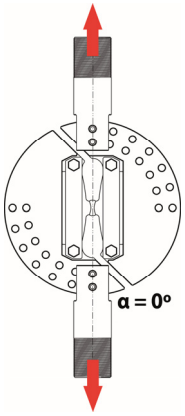
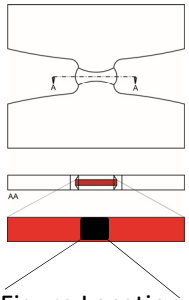
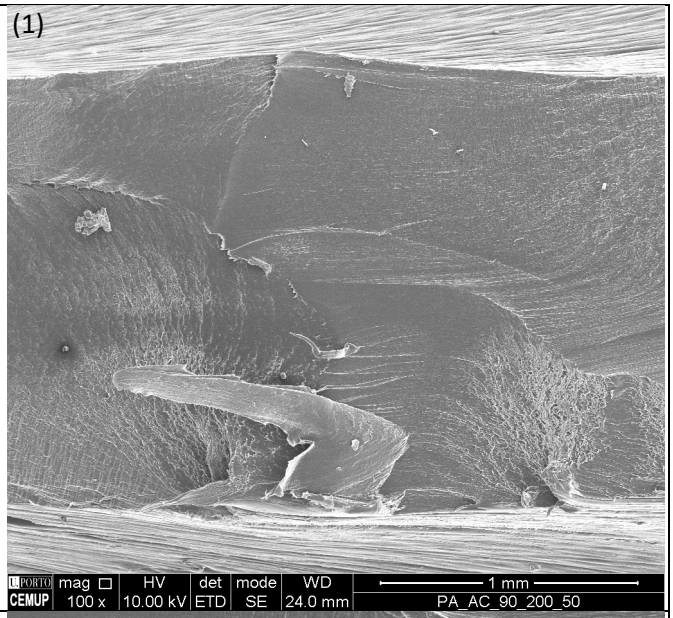
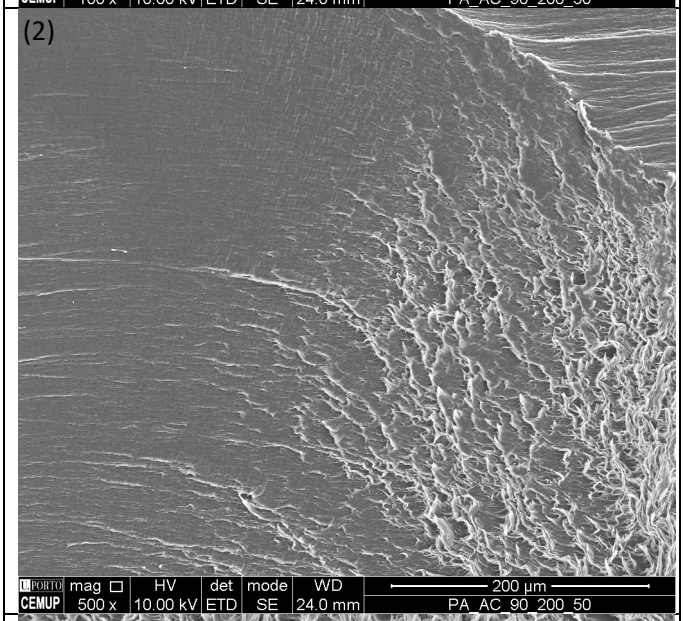


Figure 211 - SEM images of butterfly specimens fractured for combined tension/shear loading α = 30° at temperature of 50 °C for PA 6. Localization: near surface.

Pure Shear at Temperature of 50°C – PA 6

PA 6, Fracture Surface
- Temperature of 50 °C, - Pure shear, - Crosshead speed: 200 mm/min
  Figure Location
SEM micrographs. (2) Ductile pulling out of fibrils Vs brittle failure. (3) High magnification shows microfibrils.





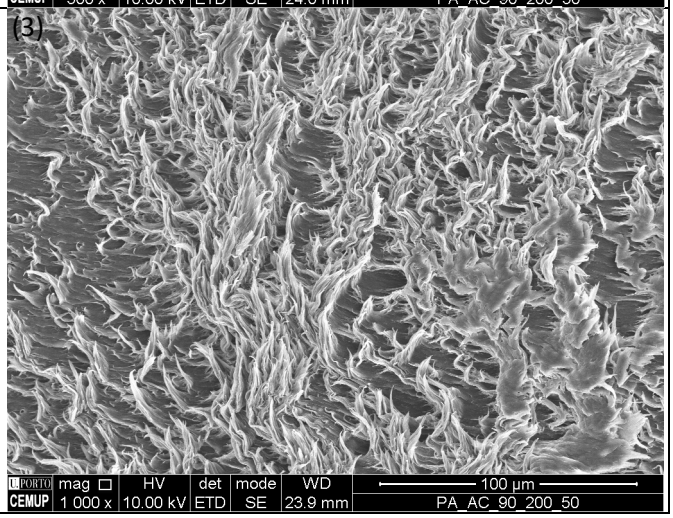


Figure 212 - SEM images of butterfly specimens fractured for shear loading at temperature of 50 °C for PA 6. Localization: near surface.

9 References

[1] H. F. Brinson and L. C. Brinson, *Polymer Engineering Science and Viscoelasticity: An Introduction*, Second. Springer Science, 2015.

[2] R. J. Crawford, *Plastics Engineering*, Third Edit. Butterworth-Heinemann, 1998.

[3] A. Kumar and R. K. Gupta, *Fundamentals of Polymer Engineering*, Second Edi. CRC Press, 2003.

[4] M. Chanda and S. K. Roy, *Plastics Fundamentals, Properties and Testing*. CRC press, 2008.

[5] K. Hachour, F. Zaïri, M. Naït-Abdelaziz, J. M. Gloaguen, M. Aberkane, and J. M. Lefebvre, 'Experiments and Modeling of High-Crystalline Polyethylene Yielding Under Different Stress States', *Int. J. Plast.*, vol. 54, pp. 1–18, 2014.

[6] S. S. Haltom, S. Kyriakides, and K. Ravi-Chandar, 'Ductile Failure Under Combined Shear and Tension', *Int. J. Solids Struct.*, vol. 50, no. 10, pp. 1507–1522, 2013.

[7] H. J. M. Caelers, L. E. Govaert, and G. W. M. Peters, 'The Prediction of Mechanical Performance of Isotactic Polypropylene on the Basis of Processing Conditions', *Polymer (Guildf).*, vol. 83, pp. 116–128, 2016.

[8] Y. Bai, 'Effect of Loading History on Necking and Fracture', *PhD Thesis*, no. 2000, pp. 1–262, 2008.

[9] B. H. Stuart, *Polymer Analysis*. John Wiley & Sons, 2002.

[10] S. B. Driscoll, *The Basics of Testing Plastics: Mechanical Properties, Flame Exposure and General Guidelines*. ASTM Manual Series, 2004.

[11] B. Demirel, 'Optimisation of Petaloid Base Dimensions and Process Operating Conditions to Minimise Environmental Stress Cracking in Injection Strerch Blow Moulded PET Bottles', School of Aerospace, Mechanical, and Manufacturing Engineering RMIT University, 2008.

[12] M. Alauddin, I. A. Choudhury, M. A. El Baradie, and M. S. J. Hashmi, 'Plastics and their Machining: A Review', *J. Mater. Process. Technol.*, vol. 54, no. 1–4, pp. 40–46, 1995.

[13] L. W. McKeen, *The Effect of Temperature and Other Factors on Plastics and Elastomers*, Second. 2007.

[14] J. M. Asua, Ed., *Polymer Reaction Engineering*. Blackwell, 2007.

[15] L. W. McKeen, *Permeability Properties of Plastic and Elastomers*, Third. William Andrew, 2012.

[16] C. Yu, Q. Xie, Y. Bao, G. Shan, and P. Pan, 'Crystalline and Spherulitic Morphology of Polymers Crystallized in Confined Systems', *Crystals*, vol. 7, no. 6, p. 147, 2017.

[17] S. Patlazhan and Y. Remond, 'Structural Mechanics of Semicrystalline Polymers Prior to the Yield Point: A Review', *J. Mater. Sci.*, vol. 47, no. 19, pp. 6749–6767, 2012.

[18] Z. Bartczak, A. S. Argon, and R. E. Cohen, 'Texture Evolution in Large Strain Simple Shear Deformation of High Density Polyethylene', *Polymer (Guildf).*, vol. 35, no. 16, pp. 3427–3441, 1994.

[19] B. Crist and J. M. Schultz, 'Polymer Spherulites: A Critical Review', *Prog. Polym. Sci.*, vol. 56, pp. 1–63, 2016.

[20] J. Xu *et al.*, 'Direct AFM Observation of Crystal Twisting and Organization in Banded Spherulites of Chiral Poly(3-hydroxybutyrate-co-3-hydroxyhexanoate)', *Macromolecules*, vol. 37, no. 11, pp. 4118–4123, 2004.

[21] Y. Fujiwara, 'The Superstructure of Melt-Crystallized Polyethylene. I. Screwlike Orientation of Unit Cell in Polyethylene Spherulites with Periodic Extinction Rings', *J. Appl. Polym. Sci.*, vol. 4, no. 10, pp. 10–15, 1960.

[22] T. Ikehara and T. Kataoka, 'Relation Between the Helical Twist and S-Shaped Cross Section of the Lamellar Crystals of Polyethylene', *Sci. Rep.*, vol. 3, no. 1, p. 1444, 2013.

[23] N. Patil, 'Flow Induced Crystallisation of Polyethylene in Presence of Nanoparticles', Loughborough University, 2010.

[24] J. M. Kim, R. Locker, and G. C. Rutledge, 'Plastic Deformation of Semicrystalline Polyethylene under Extension, Compression, and Shear Using Molecular Dynamics Simulation', *Macromolecules*, vol. 47, no. 7, pp. 2515–2528, 2014.

[25] A. Sedighiamiri, L. E. Govaert, and J. A. W. Van Dommelen, 'Micromechanical Modeling of the Deformation Kinetics of Semicrystalline Polymers', *J. Polym. Sci. Part B Polym. Phys.*, vol. 49, no. 18, pp. 1297–1310, 2011.

[26] B. A. G. Schrauwen, L. C. A. V. Breemen, A. B. Spoelstra, L. E. Govaert, G. W. M. Peters, and H. E. H. Meijer, 'Structure, Deformation, and Failure of Flow-Oriented Semicrystalline Polymers', *Macromolecules*, vol. 37, no. 23, pp. 8618–8633, 2004.

[27] S. S. Katti and M. Schultz, 'The Microstructure of Injection-Molded Semicrystalline Polymers: A review', *Polym. Eng. Sci.*, vol. 22, no. 16, pp. 1001–1017, 1982.

[28] F. Kai, Z. Liu, Q. Fu, J. Zheng, and C. Chen, 'State-of-the-Art of Fiber-Reinforced High-Pressure Hydrogen Storage Tanks', *J. Press. Equip. Syst.*, vol. 2, pp. 59–63, 2004.

[29] J. Aurrekoetxea, M. a. Sarrionandia, I. Urrutibeascoa, and M. L. Maspoch, 'Effects of Injection Moulding Induced Morphology on the Fracture Behaviour of Virgin and Recycled Polypropylene', *Polymer (Guildf).*, vol. 44, no. 22, pp. 6959–6964, 2003.

[30] M. R. Kantz, H. D. Newman, and F. H. Stigale, 'The Skin-Core Morphology and Structureproperty Relationships in Injection-Molded Polypropylene', *J. Appl. Polym. Sci.*, vol. 16, pp. 1249–1260, 1972.

[31] X. Guo, A. I. Isayev, and M. Demiray, 'Crystallinity and Microstructure in Injection Moldings of lsotactic Polypropylenes. Part II: Simulation and Experiment', *Polym. Eng. Sci.*, vol. 39, no. 71, pp. 2132–2149, 1999.

[32] J. C. Viana, 'Development of the Skin Layer in Injection Moulding: Phenomenological Model', *Polymer (Guildf).*, vol. 45, no. 3, pp. 993–1005, 2004.

[33] R. Pantani, I. Coccorullo, V. Speranza, and G. Titomanlio, 'Morphology Evolution During Injection Molding: Effect of Packing Pressure', *Polymer (Guildf).*, vol. 48, no. 9, pp. 2778–2790, 2007.

[34] C. Stern, A. Frick, and G. Weickert, 'Relationship Between the Structure and Mechanical Properties of Polypropylene: Effects of the Molecular Weight and Shear-Induced Structure', *J. Appl. Polym. Sci.*, vol. 103, pp. 519–533, 2007.

[35] L. Huang, Z. Wang, G. Zheng, J. Z. Guo, K. Dai, and C. Liu, 'Enhancing Oriented Crystals in Injection-Molded HDPE Through Introduction of Pre-Shear', *Mater. Des.*, vol. 78, pp. 12–18, 2015.

[36] A. J. Pennings and A. M. Kiel, 'Fractionation of Polymers by Crystallization from Solution, III. On the Morphology of Fibrillar Polyethylene Crystals Grown in Solution', *Kolloid-Zeitschrift Zeitschrift fur Polym.*, vol. 205, no. 2, pp. 160–162, 1965.

[37] R. H. Somani, L. Yang, L. Zhu, and B. S. Hsiao, 'Flow-Induced Shish-Kebab Precursor Structures in Entangled Polymer Melts', *Polymer (Guildf).*, vol. 46, no. 20, pp. 8587–8623, 2005.

[38] A. Galeski, 'Strength and Toughness of Crystalline Polymer Systems', *Prog. Polym. Sci.*, vol. 28, no. 12, pp. 1643–1699, 2003.

[39] B. A. G. Schrauwen, R. P. M. Janssen, L. E. Govaert, and H. E. H. Meijer, 'Intrinsic Deformation Behavior of Semicrystalline Polymers', *Macromolecules*, vol. 37, no. 16, pp. 6069–6078, 2004.

[40] H. Abdul-Hameed *et al.*, 'A Two-Phase Hyperelastic-Viscoplastic Constitutive Model for Semi-Crystalline Polymers: Application to Polyethylene Materials with a Variable Range of Crystal Fractions', *J. Mech. Behav. Biomed. Mater.*, vol. 37, pp. 323–332, 2014.

[41] S. Vishu, *Handbook of Plastics Testing and Failure Analysis*, vol. 293. JOHN WILEY & SONS, 2008.

[42] W. Grellmann and S. Seidler, *Polymer Testing*, 2nd Editio., vol. 27. Hanser Munich, 2013.

[43] Z. Bartczak and A. Galeski, 'Plasticity of Semicrystalline Polymers', *Macromol. Symp.*, vol. 294, no. 1, pp. 67–90, 2010.

[44] R. Séguéla, 'On the Natural Draw Ratio of Semi-Crystalline Polymers: Review of the Mechanical, Physical and Molecular Aspects', *Macromol. Mater. Eng.*, vol. 292, no. 3, pp. 235–244, 2007.

[45] Z. Bartczak, M. Grala, E. Richaud, and K. Gadzinowska, 'Erosion of the Molecular Network in the Amorphous Layers of Polyethylene upon High- Strain Deformation', *Polym. (United Kingdom)*, vol. 99, pp. 552–565, 2016.

[46] G. Strobl and G. Reiter, *Progress in Understanding of Polymer Crystallization*. Springer, 2007.

[47] R. Seguela, 'Critical Review of the Molecular Topology of Semicrystalline Polymers: The Origin and Assessment of Intercrystalline Tie Molecules and Chain Entanglements', *J. Polym. Sci. Part B Polym. Phys.*, vol. 43, no. 14, pp. 1729–1748, 2005.

[48] S. Humbert, O. Lame, J. M. Chenal, C. Rochas, and G. Vigier, 'New Insight on Initiation of Cavitation in Semicrystalline Polymers: In-situ SAXS Measurements', *Macromolecules*, vol. 43, no. 17, pp. 7212–7221, 2010.

[49] S. Humbert, O. Lame, and G. Vigier, 'Polyethylene Yielding Behaviour: What is Behind the Correlation Between Yield Stress and Crystallinity?', *Polymer (Guildf).*, vol. 50, no. 15, pp. 3755–3761, 2009.

[50] R. Mendoza, G. Régnier, W. Seiler, and J. L. Lebrun, 'Spatial Distribution of Molecular Orientation in Injection Molded iPP: Influence of Processing Conditions', *Polymer (Guildf).*, vol. 44, no. 11, pp. 3363–3373, 2003.

[51] A. Boger *et al.*, 'Stress-Induced Changes in Microstructure of a Low-Crystalline Polypropylene Investigated at Uniaxial Stretching', *J. Appl. Polym. Sci.*, vol. 112, pp. 188–199, 2009.

[52] P. I. Vincent, 'The Necking and Cold-Drawing of Rigid Plastics', *Polymer (Guildf).*, vol. 1, pp. 7–19, 1960.

[53] M. Makki *et al.*, 'Mullins Effect in Polyethylene and its Dependency on Crystal Content: A Network Alteration Model', *J. Mech. Behav. Biomed. Mater.*, vol. 75, pp. 442–454, 2017.

[54] C. R. López-Barrón, Y. Zeng, J. J. Schaefer, A. P. R. Eberle, T. P. Lodge, and F. S. Bates, 'Molecular Alignment in Polyethylene During Cold Drawing Using In-Situ SANS and Raman Spectroscopy', *Macromolecules*, vol. 50, no. 9, pp. 3627–3636, 2017.

[55] R. Brown, *Handbook of Polymer Testing*. CRC press, 2002.

[56] K. Hong and G. Strobl, 'Characterizing and Modeling the Tensile Deformation of

Polyethylene: The Temperature and Crystallinity Dependences', *Polym. Sci. - Ser. A*, vol. 50, no. 5, pp. 483–493, 2008.

[57] A. Pawlak and A. Galeski, 'Cavitation and Morphological Changes in Polypropylene Deformed at Elevated Temperatures', *J. Polym. Sci. Part B Polym. Phys.*, vol. 48, no. March, pp. 1271–1280, 2010.

[58] Z. Bartczak, 'Influence of Molecular Parameters on High-Strain Deformation of Polyethylene in the Plane-Strain Compression. Part II. Strain Recovery', *Polymer (Guildf).*, vol. 46, no. 23, pp. 10339–10354, 2005.

[59] A. Pawlak, A. Galeski, and A. Rozanski, 'Cavitation During Deformation of Semicrystalline Polymers', *Prog. Polym. Sci.*, vol. 39, no. 5, pp. 921–958, 2014.

[60] A. Pawlak and A. Galeski, 'Plastic Deformation of Crystalline Polymers: The Role of Cavitation and Crystal Plasticity', *Macromolecules*, vol. 38, no. 23, pp. 9688–9697, 2005.

[61] A. Pawlak, 'Cavitation During Tensile Deformation of High-Density Polyethylene', *Polymer (Guildf).*, vol. 48, no. 5, pp. 1397–1409, 2007.

[62] A. Peterlin, 'Molecular Model of Drawing Polyethylene and Polypropylene', *J. Mater. Sci.*, vol. 6, no. 6, pp. 490–508, 1971.

[63] Z. Jiang *et al.*, 'Structural Evolution of Tensile Deformed High-Density Polyethylene at Elevated Temperatures: Scanning Synchrotron Small- and Wide-Angle X-Ray Scattering Studies', *Polymer (Guildf).*, vol. 50, no. 16, pp. 4101–4111, 2009.

[64] P. Zoller and Y. A. Fakhreddine, 'Pressure-Volume-Temperature Studies of Semi-Crystalline Polymers', *Thermochim. Acta*, vol. 238, no. C, pp. 397–415, 1994.

[65] J. Wang, *PVT Properties of Polymers for Injection Molding*. In Tech, 2012.

[66] European Committee for Standardization (CEN), 'EN ISO 527-1:1993 Plastics – Determination of Tensile Properties'.

[67] J. E. Mark, *Physical Properties of Polymers Handbook*, Second. Springer, 2007.

[68] H. B. Motra, J. Hildebrand, and A. Dimmig-Osburg, 'Assessment of Strain Measurement Techniques to Characterise Mechanical Properties of Structural Steel', *Eng. Sci. Technol. an Int. J.*, vol. 17, no. 4, pp. 260–269, 2014.

[69] European Committee for Standardization (CEN), 'EN ISO 527-2:1993 Plastics – Determination of Tensile Properties'.

[70] European Committee for Standardization (CEN), 'EN ISO 604:2003 Plastics – Determination of Compressive Properties'.

[71] G. W. Ehrenstein, G. Riedel, and P. Trawiel, 'Chapter 6 Dynamic Mechanical Analysis', *Therm. Anal. Plast. Theory Pract.*, pp. 236–299, 2004.

[72] K. P. Menard, *Dynamic Mechanical Analysis : A Practical Introduction*. 2008.

[73] C. R. Siviour and J. L. Jordan, 'High Strain Rate Mechanics of Polymers: A Review', *J. Dyn. Behav. Mater.*, vol. 2, no. 1, pp. 15–32, 2016.

[74] European Committee for Standardization (CEN), 'EN ISO 6721-1:2012 Plastics – Determination of Dynamic Mechanical Properties', vol. European C.

[75] C. Schick, 'Differential Scanning Calorimetry (DSC) of Semicrystalline Polymers', *Anal. Bioanal. Chem.*, vol. 395, no. 6, pp. 1589–1611, 2009.

[76] J. E. Mark, *Polymer Data Handbook*, Second Edi. Oxford University Press, 2009.

[77] European Committee for Standardization (CEN), 'EN ISO 11375-1:1997 Plastics - Differential Scanning Calorimetry (DSC)'.

[78] P. W. Hawkes and J. C. H. Spence, *Science of Microscopy*, vol. 1. Springer, 2007.

[79] J. Sikorski, J. S. Moss, P. H. Newman, and T. Buckley, 'A New Preparation Technique for Examination of Polymers in the Scanning Electron Microscope.', *J. Sci. Instrum.*, vol. 1, no. 1, pp. 29–31, 1968.

[80] A. Dorogoy, B. Karp, and D. Rittel, 'A Shear Compression Disk Specimen with Controlled Stress Triaxiality Under Quasi-Static Loading', *Exp. Mech.*, vol. 53, no. 2, pp. 243–253, 2011.

[81] M. Ames, J. Markmann, and R. Birringer, 'Mechanical Testing Via Dominant Shear Deformation of Small-Sized Specimen', *Mater. Sci. Eng. A*, vol. 528, no. 1, pp. 526–532, 2010.

[82] Q. Duan, T. Jin, S. Chen, and X. Shu, 'Mechanical Analysis of PA66 Under Combined Shear–Compression', *Appl. Phys. A*, vol. 123, no. 5, p. 365, 2017.

[83] M. Brünig, O. Chyra, D. Albrecht, L. Driemeier, and M. Alves, 'A Ductile Damage Criterion at Various Stress Triaxialities', *Int. J. Plast.*, vol. 24, no. 10, pp. 1731–1755, 2008.

[84] A. Dorogoy and D. Rittel, 'Quasi-Static and Dynamic Large Strain Shear-Tension Testing', *Exp. Mech.*, vol. 1, pp. 1–6, 2017.

[85] I. Barsoum and J. Faleskog, 'Rupture Mechanisms in Combined Tension and Shear-Micromechanics', *Int. J. Solids Struct.*, vol. 44, no. 17, pp. 5481–5498, 2007.

[86] D. Kulawinski *et al.*, 'Characterization of stress-Strain Behavior of a Cast TRIP Steel Under Different Biaxial Planar Load Ratios', *Eng. Fract. Mech.*, vol. 78, no. 8, pp. 1684–1695, 2011.

[87] L. Leotoing, D. Guines, I. Zidane, and E. Ragneau, 'Cruciform Shape Benefits for Experimental and Numerical Evaluation of Sheet Metal Formability', *J. Mater. Process. Technol.*, vol. 213, no. 6, pp. 856–863, 2013.

[88] A. Ognedal, *Large-Deformation Behaviour of Thermoplastics at Various Stress States*, no. October. 2012.

[89] T. Børvik, O. S. Hopperstad, S. Dey, E. V. Pizzinato, M. Langseth, and C. Albertini, 'Strength and Ductility of Weldox 460 E Steel at High Strain Rates, Elevated Temperatures and Various Stress Triaxialities', *Eng. Fract. Mech.*, vol. 72, no. 7, pp. 1071–1087, 2005.

[90] M. Dunand and D. Mohr, 'Hybrid Experimental-Numerical Analysis of Basic Ductile Fracture Experiments for Sheet Metals', *Int. J. Solids Struct.*, vol. 47, no. 9, pp. 1130–1143, 2010.

[91] Y. Bai and T. Wierzbicki, 'A New Model of Metal Plasticity and Fracture with Pressure and Lode Dependence', *Int. J. Plast.*, vol. 24, no. 6, pp. 1071–1096, 2008.

[92] Y. Bao and T. Wierzbicki, 'On Fracture Locus in the Equivalent Strain and Stress Triaxiality Space', *Int. J. Mech. Sci.*, vol. 46, no. 1, pp. 81–98, 2004.

[93] R. Olsson, 'A Survey of Test Methods for Multiaxial and Out-of-Plane Strength of Composite Laminates', *Compos. Sci. Technol.*, vol. 71, no. 6, pp. 773–783, 2011.

[94] M. Arcan, Z. Hashin, and A. Voloshin, 'A Method to Produce Plane-Stress States with Applications to Fiber-Reinforced Materials', *Exp. Mech.*, pp. 141–6, 1978.

[95] D. Mohr and M. Doyoyo, 'Analysis of the Arcan Apparatus in the Clamped Configuration', *J. Compos. Mater.*, vol. 36, no. 22, pp. 2583–2594, 2002.

[96] M. Doyoyo and T. Wierzbicki, 'Experimental Studies on the Yield Behavior of Ductile and Brittle Aluminum Foams', *Int. J. Plast.*, vol. 19, no. 8, pp. 1195–1214, 2003.

[97] Z. Zhou, Z. Wang, L. Zhao, and X. Shu, 'Loading Rate Effect on Yield Surface of Aluminum

Alloy Foams', *Mater. Sci. Eng. A*, vol. 543, pp. 193–199, 2012.

[98] D. Mohr and M. Doyoyo, 'A New Method for the Biaxial Testing of Cellular Solids', *Exp. Mech.*, vol. 43, no. 2, pp. 173–182, 2003.

[99] A. Petras and M. P. F. Sutcliffe, 'Indentation Failure of Analysis of Sandwich Beams', *Compos. Struct.*, vol. 50, no. 9–10, pp. 311–318, 2000.

[100] G. Gruben, E. Fagerholt, O. S. Hopperstad, and T. Børvik, 'Fracture Characteristics of a Cold-Rolled Dual-Phase Steel', *Eur. J. Mech. A/Solids*, vol. 30, no. 3, pp. 204–218, 2011.

[101] A. Ghahremaninezhad and K. Ravi-Chandar, 'Ductile Failure Behavior of Polycrystalline Al 6061-T6 under Shear Dominant Loading', *Int. J. Fract.*, vol. 180, no. 1–2, pp. 23–39, 2013.

[102] N. Choupani, 'Experimental and Numerical Investigation of the Mixed-Mode Delamination in Arcan Laminated Specimens', *Mater. Sci. Eng. A*, vol. 478, no. 1–2, pp. 229–242, 2008.

[103] M. Nikbakht and N. Choupani, 'Fracture Toughness Characterization of Carbon-Epoxy Composite using Arcan Specimen', *Wasetacnz*, vol. 2–4, no. 5, pp. 247–253, 2008.

[104] P. B. Gning, D. Delsart, J. M. Mortier, and D. Coutellier, 'Through-Thickness Strength Measurements Using Arcan's Method', *Compos. Part B Eng.*, vol. 41, no. 4, pp. 308–316, 2010.

[105] J. Y. Cognard, L. Sohier, and P. Davies, 'A Modified Arcan Test to Analyze the Behavior of Composites and Their Assemblies Under Out-of-Plane Loadings', *Compos. Part A Appl. Sci. Manuf.*, vol. 42, no. 1, pp. 111–121, 2011.

[106] S. C. Hung and K. M. Liechti, 'An Evaluation of the Arcan Specimen for Determining the Shear Moduli of Fiber-Reinforced Composites', *Exp. Mech.*, vol. 37, no. 4, pp. 460–468, 1997.

[107] R. El-Hajjar and R. Haj-Ali, 'In-Plane Shear Testing of Thick-Section Pultruded FRP Composites Using a Modified Arcan Fixture', *Compos. Part B Eng.*, vol. 35, no. 5, pp. 421–428, 2004.

[108] H. Mae, 'Characterization of Material Ductility of PP/EPR/talc Blend Under Wide Range of Stress Triaxiality at Intermediate and High Strain Rates', *J. Appl. Polym. Sci.*, vol. 111, no. 7, pp. 854–868, 2009.

[109] B. Langrand and A. Combescure, 'Non-Linear and Failure Behaviour of Spotwelds: A "Global" Finite Element and Experiments in Pure and Mixed Modes I/II', *Int. J. Solids Struct.*, vol. 41, no. 24–25, pp. 6631–6646, 2004.

[110] T. Wierzbicki, Y. Bao, and Y. Bai, 'A New Experimental Technique for Constructing a Fracture Envelope of Metals under Multi-Axial Loading', *Proc. 2005 SEM Annu. Conf. Expo. Exp. Appl. Mech.*, pp. 1295–1303, 2005.

[111] D. Mohr and S. Henn, 'Calibration of Stress-Triaxiality Dependent Crack Formation Criteria: A New Hybrid Experimental-Numerical Method', *Exp. Mech.*, vol. 47, no. 6, pp. 805–820, 2007.

[112] M. Dunand and D. Mohr, 'Optimized Butterfly Specimen for the Fracture Testing of Sheet Materials Under Combined Normal and Shear Loading', *Eng. Fract. Mech.*, vol. 78, no. 17, pp. 2919–2934, 2011.

[113] G. Z. Voyiadjis, S. H. Hoseini, and G. H. Farrahi, 'A Plasticity Model for Metals with Dependency on all the Stress Invariants', *J. Eng. Mater. Technol.*, vol. 135, no. 1, p. 011002, 2012.

[114] J. Smith, W. K. Liu, and J. Cao, 'A General Anisotropic Yield Criterion for Pressure-

Dependent Materials', *Int. J. Plast.*, vol. 75, pp. 2–21, 2015.

[115] K. D. Pae and S. K. Bhateja, 'The Effects of Hydrostatic Pressure on the Mechanical Behavior of Polymers', *J. Macromol. Sci. Part C*, vol. 13, no. 1, pp. 1–75, 1975.

[116] C. D. Wilson, 'A Critical Reexamination of Classical Metal Plasticity', *J. Appl. Mech.*, vol. 69, no. 1, p. 63, 2002.

[117] M. Brünig, S. Berger, and H. Obrecht, 'Numerical Simulation of the Localization Behavior of Hydrostatic-Stress-Sensitive Metals', *Int. J. Mech. Sci.*, vol. 42, no. 11, pp. 2147–2166, 2000.

[118] P. B. Bowden and J. A. Jukes, 'The Plastic Flow of Isotropic Polymers', *J. Mater. Sci.*, vol. 7, no. 1, pp. 52–63, 1972.

[119] R. Raghava, R. M. Caddell, and G. S. Y. Yeh, 'The Macroscopic Yield Behaviour of Polymers', *J. Mater. Sci.*, vol. 8, no. 2, pp. 225–232, 1973.

[120] E. Ghorbel, 'A Viscoplastic Constitutive Model for Polymeric Mterials', *Int. J. Plast.*, vol. 24, no. 11, pp. 2032–2058, 2008.

[121] DS SIMULIA Corp, 'Abaqus 6.11. Theory manual', p. 1172, 2011.

[122] W. Li, F. Liao, T. Zhou, and H. Askes, 'Ductile Fracture of Q460 Steel: Effects of Stress Triaxiality and Lode Angle', *J. Constr. Steel Res.*, vol. 123, pp. 1–17, 2016.

[123] Y. Bao, 'Prediction of Ductile Crack Formation in Uncracked Bodies', *PhD Thesis*, p. 252, 2003.

[124] Y. Luo and Z. Kang, 'Topology Optimization of Continuum Structures with Drucker-Prager Yield Stress Constraints', *Comput. Struct.*, vol. 90–91, no. 1, pp. 65–75, 2012.

[125] T. Yu, J. G. Teng, Y. L. Wong, and S. L. Dong, 'Finite Element Modeling of Confined Concrete-I: Drucker-Prager Type Plasticity Model', *Eng. Struct.*, vol. 32, no. 3, pp. 665–679, 2010.

[126] D. Malpass, *Introduction to Industrial Polyethylene*. Scrivener, 2010.

[127] A. Peacock, *Handbook of Polyethylene, Structures, Properties, and Applications*. Marcel Dekker, 2000.

[128] C. Vasile and M. Pascu, *Practical Guide to Polyethylene*. 2005.

[129] Dow Plastics, 'Dow™ HDPE KT 10000 UE', *Technical Information*, 2013. [Online]. Available: http://www.dow.com/polyethylene/eu/en/prod/hdpe.htm.

[130] L. W. McKeen, *Fatigue and Tribological Properties of Plastics and Elastomers*, Second. Butterworth-Heinemann, 2010.

[131] F. M. Mirabella, 'Impact Polypropylene Copolymers: Fractionation and Structural Characterization', *Polymer (Guildf).*, vol. 34, no. 8, pp. 1729–1735, 1993.

[132] K. Chikhalikar *et al.*, 'Long Chain Branched Impact Copolymer of Polypropylene: Microstructure and Rheology', *Engineering*, vol. 55, no. 7, pp. 1463–1474, 2015.

[133] Saudi Basic Industries Corporation (SABIC), 'Sabic® pp phc27', *Technical Information*, 2014. [Online]. Available: https://www.granulat.com.pl/media/pdf/phc27.pdf.

[134] Nurel S.A., 'Promyde B30 P MI', *Technical Information*, 2012. [Online]. Available: http://promyde.com/pdfs/TDS/12.TDS Promyde B30 P MI.pdf.

[135] C. a Harper and E. M. Petrie, *Plastics Materials and Processes: a Concise Encyclopedia*. 2003.

[136] L. Lien Yu Machinery Co., 'Euro Inj G and D-Series Specifications'. 2010.

[137] T. U. Jagtap and H. A. Mandave, 'Machining of Plastics: A Review', *Int. J. Eng. Res. Gen. Sci.*, vol. 3, no. 2, pp. 577–581, 2015.

[138] European Committee for Standardization (CEN), 'EN ISO 2818: 1994 Plastics - Preparation of Test Specimens by Machining'.

[139] N. Arifin *et al.*, 'Study the Effect of CNC Milling Parameter on Surface Roughness of POM Material', *J. Eng. Appl. Sci.*, vol. 11, no. 10, pp. 6611–6614, 2016.

[140] C. G'Sell, J. M. Hiver, A. Dahoun, and A. Souahi, 'Video-Controlled Tensile Testing of Polymers and Metals Beyond the Necking Point', *J. Mater. Sci.*, vol. 27, no. 18, pp. 5031–5039, 1992.

[141] J. Faleskog and I. Barsoum, 'Tension-Torsion Fracture Experiments - Part I: Experiments and a Procedure to Evaluate the Equivalent Plastic Strain', *Int. J. Solids Struct.*, vol. 50, no. 25–26, pp. 4241–4257, 2013.

[142] S. Castagnet and Y. Deburck, 'Relative Influence of Microstructure and Macroscopic Triaxiality on Cavitation Damage in a Semi-Crystalline Polymer', *Mater. Sci. Eng. A*, vol. 448, no. 1–2, pp. 56–66, 2007.

[143] H. Fouad, 'Experimental and Numerical Studies of the Notch Strengthening Behaviour of Semi-Crystalline Ultra-High Molecular Weight Polyethylene', *Mater. Des.*, vol. 31, no. 3, pp. 1117–1129, 2010.

[144] G. Boisot, L. Laiarinandrasana, J. Besson, C. Fond, and G. Hochstetter, 'Experimental Investigations and Modeling of Volume Change Induced by Void Growth in Polyamide 11', *Int. J. Solids Struct.*, vol. 48, no. 19, pp. 2642–2654, 2011.

[145] L. Laiarinandrasana, J. Besson, M. Lafarge, and G. Hochstetter, 'Temperature Dependent Mechanical Behaviour of PVDF: Experiments and Numerical Modelling', *Int. J. Plast.*, vol. 25, no. 7, pp. 1301–1324, 2009.

[146] R. Rinaldi, R. Gaertner, M. Brunet, L. Chazeau, E. Vidal-Sallé, and C. Gauthier, 'Modeling of the Mechanical Behavior of Amorphous Glassy Polymer Based on the Quasi-Point Defect Theory-Part II: 3D Formulation and Finite Element Modeling of Polycarbonate', *Int. J. Non. Linear. Mech.*, vol. 46, no. 3, pp. 507–518, 2011.

[147] MTS Systems Corporation, 'MTS 810 & 858 Material Testing Systems', *Data Sheet*, pp. 4–9, 2006.

[148] MTS Systems Corporation, 'MTS 634.25 Axial Extensometers', 1995.

[149] Instron Testing Systems, 'INSTRON 3360 Dual Column Universal Testing Systems'. [Online]. Available: http://www.instron.us/en-us/products/testing-systems/universal-testing-systems/electromechanical/3300/3360-dual-column. [Accessed: 04-Nov-2017].

[150] TA Instruments, 'DSC Q Series Specifications', p. 29, 2012.

[151] TA Instruments, 'DMA Q 800 Specifications', no. April, pp. 1–14, 2012.

[152] FEI Company, 'Quanta 3D FEG User Operation Manual', pp. 1–192, 2008.

[153] J. C. Viana, 'Structural Interpretation of the Strain-Rate , Temperature and Morphology Dependence of the Yield Stress of Injection Molded Semicrystalline Polymers', *Polymer (Guildf).*, vol. 46, pp. 11773–11785, 2005.

[154] A. Dasari, S. J. Duncan, and R. D. K. Misra, 'Atomic Force Microscopy of Plastically Deformed Polyethylene Subjected to Tensile Deformation at Varying Strain Rates', *Mater. Sci. Technol.*, vol. 18, no. 6, 2002.

[155] J. M. Brady and E. L. Thomas, 'Deformation of Oriented High Density Polyethylene Shish-Kebab Films - Part 1 Decrystallization at Room Temperature', *J. Mater. Sci.*, vol. 24, no. 9,

pp. 3311–3318, 1989.

[156] S. C. Chou, K. D. Robertson, and J. H. Rainey, 'The Effect of Strain Rate and Heat Developed During Deformation on the Stress-Strain Curve of Plastics', *Exp. Mech.*, vol. 13, no. 10, pp. 422–432, 1973.

[157] E. M. Arruda, M. C. Boyce, and R. Jayachandran, 'Effects of Strain Rate, Temperature and Thermomechanical Coupling on the Finite Strain Deformation of Glassy Polymers', *Mech. Mater.*, vol. 19, no. 2–3, pp. 193–212, 1995.

[158] B. Wattrisse, J. M. Muracciole, and A. Chrysochoos, 'Thermomechanical Effects of Accompanying the Localized Necking of Semi-Crystalline Polymers', *Int. J. Therm. Sci.*, vol. 41, no. 5, pp. 422–427, 2002.

[159] T. B. Van Erp, L. E. Govaert, and G. W. M. Peters, 'Mechanical Performance of Injection-Molded Poly(Propylene): Characterization and Modeling', *Macromol. Mater. Eng.*, vol. 298, no. 3, pp. 348–358, 2013.

[160] H. Zhou and G. L. Wilkes, 'Orientation-Dependent Mechanical Properties and Deformation Morphologies for Uniaxially Melt-Extruded High-Density Polyethylene Films Having an Initial Stacked Lamellar Texture', *J. Mater. Sci.*, vol. 33, pp. 287–303, 1998.

[161] H. G. H. Van Melick, L. E. Govaert, and H. E. H. Meijer, 'On the Origin of Strain Hardening in Glassy Polymers', *Polymer (Guildf).*, vol. 44, no. 8, pp. 2493–2502, 2003.

[162] R. Rastogi, W. P. Vellinca, S. Rastogi, C. Schick, and H. E. H. Meijer, 'The Three-Phase Structure and Mechanical Properties of Poly(Ethylene Terephthalate)', *J. Polym. Sci. Part B Polym. Phys.*, vol. 42, no. 11, pp. 2092–2106, 2004.

[163] Hitachi High-tech Science Corporation, 'DSC Measurements of the Polyethylene, the Correlation of Polyethylene Density and Melting', *Hitachi Apllication Br.*, vol. 26, pp. 1–2, 1986.

[164] D. J. A. Senden, G. W. M. Peters, L. E. Govaert, and J. A. W. Van Dommelen, 'Anisotropic Yielding of Injection Molded Polyethylene: Experiments and Modeling', *Polym. (United Kingdom)*, vol. 54, no. 21, pp. 5899–5908, 2013.

[165] B. Hartmann, G. F. Lee, and W. Wong, 'Tensile Yield in Polypropylene', *Polym. Eng. Sci.*, vol. 27, no. 11, pp. 823–828, 1987.

[166] S. G. Lei, S. V. Hoa, and M. T. Ton-That, 'Effect of Clay Types on the Processing and Properties of Polypropylene Nanocomposites', *Compos. Sci. Technol.*, vol. 66, no. 10, pp. 1274–1279, 2006.

[167] A. Dasari and R. D. K. Misra, 'On the Strain Rate Sensitivity of High Density Polyethylene and Polypropylenes', *Mater. Sci. Eng. A*, vol. 358, no. 1–2, pp. 356–371, 2003.

[168] S. Hobeika, Y. Men, and G. Strobl, 'Temperature and Strain Rate Independence of Critical Strains in Polyethylene and Poly(ethylene-co-vinyl acetate)', *Macromolecules*, vol. 33, pp. 1827–1833, 2000.

[169] J. M. Schultz, 'Microstructural Aspects of Failure in Semicrystalline Polymers', *Polym. Eng. Sci.*, vol. 24, no. 10, pp. 770–785, 1984.

[170] B. Hartmann and R. F. Cole, 'Tensile Nield in Nylon 6,6', *Polym. Eng. Sci.*, vol. 25, no. 2, pp. 65–69, 1985.

[171] I. Narisawa and M. Ishikawa, 'Crazing in Semicrystalline Thermoplastics', *Crazing Polym. Vol. 2*, vol. 2, pp. 353–391, 1990.

[172] P. W. Bridgman, 'The Compressibility of Thirty Metals as a Function of Pressure and Temperature', *Proc. Am. Acad. Arts Sci.*, vol. 58, no. 5, pp. 165–242, 1923.

[173] R. Estevez, M. G. A. Tijssens, and E. Van Der Giessen, 'Modeling of the Competition Between Shear Yielding and Crazing in Glassy Polymers', *J. Mech. Phys. Solids*, vol. 48, no. 12, pp. 2585–2617, 2000.

[174] M. G. A. Tijssens, E. Van Der Giessen, and L. J. Sluys, 'Modeling of Crazing Using a Cohesive Surface Methodology', *Mech. Mater.*, vol. 32, no. 1, pp. 19–35, 2000.

[175] A. Dasari, J. Rohrmann, and R. D. K. Misra, 'Microstructural Evolution During Tensile Deformation of Polypropylenes', *Mater. Sci. Eng. A*, vol. 351, no. 1–2, pp. 200–213, 2003.

[176] I. Brough, R. N. Haward, G. Healey, and A. Wood, 'Scanning Electron Micrographs of High Density Polyethylene Fracture Surfaces', *Polymer (Guildf).*, vol. 45, no. 10, pp. 3115–3123, 2004.

[177] L. Dufour, B. Bourel, F. Lauro, G. Haugou, and N. Leconte, 'A Viscoelastic-Viscoplastic Model With Non Associative Plasticity for the Modelling of Bonded Joints at High Strain Rates', *Int. J. Adhes. Adhes.*, vol. 70, pp. 304–314, 2016.

[178] I. M. Ward and J. Sweeney, *Mechanical Properties of Solid Polymers*, Third Edit., vol. 13, no. 12. Wiley, 2012.

[179] A. Chan, W. K. Chiu, and X. L. Liu, 'Determining the Elastic Interlaminar Shear Modulus of Composite Laminates', *Compos. Struct.*, vol. 80, no. 3, pp. 396–408, 2007.

[180] I. M. Ward, 'Review: The Yield Behaviour of Polymers', *J. Mater. Sci.*, vol. 6, no. 11, pp. 1397–1417, 1971.

[181] M. Alves and N. Jones, 'Influence of Hydrostatic Stress on Failure of Axisymmetric Notched Specimens', *J. Mech. Phys. Solids*, vol. 47, no. 3, pp. 643–667, 1999.

[182] A. Needleman and V. Tvergaard, 'An Analysis of Ductile Rupture in Notched Bars', *J. Mech. Phys. Solids*, vol. 32, no. 6, pp. 461–490, 1984.

[183] A. C. Mackenzie, J. W. Hancock, and D. K. Brown, 'On the Influence of State of Stress on Ductile Failure Initiation in High Strength Steels', *Eng. Fract. Mech.*, vol. 9, no. 1, 1977.

[184] G. Dean and L. Crocker, 'Prediction of Impact Performance of Plastics Mouldings Part 1: Materials Models and Determination of Properties', *Plast. Rubber Compos.*, vol. 36, no. 1, pp. 1–13, 2007.